

ACTA DE EVALUACIÓN DE LA TESIS DOCTORAL
(FOR EVALUATION OF THE ACT DOCTORAL THESIS)

Año académico (academic year): 2016/17

DOCTORANDO (candidate PHD): **PÉREZ MORALES, JORGE**

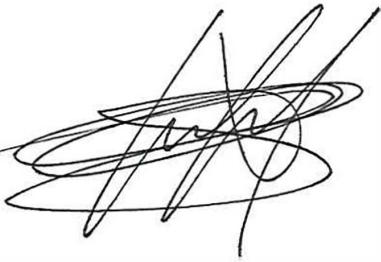
PROGRAMA DE DOCTORADO (Academic Committee of the Programme): **D332 DOCTORADO EN ELECTRÓNICA: SISTEMAS ELECTRÓNICOS AVANZADOS. SISTEMAS INTELIGEN**
DEPARTAMENTO DE (Department): **Electrónica**
TITULACIÓN DE DOCTOR EN (Phd title): **DOCTOR/A POR LA UNIVERSIDAD DE ALCALÁ**

En el día de hoy 17/07/17, reunido el tribunal de evaluación, constituido por los miembros que suscriben el presente Acta, el aspirante defendió su Tesis Doctoral **con Mención Internacional** (In today assessment met the court, consisting of the members who signed this Act, the candidate defended his doctoral thesis with mention as International Doctorate), elaborada bajo la dirección de (prepared under the direction of) FRANCISCO JAVIER RODRÍGUEZ SÁNCHEZ // SANTIAGO CÓBRECES ÁLVAREZ.

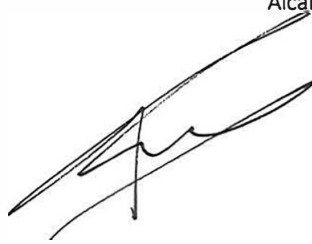
Sobre el siguiente tema (Title of the doctoral thesis): **OPTIMAL MODEL REFERENCE CONTROL DESIGN FOR GRID CONNECTED VOLTAGE SOURCE CONVERTERS**

Finalizada la defensa y discusión de la tesis, el tribunal acordó otorgar la CALIFICACIÓN GLOBAL² de **(no apto, aprobado, notable y sobresaliente)** (After the defense and defense of the thesis, the court agreed to grant the GLOBAL RATING (fail, pass, good and excellent): Sobresaliente (Excellent)

Alcalá de Henares, a 17 de Julio de 2017



Fdo. (Signed): Roberto Griño



Fdo. (Signed): Daniel Piñero



Fdo. (Signed): MARCO LISENE

FIRMA DEL ALUMNO (candidate's signature),



Fdo. (Signed): JORGE PÉREZ MORALES

Con fecha 24 de julio de 2017 la Comisión Delegada de la Comisión de Estudios Oficiales de Posgrado, a la vista de los votos emitidos de manera anónima por el tribunal que ha juzgado la tesis, resuelve:

- Conceder la Mención de "Cum Laude"
 No conceder la Mención de "Cum Laude"

La Secretaria de la Comisión Delegada



² La calificación podrá ser "no apto" "aprobado" "notable" y "sobresaliente". El tribunal podrá otorgar la mención de "cum laude" si la calificación global es de sobresaliente y se emite en tal sentido el voto secreto positivo por unanimidad. (The grade may be "fail" "pass" "good" or "excellent". The panel may confer the distinction of "cum laude" if the overall grade is "Excellent" and has been awarded unanimously as such after secret voting.)

INCIDENCIAS / OBSERVACIONES:
(Incidents

/

Comments)



Universidad
de Alcalá

COMISIÓN DE ESTUDIOS OFICIALES
DE POSGRADO Y DOCTORADO

En aplicación del art. 14.7 del RD. 99/2011 y el art. 14 del Reglamento de Elaboración, Autorización y Defensa de la Tesis Doctoral, la Comisión Delegada de la Comisión de Estudios Oficiales de Posgrado y Doctorado, en sesión pública de fecha 24 de julio, procedió al escrutinio de los votos emitidos por los miembros del tribunal de la tesis defendida por **PÉREZ MORALES, JORGE**, el día 17 de julio de 2017, titulada *OPTIMAL MODEL REFERENCE CONTROL DESIGN FOR GRID CONNECTED VOLTAGE SOURCE CONVERTERS*, para determinar, si a la misma, se le concede la mención "cum laude", arrojando como resultado el voto favorable de todos los miembros del tribunal.

Por lo tanto, la Comisión de Estudios Oficiales de Posgrado resuelve otorgar a dicha tesis la

MENCIÓN "CUM LAUDE"

Alcalá de Henares, 27 julio de 2017
EL PRESIDENTE DE LA COMISIÓN DE ESTUDIOS
OFICIALES DE POSGRADO Y DOCTORADO



Firmado digitalmente por VELASCO
PEREZ JUAN RAMON - DNI
03087239H
Fecha: 2017.07.30 18:48:58 +02'00'

Juan Ramón Velasco Pérez

Copia por e-mail a:

Doctorando: **PÉREZ MORALES, JORGE**

Secretario del Tribunal: **DANIEL PIZARRO PÉREZ.**

Directores de Tesis: **FRANCISCO JAVIER RODRÍGUEZ SÁNCHEZ // SANTIAGO CÓBRECES ÁLVAREZ**



Universidad
de Alcalá

ESCUELA DE DOCTORADO
Servicio de Estudios Oficiales de
Posgrado

DILIGENCIA DE DEPÓSITO DE TESIS.

Comprobado que el expediente académico de D./D^a _____
reúne los requisitos exigidos para la presentación de la Tesis, de acuerdo a la normativa vigente, y habiendo
presentado la misma en formato: soporte electrónico impreso en papel, para el depósito de la
misma, en el Servicio de Estudios Oficiales de Posgrado, con el nº de páginas: _____ se procede, con
fecha de hoy a registrar el depósito de la tesis.

Alcalá de Henares a _____ de _____ de 20 _____



Fdo. El Funcionario

UNIVERSIDAD DE ALCALÁ

DEPARTAMENTO DE ELECTRÓNICA

Programa de Doctorado en Electrónica: Sistemas Electrónicos
Avanzados. Sistemas Inteligentes.



“Optimal model reference control design for grid
connected voltage source converters”

Jorge Pérez Morales

2017

UNIVERSIDAD DE ALCALÁ

DEPARTAMENTO DE ELECTRÓNICA

Programa de Doctorado en Electrónica: Sistemas Electrónicos Avanzados. Sistemas Inteligentes.



“Optimal model reference control design for grid connected voltage source converters”

Author

Jorge Pérez Morales

Supervisors

Dr. Santiago Cóbrecas Álvarez
Prof. Francisco Javier Rodríguez Sánchez

2017



Universidad
de Alcalá

DEPARTAMENTO DE ELECTRÓNICA
Edificio Politécnico
Campus Universitario s/n
28805 Alcalá de Henares (Madrid)
Teléfono: 91 885 65 40
Fax: 91 885 65 91
eldep@depeca.uah.es

Dr. Sira Elena Palazuelos Cagigas, Director del Departamento de Electrónica de la Universidad de Alcalá,

INFORMA: Que la Tesis Doctoral titulada “**Optimal model reference control design for grid connected voltaje source converters**” presentada por D. Jorge Pérez Morales, y dirigida por los doctores D. Santiago Cóbreces Álvarez y D. Francisco Javier Rodríguez Sánchez, cumple con todos los requisitos científicos y metodológicos, para ser defendida ante un Tribunal, según lo indicado por la Comisión Académica del Programa de Doctorado.

Alcalá de Henares, 20 de Abril de 2017



Fdo. Sira Elena Palazuelos Cagigas



Universidad
de Alcalá

DEPARTAMENTO DE ELECTRÓNICA
Edificio Politécnico
Campus Universitario s/n
28805 Alcalá de Henares (Madrid)
Teléfono: 91 885 65 40
Fax: 91 885 65 91
eldep@depeca.uah.es

Dr. Santiago Cóbreces Álvarez, Profesor Titular de la Universidad de Alcalá, y
Dr. Francisco Javier Rodríguez Sánchez, Profesor Catedrático de la Universidad Alcalá,

INFORMAN: Que la Tesis Doctoral titulada “**Optimal model reference control design for grid connected voltaje source converters**” presentada por D. Jorge Pérez Morales, y realizada bajo la dirección de los doctores D. Santiago Cóbreces Álvarez y D. Francisco Javier Rodríguez Sánchez, dentro del campo de la aplicación de los VSCs como interfaces entre la red eléctrica y sistemas de generación de energía eléctrica, reúne los méritos de calidad y originalidad para optar al Grado de Doctor.

Alcalá de Henares, 20 de Abril de 2017

Fdo. Santiago Cóbreces Álvarez

Fdo. Francisco Javier Rodríguez Sánchez

Agradecimientos

Durante estos cuatro años he compartido muchos momentos importantes con grandes personas, tanto en mi vida académica/profesional como personal, sin cuya ayuda esta tesis no hubiese sido posible. Por lo que no me gustaría cerrar este periodo sin agradecerérselo como es debido.

En primer lugar, quiere agradecer la inmensa aportación de uno de mis tutores, el Dr. Santiago Cóbreces, tanto a nivel humano como académico. Honestamente, considero que Santi debería aparecer a mi lado como autor de este documento, pues en gran medida este trabajo ha llegado a buen puerto gracias a sus ideas y correcciones de rumbo. En segundo lugar quiero agradecer la ayuda de mi otro tutor, el Dr. Francisco Javier Rodríguez Sánchez, por sus sabios consejos y por el gran trabajo de dirección en el grupo de investigación GEISER, donde he tenido la suerte de forma parte. Quiero también agradecer la colaboración del Dr. Robert Griño, el cual ha formado parte activa de este trabajo desde el principio. No quiero olvidarme del Dr. Emilio José Bueno, que confió en mi para formar parte del grupo GEISER hace cinco años, y que desde entonces no ha dudado en ayudarme siempre que he necesitado consejo.

Hablando del grupo de investigación GEISER, quiero agradecer a cada uno de sus miembros (actuales o pasados) haberme aguantado estos cinco años: Carlos, Inés, Mario, Javi, Mouhai, Cristina, Miguel, Ana, Rocio, Paco, Pablo y Jose Manuel. Del mismo modo quiero agradecer a los integrantes del grupo GRIFO, con los que tenemos una gran relación. Me llevo muy buenos recuerdos de esta etapa, y en gran medida es gracias a vosotros.

I would also like to acknowledge the collaboration of Prof. Frede Blaabjerg and Assoc. Prof. Xiongfei Wang in the direction of part of this work. In that regard, I don't want to forget the amazing researchers I met during my stay at the University of Aalborg. Special thanks to Markus, Rodolpho and David, who made that period look much sorter than it really was. Our lab, love and life can be a mess, but at least we manage to finish our thesis.

Quiero agradecer también la enorme aportación a nivel humano de todos mis amigos, que quizás no me hayan ayudado tanto a nivel académico, pero que sin los cuales no podría haber completado mis objetivos. Traducción, que aunque no os importe lo más mínimo a que me dedico, las cañas, las pachangas futboleras y las risas absurdas me han ayudado muchísimo a hacer este periodo más ameno. Afortunada e inexplicablemente tengo muchos amigos, así que os nombraré en grupitos: la Comunidad de Murillo, Triple Embraguer, Maccabi de Levantar, tu PM mi compromiso, Comida de empresa y Machos cabríos ibéricos... quería tener un tono formal en los agradecimientos, pero me es imposible acordándome de esta fauna.

Por último, y no por ello menos importante, quiero agradecer a toda mi familia toda su ayuda. En especial a mis padres, sin cuyo apoyo tanto a nivel económico y (mucho más importante) emocional no podría haber llegado donde estoy hoy, ni ser la persona que soy. Agradecería también a mi hermano, pero ya le he nombrado indirectamente en muchos grupos... que tampoco se lo crea, que no le quiero tanto...

... ah bueno, y a mi chica Judith ¡Que no me he olvidado de tí! Cuatro años soportándome se merecen al menos un parrafito propio. Y ya basta de agradecimientos. Vamos al turrón.

Abstract

This thesis develops an \mathcal{H}_∞ optimal model-reference control design approach for its application on grid-connected Voltage-Source Converters (VSCs). Two main fields are considered: the closed-loop admittance shaping of current-controlled VSC-based applications and the optimal active damping of resonant filters.

The \mathcal{H}_∞ optimal control design paradigm gives some advantages with respect to the classical approaches when dealing with complex control problems (i.e. complex plants and/or control objectives), transferring part of the design complexity to a computational algorithm that synthesizes the optimal controller for a given set of specifications. Its presence on the control of VSC mainly centres in the \mathcal{H}_∞ minimization of the sensitivity function magnitude, which allows to shape the application loop-function, dealing effectively with different control trade-offs such as the effective reference tracking, the stand-alone stability robustness or the bandwidth limitation. This technique lacks, however, of the ability to shape the closed-loop phase, which is also important for many applications. The \mathcal{H}_∞ model-reference design approach solves this problem, allowing to shape both the gain and phase of the controlled system closed-loop dynamics over wide frequency ranges.

The main contribution of this thesis is the application of the model-reference approach for the shaping of VSCs closed-loop admittance, which have been demonstrated to play an important role on both complex networks stability and in the improvement of the grid power quality. The designer should provide the procedure with two model-reference transfer functions: one that specifies the desired input admittance and another that specifies the desired reference-tracking dynamic model. This allows an accurate shaping of both admittance modulus and phase, in addition to fulfil with traditional tracking performance specifications. The process result is a discrete-time controller suitable for being programmed and executed in a digital platform (DSP).

Several possible applications may arise from the presented methodology. This proposal is illustrated using a PWM rectifier application but is flexible enough to be applied to different control schemes and converter topologies. Three different admittance-shaping applications are explored: the design of broad-band resistive closed-loop systems, which are demonstrated to be very robust against grid uncertainties (i.e. weak grid-connection), the design of low admittance profiles, which result in a improvement in the rejection of grid-voltage (sub/inter)harmonics, and the design of high admittance profiles, which may act as good shunt grid stabilizers (i.e. dampers of grid resonances). Their respective controllers design methodology, limitations and implementation, as well as the obtained experimental results are detailed.

Complementary, the model-reference design approach is also explored for the active damping of resonant LCL filters. Once implemented, the proposed active damper shapes the LCL filter dynamic so it behaves as an L filter. That allows the use of current-controllers designed for this simpler topology, without renouncing to the higher filtering capabilities of LCL filters. The methodology is flexible enough to select the measured signals, and results, as it is demonstrated, in an improved robustness of the current-controlled system.

Index terms— Power converter, \mathcal{H}_∞ control, mixed-sensitivity, model-reference, optimal control, admittance shaping, power quality, stability robustness, active damping.

Resumen

Esta tesis se centra en el diseño de controladores \mathcal{H}_∞ basados en modelos de referencia para su aplicación en el control de convertidores electrónicos de potencia en fuente de tensión (VSC). Se persiguen dos objetivos: el conformado de la admitancia de entrada de un VSC controlado en corriente y el óptimo amortiguamiento activo de filtros resonantes.

El diseño de controladores óptimos \mathcal{H}_∞ aporta ciertas ventajas con respecto al diseño clásico, principalmente en el manejo de problemas de control complejos (i.e. plantas y/o objetivos de control complejos). La principal técnica de diseño \mathcal{H}_∞ utilizada en la literatura se centra en la minimización de la función de sensibilidad. Ésta permite lidiar con diferentes problemas de compromiso en el diseño de controladores de forma sencilla, como el conformado de la función de lazo, el seguimiento de referencias, la estabilidad del sistema o la limitación del ancho de banda de control. Sin embargo, esta técnica carece de la habilidad de conformar la fase de funciones en lazo cerrado. La técnica \mathcal{H}_∞ basada en modelos de referencia soluciona este problema.

La principal contribución de esta tesis es la aplicación de esta técnica para el moldeado de la admitancia en lazo cerrado de VSCs, la cual juega un importante papel tanto en la estabilidad de sistemas complejos como en la mejora de la calidad de energía en la red. Utilizando la técnica propuesta, el diseñador podrá especificar, en un gran ancho de banda y en un solo marco de diseño, tanto la admitancia del convertidor (en modulo y en fase), como el comportamiento del seguimiento de referencias. El proceso de diseño finaliza con la síntesis de un controlador discreto ejecutable en una plataforma digital (DSP).

Esta nueva metodología de diseño se puede aplicar en múltiples aplicaciones. La presente propuesta se ilustra con el control de un rectificador activo conectado a la red, pero es lo suficientemente flexible como para aplicarse en otros esquemas de control y topologías de convertidor. Se considerarán tres aplicaciones del control de admitancia: el diseño de aplicaciones resistivas en un gran ancho de banda, las cuales mejoran la robustez en la conexión estable a red débiles, el diseño de aplicaciones con una admitancia baja, las cuales mejoran el rechazo de (sub/inter)armónicos de la tensión de red en el control de corriente, y el diseño de aplicaciones con una admitancia alta, que al conectarse en paralelo a la red actúan como estabilizadores de ésta. La metodología de diseño de cada controlador, así como sus limitaciones, implementación y los resultados experimentales obtenidos son detallados.

De forma complementaria, se explora la técnica de diseño basada en modelos de referencia para el amortiguamiento óptimo de resonancias en filtros LCL. La idea es diseñar un amortiguador activo que, una vez conectado, moldee la dinámica del filtro LCL de tal manera que este se comporte como un filtro L. Esto permitirá el posterior uso de sencillos controladores de corriente diseñados para filtro L, evitando la complejidad del diseño de controladores para filtros LCL, sin renunciar con ello a su gran capacidad de filtrado. La metodología de diseño es lo suficientemente general como para presentar diferentes estructuras de entrada/salida para el amortiguador. Los resultados obtenidos demuestran la mejora en la robustez del sistema.

Palabras clave— Convertidor de potencia, control \mathcal{H}_∞ , conformado de función de sensibilidad, diseño basado en modelos de referencia, control óptimo, conformado de admitancia, calidad de energía, estabilidad robusta, amortiguamiento activo.

Contents

- 1 Introduction** **1**
 - 1.1 Socio-technological background 1
 - 1.1.1 Power electronic converters 1
 - 1.1.2 Current scenario: increasing presence of power electronic converters in electrical networks 4
 - 1.2 Complex networks stability problems 4
 - 1.2.1 Instability problems triggered by non-passive systems 5
 - 1.2.2 Introduction to the impedance-based stability criterion 6
 - 1.3 Introduction to admittance shaping: Thesis outline 7
 - 1.4 Thesis development context 7
 - 1.5 Document structure 9

- 2 State of the art and thesis objectives** **11**
 - 2.1 Introduction 11
 - 2.2 Networks stability analysis 12
 - 2.2.1 Impedance-based stability criterion 13
 - 2.2.2 Torsional interaction stability criterion 17
 - 2.3 Admittance shaping by means of controller design 18
 - 2.3.1 Methods 19
 - 2.3.2 Objectives/Applications 26
 - 2.4 Robust control 31
 - 2.5 Analysis of the state of the art, thesis hypothesis and objectives 32
 - 2.5.1 Analysis of the state of the art 32
 - 2.5.2 Hypothesis 33
 - 2.5.3 Objectives 34

- 3 Introduction to (sub)optimal control** **35**
 - 3.1 Introduction 35
 - 3.2 Optimal control 35
 - 3.2.1 Concept and advantages 35
 - 3.2.2 General control problem formulation 36
 - 3.2.3 Order of the synthesized controller 38
 - 3.2.4 Main optimal control approaches 38
 - 3.3 Basic \mathcal{H}_∞ control approach: Mixed-sensitivity 42
 - 3.3.1 Introduction to the method 42
 - 3.3.2 Application to a power converter current control 44
 - 3.3.3 Digital controller implementation 48
 - 3.3.4 Design limitations 49
 - 3.3.5 Results 49
 - 3.4 Introduction to \mathcal{H}_∞ model-reference approach 51

3.5	Conclusion	52
4	Model reference approach for closed-loop admittance shaping: design	55
4.1	Introduction	55
4.2	Open-loop plant modelling	56
4.2.1	Three-phase system reference frame	56
4.2.2	Filter open-loop model	56
4.3	Closed-loop dynamics	57
4.4	Controller objectives and obtaining method	58
4.5	Controller design methodology: theoretical background	60
4.5.1	Model references of the grid-current closed-loop dynamic	60
4.5.2	Frequency weights	60
4.5.3	Analysis of the controller effectiveness.	63
4.6	Controller design methodology: practical aspects	64
4.6.1	Admittance shaping versus actuation limitation trade-off	65
4.6.2	Tracking shaping versus admittance shaping trade-off	69
4.7	Sampled data problem and controller synthesis	74
4.7.1	Hybrid model of the grid-current dynamic	74
4.7.2	Search of an approximated fully continuous/discrete model	76
4.7.3	Controller synthesis	79
4.8	Design limitations	80
4.8.1	Bandwidth limitations imposed by the digital controller implementation	80
4.8.2	Influence of time delays on system passivity	83
4.8.3	Generalized plant \mathbf{P} design limitations	84
4.9	Conclusion	84
5	Model reference approach for closed-loop admittance shaping: applications	87
5.1	Introduction	87
5.2	Controller testing application	88
5.2.1	Influence of outer-loops in the design	89
5.3	Experimental platform details.	91
5.3.1	Experimental setup and results test-bench.	91
5.3.2	Controller implementation.	93
5.4	Broad band resistive designs	95
5.4.1	Motivation of broad band resistive designs	95
5.4.2	Bandwidth limitation of resistive broad band designs	97
5.4.3	L filter case	97
5.4.4	LCL filter case	99
5.4.5	Robustness toward grid uncertainties analysis	103
5.5	Low admittance designs	106
5.5.1	Motivation of low admittance designs	107
5.5.2	In a broad band	107
5.5.3	Localized at some frequencies (admittance dips)	108
5.5.4	Analysis of the proposed low admittance designs	113
5.6	High admittance designs	116
5.6.1	Motivation of high admittance designs	116
5.6.2	In a broad band	118
5.6.3	Localized at some frequencies (power pit)	120
5.6.4	Analysis of the proposed high admittance designs	121
5.7	Conclusion	126

6	Model reference approach for resonant plants active damping	129
6.1	Introduction	129
6.2	Problem description and modelling	130
6.2.1	Open-loop modelling	130
6.2.2	Inner closed-loop damped grid-current dynamic	131
6.3	Active damping design	132
6.3.1	Derivation of the augmented plant	132
6.3.2	Definition of the minimization problem	133
6.3.3	Reference model and weighting functions selection	134
6.3.4	Implementation considerations and limitations	136
6.4	Results	138
6.4.1	External control loops	138
6.4.2	Damping analysis	138
6.4.3	Stability improvement analysis	140
6.4.4	Time domain results	145
6.5	Conclusion	147
7	Conclusion and future work	149
7.1	Contributions and conclusions	149
7.1.1	\mathcal{H}_∞ model reference approach for closed-loop admittance shaping	149
7.1.2	\mathcal{H}_∞ model reference approach for resonant plants active damping	152
7.2	Future works	153
A	Background knowledge	157
A.1	Introduction	157
A.2	Generalized linear control schemes	157
A.3	Frequency response analysis [Skogestad and Postlethwaite, 2007]	161
A.4	Stand-alone stability analysis	163
A.5	Controller objectives summary: Trade-offs in terms of L	167
A.6	Bandwidth limitations of feedback control	167
A.7	Controllers design methodologies: main classical control design frameworks	170
A.8	Linear control applied to power converters	171
A.8.1	Current-controlled PECs	171
A.8.2	Voltage-controlled PECs	173
A.8.3	Application examples of controlled power electronic converters.	174
B	Publications	179
	Bibliography	221

Chapter 1

Introduction

1.1 Socio-technological background

1.1.1 Power electronic converters

Power electronic converters (PECs) are devices that work as controlled interfaces for energy conversion and conditioning. Nowadays, this task is done by means of high-efficiency semiconductor-based switching electronic devices (e.g. MOSFETs, BPTs, GTOs, IGBTs and IGCTs). However, the history of power electronics goes back to the beginning of the 20th century, with the invention of Mercury-Arc rectifiers [Rissik, 1941] used for converting high-voltage or high-current alternating current (AC) into direct current (DC). This device quickly found application in electrochemical and battery charging processes, industrial motors, railways and High-Voltage Direct Current (HVDC) power transmission.

Depending on the kind of conversion (i.e. the kind of input and output power), PECs can be classified as DC-DC (e.g. Buck, Boost and Buck-Boost converters), AC-DC (e.g. Voltage-Source (VSC) and Current-Source (CSC) converters) or AC-AC (e.g. back-to-back converters) PECs. Moreover, for multiple AC-DC, AC-AC and DC-DC systems, this conversion is bidirectional. Fig. 1.1 shows a simplified generalized connection diagram of this kind of interfaces.

In addition to the power conversion capability, PECs can be controlled to regulate the active and reactive power consumed from or injected to the considered grids. That is, PECs can control the power flow between the elements of which they act as interfaces, and, as a consequence, control the Displacement Power Factor (DPF).

Due to these interesting features, and the recent advances and fast improvements in terms of semiconductors switching speed, losses and costs reduction, the precision of actual simulation tools and the fast computational capability of digital processors in which the PECs control are implemented, the 21th century can be considered as a golden age for power electronics applications. Some of them are summarized next.

Energy generation

Until the end of the 60's, all the energy was generated in big plants (i.e. 150-1000 MW) far away from the urban centres and close to their resources, mainly fossil and nuclear, and then supplied to the different points of consumption by means of transmission and distribution (T&D) lines. The decision of keeping away these plants from the urban centres was supported by two facts;

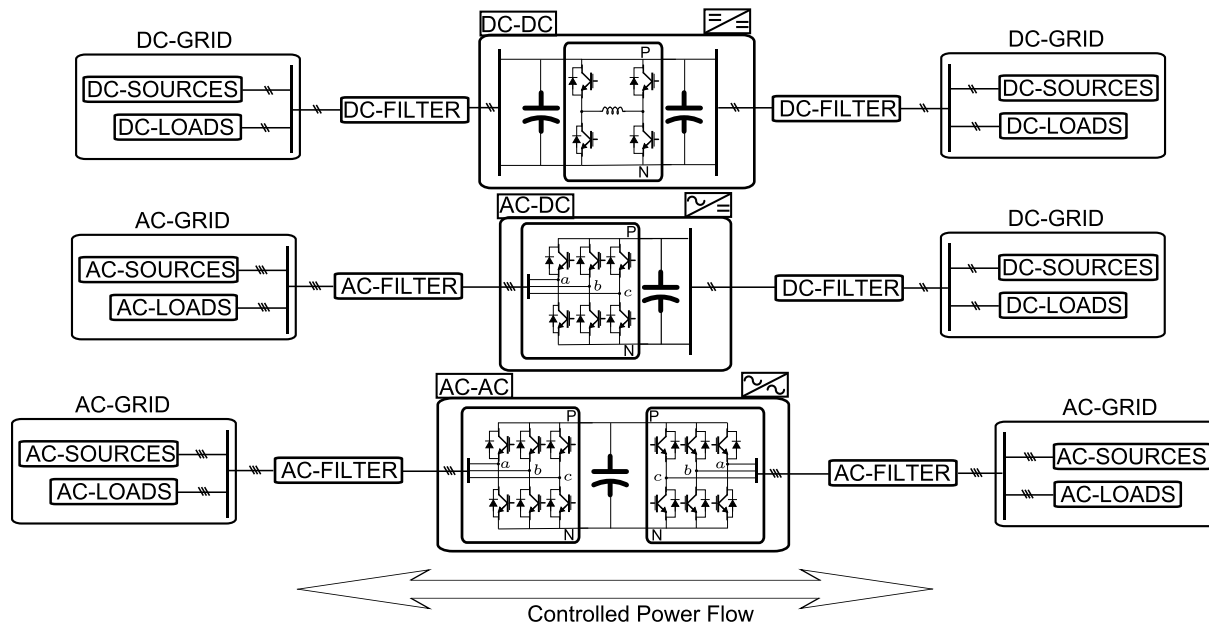


Figure 1.1. Generalized PECs connection diagram acting as an interface between different grids.

the environmental impact and contamination that they suppose and the reduced costs of the energy T&D in comparison with the incomes of the large amounts of energy there produced. This is known as centralized or traditional generation paradigm.

The electric energy consumption has highly increased over the last decades, and it is expected to increase even more in the next ones. Following the traditional approach, this tendency would end up in the fast consumption of our fossil resources, with their corresponding price increase, in addition to the big environmental hazards induced by the tones of CO_2 send to the atmosphere and the long-lived radioactive waste. Furthermore, with the necessity of supplying of energy to the most remote places, the overall energy quality was reduced and its T&D costs were increased.

In order to reduce these costs and environmental hazards, the generation paradigm is slowly changing towards a distributed one based on renewable energies, where multiple smaller plants (i.e. 1 kW-50 MW) supply energy to closer consumers, generated from (in practice) inexhaustible energy resources. In addition to these improvements, the use of this paradigm presents other advantages in comparison with the traditional one, as for example the reduction of the plant size and weight (i.e. improved mobility), the improved supply reliability (i.e. the probability of a chained fault in case of a malfunction of one of these plants is much less that in the case of a centralized generation) and the bidirectional information and power flow between big and smaller power producers (i.e. particulars) and the consumers.

However, the existing networks are not always technically prepared for the connection of multiple distributed renewable power generators which do not have a constant energy generation flow (i.e. it depends on, for example, the day lapse or the meteorological conditions). This, to some extent, unpredictable behaviour may trigger grid stability risks. It was necessary, then, to adopt certain grid connection regulations that assure the reliability, security and quality in the energy supply. These regulations form the so called grid codes¹, which imposes certain normative for the grid connection of power sources in terms of grid synchronization (i.e. same frequency, phase and voltage levels), active/reactive power injection, disconnection under over-voltages or voltage supply interruptions, current and voltage harmonics injection and continuous

¹In Spain, this is regulated by the *Procedimientos de Operación* (P.O.) defined by *Red Eléctrica de España*.

voltage/current levels.

The connection of distributed energy sources to the grid very often implies, then, the use of power electronics interfaces, as they increase the quality of the delivered energy and allow to control important connection parameters, as the aforementioned power flow control [Cóbreces, 2009].

Energy quality improvement

PECs have been also applied for the improvement of the grid power quality, minimizing some of its more common problems (e.g. voltage dips/swells, impulsive and oscillatory transients, harmonic distortion, voltage unbalance, phase angle jump or voltage flicker [Awad, 2002]).

The PEC-based applications that try to solve/mitigate these power quality problems are known as FACTS (Flexible AC Transmission Systems) or PCS (Power Conditioning Systems), depending on whether they are applied to the transmission or the distribution network, respectively [Peña, 2005]. Some examples of these PEC-based applications are the Static Synchronous Compensator (STATCOM), the Dynamic Voltage Restore (DVR), the Uninterruptible power supply (UPS), the Active Power Filter (APF) and the Unified Power Factor Controller (UPFC). A more detailed explanation of these systems is presented in section A.8.

HVDC energy transmission

Some studies demonstrated that, under certain circumstances, the DC energy transmission presents some cost/efficiency benefits with respect with the traditional three phase AC transmission. As a consequence, the use of High Voltage Direct Current (HVDC) transmission to connect distant points is thriving [Piwko and Larsen, 1982, Jiang-Häfner et al., 2002]. The HVDC topology is normally formed by two VSCs connected to each other with a common and large DC-bus (i.e. back-to-back connection) that are able to control the power flow between their respective AC-sides. PECs have also, then, an important role in energy transmission. A more detailed diagram of this topology can be found in section A.8.

Electrical loads

PECs have a very important role in electrical loads. Nowadays, it is common to find electronically controlled fluorescent lamps and light-emitting diodes (LEDs) to illuminate houses, or uncontrolled rectifiers for the connection of electronic loads (e.g. televisions, computers and other home appliances). The use of small UPS as commercial energy backup systems is also increasing.

In more industrial applications, controlled PECs are widely used as motor drivers, to achieve an adjustable speed, torque and position control [Rodríguez Monter, 2013]. This last application, and the improvement of the distributed generation paradigm in terms of mobility and efficiency, have also triggered recent research in the use of PECs in Electric Vehicles (EV) and Hybrid Electric Vehicles (HEV), like traction railways [Möllerstedt and Bernhardsson, 2000, Jansson et al., 2004] and more electric aircraft [Liu et al., 2007, Emadi et al., 1999, Areerak et al., 2012], ships [Ciezki and Ashton, 2000] and cars [Emadi et al., 2006].

1.1.2 Current scenario: increasing presence of power electronic converters in electrical networks

The presence of PEC-based application in the grid is, then, increasing. Fig. 1.2 shows this fact with a simplified diagram of the current T&D grids [Blaabjerg and Wang, 2015].

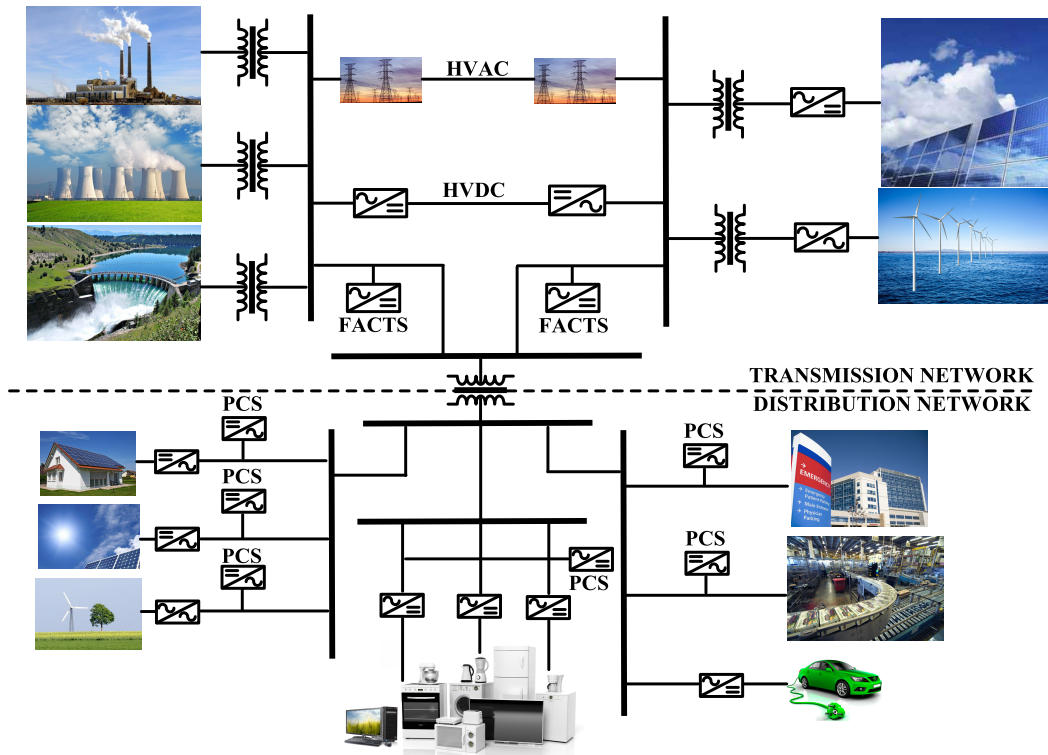


Figure 1.2. Simplified diagram of the high presence of PECs in the current T&D grids. *Source:* [Blaabjerg and Wang, 2015]

Nowadays, 15% of the electricity flows via electronics but, as the demand for electrical energy increases, high-power conversions systems based on PECs are becoming more necessary [Rodríguez Monter, 2013]. A recent Yole Développement report [Azémar et al., 2015] about PECs markets and trends has predicted a Compound Annual Growth Rate (CAGR) for the inverters (i.e. AC-DC power electronic converters) market of 6% for the period 2014 – 2020, based in the inverters market (in M\$) during the period 2010 – 2014. This market study is shown in Fig. 1.3. From this study is also deduced that the business is, and will be, dominated by industrial motor drives, UPS and the interfaces for photovoltaic (PV) and wind renewable energy generation, and that Asia (mainly China and Japan) is, by far, the main continent in integration of power electronics converters.

1.2 Complex networks stability problems

The aforementioned increasing presence of PEC-based devices in power systems is populating the grid of complex dynamics, induced by their tight regulated controllers and their, in essence, non-linear behaviour. The results of recent investigations seem to mark those kind of dynamics as contributors-triggers of power quality problems or even power system instabilities [Liutanakul et al., 2010, Cespedes et al., 2011, Wang and Howe, 2008, Sanchez et al., 2014]. As a result, the analysis of possible interactions between PEC-based applications at the interconnection point

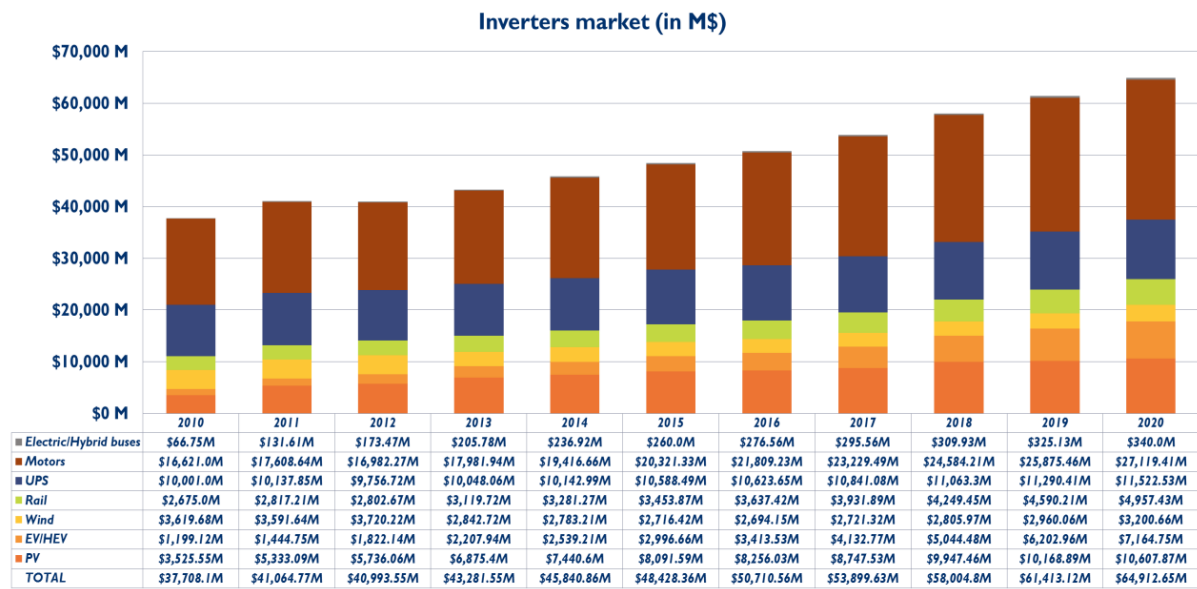


Figure 1.3. Inverter markets (in M\$) during the period 2010 – 2014 and previsions for the period 2014 – 2020, organized by the main application. *Source:* [Azémar et al., 2015].

is gaining importance to understand stability problems [Cespedes and Sun, 2009], analysing, to that end, complex networks stability as a whole and taking into account mutual coupling between elements in addition to the traditional stand-alone stability and performance analysis of each element [Wan et al., 2015].

1.2.1 Instability problems triggered by non-passive systems

Tightly regulated converters, beyond the great improvements in energy conversion and conditioning stated at the beginning of this introduction, may present a negative incremental impedance/admittance behaviour at some frequencies. An example of this behaviour are the constant power loads (CPLs). PEC-based applications that regulates the power flow between the elements of which they serve as interfaces will act like CPLs, increasing their output voltage/current in response to a decrease of their input current/voltage, respectively. This behaviour is represented in Fig. 1.4. A representative example of how CPLs affect stability can be found in [Emadi et al., 2006], and is summarized next.

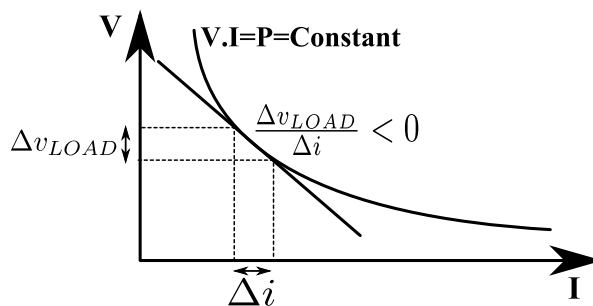


Figure 1.4. Negative impedance behaviour of constant power loads. *Source:* [Emadi et al., 2006].

Consider now the system shown in Fig. 1.5, where a load is connected to a source through an L filter (with a negligible losses resistance). Let's assume that the load follows a CPL behaviour

as the one depicted in Fig. 1.4. The V-I characteristics of both source and CPL are shown in Fig. 1.5(a), being $A = \{V_0, I_0\}$ the equilibrium or steady state operating point.

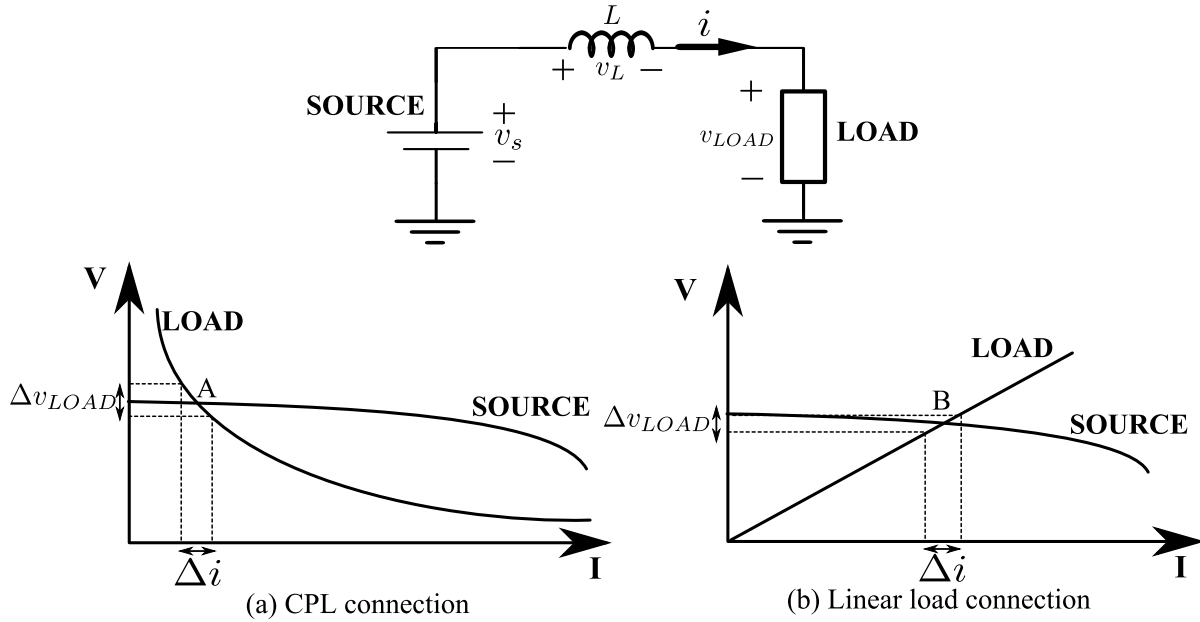


Figure 1.5. Voltage source-load series connection through an L filter (top), with the V-I characteristics of the voltage source and (a) a CPL or (b) a linear resistive load (bottom). *Source:* [Emadi et al., 2006].

Consider now a small current increment ($i = I_0 + \Delta_i$). Due to its negative impedance behaviour, the CPL will demand a decrease off its voltage (v_{LOAD}). As a consequence, the inductance voltage (v_L) and, then, the current (i) will increase. A recursive process starts, which could eventually lead to an infinite current and a null voltage. Similarly, a small current decrease ($i = I_0 - \Delta_i$) may end up in an infinite voltage and a null current. That is, the equilibrium point and, then, the aforementioned system would be unstable in the presence of a CPL. If the same analysis is done considering a resistive lineal load like the one shown in Fig. 1.5(b), it is clear that the equilibrium point B (and the system) would be steady-state stable for both current and voltage variations.

A CPL behaviour is not the only reason that may affect a PEC-based application passivity², being other triggering elements the presence of Phase-Lock Loops (PLLs) or controller delays. In any case, this non-passive behaviour always represents a risk for the stability of interconnected systems.

1.2.2 Introduction to the impedance-based stability criterion

For the stability analysis of complex networks it is important to remark the work presented in [Middlebrook, 1976], which developed a sufficient small-signal stability condition based in the relation between impedances/admittances of the systems that are to be connected. This stability condition relies on the Hurwitz condition of the polynomial $D(s) = 1 + Z_s(s)Y_l(s)$, were Z_s and Y_l are the series equivalent impedance and admittance of the energy *source* system and of the new connected *load*, respectively.

²A system is passive if its admittance($Y(j\omega)$)/impedance($Z(j\omega)$) phase is between the limits $-90^\circ \leq \angle Y(j\omega) \leq 90^\circ$ for all frequencies ω .

This is known as impedance-based stability criterion, and serves not only to predict instabilities of complex networks but also the possible frequencies of systems interaction (i.e. resonances) and the oscillations that would arise. Note the important role that is played by the systems closed-loop impedance/admittance in the overall system stability, and how a negative impedance behaviour represents, as predicted, an important risk for it.

A more detailed explanation of this criterion can be found in section 2.2.

1.3 Introduction to admittance shaping: Thesis outline

The impedance-based stability criterion has motivated the publication of several works dealing with the shaping of converter closed-loop input admittance, imposing certain conditions over its module and/or phase in order to fulfil it.

But admittance/impedance shaping is also an interesting topic in the field of power quality:

- High closed-loop impedance is preferred for the performance of current-controlled PEC-based systems, in order to reject the effect of possible voltage harmonics, in the same way that a high closed-loop admittance is desired in voltage-controlled systems.
- Shunt-connected controlled systems with high resistive admittances can improve the overall stability of weak grids, damping possible resonances that facilitate the propagation of voltage and current harmonics through distribution or transmission networks.

In addition, although they are usually approached in a different way, active damping and impedance-droop control techniques could be considered admittance shaping approaches.

This dissertation proposes a systematic design procedure that allows to shape the converter input admittance, in modulus and phase, for wide frequency bands and handling other control objectives, such as reference tracking or stand-alone stability, from a holistic point of view. Its main objective is the design of PEC controllers that, in addition to fulfil with their main application objective (see section 1.1.1 for some examples), are able to not contribute negatively to the instability problem that arises from the current complex grid dynamics (i.e. achieve an improved stability robustness towards the high presence of PEC-based applications in the grid) or, if possible, contribute positively to it (i.e. stabilize the grid). The obtained flexibility allows the use of the procedure to obtain controllers valid for some of the other admittance shaping scenarios described above, such as the voltage harmonic rejection or the active damping of resonant filters.

1.4 Thesis development context

This dissertation was developed inside the *GEISER*³ research group, an officially recognized group by the Spanish *Universidad de Alcalá* centred in electronic technologies applied to renewable energy systems.

It was, in part, supported by the next projects;

³The acronym follows the name of the group in Spanish: Electronic Engineering Applied to Renewable Energy Systems

- Project ENE2011-28527-C04-02 “*Aplicaciones de los convertidores en fuente de tensión HDVC en los sistemas eléctricos de potencia con especial atención a la operación multiterminal*”, financed by the spanish *Ministerio de economía y competitividad*.
- Project PRICAM: S2013/ICE-2933 “*Programa redes eléctricas inteligentes en la Comunidad de Madrid*”, financed by the spanish *Consejería de educación, juventud y deporte de la Comunidad de Madrid*.
- Project CONPOSITE: ENE2014-57760-C2-2-R “*Convertidores de potencia para optimizar la operación de sistemas híbridos HVDC-VSC multiterminal/HVAC*”, financed by the spanish *Ministerio de economía y competitividad*.
- Project DIANA: CCG2015/EXP-064 “*Diseño de Algoritmos para VSC con especificación de la admitancia de entrada*”, financed by the spanish *Universidad de Alcalá (UAH)*.

The author developed this Ph.D. dissertation, during the period 2013-2017, hired as a faculty researcher by the spanish *Universidad de Alcalá (UAH)* and financed, in part, by:

- Project ENE2011-28527-C04-02 “*Aplicaciones de los convertidores en fuente de tensión HDVC en los sistemas eléctricos de potencia con especial atención a la operación multiterminal*”, financed by the spanish *Ministerio de economía y competitividad*.
- Program FPI “*Contratos predoctorales de personal investigador en formación*”, financed by the spanish *Universidad de Alcalá (UAH)*.

During this period, the developed methods have been presented at different conferences and specialized journals. They are next displayed in chronological order:

1. Perez, J., Cobreces, S., and Grino, R. (2014). Admittance-shaped h-inf current controller for grid-connected vsc. In *Proc. of IEEE Emerging Technology and Factory Automation (ETFA)*, pages 1–8. IEEE
2. Perez, J., Cobreces, S., Sanchez, F. J. R., and Grino, R. (2015). H-inf simultaneous admittance and tracking current controller of three-phase active grid front-ends. In *2015 IEEE International Conference on Industrial Technology (ICIT)*, pages 2092–2097. IEEE.
3. Perez, J., Cobreces, S., Grino, R., and Rodriguez, F. (2016a). H-inf current controller for input admittance shaping of vsc-based grid applications. *IEEE Transactions on Power Electronics*, 32(4):3180–3191
4. Perez, J., Cobreces, S., Pizarro, D., Rodriguez Sanchez, F. J., and Grino, R. (2016b). Resonance damping of lcl filters via input admittance frequency shaping. In *Proc. of the 2016 IEEE 25th International Symposium on Industrial Electronics (ISIE)*, pages 516–521. IEEE
5. Pérez, J., Cóbreces, S., Wang, X., Blaabjerg, F., and Griño, R. (2017b). A robust grid current controller with grid harmonic and filter resonance damping capabilities using closed-loop admittance shaping. In *Proc. of IEEE Applied Power Electronics Conference and Exposition (APEC)*, pages 2625–2632. IEEE
6. Perez, J., Cobreces, S., Grino, R., Rodriguez, F., and Huerta, F. (2017). Active damping: an h-inf model-reference approach. *Submitted to IEEE Transactions on Power Electronics (Under review)*

7. Pérez, J., Cóbreces, S., Wang, X., Blaabjerg, F., and Griño, R. (2017a). A robust admittance shaping approach to grid harmonic attenuation and filter resonance damping. *To be submitted to IEEE Transactions on Power Electronics*

Although not directly related with the research presented in this dissertation, other works have been presented during this period in the fields of current control, robust control and optimal control:

1. Perez, J., Cobreces, S., Rodriguez, F. J., Bueno, E. J., Sanz, I., Huerta, F., and Grino, R. (2013). Static reference frame lqr optimal state-feedback control for static-series compensators. In *Proc. of 39th Annual Conference of the IEEE Industrial Electronics Society, IECON*, pages 3776–3781. IEEE
2. del Toro, J. M., Pérez, J., Cóbreces, S., and Rodríguez, F. J. (2016). Robust qft current control design for dc/ac grid converter. In *Proc. of 42nd Annual Conference of the IEEE Industrial Electronics Society, IECON 2016*, pages 7221–7226. IEEE
3. Huerta, F., Pérez, J., Moranchel, M., and Rodríguez, F. J. (2016). Two-degree-of-freedom current control for shunt active power filters. In *Proc. of the 42nd Annual Conference of the IEEE Industrial Electronics Society, IECON 2016*, pages 3787–3792. IEEE

The research presented in [Pérez et al., 2017b, Pérez et al., 2017a] was developed, in part, in the *HARMONY* (Harmonic Identification, mitigation and control in Power Electronics based Power Systems) research group of the Danish *Aalborg University*, supervised by Professor Frede Blaabjerg and Associate Professor Xiongfei Wang.

1.5 Document structure

The present document is structured in seven chapters and two annexes organized as follows:

- Chapter 2 presents a review of the state of the art of complex networks stability, robust control and admittance shaping methods and applications. The chapter ends with a summary of this thesis main hypothesis and objectives, with special attention on the advantages of the presented admittance shaping methodology.
- Chapter 3 serves as an introduction to optimal control and its main approaches and advantages, with a special focus on the \mathcal{H}_∞ framework. The classic \mathcal{H}_∞ mixed-sensitivity approach is applied to the current control of a VSC, presenting the deriving design limitation and showing the main experimental results. The end of the chapter serves as an introduction to the \mathcal{H}_∞ model-reference design approach and its application to the main proposals of this dissertation.
- Chapter 4 develops the proposed \mathcal{H}_∞ model reference method for the admittance shaping of current-controlled VSCs, focusing on the controller design methodology, with a special attention on the influence of the different design parameters and the main design limitations and trade-offs. It presents a realistic model of the controlled plant, analysing the influence of the discrete nature of the controller on the obtained admittance.
- Chapter 5 describes some applications of the proposed admittance shaping method, organized in three fields: broad band resistive designs, low admittance designs and high admittance designs. It shows the achieved experimental results of each of them.

- Chapter 6 applies the studied \mathcal{H}_∞ model reference approach for the active-damping of resonant LCL filters. Once the designed active-damper is implemented in the system, the LCL filter acts as a non-resonant L filter, making possible to design simpler current controllers and improving the overall system robustness. The effectiveness of the method is again proved with experimental results.
- Chapter 7 states the conclusions and contributions extracted from this thesis and elaborates a list of possible future lines of research and work.
- Annex A quickly introduces some of the background knowledge that the author considers useful for the understanding of this dissertation.
- Annex B collects all the publications related with the research presented in this dissertation.

Chapter 2

State of the art and thesis objectives

2.1 Introduction

As stated in this thesis introduction, the increasing presence of controlled power electronic converters (PECs) in the grid makes necessary the study of possible interactions between them, as they may lead to instability. This study is generally difficult due to the derived high order and complex dynamics, so it is usual to find in the literature simplified criteria for this stability analysis. Among them, the impedance-based stability criterion remarks the importance of the closed-loop impedance/admittance of each interconnected element as the key to the global system stability.

The impedance-based stability criterion leads to some conclusions about how PEC-based applications should behave to be stable in connection with weak grids (i.e. with high equivalent impedances). In that regard, some works have tried to improve the stability robustness of PECs towards these grid uncertainties by means of the so-called robust control techniques, either implicitly or explicitly, sacrificing, in some cases, controller performance (i.e. output reference tracking and disturbance rejection capabilities).

Given their importance on stability, some other works have focused their attention in the admittance/impedance shaping of controlled PEC-based applications by means of different control design methods. But admittance/impedance shaping is not only interesting to reduce instability risk in complex networks. Some works have remarked its importance in other power quality fields, such as disturbance rejection (e.g. voltage/current harmonics) in the controlled output, filter resonance active damping and stabilization of weak grids.

This chapter serves as a state-of-the-art report of these three interrelated fields: complex networks stability analysis, admittance shaping and robust control.

A knowledge review of networks stability analysis is done at the beginning of this chapter (section 2.2). It put into context the importance of the closed-loop admittance/impedance of PEC-based applications for the overall network stability.

The state-of-the-art of the existing admittance shaping (i.e. control) methods and their main applications are detailed in section 2.3. The different admittance shaping methods are illustrated with different control structures applied to a current-controlled VSC connected to the grid with an LCL filter.

Section 2.4 briefly analyses the main robust control design techniques presented in the literature, focusing on the stability robustness of PEC-based application connected to uncertain

grids.

Having analysed the current state-of-the-art of these fields, by means of exposing the main common disadvantages and weaknesses, a summary of the main objectives and hypothesis of this thesis are described in section 2.5, with special focus on the advantages, with respect to the aforementioned previous works, of the two main contributions of it; the optimal model reference shaping of the closed-loop admittance of PEC-based applications and their plants complex dynamics.

2.2 Networks stability analysis

The use of controlled PECs provides multiple advantages in electric applications, such as an excellent load regulation, a good transitory response and a robust tolerance to failures [Sudhoff et al., 2000]. It is understandable, then, that the presence of these systems connected to the grid is becoming more and more common [Emadi, 2004].

The classical approach to the controller design of PECs-based applications considers an ideal grid with a negligible impedance, trying to fulfil their own performance specifications [Cobreces et al., 2007] (e.g. grid power suppliers, load feeders etc.). However, the grid rarely presents an ideal behaviour, so different PECs-based applications connected to the same point of common coupling (PCC) may interact with each other through the grid, or with the grid itself. The effect of these interactions may not be negligible if the considered PEC-based system requires a high power rating from a grid with a relatively small short-circuit ratio (SCR). Moreover, they may even lead to instability problems of the global (interconnected) system.

Instability problems due to interactions between the different elements in an electrical network start as poorly damped or even amplified parasitic oscillation at a certain frequency [Harnefors et al., 2007, Harnefors, 2007]. Some papers have analysed these stability problems from a large signal point of view [Emadi et al., 2006, Belkhat et al., 1995, Sanchez et al., 2014, Acharya et al., 2008], mainly analysing the conditions for the existence of dynamic equilibria. However, in most of the cases the PECs fast non-linear dynamics, induced from their good power regulation (i.e. CPL dynamics), can be approximated through the stability analysis on an operation point, using linear criteria.

Classic LTI (Linear-Time Invariant) stability criteria (e.g. Routh-Hurwitz, Jury, Nyquist etc.) are widely known, and had been successfully applied for the stability analysis of interactions between PECs-based networks [Liserre et al., 2004b, Ariyasinghe and Vilathgamuwa, 2008, Liu et al., 2007, Kundur et al., 1994]. However, they can become prohibitively complex for electrical networks with high dynamical order (i.e. with multiple controlled PECs).

Two main simplified lineal criteria stand out over the rest; the analysis of torsional interactions, proposed in [Canay, 1982], and the impedance-based stability criterion, proposed in [Middlebrook, 1976]. While the former is mainly focused on the stability analysis of machines (generators) connected to the grid, the latter is more general and can be applied to multiple electrical scenarios. Both simplify the LTI stability analysis of complex interconnected systems by dividing the process in two steps: assuming that every interconnected system is stand-alone stable (step 1), they derive a simplified LTI condition for their interconnection stability based on individual (stand-alone) characteristics of each of them (step 2).

2.2.1 Impedance-based stability criterion

Impedance-based criterion, proposed in [Middlebrook, 1976], overcome LTI stability analysis limitations for complex systems. It is just a sufficient stability condition, applicable to both single-phase and three-phase networks, where complex dynamics can be separated in more tractable stand-alone stable subsystems modelled with their classic Norton/Thevenin equivalents (see Fig. 2.1). It established that, assuming that two electrical subsystems are stand-alone stable (see section A.4), the stability analysis of the global network resulting of their connection can be performed applying classic LTI Nyquist criterion to the loop function $L(s) = Z_s(s)Y_l(s)$, where $Z_s(s)$ is the input impedance of the subsystem acting as source and $Y_l(s)$ is the input admittance of the subsystem acting as load. Even though it was introduced for the analysis of multiple DC systems interconnection [Middlebrook, 1976, Lazbin and Needham, 1993], it was soon applied for the stability analysis of three-phase AC interconnected systems [Hiti et al., 1994, Belkhaty, 1997, Mao et al., 1998].

Illustration of the impedance-based stability criterion

To illustrate the impedance stability criterion, consider now the interconnection of a voltage-controlled system (e.g. the grid) and a current-controlled system (e.g. a grid-tied STATCOM) shown in Fig. 2.1¹.

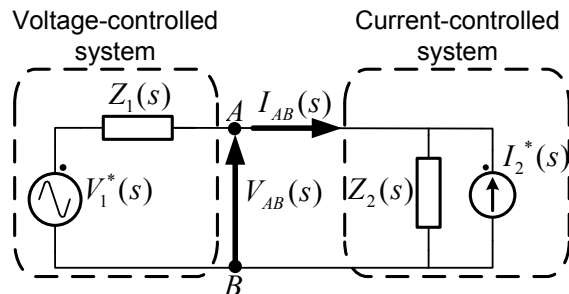


Figure 2.1. Simplified equivalent of a connection of a voltage-controlled and a current-controlled system.

For simplicity, the current-controlled and voltage-controlled systems are modelled with their Norton and Thevenin equivalent circuits, respectively². The interconnected system stability condition can be derived analysing $V_{AB}(s)$ dynamics:

$$V_{AB}(s) = \frac{Z_1(s)Z_2(s)}{Z_1(s) + Z_2(s)} I_2^*(s) + \frac{Z_1(s)}{Z_1(s) + Z_2(s)} V_1^*(s) \quad (2.1)$$

The system is stable if the characteristic polynomial $Z_1(s) + Z_2(s) = 0$ is Hurwitz.

The impedance-based stability analysis simplifies this condition, but presents a duality problem, because its correct interpretation depends on which element acts as the source and which as the load [Areerak et al., 2012] [Sun, 2011]. These definitions are derived from the conditions that make each element stand-alone stable in a certain application, rather than the intuitive assumption that the element which generate power acts as source and the one which dissipate it acts as load, even though these two definitions often coincide [Sudhoff et al., 2000]:

¹A quick summary of current-controlled and voltage-controlled PEC-based applications can be found in section A.8

²Note that Norton and Thevenin circuits are interchangeable, so the result of the impedance-based stability criterion is the same regardless of the selected equivalent circuit.

- A voltage-controlled system is stand-alone stable if $V_{AB}(s)$ is bounded when an ideal current source ($I_{AB}(s)$) is connected to its output terminals (A and B):

$$V_{AB}(s) = V_1^*(s) - Z_1(s)I_{AB}(s) \quad (2.2)$$

That is, its stability relies on $Z_1(s)$ stability.

- A current-controlled system is stand-alone stable if $I_{AB}(s)$ is bounded when an ideal voltage source ($V_{AB}(s)$) is connected to its output terminals:

$$I_{AB}(s) = \frac{1}{Z_2(s)}V_{AB}(s) - I_2^*(s) = Y_2(s)V_{AB}(s) - I_2^*(s) \quad (2.3)$$

That is, its stability relies on $Y_2(s)$ stability.

Decimating (2.1):

$$V_{AB}(s) = \frac{Z_1(s)}{Z_1(s)Y_2(s) + 1}I_2^*(s) + \frac{Z_1(s)Y_2(s)}{Z_1(s)Y_2(s) + 1}V_1^*(s) \quad (2.4)$$

Providing that both systems are stand-alone stable (i.e. Z_1 and Y_2 are stable transfer functions), its interconnection stability depends only on the loop function $L(s) = Z_1(s)Y_2(s)$, that is, in the impedance-based stability criterion with the voltage-controlled system acting as source (i.e. $Z_s(s) = Z_1(s)$) and the current-controlled system acting as load (i.e. $Y_l(s) = Y_2(s)$), independently of the power flow. Considering this interpretation, passive elements (i.e. resistances, inductors or capacitors) can act either as loads, when connected to voltage-source systems, or sources, when connected to current-controlled systems [Sun, 2011], which make the *load* and *source* concepts introduced by [Middlebrook, 1976] rather confusing. To clarify this, [Liu et al., 2014] introduces the Z-type and Y-type systems concepts to refer to the source and load systems in the impedance-based stability criterion, respectively.

When more than two systems are involved, all the voltage-controlled (i.e. *sources* or Z-type) systems are represented as a unique system characterized by its equivalent impedance (Z_t) equal to the parallel association of each system impedance. In the same way, all current-controlled (i.e. *loads* or Y-type) systems can be expressed as a unique system characterized by its equivalent admittance (Y_t) equal to the parallel association of each system admittance. The new impedance loop to predict stability is, in that case, $L(s) = Y_t Z_t$ [Liu et al., 2014].

Main advantage

Middlebrook's proposal constitutes a respected criterion for the stability analysis of complex systems. This may be partly due to the fact that information of the inner loop (i.e. controller, plant model, structure etc.) of each system, which is not always accessible by grid operators, is not necessary. Provided that the systems to be interconnected are stand-alone stable, the only necessary information to predict stability is their small signal admittance/impedance dynamic model, which can be measured experimentally by network analysers [Sun, 2011, Huang et al., 2009, Familant et al., 2009, Francis et al., 2011].

Derived practical controller design specifications

It is common to find in the literature controller design techniques that shape, in some way, the input admittance/impedance of PEC-based applications to fulfil certain limitations imposed by the impedance-based stability criterion (refer to section 2.3 to review its state of the art).

To derive this admittance/impedance limitations, sufficient (but not necessary) more conservative simplifications of the impedance-based criterion are common in the literature [Vesti et al., 2013, Haddadi et al., 2015, Liu et al., 2015]. Four conservative conditions for stability stand out over the rest [Sudhoff et al., 2000], depicted in Fig. 2.2 and detailed below:

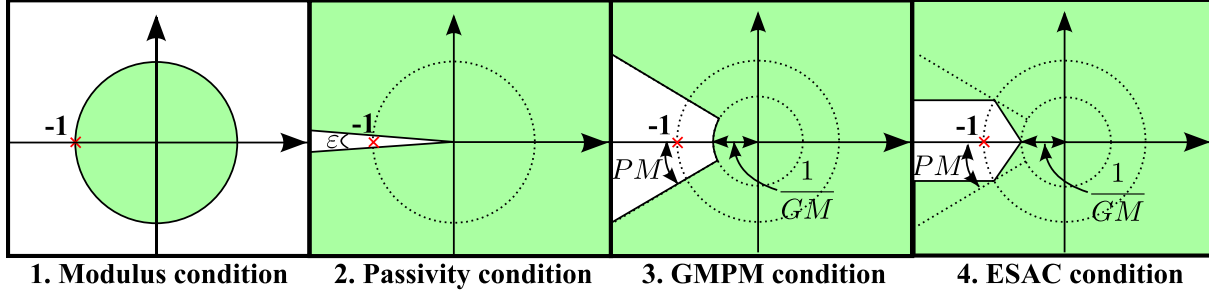


Figure 2.2. Allowed regions (green zones) for the polar representation of $L(s) = Z_g Y_l$ of different impedance-based stability criterion simplifications.

1. **Modulus condition**, which imposes:

$$|Y_l(s)| < 1/|Z_g(s)|, \quad (2.5)$$

as then $L(s)$ can not cross the unit circle, making impossible encirclement of point -1 . This condition was firstly proposed in [Middlebrook, 1976].

2. **Passivity condition**, that requires:

$$-90^\circ < \angle Z_s(j\omega) < 90^\circ, -90^\circ < \angle Y_l(j\omega) < 90^\circ, \quad (2.6)$$

, that is, that $Z_s(s)$ and $Y_l(s)$ are passive for all frequencies [Willems, 1972a] [Willems, 1972b], as then $L(s)$ will not cross the negative part of the real axis, making impossible the encirclement of point -1 .

3. **Gain and phase margin (GMPM) condition**, which imposes two restrictions [Wildrick et al., 1995]:

$$|Y_l| < \frac{GM}{|Z_l(s)|}, \quad -180^\circ + PM < \angle Y_l(j\omega) + \angle Z_g(j\omega) < 180^\circ - PM. \quad (2.7)$$

[Feng et al., 2002] expands this criterion; it considers multiple *loads* interconnected with the same *source* and derives each individual *load* admittance GMPM restrictions according to their power ratings.

4. **ESAC condition**, proposed in [Sudhoff et al., 2000]. This is the least conservative of the four but needs to be evaluated frequency by frequency by means of three-dimensional forbidden regions.

Among them, modulus and passivity conditions are the most used in the literature due to their straightforward graphic interpretation (e.g. using Bode diagram) [Liu et al., 2003, Nussbaumer et al., 2006, Harnefors et al., 2007, Burgos et al., 2010]. If at least one of these conditions are met for all frequencies, the resulting interconnected system will be stable. Normally, the modulus condition is first checked; in case it is not met at a given frequency, the phase of each system will determine the overall network stability.

Risk factors for network stability

Attending to the aforementioned simplified conditions, some stability risk factors can be identified in PEC-based applications:

- The equivalent **grid series impedance** (Z_g) is rarely negligible. A distributed parameters model of the grid impedance is shown in Fig. 2.3 [Kundur et al., 1994].

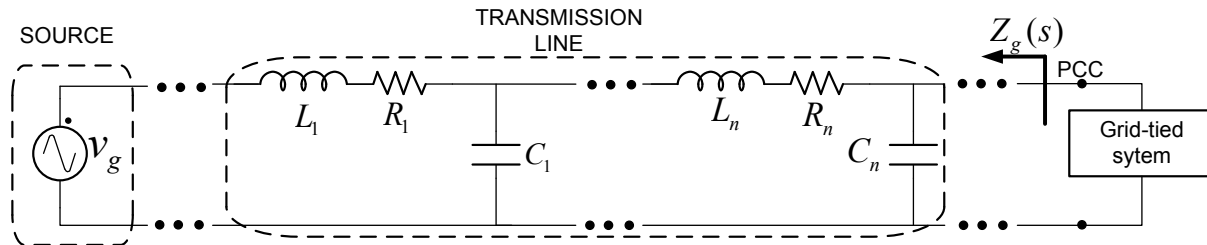


Figure 2.3. Distributed parameters model of a transmission line.

Active power losses are modelled as resistances (R_n), magnetic fields that surround the conductors are represented as inductances (L_n) and electric fields between different conductors are modelled as capacitances (C_n). The grid may present, then, one or more natural resonances, generally well above the nominal frequency (ω_1), being the exact frequency dependent on its geometry (e.g. distance to the substation transformer, loading conditions etc.). An exact model of the grid impedance seen from the PCC (Z_g) is difficult in practice [Cespedes and Sun, 2009], but it is common to simplify this distributed parameters model in two equivalents: a resonant LC-type grid model ($Z_g(s) = (L_g s) / (L_g C_g s^2 + 1)$) or an inductive L-type grid model ($Z_g(s) = L_g s$). Some studies have measured the behaviour of low voltage grids during different time lapses [Jessen and Fuchs, 2015, Akagi et al., 2007], demonstrating that the first and second models are very approximated during both light and heavy load conditions.

In any case, knowing that the grid acts as a *source* in the impedance-based criterion, a grid connected system is more likely to become unstable for weak grids (i.e. with high grid impedance values), as then it is more probable to fail with the modulus condition. The resonant behaviour of some grids are an additional instability factor.

- From the PEC-based application side, there are two major risk factors; the use of **resonant filters** and the **non-passive behaviour** of the system at some frequencies.

LCL and LC filters, commonly used in current-controlled and voltage-controlled PEC-based applications, respectively, have a high open-loop admittance and impedance, respectively, at their resonant frequencies (see G_{dLCL} and G_{dLC} in Fig. A.14). Being the current-controlled and the voltage-controlled systems considered *loads* (Y_l) and *sources* (Z_s) in the impedance-based criterion, respectively, the use of these resonant filters could potentially violate the modulus condition (i.e. $|Z_s(s)| < 1/|Y_l(s)|$).

Another risk for instability are systems with non-passive behaviour at some frequencies. This is a common problem in tightly regulated converters [Ciezki and Ashton, 2000, Harnefors, 2007, Middlebrook, 1976] which, beyond the great improvements in energy conversion and conditioning, may present negative incremental impedance behaviour (i.e. $dV/dI < 0$ [Emadi et al., 2006]) at some frequencies. These systems often act as constant power loads (CPLs) induced by the common use of outer power loops (see Fig. 1.4). But beyond the converter main controller influence, there are other factors that may induce

this non-passive behaviour, as the use of Phase-Locked Loops (PLLs) [Harnefors et al., 2007, Céspedes and Sun, 2011] or the computational delay necessary for the controller implementation in a digital platform [Harnefors et al., 2014, Wang et al., 2014b, Harnefors et al., 2017]. A possible oscillation may be fed (i.e. increased) at frequencies where the systems involved are non-passive, eventually leading to instability.

[Harnefors et al., 2007] proposes that passive behaviour of PECs at network's resonant frequencies may be probably enough to achieve stability (i.e. in frequencies where violation of modulus condition may occur, the systems passivity determines the overall stability). [Harnefors et al., 2017] expands this hypothesis to frequencies beyond the Nyquist limit (i.e. $\omega > \omega_s/2$, being ω_s the controller sampling frequency).

2.2.2 Torsional interaction stability criterion

Synchronous machines used in energy generation systems have natural mechanical resonances, usually below the synchronous frequency. That is, apart of their synchronous frequency, the shaft of these machines can vibrate at a different frequency due to their mechanical characteristics. If this mechanical resonance matches, in frequency, a grid electrical resonance, a cyclical interchange of energy between the grid and the machine shaft may occur. This produces additional torsional stress to the machine, that may lead to a possible system instability and, eventually, to the shaft rupture. This phenomenon is known as subsynchronous resonance (or torsional resonance) and it is analysed by I. Canay in [Canay, 1982].

It proposes two complex coefficients to predict this torsional interaction; $\mathbf{K}_e(j\lambda)$, associated to the system electrical torque, and $\mathbf{K}_m(j\lambda)$, associated to the system mechanical torque. The parameter λ represents the rotor frequency relative to the natural grid frequency (ω_1). Ideally, this frequency should be zero in a synchronous machine but, as introduced before, this is not the case due to small (subsynchronous) oscillations that appear in the machine rotor. $\mathbf{K}_e(j\lambda)$ and $\mathbf{K}_m(j\lambda)$ can be expressed as a function of their real and imaginary parts as follows;

$$\mathbf{K}_e(j\lambda) = K_e + j\lambda D_e \quad (2.8)$$

$$\mathbf{K}_m(j\lambda) = K_m + j\lambda D_m \quad (2.9)$$

Their real parts (K_e and K_m) represent the electrical and mechanical spring constants, respectively, and their imaginary parts divided by λ (D_e and D_m) are the electrical and mechanical damping constants, respectively. These constants may vary due to the transmission line configuration, the operation point, the machine control or the number of parallel machines. The electrical damping (D_e) at electrical resonant frequencies is inherently (i.e. without additional electrical dampers) negative (i.e. it amplifies possible disturbances), meanwhile the mechanical damping is zero at mechanical resonance frequencies, being usually positive (i.e. it reduces possible disturbances) due to the machine big inertial mass. The stability criterion proposed in [Canay, 1982] is simplified to the next condition:

$$\text{If } D(\omega) = D_e(\omega) + D_m(\omega) > 0 \text{ then the system is stable,} \quad (2.10)$$

being ω a resonant frequency (electrical or mechanical). That is, the system will be inherently stable if the mechanical damping constant (D_m) totally compensates a negative electrical damping constant (D_e).

[Tabesh and Iravani, 2005] demonstrates that, depending on the system parameters and point of operation, the criterion presented in [Canay, 1982] does not always correctly predict instability. [Tabesh and Iravani, 2004] proposes an alternative stability criterion based on the

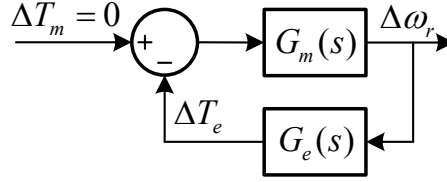


Figure 2.4. Linearized electromechanical model of the interconnected system Generator Turbine-Grid proposed in [Tabesh and Iravani, 2004].

linearisation, around an operational point, of the mechanical and electrical system. Fig. 2.4 shows the resulting electromechanical system. In it:

- ΔT_e represents small linear variations of the electrical torque,
- ΔT_m represents small linear variations of the mechanical torque, which can be approximated to zero due to its slow dynamics (in comparison with the electrical torque),
- ω_r is the rotor speed,
- $G_m(s)$ and $G_e(s)$ are the linearized models of the mechanical and electrical systems, respectively.

This criterion is based on Nyquist classic stability analysis of the feedback loop shown in Fig. 2.4. It states that, providing that $G_m(j\omega)$ and $G_e(j\omega)$ are stand-alone stables (see section A.4), the interconnected system is stable if the loop function $L(j\omega) = G_m(j\omega)G_e(j\omega)$ does not encircle the real axis point -1.

[Harnefors, 2011] demonstrates that both stability methods are equivalent for some frequencies. To that end, it proposes an equivalence between the linearized models in [Tabesh and Iravani, 2004] and the torque coefficients in [Canay, 1982]:

$$G_e(j\omega) = D_e(\omega) + jK_e(\omega) \quad (2.11)$$

$$\frac{1}{G_m(j\omega)} = D_m(\omega) + jK_m(\omega) \quad (2.12)$$

The loop function $G_m(j\omega)G_e(j\omega)$ may cross the real axis at a frequency ω_s where the next equality is fulfilled:

$$G_m(j\omega_s)G_e(j\omega_s) = \frac{D_e(\omega_s)}{D_m(\omega_s)} = \frac{K_e(\omega_s)}{K_m(\omega_s)} \quad (2.13)$$

If $D_e(\omega_s)/D_m(\omega_s) > -1$, or equivalently if $D_e(\omega_s) + D_m(\omega_s) > 0$ [Canay, 1982], the system will be stable. That is, [Canay, 1982] proposes a sufficient but not necessary condition for stability, as the loop function $G_m(j\omega)G_e(j\omega)$ may cross the real axis to the left of -1 but not encircle it. [Harnefors, 2007] proposes to use of [Canay, 1982] condition (due to its simplicity) only at frequencies where $|G_m(j\omega)G_e(j\omega)| > 1$, that is, at the open loop resonant frequencies, as those are the frequencies with a higher risk of encircling point -1 .

This criterion is still used in several works to predict instabilities between wind-power farms converters and the grid [Alawasa et al., 2013, Alawasa et al., 2014].

2.3 Admittance shaping by means of controller design

This section reviews the state of the art of the different control design techniques for the admittance shaping of PEC-based applications, organized by how they are shaped and their main

objective/application.

2.3.1 Methods

Automatic control provides of different ways to modify the closed-loop admittance/impedance of controlled PEC-based applications. This section reviews the main proposals in the literature, which can be roughly classified in three groups: the controlled output feedback loop modification, the addition of a disturbance feed-forward loop and the addition of partial/complete system states feedback loops.

To better illustrate each method and put them into context, this section presents the dynamic analysis of a current-controlled VSC connected to the grid with an LCL filter, with special attention to the effect on the system closed-loop admittance of each proposal. This is a particularly representative example, as it allows the use of all the aforementioned shaping techniques.

Even though they are not considered in this state of the art review, note that similar methods can be applied to shape the closed-loop impedance of voltage-controlled PEC-based applications. Examples can be found in [Radwan et al., 2013, Turner et al., 2013, Guerrero et al., 2005, Chiang and Chang, 2001, Radwan et al., 2012, Wen et al., 2013, Wang et al., 2012, Deng et al., 2008, He et al., 2012, He and Li, 2012].

Introduction: LCL filter open loop model

Fig. 2.5 shows the open-loop model of the LCL filter, where;

$$Y_{L_2}(s) = \frac{1}{L_2s + R_2}, \quad Y_{L_1}(s) = \frac{1}{L_1s + R_1}, \quad Z_C(s) = \frac{1}{Cs}, \quad (2.14)$$

where L_1 , L_2 are the LCL converter and grid side inductances, R_1 , R_2 are their respective losses and C is the LCL-filter capacitor.

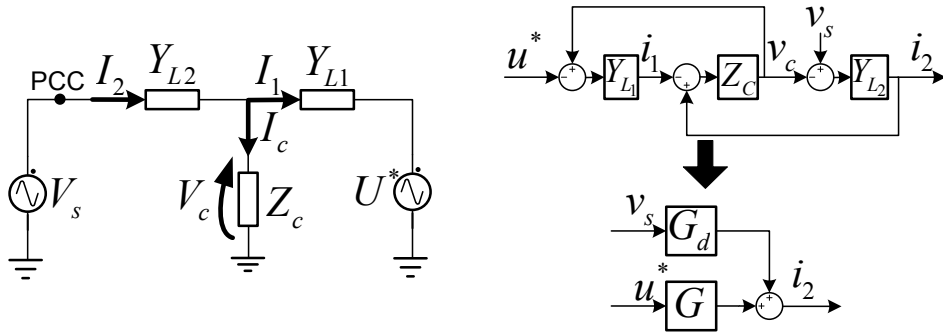


Figure 2.5. Equivalent electric circuit and block diagram of the LCL filter open-loop model.

The transfer functions that model the open-loop grid-current dynamics are:

$$G(s) = \frac{I_2(s)}{U^*(s)} = -\frac{Y_{L1}Z_cY_{L2}}{1 + Y_{L1}Z_c + Y_{L2}Z_c}; \quad G_d(s) = \frac{I_2(s)}{V_s(s)} = \frac{Y_{L2}(1 + Y_{L1}Z_c)}{1 + Y_{L1}Z_c + Y_{L2}Z_c}. \quad (2.15)$$

where $G(s)$ is named as the open-loop command-to-output transfer function and $G_d(s)$ is the system open-loop admittance. These transfer functions are equivalently defined in equation (A.51) (with the names G_{LCL} and G_{dLCL} , respectively). Refer to Fig. A.14 for information about their dynamic response.

Output feedback loop modification

It is possible to modify the closed-loop admittance to fulfil the desired objectives by modifying the grid-side current (i_2) controller.

To illustrate it, consider a classic single loop feedback structure like the one shown in Fig. 2.6, with a one degree-of-freedom (DOF) controller K_{cc} (see section A.2 for more details about this structure). The grid-current closed-loop dynamic is as follows;

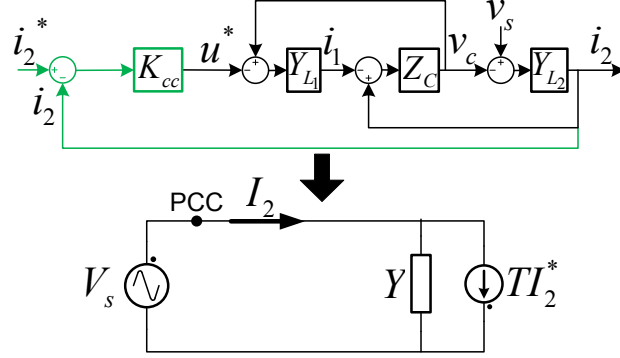


Figure 2.6. Closed-loop structure of the grid-current control with a one DOF controller. The controller and the open-loop plant are shown in green and black, respectively. The closed-loop loop system is equivalent to the Norton model shown at the bottom of the image.

$$I_2(s) = \underbrace{\frac{G(s)K_{cc}(s)}{1 + G(s)K_{cc}(s)}}_{T(s)} I_2^*(s) + \underbrace{\frac{G_d(s)}{1 + G(s)K_{cc}(s)}}_{Y(s)} V_s(s), \quad (2.16)$$

where $T(s)$ and $Y(s)$ represent the closed-loop tracking and admittance transfer functions, respectively. The closed-loop system can be expressed, then, as the Norton equivalent circuit shown at the bottom of Fig. 2.6.

To further analyse the effect of the controller (K_{cc}) in the system closed-loop admittance, it is useful to divide its action in a current reference (i_2^*) feed-forward path and a grid-current (i_2) feedback path, as shown in the top part of Fig. 2.7. The admittance (Y) is only affected by the feedback action, as it is demonstrated below:

$$I_2(s) = \underbrace{\frac{G(s)}{1 + G(s)K_{cc}(s)}}_{G'(s)} U'(s) + \underbrace{\frac{G_d(s)}{1 + G(s)K_{cc}(s)}}_{G'_d(s)=Y(s)} V_s(s) \quad (2.17)$$

where $G'(s)$ and $G'_d(s)$ can be considered as the modified LCL filter dynamics;

$$\begin{aligned} G'(s) &= \frac{I_2(s)}{U'(s)} = -\frac{Y_{L1}Z_C Y_{L2}}{1 + Y_{L1}Z_C + Y_{L2}Z_C - Y_{L1}Z_C Y_{L2}K_{cc}} \\ G'_d(s) &= \frac{I_2(s)}{V_s(s)} = \frac{Y_{L2}(1 + Y_{L1}Z_C)}{1 + Y_{L1}Z_C + Y_{L2}Z_C - Y_{L1}Z_C Y_{L2}K_{cc}} \end{aligned} \quad (2.18)$$

Comparing these modified filter dynamics ($G'(s)$ and $G'_d(s)$) with the open-loop ones ($G(s)$ and $G_d(s)$) in equation (2.15), it can be seen a new term in the denominator that depends on the controller (K_{cc}). This is equivalent to add to the filter grid-side inductance a virtual series

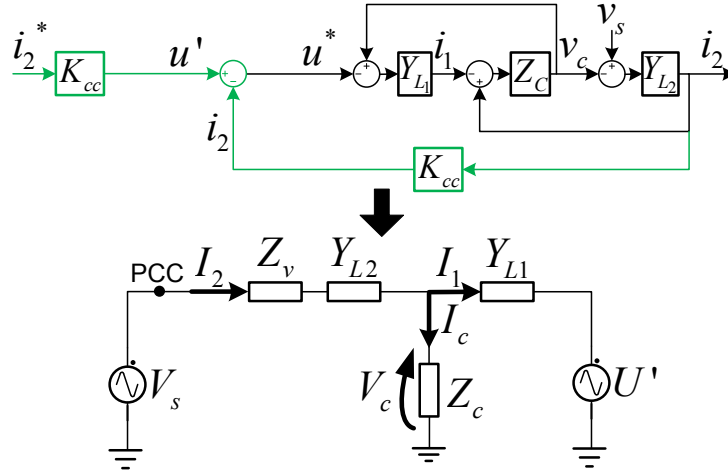


Figure 2.7. Current controller (K_{cc}) divided in its reference feed-forward and current feedback actions. The feedback action is equivalent to add a series impedance Z_v in series to the grid-side inductance (Y_{L2}).

impedance Z_v , as shown in the bottom part of Fig. 2.7:

$$Z_v(s) = -\frac{Y_{L1} Z_c K_{cc}}{1 + Y_{L1} Z_c} \quad (2.19)$$

The current controller (K_{cc}) will modify, then, the system admittance (Y) by adding a virtual series impedance (Z_v) inside its bandwidth, tending Y to its open-loop value (G_d) beyond K_{cc} cut-off frequency ($\lim_{|K_{cc} \rightarrow 0|} Y = G_d$).

This effect can be directly extrapolated to the current control of VSCs with L filters by substituting G and G_d dynamics with G_L and G_{dL} defined in (A.50). In that case, $G = -G_d$ and the virtual impedance is simplified to $Z_v = -K_{cc}$, so the closed loop admittance (Y) is simply the inverse of the series association of the filter open-loop admittance (G_d) and the negated controller (K_{cc}).

It is clear, in any case, that zeros in the current controller will decrease the closed-loop admittance magnitude (as well as its phase), unlike current controller poles, that will increase it [Céspedes and Sun, 2011].

Among the works that modify the current controller (K_{cc}) to shape the closed-loop admittance are [Dannehl et al., 2011, Liserre et al., 2002, Tang et al., 2012, Teodorescu et al., 2003, Jessen and Fuchs, 2015], that use it to actively damp the LCL filter resonance, and [Wang et al., 2014b, Kwon et al., 2014, Harnfors et al., 2014, Céspedes and Sun, 2014b], that use it to achieve passivity at certain frequencies.

Addition of a disturbance feed-forward loop

The aforementioned one DOF scheme is not very flexible, as it modifies (i.e. shapes) the closed-loop admittance (Y) but also the tracking transfer function (T) and, then, may influence the reference tracking response of the designed controller.

Some works add a new DOF to the controller by including a feed-forward path to the PCC voltage (v_s), as shown in Fig. 2.8 (see section A.2 for more details about the dynamics of this two DOF structure). This new loop may modify either the grid current reference (i^*), with the switch in position 2, or the actuation signal (u), with the switch in position 1; these two proposals are named, for now on, as external and internal feed-forward loops, respectively.

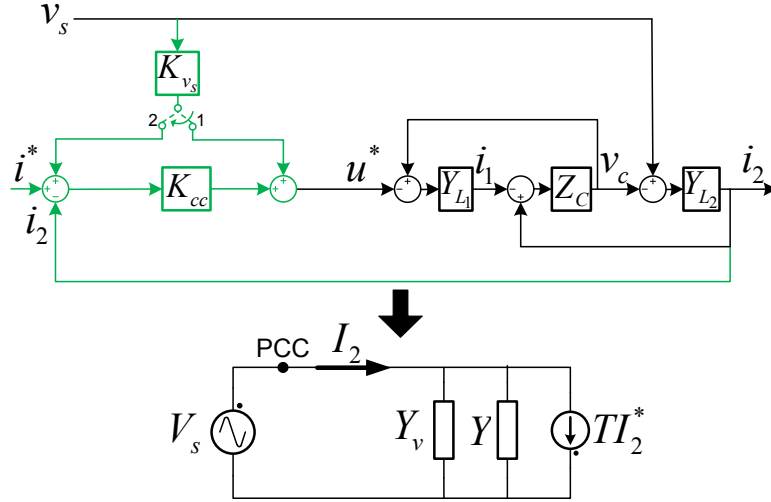


Figure 2.8. Modification of the closed-loop admittance when a feed-forward path (K_{v_s}) is included: this is equivalent to add a parallel virtual admittance ($Y_v(s)$) to the initial admittance ($Y(s)$) in the Norton equivalent circuit shown at the bottom of the image.

If an internal feed-forward path is set [Wang et al., 2014a, He and Li, 2012, Xu and Fan, 2013, Park et al., 2008, Harnefors et al., 2007, Jansson et al., 2004, Wu et al., 2015, Céspedes and Sun, 2011, Yang et al., 2014], the closed-loop grid-current dynamic changes as follows:

$$I_2(s) = \underbrace{\frac{G(s)K_{cc}(s)}{1 + G(s)K_{cc}(s)}}_{T(s)} I_2^*(s) + \left(\underbrace{\frac{G_d(s)}{1 + G(s)K_{cc}(s)}}_{Y(s)} + \underbrace{\frac{K_{v_s}(s)G(s)}{1 + G(s)K_{cc}(s)}}_{Y_v(s)} \right) V_s(s), \quad (2.20)$$

where Y' is the modified closed-loop admittance and Y_v represents a virtual admittance added to Y as a result of this new PCC voltage feed-forward loop (K_{v_s}).

On the other hand, if an external feed-forward path is set [He et al., 2012, Park et al., 2008, Alawasa et al., 2014, Takeshita and Matsui, 2003, Freijedo et al., 2015], the grid-current dynamic is simplified to:

$$I_2(s) = T(s)I_2^*(s) + \left(\underbrace{\frac{Y'(s)}{Y(s) + K_{v_s}T(s)}}_{Y_v(s)} \right) V_s(s) \quad (2.21)$$

The external feed-forward structure is more useful to modify the closed-loop admittance at frequencies where a good tracking ($|T(s)| \rightarrow 1$) is obtained thanks to a high feedback controller gain ($|K_{cc}|$), as in that case $|Y(s)| \rightarrow 0$ and the new admittance is simply $Y'(s) = K_{v_s}$. Note that, on the contrary, complete shaping of the system admittance at frequencies where $|T(s)| \rightarrow 1$ is not possible for an internal PCC voltage feed-forward, as the high value of K_{cc} at those frequencies will impose that $|Y'(s)|$ varies from 0 to 1 as a function of $|K_{v_s}|$ value.

The external feed-forward structure requires, however, a good tracking at frequencies where admittance shaping is desired. Its use is, then, not recommended if a broad bandwidth of admittance shaping is required, as it may result in poor stand-alone stability margins (see A.4 and A.5 for more details about this control trade-off), being the internal feed-forward a better choice in this case.

Regardless of the considered feed-forward path (i.e. internal or external), its use is equivalent to include a parallel virtual admittance ($Y_v(s)$) to the original closed-loop admittance ($Y(s)$), as it is shown in the new Norton equivalent circuit at the bottom of Fig. 2.8. Adding derivative terms (increasing $|K_{v_s}(s)|$) should result, then, in an increase of both admittance magnitude and phase, in opposition to integral terms.

Again, the effect of this new feed-forward loop on the closed-loop admittance can be directly extrapolated to the current control of VSCs with L filters by substituting G and G_d transfer functions with G_L and G_{d_L} defined in (A.50).

This is probably the commonest way to shape the closed-loop admittance. Other works that use this method are [Harnefors, 2007, Harnefors et al., 2008, Harnefors et al., 2014, Harnefors et al., 2015b, Céspedes and Sun, 2012, Céspedes and Sun, 2014a].

Addition of partial/complete system states feedback loops: hierarchical control

Resonant filters, as the considered LCL filter or the LC and LLCL filter topologies, have a resonance in their open-loop transfer functions $G(s)$ and $G_d(s)$. This resonance will increase the feedback controller (K_{cc}) design complexity and the risk of system instability, both from a stand-alone and complex network points of view.

To simplify this design process without the addition of passive elements to the filter, new filter state (or linear combination of states) feedback loops may be added to the initial structure shown in Fig. 2.6 (see section A.2 for more details about the dynamic modifications induced by a state regulator). This technique, widely known as active damping, introduces modifications to the controlled filter dynamic (G and G_d) by adding equivalent virtual impedances/admittances. Considering again the LCL filter case, this technique is below classified as a function of the feedback variable. Fig. 2.9 shows the control closed-loop diagram considering these new feedback loops, as well as their corresponding virtual impedance equivalences:

- **Feedback of the grid-side current** (i_2) [Dujic et al., 2013, Harnefors et al., 2008, Yang et al., 2014]: As deduced from Fig. 2.7 and equations (2.18) and (2.19), feeding-back the grid-current (i_2) is equivalent to add a virtual impedance (Z_v) in series with the grid-side inductance (Y_{L_2}). An additional grid-current feedback loop (K_{i_2}) is considered (see Fig. 2.9), which is again equivalent to add a series impedance (Z_{i_2}) to the open-loop filter³:

$$Z_{i_2}(s) = \frac{Y_{L_1} Z_c K_{i_2}}{1 + Y_{L_1} Z_c} \quad (2.22)$$

- **Feedback of the converter-side current** (i_1) [He and Li, 2012, Dahono, 2002, Rahimi and Emadi, 2009]: In a similar way, to introduce a feedback loop for the converter-side current (K_{i_1} in Fig. 2.9) is equivalent to add a virtual impedance (Z_{i_1}) in series with the converter side inductance (Y_{L_1}):

$$Z_{i_1}(s) = K_{i_1} \quad (2.23)$$

- **Feedback of the capacitor voltage** (v_c) [Radwan et al., 2013, Turner et al., 2013, Dannehl et al., 2010, Agorreta et al., 2011, Huang et al., 2016, Radwan et al., 2012, Freijedo et al., 2016]: The addition of a capacitor voltage feedback loop (K_{v_c} in Fig. 2.9) is equivalent to add a virtual admittance (Y_{v_c}) in parallel to the capacitor impedance (Z_c):

$$Y_{v_c}(s) = -Y_{L_1} K_{v_c} \quad (2.24)$$

³Note that the virtual impedance sign change with respect to (2.19) because the feedback path is, for this case, positive.

- **Feedback of the capacitor current** (i_c) [Twining and Holmes, 2003, Parker et al., 2014, Wu et al., 2015, Mohamed et al., 2012, Orellana and Griñó, 2012, Yang et al., 2014, Chen et al., 2016, Wang et al., 2015]: The addition of a capacitor current (i_c) feedback path (K_{i_c} in Fig. 2.9) can be considered a lineal combination of both grid (i_2) and converter (i_1) side current feedback loops ($i_c = i_2 - i_1$). This new loop is, again, equivalent to introduce a virtual admittance (Y_{i_c}) in parallel to the filter capacitor (Z_c):

$$Y_{i_c}(s) = -\frac{Y_{L1}K_{i_c}}{Z_c} \quad (2.25)$$

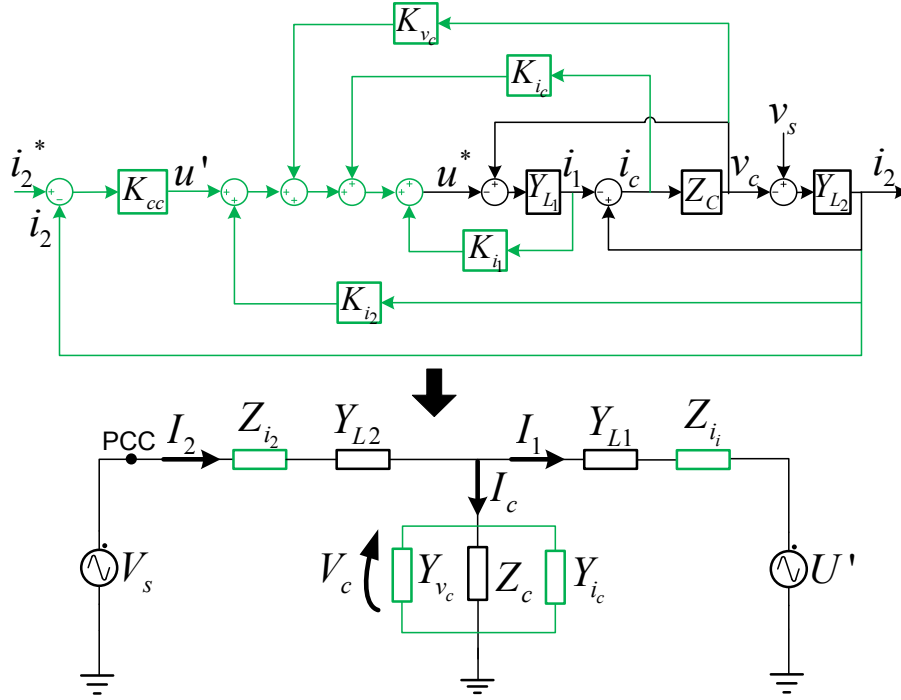


Figure 2.9. Effect of introducing additional feedback paths in the initial control structure: grid-side current (K_{i_2}), converter-side current (K_{i_1}), capacitor voltage (K_{v_c}) and capacitor current (K_{i_c}).

Considering the new virtual impedances/admittances shown at the bottom of Fig. 2.9, the LCL filter dynamic can be modelled by two modified transfer functions $G'(s) = I_2(s)/U'(s)$ and $G'_d = I_2(s)/V_s(s)$. In that case, the outer current controller (K_{cc}) will modify the grid current closed-loop dynamic to:

$$I_2(s) = \underbrace{\frac{G'(s)K_{cc}(s)}{1 + G'(s)K_{cc}(s)}}_{T'(s)} I_2^*(s) + \underbrace{\frac{G'_d(s)}{1 + G'(s)K_{cc}(s)}}_{Y'(s)} V_s(s), \quad (2.26)$$

That is, unlike feed-forward techniques, which introduce another DOF to the control, these new feedback loops will alter the closed-loop admittance (Y') but also the tracking transfer function (T'). They can be considered, then, another form of admittance shaping, even though dealing with the trade-off between tracking response and admittance shaping is more difficult using them.

The main advantage of these techniques is that they separate the initial current control design complexity in two hierarchical loops. The new inner loop, consisting of the filter state (or lineal combination of states) feedback, will actively damp the filter resonance by shaping G'

and G'_d . As a result, the design of a stable outer-loop controller (K_{cc}) that fulfil the desired closed-loop behaviour ($Y'(s)$ and $T'(s)$) is simplified.

The design of either grid-side (i_2) or converter-side (i_1) current feedback loops for the LCL filter resonance active damping (i.e. shaping of G' and G'_d) is rather difficult, at least following a classic (i.e. not optimal) control approach. It is more common to find in the literature, then, the addition of capacitor voltage (v_c) or capacitor-current (i_c) feedback loops. This is due to the well-known fact that a small resistance in parallel with the filter capacitor is the easiest resonance (passive) damping method. Regardless of the choice of i_c or v_c as the new fed-back variable, the design of K_{i_c} and K_{v_c} for active damping is simplified, then, to the obtaining of an equivalent big resistive virtual admittance (Y_{i_c} or Y_{v_c} , respectively).

Modification of outer loops

The modification of the closed-loop admittance is not an exclusive problem of the current controller. Some works have focused their attention on changing the closed-loop admittance by modifying the system outer control loops that use, in some way, a PCC voltage (v_s) measurement in their structures. That is the case of the outer DC-bus/power controller [Wan et al., 2015] and phase-locked (PLL) [Alawasa et al., 2014, Messo et al., 2013, Wu et al., 2015, Wen et al., 2013, Céspedes and Sun, 2011] loops. In them, it is necessary to deal with another trade-off, between the altered outer loop performance and the necessary admittance modification to fulfil the considered objective [Céspedes and Sun, 2012, Céspedes and Sun, 2014a, Zhang et al., 2015, Harnefors et al., 2007].

Admittance shaping bandwidth

This section has summarized the different methods to modify the closed-loop admittance of current controlled PEC-based system. For the sake of expressions simplicity, the continuous Laplace model of the full system has been considered. However, the designed current controller is usually implemented in a digital platform in discrete time.

The current (i_2) closed-loop response is, then, the result of an hybrid dynamic, where the control algorithm and the plant to be controller are modelled in discrete (z) and continuous (s) times, respectively. Fig. 2.10 shows a more realistic closed-loop diagram of a one DOF current-controlled PEC-based system.

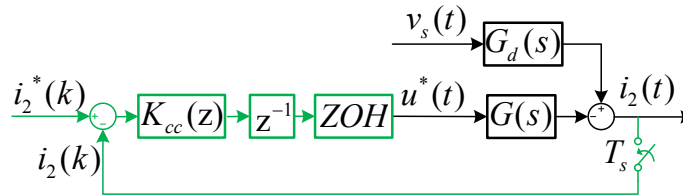


Figure 2.10. One DOF current control considering a discrete controller $K_{cc}(z)$. The discrete control loop is shown in green.

In it, the current ($i_2(t)$) is sampled ($i_2(k)$) with a period T_s and compared with the given reference ($i_2^*(k)$). The discrete controller responds to this comparison generating an actuation signal after a non-negligible fraction of the sampling period (T_s). For that reason, this signal is not usually applied until the next sample, when it is introduced into a pulse-width modulator (PWM) to modify the PEC output voltage.

To consider, then, a continuous model for both the controller and the plant will neglect important dynamics such as the one-sample delay at the controller output (z^{-1}) and the PWM dynamic that can be modelled as a Zero-Order-Hold (ZOH). The relevance of these elements are more evident in the admittance shaping problem, as they introduce important dynamic differences, mainly in phase, in the obtained admittance, as well as shaping bandwidth limitations for both feedback and feed-forward control. In practice, consider the system dynamic in its full complexity makes the admittance shaping problem a more precise but also difficult task.

This complex hybrid model is studied in more detail in section 4.7. The induced bandwidth limitations are derived in sections 3.3.4 and 4.8.1, for both feedback and feed-forward techniques, respectively.

2.3.2 Objectives/Applications

Once the different methods to shape the closed-loop admittance has been reviewed, this section summarizes the main objectives and applications of this control paradigm, as well as some of the more relevant works on each of them.

Compliance of the impedance-based stability criterion

The impedance-based stability criterion (see section 2.2.1) leads to the conclusion that the admittance/impedance of interconnected PECs plays an important role in the stability of complex networks. Multiple works have focused their attention in shaping the admittance of current-controlled applications and/or the impedance of voltage-controlled systems [Turner et al., 2013] in order to fulfil this stability criterion in either AC [Wang et al., 2014b, Messo et al., 2013, Kwon et al., 2014, Wang et al., 2014a], DC [Thandi et al., 1999, Radwan et al., 2012, Mosskull, 2014, Freijedo et al., 2016] or hybrid AC-DC [Xu and Fan, 2013] systems. Following it, they predict instabilities in complex networks and then shape (modify) the closed-loop impedance/admittance of one or a multiple number of the interconnected systems, following one of the methods summarized in section 2.3.1.

Admittance/impedance shaping can be used, then, to improve the stability robustness of the system when it is connected to complex networks. This improved stability robustness usually comes, however, in detriment of a poorer controller performance. It is necessary, then, to solve a trade-off between controller performance and the system stability robustness [Wan et al., 2015, Céspedes and Sun, 2012, Yang et al., 2014].

As stated in section 2.2.1, it is common to approach the impedance-based criterion using the modulus and/or the phase conditions; if at least one of these conditions is met at all frequencies the interconnected system should be stable.

1. **Fulfilment of the modulus condition:** Stability problems of resonant filters (e.g. LC or LCL topologies) in complex networks are a common concern in the literature, even though not many papers have treated it directly from an impedance-based stability criterion point of view. Resonant filters are characterized for having a resonant frequency with high admittance/impedance (see Fig. A.14). This behaviour may potentially violate the modulus condition, as advanced in section 2.2.1. This can be solved by damping the filter resonance, either with active [Radwan et al., 2013, Céspedes and Sun, 2011] or passive [Middlebrook, 1976, Erickson, 1999] techniques.
2. **Fulfilment of the passivity condition:** If the modulus condition is not met, phase information of the interconnected systems will determine whether the system is stable

or not. As introduced in section 2.2.1, if all the interconnected systems in a complex network are passive, the resulting network is passive and then stable [Harnefors et al., 2007]. However, this is a very conservative specification and difficult to fulfil at all frequencies. Some works, such as [Dujic et al., 2013, Harnefors et al., 2015a, Harnefors et al., 2007, Harnefors et al., 2008], have identified the elements that affect the system passivity, to then shape, using the methods showed in section 2.2.1, the admittance phase to remain passive at least at the problematic frequencies (i.e. where the modulus condition is or may not be met). The control elements that have received more attention are the outer DC-bus/power and PLL loops, and the effect of the one-sample time delay and PWM necessary for the controller discrete implementation (see Fig. 2.10):

- As introduced in section 2.2.1, and also in multiple works such as [Ciezki and Ashton, 2000, Rivetta et al., 2006, Emadi et al., 2006, Middlebrook, 1976, Sudhoff et al., 2000], the outer DC-bus/power control loops may induce a CPL or negative resistive behaviour to the system. A similar behaviour is reported in the use of PLLs to predict the grid fundamental frequency [Alawasa et al., 2014, Jansson et al., 2004, Wen et al., 2013, Céspedes and Sun, 2011], which effect is equivalent to add a parallel negative resistance to the closed-loop admittance [Zhang et al., 2015, Messo et al., 2013]. The simplest way to alter this behaviour is to reduce the considered outer controller bandwidth, generating a trade-off between the system stability robustness (from a complex network point of view) and its control performance [Mosskull, 2014], being possible to dynamically modify it by means of adaptive techniques [Céspedes and Sun, 2014a]. It is also possible to lighten this non-passive behaviour by means of introducing proportional/derivative terms in a PCC voltage feed-forward loop [Liu et al., 2007, Liutanakul et al., 2010]. Note, however, that with the introduction of these terms in the feed-forward the admittance phase is increased at the expense of an admittance magnitude increase and, then, in a decreased PCC voltage disturbance rejection capability. Additionally, the controller effort (i.e. actuation) necessary will increase, with higher risks of controller saturation.
- On the other hand, the computational delay and PWM dynamics introduce a phase lag in the system, bigger as frequency (ω) increases, that will easily result in non-passive frequency zones [Harnefors et al., 2014, Harnefors et al., 2008, Harnefors et al., 2015a, Wang et al., 2015, Harnefors et al., 2017]. In that regard, some papers [Harnefors et al., 2015b, Wang et al., 2014b] have tried to assure passivity at least below the Nyquist sampling frequency ($\omega_s/2$) by introducing derivative terms in either the PCC voltage feed-forward term or the controlled current feedback term. Again, this phase increase will result in an equivalent module increase of the admittance and controller actuation and, if feedback is involved, wider controller bandwidths and smaller stand-alone stability margins (refer to sections A.4 and A.5 for more details about this control trade-off). Additionally, even if passivity is achieved inside the Nyquist region, it is not assured beyond that frequency [Harnefors et al., 2017].

Power quality improvement

Admittance shaping is an interesting topic also in the field of power quality. It can be used to damp resonant filters, to reject the effect of voltage oscillations on the current-control or to improve the grid voltage quality:

1. **Damping of resonant filters:** The resonant frequency that appears in certain filter topologies (e.g. LC, LCL, LLCL etc.), apart of being a risk factor for the non-fulfilment

of the impedance-based stability criterion, may produce a high current/voltage oscillation even under minimum voltage/current disturbances. That is, its presence may deteriorate the performance of current/voltage controllers and its stand-alone stability. The most common approach to deal with these problems are the damping techniques, that indirectly modify the closed-loop admittance/impedance of the system. They can be classified in passive and active damping techniques:

- Passive damping techniques [Liserre et al., 2005, Middlebrook, 1976, Pena-Alzola et al., 2013, Erickson, 1999, Liserre et al., 2002] requires the introduction of passive elements (normally resistances) on the resonant filter configuration.
- Active techniques [Twining and Holmes, 2003, Liserre et al., 2006, Blasko and Kaura, 1997, Liserre et al., 2004a, Wu and Lehn, 2005, Dannehl et al., 2010] only modifies the current/voltage controller, changing the output feedback loop (see Fig. 2.7) or adding new fed-back states (or linear combination of states) to the structure (see Fig. 2.9), in order to damp the filter resonance. This is still a highly prolific research field in the control of PEC-based systems. Other more recent relevant works in this topic are [Agorreta et al., 2011, Dannehl et al., 2011, Agorreta et al., 2011, Tang et al., 2012, Parker et al., 2014, Jessen and Fuchs, 2015, Liu et al., 2016].

Note that, in fact, it is possible to make an equivalence between passive and active damping techniques with the virtual impedance concept [Orellana and Griñó, 2012, He and Li, 2012, Rahimi and Emadi, 2009, Wessels et al., 2008, Wang et al., 2015], even though this equivalence is never accurate due to the effect of the PWM modulation and the computational delay, which can not be fully compensated with a causal feedback/feed-forward loop gain [Huang et al., 2016] or with variations of the modulation signal [Chen et al., 2016].

2. **Rejection of grid voltage oscillations:** In order to reject the effect of voltage oscillations (i.e. (sub/inter)harmonics [CEI/IEC 1000-2-1:1990, 1990]) in current-controlled PEC-based applications, and satisfy grid standards such as [IEEE 519-2014, 2014], [IEEE 1547-2003, 2008] and [IEEE 929-2000, 2000], a common approach in the literature is to highly increase the system closed-loop impedance at the problematic frequencies (ω_x) [Twining and Holmes, 2003], so its admittance $|Y(j\omega_x)| \rightarrow 0$.

To achieve this, the classical approach is to design multiple PR controllers (see section A.7) tuned at those problematic frequencies (ω_x), mainly at low order harmonics. These controllers present a high feedback gain, ideally infinite, at those frequencies (see Fig. A.10), so the system is able to track null references at them (i.e. $|T(j\omega)| \rightarrow 1$), which will indirectly reject voltage oscillation effect in the controlled current (i.e. $|Y(j\omega_x)| \rightarrow 0$) [Rodriguez et al., 2008, Vidal et al., 2013, Kwon et al., 2014, Liserre et al., 2006, Harnefors et al., 2014]. Note, however, that the oscillation rejection effectiveness depends on different factors, such as the model uncertainties, the discretization process and the presence of computational delays in the system, which may result in ineffective harmonic damping due to the frequency displacement of the tuned PR [Yepes, 2011]. Additionally, the use of high feedback gains controllers may lead to poor stand-alone stability margins [Yepes et al., 2011], and its stable operation becomes more difficult for resonant filters as the harmonics to be rejected approach their resonances [Wang et al., 2015, Twining and Holmes, 2003].

The second alternative is to similarly shape the system admittance by means of feed-forward techniques. The objective is the same, achieve a shaped admittance $|Y'(j\omega_x)| \rightarrow 0$ to reject voltage oscillations in the current-controlled system, this time by introducing a virtual admittance (Y_v) that cancels (or reduces) the closed-loop admittance achieved by the current tracking feedback loop (Y) at the desired frequencies [Wu et al., 2015, Yang

et al., 2014, Park et al., 2008]. This technique considers an internal feed-forward loop like the one shown in Fig. 2.8. The shaped admittance (Y') expression is shown in equation (2.20). One advantage of this technique is that it does not rely in a feedback loop, so the system stand-alone stability margins are not affected. A similar feed-forward technique can be used to reject current oscillations in voltage-controlled systems, this time by shaping the system impedance to zero [Deng et al., 2008].

In any case, the bandwidth where an effective voltage oscillation rejection is achieved (i.e. where the admittance is low) is limited by the presence of computational delays and the usually discrete nature of the implemented controller [Yang et al., 2014], as any other admittance shaping technique. Moreover, it is important to remark that, even though these techniques enhance the voltage oscillation-rejection capability, they usually have a negative effect on the stability-robustness from a complex network (impedance-based criterion) point of view:

- The abrupt reduction of the closed-loop admittance (i.e. resonant impedance behaviour) that is achieved using multiple PR feedback gains in the controller supposes a high risk of interaction (instabilities) with weak grids, mainly because of the possible non-passive behaviour of the system around the tuned frequencies [Kwon et al., 2014, Harnefors et al., 2014].
- The use of feed-forward techniques to reject oscillations does not improve the system robustness. In that case, the *perfect* cancellation of the shaped system admittance induces a great phase-delay which may result in non-passive system behaviour (mainly in the presence of integral PI feedback controllers) [Yang et al., 2014].

3. Improvement of the grid voltage quality, filtering it from (sub/inter)harmonics so other system connected to it (via the PCC) are not affected by them:

Instead of rejecting the effect of PCC voltage oscillations in the current control, achieved by means of low admittance profiles, this third group of applications filters eventual voltage oscillations so other elements connected to the same PCC are not affected by them. The idea is to behave as a high admittance (i.e. low impedance), so this new system drains any possible current oscillation at the problematic frequencies, damping the resulting PCC voltage oscillations. These PEC-based applications can be considered, then, as effective grid stabilizers.

Consider now the structure shown in Fig. 2.11, where a non-linear load consumes a current (i_h) with harmonic content from the grid. With a non-ideal (linear) grid impedance (i.e. $Z_g(s) \neq 0$), the PCC voltage (v_s) will be affected by the same harmonics than the non-linear load current.

A classic solution to reject the effect of non-linear loads in the PCC (i.e. voltage harmonics) is the use of shunt-connected active power filters (APF) (refer to section A.8.3 for more details about this application). This method does not use any admittance/impedance shaping technique to achieve optimal results [Akagi et al., 2007, Morán et al., 1995, Akagi et al., 1986, Akagi, 2005, Lascu et al., 2009]. Its main disadvantage is that it is necessary the measurement of the non-linear load current which effect is wanted to be rejected, which is not always accessible. A very similar technique is reported in [He et al., 2012] using voltage-controlled systems. This technique does not need the measurement of the non-linear load current, but only the PCC voltage, more precisely its non-fundamental frequency oscillations. Once measured, their negated forms are injected again to the PCC to partially compensate them; how much they are compensated depends on the line impedance between the voltage-controlled system and the grid.

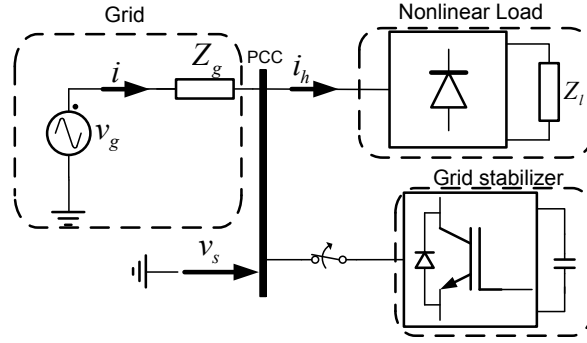


Figure 2.11. Non-linear load (e.g. a diode-rectifier) connected to the grid that may induce grid PCC voltage (v_s) harmonics. In parallel, a shunt-connected PEC-based application that filters this PCC voltage.

Similar results have been achieved using admittance/impedance shaping techniques. On [Takeshita and Matsui, 2003, Akagi et al., 2007], an external PCC voltage feed-forward loop (position 2 in Fig. 2.8) is used to shape the system closed-loop admittance; the PCC voltage (v_s) is measured, filtered (extracting the desired voltage harmonics to be compensated), passed through a feed-forward gain (K_{v_s}) and finally introduced in the reference current (i^*). If a good tracking is obtained at these harmonic frequencies (i.e. $|T(j\omega_x)| = 1$), the feed-forward gain (K_{v_s}) directly shape the system admittance at those frequencies (ω_x) (see equation 2.21). The higher K_{v_s} gain is, the higher the obtained closed-loop admittance will be at the considered harmonic frequencies, draining any possible grid current harmonics and resulting in a *cleaner* PCC voltage. This technique has, then, the big advantage of not measuring the non-linear load currents that trigger the PCC voltage harmonics. Note, however, that a good tracking is still necessary at the problematic frequencies, normally achieved using multiple PR controllers, which implies high feedback gains and the consequent reduction of the system stand-alone stability margins.

A similar concept has been used to damp eventual PCC voltage oscillations in the presence of weak resonant grids like the one shown in Fig. 2.3 [Wang et al., 2014a, Akagi et al., 2007]. Demanding current for these kind of grids may result in poorly damped PCC voltage oscillations. Again, a shunt-connected PEC-based application with a high equivalent admittance should serve as a *power pit* to any grid-current oscillations, damping possible grid impedance resonances, filtering the PCC voltage and stabilizing the weak grid. The higher is this closed-loop admittance, the *cleaner* the PCC voltage will be. As this kind of oscillations may appear at any frequency, a broader frequency band of high shaped admittance is desired. For that reason, it is more likely the use of an internal PCC voltage (v_s) feed-forward loop (position 1 in Fig. 2.8) to shape the admittance, as this technique only relies in feed-forward gains and the system stability margins are not affected by it. The closed-loop admittance gain ($|Y'|$) can be increased with higher $|K_{v_s}|$ values at the problematic frequencies, as it was demonstrated in equation (2.20).

This last objective can be also achieved by using voltage-controlled PEC-based systems with a similar impedance-shaping capability [Wang et al., 2012]. A scheme similar to the one shown in Fig. 2.8, using an external feed-forward loop (K_{i_s}) of the grid-side current (i_s in Fig. A.13), is used to shape the system impedance (Z) so that it negates the grid impedance (Z_g) effect (i.e. $Z = -Z_g$ is desired). By doing so, the PCC voltage is no longer affected by current oscillations triggered by non-linear loads (Fig. 2.11) or by resonant weak grids. However, only inductive grids are considered and a good model of the grid impedance is necessary, being possible to unstabilize the system if this impedance is over-dimensioned.

Impedance-droop control

Finally, the impedance-shaping of voltage-controlled PEC-based systems is also used in the literature to coordinate efforts in complex smart grids, by means of an impedance-droop technique [He and Li, 2012, Guerrero et al., 2005, He and Li, 2011, Chiang and Chang, 2001].

2.4 Robust control

The long-term objective of robust control applied to PEC-based systems is the design of controllers that, while maintaining a certain minimum performance regarding the converter reference tracking and disturbance rejection, are able to overcome an arbitrary amount of uncertainty in model parameters [Cóbreces, 2009].

Different design frameworks follow a robustness motivation, either implicitly or explicitly:

- **Implicitly robust frameworks:** Some examples are the Internal Model Control (IMC) [Harnefors and Nee, 1998], which present good robustness properties, even though its appliance to complex dynamics is difficult, and the Linear-Quadratic (LQ) controllers [Perez et al., 2013, Huerta et al., 2012, Alepuz et al., 2006, Wu and Lehn, 2005], that present interesting robustness properties provided that a state estimator is not used.
- **Explicitly robust frameworks:** Robust synthesis is the process that allows to extract a controller that produces a stable closed-loop when applied to an a-priori known set of plants. In other words, it can be viewed as a controller that stabilizes a plant that is *uncertain* to some extent [Cóbreces, 2009]. Some design frameworks examples of this are the non-linear sliding-mode controllers [Dias et al., 2008, Jung and Tzou, 1996, Miret et al., 2004, Moharana and Dash, 2010], the Lineal Matrix Inequalities (LMI) [Gabe et al., 2009, Gabe et al., 2007, Durrant et al., 2004], the Quantitative Feedback Theory (QFT) [del Toro et al., 2016, Altowati et al., 2007, Towati, 2008, Olalla et al., 2009] and the \mathcal{H}_∞ (sub)optimal framework [Rahim and Kandlawala, 2004, Cóbreces et al., 2010, Cóbreces, 2009].

Among them, the design technique that has received more attention in the specialised literature is the \mathcal{H}_∞ (sub)optimal framework thanks to the robustness implications of its synthesis.

Small Gain Theorem

\mathcal{H}_∞ controller synthesis, apart of achieving certain user-defined performance objectives (e.g. tracking, disturbance rejection etc.) for a nominal plant, provides of good indicators of the close-loop system robustness when this nominal plant suffers from certain known parametric uncertainties. Moreover, unlike other optimal design techniques like LQ controllers, \mathcal{H}_∞ theory provides of a way to design controllers that satisfy robustness specifications even in the case that some state variables need to be estimated.

The stability analysis of these uncertain plants is done by means of the Small Gain Theorem [Skogestad and Postlethwaite, 2007]. Applied to this scenario, the Small Gain Theorem introduces a condition to the \mathcal{H}_∞ norm of the closed-loop nominal plant (i.e. the one that results from the connection of the nominal plant and the synthesized controller) and the \mathcal{H}_∞ norm of a function that measures the *size* of the plant uncertainties, known as the l_2 -induced gap metric or v-gap [Vinnicombe, 2000], which gives an idea of how much the plant dynamic can vary as a

function of the frequency; if this condition is met, the controller will result in a robustly stable closed-loop system for all the plants within the considered uncertain set.

Robustness towards grid uncertainties

From the robustness point of view, it is known that the stability of the control loop in current-controlled grid-connected PEC-based systems may be compromised by the uncertainty in the grid equivalent impedance, which may lead to the uncontrolled displacement of resonances inside the control band [Liserre et al., 2004b]. It is possible to derive a controller that is robustly stable for different grid conditions by including these a-priory known grid parametric uncertainties in the modelled plant.

Some works have tried to propose an \mathcal{H}_∞ control design method that, given an initial expected grid impedance parameters variation range, synthesizes a controller that ensures stability for all possible conditions [Cobreces et al., 2010, Gabe et al., 2009]. However, this improvement in the system robustness comes at the cost of a conservative performance -control bandwidth-reduction (i.e. poor tracking and disturbance rejection responses), as a consequence of the need to comply with the aforementioned Small Gain Theorem.

The impedance-based stability criterion introduced in section 2.2.1 open the door to face this robustness problem from an alternative point of view; instead of the fulfilment of the conservative Small Gain Theorem, it allows to face the problem trying to comply with certain input admittance conditions (derived from the impedance-based stability criterion and the uncertain grid impedance). This may decrease the closed-loop performance reduction induced by uncertainty in the grid parameters when a classic \mathcal{H}_∞ robust design is implemented. Admittance shaping techniques detailed in section 2.3 may be of main importance to comply with these new robustness conditions. Particularly interesting proposals can be found in [Mosskull, 2014] and [Freijedo et al., 2016]. The former calculates a (theoretical) suitable closed-loop admittance of a motor drive that results in a robustly stable system when connected to a DC resonant grid for a known set of model uncertainties, using to that end the impedance-based criterion and the robust \mathcal{H}_∞ synthesis; however, the controller design to obtain this admittance is still approached from a classical point of view. The latter assesses the closed-loop poles derived from the interaction between the grid impedance (Z_s) and the converter admittance (Y_l) (i.e. zeros of the characteristic equation $1 + Z_s Y_l$) for variations of the current controller parameters. The system is considered robustly stable for a given grid impedance when the current controller makes the closed-loop poles (in the s domain) move away as far as possible from the imaginary axis. The proposed assessment shows that, for the considered converter plant and grid impedance, optimal results are obtained when the used LCL filter resonance is perfectly damped, as advanced in the risk factors for networks stability exposed in section 2.2.1.

2.5 Analysis of the state of the art, thesis hypothesis and objectives

2.5.1 Analysis of the state of the art

The aforementioned admittance shaping works share the strategy of modifying the converter admittance/impedance on a particular -problematic- frequency, or in a small set of discrete frequencies, using classical control design procedures.

In general terms, the aforementioned works offer satisfactory results on the target frequencies,

solving a particular problem scenario; but the controller design complexity induces limitations when facing wide-band (robust) designs, and also in the management of the trade-offs between the admittance/impedance shaping at different frequencies and other control objectives such as reference tracking or the system stand-alone stability.

The controller design, from a classical point of view, of controllers that has to deal with multiple objectives (e.g. reference tracking, stand-alone and complex-networks stability robustness, harmonic rejection/attenuation, resonance damping, control effort (energy) optimization etc.), and their different associated control trade-offs (some of these objectives are mutually exclusive), is very complex. Even only from an admittance shaping point of view (i.e. without considering tracking or stand-alone stability design specifications), this means that the system should follow different (complex) dynamic behaviours depending on the objective to be fulfilled and its frequency range of application. These design problems grow even more in the presence of complex plants (from a dynamic point of view).

Approaching the control design of this kind of applications from a more tractable and unified framework could be, then, an interesting field of research.

2.5.2 Hypothesis

This dissertation parts of the hypothesis that a (sub)optimal design method may simplify the achievement of admittance shaping controllers, unifying the different admittance shaping methods and their objectives in a single design framework. This design methodology should, at the same time, deal with other controller objectives, such as the reference tracking performance, the energy optimization or the stand-alone robustness of the system, solving the associated controller trade-offs in a more tractable way.

The \mathcal{H}_∞ model-reference control design framework seems like a good tool to approach to this complex control paradigm. This approach is based in the definition of dynamic model-references that define the desired closed-loop behaviour of the system in the frequency domain, both in magnitude and in phase. After this definition, a (sub)optimal \mathcal{H}_∞ algorithm synthesizes a suitable controller that achieves the desired dynamics (i.e. model-references).

That is, using this framework it should be possible to shape the closed-loop admittance (Y) of the system by defining admittance model-reference (Y_{ref}). The possibilities that may arise, from an admittance shaping point of view, of this design methodology hypothesis are wide. Theoretically, the designer has only to provide the desired behaviour of the closed-loop admittance, depending on the desired control objective/application, as well as the frequency range where this behaviour is desired; the \mathcal{H}_∞ synthesis algorithm should, then, provide of a (sub)optimal controller that achieves these objectives, by means of feedback and/or feed-forward gains, as needed. Hypothetically, complex admittance profiles may be achieved, then, by defining complex admittance reference (Y_{ref}) profiles. Moreover, good admittance shaping should be obtained in a broad band in an easier way that the aforementioned classic approaches, and the plant dynamic should have less influence in the controller design and synthesis complexity.

This thesis also states the hypothesis that the model-reference framework can be useful to shape dynamically complex open loop plants, simplifying them from a controller design point of view. Of particular interest is the shaping of resonant plants such as the LCL filter. By defining a model-reference equivalent to a simple L filter, the introduced framework should shape the LCL filter resonance in a similar fashion than active dampers do. If a successful active-damper is synthesized using this framework, its implementation should make possible to apply simpler classic current controllers (e.g. PI and/or PR) in the complex LCL filter without renouncing to

the overall system robustness, both from a stand-alone and a complex-network (i.e. impedance-based criterion) points of view.

2.5.3 Objectives

This dissertation tries to fulfil the next objectives:

1. Provide of a unified and simpler design framework for the admittance shaping of PEC-based applications in a broad band, applying modern (sub)optimal techniques.
2. Presented method should be general enough to achieve different (complex) admittance profiles to fulfil different admittance-shaping objectives. At the same time, the proposed framework should be able to achieve other control objectives, as current reference tracking, energy optimization and robust stand-alone stability.
3. Explain the design methodology and the different control trade-offs that must be faced.
4. Explore the limitations of the method and, in case they exist, provide of solutions/improvements to their performance effect.
5. Apply the proposed design methodology to different admittance shaping applications and analyse, experimentally and/or by means of realistic simulations, the obtained results.
6. Study the application of the method to other related PEC-based system problems, as the shaping of complex plant dynamics.

Chapter 3

Introduction to (sub)optimal control

3.1 Introduction

This chapter serves as a descriptive introduction to some of the concepts and control tools that are later used in this dissertation. In addition, an \mathcal{H}_∞ mixed-sensitivity controller design is applied to a power-converter based application, serving as a design example of \mathcal{H}_∞ controllers. The main control limitations are exposed and some experimental results are presented. Additionally, this chapter contextualizes the controller design framework used for the main contributions of this dissertation; the \mathcal{H}_∞ model reference approach.

Section 3.2 introduces the optimal control paradigm, its main approaches (\mathcal{H}_∞ and \mathcal{H}_2) and their advantages and the important general control problem formulation concept. Once the theoretical background of the \mathcal{H}_∞ space has been settled, section 3.3 presents a classic \mathcal{H}_∞ mixed sensitivity control approach. This design framework is explained and applied to a grid connected VSC grid current control, deriving its main design limitations. Some experimental results, both in time and frequency domains, are shown at the end of this section. Finally, section 3.4 introduces the \mathcal{H}_∞ model reference approach and its application to the main contributions of this dissertation; the closed-loop admittance shaping and the resonant plant shaping of power converter-based applications.

3.2 Optimal control

3.2.1 Concept and advantages

A control paradigm is considered optimal if its objective is to find a controller for a given system (i.e. plant) such that a certain optimality criterion is achieved. The common element in any optimal control method is the minimization of a cost function that includes both the controller and the plant dynamics, along with some plant modifiers named cost weights; the optimal controller is the one that minimize this cost function given the (modified/augmented) plant dynamics¹.

In the classical control paradigm, the designer obtains a controller for a given plant dynamic following some heuristic rules based on its knowledge and experience, so that the closed-loop system fulfils some given objectives (e.g. good reference tracking performance, robustness etc.). This task becomes harder in case of complex plant dynamics to be controlled (e.g. multiple-

¹A controller will be considered suboptimal if it does not achieve the considered cost function minimum.

inputs multiple-outputs, MIMO, plants), or if different objectives must be fulfilled, some of which may even be mutually exclusive. Modern optimal control gives a way to handle complex control problems, allowing to solve the different trade-offs between different control objectives in a more tractable way. To do that, it transfers part of the design complexity to a computational algorithm that synthesizes the (sub)optimal control for a given set of design specifications. Even though some trial and error design process (following some intuitive heuristic rules) is still usually necessary for achieving better closed-loop results, the convex nature of the underlying optimisation algorithm guarantees that an (sub)optimal controller is found. The controller obtaining complexity is, then, reduced for difficult control applications.

Optimal control reached maturity in the 1960's, with the development of the linear quadratic (LQ) optimal control methodology, for its application in spacecraft control during the Space Race between the former Soviet Union and the United States. For these kind of applications, to achieve a good rocket manoeuvring with minimum fuel consumption can be well defined and easily formulated as an optimization problem [Skogestad and Postlethwaite, 2007]. Even though LQ optimal control, in particular Linear Quadratic Gaussian (LQG) control, was proved successful for aerospace engineering and other frameworks, its use in other industrial applications is, in practice, not robust enough; accurate plant models were frequently not available, and the assumption of white noise disturbances was not always relevant or meaningful to practising control engineers [Skogestad and Postlethwaite, 2007]. This resulted in the development of other optimal control frameworks, like the \mathcal{H}_∞ control synthesis used in this dissertation.

3.2.2 General control problem formulation

Optimal control synthesis process usually depends on a common general control problem formulation, or generalised plant $\mathbf{P}(s)$, as their entry point [Skogestad and Postlethwaite, 2007]. This virtual plant is a mathematical instrument that incorporates the open-loop plant that models the system to be controlled, along with a set of extra transfer function that are defined by the designer to specify the main control objectives and restriction, defining, in some way, the desired closed-loop behaviour of the system. Structurally, \mathbf{P} is a plant with two (vector) inputs and two (vector) outputs:

$$\begin{bmatrix} \mathbf{z} \\ \mathbf{v} \end{bmatrix} = \underbrace{\begin{bmatrix} \mathbf{P}_{11} & \mathbf{P}_{12} \\ \mathbf{P}_{21} & \mathbf{P}_{22} \end{bmatrix}}_{\mathbf{P}} \begin{bmatrix} \mathbf{w} \\ \mathbf{u} \end{bmatrix}; \quad \mathbf{z} = \mathbf{N}\mathbf{w}; \quad (3.1)$$

where \mathbf{w} is called the exogenous inputs vector, usually composed of the disturbances to the closed-loop system (i.e. mainly control references and disturbances); input vector \mathbf{u} and output vector \mathbf{v} are formed by the inputs and outputs of the controller to be synthesized (\mathbf{K}), respectively; and \mathbf{z} is the vector of the so-called output *error* signals, that are to be minimised in some sense to meet control objectives. The transfer matrix \mathbf{N} is the generalized closed-loop matrix that results from the feedback interconnection of \mathbf{P} and \mathbf{K} , and relates exogenous input vector \mathbf{w} and *error vector* \mathbf{z} :

$$\mathbf{N} = \text{lft}(\mathbf{P}, \mathbf{K}) = \mathbf{P}_{11} + \mathbf{P}_{12}\mathbf{K}(\mathbf{I} - \mathbf{P}_{22}\mathbf{K})^{-1}\mathbf{P}_{21} \quad (3.2)$$

The objective of the considered optimal controller synthesis is to obtain a controller \mathbf{K} that minimize, in some way, the effect of \mathbf{w} over \mathbf{z} .

To measure how *big* this effect is, different matrix norms of the closed-loop matrix (\mathbf{N}) can be considered as the cost function to be minimized. Attending to the norm considered, the most

common control paradigms are the \mathcal{H}_2 and \mathcal{H}_∞ , explained in more detail later. The optimal controller synthesis following a general control approach can be formulated, then, as follows;

$$\min_{\mathbf{K}} \|\mathbf{N}(\mathbf{K})\|_p \leq \gamma \quad (3.3)$$

where p depends on the considered system norm (e.g. 2, ∞ , etc.) and γ is usually a sub-optimal value.

A wide set of control problems and structures can be formulated following this general scheme. Fig. 3.1 shows the translation of the classic one DOF feedback control scheme into the generalized control scheme. In this control problem, the objective is to minimize the tracking error (e), limiting the allowed controller effort (u) to elude saturation or any other physical actuation constraint. These two variables will form, then, the output vector to be minimized (\mathbf{z}). The exogenous inputs to the closed-loop system (i.e. the output reference y^* , the output disturbance signal d and the measurement noise n) form the input vector \mathbf{w} . Finally, as a one DOF controller for a SISO plant (G) is considered, the output vector \mathbf{v} and input vector \mathbf{u} are simply the controller (K) input (e) and output (u), respectively.

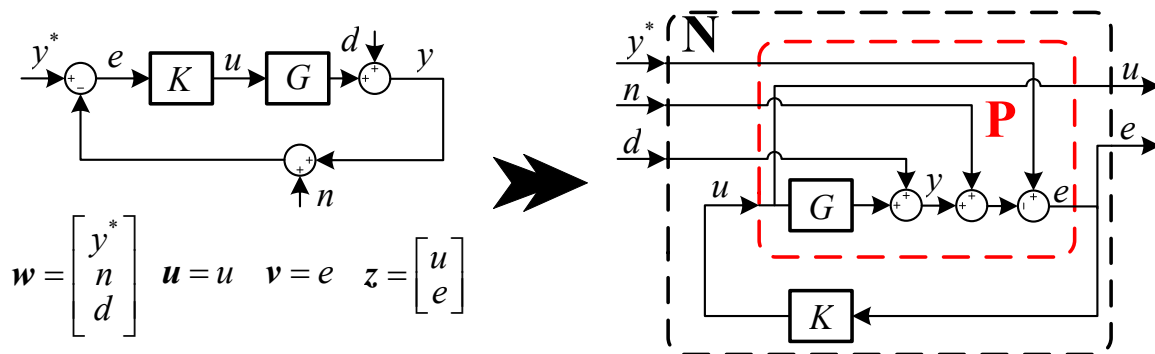


Figure 3.1. Translation of the classic one DOF feedback control scheme into the generalized control scheme.

The synthesized optimal controller (K) will try to minimize the effect of the exogenous inputs (\mathbf{w}) on both tracking error (e) and controller effort (u) attending to the considered cost function (i.e. $\|\mathbf{N}\|_p$). The minimization of both signals may not be possible at the same time; to effectively reduce the tracking error (e) a high actuation (u) may be needed. In addition, the importance of the different exogenous signals (\mathbf{w}) in the minimization problem may not be of equal importance; may be the designer prefers that the tracking error (e) is minimized with higher focus on the variations of the reference signal (y^*), rather than the measurement noise signal (n). To solve this conflicts, designer usually has to include weights in the generalized plant \mathbf{P} to normalize the exogenous inputs vector (\mathbf{w}), named $\tilde{\mathbf{W}}_w$, and/or, more commonly, to weight the errors vector (\mathbf{z}), named $\tilde{\mathbf{W}}_z$, as shown in Fig. 3.2.

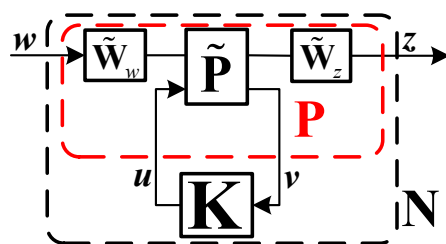


Figure 3.2. General control configuration with weighted/normalized input vector \mathbf{w} and output vector \mathbf{z} .

These weighting matrices are usually frequency-dependent and represent the main design element of the considered optimal control paradigm.

3.2.3 Order of the synthesized controller

One of the main disadvantages attributable to optimal control is the probable high order of the synthesized controller. The order of \mathbf{K} is that of the augmented plant transfer function (\mathbf{P}). That is, the controller (\mathbf{K}) in Fig. 3.2 will have the order of the sum of orders of the unmodified open-loop plant ($\tilde{\mathbf{P}}$), the normalization function ($\tilde{\mathbf{W}}_w$) and the weighting function ($\tilde{\mathbf{W}}_z$) that are contained inside \mathbf{P} . From a practical point of view, that means that complex plant dynamics (i.e. high order of $\tilde{\mathbf{P}}$) and/or complex design specifications (i.e. high order of $\tilde{\mathbf{W}}_w$ and/or $\tilde{\mathbf{W}}_z$) imply an increase in the final controller (\mathbf{K}) computational burden.

The fast improvement of digital processors computation capability, with the increase of their *flops/\$* ratio, makes this disadvantage less of an issue nowadays. In any case, order reduction techniques can be used, if necessary, to lighten the computation burden of the implemented controller. An example of this can be found in section 5.5.

3.2.4 Main optimal control approaches

\mathcal{H}_2 optimization approach

The \mathcal{H}_2^2 norm of a strictly proper stable MIMO closed-loop transfer matrix $\mathbf{N}(s)$ of dimensions $i \times j$ is defined as [Skogestad and Postlethwaite, 2007]:

$$\|\mathbf{N}(s)\|_2 = \left(\frac{1}{2\pi} \int_{-\infty}^{\infty} \sum_{ij} |N_{ij}(j\omega)|^2 d\omega \right)^{1/2} \quad (3.4)$$

which for a SISO case is simplified to:

$$\|N(s)\|_2 = \left(\frac{1}{2\pi} \int_{-\infty}^{\infty} |N(j\omega)|^2 d\omega \right)^{1/2} \quad (3.5)$$

Note how if $N(s)$ is a proper (but not strictly proper) transfer function (i.e. $\lim_{s \rightarrow \infty} N(s)$ is a non-zero constant) its \mathcal{H}_2 norm is infinite and, then, not bounded.

There are different interpretations of the \mathcal{H}_2 norm of a system that are useful from a control theory point of view. The \mathcal{H}_2 norm of $\mathbf{N}(j\omega)$ can be expressed as a function of their singular values (see section A.3):

$$\|\mathbf{N}(s)\|_2 = \left(\frac{1}{2\pi} \int_{-\infty}^{\infty} \sum_i \sigma_i^2(\mathbf{N}(j\omega)) d\omega \right)^{1/2} \quad (3.6)$$

From a frequency domain point of view, minimizing the \mathcal{H}_2 norm of $\mathbf{N}(j\omega)$ involves, then, minimizing the sum of the square of all the singular values over all frequencies. That is, the $\mathbf{N}(j\omega)$ gain will be minimized for an *average direction* and an *average frequency* of its input vector \mathbf{w} (i.e. in practice, for all \mathbf{w} directions and frequencies).

²The symbol \mathcal{H}_2 stands for the Hardy space of transfer functions with bounded 2-norm, which is the set of stable and strictly proper transfer functions [Skogestad and Postlethwaite, 2007]

From a time domain point of view, using an inverse Laplace transformation of $\mathbf{N}(j\omega)$ (i.e. $\mathcal{L}^{-1}\{\mathbf{N}(s)\} = \mathbf{n}(t)$), the \mathcal{H}_2 norm of the closed-loop system can be expressed, following Parseval's theorem, as:

$$\|\mathbf{N}(s)\|_2 = \|\mathbf{n}(t)\|_2 = \left(\sum_{ij} \int_0^\infty |n_{ij}(\tau)|^2 d\tau \right)^{1/2} \quad (3.7)$$

where $n_{ij}(t)$ is the ij^{th} element of the impulse response matrix $\mathbf{n}(t)$. That is, the \mathcal{H}_2 norm is the 2-norm of the output $\mathbf{z}(t)$ resulting from applying unit impulses $\delta_j(t)$ to each element of \mathbf{w} (i.e. $w_1(t) \dots w_j(t)$), one after another, allowing the output $\mathbf{z}(t)$ to settle to zero before applying an impulse to the next input:

$$\|\mathbf{N}(s)\|_2 = \left(\sum_j \|\mathbf{z}_j(\tau)\|_2^2 \right)^{1/2} \quad (3.8)$$

being $\mathbf{z}_j(t)$ ³ the output vector resulting from applying a unit impulse $\delta_j(t)$ to the j^{th} input ($w_j(t)$), setting the rest inputs to zero [Skogestad and Postlethwaite, 2007].

Finally, \mathcal{H}_2 norm of the system $\mathbf{N}(j\omega)$ has a stochastic interpretation. Suppose that the input vector $\mathbf{w}(t)$ is white noise of unit intensity:

$$E\{\mathbf{w}(t)\mathbf{w}(\tau)^T\} = \mathbf{I}\delta(t - \tau) \quad (3.9)$$

where $E\{\mathbf{w}(t)\mathbf{w}(\tau)^T\}$ represents the covariance or mathematical expectation of the input vector $\mathbf{w}(t)$. The expected output vector $\mathbf{z}(t)$ is, in that case, given by;

$$E \left\{ \lim_{T \rightarrow \infty} \frac{1}{2T} \int_{-T}^T \mathbf{z}(t)^T \mathbf{z}(t) dt \right\} \quad (3.10)$$

which, by Parseval's Theorem:

$$E \left\{ \lim_{T \rightarrow \infty} \frac{1}{2T} \int_{-T}^T \mathbf{z}(t)^T \mathbf{z}(t) dt \right\} = \|\mathbf{N}(s)\|_2^2 \quad (3.11)$$

Then, by minimizing the \mathcal{H}_2 norm of $\mathbf{N}(s)$, the output \mathbf{z} due to a unit intensity white noise input \mathbf{w} is minimized [Skogestad and Postlethwaite, 2007].

From the stochastic interpretation of the \mathcal{H}_2 norm, it can be deduced that the classic LQG (Lineal-Quadratic Gaussian) optimal controller is, in fact, a special \mathcal{H}_2 optimal controller. Consider the next stochastic system expressed in state-space:

$$\frac{d\mathbf{x}}{dt} = \mathbf{A}\mathbf{x} + \mathbf{B}\mathbf{u} + \mathbf{w}_d \quad (3.12)$$

$$y = \mathbf{C}\mathbf{x} + \mathbf{w}_n \quad (3.13)$$

where \mathbf{w}_d and \mathbf{w}_n are the process noise and measurement noise inputs respectively, which are assumed uncorrelated white noise processes with covariances:

$$E \left\{ \begin{bmatrix} \mathbf{w}_d(t) \\ \mathbf{w}_n(t) \end{bmatrix} \begin{bmatrix} \mathbf{w}_d(t)^T & \mathbf{w}_n(t)^T \end{bmatrix} \right\} = \begin{bmatrix} \mathbf{W} & \mathbf{0} \\ \mathbf{0} & \mathbf{V} \end{bmatrix} \delta(t - \tau) \quad (3.14)$$

³The 2-norm of a vector function of time, known as the vector energy, is $\|\mathbf{z}(t)\|_2 = (\int_0^\infty \sum_i |z_i(t)|^2 dt)^{1/2}$, being $z_i(t)$ the elements of $\mathbf{z}(t)$

where \mathbf{W} and \mathbf{V} are constant power spectral density matrices. The LQG control paradigm objective is to find a controller $\mathbf{K}(s)$ so that, for an actuation $\mathbf{u} = \mathbf{K}(s)\mathbf{y}$, the next cost function is minimized:

$$J = E \left\{ \lim_{T \rightarrow \infty} \frac{1}{T} \int_0^T (\mathbf{x}^T \mathbf{Q} \mathbf{x} + \mathbf{u}^T \mathbf{R} \mathbf{u}) dt \right\} \quad (3.15)$$

where $\mathbf{Q} = \mathbf{Q}^T$ and $\mathbf{R} = \mathbf{R}^T$ are positive semi-definite and positive definite constant matrices, respectively, defined by the designer to establish the desired closed-loop dynamics.

LQG optimization is considered a special LQR (Linear-Quadratic Regulator) problem where all system states (\mathbf{x}) are estimated by a Kalman Filter to improve the estimation in noising environments [Huerta et al., 2012]. So, after the LQG optimization, a controller \mathbf{K} which measure only the output vector \mathbf{y} is synthesised, estimating the states \mathbf{x} and filtering the effect of the previously defined white noise processes \mathbf{w}_n and \mathbf{w}_d .

Considering now a closed-loop general problem formulation $\mathbf{N}(s)$, with an error vector

$$\mathbf{z} = \begin{bmatrix} \mathbf{Q}^{1/2} & 0 \\ 0 & \mathbf{R}^{1/2} \end{bmatrix} \begin{bmatrix} \mathbf{x} \\ \mathbf{u} \end{bmatrix} \quad (3.16)$$

and representing the stochastic inputs \mathbf{w}_d and \mathbf{w}_n as

$$\begin{bmatrix} \mathbf{w}_d \\ \mathbf{w}_n \end{bmatrix} = \begin{bmatrix} \mathbf{W}^{1/2} & 0 \\ 0 & \mathbf{V}^{1/2} \end{bmatrix} \mathbf{w} \quad (3.17)$$

where \mathbf{w} is a white noise process of unit intensity, it is clear that the LQG cost function is:

$$J = E \left\{ \lim_{T \rightarrow \infty} \frac{1}{T} \int_0^T (\mathbf{x}^T \mathbf{Q} \mathbf{x} + \mathbf{u}^T \mathbf{R} \mathbf{u}) dt \right\} = E \left\{ \lim_{T \rightarrow \infty} \frac{1}{2T} \int_{-T}^T \mathbf{z}(t)^T \mathbf{z}(t) dt \right\} = \|\mathbf{N}(s)\|_2^2 \quad (3.18)$$

Fig. 3.3 shows the LQG problem formulated in the general control configuration.

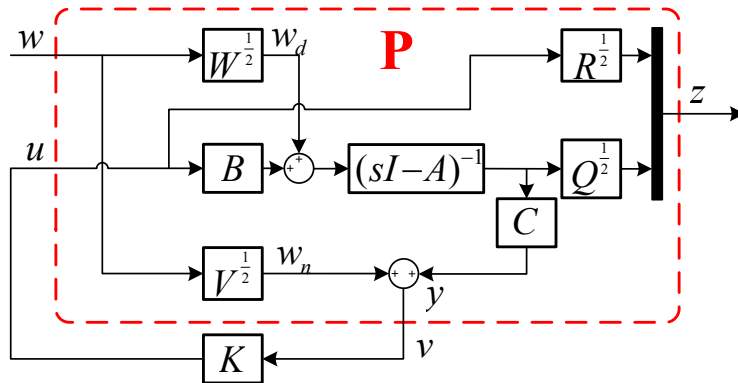


Figure 3.3. LQG problem expressed as a general control formulation.

Several works have studied the use of LQ controllers in power converter-based applications. In particular, [Perez et al., 2013, Huerta et al., 2012] were elaborated in the same research group in which this dissertation has been developed.

\mathcal{H}_∞ optimization approach

The \mathcal{H}_∞ ⁴ norm of a proper stable MIMO closed-loop transfer matrix $\mathbf{N}(s)$ of dimensions $i \times j$ is defined as:

$$\|\mathbf{N}(s)\|_\infty = \lim_{p \rightarrow \infty} \left(\int_{-\infty}^{\infty} \sum_{ij} |N_{ij}(j\omega)|^p d\omega \right)^{1/p} \quad (3.19)$$

which for a SISO case is simplified to:

$$\|N(s)\|_\infty = \lim_{p \rightarrow \infty} \left(\int_{-\infty}^{\infty} |N(j\omega)|^p d\omega \right)^{1/p} \quad (3.20)$$

Note how if $N(s)$ is a proper or strictly-proper transfer function (i.e. $\lim_{s \rightarrow \infty} N(s)$ is a constant) its \mathcal{H}_∞ norm is bounded and is, in fact, the maximum gain value ($|N(j\omega)|$) over the frequency ω [Skogestad and Postlethwaite, 2007]:

$$\|N(s)\|_\infty = \max_{\omega} |N(j\omega)| \quad (3.21)$$

For a MIMO system, the \mathcal{H}_∞ norm can be expressed as a function of $\mathbf{N}(s)$ singular values:

$$\|\mathbf{N}(s)\|_\infty = \lim_{p \rightarrow \infty} \left(\int_{-\infty}^{\infty} \sum_i \sigma_i^p(\mathbf{N}(j\omega)) d\omega \right)^{1/p} = \max_{\omega} \bar{\sigma}(\mathbf{N}(j\omega)) \quad (3.22)$$

From a frequency domain point of view, minimizing $\|\mathbf{N}(j\omega)\|_\infty$ corresponds, then, to minimizing the peak (i.e. maximum value) of its largest singular value ($\bar{\sigma}(\mathbf{N}(j\omega))$). That is, the $\mathbf{N}(j\omega)$ gain will be minimized for the *worst-case direction* and *worst-case frequency* of its input vector \mathbf{w} . Comparing with the \mathcal{H}_2 norm, we have that minimizing \mathcal{H}_∞ norm will only reduce the maximum gain peak of $\mathbf{N}(j\omega)$, meanwhile \mathcal{H}_2 will minimize it in a wider sense (i.e. all singular values over all frequencies) [Skogestad and Postlethwaite, 2007].

From a time domain point of view, the \mathcal{H}_∞ norm of $\mathbf{N}(s)$ can be simply expressed as:

$$\|\mathbf{N}(j\omega)\|_\infty = \max_{\mathbf{w}(\omega) \neq 0} \frac{\|\mathbf{z}(\omega)\|_2}{\|\mathbf{w}(\omega)\|_2} = \max_{\mathbf{w}(t) \neq 0} \frac{\|\mathbf{z}(t)\|_2}{\|\mathbf{w}(t)\|_2} = \max_{\|\mathbf{w}(t)\|_2=1} \|\mathbf{z}(t)\|_2 \quad (3.23)$$

That is, minimizing $\|\mathbf{N}(j\omega)\|_\infty$ correspond to minimize the ratio between the energy (norm-2) of the error vector ($\mathbf{z}(t)$) and the exogenous input vector ($\mathbf{w}(t)$).

This time-domain interpretation of the \mathcal{H}_∞ norm is the basis for the model reference controller design approach used in this dissertation for the shaping of closed-loop systems and plants.

Although \mathcal{H}_∞ synthesis presence on the control of DC/AC converters is still incipient, some approaches have been published in the field of current and voltage control reference tracking control, robust control, etc. [Mosskull, 2014, Zhong and Hornik, 2012, Hornik and Zhong, 2013, Weiss et al., 2004, Rigatos et al., 2014, Cobreces et al., 2010, Yang et al., 2011, Naim et al., 1997, Lee et al., 2001].

⁴The symbol \mathcal{H}_∞ stands for the Hardy space of transfer functions with bounded ∞ -norm, which is the set of stable and proper transfer functions [Skogestad and Postlethwaite, 2007].

3.3 Basic \mathcal{H}_∞ control approach: Mixed-sensitivity

This section starts with a brief introduction to the basic \mathcal{H}_∞ mixed-sensitivity controller design. Then, this design methodology is applied to a grid-connected current-controlled VSC in subsection 3.3.2. The implementation of a discrete controller obtained using these technique and the derived control limitations are detailed in subsections 3.3.3 and 3.3.4, respectively. The obtained experimental results are exposed at subsection 3.3.5.

3.3.1 Introduction to the method

Classic control objective

To illustrate the method, consider now the one DOF classic feedback scheme shown in the left part of Fig. 3.4.

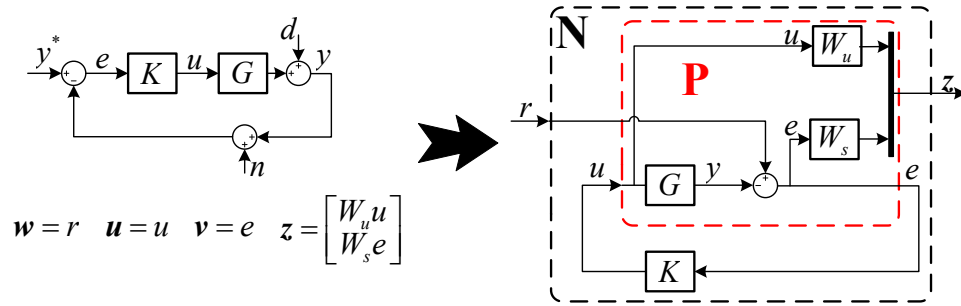


Figure 3.4. Generalized control scheme equivalent to the classic one DOF feedback scheme.

In it, the main objective is that the SISO plant (G) output (y) tracks a given reference (y^*), minimizing the tracking error (e) even for output (d) and noise (n) disturbances. This error minimization is limited by actuation constraints imposed by physical restrictions, controller saturation etc.. The system output (y), control effort (u) and tracking error (e) closed-loop dynamics are as follows;

$$U(s) = F_u(s)(Y^*(s) - D(s) - N(s)) \quad (3.24)$$

$$Y(s) = T(s)Y^*(s) + S(s)D(s) - T(s)N(s) \quad (3.25)$$

$$E(s) = S(s)(Y^*(s) - D(s) - N(s)) \quad (3.26)$$

being the sensitivity (S), tracking (T) and control effort transfer functions (F_u) defined as follows;

$$S(s) = \frac{E(s)}{R(s)} = \frac{1}{1 + L(s)} \quad (3.27)$$

$$T(s) = \frac{Y(s)}{Y^*(s)} = -\frac{Y(s)}{N(s)} = \frac{L(s)}{1 + L(s)} \quad (3.28)$$

$$F_u(s) = \frac{U(s)}{R(s)} = \frac{K(s)}{1 + L(s)} \quad (3.29)$$

being r a generalized disturbance signal:

$$r \equiv y^* \equiv -d \equiv -n, \quad (3.30)$$

and $L(s) = G(s)K(s)$ the loop function. Note that the next equality is met for this one DOF structure:

$$S(s) + T(s) = 1 \quad (3.31)$$

So the controller ($K(j\omega)$) objective inside its bandwidth (i.e. at low frequencies, where the output noise n is usually small) is to obtain a $|S(j\omega)| \rightarrow 0$ and bound, at the same time, $|F_u(j\omega)|$, in order to minimize the tracking error (e) without increasing more than necessary the controller actuation (u) for disturbances (r) transients. At high frequencies, a $|F_u(j\omega)| \rightarrow 0$ and $|T(j\omega)| \rightarrow 0$ (i.e. $|S(j\omega)| \rightarrow 1$) is usually required, so the controller actuation is limited and the effect of measurements noise is minimized.

Translation of the control objectives into an \mathcal{H}_∞ problem

An \mathcal{H}_∞ controller synthesis can be used to solve this frequency domain trade-off in a simple and compact way. Fig. 3.4 shows the translation of the one DOF feedback scheme into the generalized open-loop (**P**) and closed-loop (**N**) plants, as well as the selection of its input and output vector. The objective here is to minimize, in the frequency domain, the sensitivity ($|S(s)|$) and control effort ($|F_u(s)|$) transfer functions gains⁵. To that goal, the exogenous inputs to the system (i.e. y^* , d and n) can be unified in the generalized disturbance signal r (i.e. $\mathbf{w} = r$), being the output vector \mathbf{z} to be minimized defined as follows:

$$z_1 = W_u u = W_u F_u r \quad (3.32)$$

$$z_2 = W_s e = W_s S r \quad (3.33)$$

As explained in section 3.2.4, the \mathcal{H}_∞ synthesis algorithm will obtain a controller $K(s)$ that minimize $\|\mathbf{N}(s)\|_\infty$. That is:

$$\min_{\mathbf{K}} \|\mathbf{N}\|_\infty \leq \gamma, \text{ with } \|\mathbf{N}\|_\infty = \max_{\omega} \bar{\sigma}(\mathbf{N}) = \max_{\mathbf{w}(t) \neq 0} \frac{\|\mathbf{z}(t)\|_2}{\|\mathbf{w}(t)\|_2} = \left\| \begin{array}{c} W_u F_u \\ W_s S \end{array} \right\|_\infty \quad (3.34)$$

being γ (usually) a sub-optimal value.

Design methodology

The \mathcal{H}_∞ minimization problem in (3.34) can be expressed as follows:

$$\bar{\sigma}(\mathbf{N}(j\omega)) = \sqrt{|W_s S|^2 + |W_u F_u|^2} < \gamma, \forall \omega \quad (3.35)$$

If that condition is met (i.e. a sub-optimal controller has been achieved), the previous \mathcal{H}_∞ inequality can be expressed as a stacked problem with two single specifications to fulfil:

$$|S(j\omega)| < \frac{\gamma}{|W_s(j\omega)|}, \forall \omega \Leftrightarrow |W_s S| < \gamma, \forall \omega \Leftrightarrow \|W_s S\|_\infty < \gamma \quad (3.36)$$

$$|F_u(j\omega)| < \frac{\gamma}{|W_u(j\omega)|}, \forall \omega \Leftrightarrow |W_u F_u| < \gamma, \forall \omega \Leftrightarrow \|W_u F_u\|_\infty < \gamma \quad (3.37)$$

That is, if (3.35) is met (3.36) and (3.37) are fulfilled. The design frequency weights (W_s and W_u) can be considered, then, as inverse upper boundaries for the gain of the transfer functions to be minimized in the frequency domain (S and F_u). Higher weights values ($|W_s|$ or $|W_u|$) at a given frequency should result, then, in a higher minimization of their respective transfer functions ($|S|$ or $|F_u|$).

⁵Note that more closed-loop functions can be included in this minimization problem (e.g. the tracking transfer function $T(s)$). However, as the number of function to be minimized increased so does the controller design complexity.

Note, however, that both minimization objectives may be mutually exclusive at the same frequency or impossible to achieve due to physical limitations; for example, ideal sensitivity function minimization (i.e. $|S(j\omega)| \rightarrow 0$, so $|L(j\omega)| \rightarrow \infty$ in (3.27)), theoretically obtained if a high $|W_s(j\omega)| \rightarrow \infty$ is defined, will not be achieved at frequencies where the control effort is highly limited (i.e. $|F_u(j\omega)| \rightarrow 0$, so $|L(j\omega)| \rightarrow 0$ in (3.29)) due to a high $|W_u(j\omega)| \rightarrow \infty$ definition.

That is, the frequency weights must be defined in a complementary manner to achieve better results. In that regard, the scalar γ in (3.36) and (3.37) is an indicator that represents if the performance objectives given by the chosen weights are too demanding. In other words, a higher γ may be obtained when good sensitivity function minimization is desired (i.e. high $|W_s|$ values are defined) at frequencies where it is not possible to obtain such results, due to physical constraints (see subsection 3.3.4) or because the desired actuation minimization at that frequency, bounded by $|W_u|$ definition (3.37), is also high (i.e. a relatively high $|W_u|$ is also defined); the result, in both cases, is a poorer sensitivity function limitation than it was expected from $|W_s|$ definition.

The trade-off between good controller performance (i.e. minimization of e) and energy optimization (i.e. minimization of u) can be, in any case, easily solved by defining the adequate frequency weights.

3.3.2 Application to a power converter current control

This section applies the \mathcal{H}_∞ mixed-sensitivity design explained above to the grid current control of a grid connected VSC through an L filter. The main objective of the proposed controller is to track a given current reference (i^*) rejecting the effect of the main grid voltage (v_s) harmonics (i.e. low frequency harmonics). The system should also be stand-alone robust, with enough gain and phase margins, and with a realizable control effort (i.e. without saturating the VSC voltage limits under nominal transient and disturbance as, for example, voltage dips).

Fig. 3.5 shows a single-phase equivalent of the proposed application. This single-phase system is considered for both modelling and controller design procedures. Obtained controller can be easily translated and implemented in a three-phase system using $\alpha\beta$ stationary reference frame transformations [Krause et al., 2002] for its input and output signals.

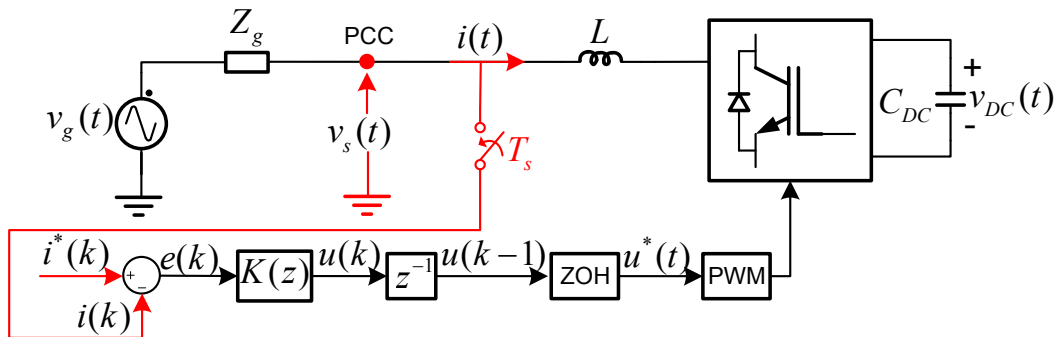


Figure 3.5. Simplified single phase equivalent of the considered system.

The grid current ($i(t)$) open-loop dynamic, in continuous Laplace domain, is as follows:

$$I(s) = \underbrace{\frac{1}{sL + R}}_{G_d(s)} V_s(s) - \underbrace{\frac{1}{sL + R}}_{G(s)} U^*(s) \quad (3.38)$$

where $I(s)$, $U^*(s)$ and $V_s(s)$ are the grid current, VSC average output voltage and point of common coupling (PCC) voltage, respectively, L and R model the filter inductance and its equivalent resistive losses, respectively, and $G(s)$ and $G_d(s)$ are the open-loop command-to-output and admittance transfer functions, respectively.

Note that, once the feedback loop is closed (see Fig. 3.5), the grid current ($i(t)$) dynamic is affected by two exogenous inputs; the current reference ($i^*(k)$), input to the discrete controller ($K(z)$), and the PCC voltage ($v_s(t)$), that is a continuous disturbance to the system. The grid current closed-loop response is, then, the result of an hybrid discrete/continuous dynamic. This sampled-data modelling problem is discussed in more detail in section 4.7. In any case, this is not a critical problem for this application controller design. So, for the sake of simplicity, let's consider for now a continuous equivalent model of the system. The discrete controller implementation and its influence in the current dynamic are addressed in sections 3.3.3 and 3.3.4, respectively.

To translate the aforementioned controller design objectives into an \mathcal{H}_∞ mixed-sensitivity problem, consider now the closed-loop dynamics of the tracking error (e) and the controller effort (u):

$$E(s) = S(s)(I^*(s) - D(s)) \quad (3.39)$$

$$U(s) = F_u(s)(I^*(s) - D(s)) \quad (3.40)$$

where the sensitivity (S) and actuation (F_u) function dynamics were defined in (3.27) and (3.29), respectively, and $D(s) = G_d(s)V_s(s)$ is the output current disturbance. For the equations above, it is clear that to obtain a good reference tracking at the fundamental frequency, rejecting the influence of the PCC voltage at fifth ($5\omega_1$) and seventh ($7\omega_1$) harmonics, the sensitivity function gain ($|S|$) must be close to zero around those frequencies as, in that case, the tracking error (e) will be close to zero for disturbances of both of the exogenous inputs (i.e. disturbances) to the system (i.e. i^* and d). Moreover, the minimization of the sensitivity maximum gain (M_s) implies good stand-alone stability margins (see section A.4). The actuation function gain ($|F_u|$) can be bounded inside the controller bandwidth, to avoid u saturation problems, and at high frequencies, to limit the controller bandwidth⁶.

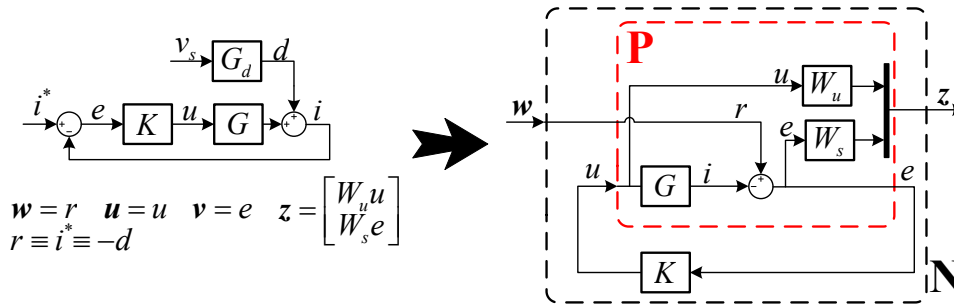


Figure 3.6. Generalized control scheme of the \mathcal{H}_∞ mixed-sensitivity problem applied to a grid current control.

⁶Note that the measurements noise (n) is not considered in this control problem, as its effect is usually negligible at low frequencies, due to sensor dynamics, and at high frequencies if the actuation is limited (i.e. $|F_u| \rightarrow 0$ and $|T| \rightarrow 0$), as it is the case considered here.

Fig. 3.6 shows the translation of the considered one DOF feedback scheme into a generalized control problem scheme used for \mathcal{H}_∞ mixed-sensitivity synthesis. The next and most important design step is to define an adequate sensitivity (W_s) and actuation (W_u) weights in order to obtain, after \mathcal{H}_∞ synthesis, a controller (K) that fulfils the aforementioned objectives.

Proposed weights and tuning methodology

To achieve the desired controller objectives, the next sensitivity weight is proposed:

$$W_s(s) = K_s R_{\omega_1}(s) R_{5\omega_1}(s) R_{7\omega_1}(s) \frac{1}{(1/\omega_s)s + 1}, \quad (3.41)$$

where

$$R_{\omega_1}(s) = \frac{s^2 + 2\zeta_{n1}\omega_1 s + \omega_1^2}{s^2 + 2\zeta_{d1}\omega_1 s + \omega_1^2} \quad (3.42)$$

$$R_{5\omega_1}(s) = \frac{s^2 + 2\zeta_{n5}(5\omega_1)s + (5\omega_1)^2}{s^2 + 2\zeta_{d5}(5\omega_1)s + (5\omega_1)^2} \quad (3.43)$$

$$R_{7\omega_1}(s) = \frac{s^2 + 2\zeta_{n7}(7\omega_1)s + (7\omega_1)^2}{s^2 + 2\zeta_{d7}(7\omega_1)s + (7\omega_1)^2} \quad (3.44)$$

This weight presents an initial gain K_s and a resonant gain at the fundamental frequency (ω_1), as well as at the most relevant grid voltage harmonic frequencies ($5\omega_1$ and $7\omega_1$). This should result in a higher minimization of the sensitivity function gain ($|S|$) at those frequencies, involving a good current reference tracking at ω_1 and a good voltage harmonic rejection at $5\omega_1$ and $7\omega_1$. The parameters ζ_{nx} and ζ_{dx} (with $x = 1, 5, 7$) will determine W_s gain at its different resonant frequencies, as well as their corresponding bandwidths:

- The ratios $n_{h1} = \zeta_{n1}/\zeta_{d1}$, $n_{h5} = \zeta_{n5}/\zeta_{d5}$ and $n_{h7} = \zeta_{n7}/\zeta_{d7}$ should determine the minimization of the tracking error (e) at ω_1 , $5\omega_1$ and $7\omega_1$ frequencies, respectively.
- Increasing ζ_{nx} value will increase the corresponding resonance bandwidth⁷.

W_s also presents a pole at ω_s that will relax the sensitivity function limitation at high frequencies.

The chosen actuation weight W_u for this application follows the next dynamic;

$$W_u(s) = K_u \frac{(1/\omega_u)s + 1}{(1/\omega_{u_p})s + 1} \quad (3.45)$$

which has a low initial gain $K_u < K_s$ to allow higher actuation (u) at low frequencies and do not interact with the sensitivity function minimization. It increases its gain at higher frequencies thanks to a zero in ω_u that will limit controller actuation, and then its bandwidth. The pole ω_{u_p} is needed to make W_u proper, as required by the \mathcal{H}_∞ synthesis algorithm (see section 3.3.4), and can be set as high as desired to limit the control effort in a broader bandwidth.

Fig. 3.7 shows the frequency domain representation of the proposed weights dynamics, as well as all the design parameters of the considered application and the expected achieved controller objectives.

The design criterion is summarized next:

⁷ ζ_{dx} must increase equally to ζ_{nx} to make the corresponding resonance wider and preserve, at the same time, the ratio n_{hx} .

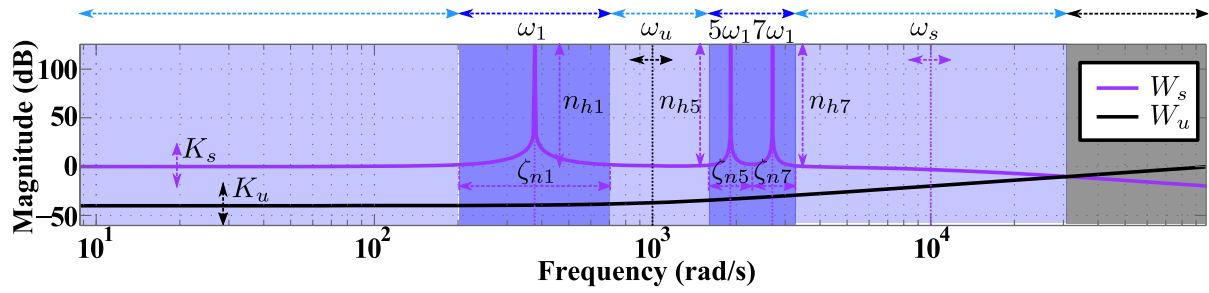


Figure 3.7. Proposed weights dynamics. The sensitivity function ($|S|$) should be highly reduced in the dark blue zones (i.e. around the fundamental frequency and the fifth and seventh harmonics) and less reduced in the light blue zones. The actuation function ($|F_u|$) should be reduced in the black zone at high frequencies.

- Higher sensitivity weight (W_s) gain ratios n_{hx} (with $x = 1, 3, 5$) at the different resonant frequencies will reduce the sensitivity function gain ($|S(j\omega)|$) at those frequencies (i.e. very high values should end up in an ideal sensitivity function $|S(j\omega)| \rightarrow 0$).
- Increase W_s resonance width ζ_{n1} results in a faster reference tracking. In a similar way, increase ζ_{n5} or ζ_{n7} will improve the corresponding voltage harmonic rejection speed.
- Following the weights proposed in Fig. 3.7, the sensitivity function should be highly reduced in the dark blue frequency zones, with an ideal sensitivity function at ω_1 , $5\omega_1$ and $7\omega_1$, and less reduced in the light blue zones.
- By reducing either ω_u or ω_s , the controller effort at high frequencies, and then its bandwidth, will be reduced (i.e. $|F_u(j\omega)| \rightarrow 0$ and $|L(j\omega)| \rightarrow 0$, so $|S(j\omega)| \rightarrow 1$). Control actuation limitation frequency zone is represented in Fig. 3.7 in black colour⁸.
- Note that following the waterbed effect (defined in section A.4) wider ranges of $|S| < 1$ will result in higher sensitivity gain peaks (M_s). That is, wider/higher W_s resonances (i.e. higher ζ_{nx}/n_{hx} values and, then, wider dark blue zones in Fig. 3.7) as well as wider controller bandwidths (i.e. higher ω_s and/or ω_u values and, then, narrower black zones in Fig. 3.7), apart of giving an improved performance in terms of current control (i.e. better feedback action), will result in poorer stability margins. The stability robustness is, in fact, a common concern for controllers with different resonant gains (e.g. multiple PR controllers tuned at different frequencies) [Yepes et al., 2011]. The designer should tune the weights values until the desired objectives in terms of performance and stability margins are met.

Fig. 3.8 shows the chosen weights for the considered application.

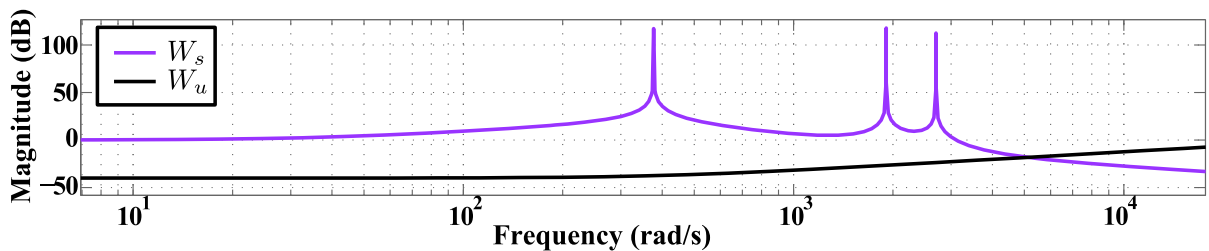


Figure 3.8. Frequency domain representation of the chosen weights.

⁸ W_u pole ω_{u_p} does not appear in Fig. 3.7 due to its high selected frequency.

3.3.3 Digital controller implementation

The synthesized controller must be implemented in a digital processor. Fig. 3.9 shows the process to translate the aforementioned continuous plant ($G(s)$) and design specifications ($W_s(s)$ and $W_u(s)$) into a discrete augmented plant ($P(z)$).

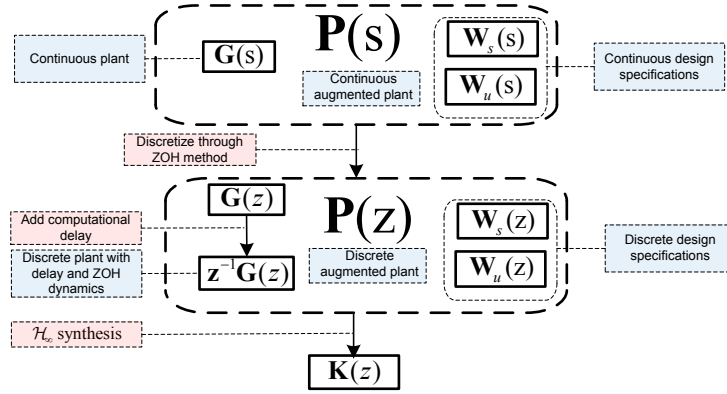


Figure 3.9. Synthesis of a discrete controller $K(z)$ from a continuous augmented plant $P(s)$ in the proposed mixed-sensitivity design.

First, the elements in the continuous augmented plant ($P(s)$) are discretized through ZOH method (see (4.26)) with a sampling period T_s . Then, one computational delay is added to the discrete version of the open-loop plant ($G(z)$). The new discrete design specifications ($W_s(z)$ and $W_u(z)$) along with the discrete and delayed plant ($z^{-1}G(z)$) will form the discrete augmented plant ($P(z)$), from which a discrete controller ($K(z)$) is synthesized using a commercial \mathcal{H}_∞ algorithm. The snippet displayed on Alg. 1 describes the procedure used to obtain the final controller using MATLAB standard library and also its Robust Control Toolbox.

Algorithm 1 Controller synthesis procedure

```

1: procedure CONTROLLER SYNTHESIS( $G, W_s, W_u, T_s$ )
2: Weight definition:
3:    $W_u = \text{tf}(\dots); W_s = \text{tf}(\dots);$ 
4: Process model:
5:    $\text{delay} = \text{tf}([1], [1 \ 0], T_s);$ 
6:    $G_z = \text{delay} * \text{c2d}(G, T_s, 'zoh');$ 
7:    $W_u_z = \text{c2d}(W_u, T_s, 'zoh');$ 
8:    $W_s_z = \text{c2d}(W_s, T_s, 'zoh');$ 
9: P assembly:
10:   $\text{systemnames} = 'G_z \ W_u_z \ W_s_z';$ 
11:   $\text{inputvar} = '[i\_ref; u]';$ 
12:   $\text{outputvar} = '[W_s_z; W_u_z; i\_ref - G_z]';$ 
13:   $\text{input\_to\_}W_s_z = '[i\_ref - G_z]';$ 
14:   $\text{input\_to\_}W_u_z = '[u]';$ 
15:   $\text{input\_to\_}G_z = '[u]';$ 
16:   $P_z = \text{sysic};$ 
17: K synthesis:
18:   $[K_z, \text{gamma}] = \text{hinfsyn}(P_z, 1, 1, \dots);$ 
19:  if ( $\text{gamma} > \text{gmax}$ ) then goto Weight definition
20:  end

```

3.3.4 Design limitations

Bandwidth limitations imposed by the digital controller implementation

The mixed-sensitivity control approach suffers, as any other feedback control technique, of a bandwidth limitation derived from its digital implementation. This limitation was first derived in [Morari and Zafriou, 1989], and it is demonstrated in section A.6.

The sampling nature of the implemented controller, as well as the presence of one-sample delay in the plant input, marks this limitation in a maximum control bandwidth of:

$$f_{c_{MAX}} \approx \frac{1}{2\pi T_s} \quad (3.46)$$

being T_s the considered sampling period. In addition, the aforementioned presence of time delays in the system bounds the sensitivity integral following the second waterbed formula. From a controller design point of view, this means that a large sensitivity peak (M_s) and, then, reduced stability margins, are unavoidable if wider control bandwidths are intended (see section A.4 for more details).

Generalized plant \mathbf{P} design limitations

In addition to the previous limitation, which actually have a clear indirect impact on the design of the weighting functions, the elements in \mathbf{P} are also subject to four additional limitations that have to be considered in the design process:

1. Elements in \mathbf{P} must be represented as state space matrices without internal delays or as polynomial transfer functions, either in the continuous or the discrete domain.
2. Elements in \mathbf{P} and, then, the design weights must be strictly stable. Pure resonators and integrators are, thus, not allowed to be included in weight functions as they present poles over the $j\omega$ axis. There is no theoretical limitation, in any case, in placing them arbitrary close to the $j\omega$ axis. From a practical point of view, this limitation has no implication as the behaviour is practically equivalent. That is one of the reason of using a damped resonant weight W_s like the one in (3.41), instead of multiple infinite PR resonant gains.
3. Weights must be proper (i.e. order of the numerator \leq order of the denominator). The only weight affected by this condition is W_u , which ideally should limit to zero the actuation at high frequencies (i.e. ideally, $\lim_{\omega \rightarrow \infty} |W_u| = \infty$). This limitation is solved by adding a high frequency pole (ω_{u_p}) in W_u definition in (3.45).
4. The order of the synthesised controller is that of the augmented plant transfer function (\mathbf{P}). The two considered design weights (W_s and W_u) are contained inside \mathbf{P} so an increase in their order implies an increase in the final controller \mathbf{K} order. The designer has to evaluate whether the performance improvement obtained by an extra state in a weight is worth the corresponding controller complexity increase.

Order reduction techniques can be used, if necessary, to lighten the computation burden of the implemented controller. An example of this can be found in section 5.5.

3.3.5 Results

This section shows the frequency and time domain results of the proposed \mathcal{H}_∞ mixed-sensitivity controller.

Fig. 3.10 and Fig. 3.11 shows the sensitivity ($|S|$) and actuation ($|F_u|$) that results for the weights selection in Fig. 3.8. As it can be seen, the sensitivity function is highly reduced at frequencies nearby ω_1 , ω_5 and ω_7 , where W_s increases. Similarly, $|F_u|$ is highly reduced at high frequencies to limit controller actuation, as expected from W_u definition. Additionally, the maximum sensitivity function gain (M_s) is less than 6 dB (marked with a blue dashed line in Fig. 3.10), that will assure a gain margin $GM > 6$ dB and a phase margin $PM > 30^\circ$, typical limits to consider a system robust (see section A.4).

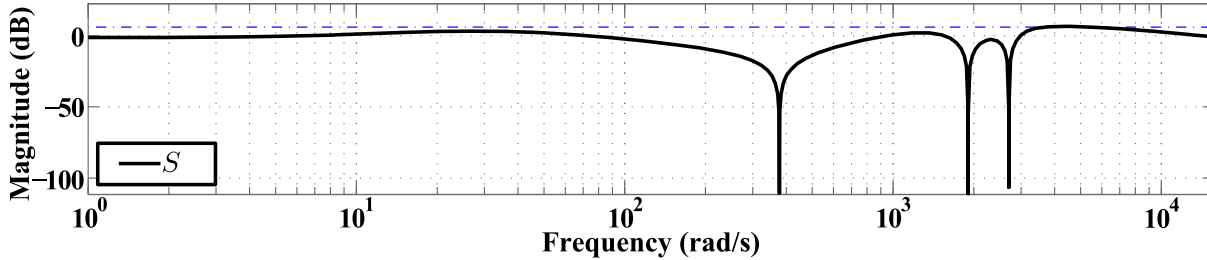


Figure 3.10. Achieved sensitivity function magnitude ($|S|$).

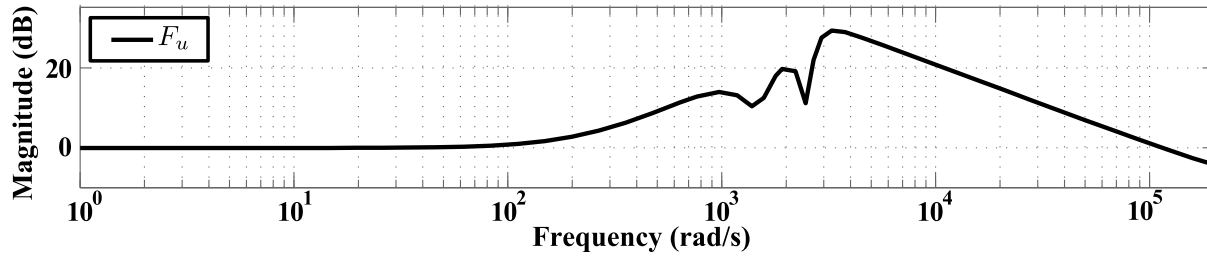


Figure 3.11. Achieved actuation function magnitude ($|F_u|$).

The controller performance is tested in a VSC connected to the grid through an L filter. A picture of the experimental set up is shown in Fig. 5.3. Its most important parameters are summarized in Table. 5.1, being the used L filter equal to the series connection of the grid-side inductance L_2 and the converter-side inductance L_1 .

Fig. 3.12 gathers the main time domain results taken from the experimental platform. Fig 3.12(a) shows the system behaviour under a reactive grid current reference change from 0 to 15 A. Top view shows the complete transient. Zoom 1 focus on the initial grid current transient. As it can be seen, the grid current quickly tracks the change in its reference in the fundamental frequency (ω_1). However, it has a slower tracking response for low frequencies, as it is deduced from the initial transitory offset (more evident in phase b). This can be explained from the sensitivity function ($|S|$) results shown in Fig. 3.10; the achieved sensitivity gain is above one at low frequencies, which implies a poor response for DC offsets. This can be solved by increasing the initial gain (K_s) of the sensitivity weight (W_s), but with the cost of smaller stability margins or poorer response at the fundamental frequency (ω_1) and/or the fifth and seventh harmonics ($5\omega_1$ and $7\omega_1$), as it is deduced from the waterbed effect defined in section A.4. In any case, Zoom 2 shows how the grid current in steady state is perfectly balanced (i.e. without DC offsets) and follows the given reactive reference.

Fig 3.12(b) shows the response of the system for a grid contaminated with 0.12 pu fifth and seventh harmonics. The grid current follows, in this case, an active reference of 19 A, neglecting perfectly the effect of the grid voltage harmonics.

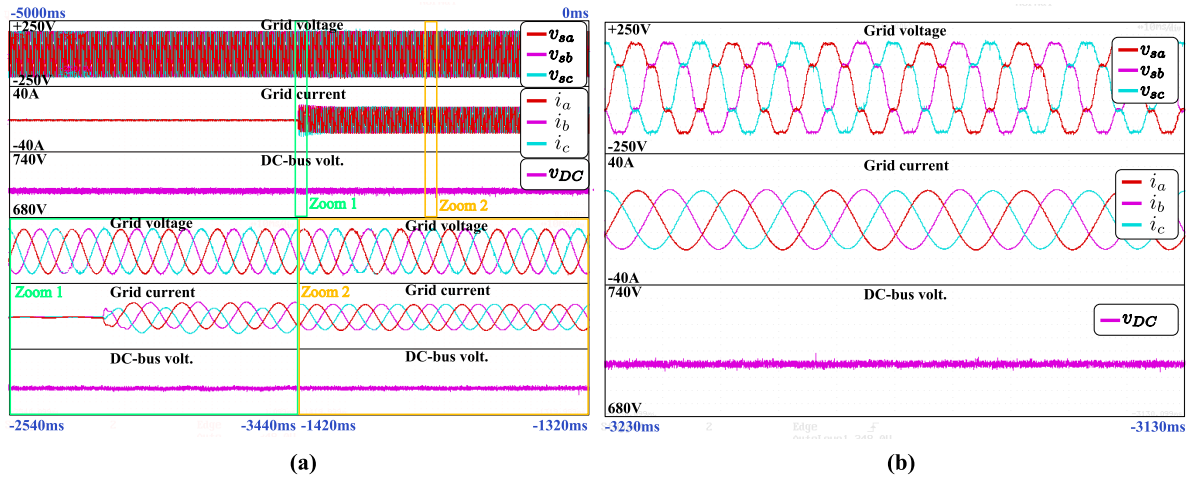


Figure 3.12. Time-domain experimental measurements of the proposed application for different test: (a) change of the current reference with a nominal grid voltage (b) influence of grid voltage harmonics in the controlled current.

3.4 Introduction to \mathcal{H}_∞ model-reference approach

The aforementioned mixed-sensitivity design approach is useful when a small number of simple control objectives are intended. If several complex objectives must be taken into account simultaneously, the signal-based \mathcal{H}_∞ approach represents a simpler design framework. In it, the focus of attention moves from the size (i.e. gain) and bandwidth of selected closed-loop transfer function to the size (i.e. magnitude) of different signals that the designer wants to keep small [Skogestad and Postlethwaite, 2007]. This section introduces the \mathcal{H}_∞ model-reference approach, which is a particular case of the signal-based \mathcal{H}_∞ approach.

Fig. 3.13 shows the generalized control structure for this new \mathcal{H}_∞ paradigm. The main difference with respect to the basic mixed-sensitivity approach is the existence of a dynamic closed-loop reference function \mathbf{F}_{ref} (with inputs \mathbf{w} and outputs \mathbf{y}^*). This function will define the desired behaviour, in the frequency domain, of a certain system closed-loop transfer function \mathbf{F} (with inputs \mathbf{w} and outputs \mathbf{y}).

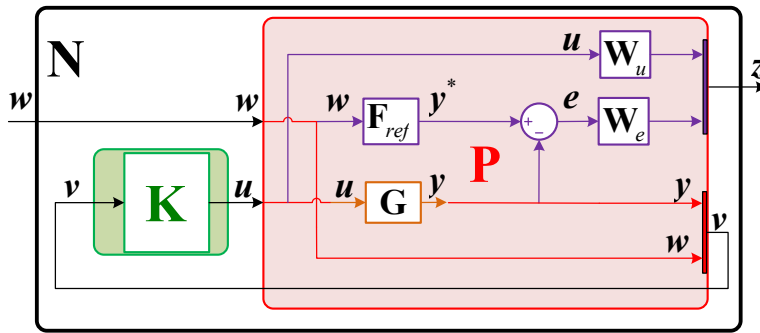


Figure 3.13. Generalized closed-loop control structure of the \mathcal{H}_∞ model reference approach. The open-loop plant and the controller are represented in orange and green, respectively. The generalized plant \mathbf{P} , shown in red, is completed by a set of weights and model reference functions, represented in purple. Those elements are added for the controller synthesis; that is, they are not present in the real closed-loop system.

The open-loop plant (\mathbf{G}) output (\mathbf{y}) is subtracted from the reference model (\mathbf{F}_{ref}) output (\mathbf{y}^*) resulting in an error signal (\mathbf{e}). If this error signal is kept small at a given frequency (ω_x), the considered closed-loop transfer function (\mathbf{F}) will be approximately equal to its reference

(\mathbf{F}_{ref}) at that frequency (i.e. $\mathbf{F}(j\omega_x) \approx \mathbf{F}_{ref}(j\omega_x)$), both in magnitude and in phase. A weight (\mathbf{W}_e) is included to specify at which frequency \mathbf{e} is minimized. Its design principle is similar than that of the previous mixed-sensitivity approach; higher \mathbf{W}_e gain values should result in higher \mathbf{e} magnitude minimization and, then, better \mathbf{F} function shaping.

A new \mathcal{H}_∞ problem is defined with the next generalized inputs and outputs definitions;

$$\begin{bmatrix} \mathbf{z} \\ \mathbf{v} \end{bmatrix} = \mathbf{P} \begin{bmatrix} \mathbf{w} \\ \mathbf{u} \end{bmatrix} \quad \mathbf{z} = \begin{bmatrix} \mathbf{W}_e \mathbf{e} \\ \mathbf{W}_u \mathbf{u} \end{bmatrix} \quad \mathbf{v} = \begin{bmatrix} \mathbf{w} \\ \mathbf{y} \end{bmatrix} \quad \mathbf{w} = \mathbf{w} \quad \mathbf{u} = \mathbf{u} \quad (3.47)$$

The controller input vector (\mathbf{v}) is usually formed by the plan output (\mathbf{y}) feedback path and an exogenous disturbance (\mathbf{w}) feed-forward path, which will provide the controller of the necessary degrees of freedom to correctly shape the considered closed-loop transfer function (\mathbf{F}). After \mathcal{H}_∞ synthesis, a controller \mathbf{K} will be obtained following the usual minimization problem;

$$\min_{\mathbf{K}} \|\mathbf{N}(\mathbf{K})\|_\infty \leq \gamma, \text{ with } \|\mathbf{N}\|_\infty = \max_{\omega} \bar{\sigma}(\mathbf{N}) = \max_{\mathbf{w}(t) \neq 0} \frac{\|\mathbf{z}(t)\|_2}{\|\mathbf{w}(t)\|_2} = \left\| \begin{bmatrix} \mathbf{W}_e \mathbf{F}_{\mathbf{w} \rightarrow \mathbf{e}} \\ \mathbf{W}_u \mathbf{F}_{\mathbf{w} \rightarrow \mathbf{u}} \end{bmatrix} \right\|_\infty \quad (3.48)$$

being $\mathbf{F}_{\mathbf{w} \rightarrow \mathbf{e}}$ an error function simply defined as $\mathbf{F}_{\mathbf{w} \rightarrow \mathbf{e}} = \mathbf{F}_{ref} - \mathbf{F}$.

It is worth to remark the importance of the error (\mathbf{e}) minimization. Unlike in the previous \mathcal{H}_∞ mixed-sensitivity approach, where certain closed-loop functions are minimized in magnitude, this new approach allows the designer to define complex model-reference transfer function (\mathbf{F}_{ref}) for a given closed-loop system transfer function (\mathbf{F}), whose magnitude can be either minimized or maximized depending on \mathbf{F}_{ref} definition. In addition, minimization of the output error (\mathbf{e}) magnitude also implies that \mathbf{F} will be equal to its reference \mathbf{F}_{ref} in phase, giving to this approach an extra design degree of freedom.

This framework is the base of the two main contribution of this dissertation. Chapter 4 applies the model-reference approach to shape, in the frequency domain, the closed-loop admittance of power converter-based systems. The applications of admittance-shaping are multiple and explored in detail in chapter 5. Chapter 6 focus, instead, on resonant plant shaping. Specifically, the model-reference approach is used to shape a grid-connected VSC through an LCL resonant filter so its behave like an equivalent L filter, damping the LCL resonance and improving the overall system robustness.

3.5 Conclusion

The next conclusions can be derived from this chapter:

- Modern optimal control simplifies the systematic controller design of complex control problems (e.g. with multiple control objectives or with dynamically complex plants to be controlled), which are difficult to approach with a classical design methodology.
- The main disadvantage attributable to optimal control is the probable high order of the synthesized controller, which is equal to the defined augmented plant (\mathbf{P}). In the present, with the fast development of digital processors, this disadvantage is less of an issue. Additionally, order reduction techniques can be used, if necessary, to lighten the computation burden of the implemented controller with an often small influence in the final performance.
- Among optimal control techniques, this dissertation is focused on the \mathcal{H}_∞ framework. Specifically, this chapter presents the good results of the basic \mathcal{H}_∞ mixed-sensitivity approach applied to the design of a grid-current control with harmonic rejection capabilities.

- The mixed-sensitivity design approach still presents some difficulties when several complex objectives must be fulfilled simultaneously. An \mathcal{H}_∞ model-reference approach is presented to overcome these difficulties. This design framework is the base of this thesis main contributions, which are presented in the next chapters.

Chapter 4

Model reference approach for closed-loop admittance shaping: design

4.1 Introduction

This chapter develops the proposed \mathcal{H}_∞ model-reference method for current-controlled power converters admittance shaping. The resulting controller is able to add to the classic reference tracking capability the ability to shape, in the frequency domain and both in magnitude and phase, the input admittance of the considered application. This is done by means of the model-reference scheme introduced in Fig. 3.13, where two reference models for the tracking transfer function (T_{ref}) and the admittance transfer function (Y_{ref}) are included to define the desired closed-loop behaviour of the grid current, as well as some frequency weights to distribute the different controller objectives in the frequency spectrum.

Fig. 4.1 shows a single-phase simplification of the considered grid-current control of a two-level three-phase VSC connected to the grid.

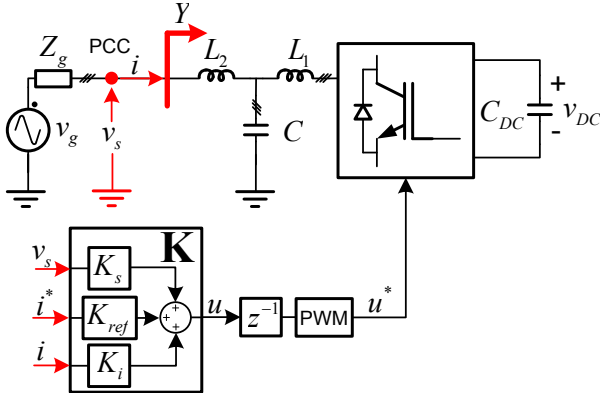


Figure 4.1. Grid-current control of a VSC connected to the grid through an L or an LCL filter.

The grid is modelled with an ideal AC voltage source (v_g) and its equivalent series impedance Z_g . The connection filter is formed by a grid-side inductance (L_2), a capacitor (C) and a converter-side inductance (L_1). It can be configured in an L or an LCL filter topology, discon-

necting the capacitor branch for the L-filter case.

Section 4.2 models the open-loop plant for both considered L and LCL filter topologies. Fig. 4.1 also considers the one-sample delay and pulse-width modulation (PWM) effects in the controller (\mathbf{K}) output (u) present in the digital implemented platform. A more detailed analysis of their effects in the open-loop grid current dynamic is done in section 4.7.

The controller (\mathbf{K}) follows a three DOF structure. It uses a point of common connection (PCC) voltage (v_s) feed-forward path (K_s), a current reference (i^*) feed-forward path (K_{ref}) and a grid current (i) feedback path (K_i). The resulting controlled current (i) and controller actuation voltage (u) closed-loop dynamics are derived in section 4.3. The controller will be designed using the model-reference approach, and synthesized using a \mathcal{H}_∞ optimization algorithm. The generalized plant \mathbf{P} (see section 3.2.2) used to synthesize the controller that fulfils the considered dual objective (i.e. admittance shaping plus current tracking) is detailed in section 4.4.

The theoretical background of the controller design methodology is detailed in section 4.5. It is further illustrated, using simple examples, in section 4.6. The proposed method is not exempt of some design limitations, some of which are typical in every discrete controller implementation (i.e. not exclusive of the presented one), as it will be lastly detailed in section 4.8.

4.2 Open-loop plant modelling

This section defines a valid open-loop linear model of the grid current dynamic for the two considered filter topologies (L and LCL).

4.2.1 Three-phase system reference frame

The three-phase system shown in Fig. 4.1 is modelled and controlled in the $\alpha\beta$ stationary reference frame [Krause et al., 2002]. Expressing a three-wire converter control problem in $\alpha\beta$ reference frame allows to operate under unbalanced conditions and in a natural way, removing component coupling and, thus, reducing the original MIMO problem to the control of two identical SISO uncoupled systems.

The theory and procedures exposed on this proposal are expressed for only one control axis (α or β) and, similarly, the obtained controller will have to be executed twice, once for each component. As a consequence, the obtained closed-loop admittance will be equal for both components, being it a balanced three-phase admittance.

It is also worth to remark that the design procedure could be translated into other typical reference frames, for instance, in synchronous dq axes.

4.2.2 Filter open-loop model

The grid current in Fig. 4.1 follows the next linear dynamic expression, expressed in Laplace domain:

$$I(s) = G(s) \cdot U^*(s) + G_d(s) \cdot V_s(s), \quad (4.1)$$

where I and V_s are the grid injected current and the PCC voltage, respectively. $U^*(s)$ represents the averaged value, over a PWM period, of the VSC output voltage that is generated by the PWM signals applied to the power device gates. Transfer functions $G(s)$ and $G_d(s)$ are the open-loop command-to-output and input open loop admittance, respectively, which model the

behaviour of the controlled current to changes of VSC output u^* and the PCC voltage v_s . These transfer functions are extracted from the differential equations that describe the system dynamics and are dependent on the grid filter that is used.

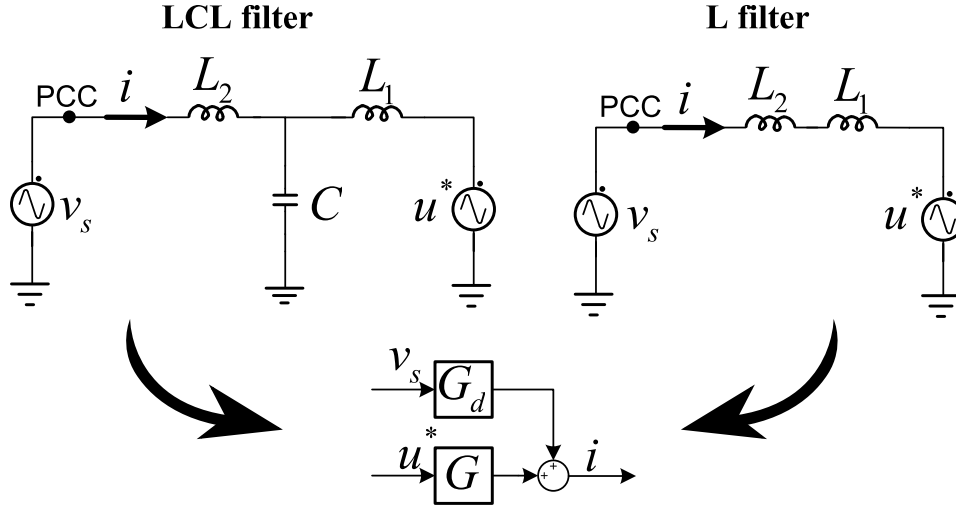


Figure 4.2. Equivalent electric circuit and block diagram of the two considered filters open-loop models.

Fig. 4.2 shows the open-loop single-phase electric diagram of the two considered filters, as well as the aforementioned transfer functions $G(s)$ and $G_d(s)$ in the equivalent block diagram. Their dynamics are modelled as follows:

- For the **L filter** case:

$$G(s) = -\frac{1}{sL_f + R_f}, \quad G_d(s) = \frac{1}{sL_f + R_f}, \quad (4.2)$$

where $L_f = L_1 + L_2$ and $R_f = R_1 + R_2$ are the filter inductance and its parasitic equivalent resistance, respectively.

- For the **LCL filter** case:

$$\begin{aligned} G(s) &= -\frac{1}{sC(R_1 + sL_1)(R_2 + sL_2) + R_f + sL_f}, \\ G_d(s) &= \frac{sC(R_1 + sL_1) + 1}{sC(R_1 + sL_1)(R_2 + sL_2) + R_f + sL_f}, \end{aligned} \quad (4.3)$$

where $L_f = L_1 + L_2$ and $R_f = R_1 + R_2$.

4.3 Closed-loop dynamics

Fig. 4.1 showed the structure where the proposed controller is integrated. As it was described in the introduction, the current controller ($\mathbf{K}(s)$) has three inputs: the PCC grid voltage measurement (v_s), the grid reference current (i^*), and the sensed grid current (i). From the information provided by these three inputs the controller computes the output voltage (u) needed to achieve the considered control objectives. The controller transfer matrix is computed as a whole by the used \mathcal{H}_∞ control design algorithm, as it is detailed in section 4.4. However, it is interesting to observe that dividing the transfer matrix in rows: $\mathbf{K}(s) = [K_s(s) \quad K_{ref}(s) \quad K_i(s)]$ the actuation signal can be calculated as:

$$U(s) = K_s(s)V_s(s) + K_{ref}(s)I^*(s) + K_i(s)I(s). \quad (4.4)$$

Controller \mathbf{K}^1 can be considered, thus, to be formed by the addition of a grid voltage feedforward action (K_s), a current reference pre-compensation action (K_{ref}) and a grid current feedback action (K_i). That is, this controller allows to shape the input admittance in two ways: by the output feedback loop modification and by the addition of an internal disturbance feed-forward loop (see section 2.3.1 and Figs. 2.7 and 2.8).

Expressing the closed-loop grid current (i) using the aforementioned three DOF controller structure, neglecting the effects of the one-sampling delay and PWM in the controller output (i.e. $u^* \approx u$) and considering an ideal grid impedance (i.e. $Z_g = 0$), the following expression is obtained:

$$I|_{Z_g(s)=0} = \underbrace{\frac{GK_{ref}}{1 - GK_i}}_{T(s)} I^* + \underbrace{\frac{G_d + GK_s}{1 - GK_i}}_{Y(s)} V_s, \quad (4.5)$$

where $T(s)$ and $Y(s)$ are the closed-loop tracking and admittance transfer functions. It is important to note that the system stability depends only on the system open-loop transfer function $L(s) = -GK_i$. As explained in section A.4, a good inverse indicator of the system stability is the maximum peak $M_s = \|S\|_\infty$ of the sensitivity transfer function $S = (1 + L(s))^{-1}$.

The closed-loop controller actuation dynamic can be expressed as:

$$U(s) = \underbrace{\frac{K_s + K_i G_d}{1 - GK_i}}_{F_{v_s \rightarrow u}} V_s(s) + \underbrace{\frac{K_{ref}}{1 - GK_i}}_{F_{i^* \rightarrow u}} I^*(s) \quad (4.6)$$

Note that a continuous controller was considered for the derivation of the aforementioned closed-loop dynamics, even though the final controller will be implemented in a digital platform. Controller discretization, as well as the existence of one-sample time delay and a PWM at its output, have influence in the grid-current response and the controller design limitations. For the sake of simplicity, the next sections will neglect the effects of the one-sampling delay and PWM in the controller output (i.e. $u^* \approx u$) and consider a continuous controller ($\mathbf{K}(s)$). The influence of the controller discretization, the time delay and the PWM is addressed in more detail in section 4.7.

4.4 Controller objectives and obtaining method

The fundamental difference of the proposed control method with respect to classical current control approaches is that, in addition to the common current controller tracking capabilities (i.e. make $T(s) \approx 1$ at some frequencies, so $i \approx i^*$), it can shape the grid-connected converter admittance (Y) so it emulates a given model-reference transfer function, namely Y_{ref} .

The \mathcal{H}_∞ synthesis process from which the controller (\mathbf{K}) is obtained uses, as introduced in section 3.2.2, the information contained in the general control problem formulation, or generalised plant (\mathbf{P}), as its entry point. The plant \mathbf{P} structure for the proposed admittance shaping method is inspired by the model-reference \mathcal{H}_∞ approach introduced in section 3.4. The principle behind this control proposal is the minimisation of the difference between the output current of the aforementioned admittance reference (Y_{ref}) and that of the actual converter (Y); if, given

¹For notation compactness, the Laplace variable 's' is omitted when its presence results obvious attending to the context.

the grid PCC voltage (v_s), this difference is *small*, the converter would be following the provided admittance model, accomplishing the main objective of this work. Current tracking is approached in a similar manner by means of a tracking reference (T_{ref}) transfer function.

Fig. 4.3 shows the proposed structure for **P**. Over the diagram;

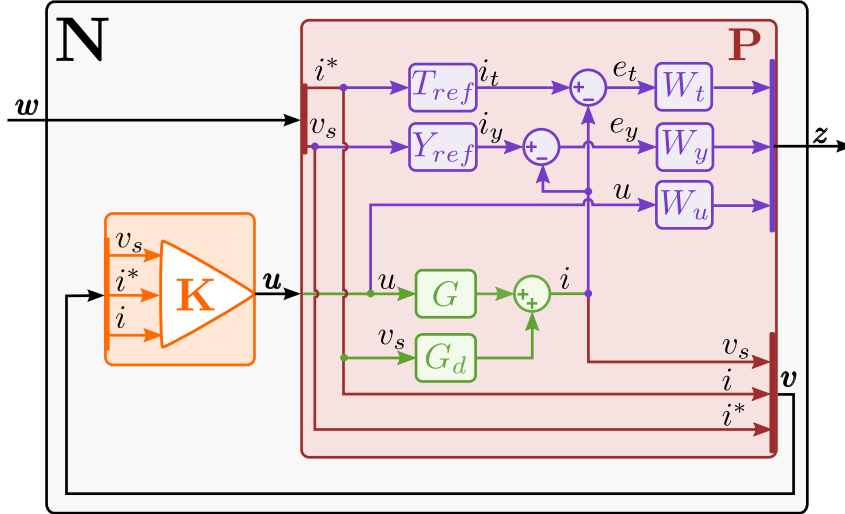


Figure 4.3. Controller structure (for any of the $\alpha\beta$ components) for the \mathcal{H}_∞ synthesis. The open-loop transfer functions are coloured in green, while the purple elements are added in the design process for controller synthesis. The generalized plant **P**, in red colour, wraps around both, while the desired controller **K** is shown in orange. Finally, the closed-loop system **N**, in black, results from connection of **P** and **K**.

- Green elements represent the actual plant under control. The plant output (i) is the result of adding the outputs of G and G_d transfer functions defined in section 4.2.
- Purple elements are added in the design process for controller synthesis. e_t is the difference between the plant output (i) and the tracking reference model (T_{ref}) output (i_t). In a similar way, e_y is the difference between i and i_y , the output of the admittance reference model (Y_{ref}). These two signals, as well as the controller actuation (u), are the variables to be minimized by the controller. They are multiplied by frequency weights (W_t , W_y , W_u , respectively), that emphasise the range of frequencies where each variable has to be minimised. Their outputs compose the generalized plant output vector \mathbf{z} .
- Finally, the controller that is produced from the synthesis process is displayed on green colour. Note that the inputs to the controller, namely \mathbf{v} in the standard notation of (3.1), are all the exogenous signals (\mathbf{w} vector) together with the plant output current measurement, i signal. The controller output (u) forms the generalized plant input vector \mathbf{u} .

Summing up, output and input signal vectors of generalised plant **P** defined in Fig. 4.3 are then:

$$\mathbf{z} = \begin{bmatrix} W_t \cdot e_t \\ W_y \cdot e_y \\ W_u \cdot u \end{bmatrix} \quad \mathbf{v} = \begin{bmatrix} v_s \\ i^* \\ i \end{bmatrix} \quad \mathbf{w} = \begin{bmatrix} v_s \\ i^* \end{bmatrix} \quad \mathbf{u} = u \quad (4.7)$$

It is important to stress on the way i_y and i are compared: e_y is calculated as the subtraction of both signals. As a consequence, good admittance control can be achieved not only in modulus but also in phase if this error magnitude ($|e_y|$) is minimized. Admittance transfer function phase

is a key parameter because important dynamical properties, as for example passivity [Willems, 1972a], depend on it.

The design of frequency weights has a strong influence on the obtained controller \mathbf{K} : the signals involved in the \mathbf{z} vector are actually incompatible from a minimisation point of view as it is not possible to mimic a certain admittance in the frequency bands where good tracking is required, in the same way that it is not possible to minimise the control effort at frequencies where a good admittance shaping or current tracking are intended. The correct design of the functions inside \mathbf{P} is, to a large extent, application dependent and is dealt in more detail in Section 4.5.

4.5 Controller design methodology: theoretical background

The synthesized current controller (\mathbf{K}) depends on a set of transfer functions defined by the designer (shown in purple in Fig. 4.3). This section summarizes, first, the controller (\mathbf{K}) design criterion attending to the choice of these elements; the model references (T_{ref} and Y_{ref}) and the frequency weights (W_y , W_t and W_u). Finally, it presents a set of performance transfer functions that the author considers useful for the analysis of the synthesized controller effectiveness.

4.5.1 Model references of the grid-current closed-loop dynamic

The first step in the design process is to define the desired tracking (T_{ref}) and admittance (Y_{ref}) references.

$Y_{ref}(s)$ represents the desired behaviour, in the frequency domain, of the closed-loop admittance ($Y(s)$), as so does $T_{ref}(s)$ for the desired tracking transfer function ($T(s)$). Obtained controller should fulfil either $T(s) \approx T_{ref}(s)$ or $Y(s) \approx Y_{ref}(s)$ at a given frequency range, resulting in the minimization of either error signals e_t or e_y .

In typical applications the grid current is required to accurately track the provided reference (i.e. $T(j\omega) = 1$ so $i(\omega) \approx i^*(\omega)$) at least in a band around the fundamental frequency (ω_1) and, possibly, also in some of its lower order harmonics ($h\omega_1$). Facing the design from a model-reference point of view, the evident approach to achieve this is to choose a $T_{ref} = 1$.

The range of possibilities for admittance reference model (Y_{ref}) is wider and more application dependent. Chapter 5 shows different example designs that can give an idea of the design method flexibility.

4.5.2 Frequency weights

This section first introduces the dynamic of the signals whose magnitude will be minimized by the synthesized controller, as a preface to the design criteria for the frequency weights.

Dynamics of the signals to be minimized

The synthesized controller should minimize one of the signal whose dynamics are derived below:

- **Admittance shaping error** (e_y) dynamic is modelled as;

$$E_y(s) = \underbrace{\frac{Y_{ref}(1 - GK_i) - G_d - GK_s}{1 - GK_i}}_{F_{v_s \rightarrow e_y}} V_s(s) - \underbrace{\frac{GK_{ref}}{1 - GK_i}}_{F_{i^* \rightarrow e_y}} I^*(s) \quad (4.8)$$

$$\mathbf{F}_{\mathbf{w} \rightarrow e_y} = [F_{v_s \rightarrow e_y} \quad F_{i^* \rightarrow e_y}] = [Y_{ref} - Y \quad -T]$$

where $\mathbf{F}_{\mathbf{w} \rightarrow e_y}$ is the transfer matrix from the disturbances vector (\mathbf{w}) to the admittance shaping error (e_y). $F_{v_s \rightarrow e_y}$ and $F_{i^* \rightarrow e_y}$ model the contribution of PCC voltage (v_s) and current reference (i^*) to this error, respectively.

- In the same way, **tracking shaping error** (e_t) dynamic in the Laplace domain is modelled by the next lineal equation:

$$E_t(s) = \underbrace{\frac{T_{ref}(1 - GK_i) - GK_{ref}}{1 - GK_i}}_{F_{i^* \rightarrow e_t}} I^*(s) - \underbrace{\frac{G_d + GK_s}{1 - GK_i}}_{F_{v_s \rightarrow e_t}} V_s(s) \quad (4.9)$$

$$\mathbf{F}_{\mathbf{w} \rightarrow e_t} = [F_{v_s \rightarrow e_t} \quad F_{i^* \rightarrow e_t}] = [-Y \quad T_{ref} - T]$$

where $\mathbf{F}_{\mathbf{w} \rightarrow e_t}$ models tracking shaping error (e_t) dynamics in response to the complete disturbances vector (\mathbf{w}), and $F_{v_s \rightarrow e_t}$ and $F_{i^* \rightarrow e_t}$ model the contribution of v_s and i^* to it, respectively.

- Finally, **actuation voltage** (u) dynamic response to changes of the disturbances vector (\mathbf{w}) is fully characterized below:

$$\mathbf{F}_{\mathbf{w} \rightarrow u} = [F_{v_s \rightarrow u} \quad F_{i^* \rightarrow u}] \quad (4.10)$$

where $F_{v_s \rightarrow u}$ and $F_{i^* \rightarrow u}$ were defined in equation 4.6.

Design criterion for the frequency weights

The \mathcal{H}_∞ problem can be partitioned as a function of the different exogenous outputs (z_n) that are wanted to be minimized:

$$\|\mathbf{N}\|_\infty = \left\| \begin{array}{l} \mathbf{N}_{\mathbf{w} \rightarrow z_1} \\ \mathbf{N}_{\mathbf{w} \rightarrow z_2} \\ \mathbf{N}_{\mathbf{w} \rightarrow z_3} \end{array} \right\|_\infty = \left\| \begin{array}{l} (W_y \mathbf{F}_{\mathbf{w} \rightarrow e_y})(j\omega) \\ (W_t \mathbf{F}_{\mathbf{w} \rightarrow e_t})(j\omega) \\ (W_u \mathbf{F}_{\mathbf{w} \rightarrow u})(j\omega) \end{array} \right\|_\infty \leq \gamma \quad (4.11)$$

Equation (4.11) establish an \mathcal{H}_∞ problem similar to the \mathcal{H}_∞ mixed-sensitivity problem introduced in section 3.3.1. This inequality can be expressed, then, as a stacked problem with three single specifications to fulfil:

$$\bar{\sigma}(\mathbf{F}_{\mathbf{w} \rightarrow e_y})(s) \leq \frac{\gamma}{|W_y(s)|} \quad (4.12)$$

$$\bar{\sigma}(\mathbf{F}_{\mathbf{w} \rightarrow e_t})(s) \leq \frac{\gamma}{|W_t(s)|} \quad (4.13)$$

$$\bar{\sigma}(\mathbf{F}_{\mathbf{w} \rightarrow u})(s) \leq \frac{\gamma}{|W_u(s)|} \quad (4.14)$$

Different conclusions can be deduced from the stacked \mathcal{H}_∞ problem above:

- Attending to the condition given by the in-equation (4.12) and $F_{\mathbf{w} \rightarrow e_y}$ definition in (4.8), it is clear that a big **admittance weight magnitude** ($|W_y|$) *should* minimize $\bar{\sigma}(\mathbf{F}_{\mathbf{w} \rightarrow e_y})^2$ and, then, the magnitude of both admittance shaping error ($|Y_{ref} - Y|$) and tracking transfer function ($|T|$). Or, in other words, high values of the admittance weight *should* result in $Y(s) \rightarrow Y_{ref}(s)$, both in magnitude and phase, and $T(s) \rightarrow 0$.
- In the same way, from (4.13) and (4.9), a big **tracking weight magnitude** ($|W_t|$) *should* minimize both tracking shaping error ($|T_{ref} - T|$) and admittance transfer function ($|Y|$) magnitudes. Then, $T(s) \rightarrow T_{ref}(s)$ and $Y(s) \rightarrow 0$ at frequencies where $|W_t|$ is high.
- Finally, from (4.14) and (4.6), a big **control effort weight magnitude** ($|W_u|$) *should* result in a minimized $\bar{\sigma}(\mathbf{F}_{\mathbf{w} \rightarrow u})$. In other words, u *should* tend to zero for changes of both disturbances (v_s and i^*) at frequencies where $|W_u|$ is high. The only way to achieve this is by decreasing all the controller terms magnitude: that is, by making $|K_i(s)|$, $|K_{ref}(s)|$ and $|K_s(s)|$ tend to zero. Then, increasing W_u *should* result in $T(s) \rightarrow 0$ and $Y(s) \rightarrow G_d(s)$ in (4.5). Additionally, the sensitivity function $S(s) \rightarrow 1$ and the loop function $L(s) \rightarrow 0$, so increasing W_u is the best way to limit the controller bandwidth, preventing the reduction of the system stability margins due to the water-bed effect (see section A.4).

Effect of control objectives interaction and design limitations

The emphasis in the word *should* in the conclusions above comes from the importance of the obtained γ (i.e. how much \mathbf{N} has been minimized with the synthesized \mathbf{K}) in the in-equations (4.12), (4.13) and (4.14). This term acts as an indicator of how *difficult* is for the \mathcal{H}_∞ synthesis algorithm to obtain a controller that fulfils the design conditions imposed by the information contained in \mathbf{P} . In other words, a big³ obtained γ means that the algorithm can not find a controller that effectively minimize the admittance shaping error function ($\bar{\sigma}(\mathbf{F}_{\mathbf{w} \rightarrow e_y})$) in (4.12), the tracking shaping error function ($\bar{\sigma}(\mathbf{F}_{\mathbf{w} \rightarrow e_t})$) in (4.13) and/or the actuation function ($\bar{\sigma}(\mathbf{F}_{\mathbf{w} \rightarrow u})$) in (4.14), independently of how big W_y , W_t and W_u have been defined. Two main factors may induce a big γ :

1. Normally, it is not possible to minimize both tracking (e_t) and admittance shaping (e_y) errors at the same frequencies. That is, they are usually incompatible objectives from a minimization point of view. In a similar way, good tracking/admittance shaping results may be incompatible with a high control effort minimization. These incompatibilities in the design objectives are one of the risk factors that may induce a big obtained γ , resulting in a poor performance of the synthesized controller. To solve this, the design weights must be defined in a complementary manner. That is, if good admittance shaping is desired, a bigger W_y and a smaller W_t and W_u have to be defined; minimization of the tracking error and the control actuation follow an equivalent design guideline.
2. The obtained controller is conditioned by some design limitations. Ignoring them will result in a high obtained γ and, then, in a controller that does not fulfil the desired objectives. These limitations are explained in Section 4.8.

So the designer must define at which frequency ranges each of the controller objectives (i.e. admittance shaping, tracking shaping or control effort limitation) is desired by means of complementary frequency weights W_y , W_t and W_u . Fig. 4.4 summarizes the expectable results of a controller (\mathbf{K}) obtained from a given set of model references and design weights. Chosen

²Refer to section A.3 for a definition of the maximum singular value operator $\bar{\sigma}$.

³A $\gamma < 1$ value is usually considered as a good result.

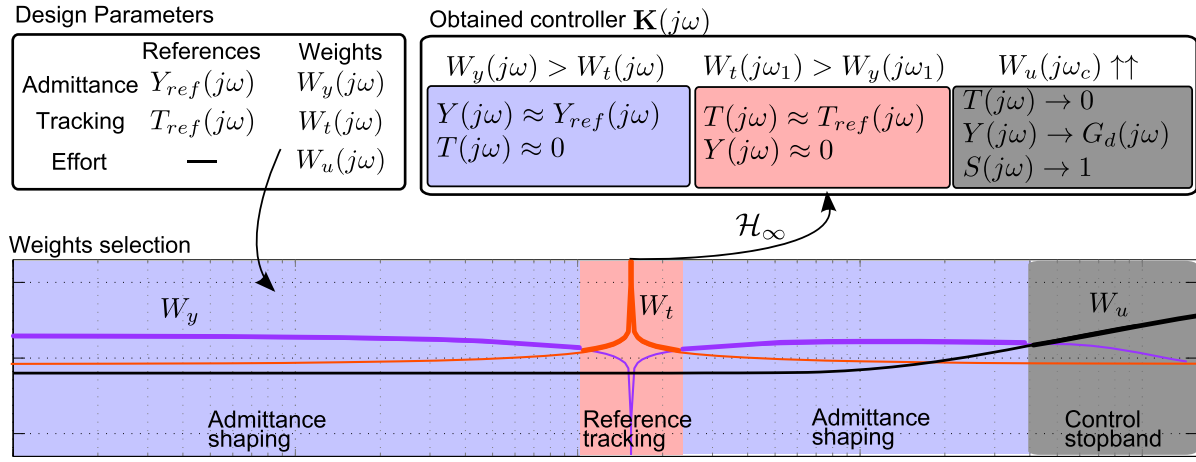


Figure 4.4. Weights selection example and the resulting separation of the controller $\mathbf{K}(s)$ objectives in frequency zones.

weights will divide the spectrum in four different frequency zones, each of which characterized by a different controller objective.

4.5.3 Analysis of the controller effectiveness.

To evaluate the obtained controller effectiveness in terms of admittance and tracking shaping this thesis proposes the magnitude analysis of two transfer functions:

$$|F_y(j\omega)| = \left| \frac{F_{v_s \rightarrow e_y}(j\omega)}{Y_{ref}(j\omega)} \right| = \left| \frac{Y_{ref}(j\omega) - Y(j\omega)}{Y_{ref}(j\omega)} \right| \quad (4.15)$$

$$|F_t(j\omega)| = \left| \frac{F_{i^* \rightarrow e_t}(j\omega)}{T_{ref}(j\omega)} \right| = \left| \frac{T_{ref}(j\omega) - T(j\omega)}{T_{ref}(j\omega)} \right| \quad (4.16)$$

, where the admittance shaping and tracking shaping errors are normalized to their respective model references magnitude (i.e. $|Y_{ref}|$ and $|T_{ref}|$). Perfect admittance or tracking shaping is obtained if $|F_y(j\omega)| \rightarrow 0$ or $|F_t(j\omega)| \rightarrow 0$ at a given frequency, respectively.

Analogously, a transfer function $F_u(s)$, whose magnitude is equivalent to the maximum singular value of $\mathbf{F}_{\mathbf{w} \rightarrow u}(s)$, is defined to evaluate the control effort minimization and bandwidth limitation:

$$|F_u(j\omega)| = \bar{\sigma}(\mathbf{F}_{\mathbf{w} \rightarrow u}(j\omega)) \quad (4.17)$$

Low values of $|F_u(j\omega)|$ will mean low allowed actuation voltages.

As stated in in-equations (4.12), (4.13) and (4.14), the magnitudes of these transfer functions are bounded by their respective frequency weights as well as the obtained γ value, which is a good indicator of incompatibilities in the design objectives. However, γ does not give additional information of which objective is *difficult* to achieve given the information contained in \mathbf{P} . For convenience in the design analysis, γ is divided in three partial values $\gamma_y = \|W_y(s)F_{v_s \rightarrow e_y}(s)\|_\infty$, $\gamma_t = \|W_t(s)F_{i^* \rightarrow e_t}(s)\|_\infty$ and $\gamma_u = \|W_u(s)\mathbf{F}_{\mathbf{w} \rightarrow u}(s)\|_\infty$. Therefore, attending to the $\|\cdot\|_\infty$ norm definition (see (3.21) and (3.22)), the next conditions are met for all frequencies (ω) and syn-

thesized controllers (\mathbf{K}):

$$|W_y(j\omega)F_{v_s \rightarrow e_y}(j\omega)| \leq \gamma_y, \forall \omega \quad \Leftrightarrow |F_y(j\omega)| \leq |L_y(j\omega)| = \frac{\gamma_y}{|W_y(j\omega)Y_{ref}(j\omega)|}, \forall \omega \quad (4.18)$$

$$|W_t(j\omega)F_{i^* \rightarrow e_t}(j\omega)| \leq \gamma_t, \forall \omega \quad \Leftrightarrow |F_t(j\omega)| \leq |L_t(j\omega)| = \frac{\gamma_t}{|W_t(j\omega)T_{ref}(j\omega)|}, \forall \omega \quad (4.19)$$

$$\bar{\sigma}(W_u(j\omega)\mathbf{F}_{\mathbf{w} \rightarrow u}(j\omega)) \leq \gamma_u, \forall \omega \quad \Leftrightarrow |F_u(j\omega)| \leq |L_u(j\omega)| = \frac{\gamma_u}{|W_u(j\omega)|}, \forall \omega \quad (4.20)$$

The next conclusions can be derived from the above in-equations:

- $L_y(s)$, $L_t(s)$ and $L_u(s)$ will act as magnitude boundaries in the frequency domain of $F_y(s)$, $F_t(s)$ and $F_u(s)$ transfer functions, respectively.
- $|W_y(j\omega)Y_{ref}(j\omega)|^{-1}$, $|W_t(j\omega)T_{ref}(j\omega)|^{-1}$ and $|W_u(j\omega)|^{-1}$ can be considered as frequency domain shapers of the admittance and tracking shaping errors and the controller actuation, respectively.
- The constants (i.e. not function of frequency) γ_y , γ_t and γ_u are indicators of possible incompatibilities in the admittance shaping, tracking shaping and actuation minimization objectives, respectively.

4.6 Controller design methodology: practical aspects

This section presents a simple example that illustrates the design methodology introduced in section 4.5. The application design specifications for this example are summarized as follows:

- A resistive behaviour is intended for the system closed-loop admittance, so a simple constant $Y_{ref}(s) = Y_{ref0}$ will be defined. A unitary tracking reference ($T_{ref} = 1$) is, as always, selected.
- Good admittance shaping (i.e. $Y(s) \approx Y_{ref}(s)$) is desired at both sub and super synchronous frequencies.
- Good tracking (i.e. $T(s) \approx T_{ref}(s)$) is desired around the grid synchronous (i.e. fundamental) frequency (ω_1).
- Control effort (u), and then controller bandwidth, must be limited at high frequencies.

The designer has to solve, in essence, two trade-offs exposed below:

1. Admittance shaping versus current reference tracking (i.e. tracking shaping): Broader range of effective tracking shaping will result in faster current reference tracking, but also in a narrower range of effective admittance shaping.
2. Performance versus energy optimization and stability margins: Good performance⁴ of the controller in broader ranges will result in smaller stand-alone stability margins (i.e. stability robustness) due to the water-bed effect (see section A.4 for more details). In addition, performance of the controller could be sacrificed, in some cases, in favour of the system energy optimization.

⁴Good controller performance is obtained, for this control paradigm, at frequencies where either good admittance or tracking shaping are achieved.

To simplify the controller design, it will be separated in two processes. First, the admittance shaping versus actuation limitation (i.e. energy and stability margins optimization) trade-off is partially solved. In a second step, the solution to the admittance shaping versus tracking shaping trade-off is pursued. This second process may slightly modify the solution of the first trade-off in terms of stability margins and energy optimization, but it can be easily corrected by minor weights modifications.

4.6.1 Admittance shaping versus actuation limitation trade-off

In this first step the trade-off between good admittance shaping and actuation limitation is discussed. Tracking weight W_t is then set to zero, resulting in a controller without any tracking capabilities.

Weights definitions

Good admittance shaping is desired in the broader bandwidth possible. W_y is then chosen as a low-pass function:

$$W_y(s) = K_y \frac{1}{(1/\omega_y)s + 1}, \quad (4.21)$$

where W_y has an initial high gain value (K_y) that will impose a low boundary ($|L_y(s)|$) to admittance shaping error magnitude ($|F_y(s)|$) at low frequencies. The pole at ω_y marks the frequency from where this boundary is less restrictive (i.e. $|F_y(s)|$ is less minimized).

W_u weights the actuation in two senses: it is used to limit the maximum control bandwidth but also to limit the maximum control effort within the control band. Thus, typically, W_u is a high-pass function:

$$W_u(s) = K_u \frac{(1/\omega_u)s + 1}{(1/\omega_{u_p})s + 1} \quad (4.22)$$

The transition between the low and high gain bands, set by the zero in ω_u , marks the frequency where control actuation is desired to be small (i.e. the stop-band beginning). The maximum control effort in the control band is adjusted by modifying the gain K_u : lower values allow a bigger control effort and vice versa (see $|F_u|$ boundary $|L_u|$ in in-equation (4.20)). This value is usually adjusted to get a control effort near the saturation limit under nominal transients and disturbances as, for instance, voltage dips. The pole ω_{u_p} is needed to make W_u proper and can be set as high as desired to limit the control effort in a broader bandwidth.

Fig. 4.5 shows the frequency domain representation of a possible choice of both admittance and control effort weights magnitudes, and the expected frequency ranges of admittance shaping and bandwidth limitation.

Note, in any case, that the admittance shaping and bandwidth limitation ranges represented here serve only as a visual guidance. That is, the exact frequency where effective admittance shaping range ends and the controller action starts to be limited may not match with the frequency where $|W_u| = |W_y|$, as the optimisation process depends on other parameters such as the admittance reference magnitude ($|Y_{ref}|$) and the obtained \mathcal{H}_∞ norms γ_y and γ_u (see in-equations (4.18) and (4.20)).

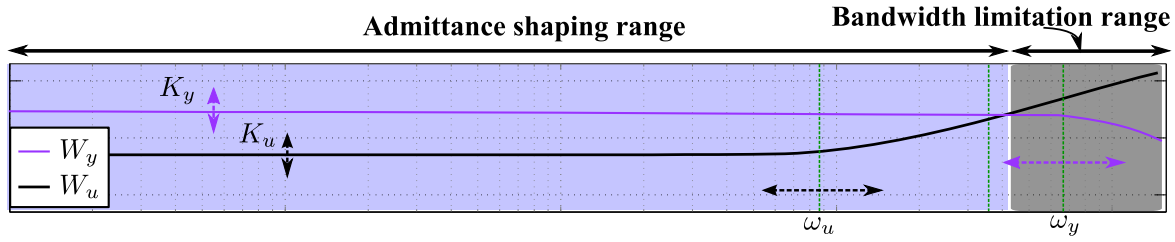


Figure 4.5. Example of the magnitude representation of the admittance W_y and control effort weight W_u , and the resulting admittance shaping (blue colour) and bandwidth limitation (grey colour) ranges.

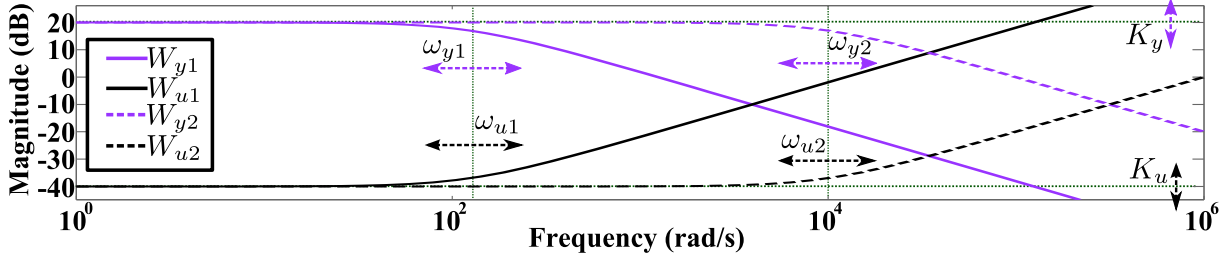


Figure 4.6. Weights example to illustrate the admittance shaping versus controller effort trade-off.

Design examples introduction

To further illustrate this first step of the weights selection and its derived design trade-off, two design examples and the comparison of their respective results are fully described next. A $K_y > K_u$ is chosen for both examples in order to obtain good admittance shaping results at low frequencies. The two examples differ in W_y pole at ω_y and W_u zero at ω_u selections. In the first example, a narrower admittance shaping range and, then, bigger bandwidth limitation are desired, defined by the choice of smaller ω_{y1} and ω_{u1} frequencies⁵. These two design elements increase their values to $\omega_{y2} > \omega_{y1}$ and $\omega_{u2} > \omega_{u1}$ for the second example, resulting in a broader admittance shaping range. Fig. 4.6 shows the frequency domain representation of the aforementioned weights.

Admittance shaping results

Fig. 4.7 shows the admittance shaping results for the two considered examples. As it can be seen on the top of the figure, the admittance shaping error magnitude $|F_y|$ is limited by $|L_y|$, as expected from in-equation (4.18). The second example has a broader effective admittance bandwidth (BW_{y2}) than the first one (BW_{y1}), shown here as light blue and dark blue frequency zones, respectively, thanks to its higher admittance weight pole value $\omega_{y2} > \omega_{y1}$ (see Fig. 4.6).

The minimum error magnitude is bounded by the obtained ratio $\gamma_y/(K_y Y_{ref0})$, which is, in this case, equal for both examples. The obtained $|F_y|$ results will mean an admittance shaping error of 0.1 p.u (-20 dB) of the given reference (Y_{ref}) at low frequencies.

Fig. 4.7 bottom shows the considered open-loop admittance (G_d), the obtained admittance (Y) for both examples and the given resistive reference (Y_{ref}). Both admittances (Y) follow the reference (Y_{ref}) inside their respective effective admittance shaping range. At high frequencies, where the control effort starts to be limited, close-loop admittance (Y) tends to its open-loop value (G_d).

⁵Design parameters and results for the first and second examples are notated with a subscripted 1 or 2, respectively.

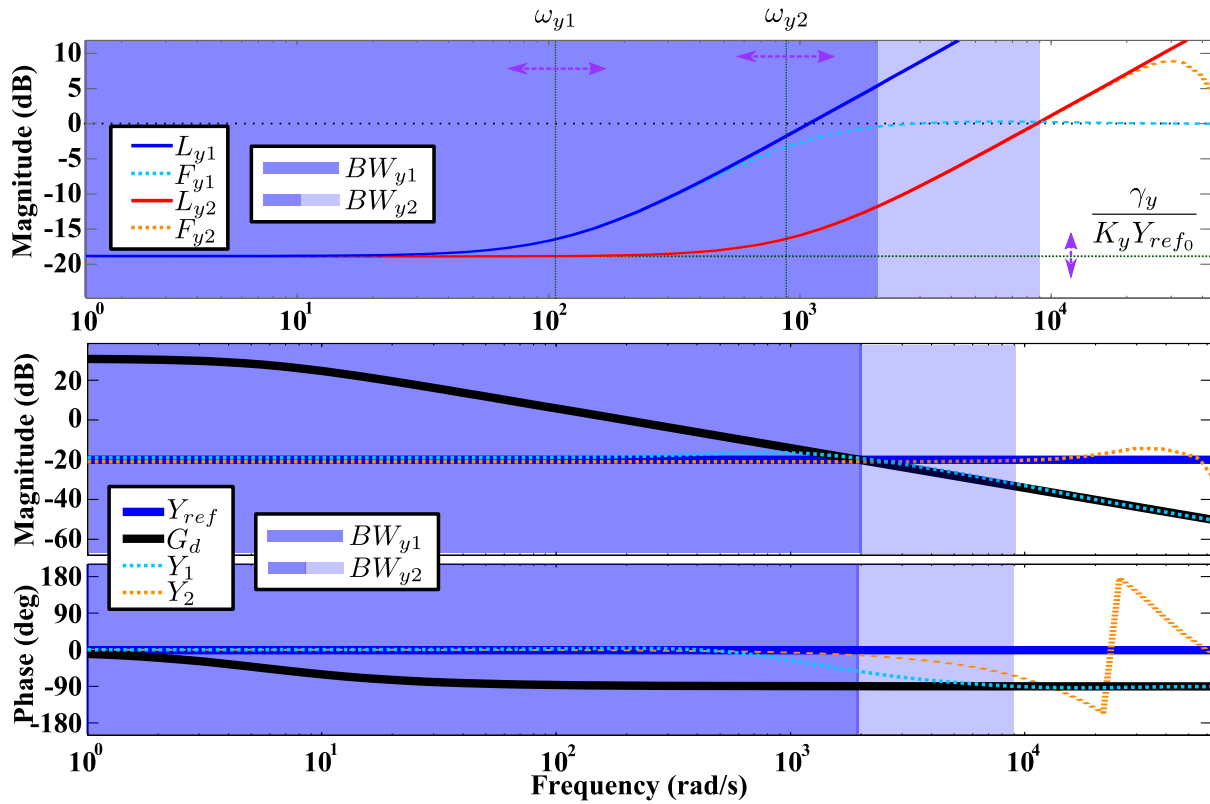


Figure 4.7. Admittance shaping results for the two considered designs. On the top, their corresponding admittance shaping error magnitudes ($|F_y|$) and their frequency domain boundaries ($|L_y|$). Effective admittance shaping ranges for both examples are shown in dark blue (BW_{y1}) and light blue zones (BW_{y2}), respectively. The figure bottom shows how the resulting admittances (Y) follows the given reference (Y_{ref}) inside their respective effective admittance shaping ranges.

Control effort limitation results

Fig. 4.8 shows the control effort results for both examples. The top of the figure shows how the controller effort function magnitude $|F_u|$ is limited by the function $|L_u|$ (see in-equation (4.20)). As a $\omega_{u2} > \omega_{u1}$ was defined (see Fig. 4.6), a higher bandwidth limitation of $|F_u|$ is obtained in first design (light grey zone) than in the second (dark grey zone).

$|F_u|$ maximum value in the frequency domain is closely related to the time domain response of its output [Skogestad and Postlethwaite, 2007], the actuation voltage (u), as it can be seen in the bottom of Fig. 4.8. It shows the actuation needed to respond to the application start conditions (i.e. controller actuation when the considered application is first connected to the grid)⁶. The small maximum peak of $|F_{u1}|$ in the first example results in a very smooth response of the controller actuation (shown in blue-dashed line at the bottom of Fig. 4.8.). However, the bigger admittance bandwidth of the second example induces a higher $|F_{u2}|$ peak, and then a bigger actuation (shown in orange-dashed line at the bottom of Fig. 4.8), which will clearly saturate the controller at the application start.

This high actuation in the second example comes from its broader effective admittance shaping range. As it can be seen in Fig. 4.7, this broader range makes the admittance (Y) follow a reference (Y_{ref}) bigger, in magnitude, than the open-loop admittance (G_d) at high frequencies. This will induce higher controller efforts at those frequencies, as seen in $|F_u|$ frequency domain

⁶This response is normalized to the half of the nominal DC-bus voltage V_{DC} , as the PWM saturation limits (shown as black horizontal lines in Fig. 4.8) are related to it

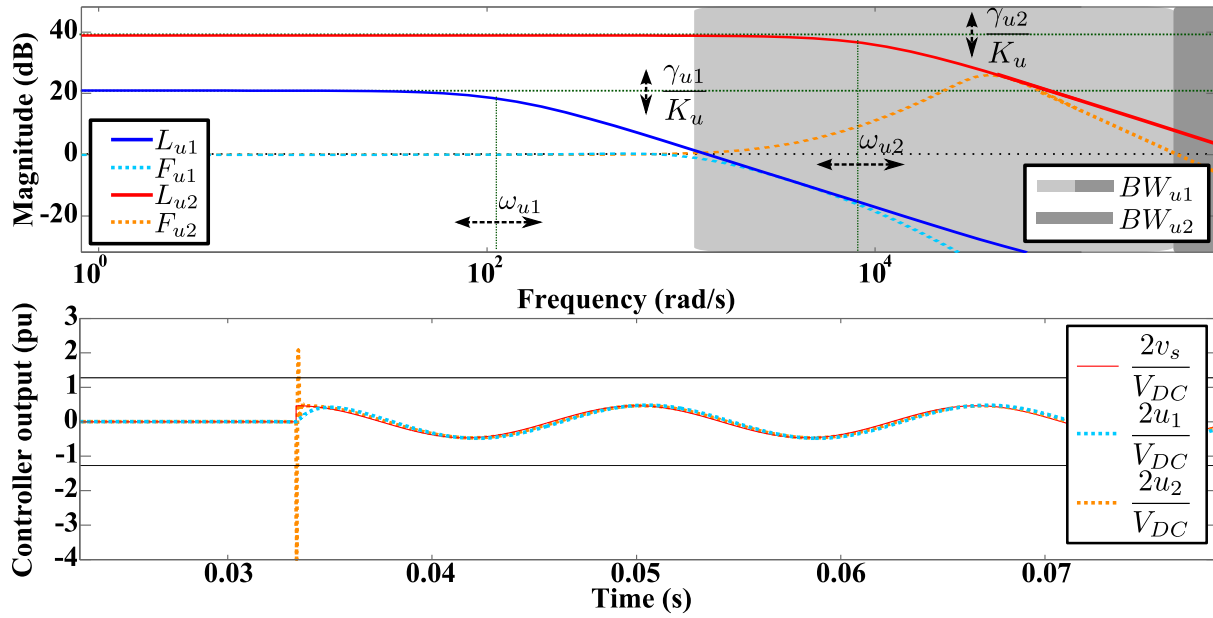


Figure 4.8. On the top, the frequency domain minimization of both examples controller effort functions ($|F_u|$). The range where each controller starts to be inactive are shown in dark grey (BW_{u2}) and light grey (BW_{u1}) zones for the second and first examples, respectively. On the bottom, the time domain results of the control effort (u) (normalized to the half of DC-bus nominal voltage V_{DC}) needed to respond to a sudden change from zero to the nominal conditions of the grid voltage (v_s) (i.e., controller start condition) for both examples. The actuation in the first and second example and the PCC voltage considered for the test are shown in blue-dashed, orange-dashed and red lines, respectively.

representation in Fig. 4.8. This is an important fact that will be later taken into account in chapter 5 for applications where high converter admittances are desired.

As a remark, note that, from Fig. 4.8 results, a $\gamma_{u2} > \gamma_{u1}$ is deduced, as K_u gain was set equal for both examples (see Fig. 4.6). This higher γ_u value is the result of the admittance shaping and controller effort limitation objectives interaction in the second example, as the \mathcal{H}_∞ synthesis can not find a controller that maintain $|Y| = |Y_{ref}|$ at high frequencies without increasing $|F_u|$ and, then, controller effort (u).

Stand-alone stability robustness analysis

Finally, Fig. 4.9 shows the obtained sensitivity function magnitude for both considered examples.

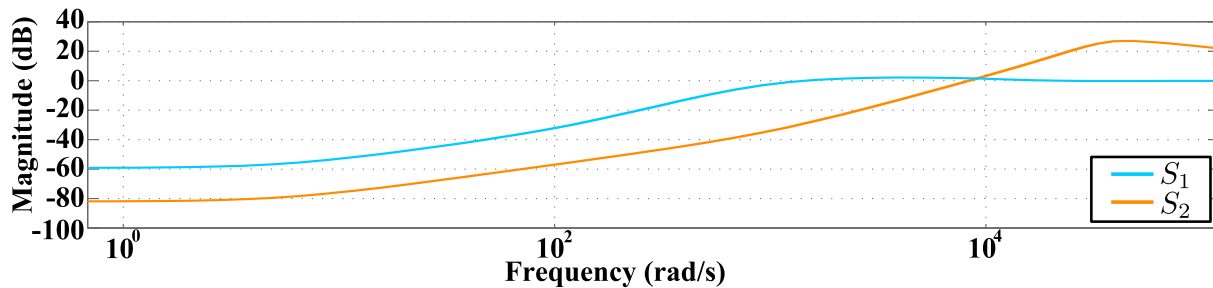


Figure 4.9. Obtained sensitivity function magnitude for both considered designs.

The broader admittance shaping bandwidth of the second example induces a bigger sensi-

tivity peak, which will mean poorer (i.e. smaller) stand-alone stability margins of the proposed controller (see water-bed effect definition in subsection A.4).

Conclusion

From the aforementioned results it is clear that, even though better admittance shaping results are obtained for the second example, the high control effort and small stability margins obtained makes this design inadvisable. The first design shows the opposite results; a very good stability margins and smooth actuation response in detriment of a poorer (narrower) effective admittance shaping range. An intermediary solution should be adopted (i.e. selection of $\omega_{y1} < \omega_y < \omega_{y2}$ and $\omega_{u1} < \omega_u < \omega_{u2}$).

4.6.2 Tracking shaping versus admittance shaping trade-off

Once the admittance shaping and control effort trade-off has been studied, this section will introduce the current reference tracking objective in the controller design process, which will induce a new trade-off between admittance and tracking shaping, as both can not be obtained in the same frequencies.

Weights definition

A perfect tracking shaping is obtained if $|F_t| \rightarrow 0$. This objective is desired, for these design examples, around the fundamental synchronous frequency (ω_1). The resonant-like tracking weight (W_t) presented below is suitable for this task:

$$W_t(s) = K_t \frac{s^2 + 2\zeta_n \omega_1 s + \omega_1^2}{s^2 + 2\zeta_d \omega_1 s + \omega_1^2} \quad (4.23)$$

This weight has an initial low gain ($K_t < K_y$) that will allow good admittance shaping results in the rest of frequencies (i.e. sub and super synchronous). The parameters ζ_n and ζ_d will determine W_t gain at ω_1 and its resonance bandwidth:

- How much the tracking shaping error is minimized at ω_1 depends on the W_t resonance peak, that is, the ratio $n_h = \zeta_n/\zeta_d$: the higher this ratio is, the smaller the error (i.e. perfect current tracking ($i \approx i_{ref}$) can be obtained for very high n_h values).
- Increasing ζ_n value will increase the resonance bandwidth of the proposed weight and, then, the range where good tracking shaping is obtained⁷.

A modification of the admittance weight (W_y) presented in (4.21) is proposed below:

$$W_y(s) = K_y \frac{s^2 + 2\zeta_d \omega_1 s + \omega_1^2}{s^2 + 2\zeta_n \omega_1 s + \omega_1^2} \cdot \frac{1}{(1/\omega_y)s + 1} \quad (4.24)$$

It presents a notch-like part, complementary to W_t resonance, that will decrease W_y gain around the fundamental frequency.

Fig. 4.10 shows a frequency domain representation of W_t , W_y and W_u magnitudes defined in (4.23), (4.24) and (4.22), respectively.

⁷In order to preserve the ratio n_h , ζ_d must increase equally to ζ_n to make W_t resonance wider.

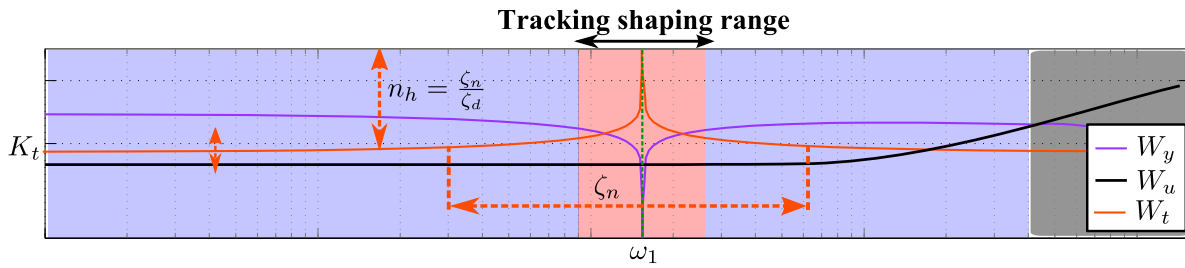


Figure 4.10. Example of the magnitude representation of the new tracking weight (W_t), along with admittance shaping (W_y) and control effort (W_u) weights, and the resulting, a priori, tracking shaping (red colour), admittance shaping (blue colour) and bandwidth limitation (grey colour) ranges.

The new tracking shaping zone is, a priori, defined by the range where $|W_t| > |W_y|$. Increase W_t resonance bandwidth by means of increasing ζ_n value is the best option to obtain a broader tracking bandwidth in detriment of a narrower admittance shaping range

Design examples introduction

To further analyse the consequences of this new tracking shaping zone in the controller performance, two new design examples and their corresponding results are described next. Starting from the admittance shaping results and weights definitions of the previous step, a tracking weight W_t like the one in (4.23) is introduced, along with a W_y modification following (4.24) dynamic. The two proposed examples differ in the resonance/notch width defined by changes of ζ_n parameter. Fig. 4.11 shows the frequency domain magnitude representation of these new weights.

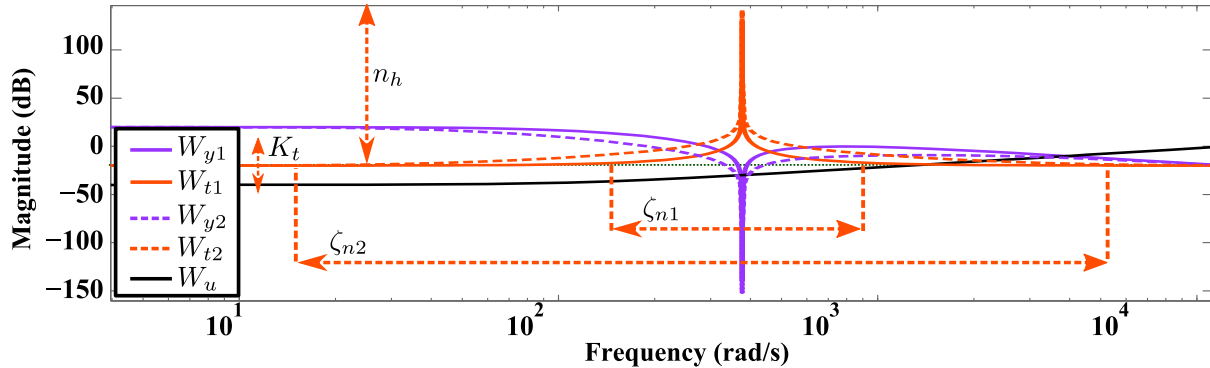


Figure 4.11. Chosen weights to illustrate the admittance shaping versus tracking shaping trade-off.

Tracking shaping results

Fig. 4.12 shows the obtained tracking results for both considered examples. The top part of the figure shows the minimization of the tracking error magnitude ($|F_t|$), and how it is bounded by $|L_t|$ defined in (4.19). As it can be seen, $|F_t| \rightarrow 0$ in ω_1 for both examples, which means a tracking error approximately zero (i.e. $T \approx 1$ and $i \approx i^*$) at that frequency. The middle part of Fig. 4.12 shows how the obtained tracking transfer function (T) follows its reference (T_{ref}) around the fundamental frequency (ω_1). The obtained tracking bandwidth⁸ marks the effective

⁸Tracking bandwidth of a controller is typically defined as the frequency range where $-3 \text{ dB} < |T| < 0 \text{ dB}$ is fulfilled.

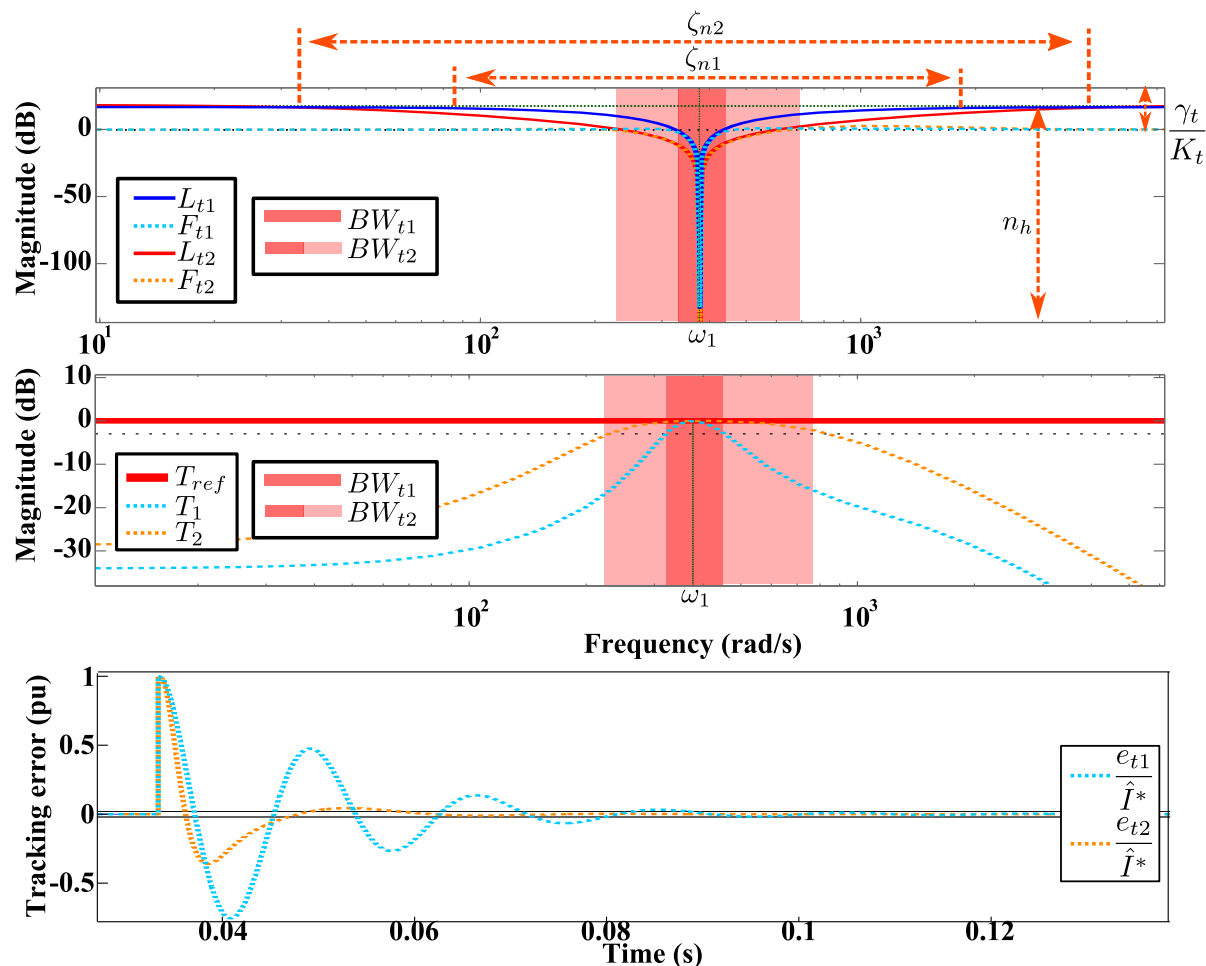


Figure 4.12. Frequency and time domain tracking results. In the figure, tracking error $|F_i|$ magnitude minimization in the frequency domain (top), tracking shaping results (middle), and tracking error e_t time domain results for changes of the tracking reference i^* (bottom). The black horizontal lines in the latter mark the standard error for measuring the tracking settling time (t_s) (i.e. 0.02 p.u of the current reference magnitude \hat{I}^*).

tracking shaping frequency ranges, shown in a dark red zone (BW_{t1}) for the first design and in a light red zone for the second design (BW_{t2}). Finally, the bottom part of Fig. 4.12 shows the time domain response of the tracking error (e_t) normalized to a sudden change of the current reference ($i^*(t) = \hat{I}^* \sin(\omega_1 t)$). The wider tracking shaping range of the second example allows a faster tracking response.

Admittance shaping results

Fig. 4.13 shows the obtained admittance shaping results, and how they are affected by the new tracking shaping zone around the fundamental frequency. As it can be seen, the effective admittance shaping range in both designs (BW_{y1} and BW_{y2}) is reduced, as Y tends to zero around ω_1 instead of to its reference (Y_{ref}). The wider tracking shaping range of the second example makes not possible a super synchronous effective admittance shaping range before the controller effort starts to be limited at high frequencies, where $Y \rightarrow G_d$. That is not the case for the narrower tracking shaping range of the first example, where an effective admittance shaping is still possible at super synchronous frequencies, even though with bigger relative admittance shaping error magnitude ($|F_y|$) than at low frequencies.

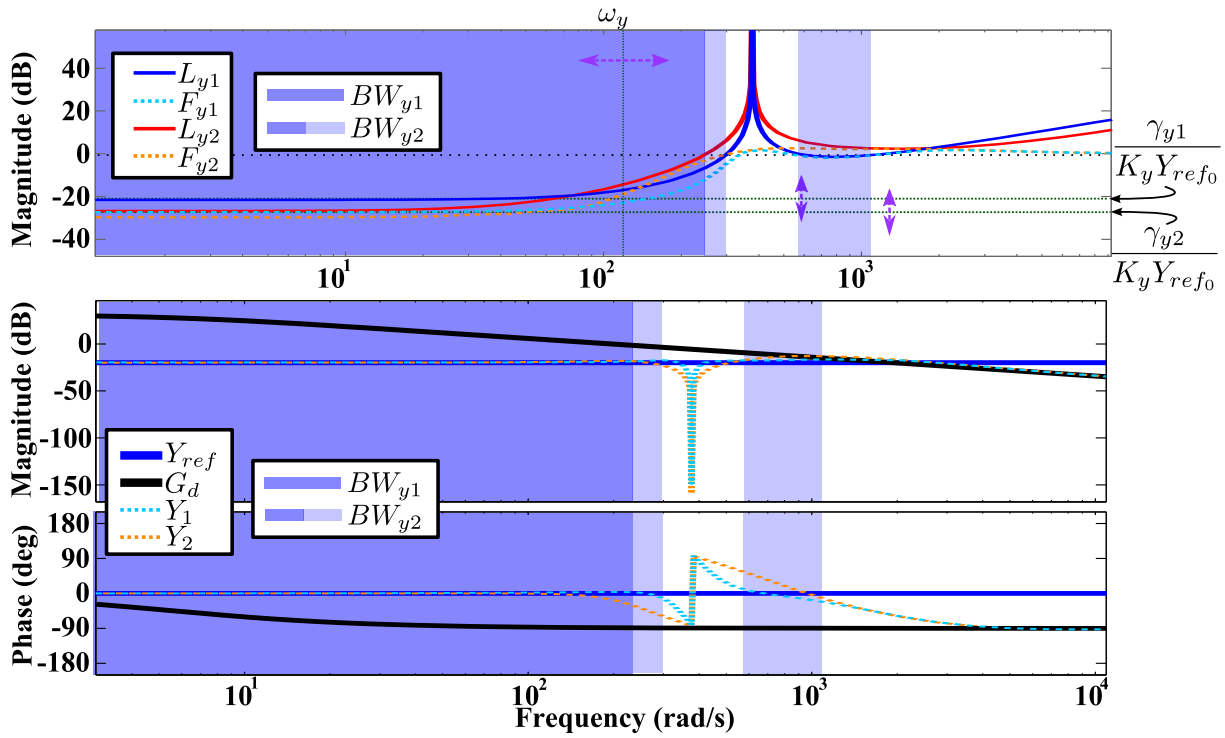


Figure 4.13. Obtained admittance results once controller tracking capabilities are considered. The new admittance shaping range of the first (BW_{y1}) and second (BW_{y2}) examples are showed in light blue and dark blue, respectively.

Control effort limitation results

Fig. 4.14 shows the controller effort limitation results. The broader tracking bandwidth of the

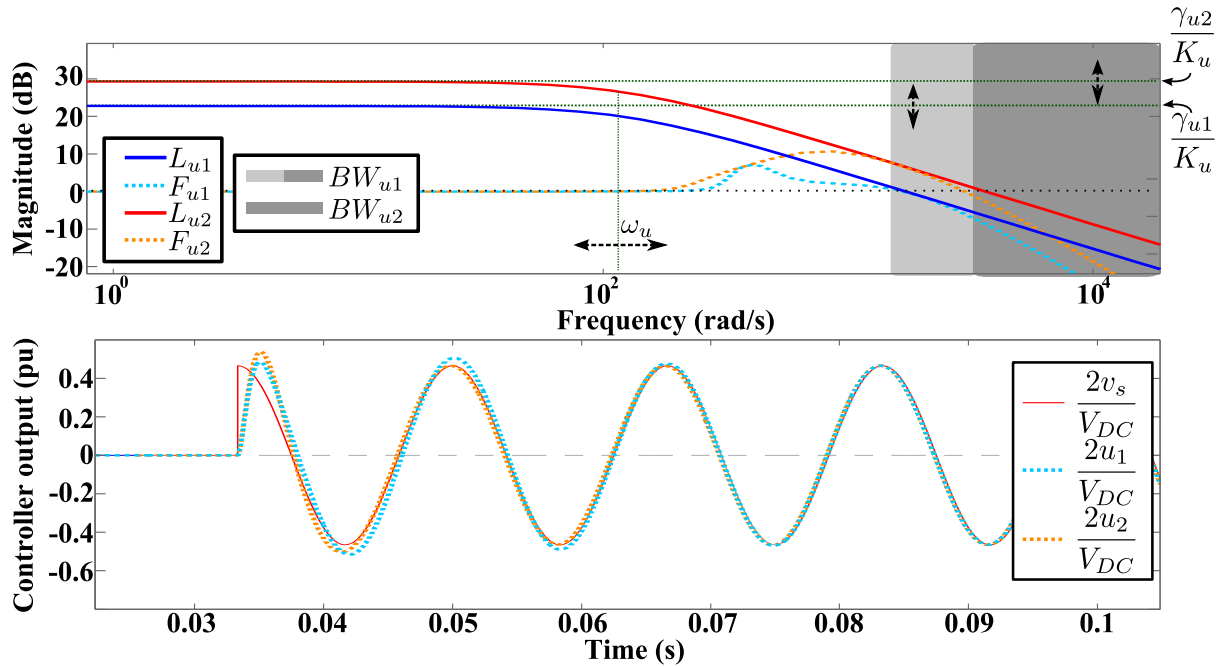


Figure 4.14. Controller effort limitation results for the two considered tracking shaping examples.

second example induces a broader range where actuation is not limited than in the first example,

showed in dark grey (BW_{u2}) and light grey (BW_{u1}) frequency zones, respectively. It also induces a slightly bigger $|F_u|$ peak, which triggers a bigger actuation when the application start (bottom part of Fig. 4.14).

Fig. 4.15 shows the frequency domain representation of the magnitudes $|F_{v_s \rightarrow u}|$ and $|F_{i^* \rightarrow u}|$, which will measure the actuation response to changes of PCC voltage (v_s) and current reference (i^*), respectively, for the first considered example. $|F_u|$ is defined by the maximum gain value,

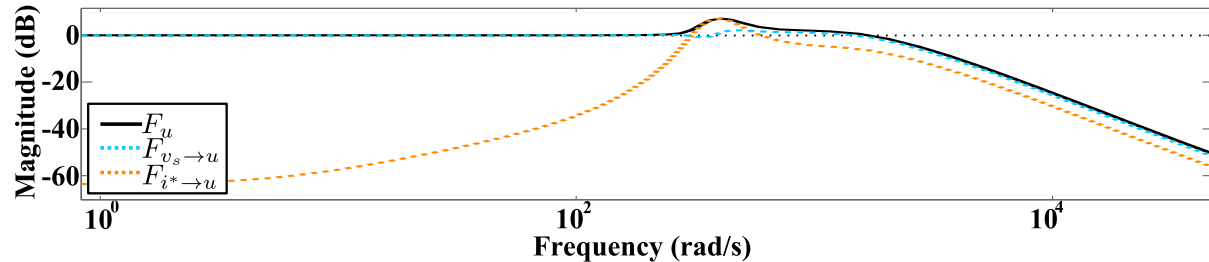


Figure 4.15. Influence of PCC voltage v_s and current reference i^* disturbances in the controller actuation u magnitude ($|F_{v_s \rightarrow u}|$ and $|F_{i^* \rightarrow u}|$ results, respectively) and, then, their frequency domain contribution to the function $|F_u|$.

frequency by frequency, of these two transfer functions (see (4.17) and section A.3). As it can be seen, the new tracking shaping zone increases $|F_{i^* \rightarrow u}|$ and, then, $|F_u|$ around the fundamental frequency. $|F_u|$ frequency domain shape is determined by $|F_{v_s \rightarrow u}|$ for the rest of frequencies (i.e. the admittance shaping sub and super synchronous ranges). It can be concluded that, even though tracking shaping affects the controller effort at synchronous frequencies, the controller bandwidth for this example and, normally, the maximum controller effort needed (see the high $|F_{u2}|$ peak in the second example in Fig. 4.8) are more dependent on the admittance shaping range at super synchronous frequencies. Therefore, the controller effort limitation specifications (i.e. definition of W_u) can be usually fixed before defining the tracking capabilities.

Stand-alone stability robustness analysis

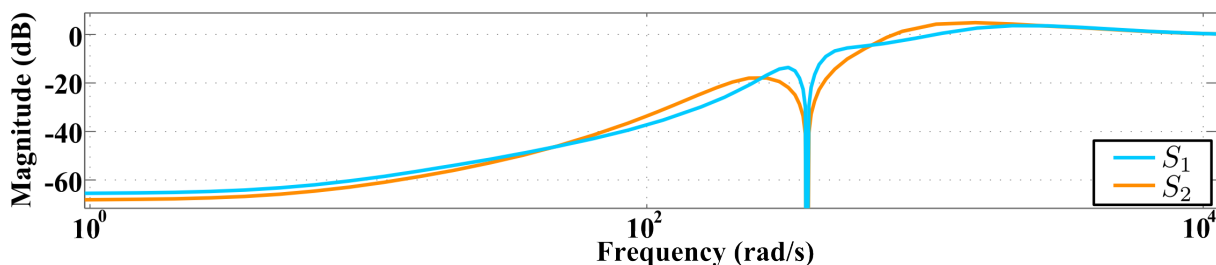


Figure 4.16. Sensitivity function results for the two considered tracking shaping designs.

Finally, Fig. 4.16 shows the sensitivity function magnitude for the two considered examples. As good tracking strongly depends on feedback action (see how $|S| \rightarrow 0$ for both examples at ω_1), the maximum sensitivity peak is higher in the second example, where the tracking bandwidth is bigger, than in the first. This would be more evident if tracking was desired at other frequencies (e.g. in selective harmonic compensation designs).

Conclusion

For this second trade-off, selection of the first or second designs is more a matter of the considered application. The second example has a faster tracking response than the first, but also a narrower effective admittance shaping range. It has also slightly smaller stability margins, but as long as multiple frequencies are not intended to be tracked (e.g. to reject grid voltage harmonics) the differences should be small. The controller effort is also slightly affected by the controller new tracking capability in comparison with the influence of effective admittance shaping ranges on it.

4.7 Sampled data problem and controller synthesis

Even though a continuous Laplace modelling has been considered in the previous sections, the real open-loop current dynamic follows a more complex pattern. That is due to the discrete nature of the actuation voltage (u) when the controller (\mathbf{K}) is implemented in a digital platform.

This section tries to derive, first, a valid open-loop model of the grid current dynamic for the two considered filter topologies (L and LCL) taking into account this more realistic scenario. Then, it studies different equivalent open-loop models, either in continuous or discrete time, that can be included in the augmented plant (\mathbf{P}) to synthesize a valid controller (\mathbf{K}). The synthesis process of the final discrete controller is detailed at the end of the section.

4.7.1 Hybrid model of the grid-current dynamic

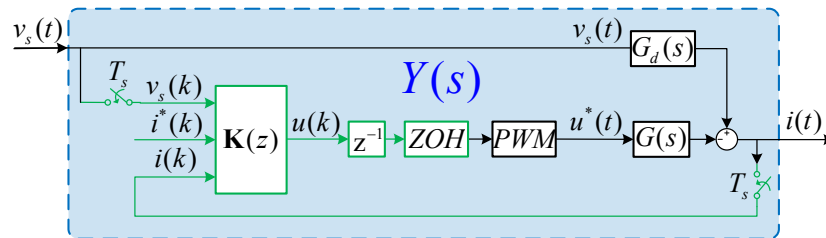


Figure 4.17. Hybrid continuous/discrete closed-loop diagram of the considered grid-current control. The blue box mark the closed-loop admittance ($Y(s)$) dynamic, defined as the relation between a continuous input, the PCC voltage ($v_s(t)$), and a continuous output, the grid current ($i(t)$).

Fig. 4.17 shows a more realistic diagram of the considered grid-current control once a discrete controller ($\mathbf{K}(z)$) is contemplated. The open-loop admittance ($G_d(s)$) can be directly modelled in the Laplace domain, as the PCC voltage (v_s) is, in fact, a continuous disturbance to the system. However, the other open-loop disturbance to the current, the controller output ($u(k)$), is a delayed discrete signal because the presented controller is executed in a digital signal processor (DSP) that requires time for its execution. So, even though the closed-loop admittance to be shaped is still a continuous transfer function (i.e. it models the relation between $v_s(t)$ and $i(t)$ once the control loop is closed), its dynamic (marked as a blue box in Fig. 4.17) includes both continuous and discrete systems. The transfer function that models the dynamic from the actuation voltage ($u(k)$) to the grid current ($i(t)$) should be, then, modified to represent a closer approximation to the realistic hybrid scenario.

PWM effect modelling

The plant model should consider, first, the PWM modulator effect in the controller actuation u . A common and approximated choice is to consider this effect equal to a Zero-Order Hold (ZOH) applied to the discrete controller output u :

$$ZOH(s) = \frac{1 - e^{-T_s s}}{s}, \quad (4.25)$$

where $ZOH(s)$ is the Laplace equivalent of the ZOH dynamic. The simplest way to include this ZOH effect is to transform $G(s)$ in equations 4.2 and 4.3 to its zero-order hold discrete-time equivalent $G(z)|_{ZOH}$ in the z -domain:

$$G(z)|_{ZOH} = \mathcal{Z} \{ \mathcal{L}^{-1} \{ ZOH(s)G(s) \} \}, \quad (4.26)$$

where \mathcal{Z} and \mathcal{L}^{-1} represents the z -transform and inverse Laplace-transform, respectively.

One-sample delay effect modelling

An inherent limitation in the practical implementation of discrete-time controllers is the impossibility of applying to the plant, in time k , an actuation computed with measurements also acquired in time k . In most power converter control scenarios signal acquisition time and controller actuation computation last for a non-negligible part of the controller sample time. The typical workaround is to postpone the actuation application until the arrival of the next sampling period. This is usually modelled placing a one-sample pure delay in the control input of the plant discrete-time equivalent model in the z -domain (i.e. adding z^{-1} to $G(z)|_{ZOH}$).

Model accuracy analysis

Fig. 4.18 shows a comparison of the frequency responses of $G(s)$, $G(z)|_{ZOH}$ and $z^{-1}G(z)|_{ZOH}$ for the LCL filter topology.

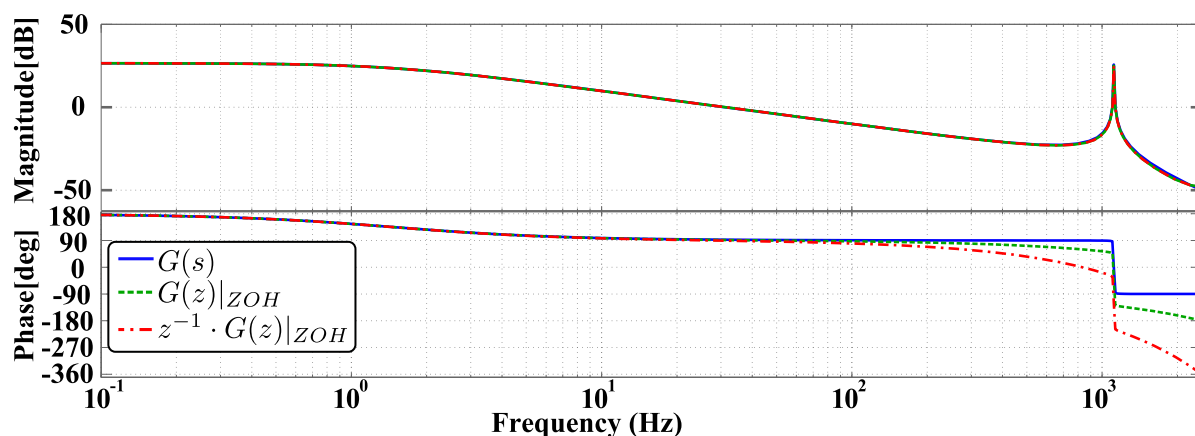


Figure 4.18. Frequency responses of the continuous open-loop plant $G(s)$, the Zero-Order Hold discrete-time equivalent $G(z)|_{ZOH}$ plant and the delayed ZOH discrete-time equivalent $z^{-1}G(z)|_{ZOH}$ for the LCL filter.

It can be observed that, while the modulus of the transfer functions are similar, there are important differences in their phases that increase with frequency. While these differences could be neglected in the case of a reference-tracking controller with a conservative tracking bandwidth

(relative to the switching frequency), in the case of the admittance shaping it would yield phase errors in the obtained closed-loop admittance.

To further prove the precision of the above model, a commutated system equivalent to the real plant, formed by a switching VSC, the LCL filter and the grid, is implemented in MATLAB[®] *Simulink* using MATLAB[®] *SimPowerSystems* toolbox. It includes both PWM modulation and the one-sample delay presented in the digital platform, so it represents a very close approximation to the implemented plant. The *Identification* toolbox is used, then, to identify the grid current i response to a discrete actuation $u(k)$ and a continuous PCC voltage $v_s(t)$ disturbances at different frequencies. Fig. 4.19 compares these frequency domain identification results with the proposed model.

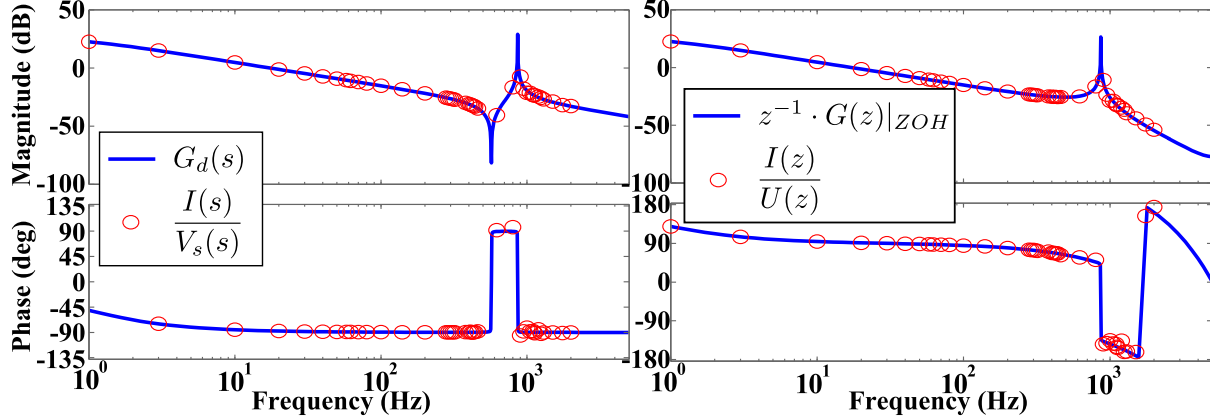


Figure 4.19. Identification of the LCL filter open-loop frequency response and its comparison to the considered command-to-output and input open-loop admittance models.

4.7.2 Search of an approximated fully continuous/discrete model

From the results in Fig. 4.19, it can be concluded that the grid current dynamic can be modelled by the outputs addition of a continuous transfer function, $G_d(s)$, and a discrete transfer function, $z^{-1}G(z)|_{ZOH}$. This hybrid model is non practical from a controller design point of view, being necessary to either transform all the elements in the augmented plant (\mathbf{P}) to the discrete z -domain or to the continuous Laplace s -domain before using the considered \mathcal{H}_∞ synthesis algorithm. This section presents different fully continuous and fully discrete approximated models, and compares them with the real hybrid dynamic shown in Fig 4.19.

Continuous time models

The effect of both PWM and computational delay in the controller output voltage ($U(s)$) can be modelled, in the continuous Laplace domain, as:

$$G_{del}(s) = \frac{U^*}{U} = \underbrace{\frac{1 - e^{-T_s s}}{T_s s}}_{ZOH(s)} \underbrace{e^{-T_s s}}_{\text{Delay}} \quad (4.27)$$

where $U^*(s)$ represents the averaged value of the VSC output voltage.

Dynamics from the controller output (u) to the grid current (i) in the L and LCL filter

topologies change, then, to equations (4.28) and (4.29), respectively:

$$G_{real}(s) = -\frac{G_{del}(s)}{sL_f + R_f} \quad (4.28)$$

$$G_{real}(s) = -\frac{G_{del}(s)}{sC(R_1 + sL_1)(R_2 + sL_2) + R_f + sL_f}, \quad (4.29)$$

where $G_{real}(s)$ models the effect of $G_{del}(s)$ in $G(s)$ in equations (4.2) and (4.3), respectively.

As it was described in Section 3.3.4, one of the requisites of the \mathcal{H}_∞ synthesis tool is that the elements in the generalized transfer function \mathbf{P} must be represented as state space matrices without internal delays or as polynomial transfer functions. This means that the effect of the delay terms ($e^{-T_s s}$) in $G_{del}(s)$ must be approximated as polynomial functions before being included in $\mathbf{P}(s)$. Two methods have been considered to obtain an approximated version of $G_{real}(s)$:

- The first method uses a **Padé approximation**:

$$e^{-T_s s} \approx \frac{\sum_{i=0}^n \frac{(T_s)^i (2n-i)! n!}{(2n)!(n-i)! i!} (-s)^i}{\sum_{i=0}^n \frac{(T_s)^i (2n-i)! n!}{(2n)!(n-i)! i!} (s)^i}, \quad (4.30)$$

where n marks the order of the resultant s-domain lineal transfer function. For a $n = 1$ Padé approximation, $G_{del}(s)$ can be approximated to:

$$G_{del}(s) \approx \frac{1 - \frac{T_s}{2}s}{\left(1 + \frac{T_s}{2}s\right)^2} \quad (4.31)$$

Substitution of (4.31) in $G_{real}(s)$ (equations (4.28) and (4.29)) results in the first order Padé approximation ($G(s)|_{Padé}$).

- The second method for the obtaining of a proper continuous approximated model is the **transformation of $z^{-1}G(z)|_{ZOH}$** into its continuous s-domain approximation. To preserve the ZOH and delay effects, a Bilinear (Tustin) transformation is used:

$$z \rightarrow e^{sT_s} \approx \frac{1 + \frac{T_s s}{2}}{1 - \frac{T_s s}{2}} \quad (4.32)$$

This transformation maps every point of the frequency response, both in magnitude and phase, of $z^{-1}G(z)|_{ZOH}$ to a point in the frequency response of a continuous-time equivalent ($G(s)|_{Tustin}$). Unfortunately, these two frequency points does not match, being the magnitude and phase at frequency ω_a of $G(s)|_{Tustin}$ equal to the magnitude and phase at frequency $\omega_b = ((2/T_s) \tan(\omega_a T_s/2))$ of its discrete equivalent $z^{-1}G(z)|_{ZOH}$. This phenomenon in the bilinear transform is called frequency warping. Even though it will not have much influence in the L filter model, this phenomenon becomes more evident if the plant to be transformed has resonant poles/zeros (i.e. sudden changes in phase/magnitude in the frequency domain) at high frequencies. For that reason, a modification of the bilinear transformation is done at the resonant frequency (ω_{res}) of the LCL filter case, called

pre-warping:

$$z \rightarrow \frac{1 + \frac{\tan(\omega_{res} \frac{T_s}{2})}{\omega_{res}} s}{1 - \frac{\tan(\omega_{res} \frac{T_s}{2})}{\omega_{res}} s} \quad (4.33)$$

For the sake of notation simplicity, both filters continuous models $G(s)$ that takes into account an approximated version of the PWM and delay dynamics using Tustin(4.32) or Tustin+pre-warping(4.33) methods will be named $G(s)|_{Tustin}$.

Discrete time model

These models consider a discrete version of the continuous s-domain open-loop admittance ($G_d(s)$), named $G_d(z)$. Three approximations have been considered:

- The inverse Tustin transformation (relation $s \rightarrow z$ in (4.32)) and the inverse Tustin+pre-warping at ω_{res} (relation $s \rightarrow z$ in (4.33)) for the L and LCL filter topologies, respectively. Both resulting functions are named $G_d(z)|_{Tustin}$.
- The impulse-invariant transformation, which matches the discretized impulse response of $G_d(z)$ to that of the continuous time system $G_d(s)$. To do this, it maps all $G_d(s)$ poles in the continuous domain (p_{s_i}) to the discrete domain (p_{z_i}) following:

$$p_{z_i} = e^{p_{s_i} T_s} \quad (4.34)$$

The resulting function is named $G_d(z)|_{Impulse}$.

- The zero-pole matching transformation, which will map all the zeros (z_{s_i}) and poles (p_{s_i}) of $G_d(s)$ to their discrete domain equivalents (z_{z_i} and p_{z_i}) following (4.34) equality. The resulting function is named $G_d(z)|_{Matching}$.

Models comparison

Fig. 4.20 shows a frequency-domain comparison of the different open-loop models considered. Some information can be extracted for its analysis:

- For the open-loop command-to-output ($G = F_{u \rightarrow i}$) dynamic, the more realistic models (i.e. the ones that accurately model the identified dynamic $I(z)/U(z)$) are $z^{-1}G(z)|_{ZOH}$ and $G_{real}(s)$, in discrete and continuous time respectively. These two models are very close in phase and magnitude inside the Nyquist frequency $f_s/2$. However, $G_{real}(s)$ includes internal delays and, then, can not be used in the \mathcal{H}_∞ synthesis algorithm, so two continuous time approximated systems, $G(s)|_{Tustin}$ and $G(s)|_{Padé}$, have been considered. Both are very close in magnitude to $G_{real}(s)$, but $G(s)|_{Tustin}$ has improved results in terms of phase.
- For the open-loop admittance ($G_d = F_{v_s \rightarrow i}$) dynamic, the more realistic model is the continuous model $G_d(s)$, as the PCC voltage (v_s) is, in fact, a continuous disturbance. The frequency domain response of the discrete equivalents obtained using the zero-pole matching ($G_d(z)|_{Matching}$) and the impulse-invariant ($G_d(z)|_{Impulse}$) are close in magnitude but very different in phase to their continuous equivalent $G_d(s)$. The discrete equivalent $G_d(z)|_{Tustin}$, obtained following a Tustin or a Tustin+pre-warping transformation, is very close in phase to $G_d(s)$ and differs slightly in magnitude, so it is its closest discrete approximation.

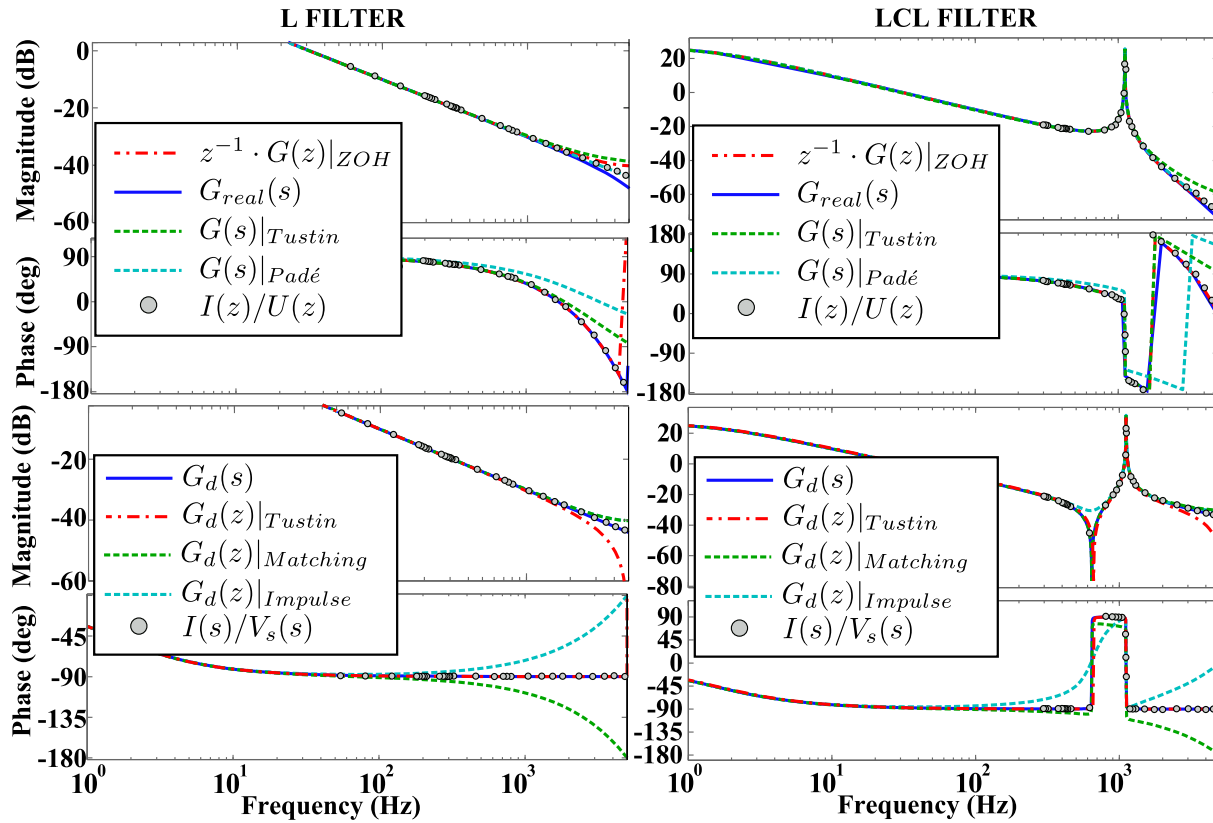


Figure 4.20. Frequency-domain comparison of the different open-loop models, both in continuous and discrete time and for both L and LCL filter topologies.

4.7.3 Controller synthesis

As concluded in the previous section, the more accurate models that can be used for the controller \mathcal{H}_∞ synthesis are the set formed by $G(s)|_{Tustin}$ and $G_d(s)$, considering the continuous s -domain, and the set formed by $z^{-1}G(z)|_{ZOH}$ and $G_d(z)|_{Tustin}$, for the discrete z -domain. Both models are ready to be included, along with model-references and frequency weights, in the model-reference structure saw in Fig. 4.3, forming a continuous $\mathbf{P}(s)$ and a discrete $\mathbf{P}(z)$ version of the generalized plant \mathbf{P} . These generalized plants are the entry points to an \mathcal{H}_∞ synthesis algorithm that will compute a continuous time $\mathbf{K}(s)$ or a discrete time $\mathbf{K}(z)$ version of the controller, respectively.

Fig. 4.21 summarizes how to obtain a final discrete controller $\mathbf{K}(z)$ for the two considered options.

Even though designing the controller directly in discrete time require less steps (continuous controller version $\mathbf{K}(s)$ on the left part of Fig. 4.21 must be discretized through Tustin method before it can be implemented in a digital platform), the continuous version of the \mathcal{H}_∞ synthesis algorithm has proven better admittance shaping results, mostly at high frequencies, than its discrete counterpart. This is probably due to the fact that the closed-loop admittance is, actually, a continuous transfer function.

So the continuous model of the plant, formed by $G(s)|_{Tustin}$ and $G_d(s)$, is the one used in the rest of this dissertation for the obtaining of current controllers $\mathbf{K}(z)$. For the sake of notation simplicity, $G(s) \equiv G(s)|_{Tustin}$ for the rest of this chapter.

The algorithm synthesis is performed using MATLAB standard library and also its Robust

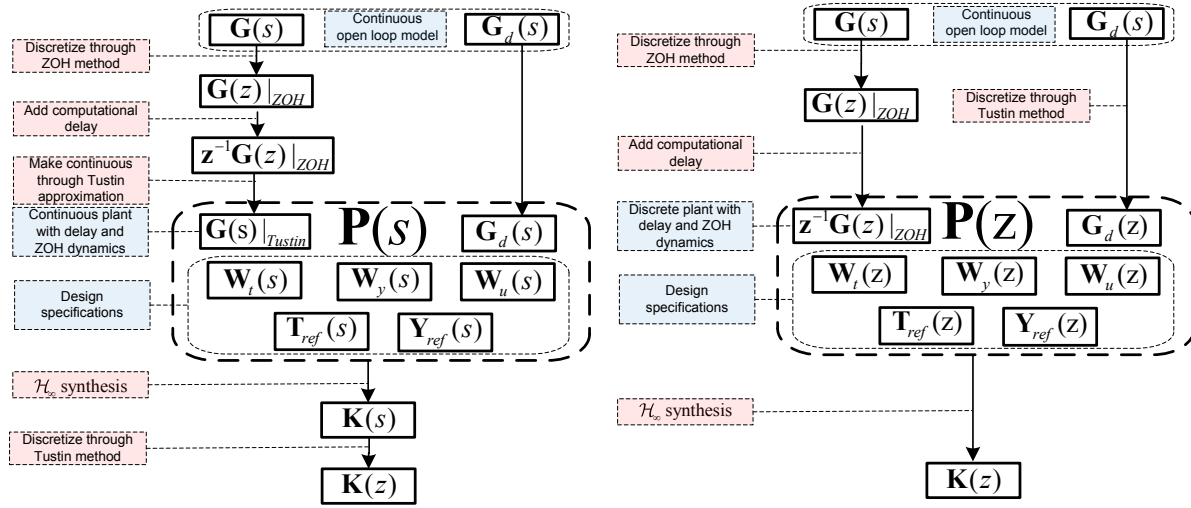


Figure 4.21. Flux diagram of the discrete controller $\mathbf{K}(z)$ synthesis from a continuous $\mathbf{P}(s)$ (left) and a discrete $\mathbf{P}(z)$ (right) generalized plant.

Control Toolbox⁹. The transfer functions used in \mathbf{P} are created using standard `tf` and `ss` commands. Continuous to discrete conversions, and vice-versa, are performed using `c2d` and `d2c`. Once they are created, process \mathbf{P} is assembled using the scripting tool `sysic`. The controller is then synthesised using `hinfscn` command. The snippet displayed on Alg. 2 describes the procedure used to obtain the final controller.

4.8 Design limitations

4.8.1 Bandwidth limitations imposed by the digital controller implementation

The proposed solution relies on the use of a discrete LTI controller and, thus, is subjected to bandwidth limitations. This limitation was derived in section 3.3.4 for a discrete feedback controller and a plant with time delays, following [Morari and Zafiriou, 1989] demonstration (see section A.6), being the maximum control bandwidth:

$$f_{c_{MAX}} \approx \frac{1}{2\pi T_s} \rightarrow \omega_{c_{MAX}} \approx \frac{\omega_s}{6}, \quad (4.35)$$

where ω_s is the sampling frequency in radians per second.

This section demonstrates that the proposed admittance shaping method is also subjected to this limitation. To do that, consider now an open-loop command-to-output transfer function (G) with a real RHP-zero at z and a LHP-pole at p , and an open-loop admittance (G_d) with a LHP-pole at p :

$$G(s) = \frac{-s + z}{s + p} \quad G_d(s) = \frac{1}{s + p} \quad (4.36)$$

The objective is to obtain an ideal two DOF controller ($\mathbf{K}_{ideal} = [K_{s_{ideal}} \quad K_{i_{ideal}}]$) with the broader admittance shaping bandwidth possible, derived from an admittance shaping error func-

⁹The synthesis procedure here described represents only one alternative that has been found particularly intuitive by the author; similar results could be obtained by different approaches.

Algorithm 2 Controller synthesis procedure

```

1: procedure CONTROLLER SYNTHESIS(G,GD,TS)
2: Weights and model references definition:
3:   Wu=tf(...); Wt=tf(...); Wy=tf(...);
4:   Yref=tf(...); Tref=tf(1);
5: Process model:
6:   delay=tf([1],[1 0],ts);
7:   G_z=delay*c2d(G,ts,'zoh');
8:   G= d2c(G_z,'bilin',...);
9: P assembly:
10:  systemnames='G Gd Yref Wy Tref Wt Wu';
11:  inputvar = '[vs;i_ref;u]';
12:  outputvar = '[Wy;Wt;Wu;vs;i_ref;G+Gd]';
13:  input_to_Wy='[Yref-G-Gd]';
14:  input_to_Wt='[Tref-G-Gd]';
15:  input_to_Wu='[u]';
16:  input_to_Yref='[vs]';
17:  input_to_Tref='[i_ref]';
18:  input_to_G= '[u]';
19:  input_to_Gd= '[vs]';
20:  P=sysic;
21: K synthesis:
22:  [K_cont,gamma]=hinfosyn(P,3,1...);
23:  if (gamma>gmax) then goto Weight definition
24:  K=c2d(K_cont,ts,'bilin',...);
25:  end

```

tion (F_y) equal to zero¹⁰:

$$F_y(s) = 0 = \frac{Y_{ref} - Y}{Y_{ref}} = Y_{ref} - \frac{G_d + GK_{s_{ideal}}}{1 + GK_{i_{ideal}}} = Y_{ref} - (G_d + GK_{s_{ideal}})S_{ideal} \quad (4.37)$$

$$S_{ideal} = \frac{1}{1 + GK_{i_{ideal}}} \quad (4.38)$$

$$K_{s_{ideal}} = \frac{Y_{ref}/S_{ideal} - G_d}{G} \quad (4.39)$$

where $K_{i_{ideal}}$ and $K_{s_{ideal}}$ are the ideal grid current (i) feedback term and the ideal PCC voltage (v_s) feed-forward term, respectively, and S_{ideal} is the ideal sensitivity function.

So perfect admittance shaping (equation (4.37)) may rely on both feedback (K_i) and feed-forward (K_s) terms or only in the feed-forward term (i.e. with $K_i = 0$ and $S = 1$). A controller that only relies on a feed-forward term would be very sensitive to plant parameters changes, so let's consider now the case of a controller with the broadest feedback bandwidth (i.e. frequency range where $|S| < 1$). This ideal feedback term ($K_{i_{ideal}}$) can be obtained from the ideal feedback IMC controller derived in [Morari and Zafriou, 1989] (i.e. from $Q(s)$ in equation A.43):

$$K_{i_{ideal}} = \frac{Q}{1 - GQ} = \frac{s + p}{2s} \quad (4.40)$$

¹⁰The two DOF controller \mathbf{K}_{ideal} is equivalent to the presented three DOF current controller ($\mathbf{K} = [K_s(s) \ K_{ref}(s) \ K_i(s)]$) for a $K_s = K_{s_{ideal}}$, $K_{ref} = K_{i_{ideal}}$ and $K_i = -K_{i_{ideal}}$. See section A.2 for more details.

The ideal sensitivity function for that term is:

$$S_{ideal} = \frac{1}{1 + GK_{i_{ideal}}} = \frac{2s}{s + z} \quad (4.41)$$

Following a similar design process to the aforementioned IMC feedback controller (see section A.6), the ideal term $K_{s_{ideal}}$ for the above S_{ideal} is:

$$K_{s_{ideal}} = \left(\frac{s + p}{s + z} \right) \left(\frac{Y_{ref}}{S_{ideal}} - G_d \right) \quad (4.42)$$

The resulting admittance transfer function (Y_{ideal}) for these two ideal controller terms is, then:

$$Y_{ideal} = (G_d + GK_{s_{ideal}})S_{ideal} = G_d S_{ideal} + \frac{-s + z}{s + z} (Y_{ref} - G_d S_{ideal}) \quad (4.43)$$

Y_{ideal} in (4.43) is defined as the ideal admittance transfer function for a particular command-to-output transfer function (G) with a real RHP-zero, an open-loop admittance (G_d), a given admittance reference (Y_{ref}) and the broader feedback action possible. Fig. 4.22 shows different ideal admittances (dashed lines) for a plant (G) with a RHP-zero at $z = 2 \times 10^4$, an open-loop admittance (G_d) and different levels of a resistive admittance reference ($Y_{ref} = Y_{refn}$).

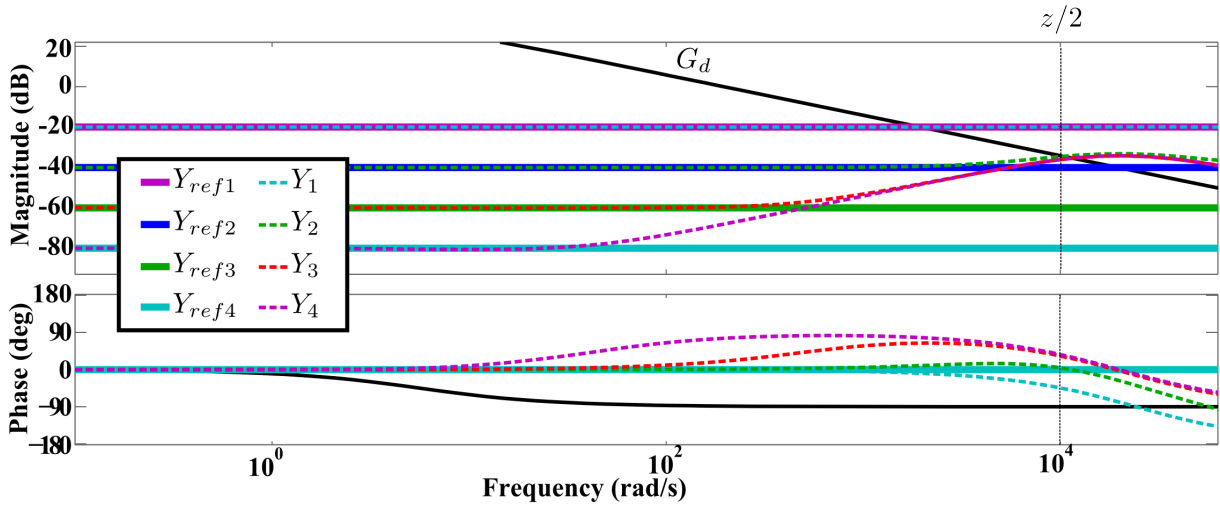


Figure 4.22. Ideal admittance Y_n for a given command-to-output plant G with a RHP-zero at z , an open-loop admittance G_d and different admittance reference Y_{refn} .

These results lead to the next conclusions:

- A RHP-zero in G at a frequency z imposes a minimum achievable admittance magnitude at ω_c equal to the open-loop admittance magnitude at that frequency (i.e. $|Y(j\omega_c)|_{MIN} = |G_d(j\omega_c)|$), where $\omega_c = z/2$. This induces an admittance shaping bandwidth limitation for low admittance references (i.e. for $|Y_{ref}(j\omega_c)| < |G_d(j\omega_c)|$), as the admittance abandons its reference at some frequency $\omega_x < \omega_c$: the lower is the reference the sooner the admittance abandons it (i.e. the smaller ω_x is). Admittance phase is affected about one decade before its magnitude.
- This RHP-zero in G does not impose, a priori, any limitation for achieving higher admittance magnitudes. That is, good admittance shaping can be achieved in magnitude at

frequencies beyond ω_c for $|Y_{ref}(j\omega_c)| \geq |G_d(j\omega_c)|$ definitions. In any case, it is still not possible to track a given admittance reference phase above $0.1\omega_c$. Moreover, as shown in Fig. 4.8, an admittance (Y) whose magnitude ($|Y|$) is greater than its open-loop value ($|G_d|$) require a bigger control effort. So chances are that admittance shaping of high reference (Y_{ref}) are not feasible for broad bandwidths, even more for low-pass G_d dynamics.

These conclusions are similar for a plant (G) with a time delay (θ), in that case with a bandwidth $\omega_c = 1/\theta$, and whether the controller only uses a feed-forward term or both feedback and feed-forward terms.

The continuous plant model ($G(s)$) presented in section 4.7.3 has a RHP-zero at frequency $z = 2/T_s$ (from the approximation of the time delay and the PWM effects), so an admittance shaping limitation frequency $\omega_c \approx \omega_s/6$ is also induced for the controller \mathcal{H}_∞ synthesis. Note that this limitation is common for every feedback/feed-forward discrete controllers and plants (G) with time delays/RHP-zeros. That is, it is not exclusive of the presented admittance shaping technique.

4.8.2 Influence of time delays on system passivity

As explained in [Harnefors et al., 2014, Harnefors et al., 2015b, Wang et al., 2014b] the time delay included in the controller digital implementation introduces non-passive frequency ranges (i.e. ranges where $\Re\{Y(j\omega)\} < 0$). These non-passive zones can trigger instabilities if the grid to which the power converter is connected has resonances at the same frequencies.

As demonstrated in the cited papers, for simple proportional one DOF controllers¹¹, these non-passive frequency ranges are $\Delta\omega = [\omega_s/6, \omega_s/2]$ for the L filter topology, and $\Delta\omega = [\omega_{dip}, \omega_s/6]$ for the LCL filter, where ω_s is the sampling frequency and $\omega_{dip} = 1/\sqrt{L_1 C}$ is the dipping frequency of the LCL open-loop admittance (G_d). If PR controllers are used (see section A.7), additional non-passive frequencies will appear around their resonant frequencies (i.e. the frequencies to be tracked).

The most common approach to compensate these frequency zones, at least below the Nyquist frequency $\omega_s/2$, are the addition of derivative terms in the current controller, either in the feedback term [Wang et al., 2014b] or the PCC feed-forward term [Harnefors et al., 2014, Harnefors et al., 2015b]¹². This will increase the admittance phase until the system becomes passive inside those ranges but, at the same time, will increase its magnitude. So these kind of techniques will increase the total controller effort (u) needed and, if feedback is involved, they may reduce the stand-alone stability margins.

Using the presented technique, the high frequency non-dissipative ranges can be avoided:

- By increasing, in the same way that the cited papers, the obtained admittance magnitude (i.e. its reference) enough, so its phase remains passive at least below the Nyquist frequency $\omega_s/2$. To that end, it must be taken into account the admittance shaping bandwidth limitations derived in the previous section, where the admittance phase can not track a given reference for frequencies above $0.1\omega_c$, being $\omega_c \approx \omega_s/6$ for the considered delayed plant.

¹¹These controllers are equivalent to a $K_i = -K_{ref} \in \mathbb{R}$ and $K_s = 0$ in the presented three DOF controller. See section A.2 for more details

¹²The system will be non-passive at some frequency above the Nyquist limit $\omega_s/2$ for plants (G) with time delays. In fact, these techniques only delay in frequency the non-passive frequency ranges above the Nyquist limit.

- By highly limiting the controller action, so controller $\mathbf{K} \rightarrow 0$ at the problematic frequencies and $Y \rightarrow G_d$, which is, obviously, passive.

Both solutions will result in a poor admittance shaping controller, as the obtained admittance will follow the given reference in a very narrow bandwidth. As this dissertation objective is the opposite (i.e. obtain a controller with the broader admittance shaping bandwidth), the compensation of the non-dissipative frequency zones is not considered.

This zones, in any case, can be reduced (but not avoided) by defining an admittance reference $Y_{ref} \approx G_d$ at high frequencies (i.e. when the maximum controller bandwidth ω_c is achieved) as, in that case, Y transition between Y_{ref} and G_d will be less abrupt, both in phase and in magnitude.

4.8.3 Generalized plant \mathbf{P} design limitations

Controller synthesis limitations in terms of the generalized plant \mathbf{P} definition are the same that the ones presented in section 3.3.4, so the reader can refer to that section for more details.

4.9 Conclusion

The next conclusions can be derived from this chapter:

- This chapter proposes a (sub)optimal \mathcal{H}_∞ method, following a model-reference approach, that allows to shape, both in magnitude and in phase, the admittance of current-controlled PEC-based applications. The designer should specify the desired behaviour of the closed-loop admittance (Y) and tracking (T) transfer functions by means of an admittance (Y_{ref}) and tracking ($T_{ref} = 1$) reference models. The synthesized controller should fulfil either ($Y \approx Y_{ref}$) or ($T \approx T_{ref}$) inside its control bandwidth, in addition to have feasible actuation levels, to avoid saturation problems, and enough stability margins.
- The designer should deal with two main design trade-offs: the admittance vs reference tracking trade-off and the controller performance vs stability robustness and energy minimization trade-off. To that end, three different frequency weights are defined (i.e. W_y , W_t and W_u) that emphasize the range of frequencies where each controller objective (i.e. admittance shaping, reference tracking and energy/bandwidth limitation) is intended. This chapter introduces different examples to illustrate these trade-offs and the controller design methodology.
- The results of the proposed method depend on the precision of the modelled system. The hybrid continuous/discrete nature of it makes not possible its use for the \mathcal{H}_∞ optimal controller synthesis. This chapter proposes different fully continuous and fully discrete approximations of this hybrid model and compares them in the frequency domain. It is concluded that, among the considered models, a continuous Laplace model that includes both the time-delay and PWM effects of the digital platform presents better admittance shaping results.
- The proposed method is subjected to a bandwidth limitation induced by the implementation of the discrete controller in a digital platform. This limitation is not exclusive of the presented admittance shaping technique.

- The accuracy of the presented preliminary results, as well as the flexibility of the controller design method, makes the proposed admittance shaping technique a promising tool to solve different objectives of grid-connected PEC-based applications.

Chapter 5

Model reference approach for closed-loop admittance shaping: applications

5.1 Introduction

Chapter 4 introduced the proposed admittance shaping technique. In addition, it shows some preliminary simulated results to illustrate the design methodology. The presented technique seems like a promising tool to solve different grid-connected PEC-based applications objectives, some of which can be translated into admittance/impedance specifications. The purpose of this chapter is to present different experimental admittance shaping applications in order to demonstrate the flexibility of the proposed technique with respect to the current controller objective.

Note that the previous chapter has only considered the inner current controller design. However, other outer control loops (e.g. voltage, power or phase-locked loops) are usually necessary in PEC-based applications to fulfil their objectives. Section 5.2 presents the considered controller testing application, a VSC-based active rectifier connected to the grid, and the effect of its outer control loop in the obtained admittance.

Some information of the experimental platforms, the controllers implementation and the method to obtain experimental frequency domain admittance results is given in section 5.3.

Once the considered PEC-based application and its experimental platform are detailed, different control motivations of admittance shaping are studied. They will be organized in three categories depending on their main characteristics and desired objectives:

- Section 5.4 explores the advantages of **broad band resistive designs**, defined by constant admittance profiles (Y_{ref}). These kind of designs are convenient to improve the robustness of the controlled grid-connected application towards weak grids. This section also studies the influence of the selected filter open-loop admittance (G_d) and the discrete controller sampling period (T_s) in this broad-band resistive behaviour. Results are obtained for both L and LCL filter topologies.
- Section 5.5 focuses on **low admittance designs**. The main application of this kind of designs is the grid voltage (v_s) (sub/inter) harmonic effect attenuation/rejection in the controlled grid current (i). Due to the aforementioned advantages of resistive designs,

minimization of the closed-loop admittance is first pursued by the definition of a resistive low admittance (Y_{ref}), taking into account the limitations imposed by the used filter and the controller digital implementation. This section also explores a second design that introduces different admittance dips at selected frequencies by means of a more complex admittance reference (Y_{ref}), resulting in an improved voltage disturbance rejection but also in poorer robustness toward weak grids.

- Finally, section 5.6 studies possible applications of **high admittance designs**. These designs serve as grid stabilizers, damping possible grid impedance resonances that may destabilize other grid-connected systems. In a similar way that in the previous section, this section explores two different high admittance profiles, one focused in a given frequency (i.e. power pit) and another that tries to behave like a resistive high admittance in the broadest region possible given the limitations imposed by the used grid filter and the sampling period of the implemented discrete controller.

The obtained experimental results for every admittance shaping design considered, both in time and frequency domain, are detailed. The motivation of each application category is, then, studied, analysing the effectiveness of the obtained designs considering their respective objectives.

5.2 Controller testing application

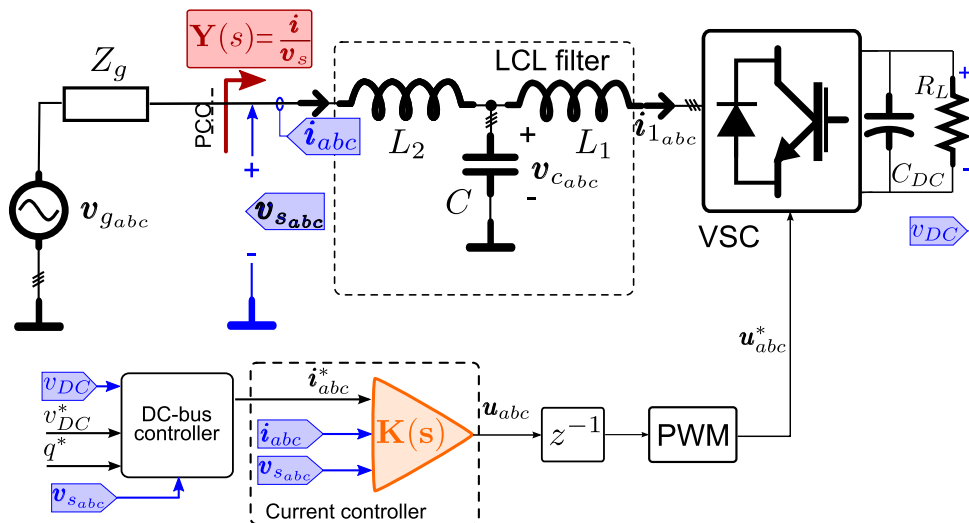


Figure 5.1. Proposal block diagram: Active rectifier connected to the grid via L or LCL filter. In orange colour the proposed controller. In blue colour the measured signals.

Even though this dissertation is mainly centred in the design of the inner current controller to shape the system input admittance, PEC-based applications need, usually, additional outer loops that may influence the achieved results. To test the proposed admittance shaping technique, the obtained current controller has been applied to a PWM VSC-based active rectifier (see Fig. 5.1), connected to the grid with an L or an LCL filter. This application represents a good benchmark plant, allowing a simultaneous testing of the current reference tracking capabilities and of the admittance emulation accuracy of the method.

The control structure is divided in a classical two-hierarchical-levels control scheme: in the highest level, the load voltage is regulated to a given reference v_{DC}^* by the DC-bus controller. This voltage reference, together with a possible reactive power reference q^* , will serve as inputs

for the DC-bus controller block that will generate an AC current reference, namely \mathbf{i}_{abc}^* , that satisfies the desired power balance for a given -measured- Point of Common Connection (PCC) voltage, $\mathbf{v}_{s_{abc}}$.

5.2.1 Influence of outer-loops in the design

The admittance of grid tied current controlled power converter is also affected by outer loops, like DC-bus controllers and phase locked loops (PLL). This section introduces some design guidelines for the outer DC-bus voltage (i.e. power) controller of the proposed active rectifier (Fig. 5.1), analysing its influence in the input admittance and the grid current in general. As the proposed active rectifier does not need of an outer PLL to obtain the innermost loop current references (i^*), its influence in the input admittance is not analysed.

DC-bus model.

The DC-bus voltage (v_{DC}) dynamic is deduced next. Considering the bus capacitor (C_{DC}) energy ($E_{C_{DC}} = \frac{1}{2}C_{DC}v_{DC}^2$) and a negligible power dissipation in the filter and the converter, the power balance equation of the active rectifier is:

$$\frac{1}{2}C_{DC}\frac{dw}{dt} = p - p_L \quad (5.1)$$

where $w = v_{DC}^2$, p_L is the power consumed by the DC-load (i.e. R_L in Fig. 5.1) and p is the active power delivered by the grid. In steady state (i.e. $\frac{dw}{dt} = 0$ and v_{DC} constant) the power converter will obtain from the grid an active power (p) equal to the DC-load demand (p_L) (i.e. $p \approx p_L$):

$$\underbrace{i_\alpha v_{s\alpha} + i_\beta v_{s\beta}}_p \approx \underbrace{\frac{w}{R_L}}_{p_L} \quad (5.2)$$

where p dynamic shown above is fulfilled only for power invariant $\alpha\beta$ transformation [Krause et al., 2002].

Considering the load power as an unknown disturbance, a DC-bus model can be obtained:

$$G_{DC}(s) = \frac{W(s)}{P(s)} = \frac{2}{sC_{DC}} \quad (5.3)$$

This simple linear model should be enough for the design of an outer DC-bus voltage controller in the considered application.

DC-bus voltage control structure and design.

The objective now is to design a controller K_{DC} , like the one shown in the bottom right part of Fig. 5.2, which will maintain w , and then v_{DC} , equal to a given reference ($W^* = (V_{DC}^*)^2$) by demanding from the grid an active power (p^*). The top part of Fig. 5.2 shows the complete cascade control structure, with the proposed three DOF inner current controller (\mathbf{K}) and the new DC-bus voltage controller (K_{DC}): the bottom left part is a simplification of this structure considering the inner close-loop current dynamics \mathbf{T} and \mathbf{Y} .

The outer controller generates an active power reference (p^*) that, along with a reactive power reference (q^*) introduced by the designer, generates the current references ($\mathbf{i}_{\alpha\beta}^*$) for the

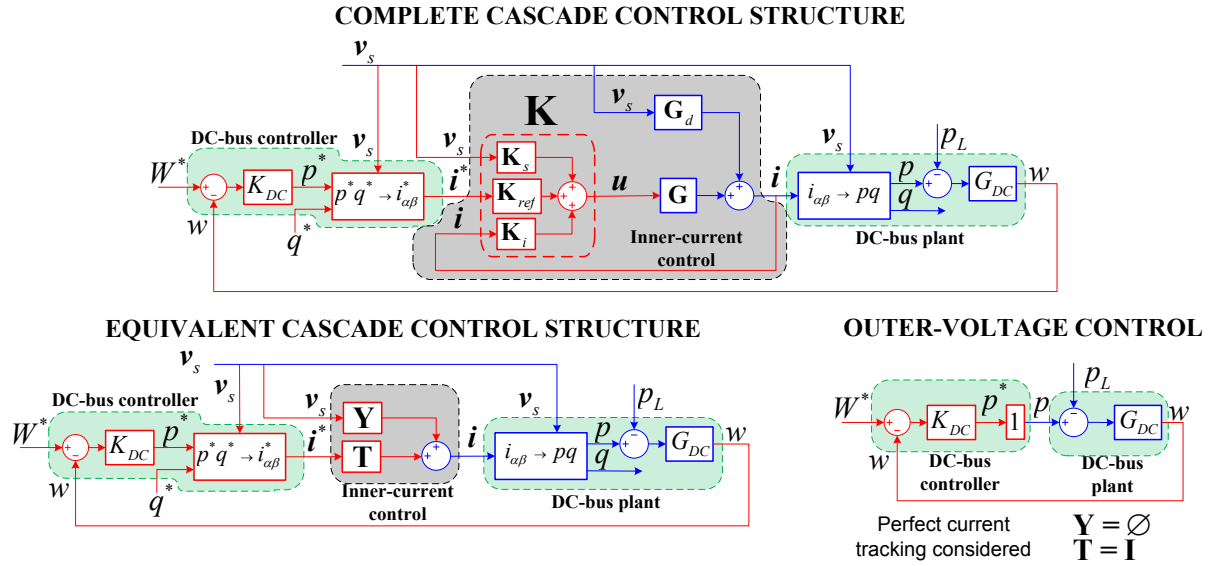


Figure 5.2. Complete cascade control structure of the proposed active rectifier.

inner controller (\mathbf{K}) following the next power theory equations [Akagi et al., 2007];

$$i_{\alpha}^* = \frac{v_{s\alpha}p^* + v_{s\beta}q^*}{v_{s\alpha}^2 + v_{s\beta}^2} \quad (5.4)$$

$$i_{\beta}^* = \frac{v_{s\beta}p^* - v_{s\alpha}q^*}{v_{s\alpha}^2 + v_{s\beta}^2} \quad (5.5)$$

The equivalent cascade control structure and the outer controller loop showed in Fig. 5.2 are equivalent if perfect current tracking (i.e. $\mathbf{T} = \mathbf{I}$ and $\mathbf{Y} = \emptyset$) is achieved. In that case, the inner loop will not affect the outer loop dynamic. To assure this, the outer controller (K_{DC}) must track its given reference (W^*) ten times slower than the inner current controller (\mathbf{K}) tracks its reference ($i_{\alpha\beta}^*$) (i.e. $t_{s_{outer}} \leq 0.1t_{s_{inner}}$, being t_s the settling time). A PI controller is proposed to achieve this objective:

$$K_{DC}(s) = k_p + \frac{k_i}{s} \quad (5.6)$$

where k_p and k_i are the proportional and integral parts of the proposed controller. Note that, as the tracking response of the proposed current controller is usually slow in favour of a bigger admittance shaping bandwidth, the resultant DC-bus voltage dynamic will be even slower.

Influence of the outer controller in the active rectifier input admittance.

As it can be seen in equations (5.4) and (5.5), the current reference is function of both active and reactive power references, but also of the PCC voltage (i.e. $\mathbf{i}^* = f_1(p^*, q^*, \mathbf{v}_s)$).

Additionally, the active power reference (p^*) depends on the outer controller (K_{DC}), the measured DC-bus voltage squared (w) and its reference (W^*). w depends on the DC-load (R_L), the grid current (i) and, again, the PCC voltage (v_s) (see equation (5.2)). So $p^* = f_2(\mathbf{v}_s, \mathbf{i}, W^*, K_{DC}, R_L)$. The reactive power (q^*) does not depend of any other variable or transfer function, as it is, in this case, generated by the designer.

So the current reference can be roughly expressed as $\mathbf{i}^* = f_1(\mathbf{v}_s, \mathbf{i}, K_{DC}, q^*, W^*, R_L)$, where q^* , R_L and W^* are considered constants. This function is not lineal (due to (5.4) and (5.5)) and

is dependent on time domain periodic signals (\mathbf{v}_s and \mathbf{i}), but can be linearized using techniques as the harmonic linearisation [Sun, 2009].

Let's denote the linear model from the PCC voltage (\mathbf{v}_s) to the current reference (\mathbf{i}^*) as $\mathbf{F}_{\mathbf{v}_s \rightarrow \mathbf{i}^*}$, whose dynamic is mainly affected by the outer loop controller (K_{DC}). The lineal grid current dynamics considering the outer loop, and neglecting the effect of constant outer references (i.e. W^* and q^*), will change, then, to:

$$\mathbf{i} = \mathbf{T}\mathbf{i}^* + \mathbf{Y}\mathbf{v}_s = \underbrace{(\mathbf{T}\mathbf{F}_{\mathbf{v}_s \rightarrow \mathbf{i}^*} + \mathbf{Y})}_{\mathbf{Y}'}\mathbf{v}_s \quad (5.7)$$

where \mathbf{Y}' is the new application input admittance, once the outer DC-bus controller is considered. The complete modelling of $\mathbf{F}_{\mathbf{v}_s \rightarrow \mathbf{i}^*}$ is out of the scope of this thesis. However, it can be derived from the above grid current dynamics, that the greatest effect of the outer loop in the admittance will be around the tracking frequencies (i.e. where $\mathbf{T} \approx \mathbf{I}$). At those frequencies the grid power (p) will be equal to the reference (p^*), which will be constant in the steady-state.

The active rectifier will behave then, as a constant power load (CPL) at frequencies around current tracking frequencies. Following equation (5.2), this will mean that a small signal increase of the PCC voltage (\mathbf{v}_s) will decrease the power converter grid current demand (\mathbf{i}), and vice-versa, to maintain p constant and equal to p_L . The CPL behaviour of the active rectifier at current tracking frequencies, from a small signal point of view, is, then, equivalent to a negative admittance. That is, the outer DC-bus controller will make the input admittance non-passive at frequencies around the tracking frequencies.

Structure non-linearity analysis.

Even though equations (5.4) and (5.5) are lineal for a balanced PCC voltage (i.e. $v_{s\alpha}$ and $v_{s\beta}$ equal in amplitude and in quadrature), that is not the case:

- if the PCC voltage is not balanced, as a second harmonic $2\omega_1$ will appear in the DC-bus voltage, which will no longer be constant in steady state.
- if the PCC voltage has an harmonic at a frequency $h\omega_1$, as it will be transferred to a current reference (i^*) with harmonics at $h\omega_1$ and its lateral bands.

To minimize the non-lineal effect of PCC voltage disturbances in the obtained grid current, a band-pass filter of the current reference (i^*) is proposed:

$$B_P = \frac{\omega_f s}{s^2 + \omega_f s + \omega_o^2} \quad (5.8)$$

where ω_f is the bandwidth of the filter and ω_o is the frequency to be filtered or, saying the same, the current reference (i^*) frequency to be tracked (e.g. the fundamental frequency (ω_1)). The filter (B_P) introduces a trade-off between filtering capabilities (small values of ω_f) and fast current references (i^*) response (big values of ω_f) for disturbances of the system (i.e. changes in PCC voltage, the DC-load etc.).

5.3 Experimental platform details.

5.3.1 Experimental setup and results test-bench.

Three different experimental setups are considered to test the performance of the proposed admittance shaping controllers.



Figure 5.3. Experimental *Semikron* and *Sedecal* setups

Semikron setup

This setup, shown in Fig. 5.3, constitutes the main source of experimental results of this dissertation. It consists of the connection between an AC programmable power supply Pacific SmartSource 345-AMX, emulating the grid, and a 17.5 kVA two-level *Semikron* VSC connected to it through an LCL or an L filter (Table 5.1 shows the main parameters of the setup). A bank of passive loads is connected to the DC-bus to test the application under different operating points. The controller is programmed in C-code and implemented on a Texas Instruments DSP TMS320DSK6713 based control platform described in detail in [Bueno et al., 2009]. More details can be found in section 5.3.2.

Table 5.1. Experimental *Semikron* setup parameters

S_N	17.5 kVA	L_1	3.4 mH
V_{gN}	120 V	R_1	28.8 m Ω
ω_1	$2\pi 60$ rad/s	L_2	1.7 mH
V_{DC}^*	700 V	R_2	18.6 m Ω
T_s	$200 \parallel 100$ μ s	C	18 μ F
T_{sw}	$2T_s$	C_{DC}	4.7 mF
$K_{DC}(z)$	$K_p + \frac{K_I T_s}{(z-1)}$	K_I, K_P	0.2893, 0.0369

The experimental values of the closed-loop system admittance are obtained by adding a three phase controlled sinusoidal signal to the voltage generated by the AC power supply. The AC power supply has a connector (P5), with three analog inputs where the user can place reference voltage signals. These voltage signals are internally amplified and then added to each one of the phases of the main power supply output. The analog outputs of a National Instruments Data Acquisition card (DAQ) controlled by a very simple LabView GUI (specially designed for this thesis) are connected to that port.

To obtain the experimental admittance value on a particular frequency, the DAQ card is configured to add, after amplification, a three-phase 10 V balanced sinusoidal signal to the AC signal of the desired frequency. The generated voltage signal and the corresponding injected currents are then acquired at a frequency $f_s = 1/T_s$, ensuring that the possible transient effects have already finished and that the data registry contains several cycles of the injected signal. Voltage and current data are, then, converted to the $\alpha\beta$ reference frame, analysed with the MATLAB `fft` command, and divided to obtain the experimental value of the converter input impedance/admittance.

Sedecal setup

The main difference with respect to the aforementioned *Semikron* set-up is the use of a 100 kVA three-level NPC *Sedecal* VSC (which is also shown in Fig. 5.3) connected to the grid (emulated by the same AC programmable power supply Pacific SmartSource 345-AMX) through a different L/LCL filter configuration. The controller is also implemented on a Texas Instruments DSP TMS320DSK6713. The main parameters of this setup are shown in table 5.2.

Table 5.2. Experimental *Sedecal* setup parameters

S_N	100 kVA	L_1	0.5 mH
V_{gN}	120 V	R_1	1.55 m Ω
ω_1	$2\pi 60$ rad/s	L_2	0.25 mH
V_{DC}^*	700 V	R_2	2.08 m Ω
T_s	200 μ s	C	100 μ F
T_{sw}	$2T_s$	C_{DC}	2.2 mF
$K_{DC}(z)$	$K_p + \frac{K_I T_s}{(z-1)}$	K_I, K_P	0.2893, 0.0369

Danfoss setup

A two-level *Danfoss* VSC is used in this case. The controller is implemented in a DS1007 dSPACE system. An AC programmable power supply Chroma 61845 is used to emulate the grid. The experimental admittance values are obtained adding three phase small controlled voltage signals to the nominal grid voltage at different frequencies using this AC power supply. The steady-state current response is, then, measured. The magnitude/phase relation between the introduced voltage and measured current at each frequency represents the experimental admittance at the corresponding frequency. Table 5.3 shows the main parameters considered for this experimental setup.

5.3.2 Controller implementation.

Once the proposed three DOF inner current controller (\mathbf{K}) is synthesized (see section 4.7.3), it is implemented, along with the outer DC-bus voltage controller, in either the Texas Instruments DSP TMS320DSK6713 based control platform or the DS1007 dSPACE based control platform. In the latter, the controllers are easily implemented thanks to the dSPACE libraries available in MATLAB[®] *Simulink*, which generate the controllers' C code directly from the *Simulink* block diagrams previously used to simulate the considered applications. In the DSP based control

Table 5.3. Experimental Danfoss setup parameters

S_N	2.6 kVA	L_1	5.2 mH
V_{gN}	120 V	R_1	28.8 m Ω
ω_1	2 π 60 rad/s	L_2	4 mH
V_{DC}^*	650 V	R_2	18.6 m Ω
T_s	100 μ s	C	15 μ F
T_{sw}	$2T_s$	C_{DC}	600 μ F
$K_{DC}(z)$	$K_p + \frac{K_I T_s}{(z-1)}$	K_I, K_P	0.2893, 0.0369

platform, the controllers are programmed in C code using its state-space description:

$$\begin{aligned} \mathbf{x}_{k+1} &= \mathbf{A}\mathbf{x}_k + \mathbf{B}\mathbf{v}_k \\ \mathbf{u}_k &= \mathbf{C}\mathbf{x}_k + \mathbf{D}\mathbf{v}_k \end{aligned} \quad (5.9)$$

where, \mathbf{x} , \mathbf{v} and \mathbf{u} vectors stand for the controller state, plant outputs measured by the sensors and controller actuation, respectively, and $[\mathbf{A}, \mathbf{B}, \mathbf{C}, \mathbf{D}]$ are the controller state matrices.

Fig. 5.4 shows a diagram of the different tasks executed during a sample period in the DSP.

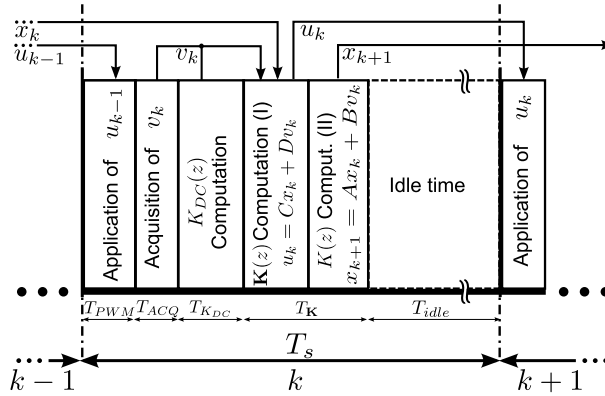


Figure 5.4. Chronogram of the implemented control algorithm. The blocks show the different tasks executed in the processor unit. The arrows show the data flow between tasks and sample periods.

The period starts updating PWM signals with the actuation computed during the previous sampling period, u_{k-1} . This time-shift is reflected as the one-sample delay at the plant input. Next, signals from sensors are acquired. With those data, higher hierarchy loops, in this case the DC-bus voltage controller, are computed, obtaining the appropriate references for the current controller. The controller is executed in two steps. First the actuation to be applied in the next period, u_k , is computed. Finally, the controller internal states are updated, calculating x_{k+1} , before the DPS goes idle until the next period arrives.

Fig. 5.5(a) shows the percentage over one sample time of all the control algorithm tasks for three different designs (i.e. different values of \mathbf{K}) implemented in the aforementioned DSP based control platform. As it can be seen, in all the designs the most time-consuming state is the inner loop controller (i.e. time $T_{\mathbf{K}}$). Fig. 5.5(b) shows the relation between \mathbf{K} number of states and its time consumption $T_{\mathbf{K}}$: as it can be seen, $T_{\mathbf{K}}$ almost linearly increases with \mathbf{K} number of states. In any case, there are no problems related to execution time constraints even

for high order controllers, as can be seen in the enough idle time remaining during one sampling time. In case its necessary, order reduction techniques can be applied to \mathbf{K} to reduce its states number and, then, $T_{\mathbf{K}}$. Section 5.5.3 shows an example of that kind of techniques.

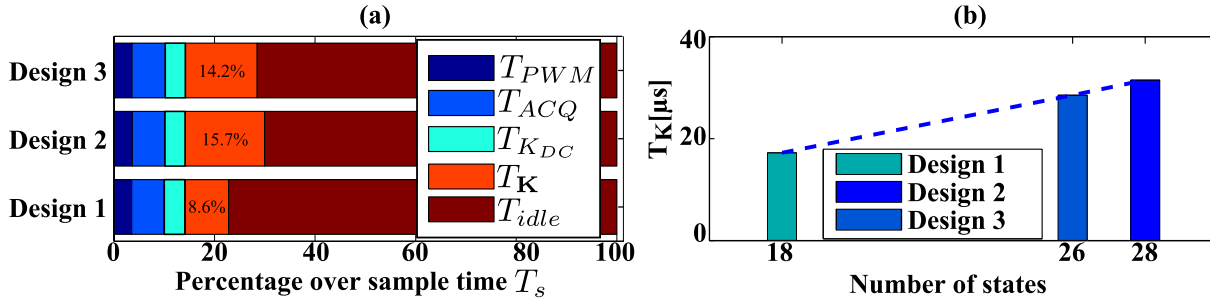


Figure 5.5. (a) Percentage over one sample time T_s of the different states of the control algorithm depicted in Fig. 5.4 and (b) inner current execution time $T_{\mathbf{K}}$ related to number of states of \mathbf{K} for the three designs considered.

5.4 Broad band resistive designs

This section studies the advantages of a resistive behaviour in a wide range of PEC-based applications. The motivation of this kind of designs, the system robustness improvement towards weak grids, is first addressed in section 5.4.1. Then, its bandwidth limitation is derived in section 5.4.2. Attending to this limitation, two designs that try to obtain a resistive behaviour in the broader bandwidth possible, one for the L filter and another for the LCL filter topology, are presented in sections 5.4.3 and 5.4.4, respectively. Finally, an analysis of the robustness improvement towards weak grids of the two proposed designs is done in section 5.4.5.

5.4.1 Motivation of broad band resistive designs

Considering a non-ideal grid, the closed-loop grid current dynamics derived in (4.5) changes to:

$$I|_{Z_g(s) \neq 0} = \underbrace{\frac{T}{1 + Z_g Y}}_{T'(s)} I^* + \underbrace{\frac{Y}{1 + Z_g Y}}_{Y'(s)} V_g, \quad (5.10)$$

where V_g is the ideal grid voltage, Z_g is the equivalent grid series impedance and $Y'(s)$ and $T'(s)$ are the modified closed-loop admittance and tracking transfer functions, respectively. From (5.10), it can be seen that the system stability no longer depends only on the loop function $L(s) = -GK_i$ in (4.5), but also on the new impedances loop $L'(s) = Z_g Y$. Provided that the system is stand-alone stable (i.e. analysing $L(s) = -GK_i$), the impedance stability criterion (see section 2.2.1) focus on this new loop ($L'(s)$) in order to predict the stability of the interconnected system. Fig. 5.6 shows the block diagram of the new grid current dynamic.

From a current controller design point of view, the easiest way to assure the system stability with weak grid conditions (i.e. high grid impedance) is to make the input admittance resistive and as low as possible in a wide frequency range, as discussed in [Harnefors et al., 2007, Middlebrook, 1976].

A graphical demonstration of this is depicted in Fig. 5.7. Fig. 5.7(a) shows the frequency-domain representation of a weak grid admittance ($Y_g = 1/Z_g$) and its interaction with a given converter admittance (Y). In this case, the converter uses a classical proportional plus integral

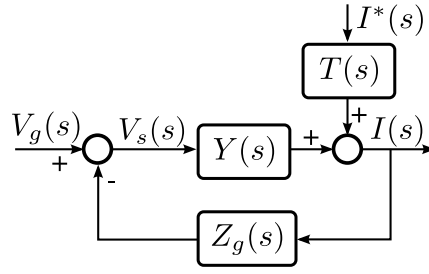


Figure 5.6. Block diagram representation of the interconnection of a current-controlled VSC to a non-ideal grid with an equivalent serial impedance $Z_g(s)$.

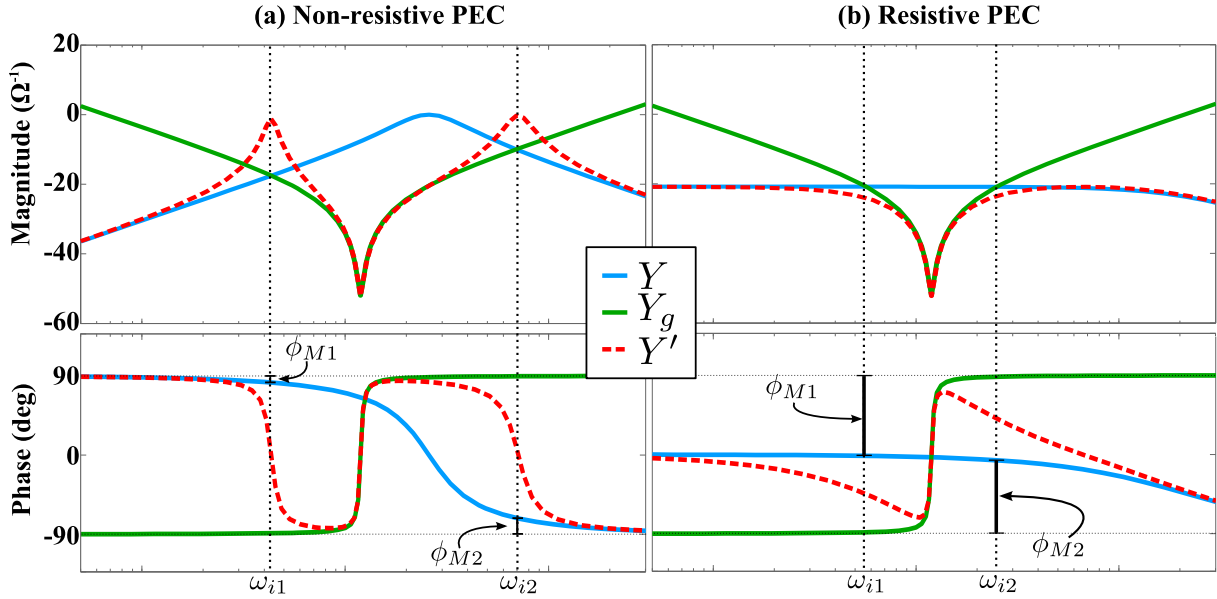


Figure 5.7. Frequency domain representation of the interaction phenomenon between the VSC admittance (Y) (blue line) and the grid admittance ($Y_g = Z_g^{-1}$) (green line), resulting in the equivalent modified admittance (Y') (red line) for two cases: (a) connection of a non-resistive PEC-based application (e.g. PI current controlled PEC) and (b) connection of a resistive PEC. ϕ_M represents the stability phase margin of the new complex system at each point of interaction (ω_i).

(PI) current controller (see section A.7) for an L filter, so its admittance (Y) is small at low frequencies (i.e. inside PI bandwidth) to reject PCC voltage disturbances and at high frequencies to filter the PWM commutation noise (i.e. open-loop filter dynamic G_d) [Céspedes and Sun, 2012]. The resulting modified admittance (Y') is shown in red.

The interaction frequencies ω_i , where $|Y(j\omega_i)| = |Y_g(j\omega_i)|$ and $|L'(j\omega_i)| = 1$, are of main importance for the stability analysis. The system will be stable as long as:

$$-180^\circ < \angle Y(j\omega_i) - \angle Y_g(j\omega_i) < 180^\circ \quad (5.11)$$

is fulfilled. This condition can be compromised by the non-passive behaviour of power converters [Harnefors et al., 2015b]. Additionally, the closer is the system to the previous stability phase boundaries ($\pm 180^\circ$), represented by the phase margin (ϕ_M) in Fig. 5.7, the bigger the admittance resonance in Y' will be, resulting in poorer rejection of grid voltage disturbances at those frequencies [Yang et al., 2014].

On the other hand, Fig. 5.7(b) shows an alternative resistive converter admittance and its interaction with the previous grid. As it can be seen, this admittance profile improves both stability robustness, increasing ϕ_M , and the rejection of voltage disturbances.

5.4.2 Bandwidth limitation of resistive broad band designs

As stated in subsection 4.8.1, the admittance shaping capability (both in magnitude and in phase) is only possible within a certain frequency range, which mainly depends on the admittance reference (Y_{ref}), the open-loop admittance (G_d) and the maximum controller bandwidth ($\omega_c \approx \omega_s/6$, where ω_s is the sampling frequency in radians per second).

Fig. 4.22 showed the ideal admittances achievable for a fixed open-loop admittance (G_d) and maximum bandwidth (ω_c), and different values of the admittance reference (Y_{ref}). From it, it can be deduced that the minimum achievable admittance at frequency ω_c is approximately equal to the open-loop admittance of the system at this frequency (i.e. $Y_{min}(j\omega_c) \approx G_d(j\omega_c)$). Therefore, it can be deduced that the minimum resistive admittance reference achievable in the broadest bandwidth (ω_c) is equal to the filter open-loop admittance at frequency ω_c (i.e. $Y_{ref_{MIN}} = |G_d(j\omega_c)|$), as it is shown in Fig. 5.8.

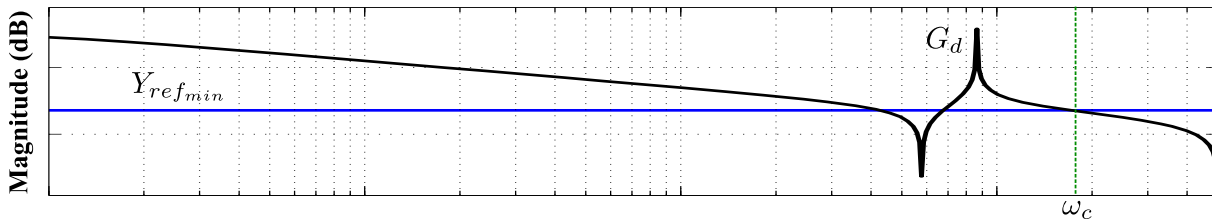


Figure 5.8. Minimum obtainable resistive admittance reference ($Y_{ref_{min}}$) as a function of the open-loop admittance (G_d) and the maximum admittance shaping bandwidth (ω_c).

Note that it is possible to achieve a smaller resistive admittance reference ($Y_{ref} < Y_{ref_{min}}$) in a narrower band. But to reduce this reference and still obtain the broadest bandwidth possible (ω_c), either the sampling time (T_s) must be reduced or the filter inductances must be increased, as both will result in a smaller magnitude of $G_d(s)$ at ω_c .

From Fig. 4.22, it is also deduced that it is possible to follow a bigger resistive admittance reference that the minimum (i.e. $Y_{ref} > Y_{ref_{min}}$) in the broadest bandwidth possible (ω_c) without theoretical limitations. However, note that an admittance ($|Y|$) bigger than its open-loop value ($|G_d|$) will require bigger actuation voltages (see Fig. 4.8), so this solution may not be feasible in practice.

5.4.3 L filter case

Model references and weights definition

This design considers the *Semikron* setup described in section 5.3, an active rectifier connected to the grid by an L filter (i.e. disconnecting the capacitor C in Fig. 5.1). Its admittance, outside the fundamental frequency range, will present a purely resistive behaviour of $Y_{ref} = 0.1U$, which is slightly above the minimum and broadest achievable resistive behaviour for the used filter open-loop admittance G_d and sampling time T_s (i.e. $Y_{ref} \gtrsim |G_d(j\omega_c)|$).

The energy absorbed by the converter due to this dissipative behaviour is evacuated, by the DC-bus voltage controller, through the grid fundamental frequency. To that end, it is necessary to provide the controlled system with fundamental frequency tracking capabilities. The simplest way to achieve this objective is by selecting a tracking reference $T_{ref} = 1$.

To distribute the different objectives along the spectrum this design uses the weights displayed on Fig. 5.9 (i.e. similar to the ones presented in section 4.6 example to illustrate the

different design trade-offs):

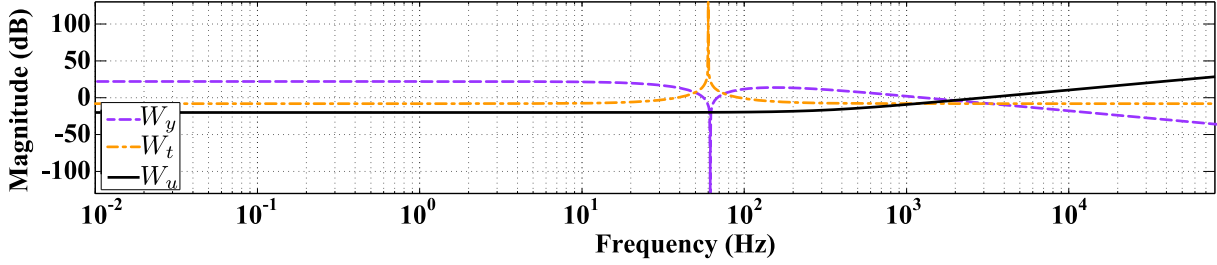


Figure 5.9. Frequency weights for the broad-band resistive design with the L filter.

- W_t is chosen as a resonance in the grid fundamental frequency. A high gain ensures an accurate tracking. Its resonance bandwidth controls tracking transient response. Concretely it follows the structure:

$$W_t(s) = K_t \frac{s^2 + 2\zeta_n \omega_1 s + \omega_1^2}{s^2 + 2\zeta_d \omega_1 s + \omega_1^2}, \quad (5.12)$$

where $\omega_1 = 2\pi 60$ rad/s is the grid fundamental frequency, ζ_n varies the resonance bandwidth and ζ_n/ζ_d can be used to adjust the resonance peak maximum value.

- Similarly, a complementary admittance weight W_y is defined using a notch-like function in the fundamental frequency.

$$W_y(s) = K_y \frac{s^2 + 2\zeta_d \omega_1 s + \omega_1^2}{s^2 + 2\zeta_n \omega_1 s + \omega_1^2} \cdot \frac{1}{(1/\omega_y)s + 1} \quad (5.13)$$

where ω_y marks the maximum frequency where admittance emulation is desired. The notch part of the transfer function is complementary to W_t resonance (i.e. equal ζ_n and ζ_d values).

- Finally, control effort is limited by the next weight:

$$W_u(s) = K_u \frac{(1/\omega_{u1})s + 1}{(1/\omega_{u2})s + 1}, \quad (5.14)$$

where the zero in ω_{u1} defines the frequency where control effort starts to be limited. The pole in ω_{u2} is needed to make W_u (and \mathbf{P}) proper, as required by \mathcal{H}_∞ synthesis algorithm.

A discrete controller with a sampling time $T_s = 200 \mu\text{s}$ is obtained from the weights and model references defined before.

Frequency domain results

Fig. 5.10 shows the obtained closed-loop tracking function $(T)^1$. It can be observed that the design achieves good tracking capabilities around the fundamental frequency ω_1 .

Similarly, Fig. 5.11 shows the achieved admittance shaping results. In the figure, it can be seen the open-loop admittance (G_d), the desired admittance reference model (Y_{ref}), the theoretical closed-loop admittance $(Y)^1$ and the experimentally identified system admittance

¹ Y and T are calculated using equation (4.5) from the theoretical plant dynamics (G and G_d) and the synthesized controller (\mathbf{K})

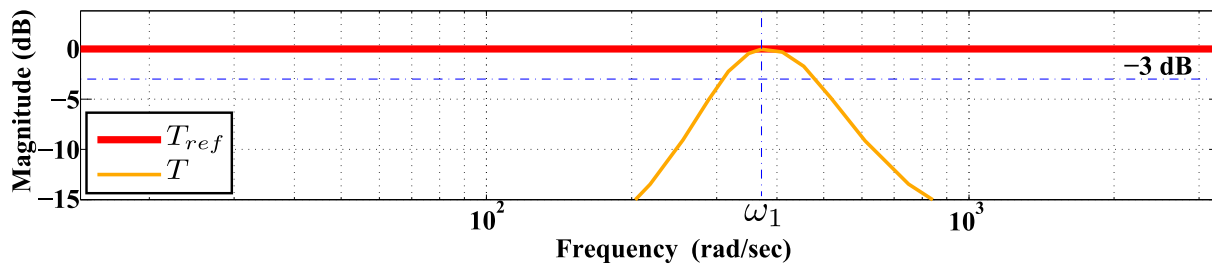


Figure 5.10. Tracking shaping result for the resistive design in the L filter topology.

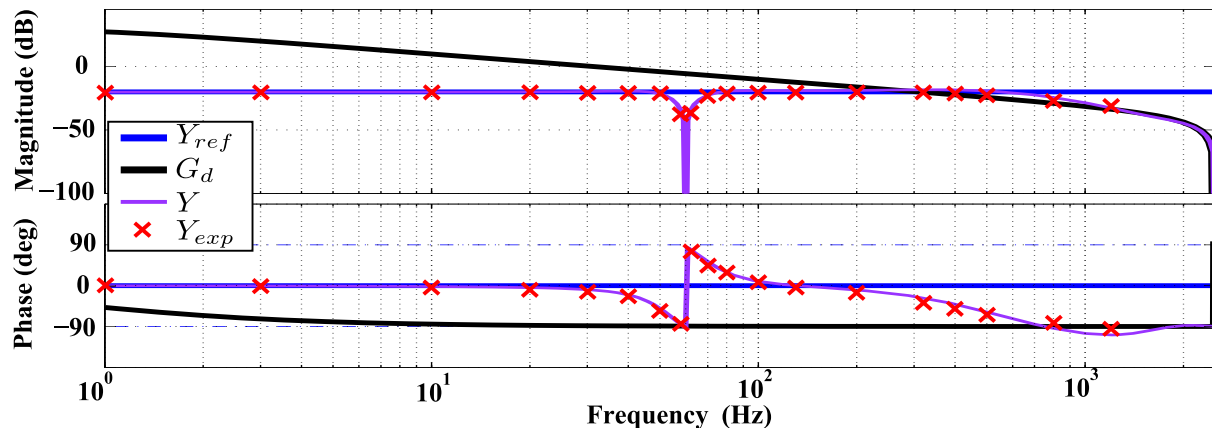


Figure 5.11. Admittance shaping result for the resistive design in the L filter topology.

(Y_{exp}) for a discrete number of frequencies. It can be observed that the synthesised controller effectively shapes the system admittance: as expected the admittance follows the reference below and above the fundamental frequency up to the system maximum control bandwidth (around the fundamental frequency there is a transition zone where $Y \rightarrow 0$ due to tracking shaping).

Finally, Fig. 5.12 shows the achieved sensitivity function. Its magnitude is below the 6 dB limit usually defined to consider a system robust.

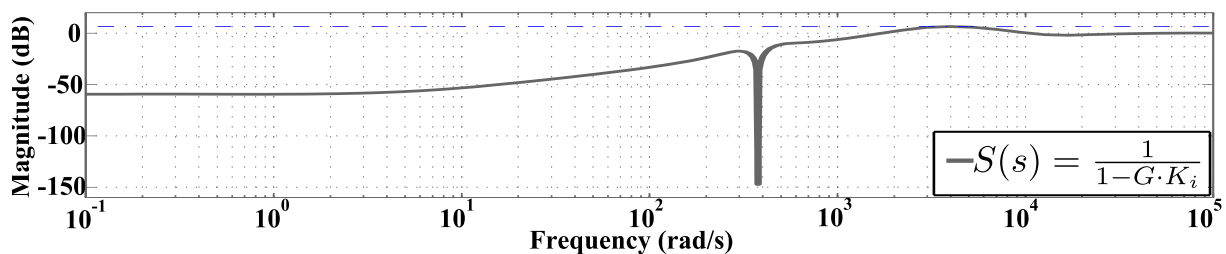


Figure 5.12. Achieved sensitivity function magnitude for the resistive design in the L filter topology.

5.4.4 LCL filter case

Model references and weights definition

Using again the *Semikron* setup (see parameters in table 5.1), the same resistive admittance reference $Y_{ref} = 0.1\mathcal{U}$ is now considered for the LCL filter topology, as it is still a close value to the broadest and minimum achievable resistive behaviour for this filter and sampling time (i.e. $Y_{ref} \gtrsim |G_d(j\omega_c)|$).

The design flow is almost unaffected by the more complex dynamics of the LCL filter. In this case, control objectives spread over a wider band, using a W_y equal to (5.13) but with a bigger ω_y , so the LCL resonance can be also shaped adequately. Tracking reference is also kept as $T_{ref} = 1$. This example has been designed to present a faster tracking behaviour than the previous design. W_t follows, thus, (5.12) but selecting a wider resonance bandwidth (i.e. increasing ζ_n). Control effort is shaped with a W_u equal to (5.14), with an also higher ω_{u1} value. Fig. 5.13 shows the frequency domain representation of the aforementioned weights.

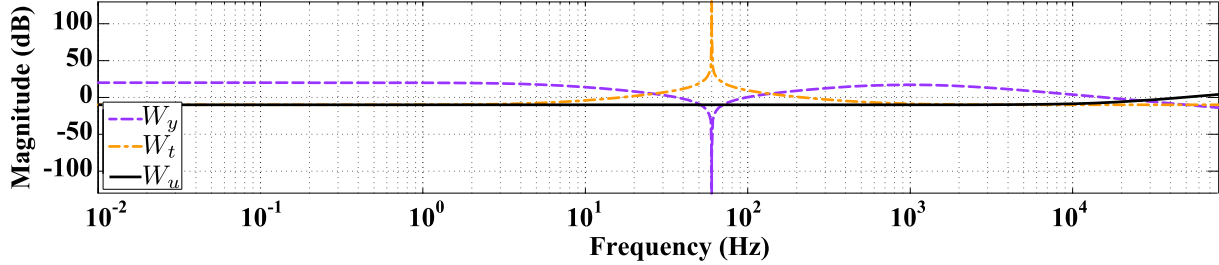


Figure 5.13. Frequency weights for the broad-band resistive design with the LCL filter.

A discrete controller with a sampling time $T_s = 200 \mu s$ is obtained from the above weights and model references selection.

Frequency domain results

Fig. 5.14 shows the obtained tracking shaping results: the tracking bandwidth is bigger than for L filter case, as expected from the wider W_t resonance width.

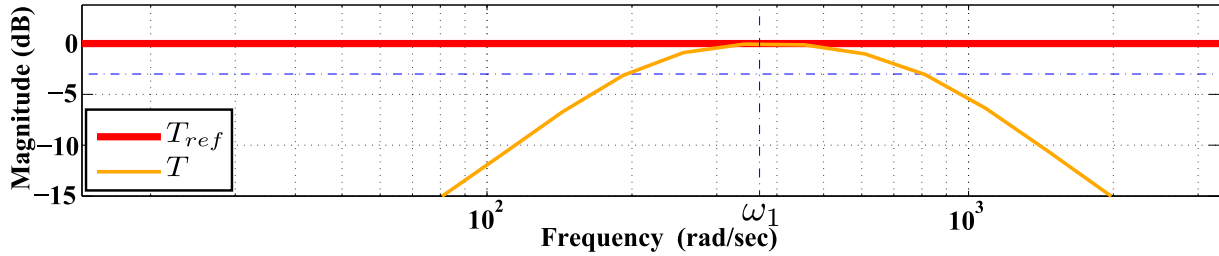


Figure 5.14. Tracking shaping result for the resistive design in the LCL filter topology.

Fig. 5.15 shows the achieved admittance shaping results. Theoretical admittance (Y) is equal to the given reference (Y_{ref}) at both sub and super synchronous frequencies. The experimental admittance results (Y_{exp}) are similar to the expected ones, with a small mismatch in phase probably for the non-exact filter modelling, more precisely the LCL resonance. Note how the resonance frequency ($\omega_{res} = \sqrt{(L_1 + L_2)/(L_1 L_2 C)}$) in G_d , is actively damped by the proposed method thanks to the resistive reference definition ($Y_{ref}(j\omega_{res}) = 0.1\bar{U}$).

Fig. 5.16 shows the sensitivity function magnitude, which again fulfil the robustness standards.

Time domain results

This design is used to validate, in the time domain, the experimental transient and tracking capabilities of the active rectifier obtained with the proposed design procedure. Results are gathered in Fig. 5.17:

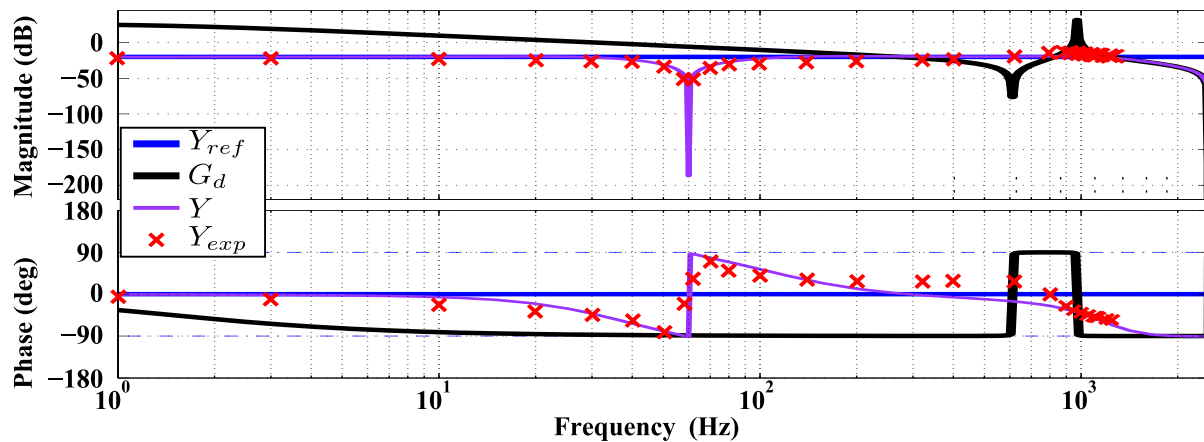


Figure 5.15. Admittance shaping result for the resistive design in the L filter topology.

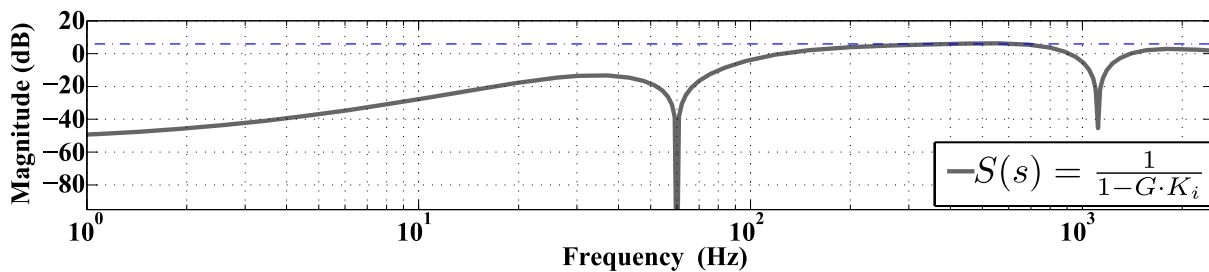


Figure 5.16. Achieved sensitivity function magnitude for the resistive design in the LCL filter topology.

- Fig. 5.17(a) shows the initial converter connection and DC-bus charging to its nominal value (700 V). General view shows how the DC-bus is charged from the diode-rectified level to the nominal value. Zoom 1 shows the current transient when PWM starts. Zoom 2 details system signals during bus boosting. After elevation, currents go null because bus is initially unloaded (i.e. $R_L = 0$).
- Fig. 5.17(b) shows the system behaviour under a soft reactive power change. With the DC-bus still unloaded, reactive power reference goes from 4 to -4 kVar. Power controller forces the transient to follow a slope. Top view shows the complete transient. Zoom 1 and 2 focus on the phase between the grid voltage and currents for both references.
- Fig. 5.17(c) shows the system behaviour when a 4.2 kW load (R_L) is connected to the DC-bus with a null reactive reference. The top shows the complete transient. Zoom 1 focuses on the currents and DC-voltage evolution after the connection. Zoom 2 shows grid currents and voltage in steady-state. Fig. 5.17(d) shows the $\alpha\beta$ components evolution for the results shown in Fig. 5.17(c): the top part shows the PCC and grid consumed currents and their reference in $\alpha\beta$ reference frame for Zoom 1; the bottom part shows the grid consumed current and the reference provided by the outer controller for the α and β components during Zoom 2 time ranges. As it can be seen the currents follows their references accurately.
- Fig. 5.17(e) and 5.17(f) show system evolution when the grid suffers a balanced and unbalanced (type E [Bollen, 2000]), respectively, with a loaded 4.2 kW DC-bus. Top view shows the complete transient in grid voltages, currents and DC-bus voltage, meanwhile the lower view focuses on the dip initial edge. For the balanced case, all phases fall to 60% of its value keeping their phases untouched. In the unbalanced dip test, phases b and c fall to 30% of its value, again with no changes in their phases. As it can be seen, a small

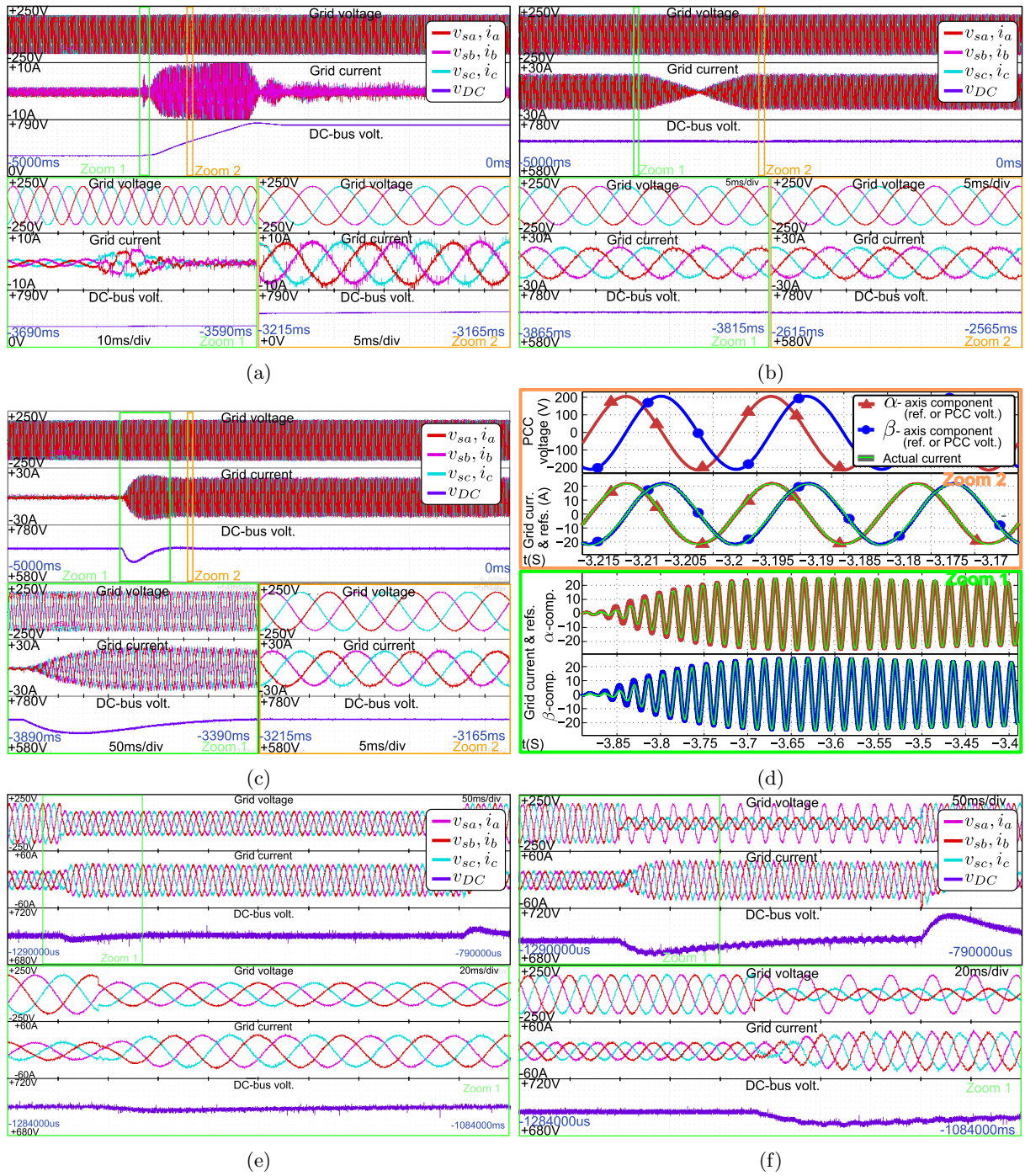


Figure 5.17. Time-domain experimental measurements of the active rectifier response to different tests: (a) start (b) reactive power reference change (c) active power (DC-load) reference change (d) $\alpha\beta$ grid current components evolution for the previous active power reference transient (e) balanced dip (f) unbalanced dip.

oscillation (with a frequency $2\omega_1$) appears in the DC-bus with an unbalanced dip. The grid current response is, on the other hand, smooth and sinusoidal for both balanced and unbalanced dip tests. Additionally, no oscillation at frequency ω_{res} can be appreciated, which proves again the good obtained resonance damping.

5.4.5 Robustness toward grid uncertainties analysis

The robustness improvement of the proposed resistive admittance shaping method towards weak grids is analysed below. The current-controlled grid-connected VSCs, for both L and LCL filter topologies, are next tested for two different grid series impedance dynamics: a purely inductive grid $Z_g(s) = L_g s$ and a resonant inductive-capacitive grid $Z_g(s) = (L_g s)/(L_g C_g s^2 + 1)$. For the sake of notation simplicity, these grids will be named as L-type and LC-type grids in the rest of the chapter.

L filter case

Fig. 5.18 shows the modified admittance ($Y'(s)$) closed loop poles (i.e. roots of $1 + Z_g Y$ in equation (5.10)) for changes of L_g in the L-type grid and C_g in the LC-type grid (with L_g fixed to 0.74 pu^2), considering an L-filter connection with the grid.

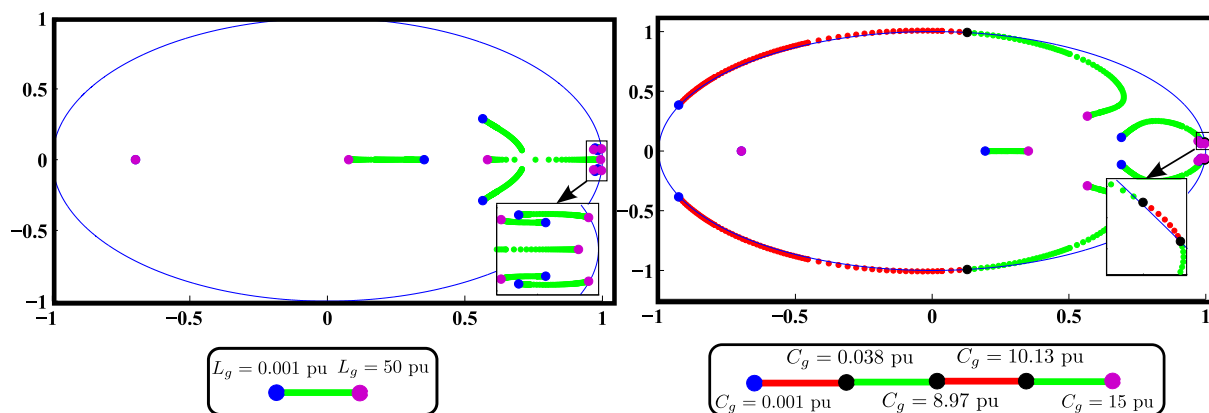


Figure 5.18. $Y'(s)$ poles for changes of the L-type grid (left) and changes of the LC-type grid (right) using the L filter topology. The red lines represents unstable cases.

The system is stable for all L-type grids considered. However, it has some unstable zones for LC-type grids (red lines in Fig. 5.18). These instabilities appear when the resonance of Z_g matches, in frequency, the two non-dissipative zones of the obtained admittance (Y) in Fig. 5.11: the first in the fundamental frequency (ω_1), that interacts with the grid for a C_g inside the interval $[8.97, 10.13] \text{ pu}^2$, and the second at high frequencies outside the controller bandwidth (f_c), for a C_g inside the interval $[0.001, 0.038] \text{ pu}^2$.

Fig. 5.19 shows $Y'(s)$ magnitude for some of the previous L-type (left side) and LC-type (right side) grid changes. As it can be seen, an inductive behaviour of the grid decreases the obtained admittance at high frequencies. However, the interaction between the LC-type grid and the converter admittance generates a resonance in Y' : the red box in the right side of Fig. 5.19 represents the zone where this resonance is unstable. The capacitive behaviour of Z_g interacts in this case with the inductive and non-passive behaviour of the converter at high frequencies.

LCL filter case

Fig. 5.20 and Fig. 5.21 show $Y'(s)$ closed-loop poles and magnitude evolution for the same changes of the grid series impedance, in this case for the LCL filter topology, which admittance

²Grid impedance parameters are expressed in per unit values of the *Semikron* VSC nominal impedance $Z_N = 3V_{gN}^2/S_N$ (i.e. $L_N = Z_N/\omega_1 = 6.5 \text{ mH}$ and $C_N = 1/(Z_N\omega_1) = 1.1 \text{ mF}$)

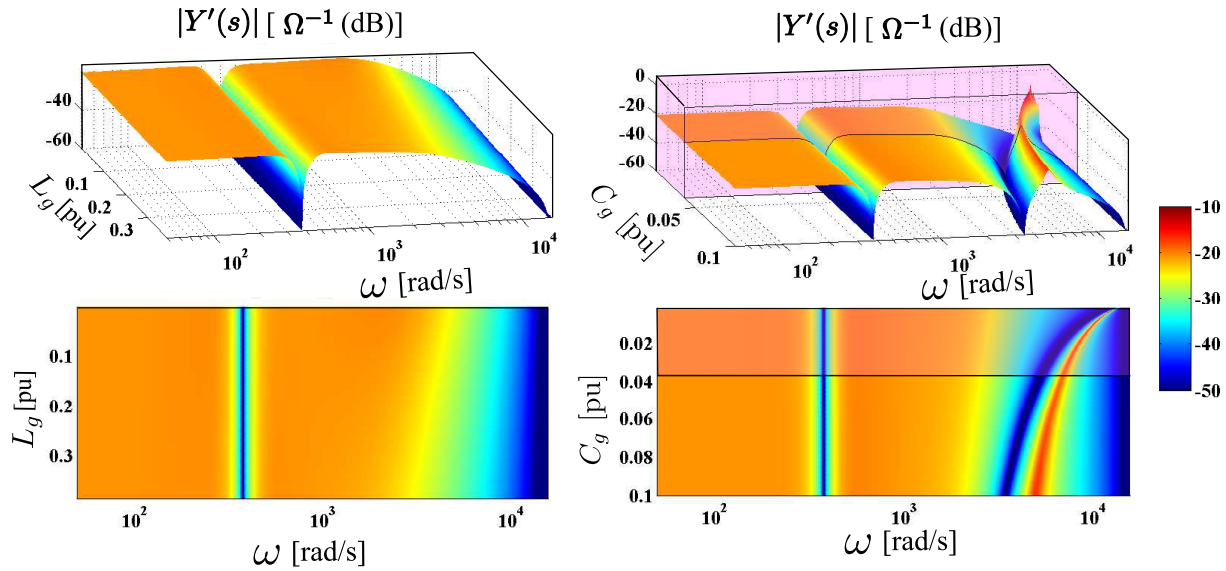


Figure 5.19. $|Y'(s)|$ for changes of an inductive grid (left) and an inductive-capacitive grid (right) using the L filter topology. The red box in the right represents C_g interval where the interconnected system becomes unstable.

results were shown in Fig. 5.15.

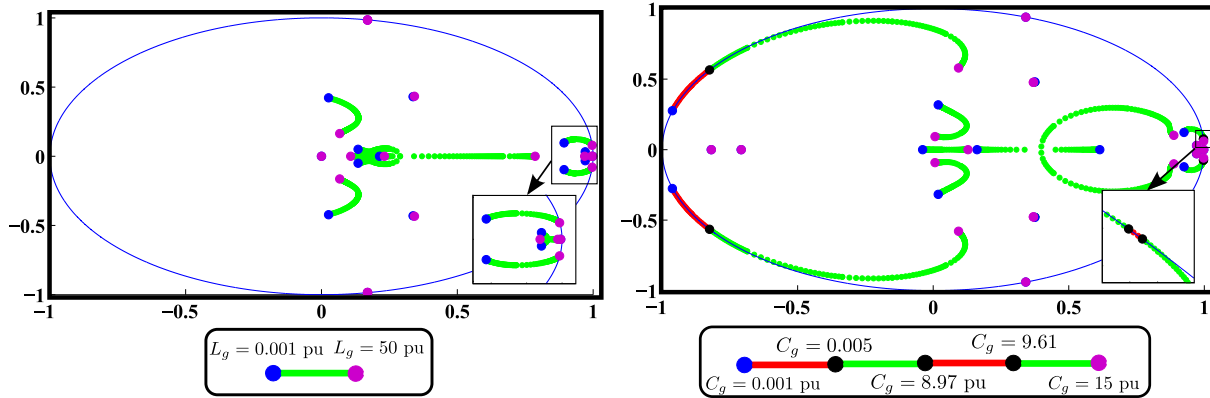


Figure 5.20. The admittance $Y'(s)$ poles for changes of inductive grid (left) and changes of capacitive grid (right) using the LCL filter topology.

Again, the system is stable when connected to a wide range of inductive-grids. It becomes unstable if the resonance of an LC-type grid impedance matches, in the frequency domain, the non-passive zones of the active rectifier (see Fig. 5.15) at fundamental frequency and at high frequencies.

Experimental time domain demonstration of the system robustness

The robustness of the grid-current controller is now experimentally tested in the time domain for the LCL filter case. Fig. 5.22(a) shows the tracking results for a sudden change of the grid current reference (i^*) with ideal grid conditions (i.e. $Z_g = 0$ and PCC voltage (v_s) equal to its nominal value). Fig. 5.22(b) shows a similar experiment, this time with an LC-type resonant grid impedance connected between the LCL filter and the AC power supply. The current is stable and quickly tracks the given reference for both cases. Note that the grid impedance resonance is perfectly damped by the converter resistive admittance. This behaviour is expected attending to

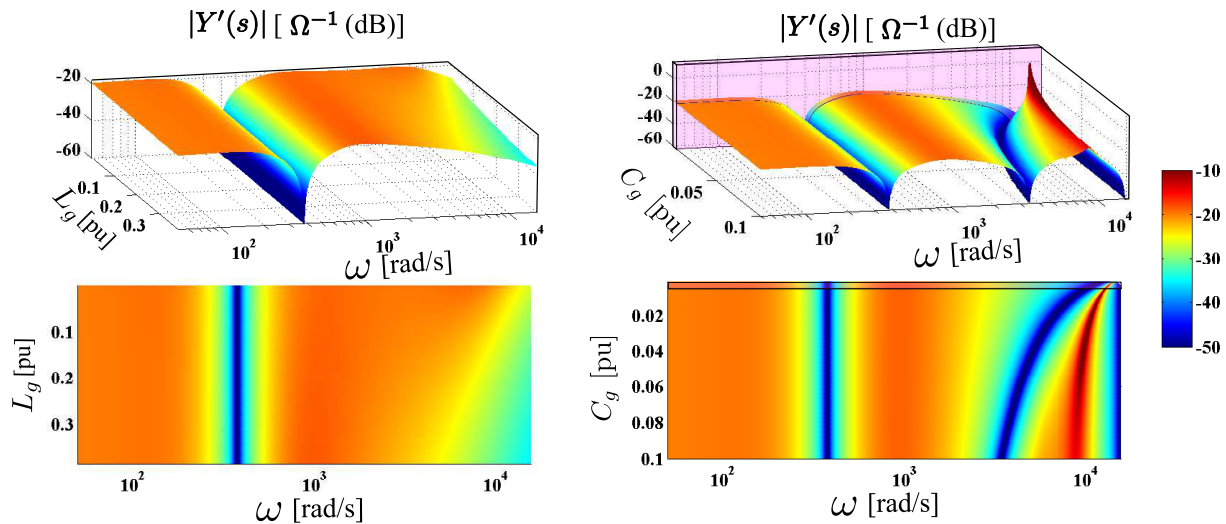


Figure 5.21. $|Y'(s)|$ for changes of an inductive grid (left) and an inductive-capacitive grid (right) using the LCL filter topology.

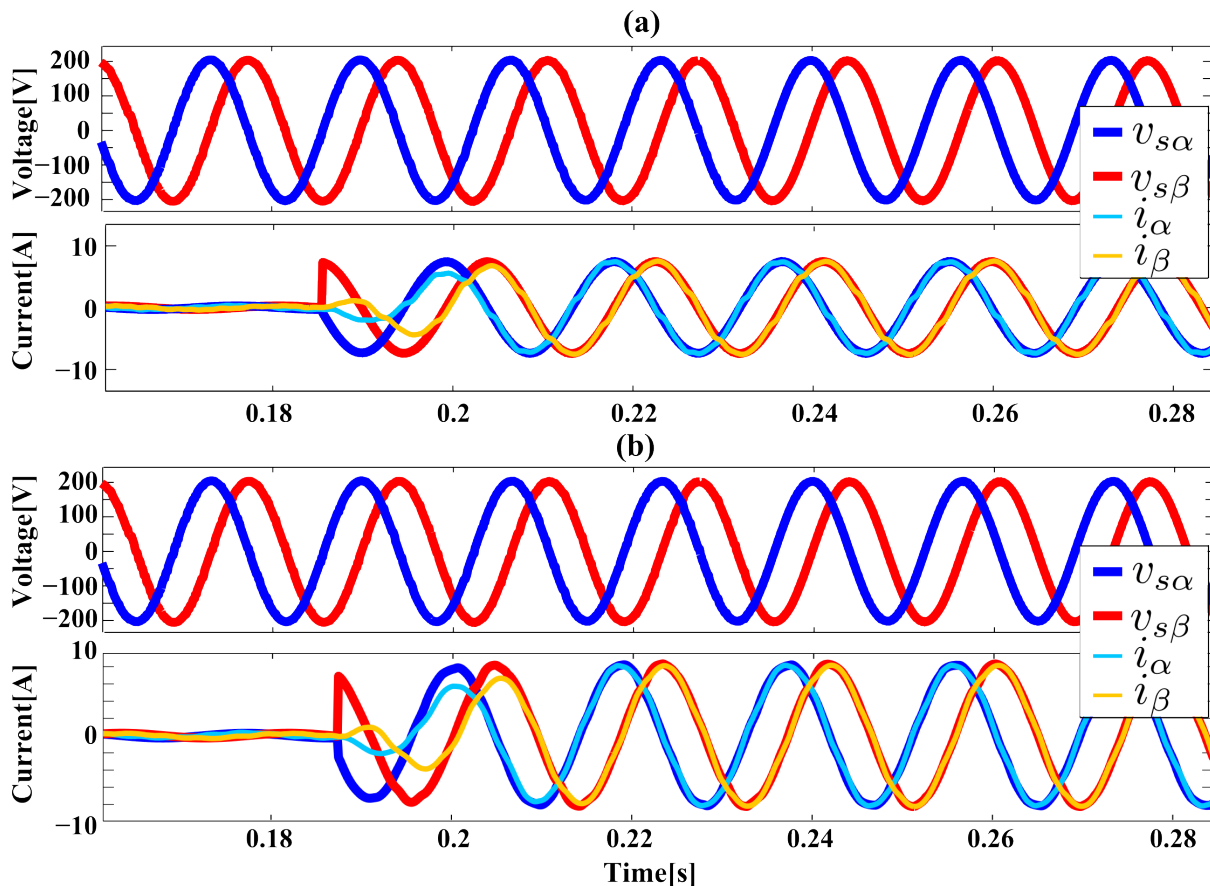


Figure 5.22. (a) Experimental time domain tracking results for an ideal grid impedance ($Z_g = 0$) (b) Experimental time domain tracking results for a resonant LC-type grid: $L_g = 0.74 \text{ pu}^2$ and $C_g = 0.33 \text{ pu}^2$.

admittance magnitude ($|Y'(s)|$) evolution in Fig. 5.21 for the chosen grid impedance parameters: $L_g = 0.74 \text{ pu}^2$ and $C_g = 0.33 \text{ pu}^2$.

Conclusions of the robustness analysis

The achieved broad-band resistive designs only present some instabilities whenever the resonant of an LC-type grid matches one of the non-passive zones of the controlled system:

- The first non-passive zone, around the fundamental frequency (ω_1), comes from the current reference tracking control (i.e. admittance control is not desired at these frequencies) and is unavoidable due to the CPL behaviour of the active rectifier (see subsection 5.2.1).
- The zone at high frequencies is beyond the admittance control bandwidth (see subsections 4.8.1 and 4.8.2) and can only be reduced by a more complex admittance reference that increases system admittance phase (and, then, magnitude) enough prior to the end of controller bandwidth. Some previous works have study this by including derivative terms in their current controllers [Harnfors et al., 2015b, Wang et al., 2014b]. However, this phase increase will trigger bigger actuations and, if feedback is involved, smaller stand-alone margins.

The resonant frequency of the grid (i.e. $\omega_{res_{Z_g}} = 1/\sqrt{L_g C_g}$) decreases as C_g increases. This resonance will be damped if it matches the resistive admittance shaping zones of the converter (i.e. sub and super synchronous frequencies below the controller bandwidth). This can be seen in 5.18 and Fig. 5.20, where the unstable (poorly damped) poles for low values of C_g gradually tend to stability as C_g increases. This resonant poles damping phenomenon can be also seen in $|Y'(s)|$ evolution (see Fig. 5.19 and Fig. 5.21), which resonance at high frequencies gradually decreases as C_g increases. This also explain how the unstable zones, in terms of grid impedance values modification, are narrower for the LCL filter case than for the L filter case (compare right side of Fig. 5.18 and Fig. 5.20) due to its broader band of resistive/passive behaviour (compare admittance phases of Fig. 5.11 and Fig. 5.15).

It is important to remark that the results from Fig. 5.18 to Fig. 5.21 show the worst case scenario, where the considered grid resonance is not damped by any resistive element, which is rarely the real case. In a more realistic scenario, the resonant unstable poles in Fig. 5.18 and Fig. 5.20 may lay inside the unit stability circle. Additionally, as shown in Fig. 5.11 and 5.15, the experimental admittance (Y_{exp}) presents a more resistive behaviour at high frequencies than the theoretical obtained admittance (Y), which means that this non-passive zone could be narrower in the real application.

The proposed controller, that shapes the converter admittance to behave as a resistance in a broad band, is, then, proven to be very robust for a wide range of grid impedance uncertainty, both for L and LCL filter topologies. It is important to remark that some of the considered grid impedances are not feasible in practice, as their high values will require huge controller actuation for grid current tracking. The aforementioned analysis only shows the stability robustness of the method.

5.5 Low admittance designs

This section explores the design of PEC-based applications with a low closed-loop admittance. The motivation of this kind of designs, rejection of PCC voltage (sub/inter) harmonics, is stated in section 5.5.1. Given the advantages of resistive broad band design in term of robustness towards grid uncertainties (see section 5.4), a broad-band resistive admittance is first studied in section 5.5.2, trying to minimize the admittance reference (Y_{ref}) to improve the (sub/inter) harmonic rejection results. Even though the harmonic rejection capability of this design extends

into a wider bandwidth than the common proposals, it is probably not enough to fulfil the strict grid standards. For that reason, a second design is explored in section 5.5.3, which defines a more complex admittance reference (Y_{ref}) with a dip-like behaviour at some discrete frequencies (i.e. low order harmonics), resulting in an improved harmonic rejection capability at these frequencies. Proposed controllers are designed and tested for the LCL filter topology active rectifier. In addition to the (sub/inter) harmonics rejection capability, the obtained systems should fulfil some stability and performance requirements, such as good tracking of the current reference (i^*), LCL filter resonance damping and stability robustness both in grid-connected and stand-alone conditions. The analysis of some of these objectives fulfilment is addressed in section 5.5.4, comparing the obtained results of the two proposed low admittance designs.

5.5.1 Motivation of low admittance designs

The presence of grid current (sub/inter) harmonics in current-controlled grid-connected PEC-based applications is regulated by strict grid standards such as [IEEE 519-2014, 2014], [IEEE 1547-2003, 2008] and [IEEE 929-2000, 2000]. The controlled grid current (i) is affected by the PCC voltage (v_s) as it can be derived from equations (4.5) and (5.10). To reject the effect of PCC voltage (sub/inter) harmonics in the controlled current, it is clear that a low admittance, ideally zero, is desired, at least in the grid low order harmonics (commonly $5\omega_1$ and $7\omega_1$).

As stated in section 2.3.2, the commonest way to reject grid voltage harmonics is to include multiple PR feedback controllers tuned at the problematic frequencies, whose high magnitude will indirectly reduce the closed-loop admittance at the tuning frequencies. Note, in any case, that the use of these controllers would only result in a rejection of voltage oscillations in the tuned frequencies. Moreover, even the rejection effectiveness at those frequencies depend on different factors, such as the model uncertainties, the discretization process and the presence of computational delays in the system, which may result in frequency displacement of the tuned PR and, then, in an ineffective harmonic attenuation. Additionally, the use of high feedback gains controllers may lead to poor stand-alone stability margins (see water-bed effect in section A.4), so its use is not recommended when a wide frequencies range of grid voltage oscillation is wanted to be rejected. Finally, the stable operation of PR controllers becomes more difficult for resonant filters as the harmonics to be rejected approach their resonances.

5.5.2 In a broad band

Model references and weights definition

This first design objective is to behave as a low resistive admittance in a broad frequency range. In that regard, it is very similar to the LCL filter design presented in subsection 5.4.4. The only difference is that, in this case, an admittance as low as possible to reject grid voltage (sub/inter) harmonics inside the controller bandwidth is intended.

Taking into account the bandwidth limitations for a broad-band resistive design addressed in section 5.4.2, the filter inductances are increased and the sampling time is decreased for this design, using to that end the *Danfoss* experimental setup shown in section 5.3 (refer to table 5.3 for its main parameters values). The capacitor value is also decreased to reduce the new LCL filter resonant frequency within the controller bandwidth. The minimum resistive admittance reference for this new filter and sampling time is $Y_{ref} = 0.06 \Omega^{-1}$, which, along with the common tracking reference selection $T_{ref} = 1$, will constitute the desired behaviour of the closed-loop grid current dynamic.

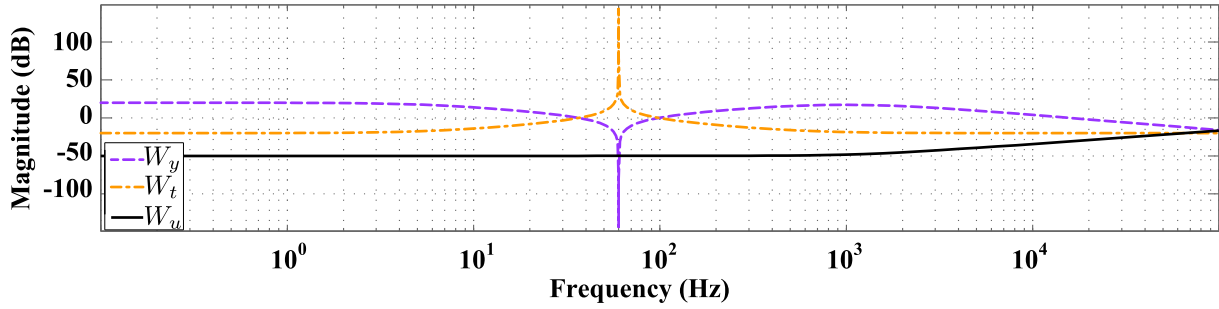


Figure 5.23. Frequency weights for the low admittance broad-band resistive design with the LCL filter.

Admittance shaping is again desired at both sub and super synchronous frequencies (including the filter resonant frequency), tracking shaping is desired around the fundamental frequency and control effort is limited at high frequencies. Tracking ($W_t(j\omega)$), admittance ($W_y(j\omega)$) and control effort ($W_u(j\omega)$) weights follow, then, the same dynamics than (5.12), (5.13) and (5.14), respectively. Fig. 5.23 shows the frequency domain representation of the selected weights.

A discrete ($T_s = 100 \mu s$) controller is obtained from the aforementioned design parameters.

Frequency domain results

Fig. 5.24 and Fig. 5.25 show the obtained tracking and admittance shaping results, respectively. As expected from the selected weights, the tracking transfer function (T) is equal to one (i.e. perfect current tracking is achieved) at the fundamental frequency (ω_1), meanwhile the closed-loop admittance (Y) follows its low resistive reference (Y_{ref}) at both sub and super synchronous frequencies, damping the LCL filter open-loop resonance. The obtained experimental admittance (Y_{exp}) demonstrates that any (sub/inter) harmonic in the PCC will be attenuated to a current oscillation of, at most, 6% of the introduced voltage disturbance thanks to the low defined admittance reference $Y_{ref} = 0.06 \Omega^{-1}$.

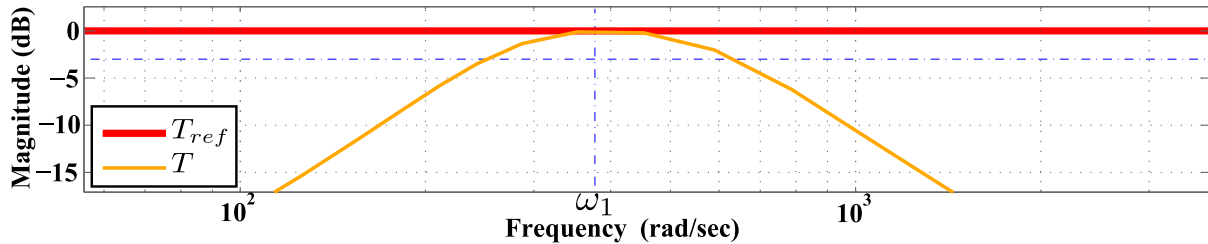


Figure 5.24. Tracking shaping result for the low admittance broad-band resistive design with the LCL filter.

Finally, Fig. 5.26 shows the achieved sensitivity function magnitude ($|S|$), which again fulfils the stand-alone stability robustness standards.

5.5.3 Localized at some frequencies (admittance dips)

Model references and weights definition

A higher order admittance reference (Y_{ref}) is considered for this design, with lower gain values at the main grid voltage 5th and 7th harmonic frequencies. This kind of admittance profile may lose the higher robustness towards weak grids obtained with the previous resistive design, but

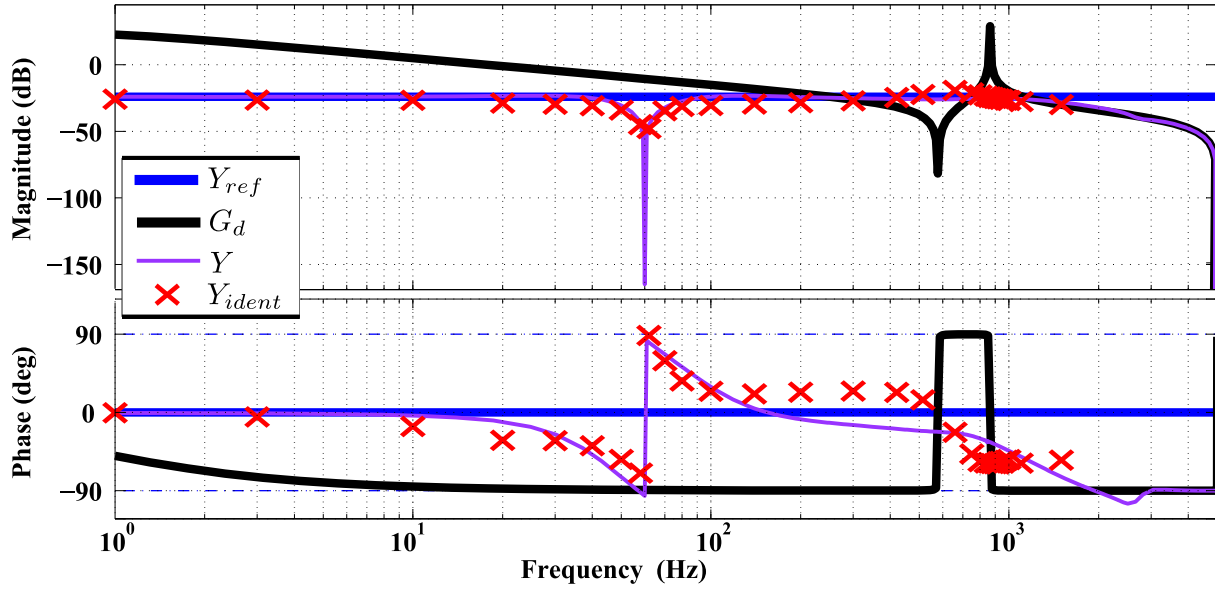


Figure 5.25. Admittance shaping result for the low admittance broad-band resistive design with the LCL filter.

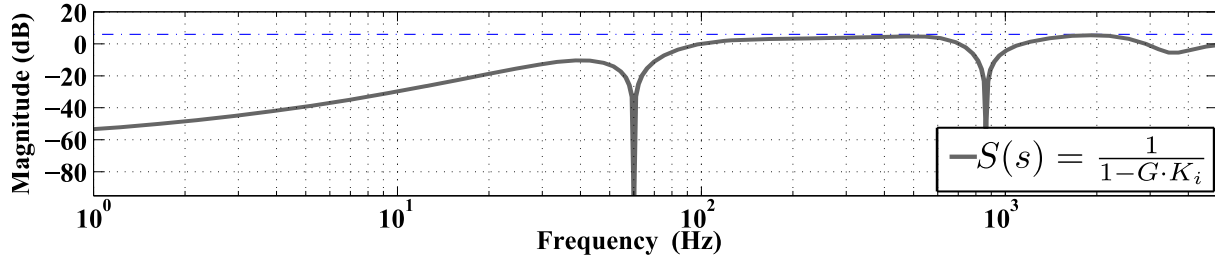


Figure 5.26. Achieved sensitivity function magnitude for low admittance broad-band resistive design with the LCL filter.

produces a bigger attenuation of the grid voltage influence in the controlled grid current without increasing the filter inductances. The proposed admittance reference dynamic is as follows:

$$Y_{ref}(s) = 0.1 \left(\frac{s^2 + 2\zeta_d(5\omega_1)s + (5\omega_1)^2}{s^2 + 2\zeta_n(5\omega_1)s + (5\omega_1)^2} \right) \left(\frac{s^2 + 2\zeta_d(7\omega_1)s + (7\omega_1)^2}{s^2 + 2\zeta_n(7\omega_1)s + (7\omega_1)^2} \right), \quad (5.15)$$

which has a resistive behaviour of $0.1 \Omega^{-1}$ at all frequencies except for the fifth ($5\omega_1$) and seventh ($7\omega_1$) harmonic frequencies, where two admittance dips are placed. These dips have the same dynamic than the notch at fundamental frequency in W_y (see equation (5.13)); that is, $n_h = \zeta_n/\zeta_d$ will define the dip minimum value and ζ_n the dip bandwidth. In this case, both dips are designed equally, with a minimum gain value $n_h = 10^{-2}$ and enough width to quickly damp the 5th and 7th grid voltage harmonics influence in the controlled current. Additionally, Y_{ref} parameters are selected so that the desired system is always inside the passivity limits (i.e. $-90 < \angle Y_{ref} < 90$), in order to increase its stability robustness towards weak grids.

The proposed design is again applied to the LCL filter topology of the *Semikron* setup (refer to table 5.1 for its main parameter values), with a sampling time $T_s = 100 \mu\text{s}$. The selected admittance reference should result in a current oscillation of 0.1% of the magnitude of eventual 5th and 7th harmonic voltage disturbances ($Y_{ref}(j5\omega_1) = Y_{ref}(j7\omega_1) = 0.001 \Omega^{-1}$), and an attenuation of 10% for the rest of controlled frequencies ($Y_{ref}(j\omega) = 0.1 \Omega^{-1}$ for all frequencies except for $5\omega_1$ and $7\omega_1$). A tracking reference $T_{ref} = 1$ is chosen, as always.

Good admittance shaping is desired again at sub and super synchronous frequencies (includ-

ing the LCL filter resonance), with a good tracking at the fundamental frequency (ω_1) and higher control effort limitation at high frequencies. Tracking (W_t) and control effort (W_u) weights dynamics are, then, equal to the ones presented in (5.12) and (5.14), with a necessary modification in the admittance weigh (W_y):

$$W_y(s) = K_y N_{\omega_1}(s) R_{5\omega_1}(s) R_{7\omega_1}(s) \frac{1}{(1/\omega_y)s + 1}, \quad (5.16)$$

where

$$N_{\omega_1}(s) = \frac{s^2 + 2\zeta_{d1}\omega_1 s + \omega_1^2}{s^2 + 2\zeta_{n1}\omega_1 s + \omega_1^2} \quad (5.17)$$

$$R_{5\omega_1}(s) = \frac{s^2 + 2\zeta_{n5}(5\omega_1)s + (5\omega_1)^2}{s^2 + 2\zeta_{d5}(5\omega_1)s + (5\omega_1)^2} \quad (5.18)$$

$$R_{7\omega_1}(s) = \frac{s^2 + 2\zeta_{n7}(7\omega_1)s + (7\omega_1)^2}{s^2 + 2\zeta_{d7}(7\omega_1)s + (7\omega_1)^2} \quad (5.19)$$

The main difference between this new admittance weight and the one used in the previous designs (equation (5.13)) is the two resonant-like gain increments at the 5th ($R_{5\omega_1}(s)$) and 7th ($R_{7\omega_1}(s)$) harmonic frequencies. Fig. 5.27 shows the frequency domain representation of the selected weights for this design.

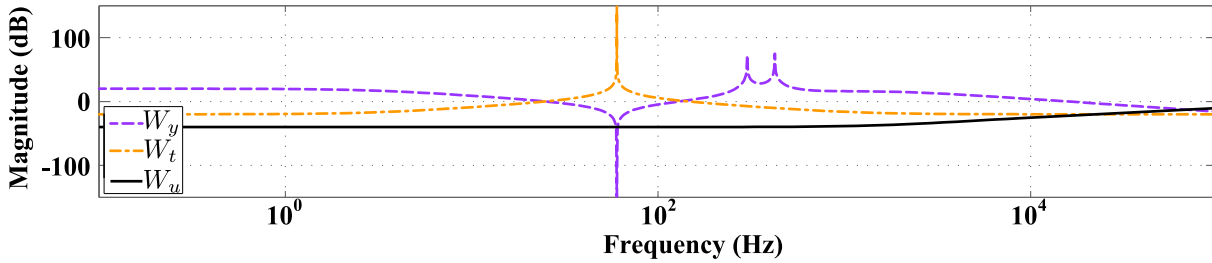


Figure 5.27. Frequency weights for the admittance dips design with the LCL filter.

Justification of the use of a higher order generalized plant

The addition of these new resonant parts in W_y is justified next. As introduced in subsection 4.5.3, an effective admittance shaping is obtained at frequencies where $|F_y(s)|$ is low, being $F_y(s)$ the normalized admittance shaping error transfer function defined in (4.15). $F_y(s)$ magnitude is shaped, in the frequency domain, by the inverse magnitude product $|W_y(s)Y_{ref}(s)|^{-1}$, as demonstrated in the admittance shaping error magnitude boundary ($|L_y|$) defined in in-equation (4.18). This means that when a low admittance reference is desired at a given frequency the admittance weight must increase accordingly in order to achieve a good admittance shaping: that is, designer must increase $|W_y(s)|$ to decrease $|W_y(s)Y_{ref}(s)|^{-1}$ for low $|Y_{ref}(s)|$ values, and then achieve low $|F_y(s)|$ values.

Fig. 5.28 demonstrates this further by means of frequency domain results. It shows the admittance shaping error ($|F_y|$) minimization (top) and the obtained closed-loop admittance (Y) (bottom) for the desired admittance reference (Y_{ref}) with (Fig. 5.28(b)) and without (Fig. 5.28(a)) the resonant parts in $W_y(s)$. As it can be seen in Fig. 5.28(a), if a plain admittance weight is defined (like the one in (5.13)) the dips in $Y_{ref}(s)$ will result in a poor minimization of the admittance shaping error (i.e. high values of the error boundary ($|L_y(s)|$) and, then, of $|F_y(s)|$). This is solved by the addition of the proposed resonant weights, leading to the good admittance shaping results shown in Fig. 5.28(b).

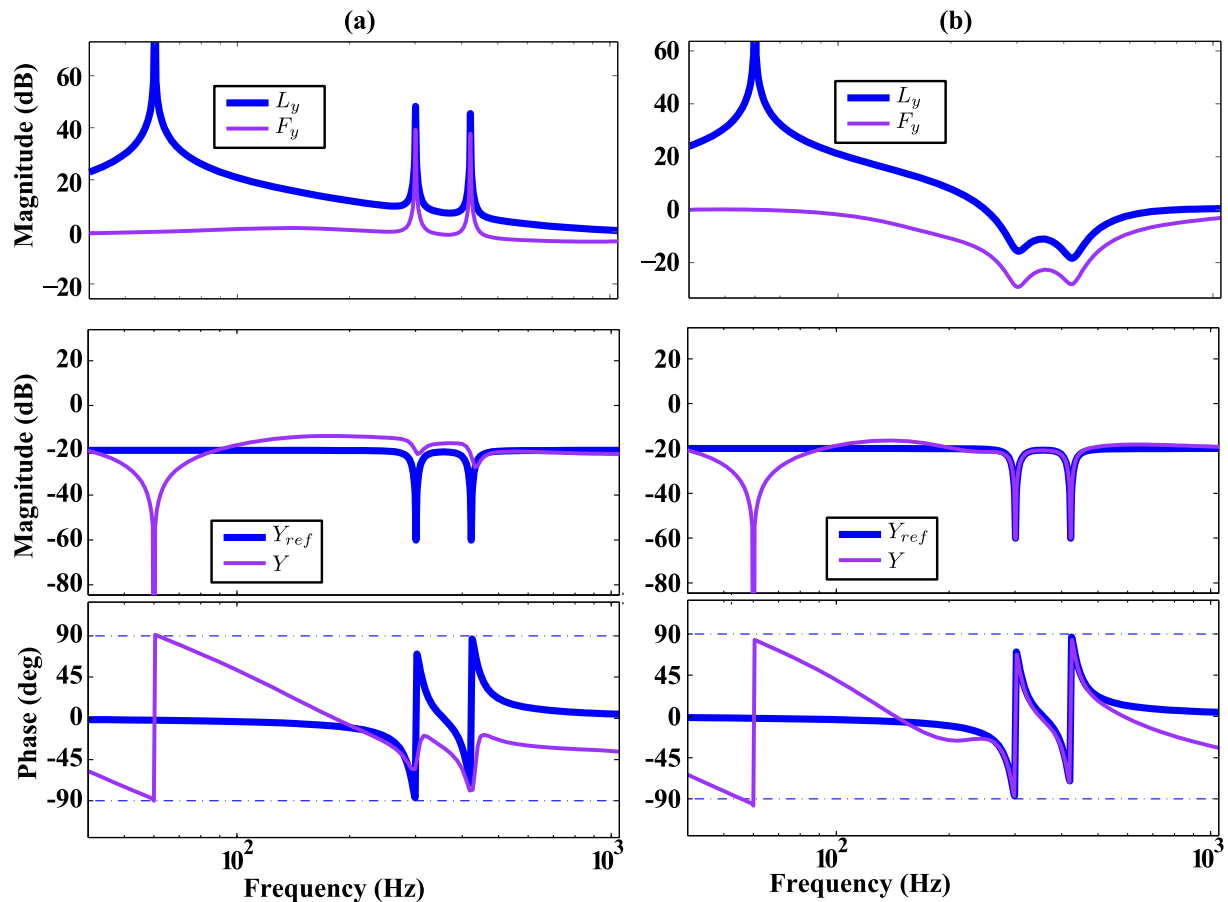


Figure 5.28. Admittance shaping results (a) without introducing resonant parts in the admittance weight and (b) introducing resonant parts in the admittance weight.

Order reduction of the synthesized controller

As stated in subsection 3.3.4, the synthesized \mathcal{H}_∞ controller (\mathbf{K}) has the same order than the generalized plant (\mathbf{P}) which, at the same time, depends on the chosen design parameters (i.e. model references and weights). The aforementioned selection of tracking (T_{ref}) and admittance (Y_{ref}) references, and tracking (W_t), admittance (W_y) and control effort (W_u) weights, along with the LCL filter model (G and G_d) will result in a single-phase controller of 21 states (42 if the two axes of the $\alpha\beta$ reference frame are considered). Even though the used DSP can compute the operations of this large controller within the selected sampling time T_s (see Fig. 5.5), a reduction of the controller order is recommended.

To do so, the command `reduce` of MATLAB Robust Control Toolbox was used. This command uses a balanced model reduction technique based on the Hankel singular values of the transfer function to be reduced, which provide a measure of energy for each state in a system. The high energy states of a system are of main importance for its dynamic, and then must be retained, in opposition to low energy states, which can be discarded without affecting the overall performance. Let's name the controller to be reduced \mathbf{K}_n and its reduced version \mathbf{K}_{red} : using `reduce` a controller \mathbf{K}_{red} that minimize the additive error $\|\mathbf{K}_n - \mathbf{K}_{red}\|_\infty$ will be obtained attending to the Hankel singular values of \mathbf{K}_n .

Fig. 5.29(a) shows the 21 Hankel singular values of the initial controller (\mathbf{K}_n) distributed with respect to its absolute value (i.e. from biggest to smallest state energy). A reduced 15th order controller can be obtained with negligible modifications in the performance, as shown

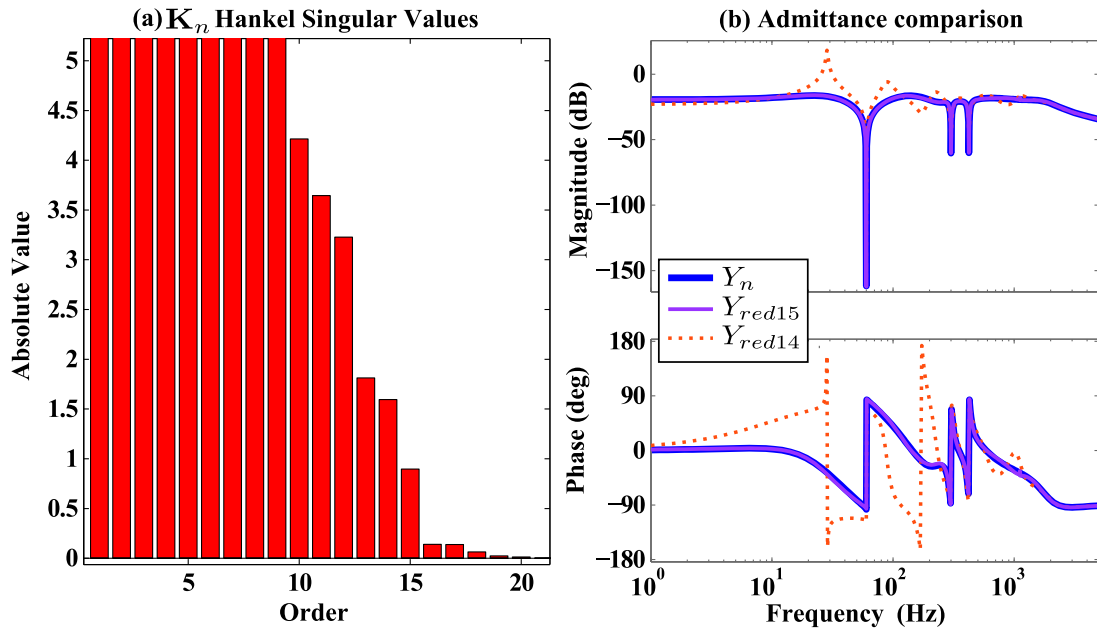


Figure 5.29. (a)Hankel singular values magnitude of the high-order controller (\mathbf{K}_n). Only 15 of them contribute significantly to the overall controller performance (b)Comparison between the high-order 21 states controller (Y_n), reduced 15 states controller (Y_{red15}) and 14 states controller (Y_{red14}) obtained admittances.

in the comparison of the obtained closed-loop admittance for the nominal (Y_n) and reduced (Y_{red15}) controllers in Fig. 5.29(b). However, a reduction to a 14th (or lower) order controller results in a different admittance (Y_{red14}) in the transition between the tracking bandwidth (i.e. around the fundamental frequency ω_1) and the admittance shaping in sub and super synchronous frequencies.

Frequency domain results

Fig. 5.30 shows the obtained experimental admittance results (Y_{exp}), along with its expected values (Y), the proposed reference (Y_{ref}) and the filter open-loop admittance (G_d). The admittance follows its reference at both sub and super synchronous frequencies, damping the LCL filter resonance and rejecting, as expected, any PCC voltage disturbance at the 5th and 7th harmonic frequencies to a 0.1% of its magnitude.

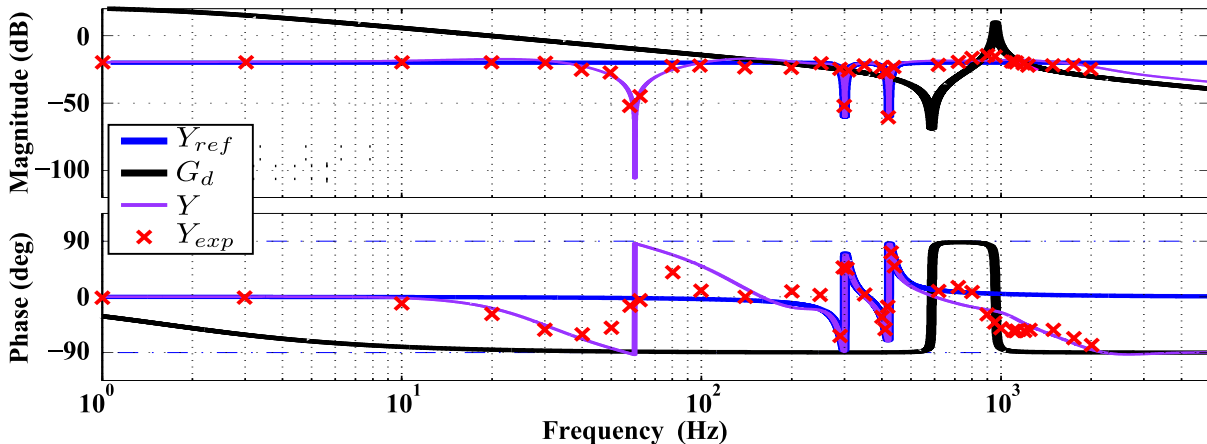


Figure 5.30. Admittance shaping result for the admittance dips design with the LCL filter.

Fig. 5.31 shows the obtained tracking shaping results. Again, tracking transfer function (T) is close to unity around the fundamental frequency, providing a good current reference tracking response.

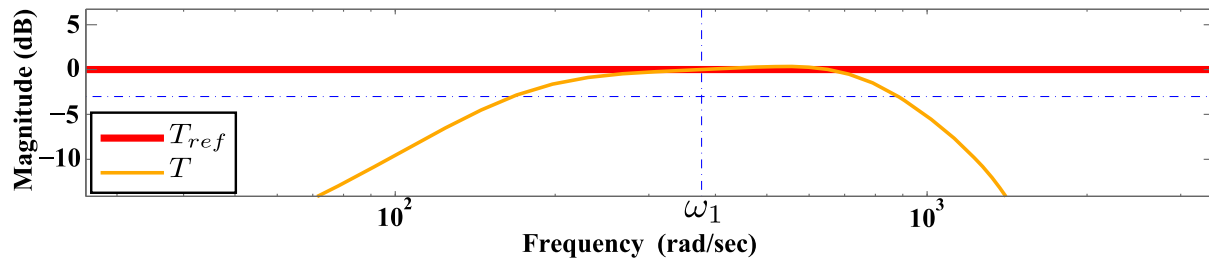


Figure 5.31. Tracking shaping result for the admittance dips design with the LCL filter.

Fig. 5.32 shows the sensitivity results of the proposed design. The additional feed-back needed at the harmonic frequencies (see how $|S(j5\omega_1)|$ and $|S(j7\omega_1)|$ are very small compared to the previous resistive design Fig. 5.26) causes that the sensitivity magnitude no longer fulfils the robustness boundary $\|S\|_\infty < 6$ dB (marked in Fig. 5.32 with an horizontal blue dashed line). The loss of stand-alone stability robustness is, then, one of the drawback of this design.

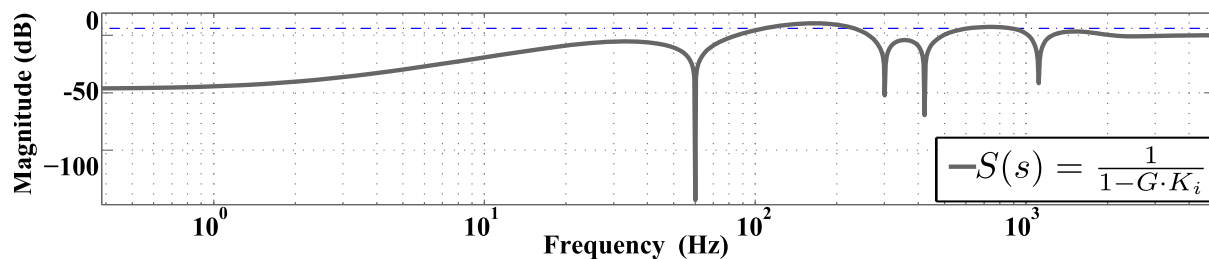


Figure 5.32. Achieved sensitivity function magnitude for the admittance dips design with the LCL filter.

5.5.4 Analysis of the proposed low admittance designs

This subsection tests the grid voltage disturbance rejection capability of both presented low admittance designs. In addition, it analyses their stability robustness towards grid impedances changes.

Grid voltage disturbance rejection capability analysis

The grid voltage harmonic rejection capabilities of the proposed designs are tested below. Fig. 5.33 shows the total harmonic distortion (THD) for four different simulated test cases and different operational points:

In test 1 (T1) a 5th harmonic of 0.12 pu³ is introduced in the grid; in test 2 (T2) a 7th harmonic of 0.1 pu is added to T1; in test 3 (T3) two more harmonics, 11th = 0.7 pu and 13th = 0.6 pu, are added; finally test 4 (T4) is completed with many high frequency harmonics 17th = 0.6 pu, 19th = 0.6 pu, 23th = 0.6 p.u, 25th = 0.6 pu, 29th = 0.5 pu, 31th = 0.3 pu, 35th = 0.3 pu and 37th = 0.3 pu. The *Admittance Dips* design has a lower THD for low order harmonics, thanks to their lower admittance values at 5th and 7th grid harmonic frequencies.

³With respect to the nominal grid voltage ($V_{gN} = 120$ V) at the nominal frequency (ω_1).

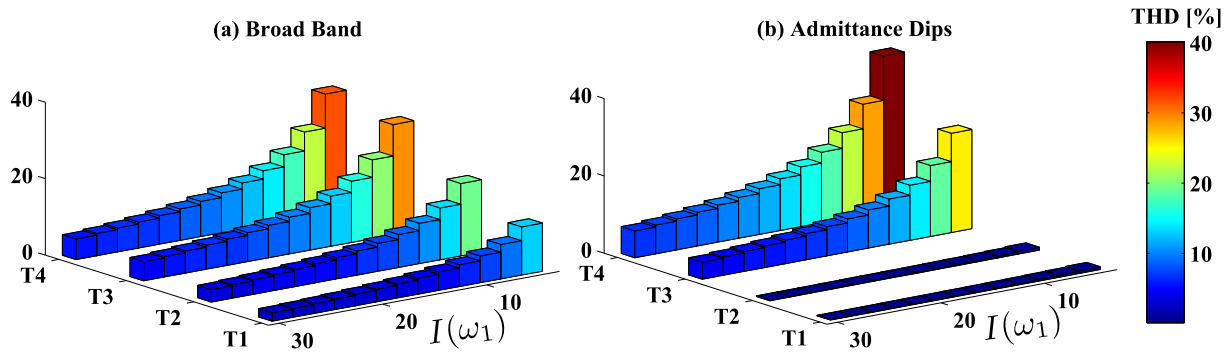


Figure 5.33. Obtained THD of the proposed low admittance designs for different harmonic test.

The smaller resistive admittance reference in the *Broad Band* design reduces the THD for higher order harmonics, as it can be seen in the results for T4.

Fig. 5.34 and Fig. 5.35 show the experimental time domain results to T2 and T4, respectively, considering an ideal grid impedance ($Z_g = 0$).

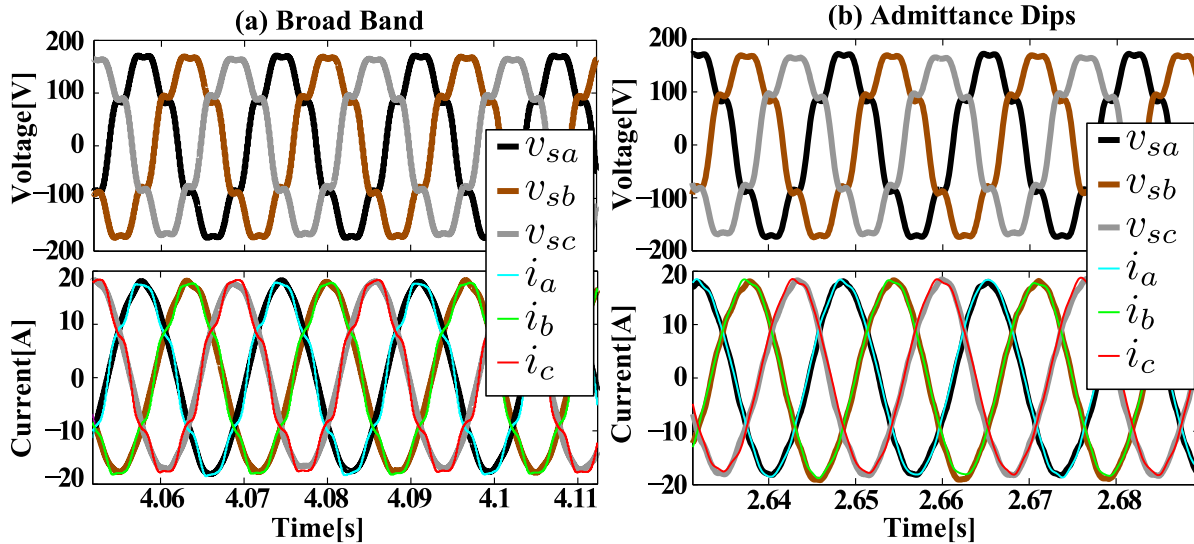


Figure 5.34. Experimental time domain results to test 2 with an ideal grid impedance $Z_g = 0$.

The grid currents (i) still follows its (active) reference (i^*) after the introduction of harmonics in the grid voltage (v_s), with reduced current distortion thanks to the achieved low admittance profiles. The second design (i.e. *Admittance Dips*) rejects better the grid fifth and seventh harmonics in T2 (Fig. 5.34). When higher order harmonics are introduced (T4), the response of both designs is very similar, being slightly better for the *broad band* design (Fig. 5.35).

Robustness towards grid uncertainties analysis

Fig. 5.36 and Fig. 5.37 show the modified admittance ($Y'(s)$, see equation(5.10)) closed-loop poles evolution for changes of the inductance (L_g) in an L-type grid impedance ($Z_g(s) = L_g s$) and the capacitance (C_g) in a resonant LC-type grid impedance ($Z_g(s) = (L_g s)/(L_g C_g s^2 + 1)$),

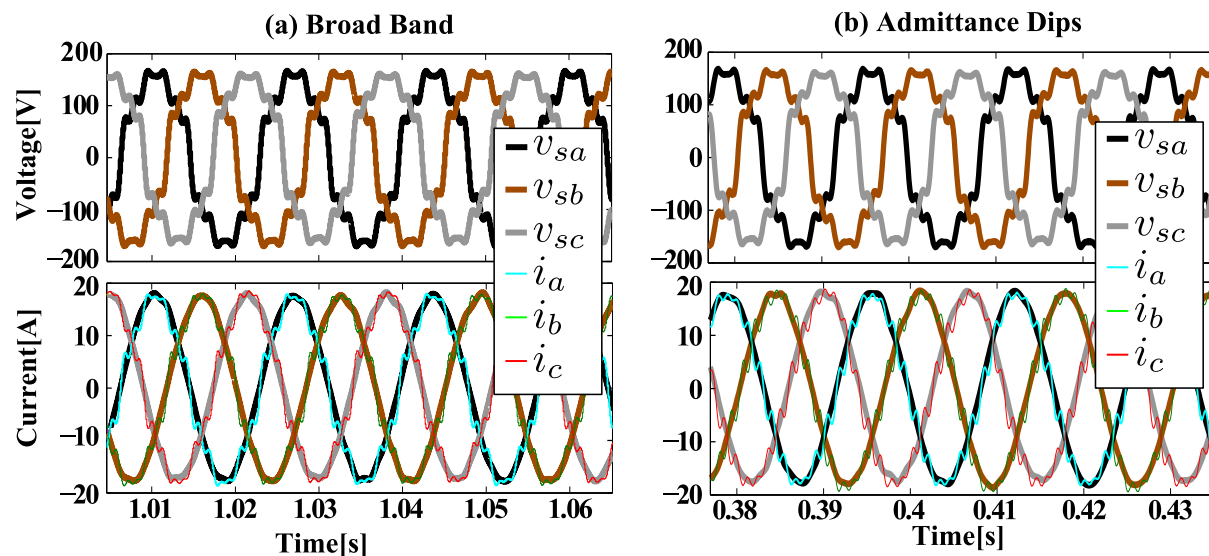


Figure 5.35. Experimental time domain results to test 4 with an ideal grid impedance $Z_g = 0$.

respectively: L_g is fixed in the latter to 0.11 pu^4 .

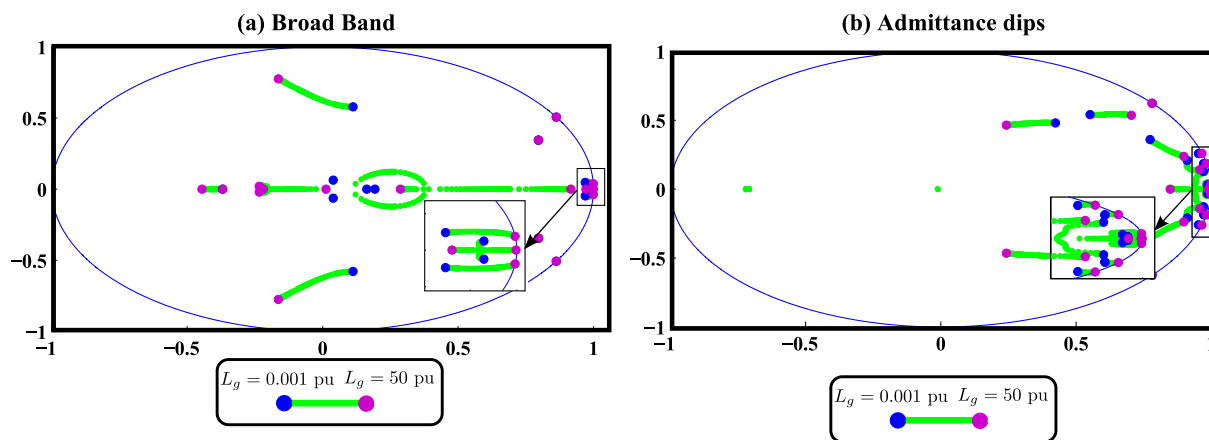


Figure 5.36. $Y'(s)$ poles for changes of an inductive grid in (a) the broad band design and (b) the admittance dips design.

The system is again stable for a large variation of L-type grids, and unstable for changes of LC-type grids if its resonance matches the non-passive frequency zones of the converter (i.e. the fundamental frequency (ω_1) and frequencies above the controller bandwidth ($\omega_c \approx \omega_s/6$)). The *Admittance Dips* design introduces two pairs of complex-conjugate resonant poles at the 5th and 7th grid harmonic frequencies which are close to destabilize the system for C_g variations (compare first zoom in Fig. 5.37 for both design). The system remains stable, in any case, due to the passive behaviour of the converter at those frequencies (thanks to the passive admittance reference (Y_{ref}) definition in (5.15)).

⁴These results were not taken in the same experimental setup, using a *Danfoss* VSC of nominal power $S_N = 2.6$ kVA for the *broad-band* design and a $S_N = 17.5$ kVA *Semikron* VSC for the *admittance dips* design. Grid impedance parameters are expressed in per unit values of the *Danfoss* VSC nominal impedance, so the stability robustness analysis of the two designs can be comparable. L-type grid impedance changes are then expressed in per unit values of its nominal inductance $L_N = 44.1$ mH, meanwhile LC-type impedance changes are expressed as a function of its nominal capacitance $C_N = 0.16$ mF)

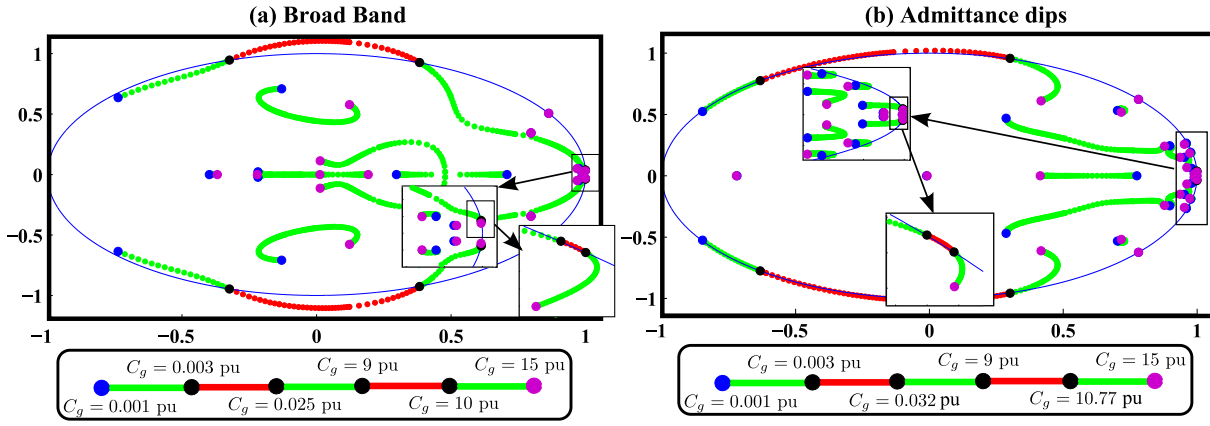


Figure 5.37. $Y'(s)$ poles for changes of an inductive-capacitive grid in (a) the broad band design and (b) the admittance dips design. The red lines represents unstable cases.

Conclusion

Both designs are, then, robust towards weak grids. The *Admittance Dips* design has an improved voltage harmonic rejection capability around the tuned frequencies ($5\omega_1$ and $7\omega_1$) than the *Broad Band* design, but poorer at the rest of frequencies. The *Admittance Dips* design lacks, on the other hand, of the stand-alone stability robustness of the *Broad Band* design (compare sensitivity results in Fig. 5.26 and Fig. 5.32).

5.6 High admittance designs

This third application considers high admittance profiles for the grid-connected VSC. This kind of designs will serve as weak grid stabilizers, as section 5.6.1 demonstrates. Again, two designs are presented, one with a high-admittance in broad resistive band (section 5.6.2) and another following a resonant-like behaviour centred in a known grid series impedance resonance (section 5.6.3). Both designs use the L filter topology and a sampling time $T_s = 200 \mu\text{s}$. In addition, they are able to track a given current reference (i^*) at the fundamental frequency (ω_1) and, then, control their own DC-bus voltage (i.e. they will act as active rectifiers like the one shown in Fig. 5.1). The effectiveness of the proposed grid stabilizers is demonstrated in section 5.6.4.

5.6.1 Motivation of high admittance designs

Consider a weak grid like the one shown in Fig. 5.38(a), with a resonant LC series impedance ($Z_g(s) = (L_g s)/(L_g C_g s^2 + 1)$). A controlled VSC, named VSC1 and modelled with its Norton equivalent in Fig. 5.38(a), connected to this weak and resonant grid may be unstable if the impedance stability criterion (analysis of $L'(s) = Z_g Y_c$ interconnection loop in (5.10)) is not met. As demonstrated in the previous applications, the resonant behaviour of this weak grid is a risk factor for the stability of the interconnected system. Fig. 5.38(b) demonstrates this interaction graphically.

This thesis proposes the design of a shunt-connected VSC, named VSC2 in Fig. 5.38(c), with a big equivalent admittance (Y). This converter will provide of a low impedance path to the system, which will damp the weak grid resonance so a new stronger grid series impedance

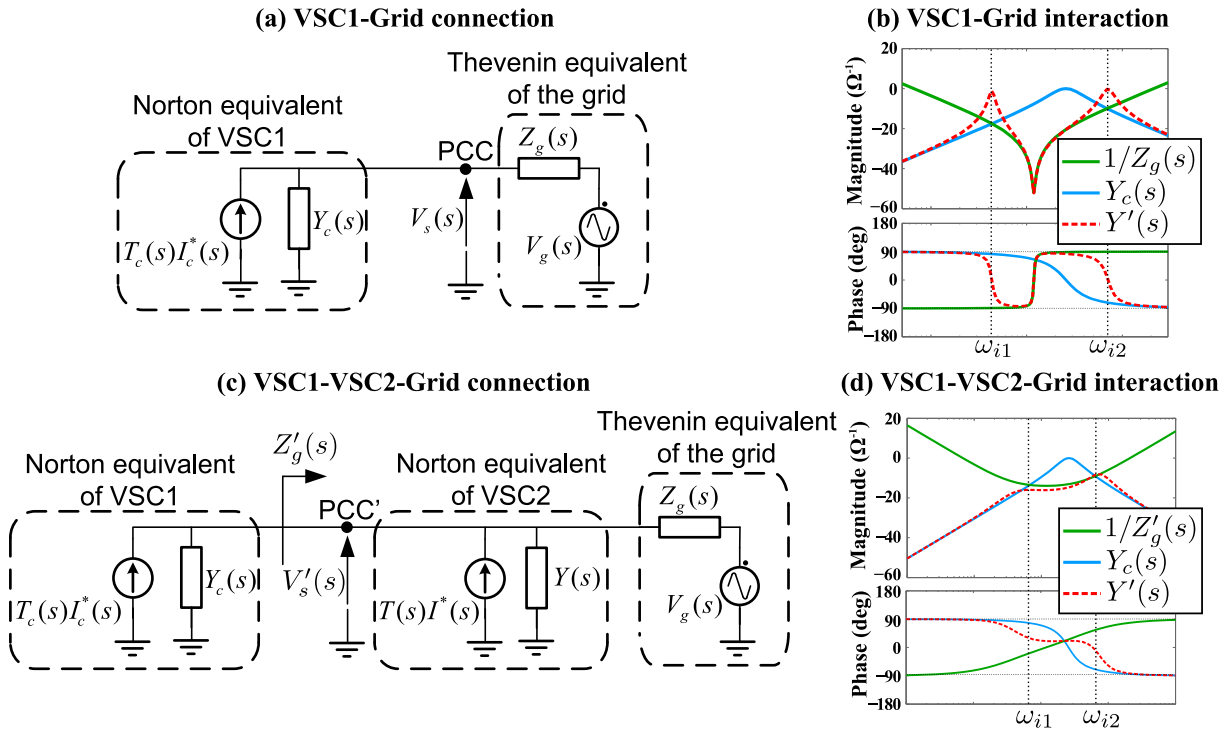


Figure 5.38. (a) Connection of a VSC (VSC1) to a weak grid and (b) its interaction in the frequency domain: where $Y'(s) = Y_c(s)/(1 + Z_g(s)Y_c(s))$. (c) Connection of a high-admittance converter (VSC2) to stabilize the system and (d) interaction of the new strong grid ($Z'_g(s)$) with VSC1: where $Y'(s) = Y_c(s)/(1 + Z'_g(s)Y_c(s))$.

(Z'_g) may be considered:

$$Z'_g(s) = \frac{Z_g(s)}{Y(s)Z_g(s) + 1} \quad (5.20)$$

This stronger grid is less likely to interact with other VSC connected to it, like the previously considered VSC1: Fig. 5.38(d) demonstrates this graphically.

It is important to remark that the connection VSC2-grid must be also stable (analysis of $L'(s) = Z_g Y$ interconnection loop). To assure this, the new big-admittance converter (VSC2) should be resistive at least around the grid resonant frequency to be damped as, if not, it may interact (i.e. become unstable) with the very same grid it tries to stabilize. This was graphically demonstrated in Fig. 5.7 (section 5.4), which shows the convenience of a resistive converter behaviour to increase the interconnected system stability margins.

The final complex system stability (Grid-VSC1-VSC2) can be derived, in fact, from an impedance stability criterion point of view (section 2.2.1). In this case, the *load* admittance is equal to the sum of converters admittances ($Y_l = Y + Y_c$) and the *source* impedance is equal to the grid impedance ($Z_s = Z_g$). If $|Y|$ is designed to be much higher than $|Y_c|$, the contribution of the latter to the *load* admittance can be neglected. In that case, it is possible to assert that the interconnection Grid-VSC1-VSC2 will be stable providing that the interconnection Grid-VSC2 is stable.

5.6.2 In a broad band

Model references and weights definition

This design considers again a broad band resistive design, this time with a higher admittance reference (Y_{ref}). As exposed in section 4.8.1 (see Fig. 4.22), and again reminded in section 5.4.2, small filter inductances (increasing $|G_d|$ value) are preferred to maximize the effective shaping bandwidth and still avoid high actuation signals in this kind of designs. For that reason, the *Sedecal* setup is used for this design, so the filter inductances (L_1 and L_2) decrease their values to the ones shown in table 5.2.

The selected admittance reference is $Y_{ref}(s) = 1 \Omega^{-1}$. Tracking reference (T_{ref}) is again defined constant and equal to one.

The design weights (W_y , W_t and W_u) are selected to achieve a good tracking at the synchronous frequency (ω_1) and good admittance shaping at both sub and super synchronous frequencies, limiting control effort, and then controller bandwidth, at high frequencies. The tracking (W_t) and control effort (W_u) weights dynamics presented in (5.12) and (5.14), respectively, are still suitable for this task. Admittance weight (W_y) dynamic is slightly modified with respect to (5.13).

The high admittance reference of this design positively contributes to the admittance shaping error minimization, as it reduces the admittance shaping error boundary ($|L_y|$, defined in (4.18)) at all frequencies⁵. This makes possible to decrease the admittance shaping weight initial gain (K_y in (5.13)) and still obtain good admittance shaping results. The reduction of W_y magnitude also implies that good tracking bandwidth (i.e. fast tracking response) can be obtained even without the notch defined in (5.13)⁶. Proposed admittance weight dynamic for this design is, then, as follows:

$$W_y(s) = K_y \frac{1}{(1/\omega_y)s + 1} \quad (5.21)$$

Fig. 5.39 shows the frequency-domain representation of the chosen weights for this broad band high admittance design.

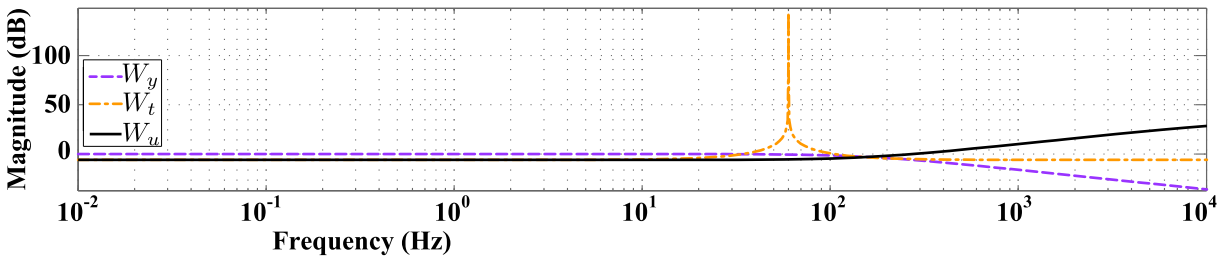


Figure 5.39. Frequency weights for the high admittance broad-band resistive design with the L filter.

A discrete controller ($\mathbf{K}(z)$) with a sampling time $T_s = 200 \mu s$ is obtained from the above weights and model-references selection.

⁵Note how a high Y_{ref} decreases the inverse magnitude product $|W_y(s)Y_{ref}(s)|^{-1}$ on which $|L_y|$ depends.

⁶As defined in section 4.6.2, the tracking bandwidth mainly depends on the frequency range where $|W_t| > |W_y|$, so a fast enough tracking can be obtained without the notch part in W_y providing that K_y is small.

Frequency domain results

After \mathcal{H}_∞ synthesis and discretization, the obtained controller produces the admittance and tracking shaping results shown in Fig. 5.40 and Fig. 5.41, respectively.

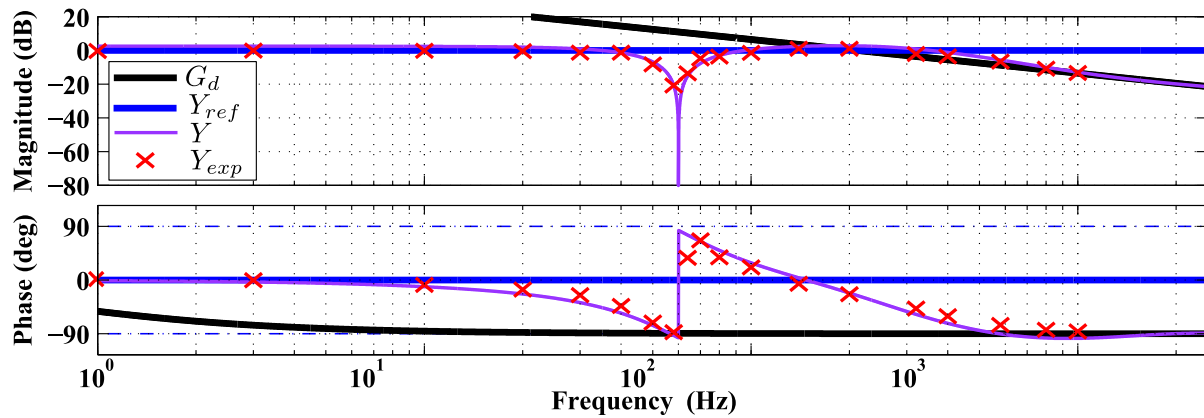


Figure 5.40. Admittance shaping result for the high admittance broad-band resistive design with the L filter.

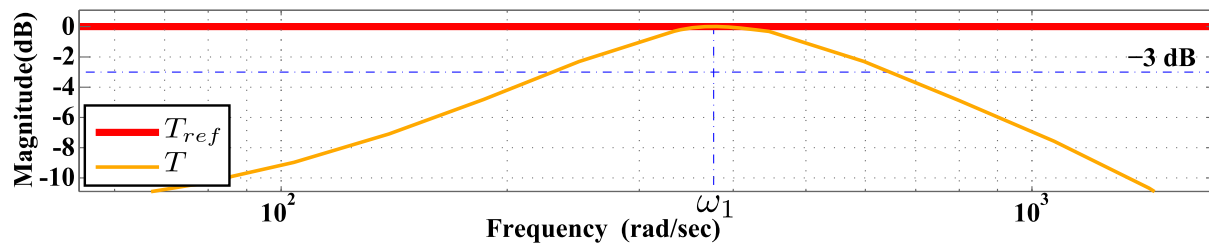


Figure 5.41. Tracking shaping result for the high admittance broad-band resistive design with the L filter.

Both admittance (Y) and tracking (T) closed-loop transfer functions follow their respective references (Y_{ref} and T_{ref}) at the desired frequencies. The admittance values measured in the experimental platform (Y_{exp}) demonstrates the effectiveness of the method.

Finally, Fig. 5.42 shows the achieved sensitivity function, which maximum gain value fulfils the standard stand-alone robustness requirements (i.e. $\|S\|_\infty < 6$ dB).

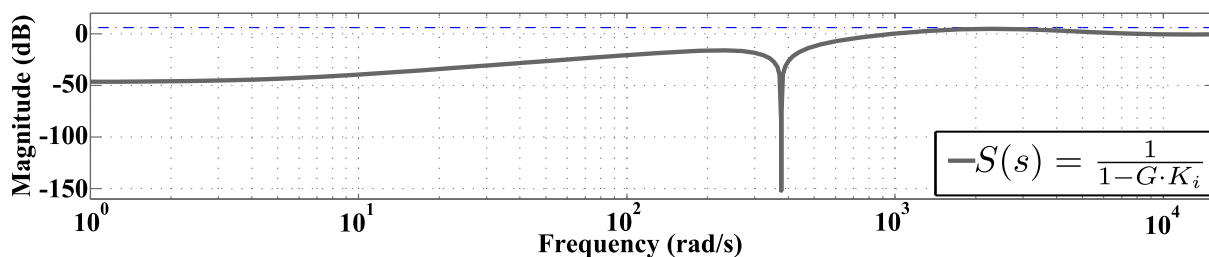


Figure 5.42. Achieved sensitivity function magnitude for a high admittance broad-band resistive design with the L filter.

5.6.3 Localized at some frequencies (power pit)

Model references and weights definition

This design considers a higher-order reference model: process model is again the *Semikron* L-filter grid-connected VSC (see table 5.1), but the desired admittance (outside the fundamental frequency) shows, this time, a resonant-like behaviour. From an application point of view, this could be used as a loss-less damper for a grid resonance placed at a known frequency. The new admittance reference is:

$$Y_{ref}(s) = 0.01 \frac{s^2 + 2\zeta_n \omega_{res} s + \omega_{res}^2}{s^2 + 2\zeta_d \omega_{res} s + \omega_{res}^2} \cdot \frac{1}{(1/\omega_{yref})s + 1} \quad (5.22)$$

where ω_{res} is the frequency where the maximum admittance is reached (i.e. the frequency where the grid will be damped). For this design, an $\omega_{res} = 5\omega_1$ is considered. That is, the proposed VSC should damp any grid impedance resonance at ω_{res} by consuming any 5th grid current harmonic.

The high frequency pole at ω_{yref} is used to make the admittance reference-model (Y_{ref}) more similar to the open-loop one (G_d), making the admittance (Y) transient between both less abrupt. This will reduce the non-dissipative behaviour at high frequencies, as advanced in subsection 4.8.2.

Note that the admittance reference (Y_{ref}) defined in (5.22) has a small initial gain value ($Y_{ref}(0) = 0.01 \Omega^{-1}$). This makes this grid current control less sensitive to grid voltage disturbances than the previous broad band design; the controlled VSC will ideally act as a high impedance (low admittance) path at frequencies outside a certain frequency (ω_{res}) where the system behaves like a *power pit* (i.e. it provides a low impedance path). This will result, obviously, in a smaller effective frequency range of the considered objective; that is, this design acts as a less robust grid stabilizer as it is centred in a known grid resonant frequency.

The frequency range of admittance control is defined by a W_y equal in structure to (5.13). In this case, W_y magnitude will be much bigger at low than at high frequencies, in order to level the admittance shaping error boundary ($|L_y|$, defined in (4.18)) between sub and super synchronous frequencies⁷. A big K_y and a small ω_y are, then, chosen for the admittance weight (W_y) in (5.13).

Tracking reference is, again, $T_{ref}(s) = 1$. W_t changes slightly:

$$W_t(s) = K_t \frac{s^2 + 2\zeta_n \omega_1 s + \omega_1^2}{s^2 + 2\zeta_d \omega_1 s + \omega_1^2} \cdot \frac{1}{(1/\omega_t)s + 1}, \quad (5.23)$$

The new pole at ω_t makes the admittance control more dominant at frequencies above the fundamental frequency (i.e. at super-synchronous frequencies, where admittance resonance peak is placed) and below the control band upper limit (where W_u is dominant).

Control effort is again limited at high frequencies, with a weight (W_u) with similar dynamics to (5.14). This time it has a double order to reduce the loop gain ($L(s) = -GK_i$), and then the controller bandwidth, faster, being able to control the admittance at the resonant frequency without increasing to much the sensitivity peak (i.e. without reducing the system stand-alone stability margins) and the control effort (u).

$$W_u(s) = K_u \left(\frac{(1/\omega_{u1})s + 1}{(1/\omega_{u2})s + 1} \right)^2, \quad (5.24)$$

⁷Note how Y_{ref} in (5.22) contributes much more to the inverse magnitude product $|W_y(s)Y_{ref}(s)|^{-1}$ at the super synchronous resonant frequency ($\omega_{res} = 5\omega_1$) than at sub synchronous frequencies.

Fig. 5.43 shows the aforementioned weights selection in the frequency domain.

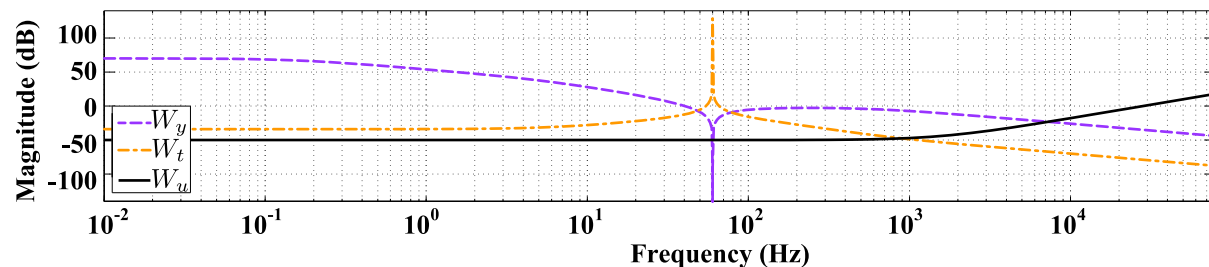


Figure 5.43. Frequency weights for the power pit design with the L filter.

A discrete controller ($\mathbf{K}(z)$) with a sampling time $T_s = 200 \mu\text{s}$ is synthesized from the resulting generalized plant (\mathbf{P}).

Frequency domain results

The tracking shaping results are shown in Fig. 5.44. Again, the controller is able to track a given current reference (i^*) in the fundamental frequency (i.e. $T(j\omega_1) = 1$)

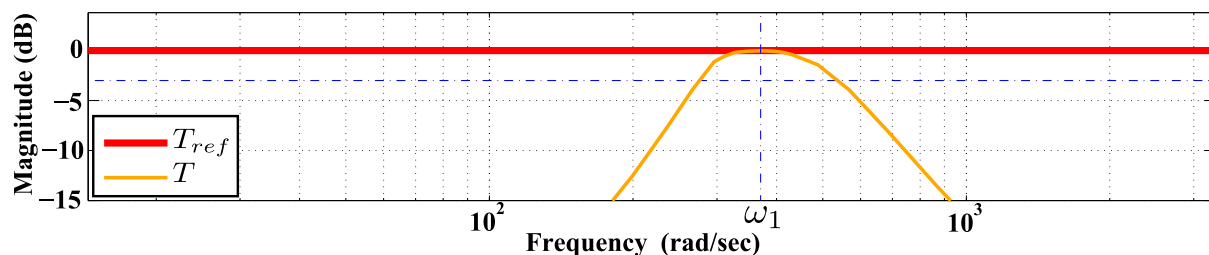


Figure 5.44. Tracing shaping result for the power pit design with the L filter.

Fig. 5.45 shows the admittance shaping results of the proposed design. The admittance (Y) follows its reference (Y_{ref}) at both sub and super synchronous frequencies, including its resonant frequency ω_{res} . The experimental results (Y_{exp}) demonstrate the efficiency of the method. Note, on the other hand, how the complex admittance reference affects negatively to the system passivity around the fundamental frequency (ω_1), where the admittance is not controlled. This may affect the system stability when connected to the grid.

Finally, Fig. 5.46 shows the sensitivity results of the system. It proves the stand-alone robustness of the proposed design.

5.6.4 Analysis of the proposed high admittance designs

Grid stabilization effect analysis

This subsection shows the simulated results of the proposed grid stabilizers effectiveness. To test the efficiency of the two proposed designs (named broad band and power pit), the interconnected system shown in Fig. 5.38 is again considered, where a PI-controlled power-converter (VSC1 in Fig. 5.38(a)) is connected through an L filter to a weak grid, whose LC-type impedance ($Z_g(s) = (L_g s)/(L_g C_g s^2 + 1)$) has a resonance at frequency $5\omega_1$. A current reference (i_c^*) of 20 A (RMS) is applied to VSC1. The PCC voltage is, then, measured without the proposed

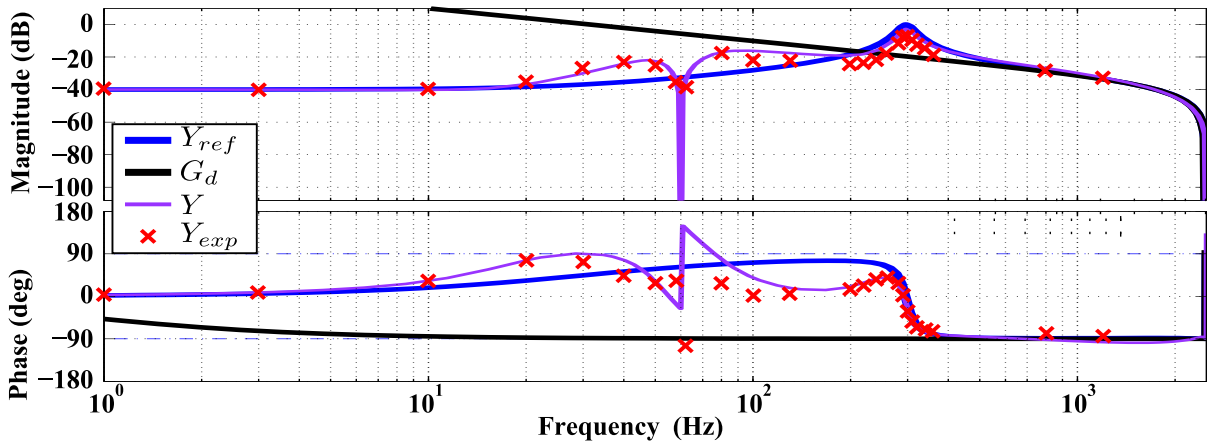


Figure 5.45. Admittance shaping result for the power pit design with the L filter.

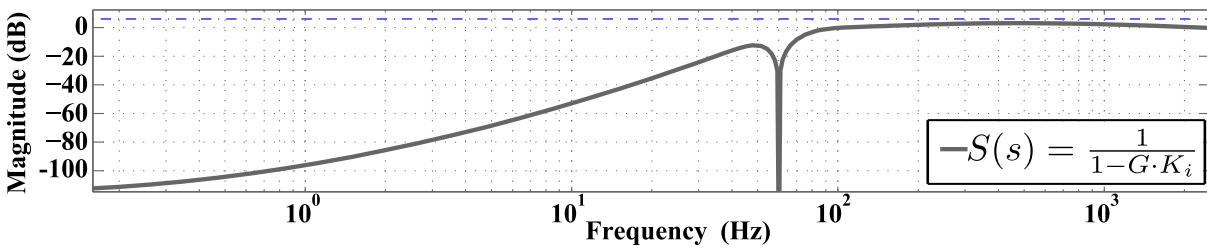


Figure 5.46. Achieved sensitivity function magnitude for power pit design with L filter.

grid stabilizers and with them (i.e. analysis of v_s and v'_s in Fig. 5.38(a) and Fig. 5.38(c), respectively). Fig. 5.47 and Fig. 5.48 show the results of the aforementioned test (left part) for both considered grid stabilizers, along with the equivalent damped grid impedance (Z'_g), defined in equation (5.20) (right part). The PCC voltage (v_s) shows an oscillation triggered by the resonance in the grid impedance (Z_g) at frequency $5\omega_1$. Once either of the grid stabilizers are connected, their high admittance profiles at $5\omega_1$ damp this resonance, resulting in a clean PCC voltage (v'_s (equal to the nominal grid voltage v_g in Fig. 5.38)).

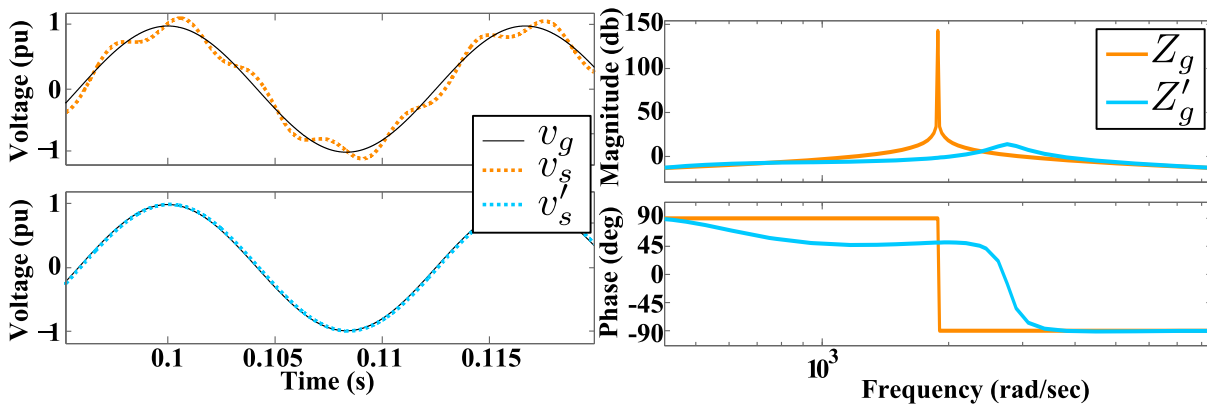


Figure 5.47. (Left) PCC voltage with (v'_s) and without (v_s) the proposed broad band high admittance design connected to it and (right) equivalent damped grid impedance (Z'_g).

The grid stabilization of the proposed designs is further proved in Fig. 5.49. It shows the PCC voltage (v_s) and the PI-controlled VSC (VSC1 in Fig.5.38(a)) current (i_c) before and after the broad-band high admittance design (VSC2 in Fig.5.38(c)) stabilizes them. At the beginning of the experiment only the PI-controlled VSC is connected to the grid, following a current

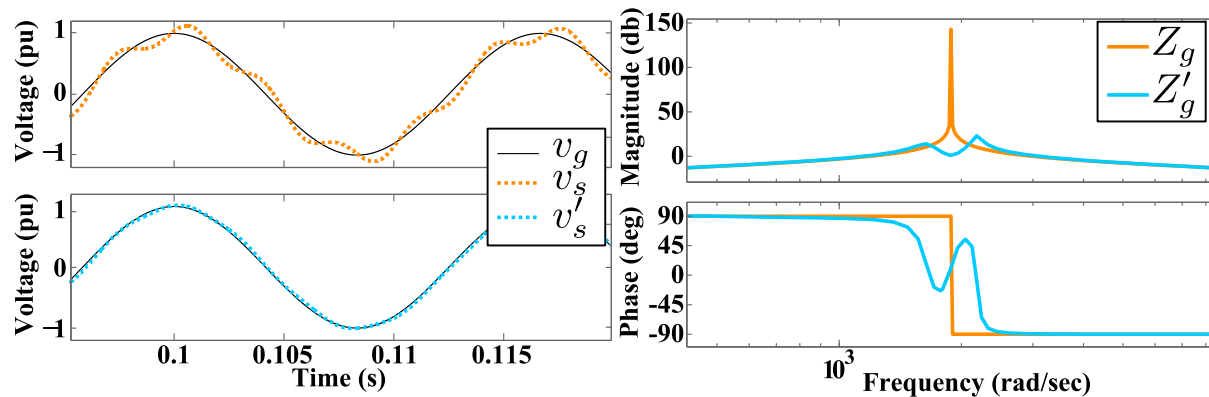


Figure 5.48. (Left) PCC voltage with (v'_s) and without (v_s) the proposed power pit design connected to it and (right) equivalent damped grid impedance (Z'_g).

reference (i_c^*) of 20 A (RMS) and inducing a PCC voltage oscillation due to the weakness of the considered grid. Once the proposed design is connected, it drains (i.e. dissipates) these voltage oscillations, resulting in the grid stabilization. Similar results are obtained considering the connection of the power-pit design.

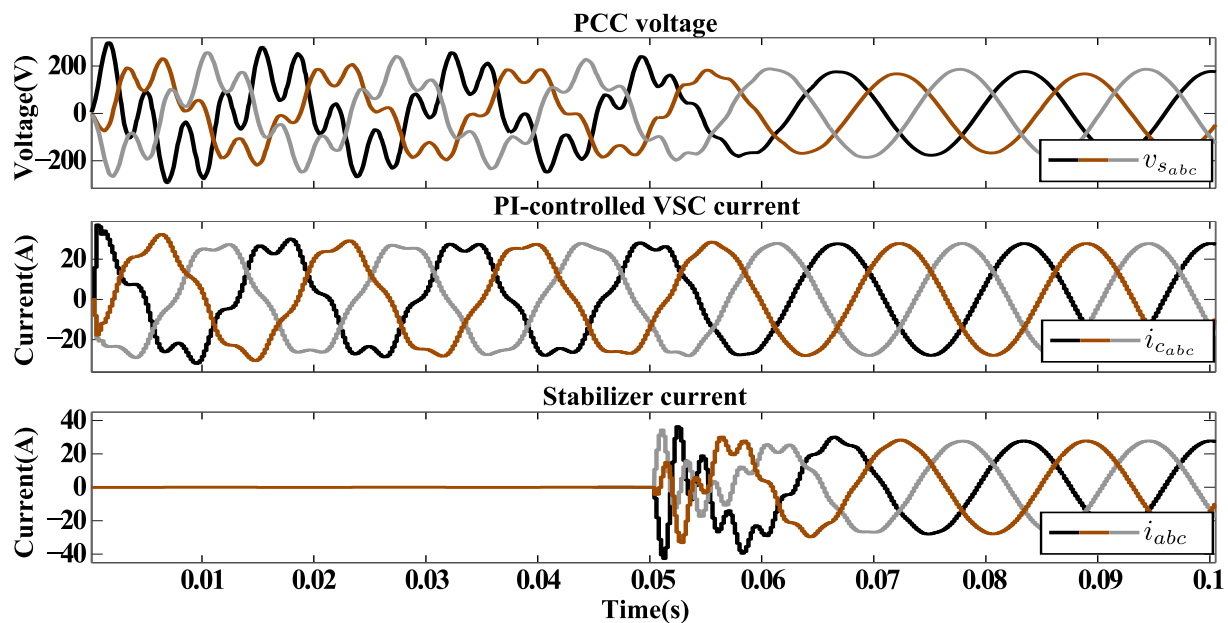


Figure 5.49. Effect of the connection of the broad-band high admittance design to a weak grid. During the first periods, the connection between a PI-controlled VSC to this weak grid results in a very distorted PCC voltage. Once connected, the proposed grid stabilizer drains these oscillations thanks to its low resistive behaviour.

The grid resonance damping robustness of both designs is now tested. Fig. 5.50 shows the grid impedance magnitude ($|Z_g|$) for changes of its resonance frequency (i.e. modifications of C_g ⁸) and the resulting damped grid impedance ($|Z'_g|$) once the broad band stabilizer is connected. Fig. 5.51 repeats the test for the power pit stabilizer. The former presents a high admittance in a broader frequency range than the latter (compare Fig. 5.40 and Fig. 5.45), resulting in a more robust grid impedance resonance damping. Fig. 5.51 makes clear, then, that the power pit design is only effective at its admittance resonant frequency ($\omega_{res} = 5\omega_1$ in (5.22)). That is, the grid impedance (i.e. its resonant frequency) must be known before defining the power pit converter admittance reference (Y_{ref}) to obtain a good grid stabilization result.

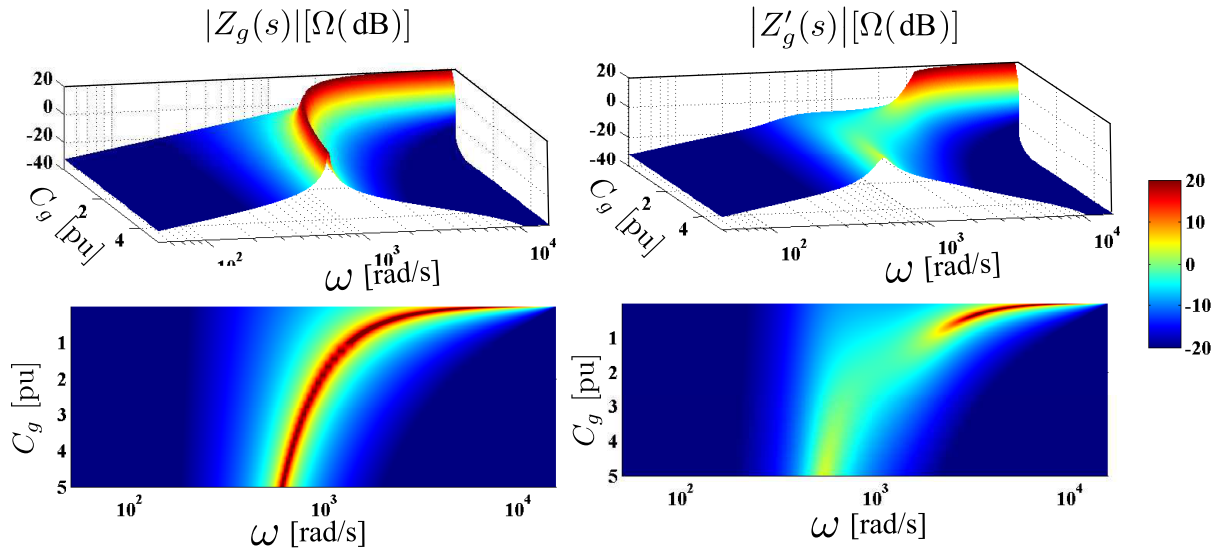


Figure 5.50. Grid impedance resonance damping robustness of the proposed high admittance broad band design.

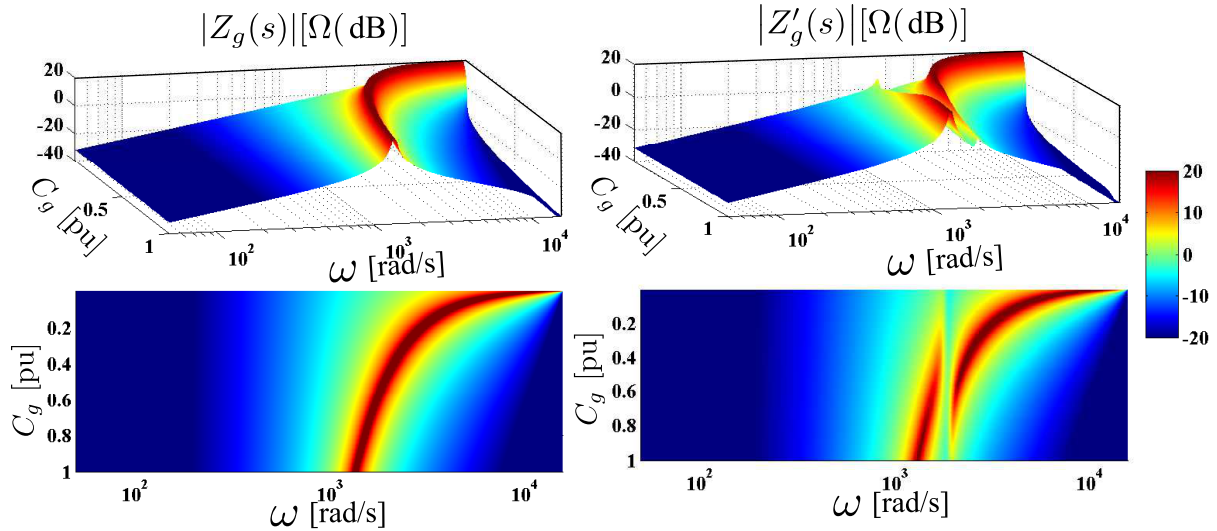


Figure 5.51. Grid impedance resonance damping robustness of the proposed power pit design.

Robustness toward grid uncertainties analysis

As introduced in section 5.6.1, the interconnected system VSC1-grid-VSC2 in Fig. 5.38 is likely to be stable if the connection VSC2-grid is stable. Fig. 5.52 and Fig. 5.53 show the stability analysis (roots of $1 + Y(s)Z_g(s)$) of the interconnection between the grid and its proposed stabilizer (VSC2 in Fig. 5.38) for changes of the grid impedance (Z_g).

Fig. 5.52(a) considers the influence of changes of L_g value in an L-type grid ($Z_g = L_g s$) for the broad band design, as so does Fig. 5.52(b) considering the power pit design⁸. As expected, the resistive behaviour of the former makes it very robust for changes of the inductive grid. The broad range of non-passive behaviour of the power pit design around the fundamental frequency (ω_1) (see Fig. 5.45) triggers, on the other hand, instabilities for some of the considered L-type grid impedance values, making it less robust than the broad band design.

⁸Grid impedance parameters are expressed in per unit values of the *Semikron* VSC nominal impedance, that is, $L_N = 6.5$ mH and $C_N = 1.1$ mF

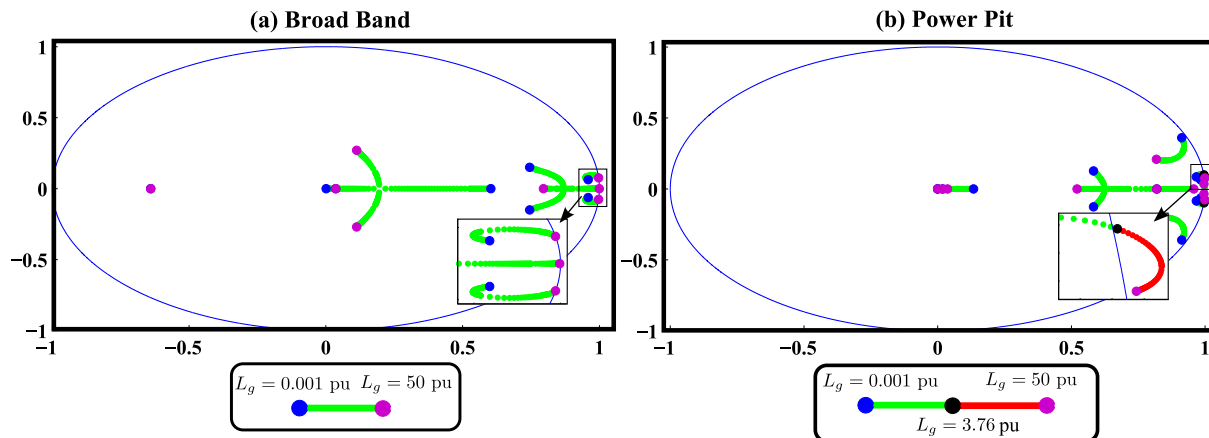


Figure 5.52. Roots of $1 + Y(s)Z_g(s)$ (interconnection VSC2-grid) for changes of an inductive grid in (a) the high admittance broad band design and (b) the power pit design. The red lines represent unstable cases.

Fig. 5.53 shows the results for a similar test, this time considering variations of C_g value in a resonant LC-type grid impedance ($Z_g(s) = (L_g s)/(L_g C_g s^2 + 1)$): a $L_g = 0.07$ pu⁸ value is fixed in this case, which is proved to be stable for both designs in Fig. 5.52. Again, the broad band design is demonstrated to be more robust than the power pit design, even though both designs are stable for a wide range of grid impedance values.

In any case, as advanced in section 5.4, the real grid impedance resonance is likely to be damped by some resistive element. So, in a more realistic scenario, the resonant unstable poles in Fig. 5.53 may lay inside the unit stability circle.

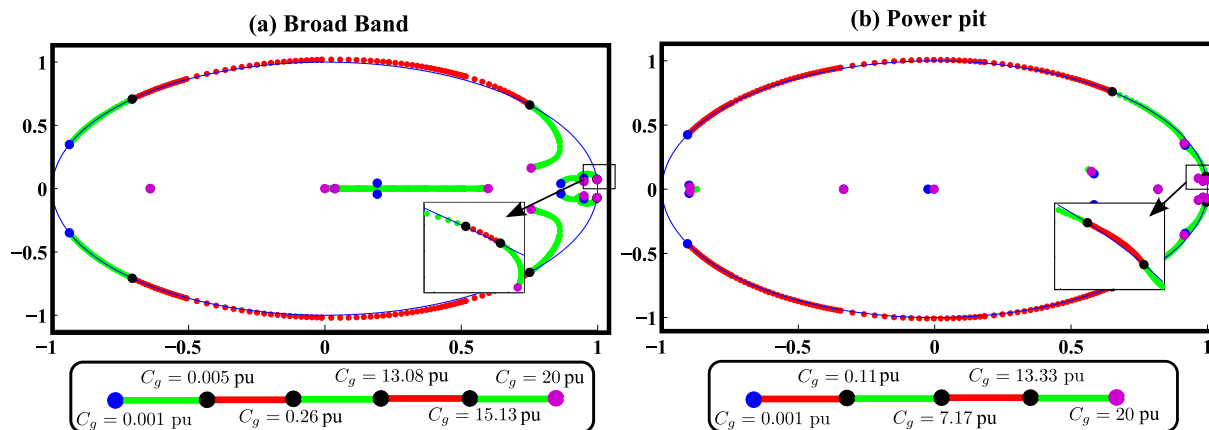


Figure 5.53. Roots of $1 + Y(s)Z_g(s)$ (interconnection VSC2-grid) for changes of an inductive-capacitive resonant grid in (a) the high admittance broad band design and (b) the power pit design. The red lines represent unstable cases.

Response to grid voltage dips analysis

Finally, Fig. 5.54 shows the response of both designs current control for disturbances of the grid voltage, considering VSC1 disconnected. A dip of 60% is simulated in the grid voltage when the proposed grid stabilizer is tracking a current reference (i^*) of 10 A. The higher admittance value of the broad band design around the fundamental frequency (see Fig. 5.40) makes the system more sensitive to variations of the grid voltage, as it can be seen in the over-current that appears after the voltage dip transients (Fig. 5.54(a)). The power pit design does not suffer

of these over-currents (Fig. 5.54(b)), being its response softer, but with small oscillations at a frequency $5\omega_1$ induced by its admittance (Y) resonant behaviour (see Fig. 5.45).

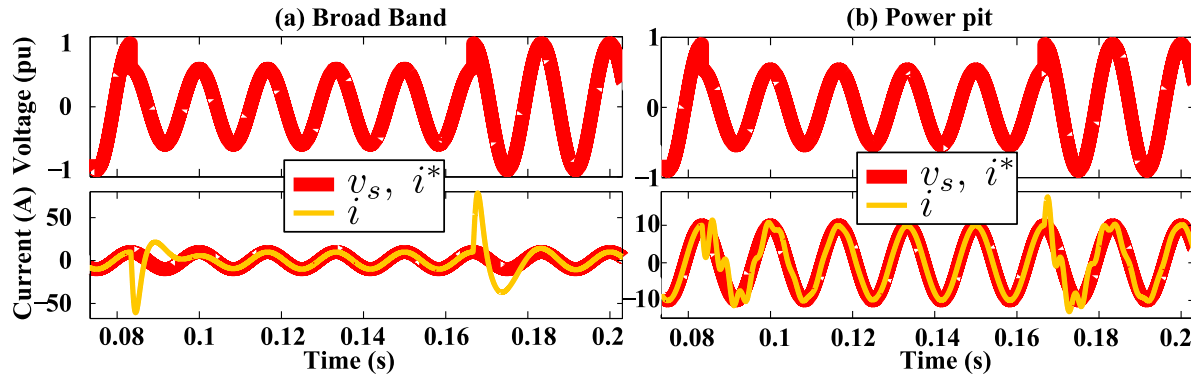


Figure 5.54. Grid current (i) response to a grid voltage (v_s) dip for both considered high admittance designs.

Conclusion

It can be concluded that both designs serve as grid stabilizers if the grid impedance is known (see Fig. 5.47 and Fig. 5.48). However, the broad band design brings advantages in terms of grid impedance damping robustness (see Fig. 5.50) and stability robustness toward changes in the grid impedance (see Fig. 5.52(a) and Fig. 5.53(a)). Even though the power pit design is a good grid damper if the grid impedance resonance is known (Fig. 5.48), it is ineffective if this resonance varies in frequency (see Fig. 5.51). It has the advantage, on the other hand, of having a better current tracking performance than the broad band design, as it is more immune to grid voltage disturbances (see Fig. 5.54).

5.7 Conclusion

The next conclusions can be derived from this chapter:

- The proposed admittance shaping has been tested to solve different objectives: improvement of the robustness towards weak grids of grid-connected PEC-based applications, achieved by means of broad-band resistive designs, rejection/attenuation of the effect of grid voltage (sub/inter) harmonics in the controlled current, achieved by means of low admittance profiles, and the stabilization of weak grids, achieved by means of high admittance designs. All the proposed designs should, in addition, track a given current reference (i^*) at the fundamental frequency (ω_1), have enough stand-alone stability margins and limit the actuation voltage to avoid possible controller saturation problems.
- Three different platforms have been used to obtain the experimental results. All of them act as active rectifiers connected to the grid through an L or an LCL filter. The influence of the outer DC-bus voltage loop in the controlled admittance is briefly explained. It mainly affects the admittance around the fundamental grid frequency (ω_1), where the current reference (i^*) is tracked and the active rectifier behaves like a CPL (i.e. negative resistance).
- The achieved simulated and experimental results demonstrate the flexibility and effectiveness of the proposed method to fulfil the aforementioned objectives. In particular, the

proposed method has been proved effective for both L and LCL grid connections, with small difference in the design methodology for the more complex dynamic of the latter with respect to the former. Moreover, the LCL filter resonance can be indirectly damped by means of the proposed admittance shaping method.

- The filter open-loop admittance (G_d) and the sampling time (T_s) are the main conditioners of the achievable admittance shaping. This is more evident when broad band resistive designs are intended.

The minimum resistive admittance achievable in the broadest bandwidth (ω_c) is equal to the filter open-loop admittance at frequency ω_c (i.e. $Y_{ref_{min}} = |G_d(\omega_c)|$), with ω_c equal to the maximum bandwidth of the controller. To reduce this reference and still obtain the broadest bandwidth possible, either the sampling time (T_s) must be reduced or the filter inductances must be increased, as both will result in a smaller magnitude of $G_d(s)$ at ω_c .

Higher resistive reference (i.e. $Y_{ref} > Y_{ref_{min}}$) can be achieved in the broadest bandwidth possible (ω_c) without theoretical limitations imposed by the open-loop admittance (G_d). In practice, however, these designs may result in high actuation voltages at frequencies where $|G_d| < |Y_{ref}|$, so it is recommended to decrease the filter inductances if broad band high admittance design are intended.

All the broad-band resistive designs have been proven to be very robust to uncertainties in the grid series impedance. Instabilities may still occur if poorly damped grid resonance match in frequency with the non-passive zones of the converter.

- Both considered low admittance designs present good rejection/attenuation of the effect of grid voltage (sub/inter) harmonics in the controlled current; the *Admittance Dips* design has an improved voltage harmonic rejection capability around the tuned frequencies ($5\omega_1$ and $7\omega_1$) than the *Broad Band* design, but poorer at the rest of frequencies. In addition, the *Admittance Dips* design lacks of the stand-alone stability robustness of the *Broad Band* design. Both designs are, in any case, very robust toward weak grids.
- Both considered high admittance designs serve as grid stabilizers if the grid impedance is known, even though the *broad band* design brings advantages in terms of grid impedance damping robustness and stability robustness toward changes in the grid impedance and its resonance. The *power pit* design, on the other hand, has the advantage of having a better current tracking performance than the *broad band* design, as it is more immune to grid voltage disturbances.

Chapter 6

Model reference approach for resonant plants active damping

6.1 Introduction

This chapter applies the model-reference \mathcal{H}_∞ design approach to the optimal active damping of resonant LCL filters to improve the performance of the controlled grid-current.

In opposition to the simpler L filter, the use of an LCL filter for the grid - VSC connection, apart of ensuring low THD grid currents, increases control complexity as it introduces a pair of complex-conjugated poles close to the $j\omega$ axis that may cause current oscillations in response to system disturbances, which may lead to system instability both from a stand-alone (section A.4) and an impedance-based (2.2.1) stability criteria.

This can be effectively solved by damping the resonant poles, either passively or actively. Passive damping adds passive elements, commonly resistances, to the filter. This simple solution, comes at the cost of extra power losses and, in some cases, reduction of the high-frequency attenuation capability. Active damping techniques follow the same strategy, now emulating a virtual (i.e. software) resistor in some position of the grid filter. Approaches usually feed-back at least one of the LCL-filter states, commonly the capacitor voltage (or current), in addition to the controlled (grid-side or converter-side) current (refer to section 2.3.1 for more details).

In both cases, if the LCL resonance is perfectly damped, its grid current dynamic resembles the one of an equivalent L-filter formed by the series connection of converter and grid side inductances. This situation allows to design simple proportional plus resonant (PR) or proportional plus integral (PI) controllers (see section A.7) to regulate the grid injected/absorbed current, reject voltage harmonics etc., with small penalties in both performance and stability margins.

This chapter uses the latter concept to propose an alternative active damping formulation: instead of trying to emulate a resistor, it proposes to design an inner loop that makes the plant under control mimic an L-filter connection. On this model-reference approach the designer specifies the desired grid current dynamic (i.e. the one equivalent to an L filter) and an \mathcal{H}_∞ algorithm synthesizes the (sub)-optimal inner controller that minimizes the error between the closed-loop plant and the model.

This method brings some important advantages over classical approaches: it removes the virtual resistor concept, that actually was misleading in the most common digital scenario. It also allows to take into account some digital control particularities such as the zero-order hold and the computational delay. The emulation of an L-filter connection, additionally, makes

the inner closed-loop plant be passive in a wide band and also reduces the influence of grid parameters over the system stability, greatly improving system robustness.

Casting the problem in the \mathcal{H}_∞ framework makes the method flexible enough to allow choosing the input measurements, being possible to select the number of states (or lineal combination of states) fed-back to the active damper and combine them with a disturbance (i.e. PCC voltage) feed-forward path, improving the damping robustness of the method.

Even though good inherent damping results were obtained shaping the closed-loop admittance so it follows a resistive reference in the resonant frequency (see section 5.4.4 and Fig. 5.15), the methodology presented in this chapter focuses only on the resonance damping design, allowing to deal with the reference tracking problem separately by means of classic design methodologies.

Next section develops the open and closed-loop dynamics of the proposed application. Section 6.3 centres on the proposed controller, giving a brief explanation of its design, synthesis, implementation and limitations. Experimental results of the proposed method, both in time and frequency domains, are shown in Section 6.4, as well as the analysis of its stability and damping robustness.

6.2 Problem description and modelling

Fig. 6.1 shows a simplified scheme of the considered application: a current-control loop of a VSC connected to the grid through an LCL filter.

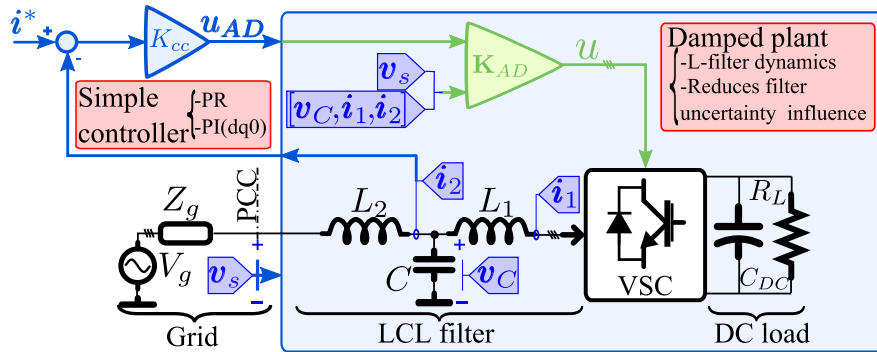


Figure 6.1. Block-diagram description of the proposed active-damping approach.

Instead of facing this objective directly in a single loop like in section 5.4.4, this chapter proposes to follow a double loop approach, much in line with the philosophy of classical active damping approaches. In the innermost layer of the control scheme shown in Fig. 6.1, the damping controller (\mathbf{K}_{AD}) will reshape the LCL-filter open-loop dynamic so it resembles the one of a simpler L filter. A simple outer grid-current controller (K_{cc} in Fig. 6.1), such as classic PR and PI regulators, can be designed, next, for this emulated L-filter dynamic.

6.2.1 Open-loop modelling

The system is characterized by three states: the grid and converter side currents (i_2 and i_1), and the capacitor voltage (v_c). Each of the states dynamic is affected by two disturbances: the VSC average output voltage over a PWM period (u) and the measured point of common coupling

(PCC) voltage (v_s), as it is showed below:

$$\underbrace{\begin{bmatrix} I_2 \\ I_1 \\ V_c \end{bmatrix}}_{\mathbf{X}(s)} = \underbrace{\begin{bmatrix} F_{u \rightarrow i_2} \\ F_{u \rightarrow i_1} \\ F_{u \rightarrow v_c} \end{bmatrix}}_{\mathbf{G}(s)} U(s) + \underbrace{\begin{bmatrix} F_{v_s \rightarrow i_2} \\ F_{v_s \rightarrow i_1} \\ F_{v_s \rightarrow v_c} \end{bmatrix}}_{\mathbf{G}_d(s)} V_s(s), \quad (6.1)$$

where $\mathbf{G}(s)$ and $\mathbf{G}_d(s)$ are the MIMO dynamics from $U(s)$ and $V_s(s)$, respectively, to the states vector $\mathbf{X}(s)$, represented in the Laplace domain¹. These matrices are broken down below:

$$F_{u \rightarrow i_2}(s) = -\frac{Y_{L_2} \cdot Z_C \cdot Y_{L_1}}{1 + Z_C \cdot (Y_{L_1} + Y_{L_2})}, \quad F_{v_s \rightarrow i_2}(s) = \frac{Y_{L_2} \cdot (1 + Y_{L_1} \cdot Z_C)}{1 + Z_C \cdot (Y_{L_1} + Y_{L_2})}, \quad (6.2)$$

$$F_{u \rightarrow i_1}(s) = -\frac{Y_{L_1} \cdot (1 + Y_{L_2} \cdot Z_C)}{1 + Z_C \cdot (Y_{L_1} + Y_{L_2})}, \quad F_{v_s \rightarrow i_1}(s) = \frac{Y_{L_2} \cdot Z_C \cdot Y_{L_1}}{1 + Z_C \cdot (Y_{L_1} + Y_{L_2})}, \quad (6.3)$$

$$F_{u \rightarrow v_c}(s) = \frac{Y_{L_1} \cdot Z_C}{1 + Z_C \cdot (Y_{L_1} + Y_{L_2})}, \quad F_{v_s \rightarrow v_c}(s) = \frac{Y_{L_2} \cdot Z_C}{1 + Z_C \cdot (Y_{L_1} + Y_{L_2})}, \quad (6.4)$$

being Y_{L_2} , Y_{L_1} and Z_C defined in 2.14.

The considered three-phase system is, again, modelled in uncoupled $\alpha\beta$ axes [Krause et al., 2002], reducing the original MIMO control problem to two identical SISO problems. For notation simplicity, only one of the controlled channels is considered in this chapter for both plant modelling and controller design.

6.2.2 Inner closed-loop damped grid-current dynamic

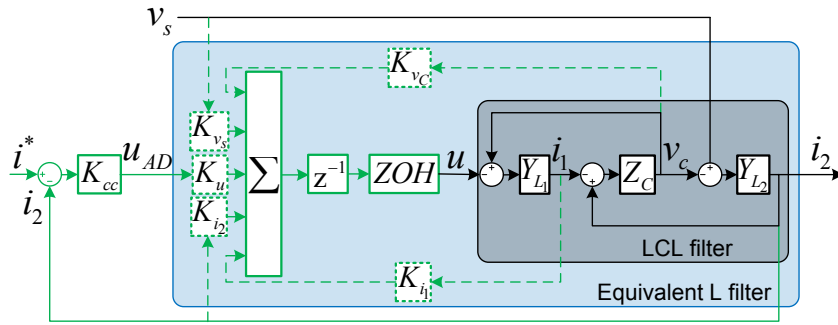


Figure 6.2. Proposed grid current control. The black and green lines represent signals or transfer functions in the continuous and discrete time domain, respectively. The proposed internal active damper (\mathbf{K}_{AD}) is represented by dashed green boxes, and its possible inputs by dashed green lines. The proposed active damping should shape the LCL filter dynamic, represented as a filled black box, so it behaves like an equivalent L filter, represented as a filled light blue box, simplifying the design of an outer loop grid current controller (K_{cc}).

Fig. 6.2 shows the proposed grid current control. The VSC average output voltage (u) is calculated by the inner active damping controller (\mathbf{K}_{AD}), which, to obtain it, will feed-back the selected filter measurements (i.e. linear combination of the states vector \mathbf{x}) and feed-forward the

¹For the sake of the chapter notation coherence, the command-to-output (G) and the open-loop admittance (G_d) transfer functions, defined in (4.3) for the LCL filter case, changes their names to $F_{u \rightarrow i_2}$ and $F_{v_s \rightarrow i_2}$, respectively, but their dynamics are equivalent.

PCC voltage (v_s) and the output (u_{AD}) of the outer grid-current controller (K_{cc}). Its dynamic expression, neglecting for now the effect of the one-sample time (z^{-1}) and ZOH, is as follows:

$$U = K_{v_s} V_s + K_u U_{AD} + K_{i_2} I_2 + K_{v_c} V_c + K_{i_1} I_1. \quad (6.5)$$

It has to be remarked that, while (6.5) shows the actuation (u) expression measuring all the filter states, the proposed methodology is flexible enough to allow, instead, the selection of a subset or a linear combination of them.

Substituting (6.5) in (6.1), a new grid-current (i_2) dynamic can be derived:

$$I_2(s) = G_{AD}(s) \cdot U_{AD}(s) + G_{d_{AD}}(s) \cdot V_s(s), \quad (6.6)$$

where $G_{AD}(s)$ and $G_{d_{AD}}(s)$ expressions are shown below:

$$\begin{aligned} G_{AD}(s) &= -\frac{K_u \cdot Y_{L_2} \cdot Z_C \cdot Y_{L_1}}{1 + Z_C \cdot (Y_{L_1} + Y_{L_2}) + (K_{i_1} \cdot (1 + Z_C \cdot Y_{L_2}) + (K_{i_2} \cdot Y_{L_2} - K_{v_c}) \cdot Z_C) \cdot Y_{L_1}}, \\ G_{d_{AD}}(s) &= \frac{Y_{L_2} \cdot (1 + Y_{L_1} \cdot Z_C) + (K_{i_1} - (K_{v_c} + K_{v_s}) \cdot Z_C) \cdot Y_{L_2} \cdot Y_{L_1}}{1 + Z_C \cdot (Y_{L_1} + Y_{L_2}) + (K_{i_1} \cdot (1 + Z_C \cdot Y_{L_2}) + (K_{i_2} \cdot Y_{L_2} - K_{v_c}) \cdot Z_C) \cdot Y_{L_1}}. \end{aligned} \quad (6.7)$$

From the outer current controller (K_{cc}) perspective, G_{AD} and $G_{d_{AD}}$ represent the dynamic model of a new grid-current plant with two inputs: one controlled by K_{cc} , its output u_{AD} , and one that acts as an external uncontrolled disturbance, the PCC voltage v_s .

The active damper actuation voltage (u) can be expressed then as:

$$U(s) = F_{u_{AD} \rightarrow u}(s) U_{AD}(s) + F_{v_s \rightarrow u}(s) V_s(s), \quad (6.8)$$

where $F_{u_{AD} \rightarrow u}$ and $F_{v_s \rightarrow u}$ represent the dynamic from the outer current controller (K_{cc}) output (u_{AD}) and the PCC voltage (v_s) to the actuation voltage (u), respectively:

$$\begin{aligned} F_{u_{AD} \rightarrow u} &= -\frac{K_u \cdot (1 + Z_C \cdot (Y_{L_1} + Y_{L_2}))}{1 + Z_C \cdot (Y_{L_1} + Y_{L_2}) + (K_{i_1} \cdot (1 + Z_C \cdot Y_{L_2}) + (K_{i_2} \cdot Y_{L_2} - K_{v_c}) \cdot Z_C) \cdot Y_{L_1}}, \\ F_{v_s \rightarrow u} &= \frac{K_{v_s} \cdot (1 + Z_C \cdot (Y_{L_1} + Y_{L_2})) + (K_{i_2} \cdot (1 + Y_{L_1} \cdot Z_C) + (K_{v_c} + K_{i_1} \cdot Y_{L_1}) \cdot Z_C) \cdot Y_{L_2}}{1 + Z_C \cdot (Y_{L_1} + Y_{L_2}) + (K_{i_1} \cdot (1 + Z_C \cdot Y_{L_2}) + (K_{i_2} \cdot Y_{L_2} - K_{v_c}) \cdot Z_C) \cdot Y_{L_1}}. \end{aligned} \quad (6.9)$$

This chapter will present a methodology to find an active damping controller (\mathbf{K}_{AD}) so that G_{AD} and $G_{d_{AD}}$ are as close as possible to the dynamic model of an L-connected VSC from both the grid and the converter side.

6.3 Active damping design

6.3.1 Derivation of the augmented plant

The design of the active-damper is approached following the \mathcal{H}_∞ model-reference framework presented in section 3.4. Fig. 6.3 shows the proposed structure for \mathbf{P} (displayed in red color) used as the entry point to the used \mathcal{H}_∞ controller synthesis algorithm. The original LCL plant ($\mathbf{G}(s)$ and $\mathbf{G}_d(s)$, described in (6.1)) is displayed in orange. The extra elements added to incorporate design objectives into the problem are drawn in purple. Those elements generate an error signal (e_d) that compares the output current (i_d) of a reference model (G_{ref}) with that of the actual plant (i_2).

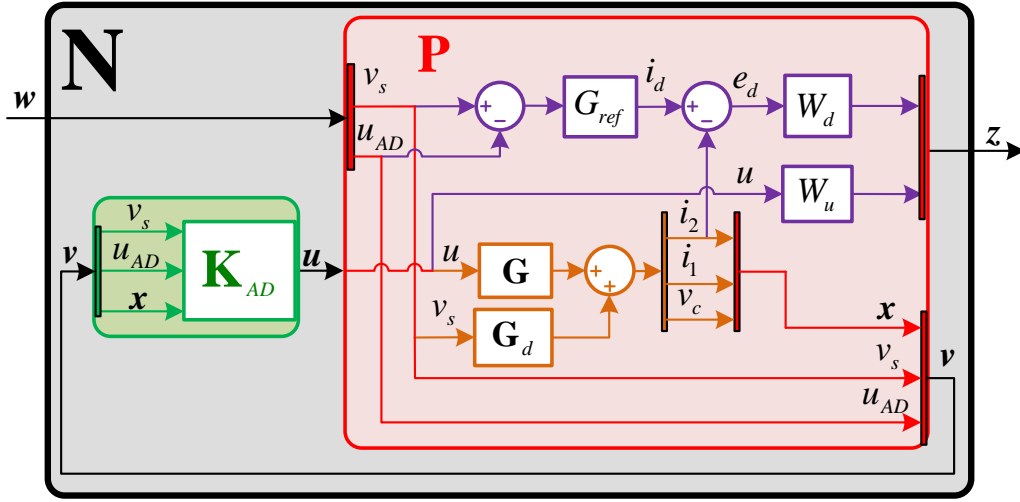


Figure 6.3. Proposed generalized plant \mathbf{P} is represented in red. Wrapped inside, the open-loop LCL plant (in orange) and a set of elements (in purple) added in the design process for controller synthesis. The desired active damper \mathbf{K}_{AD} is shown in green. Connection of \mathbf{P} and \mathbf{K}_{AD} results in the virtual closed-loop system \mathbf{N} , in black.

A controller yielding a small shaping error (e_d) will make the closed-loop system mimic the dynamic behaviour of the reference model (G_{ref}), so e_d is included in the vector to be minimized, \mathbf{z} . Actuation signal (u) needs to be also included in \mathbf{z} to avoid falling in a solution (i.e. damper) that needs of an unrealistic actuation level and, also, to limit the effective control bandwidth. Transfer functions W_d and W_u are weighting functions that determine the range of frequencies where the reference model will be imitated (i.e. e_d is minimized) and the actuation signal (u) will be limited, respectively.

The exogenous inputs vector \mathbf{w} is formed by the two disturbances to the damped plant, u_{AD} and v_s (see (6.6)). In addition to feed-forward these signals, \mathbf{K}_{AD} will feed-back some filter measurements. In Fig. 6.3, as well as in (6.5), (6.6) and (6.7), a complete states vector \mathbf{x} feed-back was considered to not lose generality. The method is, in any case, quite flexible and allows feeding-back a subset of the state vector (e.g. the grid current i_2) or a linear combination of their elements (e.g. the capacitor current i_c).

Plant \mathbf{P} inputs and outputs are summarized below:

$$\mathbf{z} = \begin{bmatrix} W_d \cdot e_d \\ W_u \cdot u \end{bmatrix}, \quad \mathbf{v} = \begin{bmatrix} v_s \\ u_{AD} \\ \mathbf{x} \end{bmatrix}, \quad \mathbf{w} = \begin{bmatrix} v_s \\ u_{AD} \end{bmatrix}, \quad \mathbf{u} = u. \quad (6.10)$$

6.3.2 Definition of the minimization problem

The shaping error (e_d) response to the exogenous inputs (\mathbf{w}) is derived below:

$$E_d = \mathbf{F}_{\mathbf{w} \rightarrow e_d} \mathbf{w} = \underbrace{(G_{ref} - G_{dAD})}_{F_{v_s \rightarrow e_d}} V_s + \underbrace{(-G_{ref} - G_{AD})}_{F_{v_s \rightarrow e_d}} U_{AD} \quad (6.11)$$

On the other hand, the active damper actuation voltage (u) response to \mathbf{w} is as follows:

$$U = \mathbf{F}_{\mathbf{w} \rightarrow u} \mathbf{w} = F_{u_{AD} \rightarrow u} U_{AD} + F_{v_s \rightarrow u} V_s, \quad (6.12)$$

where $F_{u_{AD} \rightarrow u}$ and $F_{v_s \rightarrow u}$ were defined in (6.9). Therefore, the \mathcal{H}_∞ minimization problem can be expressed as:

$$\min_{\mathbf{K}_{AD}} \|\mathbf{N}\|_\infty \leq \gamma, \text{ with } \|\mathbf{N}\|_\infty = \max_{\omega} \bar{\sigma}(\mathbf{N}) = \max_{\mathbf{w}(t) \neq 0} \frac{\|\mathbf{z}(t)\|_2}{\|\mathbf{w}(t)\|_2} = \left\| \begin{matrix} W_u \mathbf{F}_{\mathbf{w} \rightarrow u} \\ W_d \mathbf{F}_{\mathbf{w} \rightarrow e_d} \end{matrix} \right\|_\infty \quad (6.13)$$

It can be partitioned, then, into two single specifications to fulfil:

$$\bar{\sigma}(\mathbf{F}_{\mathbf{w} \rightarrow e_d})(s) \leq \frac{\gamma}{|W_d(s)|} \quad (6.14)$$

$$\bar{\sigma}(\mathbf{F}_{\mathbf{w} \rightarrow u})(s) \leq \frac{\gamma}{|W_u(s)|} \quad (6.15)$$

That is, high values of $|W_d|$ should result in the minimization of the shaping error (e_d), in the same way that high values of $|W_u|$ should minimize the actuation voltage (u), as long as the obtained γ is relatively low. Again, this value serves as an indicator of how *difficult* is for the \mathcal{H}_∞ synthesis algorithm to obtain a controller given W_d and W_u values.

6.3.3 Reference model and weighting functions selection

The proposed generalised plant (\mathbf{P}) involves the selection of three transfer functions: the model-reference transfer function (G_{ref}) and the two involved weighting functions (W_d and W_u).

G_{ref} is the way the designer specifies the damping strategy of the plant. This chapter proposes to use the transfer function relating the grid voltage and the grid current in a L-connection scenario where the inductance and resistance match the addition of the actual LCL filter inductances and resistances:

$$G_{ref}(s) = \frac{1}{R_{ref} + sL_{ref}} = \frac{1}{(R_1 + R_2) + s(L_1 + L_2)}. \quad (6.16)$$

This transfer function closely resembles that of a damped version of the LCL one as it shown in Fig. 6.4.

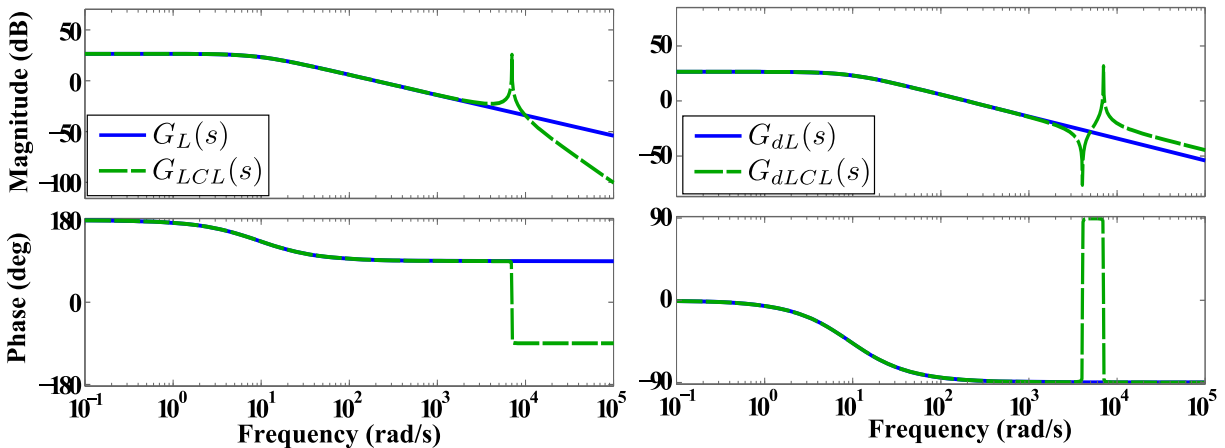


Figure 6.4. Frequency domain representation of the L and LCL filter plants.

Moreover, given the dipole nature of the L filter, a single reference model (G_{ref}) is enough to shape both G_{AD} and G_{dAD} , as it can be observed in Fig. 6.3, subtracting, to that end, u_{AD} from v_s .

The objective of the W_d and W_u weighting functions is to specify the control band where the model is going to be emulated and, also, to limit the actuation level inside the control band to avoid undesired saturation in the plant actuator (maximum duty cycle, in this case).

W_d should be, thus, a low-pass filter, to emphasise the importance of e_d minimization (see Fig. 6.3) inside the control band. The proposed transfer function is

$$W_d(s) = K_d \frac{1}{(1/\omega_d)s + 1}, \quad (6.17)$$

where K_d and ω_d are constants that should be chosen to match the design objectives in emulation error and control bandwidth, respectively.

The design of W_u should be complementary: a high-pass filter, so outside of the control band the actuation is small. A possible choice is

$$W_u(s) = K_u \frac{(1/\omega_{u1})s + 1}{(1/\omega_{u2})s + 1}. \quad (6.18)$$

An example bode plot of the aforementioned weighting function is shown in Fig. 6.5.

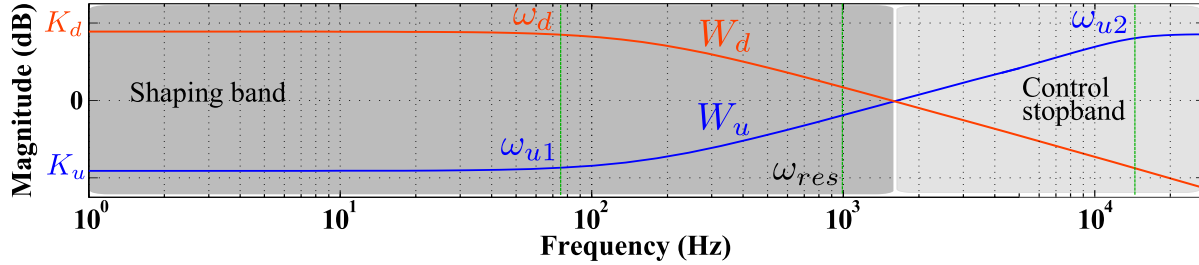


Figure 6.5. Frequency representation of the considered weights W_d and W_u .

The design methodology of these weights is very similar to the one presented in section 4.6 for the closed-loop admittance shaping:

- Higher values of $|W_d|$ should result in a greater minimization of the shaping error (e_d) and, then, in a $G_{AD} \approx -G_{ref}$ and a $G_{dAD} \approx G_{ref}$ (see (6.11) and (6.14)). On the other hand, higher values of $|W_u|$ should minimize the actuation voltage (u) (see (6.12) and (6.15)). W_u is used, then, to bound the actuation level inside the control band and to not allow it at high frequencies (i.e. limit shaping bandwidth).
- The weights defined in Fig. 6.5 will divide the \mathcal{H}_∞ synthesis objectives in two frequency bands; the shaping band and the control stop band, where e_d and u are minimized, respectively. Note that the ranges shown in Fig. 6.5 serve only as a visual guidance, as the exact width of this frequency bands not only depend on the defined weights but also in the obtained γ (see (6.14) and (6.15)).
- In order to obtain a low γ , and then fulfil the desired design specifications, W_d and W_u have to be defined in a complementary way, as shaping error (e_d) and actuation (u) minimizations are, usually, mutually exclusive.
- Additionally, as the proposed method is subjected to bandwidth limitation derived from the discrete nature of the active damper (see section 6.3.4), the band over which the shaping error is minimized (shaping band in Fig. 6.5) must be limited to not increase the obtained γ .

6.3.4 Implementation considerations and limitations

The design procedure here proposed is subjected to several limitations. While some of them are inherent to any LTI control loop, other important limitations and considerations are due to the final sampled-data nature of the algorithm to be implemented.

Sampled-time implementation and controller synthesis

The damper (\mathbf{K}_{AD}) will be coded and executed in a Digital Signal Processor (DSP), and, consequently, a discrete-time controller transfer function is needed. An approach that considers the problem to be continuous and, after the synthesis, obtains a discrete-time approximation of the controller neglects important dynamic components such as the presence of a PWM modulator, that may be modelled as a Zero-Order Hold (ZOH), and the computational delay at the damper (\mathbf{K}_{AD}) output (u_{AD}), input to the plant (\mathbf{G}) (see section 4.7 for more details about the effect of these dynamics in the controlled plant). These modelling errors would induce inaccuracies in the model emulation performance of the synthesised controller.

This chapter uses the approach described in section 4.7.3 to include these important dynamics in the plant. The ZOH discrete-time equivalent of $\mathbf{G}(s)$ is computed and a one-sample delay, z^{-1} , is added to it in the z domain. After introducing these dynamic elements in the process, a continuous approximation of this plant is obtained via Bilinear (i.e. Tustin) transformation, making a frequency pre-warping to accurately preserve LCL resonance frequency. \mathbf{G}_d transfer matrix can be included directly into the generalized plant $\mathbf{P}(s)$ as the grid voltage is, in fact, a continuous disturbance to the process. An optimal continuous controller ($\mathbf{K}_{AD}(s)$) is obtained through a regular \mathcal{H}_∞ process. The final discrete controller ($\mathbf{K}_{AD}(z)$) is, then, obtained by computing a Bilinear transformation. The process is equivalent to the one shown in the left part of Fig. 4.21.

A similar rationale can be applied to the selection of the model reference plant (G_{ref}). As long as the ZOH and the delay exists in the plant under control, they would also exist in an hypothetical L-connection case that is used as the reference model. The synthesis process yields better results if the reference-model (G_{ref}) is built following the same principles to include these dynamics.

The snippet displayed on Alg. 3 describes the procedure used to synthesize the final controller using MATLAB standard library and also its Robust Control Toolbox.

Bandwidth limitations of the active damper

The dynamic particularities derived from the sampled-time nature of the controller are also the cause of one fundamental limitation of the closed-loop system. The sampling frequency of the controller, together with the delay at the plant input, induces a limitation on the maximum achievable controller bandwidth (f_c) of:

$$f_{c_{MAX}} \approx \frac{1}{2\pi T_s}, \quad (6.19)$$

being T_s the sample time of the digital system. It is important to remark that this bandwidth limitation affect both feedback (see section 3.3.4) and feed-forward paths (see section 4.8.1). Good damping results can not be assured, then, if the LCL resonance frequency (f_{res}) is above $f_{c_{MAX}}$. Fig. 6.6 represents this limitation in the frequency domain.

Algorithm 3 Controller synthesis procedure

```

1: procedure ACTIVE DAMPER SYNTHESIS( $G, G_d, TS$ )
2: Weights and model references definition:
3:    $W_u = \text{tf}(\dots)$ ;  $W_d = \text{tf}(\dots)$ ;
4:    $G_{ref} = \text{tf}(\dots)$ ;
5: Process model:
6:    $\text{delay} = \text{tf}([1], [1 \ 0], ts)$ ;
7:    $G_z = \text{delay} * \text{c2d}(G, ts, 'zoh')$ ;
8:    $G = \text{d2c}(G_z, 'bilin', \dots)$ ;
9:    $G_{ref}_z = \text{delay} * \text{c2d}(G_{ref}, ts, 'zoh')$ ;
10:   $G_{ref} = \text{d2c}(G_{ref}_z, 'bilin', \dots)$ ;
11: P assembly:
12:   $\text{systemnames} = 'G \ G_d \ G_{ref} \ W_u \ W_d'$ ;
13:   $\text{inputvar} = '[vs; uAD; u]'$ ;
14:   $\text{outputvar} = '[W_d; W_u; vs; uAD; G+G_d]'$ ;
15:   $\text{input\_to\_}W_d = '[G_{ref} - G - G_d]'$ ;
16:   $\text{input\_to\_}W_u = '[u]'$ ;
17:   $\text{input\_to\_}G_{ref} = '[vs - uAD]'$ ;
18:   $\text{input\_to\_}G = '[u]'$ ;
19:   $\text{input\_to\_}G_d = '[vs]'$ ;
20:   $P = \text{sysic}$ ;
21: KAD synthesis:
22:   $[KAD\_cont, \gamma] = \text{hinfosyn}(P, 3, 1, \dots)$ ;
23:  if ( $\gamma > \gamma_{max}$ ) then goto Weight definition
24:   $KAD = \text{c2d}(KAD\_cont, ts, 'bilin', \dots)$ ;
25:  end

```

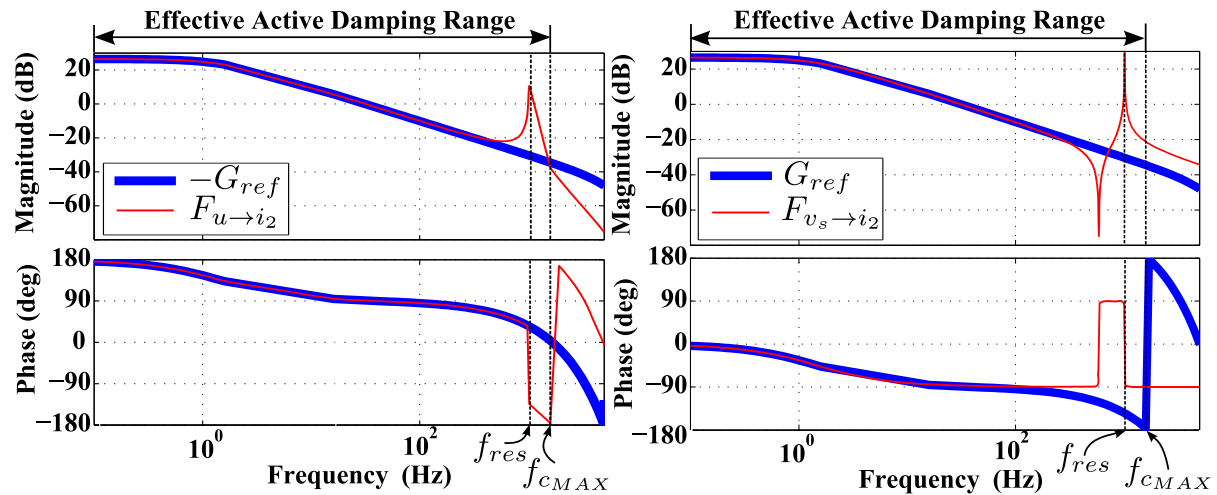


Figure 6.6. Effective active damping bandwidth limitation. If $f_{res} > f_{cMAX}$ an effective active damping of the filter resonance is not guaranteed.

Consequently, the LCL resonant frequency imposes a minimum sampling and control frequency to achieve good active damping results. This is a classical theoretical limitation and affects to any sampled-data linear strategy to achieve LCL resonance damping; that is, it is not exclusive of the proposed method. In that regard, the effective active damping bandwidth limitation proposed here represents an alternative verification of the active damping regions

proposed in [Parker et al., 2014].

Generalized plant \mathbf{P} design limitations

Controller synthesis limitations in terms of the generalized plant (\mathbf{P}) definition are the same that the ones presented in section 3.3.4, so the reader can refer to this section for more details.

6.4 Results

The presented active damper is now tested in the *Semikron* experimental platform detailed in section 5.3: its main parameters are listed in Table 5.1. Two different sampling periods (T_s) are considered, 200 and 100 μs , in order to evaluate the presented bandwidth limitations and the influence of the sampling time in the active damper performance.

6.4.1 External control loops

The reference tracking is accomplished by a classical outer PR grid current controller, designed for the L equivalent filter reference in (6.16) [Parker et al., 2014]:

$$K_{cc}(z) = K_p \left(1 + \frac{\sin(\omega_1 T_s)(z^2 - 1)}{T_r 2\omega_1 (z^2 - 2z \cos(\omega_1 T_s) + 1)} \right), \quad (6.20)$$

where the resonant time constant and the proportional gain are fixed for both sampling times to $T_r = 0.004$ and $K_p = 12.648$, respectively. The controller bandwidth is the same, then, for both considered sampling times. The resonant time constant (T_r) is chosen for a fast reference tracking. The proportional gain (K_p) is tuned so applying K_{cc} to the LCL filter (without damping) for a sampling time $T_s = 200 \mu\text{s}$ results in an unstable system with stability margins close to zero. This is done to test the active damping efficiency as a system stabilizer (see the test in Fig. 6.15).

Considering the damped LCL plant, the closed-loop dynamic of the controlled current (i_2) follows the expression:

$$I_2 = \underbrace{\frac{G_{AD} \cdot K_{cc}}{1 + G_{AD} \cdot K_{cc}}}_{T(s)} I^* + \underbrace{\frac{G_{dAD}}{1 + G_{AD} \cdot K_{cc}}}_{Y(s)} V_s, \quad (6.21)$$

where $T(s)$ and $Y(s)$ are the closed-loop tracking and admittance transfer functions. The stability of the damped system can be obtained by means of linear time invariant (LTI) analysis of the loop function $L_{AD} = K_{cc} \cdot G_{AD}$. A perfect damping and improved stability margins would be obtained if L_{AD} is equal to its reference value $L_{ref} = -K_{cc} \cdot G_{ref}$. If the inner active damping loop is not considered, L_{AD} would be equal to $L = K_{cc} \cdot F_{u \rightarrow i_2}$.

An outermost active (p) and reactive (q) power controller is implemented to regulate the power flow between the grid and the VSC. Its design was addressed in section 5.2.1. A more detailed explanation of the controllers implementation can be found in section 5.3.2.

6.4.2 Damping analysis

Fig. 6.7 shows the frequency domain results of the synthesized active dampers for the two considered sampling times. As it can be seen, both modified LCL-filter dynamics (G_{AD} and

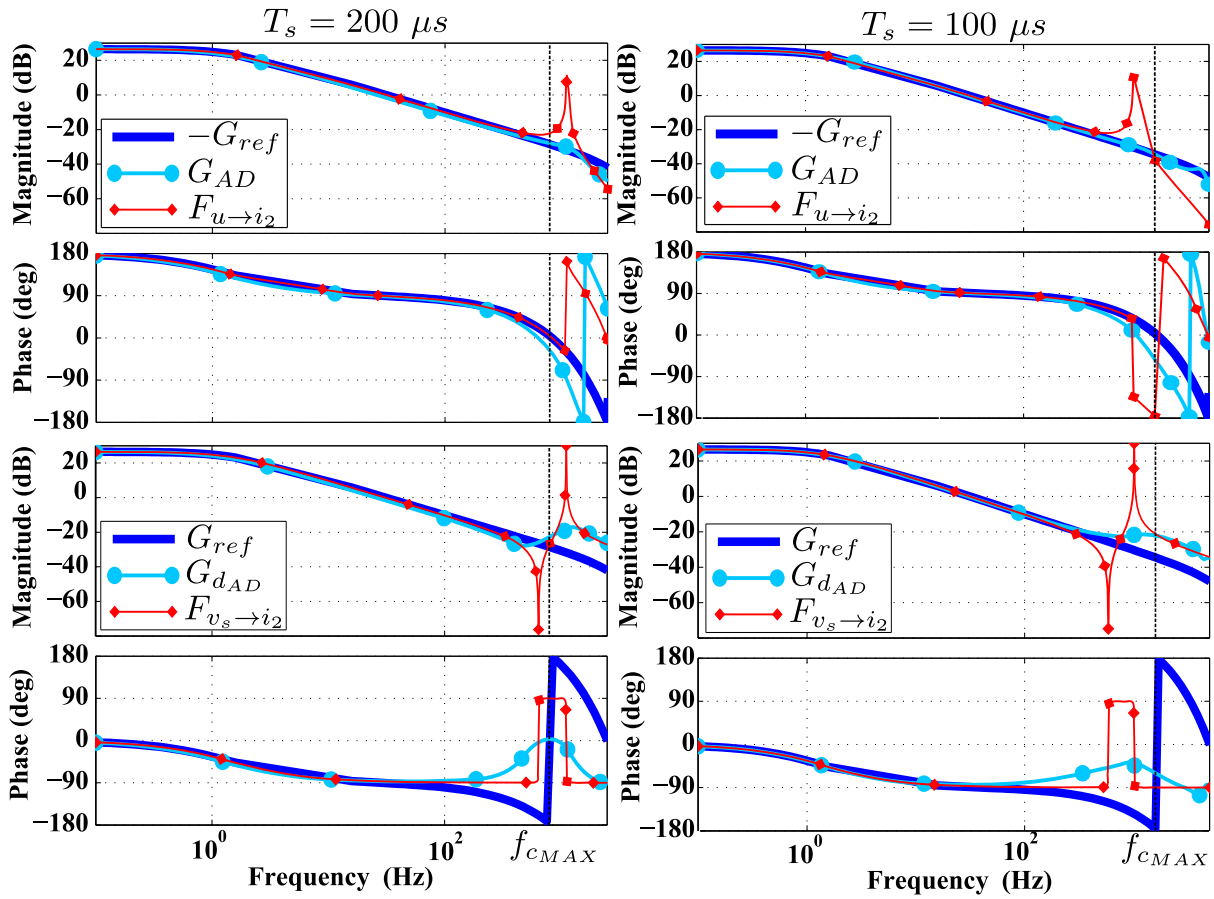


Figure 6.7. LCL dynamic shaping results for the two different considered sample times. Dynamic references (i.e. the one of an L filter) are represented in dark blue, the open loop LCL dynamic is represented in red and the obtained modified LCL dynamic is shown in light blue. Damping results improves for a smaller sample time, thanks to the higher \mathbf{K}_{AD} maximum bandwidth f_{cMAX}

G_{dAD}) follow the L-filter reference (G_{ref}), damping the resonance of the unmodified LCL-filter dynamics ($F_{u \rightarrow i_2}$ and $F_{v_s \rightarrow i_2}$). Note that the proposed controller loses effectiveness around the maximum bandwidth (f_{cMAX}) (i.e. all \mathbf{K}_{AD} terms magnitude in (6.7) tends to zero, and so does its output u), so the modified LCL plant dynamics G_{AD} and G_{dAD} tends to zero and its open loop value $F_{v_s \rightarrow i_2}$, respectively. The results are better, then, for the smaller sample time case ($T_s = 100 \mu s$), as the resonance frequency (f_{res}) is inside the achievable controller bandwidth. Damping results can be further improved for LCL filters with lower resonance frequencies and/or for lower implementation sampling times.

The result shown in Fig. 6.7 correspond to a design where only the grid-current (i_2) is fed-back to the synthesized active-damper (i.e. $\mathbf{x} = i_2$ for the generalized plant (\mathbf{P}) definition in Fig. 6.3), reducing, then, the number of sensors needed for its implementation. In any case, the design is flexible enough to achieve similar results feeding-back any linear combination of the filter states vector, as it is demonstrated in Fig. 6.8. In it, the frequency domain results of the damped dynamics (G_{AD} and G_{dAD}) are shown for a sampling time $T_s = 200 \mu s$ and different fed-back states (identified in parentheses). Poorer results are obtained when only the converter current (i_1) is fed-back. In any case, the results are very similar, being almost equivalent if the proposed active damping feeds-back only the grid current (i_2), only the capacitor voltage (v_c) or all the states of the LCL filter (\mathbf{x}).

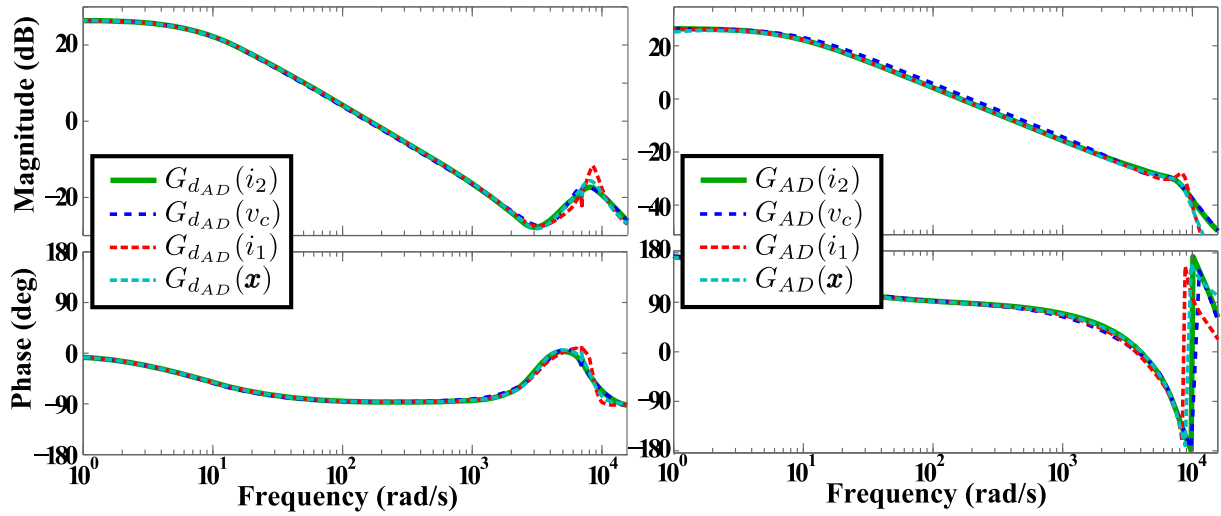


Figure 6.8. Modified (i.e. damped) LCL dynamic considering different feedback loops: (green) only the grid current i_2 (dark blue) only the capacitor voltage v_c (red) only the converter current i_1 (light blue) the complete LCL filter states vector \mathbf{x} .

Order reduction

One of the main disadvantages attributable to the presented active damping method with respect to classical approaches is its probable high order. For that reason, the order reduction techniques introduced in section 5.5.3 are now applied to the synthesized active dampers (\mathbf{K}_{AD}). Fig. 6.9 shows the order reduction results for the active damper (\mathbf{K}_{AD}) synthesized with a sampling time $T_s = 200 \mu\text{s}$ considering (a) the feedback of the grid current (i_2) and (b) the feedback of the complete state vector (\mathbf{x}).

\mathbf{K}_{AD} Hankel singular values magnitude for both considered designs are shown at the top of the figure. As it can be seen, their magnitudes decrease if the complete state vector is fed-back. That is, the active damper (\mathbf{K}_{AD}) order can be reduced further if the number of filter states sensed increases, as it is demonstrated in the damped LCL filter dynamics (G_{AD} and G_{dAD}) shown at the bottom of the figure:

(a) Feeding-back only the grid current (i_2) the 10^{th} order nominal damper can be reduced to an 8^{th} order damper without damping performance degradation.

(b) Feeding-back the complete state vector (\mathbf{x}) this 10^{th} order nominal damper can be reduced to a 5^{th} order damper without degradation.

This three orders difference between dampers are, precisely, the order of the LCL-filter plant; as all its states are measured, the synthesized active damper (\mathbf{K}_{AD}) does not need all the information of the plant dynamic (i.e. it does not need to estimate it) to achieve good results. This is one of the identified advantages of using the complete state vector as part of the active damper input variables. However, as this order difference is not an issue for the DSP where the active damper is implemented, the results shown in the next sections only consider the grid current (i_2) feedback, reducing as a result the number of sensor needed.

6.4.3 Stability improvement analysis

Fig. 6.10 shows different loop functions, and their deduced stability margins, when the designed grid current controller (K_{cc}) is: applied to the damped LCL plant G_{AD} ($L_{AD} = K_{cc} \cdot G_{AD}$);

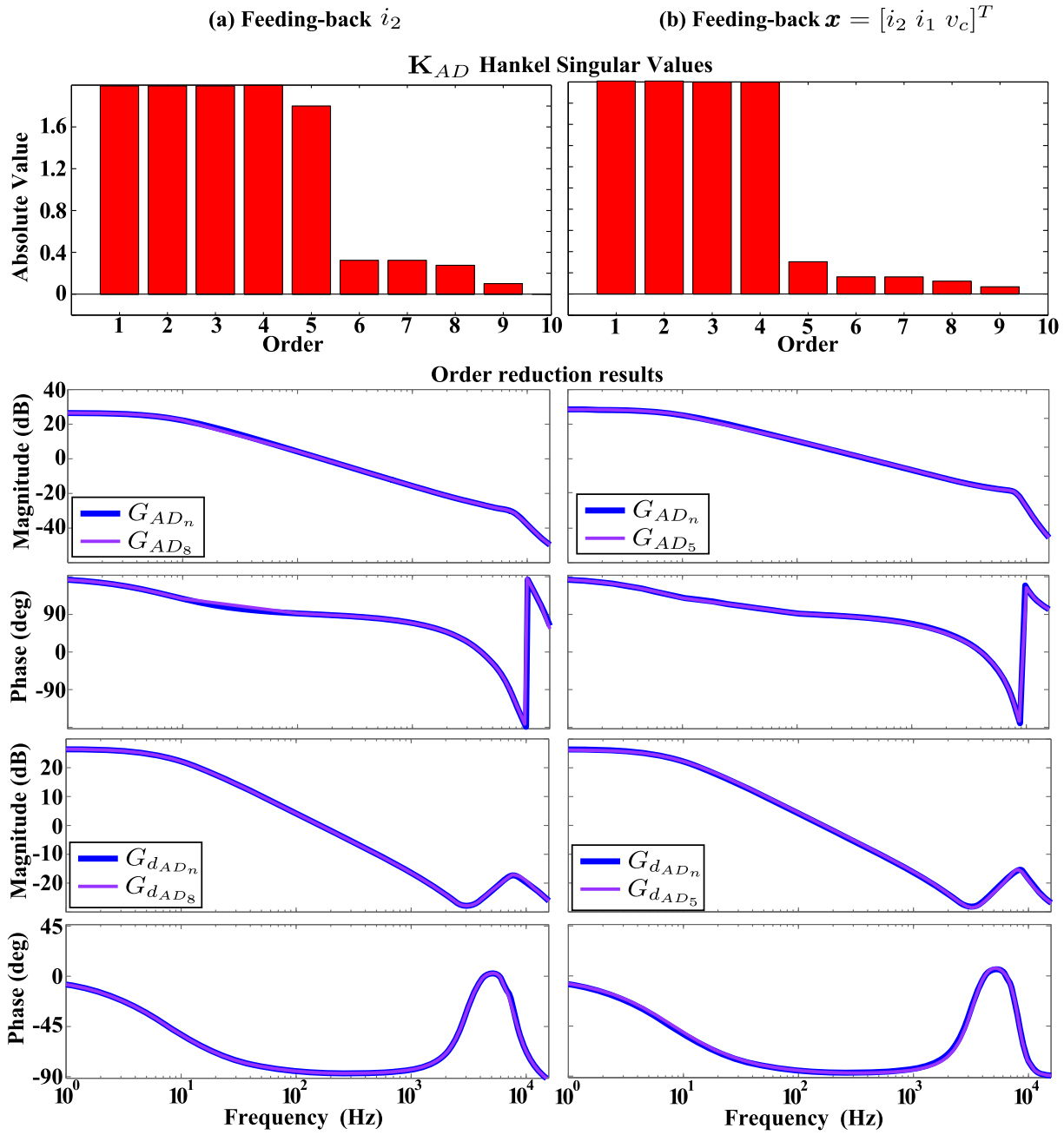


Figure 6.9. \mathbf{K}_{AD} ($T_s = 200 \mu s$) Hankel singular values and damped LCL dynamics (G_{AD} and G_{dAD}) after \mathbf{K}_{AD} order reduction (a) feeding-back only i_2 and (b) feeding-back the complete states vector \mathbf{x} . \mathbf{K}_{AD} can be reduced from its 10th nominal order (with G_{ADn} and G_{dADn} damped dynamics) to (a) an 8th order damper (resulting in G_{AD8} and G_{dAD8}) and (b) a 5th order damper (resulting in G_{AD5} and G_{dAD5}) without damping performance degradation, depending on the number of variables sensed.

applied to the L filter reference G_{ref} ($L_{ref} = -K_{cc} \cdot G_{ref}$); and applied to the unmodified LCL plant $F_{u \rightarrow i_2}$ ($L = K_{cc} \cdot F_{u \rightarrow i_2}$).

As stated before, K_{cc} is designed to be unstable if applied to the unmodified LCL plant with a sample time $T_s = 200 \mu s$, being $L = K_{cc} \cdot F_{u \rightarrow i_2}$ gain and phase margins, GM and PM , negative but close to zero in that case. K_{cc} is again designed for a sampling time $T_s = 100 \mu s$, following (6.20), with the same design parameters K_p and T_r . This will also result in an unstable system if it is directly applied to the undamped plant, but with poorer stability margins in L

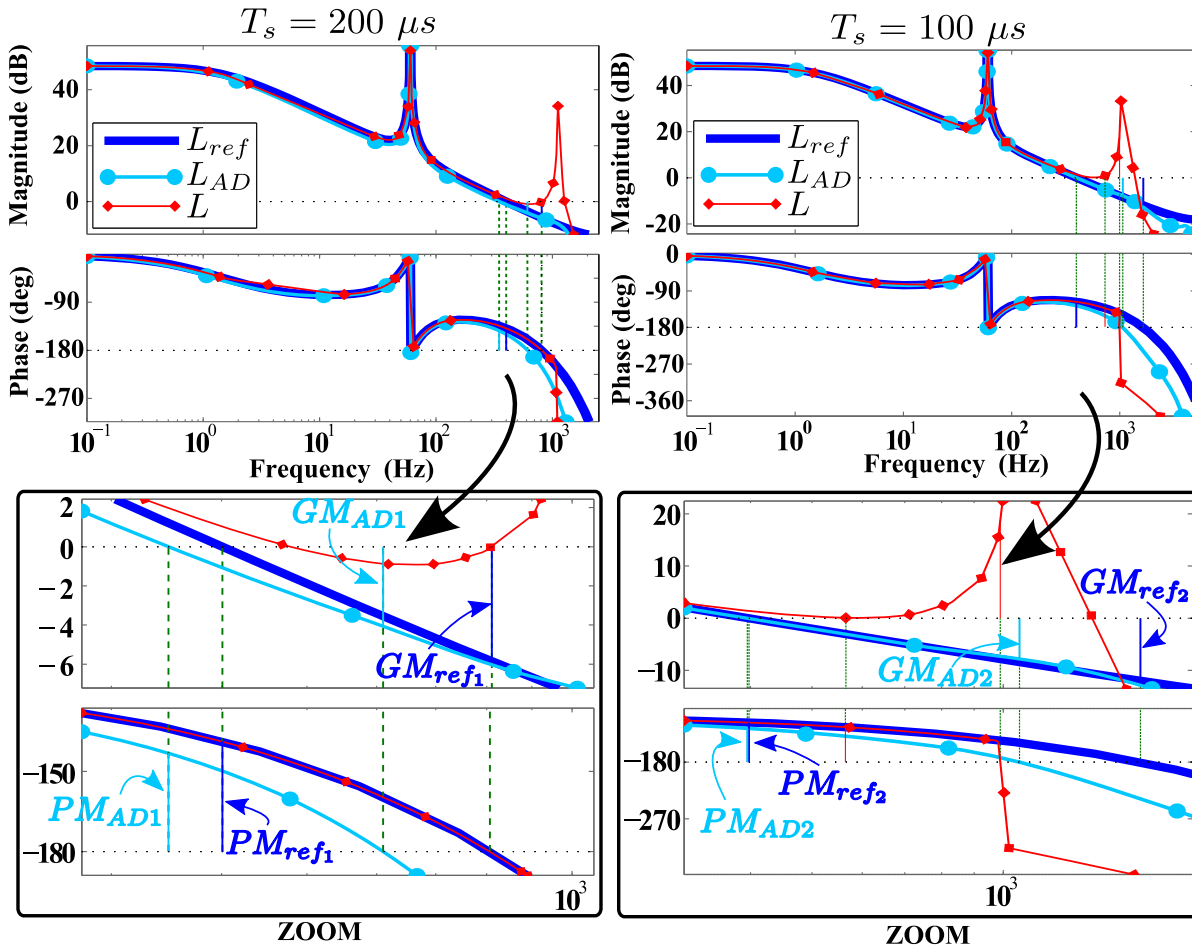


Figure 6.10. Loop function frequency representation for the unmodified LCL filter (red), the reference L filter (dark blue) and the modified LCL filter (light blue). Their corresponding stability margins are detailed in TABLE 6.1.

than the design with $T_s = 200 \mu s$. The left part of table 6.1 collects the stability margins (GM and PM) of the system without the proposed active damper, where the sub-index 1 and 2 stand for sampling times $T_s = 200 \mu s$ and $T_s = 100 \mu s$ cases, respectively.

Table 6.1. Stability margins.

PM_1	-0.31°	PM_{AD1}	36.8°	PM_{ref1}	41.3°	$\frac{PM_{AD1}}{PM_{ref1}}$	0.891
PM_2	44.3°	PM_{AD2}	58.4°	PM_{ref2}	63°	$\frac{PM_{AD2}}{PM_{ref2}}$	0.927
GM_1	0.05 dB	GM_{AD1}	4.07 dB	GM_{ref1}	5.86 dB	$\frac{GM_{AD1}}{GM_{ref1}}$	0.694
GM_2	-17.2 dB	GM_{AD2}	8.9 dB	GM_{ref2}	12 dB	$\frac{GM_{AD2}}{GM_{ref2}}$	0.741

Designed damping controller stabilizes both cases. Table 6.1 summarizes the achieved improvement of the stability margins seen in Fig. 6.10. In it, sub-index AD and ref stands for damped LCL filter case (loop L_{AD}) and L filter reference case (loop L_{ref}), respectively, meanwhile the sampling times $T_s = 200 \mu s$ and $T_s = 100 \mu s$ are again identified by sub-index 1 and 2, respectively. Both designed controllers increase stability margins almost to their respective reference values, with better results for the smaller sampling time design, as can be seen in the rightmost column that shows a performance index that compares the achieved stability margins

to its reference values.

The improvement of the system robustness when the sampling period (T_s) is reduced is further demonstrated in the sensitivity functions comparison between the reference L-filter dynamic ($S_{ref} = (1 + L_{ref})^{-1}$) and the damped LCL-filter dynamic ($S_{AD} = (1 + L_{AD})^{-1}$) shown in Fig. 6.11.

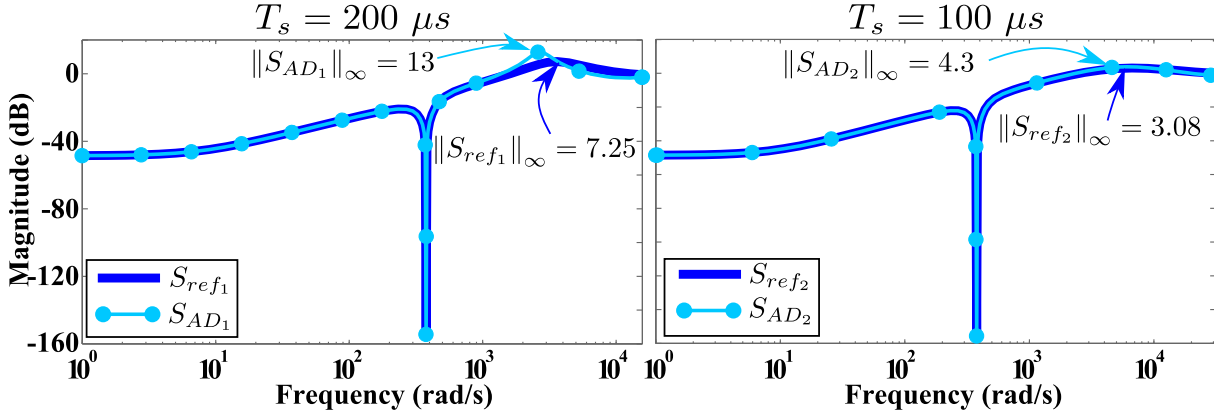


Figure 6.11. Comparison between the sensitivity functions of the reference L-filter system (S_{ref}) and the damped LCL-filter system (S_{AD}) for the two sampling times considered.

As it can be seen, the maximum sensitivity gain of the actively damped design ($\|S_{AD_2}\|_{\infty}$) decreases when the sampling period is reduced to $T_s = 100 \mu s$, being its value much closer to its reference at that sampling period ($\|S_{ref_2}\|_{\infty}$).

Fig. 6.12 shows the close-loop frequency results of the considered system (a) without the proposed active damping and (b) with the proposed active damping (K_{AD}) for a sampling time $T_s = 200 \mu s$.

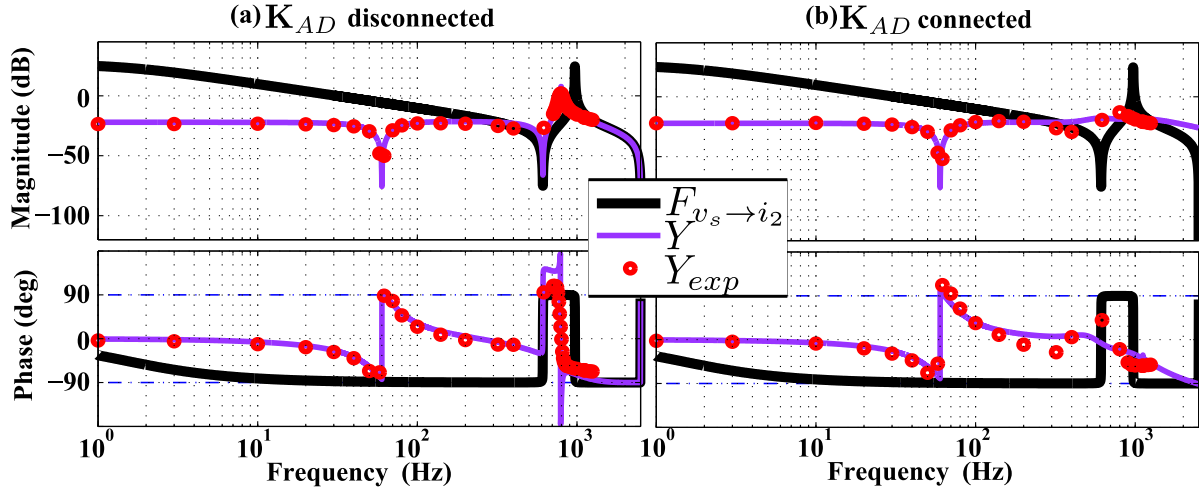


Figure 6.12. Close-loop frequency results for $T_s = 200 \mu s$ (a) without the proposed active damping (b) with the proposed active damping. In black, the open-loop resonant LCL filter admittance. Close-loop theoretical admittance is shown in purple, being the red circles experimentally measured values of it.

The purple line represents the analytical value of the obtained admittance (Y), whose dynamic was defined in (6.21), meanwhile red circles represents experimental identified values of it (Y_{exp}) taken at different frequencies. The resonance in the LCL open loop admittance ($F_{vs \rightarrow i_2}$), in black, is highly damped with the designed active damping connected, as can be deduced from

the experimental results. The undamped system (i.e. with \mathbf{K}_{AD} disconnected) considering a $T_s = 200 \mu s$ is stable in the tested experimental platform, even though it is not theoretically (see GM_1 and PM_1 in table 6.1), allowing to measure the experimental admittance (Y_{exp}) shown in 6.12(a). That is probably due to the more damped experimental behaviour of the system (compare Y_{exp} and Y phase around the resonant frequency).

Fig. 6.13 repeats the results shown in Fig. 6.12, this time for a reduced sampling time $T_s = 100 \mu s$. In this case, the undamped system is unstable in the experimental platform (as predicted theoretically, see GM_2 and PM_2 in table 6.1), not allowing to measure experimentally the obtained closed-loop admittance. Fig. 6.13 shows, then, only the results when the proposed active damping (\mathbf{K}_{AD}) is connected. As it can be seen, the LCL filter resonance (see $F_{v_s \rightarrow i_2}$) is slightly better damped experimentally for this reduced sampling time.

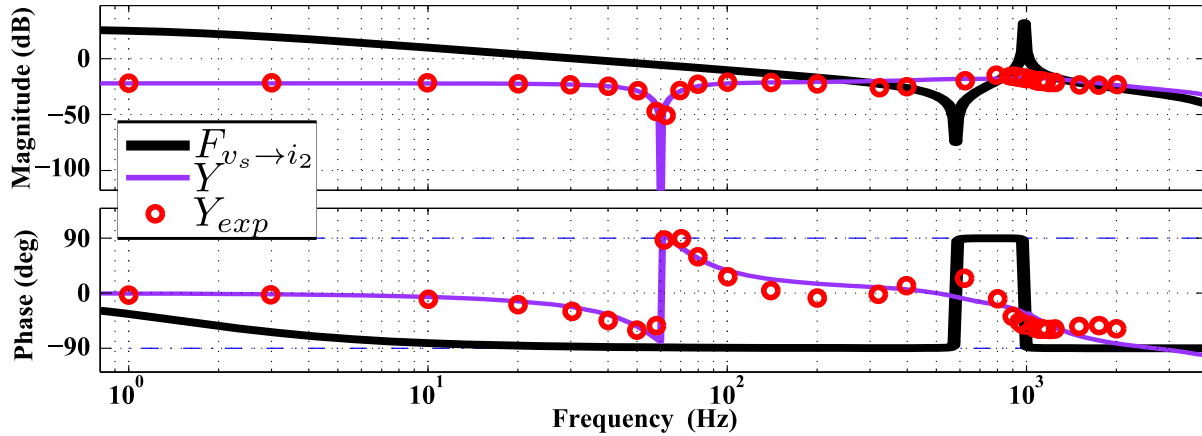


Figure 6.13. Close-loop frequency results. In black, the open-loop resonant LCL filter admittance. Close-loop theoretical admittance is shown in purple, being the red circles experimentally measured values of it. The system is well damped with a minimum deviation in the phase experimental results.

Finally, Fig. 6.14 proves the damping and stability robustness of the method towards parametric variations of the LCL filter.

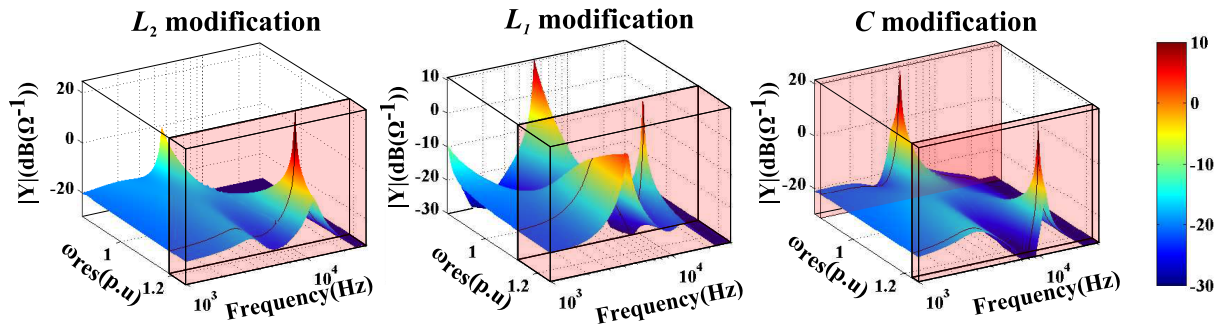


Figure 6.14. Expected admittance magnitude modification for changes of the LCL resonance frequency. High (resonant) values would indicate ineffective action of the designed active damping. Red boxes represent unstable cases.

It represents the close-loop frequency response of the expected (i.e. not experimental) admittance magnitude ($|Y|$) for changes of the LCL parameters L_1 , L_2 and C . High (resonant) values of $|Y|$ in Fig. 6.14 would indicate ineffective action of the designed active damping. A sampling time of $T_s = 100 \mu s$ was considered for the grid current controller (K_{cc}) and the damping controller (\mathbf{K}_{AD}) designs. Then, the resonance frequency (ω_{res}) is changed from 0.85 to 1.25

pu of its nominal value by modifying each of the LCL elements². $|Y|$ in Fig. 6.14 for $\omega_{res} = 1$ pu² is, then, equivalent to $|Y|$ in Fig. 6.13. The red boxes represent resonance frequency limits from which the system becomes unstable. System is stable, and well damped, for changes of the resonance frequency inside the range $[0.87, 1.12]$ pu², for the most unfavourable cases.

6.4.4 Time domain results

As it was previously stated, if the designed grid current control (K_{cc}) at sampling time $T_s = 200 \mu s$ is applied to the undamped LCL filter, the resultant system will be unstable, but with a close to zero stability margins (see GM_1 and PM_1 in table 6.1). Fig. 6.15 shows simulated³ time domain results of the action of the designed active-damping (\mathbf{K}_{AD}) in that case.

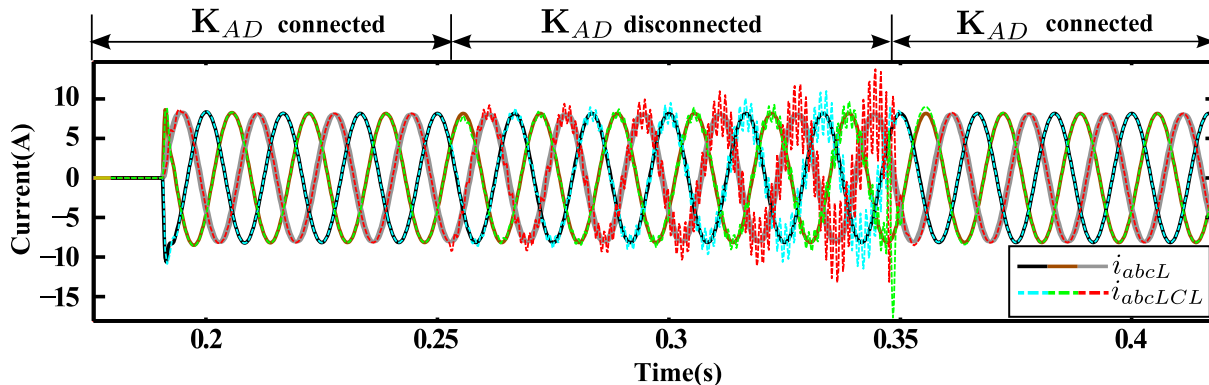


Figure 6.15. Time domain active damping results. i_{abcL} and i_{abcLCL} represent the grid current for the emulated L-filter and the considered LCL-filter, respectively. Both are equivalent if \mathbf{K}_{AD} is connected. An unstable oscillation grows if \mathbf{K}_{AD} is disconnected. This oscillation is quickly dissipated if \mathbf{K}_{AD} is again connected.

Two applications were simulated simultaneously for the results in Fig. 6.15: one VSC connected to an ideal grid (i.e. $Z_g = 0$) through the equivalent L filter, controlling its grid current (i_{abcL}) with only the proposed external current controller (K_{cc}), and another VSC connected to the same grid through the considered LCL filter, controlling its current (i_{abcLCL}) with the proposed active damper (\mathbf{K}_{AD}) and the aforementioned outer current controller (K_{cc}). At the beginning of the experiment, \mathbf{K}_{AD} is connected and a non-zero reference current (i^*) is introduced at the fundamental frequency (ω_1) in both applications. The response of the LCL-filter grid current (i_{abcLCL}) is very similar to the one of the emulated L-filter (i_{abcL}), demonstrating the good dynamics shaping achieved with \mathbf{K}_{AD} . It can be seen how the grid current of the LCL-filter (i_{abcLCL}) starts to oscillate at the resonant frequency if \mathbf{K}_{AD} is disconnected. If \mathbf{K}_{AD} is connected again, this oscillation is quickly dissipated. Experimental results are not equivalent in this case because the real LCL filter is more damped than it was considered in its model (i.e. the losses resistances are higher than expected), as it can be deduced from the experimental admittance values shown in Fig. 6.12(a). For that reason, the damping effect is not seen so clearly in the experimental platform as in the simulated results shown in Fig. 6.15.

Fig. 6.16 shows the experimental results of the implemented damped LCL grid current control at sampling time $T_s = 100 \mu s$ for different tests; Fig. 6.16(a) shows the response to a change of the passive DC-load active power demand from $p^* = 0$ to $p^* = 4.2$ kW, Fig. 6.16(b)

²The nominal value of the filter resonance is $\omega_{resN} = \sqrt{(L_{1N} + L_{2N}) / (L_{1N} L_{2N} C_N)} \approx 7000$ rad/s, where L_{1N} , L_{2N} and C_N are the filter nominal parameters shown in table 5.1. The system is stable for the next variations of the filter parameters: $L_1 = [5.97, 0.56]$ pu, $L_2 = [1.71, 0.62]$ pu and $C = [1.32, 0.66]$ pu.

³Simulated results were obtained through a complete system model, including switching VSCs and equivalent digital controllers, implemented in MATLAB SimPowerSystem.

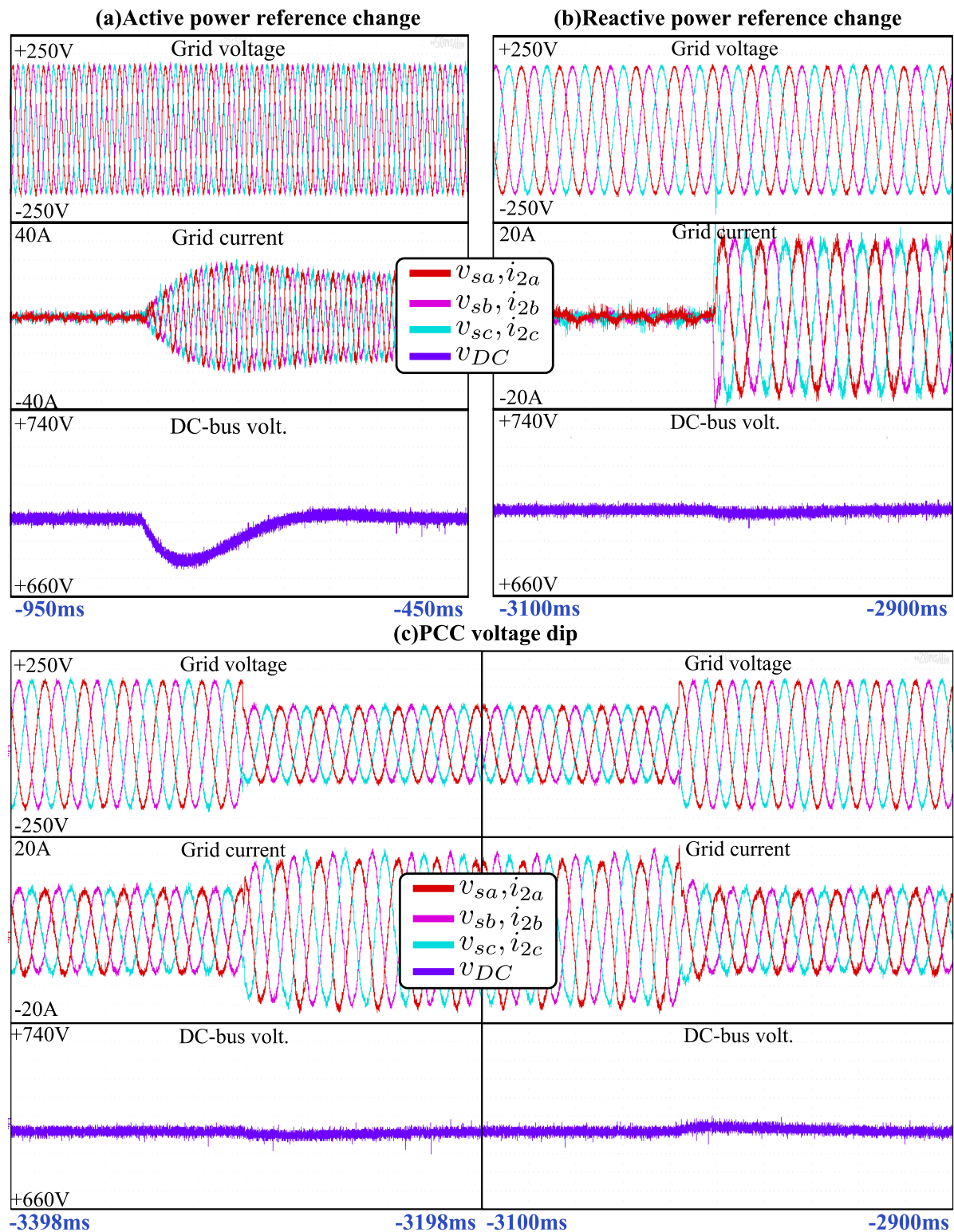


Figure 6.16. (a) Connection of a 4.2 kW DC-load with a null reactive reference. The grid current increases to supply the DC-load, maintaining the DC-bus voltage v_{DC} constant. (b) Sudden change to a reactive power reference of $q^* = 4$ kVAr with a null active power reference. The grid current quickly tracks the new reactive power demand. (c) Initial response and recovery to a balanced grid voltage dip of 60%. The active power reference is set to $p^* = 4.2$ kW. The grid current increases to compensate the power lost with the voltage dip.

shows the results of a sudden change of the reactive power reference from $q^* = 0$ to $q^* = 4$ kVAr, and Fig. 6.16(c) shows the response of the system to a balanced grid voltage dip of 60% of its nominal value (with a power reference set to $p^* = 4.2$ kW). The damped system is proven to be stable and without grid current oscillation at the resonant frequency, in opposition to the unstable system that results when \mathbf{K}_{AD} is disconnected (see GM_2 and PM_2 in table 6.1).

6.5 Conclusion

The next conclusions can be derived from this chapter:

- This chapter presents an active damping controller design for the grid current control of a grid-connected VSC with an LCL-filter topology. Designed active damping modifies the LCL resonant grid current dynamic so it mimics the one of an equivalent L filter, making possible the use of simple pre-designed PI and/or PR controllers to track the desired current with minimum stability and performance penalties.
- Proposed controller is obtained by (sub)optimal \mathcal{H}_∞ synthesis following a model-reference design. The designer specifies the desired LCL grid current dynamic, in this case one equivalent to an L filter. Afterwards, an \mathcal{H}_∞ synthesis algorithm obtain a (sub)optimal active damper that complies with the specifications.
- The presented design methodology allows to easily specify the number of inputs to the active damper. For the results shown here, both grid-current feedback and PCC voltage feedforward are considered, reducing the number of sensors needed, but the design is flexible enough to achieve similar results feeding-back any linear combination of the filter states vector.
- Limitations of the method are presented, being the most important a bandwidth limitation coming from the discrete implementation of the controller. By reducing the sample time, the effectiveness of the method is improved.
- Obtained frequency results show the damping capabilities of the presented method. Stability margins are improved when a classic PR, previously designed for the reference L-filter dynamics, is used to control the grid current. Moreover, this stability margins are close to the ones that would be obtained if the designed PR current controller was applied to the reference L-filter equivalent.
- Damping and stability robustness of the method is proved for variations of the LCL filter parameters.
- Finally, good time domain results are demonstrated by simulated and experimental tests.

Chapter 7

Conclusion and future work

7.1 Contributions and conclusions

This section presents the main contributions and conclusions that can be derived from this Ph.D. dissertation.

7.1.1 \mathcal{H}_∞ model reference approach for closed-loop admittance shaping

Contributions

An \mathcal{H}_∞ model-reference controller design approach is proposed for the admittance shaping of grid-connected current-controlled VSCs. Based on the definition of a frequency shaped admittance reference (Y_{ref}), an \mathcal{H}_∞ synthesis algorithm will compute the (sub)optimal controller that shapes the closed-loop admittance to resemble this reference model both in magnitude and in phase.

Additionally, the designer can provide to the current-controller of the desired current reference tracking capabilities and limit the controller actuation at certain frequency bands to avoid saturation problems, using to that end the same model-reference design framework. Using the proposed method is possible, then, to deal with the tracking vs admittance shaping trade-off, as well as the classic controller performance vs stability robustness and energy optimization trade-off, in a more intuitive and tractable way than with the classical approaches. As inexperienced designers may still require of some heuristic rules to face the different design trade-offs and achieve the best solution to the desired complex objectives, this dissertation proposes some design guidelines and performance analysis tools to simplify this task even more.

The proposed design method is very flexible with respect to the plant to be controlled and the number of sensed variables. In that regard, this dissertation proposes a three DOF current-controller that only feeds-back the controlled grid-current, in addition to feed-forward the sensed grid PCC voltage and pre-compensate the desired current reference. The design methodology is very similar for the two filter topologies considered, the simpler L filter and the higher order resonant LCL filter.

The discrete nature of the synthesized three DOF controller is reflected in an hybrid dynamic of the controlled current, whose response is affected by a continuous disturbance (the PCC voltage) and the discrete output of the controller. In order to improve the admittance shaping performance of the proposed method, this dissertation considers this hybrid nature of the con-

trolled current. To that end, it proposes different fully continuous and fully discrete models for both considered filter topologies (i.e. L and LCL) and compares them with the realistic hybrid scenario. From the obtained results, it is deduced that the use of a continuous approximated model that takes into account the effect of both computational delay and PWM modulation present in any digital platform implementation will positively affect the obtained experimental admittance shaping results. The synthesized continuous controller can be then discretized for its future implementation in a digital platform.

Another important advantage of the proposed admittance shaping method is that it allows the achievement of more complex designs and objectives by simply defining more complex admittance reference profiles (Y_{ref}). It is possible, then, to fulfil classic grid-connected applications objectives if they can be cast in terms of closed-loop admittance specifications. In that regard, this dissertation proposes three admittance shaping objectives:

1. Improvement of the stability robustness toward grid uncertainties and good damping capabilities for resonant filters, which can be achieved by means of broad-band resistive designs.
2. Improvement of the rejection/attenuation of the grid voltage disturbances effect in the controlled current, which can be achieved by means of low admittance designs.
3. The design of effective grid stabilizers, which may be able to damp possible grid impedance resonant behaviours and filter the grid voltage of possible oscillations at non-fundamental frequencies. This can be achieved by means of high admittance profiles.

The main difference in the design process between each considered application is, as stated before, the admittance reference (Y_{ref}) definition.

The proposed controllers performance is verified experimentally both in time and frequency domains. Good experimental admittance shaping results were obtained, as the proposed method for the closed-loop admittance frequency domain identification demonstrates. In addition, proposed controllers are able to track given current references and have enough stability margins to be considered stand-alone robust systems. The improved stability robustness toward weak grid of the proposed broad-band resistive designs, the rejection/attenuation capabilities of proposed low admittance designs and the stabilization of weak grids of the high admittance designs are also proved by means of simulated/experimental results.

Conclusions

The admittance shaping of PEC-based application by means of the proposed method has proven to have the next main advantages with respect to classical control paradigms:

1. The desired closed-loop admittance can be easily defined, both in magnitude and in phase, by means of reference frequency models
2. It is easier to deal with the different derived control objective trade-offs, such as the trade-off between the tracking capabilities and the desired admittance shaping or the classic performance vs stability margins and energy optimization trade-off.
3. It is easier to control complex plants dynamics (e.g. MIMO plants, high order filters etc.) and to achieve complex admittance profiles.

The main disadvantage that can be attributed to the presented method is that the used convex \mathcal{H}_∞ controller synthesis algorithm will compute a controller of the same order than the defined generalized (i.e. augmented) plant. Then, the synthesized controller order using this method may be considered high for certain designs with respect to classic controllers, as the controller has, at least, the order of the open-loop plant to be controlled, in the same way that full order plant states estimators do. The designer should decide whether higher orders design specifications to improve the controller performance worth the increase in the computational burden. The fast computation capability of current digital processors makes of this disadvantage a less important issue. In any case, order reduction techniques can be usually used, if necessary, with small influence in the desired controller performance.

The discrete nature of the synthesized controller imposes some design limitations, mainly in the limited admittance shaping bandwidth; the smaller the sampling time (T_s) is the broader the admittance shaping bandwidth ($\omega_{c_{MAX}}$) could be. In the same line, it can be derived that the minimum achievable closed-loop admittance at this maximum bandwidth frequency is approximately equal to the open-loop admittance (i.e. $Y_{min}(j\omega_{c_{MAX}}) \approx G_d(j\omega_{c_{MAX}})$). Due to the low pass nature of the filter open-loop admittance (G_d), either the sampling time must be decreased or the filter inductances must be increased to obtain a smaller closed-loop admittance at $\omega_{c_{MAX}}$, as both results in a smaller $G_d(j\omega_{c_{MAX}})$ value. On the other hand, higher closed-loop admittance profiles can be achieved without theoretical limitation up to the maximum bandwidth limitation ($\omega_{c_{MAX}}$), but it is important to take into account that a closed-loop admittance (Y) bigger in magnitude than its open-loop value (G_d) will result in a high controller actuation, increasing the risk of controller saturation problems. It is concluded, then, that small filter inductances values (i.e. increase G_d) is preferred for high admittance designs. Note that these are common limitations for every admittance shaping design framework, so they are not exclusive of the proposed method.

This dissertation proposes to fulfil three different admittance shaping objectives to demonstrate the effectiveness and flexibility of the proposed method. From the achieved results, the next conclusions can be derived:

1. The proposed broad-band resistive designs, implemented for both L and LCL filter topologies, present a very strong stability robustness towards inductive changes of L-type grid series impedances and a slightly weaker (but still very strong) stability robustness for capacitive changes of undamped LC-type grid series impedances. The latter can be explained, from an impedance-based stability criterion point of view, by the interaction of the undamped grid resonance with the narrow non-passive frequency zones of the obtained applications. As this is a worst case scenario (a probable grid impedance resonance would be, most likely, damped by losses resistance in the model), it is concluded that the proposed designs have a very strong robustness towards any kind of weak grids, and a less limited controller performance compared with other robust techniques.
2. The proposed low admittance designs, implemented only in an LCL filter topology, present a good rejection/attenuation of the effect of grid voltage oscillations in the controlled current. If broad-band low resistive admittance systems are pursued, the grid voltage attenuation robustness will be improved, as these designs present a low admittance profile in a wider frequency range. The attenuation level of these grid voltage oscillations effect is, however, poorer in favour of this resistive behaviour. If a low admittance profile localized only at the main grid voltage harmonics (i.e. 5th, 7th etc.) is intended, a higher order controller will be required. This design presents, on the other hand, a higher attenuation of the tuned voltage harmonics influence in the current control.

3. The proposed high admittance designs, implemented only for an L filter topology, act as very effective grid stabilizers, making the grid look stronger for other systems connected to the same PCC. If a high resistive admittance profile in a broad-band is intended, the robustness from a grid impedance resonance damping / PCC voltage filtering capability point of view will be improved, as the frequency range where a high admittance is obtained will be wider. It will have, in addition, the good stability robustness towards weak grids of resistive broad-band designs. This design is, on the other hand, more sensitive to grid voltage dips. If a high admittance profile is, otherwise, only desired at some localized frequencies, the design will require of a higher order controller to obtain a good performance, but it may have an improved response against grid voltage dips and an improved overall current reference tracking capability, as these designs are able to damp a given grid resonance (or filter the PCC voltage) at a given frequency (with a high admittance value) and still reject the grid voltage disturbances effect in the controlled current at other frequencies (with a low admittance value).

7.1.2 \mathcal{H}_∞ model reference approach for resonant plants active damping

Contributions

The \mathcal{H}_∞ model reference design approach is also applied for the optimal active damping of the resonant LCL filter. The objective is to design an active-damper that shapes the LCL filter dynamic so it resembles an equivalent L filter dynamic.

The proposed method approaches, then, the active damping of resonant filters for an alternative point of view; instead of using the classic virtual impedance concept, which is actually misleading once a digital control scenario is taken into account, it tries to shape the LCL filter dynamics in response to the two disturbances of the grid current, the PCC voltage and the VSC average output voltage (actuation of an outer grid current controller), so it resembles the ones of a non-resonant filter. By doing so, it is possible to apply fast classic PI and/or PR outer current controllers, which design for L filter is amply studied due to their simplicity, without renouncing to the higher filtering capabilities of the LCL filter.

The proposed method is flexible enough to feedback different linear combination of the filter state vector. For the majority of the presented results, a single grid-current (i_2) loop is used, reducing, then, the number of sensed variables. That is, additional feedback loops are not necessary in opposition to most of the previously proposed active damping works. In any case, the method is flexible enough to use other measured variables depending on the considered application.

In opposition to most of the classical active damping approaches, this method takes into account some digital control particularities such as the presence of a PWM and a computational delay at the control output. In that regard, it improves the classic virtual impedance concept, that, as advanced, is not formally correct when a digital active damping implementation is considered. A more realistic active damping design scenario (i.e. more approximated to its physical implementation) was achieved, then, by considering these important plant dynamics.

The design methodology for the proposed method, very similar to the aforementioned admittance shaping method, is enumerated, and the main limitations of the method are derived. In that regard, an alternative verification of the active damping regions proposed in [Parker et al., 2014] was derived, proposing an effective active damping bandwidth limitation induced by the discrete nature of the implemented controller.

Conclusions

The achieved frequency domain experimental results proved the efficiency and robustness of the method. The stability margins are highly improved using the proposed active-damper, as it can be also checked from the improved time-domain current tracking response. The use of widely known simpler PR and/or PI controllers is, then, compatible with the proposal due to the resemblance of the actively damped LCL filter to an equivalent L filter.

The discrete nature of the presented active damping technique imposes, again, a maximum bandwidth (ω_{cMAX}) limitation. As long as the LCL filter resonance is placed within this bandwidth, the method will optimally damp it. If its above, the sampling time should be reduced if the optimal results are intended. This limitation is, in any case, common to every active damping method.

Another important advantage of the proposed method is its flexibility towards the measured filter states (or linear combination of states) fed-back to the active damper. In that regard, the obtained results demonstrate equivalent damping results feeding-back the grid-current (i_2), the capacitor voltage (v_c) or the complete states vector ($\mathbf{x} = [i_2 \ i_1 \ v_c]^T$), with poorer results if only the converter-current (i_1) is fed-back. Then, even though feeding-back only the grid current (i_2) seems like the best option, as it implies a reduction of the number of sensors used, the proposed method can be adapted to other necessities.

The main disadvantage attributable to the method is the probable high order of the obtained active damper. Even though only one reference model (G_{ref}) is enough to define the grid current dynamics from both external inputs (PCC voltage and outer current controller output), the order of the proposed active damping can be considered high in comparison with the classical active damping approaches. As it was stated previously, this limitation is less important nowadays due to the fast computation of current digital processor, being possible the use of order reduction techniques, if necessary, to lighten the computational burden of the proposed active damper. This order reduction is more effective if multiple variables are fed-back to the active damper.

Finally, the wide bandwidth of the proposal results in an improved robustness of the method towards changes of the filter resonant frequency, as it is demonstrated in the damping result shown for parametric variations of the modelled LCL filter.

7.2 Future works

The author considers that the next related topics could be of interest for future theoretical or practical research work.

Due to the \mathcal{H}_∞ model-reference approach design methodology flexibility, there are multiple variations of the proposed admittance shaping and resonant plant damping methods that can be studied:

- Application of the methods to higher order filter topologies (e.g. LLCL topology) or other PECs topologies (e.g. CSC, MMC, DC-DC etc.).
- The admittance shaping technique was applied to the AC-side of a two level VSC. However, the source of instabilities can be in the DC-side. It would be interesting the study of this admittance shaping technique from the DC-side.
- Application of the admittance shaping method to follow complex MIMO admittance references (i.e. with coupled admittances between axis). Good initial experimental results

were obtained in the considered $\alpha\beta$ axis, but its field of application for this reference frame is still under study. It is clear, in any case, its application importance in the dq reference frame, where the d and q axis are coupled by default (i.e. without using any uncoupling technique).

- A three DOF controller was considered as the best suited structure for the simultaneous admittance shaping and current reference tracking control. However, if the tracking performance is set aside, relying this task to an already designed one DOF controller, a PCC voltage feed-forward external loop can be synthesized, using the \mathcal{H}_∞ model-reference approach, for the admittance shaping of the system. This structure has the main advantage of not dealing with the performance vs stand-alone stability robustness trade-off, as feed-forward techniques does not affect it. On the other hand, the obtained admittance shaping is expected to be less robust to parametric uncertainties as feed-forward techniques are more sensitive to them.
- The presented admittance-shaping method can be easily applied to the impedance-shaping of voltage-controlled PEC-based applications, such as the Dynamic Voltage Restorer (DVR) and the Uninterruptible Power Supply (UPS). Good preliminary simulated results were obtained in the application of the method to a DVR.
- Three different admittance profiles were considered in this work. However, a further study of admittance shaping applications can result in other interesting admittance profiles. The flexibility of the proposed design framework make it specially suited for this study.

Other related improvements of the topics addressed in this dissertation would be:

- In grid-connected PEC-based applications, the main source of uncertainty is the grid impedance. As this uncertainty can be considered passive, the passivity of the controlled application is of main importance for its stability robustness. The proposed \mathcal{H}_∞ admittance shaping method can obtain passivity in a wide range, resulting in the presented broadband resistive designs, which are very robust towards grid uncertainties. However, passivity, and then dissipativity, can be addressed in a more formal and effective way applying the Kalman-Yakubovich-Popov lemma in the Linear Matrix Inequalities (LMI) controller design framework. This framework is compatible with (sub)optimal minimization problems, such as the \mathcal{H}_∞ synthesis considered here, and allows to impose, in addition, certain conditions to the obtained closed-loop systems, such as the aforementioned dissipativity condition.
- Moreover, even though the proposed admittance shaping techniques has been proven effective to increase the stability robustness of PEC-based applications towards weak grids, more explicit \mathcal{H}_∞ robust techniques, applying the small gain theorem, can be used to obtain a controller that shapes a current-controlled system admittance so its stability when connected to the grid can be assured for a set of grid impedance uncertainties. The key fact of this study is that, following the impedance criterion, the considered current-controlled system admittance and the grid impedance form a complex stability loop function ($L = YZ_g$) that could be shaped using these techniques to assure stability.
- The controllers proposed in this dissertation were computed following a convex \mathcal{H}_∞ synthesis algorithm provided by MATLAB[®] *Robust toolbox*. One of the main disadvantages of this optimal framework is that the order of the synthesized controller is that of the given augmented plant \mathbf{P} . The study of more complex and non-convex synthesis tools to compute the proposed controllers, such as the *Fixed-order* \mathcal{H}_∞ technique, where the maximum order of the obtained controller can be fixed is another interesting field of research.

- In the admittance shaping paradigm, the hybrid continuous/discrete dynamic of the closed-loop controlled current plays an important role in the performance of the proposed controllers, even more as the frequency approximates to the Nyquist limit. Even though an approximated fully continuous model of the open-loop grid current was proposed in section 4.7, the author is aware of other more complex techniques, such as the Lineal Time Periodic Variant (LTPV) transform [Rosenwasser and Lampe, 2012] or the Frequency Lifting transform [Chen and Francis, 2012], that can address the modelling of this hybrid dynamic in a more efficient and formal way. This is, then, another field of interest for future research.
- Finally, the high broad-band resistive admittance design has an important industrial application interest as a grid stabilizer. It would be interesting the study and design of an specially-dedicated (i.e. stand-alone) product for this task, analysing topics like the ideal filter size and topology, the converter topology, the energy consumption, the protection against operation point changes, the costs and the viability in general.

Appendix A

Background knowledge

A.1 Introduction

This annex quickly introduces some of the background knowledge that the author considers necessary for the full understanding of this dissertation. It focuses on lineal control, its generalized control structures (section A.2), the frequency domain response (section A.3) and the derived stand-alone stability analysis (section A.4), the different controller objectives trade-offs (section A.5), the feedback bandwidth limitations of systems with time delays or RHP-zeros (section A.6) and some of the most representative classical controller design approaches (section A.7). These lineal control concepts are applied in section A.8 to power electronic converter (PEC) based applications, presenting the diagrams and main functions of some of them.

A.2 Generalized lineal control schemes

One degree-of-freedom control structure

Fig. A.1 shows a generalized one degree-of-freedom (DOF) control structure¹.

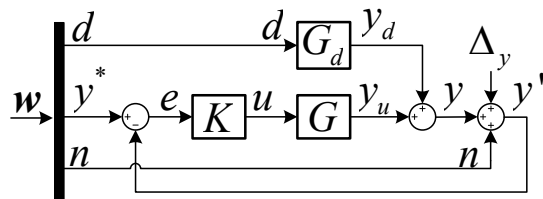


Figure A.1. One DOF generalized controller structure.

On it, the plant, which output ($y(t)$) is going to be controlled, is modelled by two transfer functions: the command-to-output transfer function $G(s)$, with a controlled input $u(t)$ (output of the controller $K(s)$), and the disturbance-to-output transfer function $G_d(s)$, whose input $d(t)$ is not controlled in the process (i.e. acts as an external disturbance). The classic objective of this structure is to control the plant output ($y(t)$) so it tracks a given reference ($y^*(t)$) at the desired frequencies (ω), minimizing the tracking error ($e(t)$) even under changes of the disturbance ($d(t)$)

¹For simplicity in the derived closed-loop dynamics, all the transfer functions in this section are considered single-input single-output (SISO) functions

and measurement noise ($n(t)$) signals. To achieve this, the measured output ($y'(t)$) is fed-back to the controller ($K(t)$), which will *integrate* the tracking error ($e(t)$) until it becomes zero ².

The closed-loop is disturbed, then, by three external inputs; the noise (n), the output disturbance (d) and the output reference (y^*) signals. These signals form the exogenous input vector \mathbf{w} . Different closed-loop transfer functions can be derived from this first structure:

$$T(s) = F_{y^* \rightarrow y}(s) = \frac{G(s)K(s)}{1 + G(s)K(s)} \quad (\text{A.1})$$

$$D(s) = F_{d \rightarrow y}(s) = \frac{G_d(s)}{1 + G(s)K(s)} \quad (\text{A.2})$$

$$N(s) = F_{n \rightarrow y}(s) = -\frac{G(s)K(s)}{1 + G(s)K(s)} \quad (\text{A.3})$$

where $T(s)$, $D(s)$ and $N(s)$ are known as the tracking, disturbance and noise transfer functions, respectively. To partially achieve the aforementioned classic controller objective (i.e. track the given reference y^* rejecting other external disturbances), a controller with high gain values (i.e. high $|K(j\omega)|$ ³), ideally infinite, should be defined, as it will achieve a $|T(j\omega)| \approx 1$ and $|D(j\omega)| \approx 0$ at the desired frequencies (ω). Note, on the other hand, that this will result in a poor noise rejection (i.e. $|N(j\omega)| \approx 1$).

The controller is, in addition, attached to other external design limitations and trade-offs that make not possible to achieve this classic objective at all frequencies. One of them is the limitation in the controller actuation (u), which is usually bounded by physical constraints and saturation limits. Its value is determined by two transfer functions;

$$F_{y^* \rightarrow u}(s) = -F_{n \rightarrow u}(s) = \frac{K(s)}{1 + G(s)K(s)}; \quad F_{d \rightarrow u}(s) = -\frac{G_d(s)K(s)}{1 + G(s)K(s)} \quad (\text{A.4})$$

High values of these transfer functions at a given frequency will result in high values of the actuation signal (u) and possible controller saturation. Another important limitation in the control is the achievable bandwidth, which can be defined as the frequency where the loop function gain is above one ($|L(s)| > 1$) or, analogously, where the sensitivity function gain is below one ($|S(s)| < 1$). These new transfer functions are defined as follows;

$$L(s) = G(s)K(s); \quad S(s) = F_{\Delta y \rightarrow y'}(s) = F_{i^* \rightarrow e}(s) = -F_{y_d \rightarrow e}(s) = -F_{n \rightarrow e}(s) = \frac{1}{1 + L(s)}, \quad (\text{A.5})$$

where Δy represents any output disturbance (e.g. n , y_d etc.). As it will be seen in section A.4, these functions are the basis for the stand-alone stability analysis of the closed loop system. In addition, both functions are good indicators of the feedback action of the controller; higher values of $|L(s)|$ and, then, lower values of $|S(s)|$ results on higher reduction of the tracking error (e) for changes of all the exogenous inputs \mathbf{w} . That is, using this one DOF structure, achieving a $|S(j\omega)| \rightarrow 0$ implies that $|T(j\omega)| \rightarrow 1$ and $|D(j\omega)| \rightarrow 0$ at frequencies ω , which is the aforementioned classic control objective. Moreover, the wider the controller bandwidth is the faster the controlled output (y) will track its given reference (y^*).

Note that $|S(j\omega)| \rightarrow 0$ also implies that a bad noise rejection function $|N(j\omega)| \rightarrow 1$ (see (A.3)) will be obtained, even though a good reduction of the noise (n) effect on the tracking

²For the sake of compactness, the time domain (t) and Laplace (s) operators will be omitted whenever its presence results obvious attending to the context.

³ $K(j\omega)$ is obtained from $K(s)$ with a simple variable substitution $s \rightarrow j\omega$. The continuous time Laplace operator s is substituted by the complex operator $j\omega$ whenever a frequency domain implication can be drawn from the context.

error (e) is apparently achieved (i.e. $|F_{n \rightarrow e}(s)| \rightarrow 0$ in (A.5)). In fact, what the controller does when a noise signal (n) is added to the output (y) inside its bandwidth is to try to compensate this noise in the fed-back (measured) output ($y' = y + n$) by obtaining a real (undisturbed) output ($y = y^* - n$). This is, obviously, an undesired behaviour of the controlled output (y). Fortunately, the effect of the measurement noise (n) in the output (y) is often not considered due to the operating characteristics of most of the commercial sensors, which only introduce noise at frequencies (ω) far beyond of the controller bandwidth, where $|K(j\omega)| \rightarrow 0$ and, then, $|N(j\omega)| \rightarrow 0$. For that reason and for the sake of the section brevity, the noise signal is no longer considered in next analysis.

Two degrees-of-freedom control structure

Fig. A.2 shows a two DOF generalized control structure, where a disturbance signal (d) feed-forward path (K_d) is introduced.

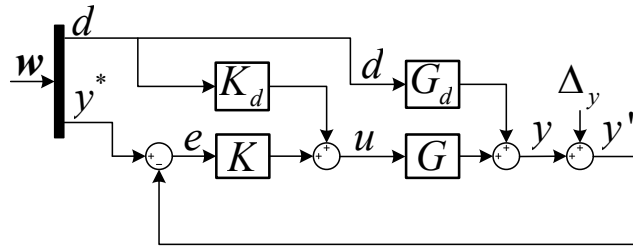


Figure A.2. Two DOF generalized controller structure.

This feed-forward path is usually implemented to quickly reject the effect of the disturbance (d) on the output (y) by defining a $K_d = -G_d/G$, as long as the plant dynamics are perfectly modelled and the resulting K_d is implementable⁴.

However, as it is shown throughout this dissertation, a null disturbance function (i.e. $|D(s)| = 0$) is not always desirable from a control point of view. In that regard, this structure provides of a new degree of freedom to the controller to modify the disturbance function (D) independently of the tracking function (T), up to certain limits. Using this structure, then, the only closed-loop transfer functions that are modified are;

$$D(s) = \frac{G_d(s) + G(s)K_d(s)}{1 + G(s)K(s)} \quad F_{d \rightarrow u}(s) = \frac{K_d(s) - G_d(s)K(s)}{1 + G(s)K(s)} \quad (\text{A.6})$$

Three degrees-of-freedom control structure

To further separate the tracking (T) and disturbance (D) transfer functions control (i.e. shaping), a three DOF generalized controller structure is proposed in Fig. A.3.

It basically splits the controller K of the one and two DOF aforementioned structures into two new transfer functions; a feedback path (K_y) for the controller output and a feed-forward path (K_{y^*}) for its reference. The tracking (T) and disturbance (D) transfer function are modified

⁴This serves also as an effective controller soft start technique, setting an initial actuation u that produces a safe output $y = y^* = 0$.

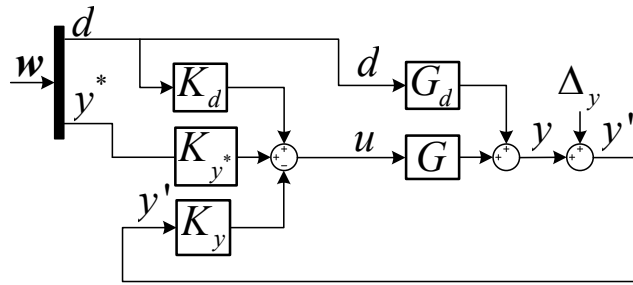


Figure A.3. Three DOF generalized controller structure.

as follows;

$$T(s) = \frac{G(s)K_{y^*}(s)}{1 + G(s)K_y(s)} \quad D(s) = \frac{G_d(s) + G(s)K_d(s)}{1 + G(s)K_y(s)} \quad (\text{A.7})$$

To achieve the aforementioned classic control objective (i.e. $|T(s)| \approx 1$ and $|D(s)| \approx 0$) high values of the feed-back gain ($|K_y|$) and the reference feed-forward gain ($|K_{y^*}|$) are needed. The actuation functions change to;

$$F_{y^* \rightarrow u}(s) = \frac{K_{y^*}(s)}{1 + G(s)K_y(s)} \quad F_{d \rightarrow u}(s) = \frac{K_d(s) - G_d(s)K_y(s)}{1 + G(s)K_y(s)}, \quad (\text{A.8})$$

whereas the loop and sensitivity functions change to;

$$L(s) = G(s)K_y(s) \quad S(s) = F_{\Delta_y \rightarrow y'}(s) = \frac{1}{1 + L(s)} \quad (\text{A.9})$$

The sensitivity function no longer serves as a tracking performance indicator (i.e. how much the tracking error (e) is reduced), as this does not only depend on the output feedback gain ($|K_y|$) but also on the reference feed-forward gain ($|K_{y^*}|$). L and S are both, still, the basis of the system stand-alone stability analysis and good indicators of the efficiency of the feedback action (i.e. its bandwidth).

States regulation

Finally, some control structures use plant states (x) regulators. This is represented in Fig. A.4 as a new feedback path (K_x).

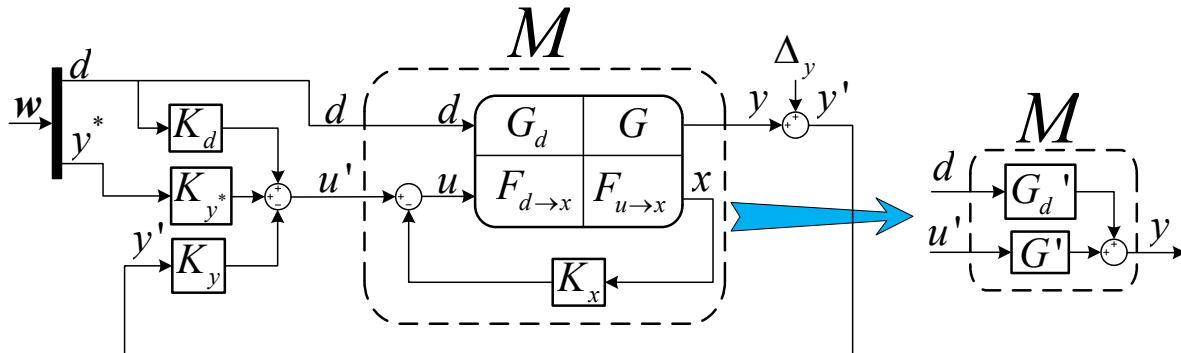


Figure A.4. Three DOF generalized controller structure plus a state regulator.

The system states dynamics are defined by two new transfer function: the disturbance-to-state ($F_{d \rightarrow x}$) and the command-to-state ($F_{u \rightarrow x}$) transfer functions. This new feed-back loop serves as a *plant regulator*, whose dynamics change as follows;

$$G'_d(s) = F_{d \rightarrow y}(s) = G_d(s) - \frac{G(s)F_{d \rightarrow x}(s)K_x(s)}{1 + F_{u \rightarrow x}(s)K_x(s)} \quad (\text{A.10})$$

$$G'(s) = F_{u' \rightarrow y}(s) = G(s) - \frac{G(s)F_{u \rightarrow x}(s)K_x(s)}{1 + F_{u \rightarrow x}(s)K_x(s)} \quad (\text{A.11})$$

The addition of this new feedback loop allows, then, to modified the plant, altering, in some way, its output (y) dynamic. In a second step, a three DOF controller can be designed for this new regulated plant, modifying the tracking (T) and disturbance (D) transfer functions dynamics as follows;

$$T(s) = \frac{G'(s)K_{y^*}(s)}{1 + G'(s)K_y(s)} \quad D(s) = \frac{G'_d(s) + G'(s)K_d(s)}{1 + G'(s)K_y(s)} \quad (\text{A.12})$$

Meanwhile, the new loop (L) and sensitivity (S) functions are defined as;

$$L(s) = G'(s)K_y(s) \quad S(s) = F_{\Delta y \rightarrow y'}(s) = \frac{1}{1 + L(s)} \quad (\text{A.13})$$

Again, the stand-alone stability analysis of the system output (y) can be derived from these transfer functions. Finally, with this new feed-back loop the controller output (u) dynamics change to:

$$F_{y^* \rightarrow u}(s) = \frac{K_{y^*}(s)}{1 + G(s)K_y(s) + F_{u \rightarrow x}(s)K_x(s)} \quad (\text{A.14})$$

$$F_{d \rightarrow u}(s) = \frac{K_d(s) - G_d(s)K_y(s)}{1 + G(s)K_y(s) + F_{u \rightarrow x}(s)K_x(s)} \quad (\text{A.15})$$

A.3 Frequency response analysis [Skogestad and Postlethwaite, 2007]

Consider a single-input single-output (SISO) lineal system modelled by the transfer function $G(s)$, so that;

$$Y(s) = G(s)D(s), \quad (\text{A.16})$$

where $Y(s)$ and the $D(s)$ are the output and the input to the considered system, which (without losing generality) follows the next sinusoidal patterns in the time domain for a given frequency ω :

$$d(t) = D_0 \sin(\omega t + \alpha) \quad (\text{A.17})$$

$$y(t) = Y_0 \sin(\omega t + \beta) \quad (\text{A.18})$$

The frequency domain response of the system $G(j\omega)$ is compactly described for all given frequencies (ω) as:

$$y(\omega) = G(j\omega)d(\omega) \quad (\text{A.19})$$

, where $d(\omega) = D_0 e^{j\alpha}$ and $y(\omega) = Y_0 e^{j\beta}$ are the phasor representations of the sinusoidal input and output signals, respectively. It is well-known in control theory that:

$$|G(j\omega)| = \frac{Y_0}{D_0} = \frac{|y(\omega)|}{|d(\omega)|} = \frac{|G(j\omega)d(\omega)|}{|d(\omega)|} \quad \angle G(j\omega) = \beta - \alpha = \angle y(\omega) - \angle d(\omega) \quad (\text{A.20})$$

where $|G(j\omega)|$ and $\angle G(j\omega)$ are the gain (amplification) and phase shift of the considered linear system $G(j\omega)$, respectively, which depend on the input (and output) signal frequency (ω), but not on its amplitude (D_0) and phase (α) at that frequency.

If a multiple-input multiple-output (MIMO) system is considered instead, the frequency response is described as follows:

$$\underbrace{\begin{bmatrix} y_1(\omega) \\ \vdots \\ y_i(\omega) \end{bmatrix}}_{\mathbf{y}(\omega)} = \underbrace{\begin{bmatrix} G_{11}(j\omega) & \dots & G_{1j}(j\omega) \\ \vdots & \ddots & \vdots \\ G_{i1}(j\omega) & \dots & G_{ij}(j\omega) \end{bmatrix}}_{\mathbf{G}(j\omega)} \underbrace{\begin{bmatrix} d_1(\omega) \\ \vdots \\ d_j(\omega) \end{bmatrix}}_{\mathbf{d}(\omega)} \quad (\text{A.21})$$

where $G_{ij}(j\omega)$ represents the frequency response from the input $d_j(\omega)$ to the output $y_i(\omega)$. The response of the output $y_i(\omega)$ to a set of inputs $\mathbf{d}(\omega)$ is, applying the superposition principle for linear systems, equal to the sum of the individual responses for each input:

$$y_i(\omega) = \sum_j G_{ij}(j\omega) d_j(\omega) \quad (\text{A.22})$$

The phase shift concept is, then, lost from a MIMO point of view. It can be defined, however, how much the inputs affect the outputs in magnitude at each frequency ω , by considering the quotient between the vector 2-norm (i.e. vector classic measure of length) of $\mathbf{y}(\omega)$ and $\mathbf{d}(\omega)$:

$$\frac{\|\mathbf{y}(\omega)\|_2}{\|\mathbf{d}(\omega)\|_2} = \frac{\|\mathbf{G}(j\omega)\mathbf{d}(\omega)\|_2}{\|\mathbf{d}(\omega)\|_2} = \frac{\sqrt{Y_{01}^2 + \dots + Y_{0i}^2}}{\sqrt{D_{01}^2 + \dots + D_{0j}^2}} \quad (\text{A.23})$$

This is considered the gain of the MIMO system, which again depends on the frequency ω but also on the *direction* of the input vector $\mathbf{d}(\omega)$ (i.e. $d_1(\omega) \dots d_j(\omega)$ values). That is, unlike the SISO case, the gain of a MIMO system is not unique for a given frequency ω . The singular value decomposition (SVD) of the matrix transfer function $\mathbf{G}(j\omega)$ gives, on the other hand, an important physical interpretation of the system frequency response:

$$\mathbf{G}(j\omega) = \mathbf{U}(\omega)\mathbf{\Sigma}(\omega)\mathbf{V}(\omega)^H \quad (\text{A.24})$$

where:

- $\mathbf{\Sigma}(\omega)$ is a $i \times j$ matrix with $k = \min\{i, j\}$ non-negative singular values⁵ ($\sigma_k(\mathbf{G}(j\omega))$) of $\mathbf{G}(j\omega)$ arranged in descending order along its main diagonal; the other entries are zero. For example, for a 2×3 matrix $\mathbf{G}(j\omega)$:

$$\mathbf{\Sigma}(\omega) = \begin{bmatrix} \sigma_1(\mathbf{G}(j\omega)) & 0 & 0 \\ 0 & \sigma_2(\mathbf{G}(j\omega)) & 0 \end{bmatrix} \quad (\text{A.25})$$

, where the non-zero elements of $\mathbf{\Sigma}(\omega)$ are scalars dependent on the frequency ω , which fulfil $\sigma_1(\mathbf{G}(j\omega)) \geq \sigma_2(\mathbf{G}(j\omega))$ for all frequencies ω .

- $\mathbf{U}(\omega)$ is an $i \times i$ unitary matrix (i.e. $\mathbf{U}(\omega)^H \mathbf{U}(\omega) = \mathbf{I}$) of output singular vectors ($\mathbf{u}_i(\omega)$) arranged in columns. For a 2×3 matrix $\mathbf{G}(j\omega)$:

$$\mathbf{U}(\omega) = \left[\underbrace{\begin{bmatrix} u_{11}(\omega) \\ u_{21}(\omega) \end{bmatrix}}_{\mathbf{u}_1(\omega)} \mid \underbrace{\begin{bmatrix} u_{12}(\omega) \\ u_{22}(\omega) \end{bmatrix}}_{\mathbf{u}_2(\omega)} \right] \quad (\text{A.26})$$

These columns vectors ($\mathbf{u}_i(\omega)$) represent the *output directions* of the plant $\mathbf{G}(j\omega)$, and are orthogonal and of unit length.

- $\mathbf{V}(\omega)$ is a $j \times j$ unitary matrix (i.e. $\mathbf{V}(\omega)^H \mathbf{V}(\omega) = \mathbf{I}$) of input singular vectors ($\mathbf{v}_j(\omega)$) arranged in columns. For a 2×3 matrix $\mathbf{G}(j\omega)$:

$$\mathbf{V}(\omega) = \left[\begin{array}{c|c|c} v_{11}(\omega) & v_{12}(\omega) & v_{13}(\omega) \\ v_{21}(\omega) & v_{22}(\omega) & v_{23}(\omega) \\ v_{31}(\omega) & v_{32}(\omega) & v_{33}(\omega) \end{array} \right] \quad (\text{A.27})$$

$$\underbrace{\qquad\qquad\qquad}_{\mathbf{v}_1(\omega)} \quad \underbrace{\qquad\qquad\qquad}_{\mathbf{v}_2(\omega)} \quad \underbrace{\qquad\qquad\qquad}_{\mathbf{v}_3(\omega)}$$

These columns vectors ($\mathbf{v}_j(\omega)$) represent the *input directions* of the plant $\mathbf{G}(j\omega)$, and are orthogonal and of unit length.

These inputs ($\mathbf{u}_i(\omega)$) and outputs ($\mathbf{v}_j(\omega)$) directions are related through their corresponding singular value⁵ ($\sigma_k(\mathbf{G}(j\omega))$) in $\mathbf{\Sigma}(\omega)$, as it is demonstrated next. As \mathbf{V} is a unitary matrix, from (A.24) it is deduced that:

$$\mathbf{G}(j\omega)\mathbf{V}(\omega) = \mathbf{U}(\omega)\mathbf{\Sigma}(\omega) \quad (\text{A.28})$$

which for an element $\sigma_x(\mathbf{G}(j\omega))$:

$$\mathbf{G}(j\omega)\mathbf{v}_x(\omega) = \sigma_x(\mathbf{G}(j\omega))\mathbf{u}_x(\omega) \quad (\text{A.29})$$

Furthermore, since $\|\mathbf{v}_j(\omega)\|_2 = \|\mathbf{u}_i(\omega)\|_2 = 1$ and $\sigma_k(\mathbf{G}(j\omega))$ is a scalar (function of the frequency ω);

$$\sigma_x(\mathbf{G}(j\omega)) = \|\mathbf{G}(j\omega)\mathbf{v}_x(\omega)\|_2 = \frac{\|\mathbf{G}(j\omega)\mathbf{v}_x(\omega)\|_2}{\|\mathbf{v}_x(\omega)\|_2} \quad (\text{A.30})$$

That means that if the input vector $\mathbf{d}(\omega)$ to the system $\mathbf{G}(j\omega)$ has the direction $\mathbf{v}_x(\omega)$, its output $\mathbf{y}(\omega)$ will have the direction of $\mathbf{u}_x(\omega)$, with an amplification gain $\|\mathbf{y}(\omega)\|_2/\|\mathbf{d}(\omega)\|_2 = \sigma_x(\mathbf{G}(j\omega))$.

More importantly, the first non-zero element of $\mathbf{\Sigma}(\omega)$, known as the maximum singular value and noted as $\bar{\sigma}(\mathbf{G}(j\omega))$, represents the maximum gain of $\mathbf{G}(j\omega)$ as the direction of the input vector varies. Analogously, the last non-zero element is the minimum singular value, noted as $\underline{\sigma}(\mathbf{G}(j\omega))$, and represents the minimum gain value of $\mathbf{G}(j\omega)$ for input vector ($\mathbf{d}(j\omega)$) variations. The maximum and minimum singular values of $\mathbf{G}(j\omega)$ establish, then, the next gain boundaries:

$$\underline{\sigma}(\mathbf{G}(j\omega)) \leq \frac{\|\mathbf{y}(\omega)\|_2}{\|\mathbf{d}(\omega)\|_2} = \frac{\|\mathbf{G}(j\omega)\mathbf{d}(\omega)\|_2}{\|\mathbf{d}(\omega)\|_2} \leq \bar{\sigma}(\mathbf{G}(j\omega)), \quad (\text{A.31})$$

So $\bar{\sigma}(\mathbf{G}(j\omega))$ represents a maximum gain (i.e. input amplification) value of $\mathbf{G}(j\omega)$, corresponding to an input vector $\mathbf{d}(\omega) = k\mathbf{v}_1(\omega)$ (with $k \in \mathbb{R}$), and $\underline{\sigma}(\mathbf{G}(j\omega))$ represents a minimum gain value of $\mathbf{G}(j\omega)$, corresponding to an input vector $\mathbf{d}(\omega) = k\mathbf{v}_j(\omega)$ (where j is the number of inputs of $\mathbf{G}(j\omega)$).

A.4 Stand-alone stability analysis

Methods

There are two methods that are commonly used in the literature for LTI closed-loop stand-alone stability analysis of SISO systems [Skogestad and Postlethwaite, 2007].

⁵The singular values of a matrix \mathbf{G} are defined as $\sigma_k(\mathbf{G}) = \sqrt{\lambda_k(\mathbf{G}\mathbf{G}^H)}$, where $\lambda_k(\mathbf{G}\mathbf{G}^H)$ are the eigenvalues of $\mathbf{G}\mathbf{G}^H$, and \mathbf{G}^H is the complex conjugate transpose of \mathbf{G} .

The first implies the analysis of the closed-loop poles, given by the roots of the characteristic equation:

$$1 + L(s) = 0 \quad (\text{A.32})$$

The system will be stable if and only if all the closed-loop poles are in the open left-half plane (LHP) (i.e. their real parts are negative).

The second method, known as Nyquist's stability criterion, counts the number of encirclements of the complex polar plot $L(j\omega)$ to the point -1 of the real axis. If it is equal to the number of right-half plane (RHP) (i.e. unstable) poles of $L(s)$ the system will be stable. For stable loops, the method is simplified to:

$$\text{The system is stable} \iff |L(j\omega_{180})| < 1 \quad (\text{A.33})$$

where ω_{180} is the phase crossover frequency where $\angle L(j\omega_{180}) = -180^\circ$. This is known as Bode's stability condition.

The first method is better for numerical calculations. It lacks, however, of the good graphical interpretation of the second method, which additionally provides useful insight of the stability robustness of the system relative to gain a phase changes of the loop function $L(s)$.

Stability margins definition

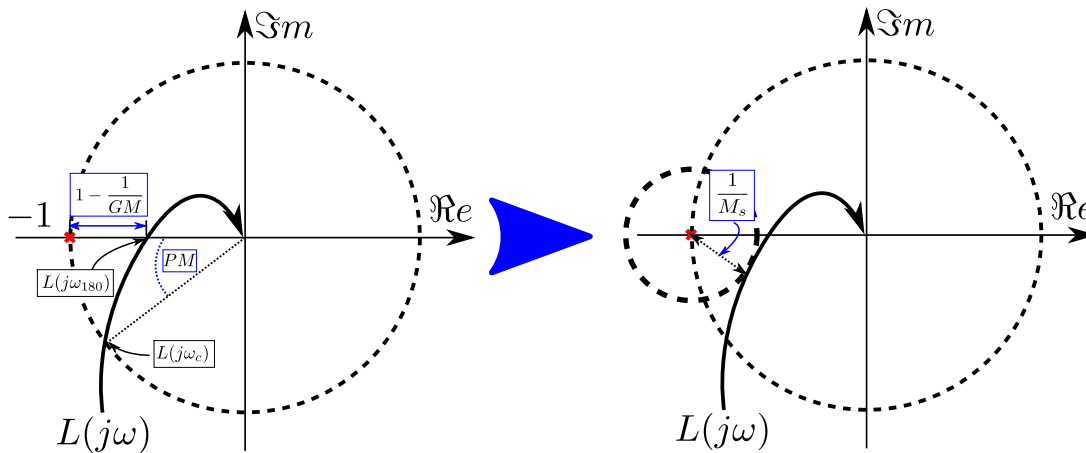


Figure A.5. Nyquist polar plot of a loop function $L(s)$. The left part of the figure shows the phase ω_{180} and gain ω_c crossover frequencies, and derives the gain GM and phase PM stability margins. The right part of the figure shows the graphical interpretation of the gain peak value M_s of the sensitivity function S .

Fig. A.5 shows the Nyquist polar plot of a given loop function $L(s)$. From it, two stability margins can be defined.

The gain margin GM is the factor by which the loop gain $|L(j\omega)|$ may be increased before the closed-loop system becomes unstable:

$$GM = \frac{1}{|L(j\omega_{180})|} \quad (\text{A.34})$$

Big GM values indicate good stability robustness against steady-state gain uncertainty. Usually, a good gain margin is considered if $GM > 2$ in natural units (i.e. $GM > 6$ dB) [Skogestad and Postlethwaite, 2007].

The phase margin is defined as the phase lag it can be added to $L(s)$ at the gain crossover frequency ω_c (i.e. the frequency where $|L(j\omega_c)| = 1$ in Fig. A.5) before the phase at this

frequency becomes -180° (i.e. $\angle L(j\omega_c) = -180^\circ$), which will result in an unstable closed-loop system:

$$PM = \angle L(j\omega_c) + 180^\circ \quad (\text{A.35})$$

Big PM values indicate good stability robustness against time delay uncertainty. Normally, a phase margin $PM > 30^\circ$ is required for robust systems [Skogestad and Postlethwaite, 2007].

Sensitivity function: analysis of controller performance versus stand-alone stability robustness trade-off

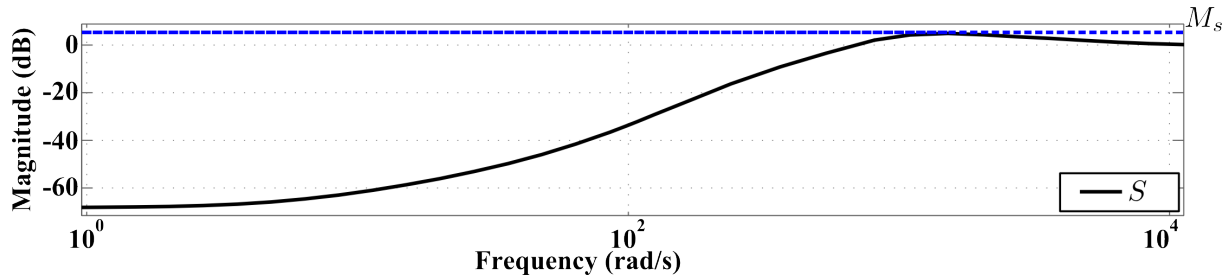


Figure A.6. Typical sensitivity function gain plot.

The sensitivity function $S(s)$ defined in section A.2, apart of giving a good insight of the controller performance, is a good indicator of the system robustness. Fig. A.6 shows the frequency domain representation of a typical SISO system sensitivity gain $|S(s)|$, with a good controller performance at low frequencies (i.e. $|S(s)| \rightarrow 0$, so $|T(s)| \rightarrow 1$ and $|D(s)| \rightarrow 0$). In it, the inverse of the maximum gain value M_s is equal to the minimum distance between the loop function polar plot $L(j\omega)$ and the point -1 , as it is showed in the right part of Fig. A.5. From this equivalence, a minimum gain and phase margins can be derived from an obtained M_s :

$$GM \geq \frac{M_s}{M_s - 1} \quad PM \geq 2 \sin^{-1} \left(\frac{1}{2M_s} \right) \quad (\text{A.36})$$

with GM and M_s expressed in natural units. The conditions to consider a system robust given above, $GM > 2$ (natural units) and $PM > 30^\circ$, are assured, then, if $M_s < 2$ (natural units).

The sensitivity function is affected by what is known as *the waterbed effect* if one of these conditions are met [Skogestad and Postlethwaite, 2007]:

1. $L(s)$ has at least two more poles than zeros (first waterbed formula). This is usually the case, due to the low-pass behaviour of the controller and the measurements dynamics.
2. $L(s)$ has a RHP-zero (second waterbed formula).

The waterbed effect essentially says that if we want to decrease the sensitivity function at some frequencies to obtain a good controller performance (i.e. $|S(s)| < 1$) it must increase at others. This is similar to the effect of sitting in a waterbed: pushing it down at one point will result in an increased level somewhere else on the bed [Skogestad and Postlethwaite, 2007].

Mathematically, if the first waterbed formula is fulfilled:

$$\int_0^\infty \ln |S(j\omega)| d\omega = \pi \sum_{i=1}^{N_p} \Re(p_i) \quad (\text{A.37})$$

where p_i is the location of the N_p RHP-poles of $L(s)$ and $\Re(p_i)$ represents their real part. For stable loops (i.e. $N_p = 0$), it is simplified to:

$$\int_0^{\infty} \ln|S(j\omega)|d\omega = 0 \quad (\text{A.38})$$

where the area of sensitivity reduction (i.e. $|S(j\omega)| < 1$ and $\ln|S(j\omega)| < 0$) must equal the area of sensitivity increase (i.e. $\ln|S(s)| > 0$). In other words, an increase of the maximum gain peak M_s , and then reduction of stability margins, is expected for big areas of controller good performance (i.e. wide feedback bandwidths). However, equation (A.38) establish an improper (i.e. unbounded) integral, as the maximum frequency ω is ∞ . So, theoretically, a good performance can be obtained in broad bands without increasing too much M_s , as the frequency range of $\ln|S(s)| < 0$ can be compensated with an infinity frequency range of $\ln|S(s)| > 0$. Following the waterbed analogy, this is similar to the effect of sitting in a waterbed of infinite surface.

This is not the case for the second waterbed formula. For an $L(s)$ with a single RHP-zero z :

$$\int_0^{\infty} \ln|S(j\omega)|w(z, \omega)d\omega = \pi \prod_{i=1}^{N_p} \left| \frac{p_i + z}{\bar{p}_i - z} \right| \quad (\text{A.39})$$

where:

- N_p is, again, the number of RHP-poles (p_i) in $L(s)$.
- \bar{p}_i denote the complex conjugate of p_i .
- $w(z, \omega)$ is a function, whose formula depends on whether z is real or complex, that makes the contribution from $\ln|S(j\omega)|$ to the sensitivity integral to tend to zero at frequencies $\omega > z$. That is, $w(z, \omega)$ effect in $\ln|S(j\omega)|$ is similar to bound the maximum integral limit to $\omega = z$ instead of ∞ .

Then, for stable loops (i.e. $N_p = 0$) the above second waterbed formula is approximately simplified to:

$$\int_0^z \ln|S(j\omega)|d\omega \approx 0, \quad (\text{A.40})$$

As the waterbed is, in this case, finite, a large peak M_s is unavoidable if we want good performance in a broad frequency range.

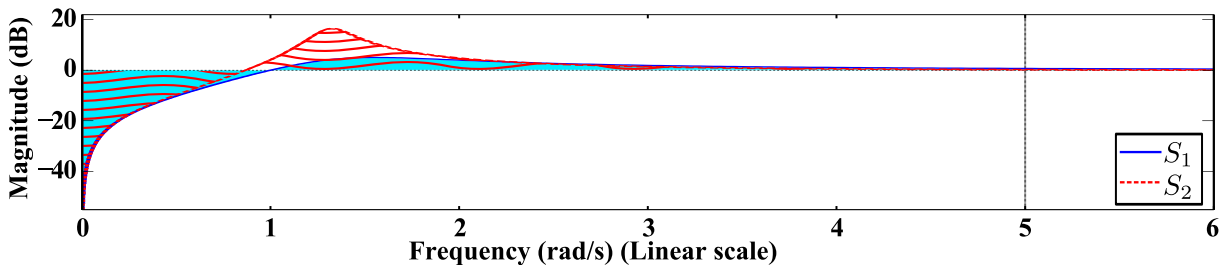


Figure A.7. Sensitivity functions S_1 and S_2 magnitude representation, which fulfil the first and second (S_2) waterbed formulas, respectively [Skogestad and Postlethwaite, 2007].

Fig. A.7 shows the sensitivity function frequency domain representation for two loop functions: $L_1(s) = \frac{2}{s(s+1)}$ fulfil the first waterbed formula and $L_2(s) = L_1(s) \frac{-s+5}{s+5}$ has the same gain representation that $L_1(s)$, but introduces a RHP-zero in $z = 5$, fulfilling the second waterbed formula. As it can be seen, the closed areas between $S_2 = \frac{1}{1+L_2(s)}$ contour and 0 dB, for a

frequency ranges $w = [0, z]$ (red waves), are equal. The same is fulfilled for S_1 , but this time for an unbounded frequency range $w = [0, \infty]$ (light blue fill).

It can be concluded that there is, normally, a control trade-off between good controller performance and good system stability margins.

A.5 Controller objectives summary: Trade-offs in terms of L

As it was advanced in section A.2, the most classic control objective is to reduce the tracking error (e), by obtaining a tracking transfer function $|T(s)| \approx 1$ and disturbance transfer function $|D(s)| \approx 0$. This can be achieved, using the one (Fig. A.1) or two (Fig. A.2) DOF structures, by defining big feedback gains (i.e. $|K| \rightarrow \infty$) and, then, big loop function gains (i.e. $|L(s)| \rightarrow \infty$) or, analogously, small sensitivity function gains (i.e. $|S(s)| \rightarrow 0$). This objective is, on the other hand, in conflict with other controller objectives, such as the minimization of the controller effort (i.e. $|F_{d \rightarrow u}| \rightarrow 0$ and $|F_{y^* \rightarrow u}| \rightarrow 0$) or the rejection of the measurement noise (i.e. $|N| \rightarrow 0$), which are obtained for low controller gains ($|K| \rightarrow 0$) and, then, low loop gains ($|L| \rightarrow 0$).

In the end, independently of the control structure used (see section A.2), the most important design objectives are bonded to trade-offs in terms of the loop function gain ($|L|$), which are summarized below [Skogestad and Postlethwaite, 2007];

1. Good disturbance rejection (i.e. $|D(j\omega)| \rightarrow 0$): $|L(j\omega)| \rightarrow \infty$.
2. Good reference tracking (i.e. $|T(j\omega)| \rightarrow 1$): $|L(j\omega)| \rightarrow \infty$.
3. Mitigation of measurement noise (i.e. $|N(j\omega)| \rightarrow 0$): $|L(j\omega)| \rightarrow 0$.
4. Reduction of the controller effort (i.e. $|F_{d \rightarrow u}| \rightarrow 0$ and $|F_{y^* \rightarrow u}| \rightarrow 0$): $|L(j\omega)| \rightarrow 0$.
5. Implementable controller: $|L(j\omega)| \rightarrow 0$ as $\omega \rightarrow \infty$.
6. Robust stand-alone stability margins against uncertain or neglected plant dynamics (i.e. reduction of maximum sensitivity gain peak M_s): $|L(j\omega)| \rightarrow 0$.

Fortunately, this conflicting objectives are generally in different frequencies ranges, so it is possible to fulfil all of them by a proper loop function ($L(s)$) design.

A.6 Bandwidth limitations of feedback control

Feedback control has a limited bandwidth (i.e. range where $|S(j\omega)| < 1$) in the presence of time delays or RHP-zeros in the loop function $L(s)$.

This limitation was deduced by [Morari and Zafriou, 1989]. It presents the internal model control (IMC), which structure is shown in Fig. A.8. This technique obtains a controller $C(s)$ that includes in its dynamic a model $\tilde{G}(s)$ of the open-loop command-to-output transfer function $G(s)$. The main advantage of this control process is that, for a perfect model $\tilde{G}(s) = G(s)$ and without considering the output disturbance (i.e. G_d effect), the tracking transfer function $T(s) = \tilde{G}(s)Q(s)$, being possible to design $Q(s)$ from an open-loop (i.e. feedforward) point of view. That is, if perfect tracking $T(s) = 1$ is desired, $Q(s) = \tilde{G}(s)^{-1}$.

In any case, in order for $Q(s)$ to be physically implementable, it must be:

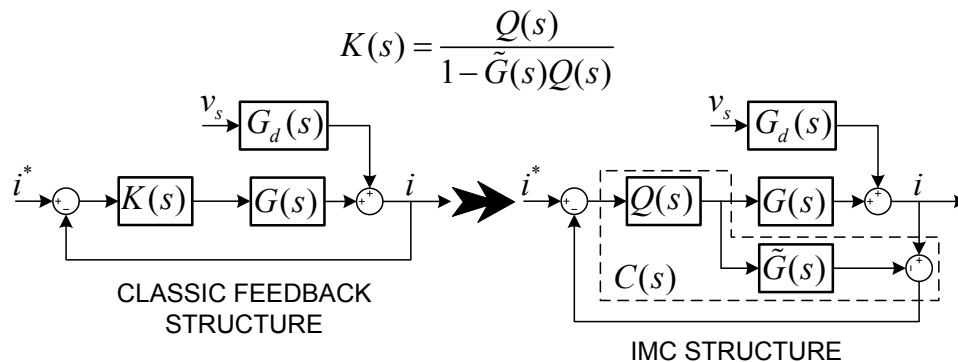


Figure A.8. Internal model control structure and its equivalence with a classic one DOF feedback controller.

- Stable, to not make the closed loop $T(s)$ unstable;
- Proper (i.e. order of numerator \leq order of the denominator), as pure differentiation cannot be implemented in practice, and
- Causal, which means that $Q(s)$ must not require prediction (i.e. must only rely in current and past plant measurements.)

If the system to be controlled $G(s)$ has RHP-zeros, time delays or is strictly proper (i.e. order of numerator $<$ order of the denominator) a $Q(s) = \tilde{G}(s)^{-1}$ for perfect tracking can not be implemented, as the resulting $Q(s)$ will be unstable, non-causal or improper, respectively.

To solve this problem, the IMC control design procedure proposes a factorization of $\tilde{G}(s) = \tilde{G}_+(s)\tilde{G}_-(s)$, where transfer function $\tilde{G}_+(s)$ contains all non-minimal phase elements of the plant model (i.e. all RHP-zero and time delays) and $\tilde{G}_-(s)$ is equal to the minimum phase, and then invertible, part of \tilde{G} . The designed $Q(s)$ should, at the same time, invert $\tilde{G}_-(s)$, try to minimize the effect of $\tilde{G}_+(s)$ in $T(s)$ and include new poles by means of low pass filters to make $Q(s)$ proper (in case $G(s)$ is strictly proper).

To deduct the aforementioned sensitivity (i.e. feedback) bandwidth limitation, consider now a plant G with a time delay θ , a real RHP-zero at z and a LHP-pole at p :

$$G(s) = \frac{-s + z}{s + p} e^{-\theta s} \quad (\text{A.41})$$

The objective is to obtain an ideal⁶ IMC controller $Q(s)$ that obtains a perfect tracking in the broader bandwidth possible. The ideal IMC controller $Q(s)$, calculated for a $T(s) = 1$, is then:

$$Q(s) = \tilde{G}(s)^{-1} = G(s)^{-1} = \frac{s + p}{-s + z} e^{\theta s} \quad (\text{A.42})$$

But, as explained before, this controller is not realizable for two reasons: it has a predictive term $e^{\theta s}$ and a RHP-pole at z , which will make the closed-loop system unstable. The effect of the RHP-zero of the plant in $T(s)$, however, can be partially compensated (in module, but not in phase) by adding a LHP-pole at z in $Q(s)$ instead of the ideal RHP-pole⁷. So the final ideal

⁶The obtained $Q(s)$ is considered ideal as its output $u(s)$ is not limited.

⁷In [Morari and Zafiriou, 1989] different techniques are presented to obtain a controller $Q(s)$ that minimize the effect of G RHP-zeros and delays (i.e. $\tilde{G}_+(s)$ part) in the obtained closed-loop $T(s)$. The addition of a LHP-pole in $Q(s)$ tries to minimize the integral square error (i.e. ISE optimal control) between the system output y and its reference y^* (i.e. minimize the gain difference between $|T(s)|$ and its ideal unity response).

controller, and the resulting tracking transfer functions, will be as follows:

$$Q(s) = \frac{s+p}{s+z} \rightarrow T(s) = e^{-\theta s} \frac{-s+z}{s+z} \quad (\text{A.43})$$

$T(s)$ in (A.43) represents the ideal tracking transfer function for a plant $G(s)$ with time delays and RHP-zeros. Its most general form is:

$$T(s) = \prod_{j=0}^{N_p-1} \frac{-s+z_j}{s+\bar{z}_j} e^{-\theta s} \quad (\text{A.44})$$

where N_p is the number of z_j RHP-zeros (real or complex) in $G(s)$, \bar{z}_j their complex conjugate and θ the total $G(s)$ time delay.

From (A.43), it is easy to derived the feedback limitations of a system with time delays or RHP-zeros. Knowing that the sensitivity function $S(s) = 1 - T(s)$ for the considered one DOF control scheme [Skogestad and Postlethwaite, 2007]:

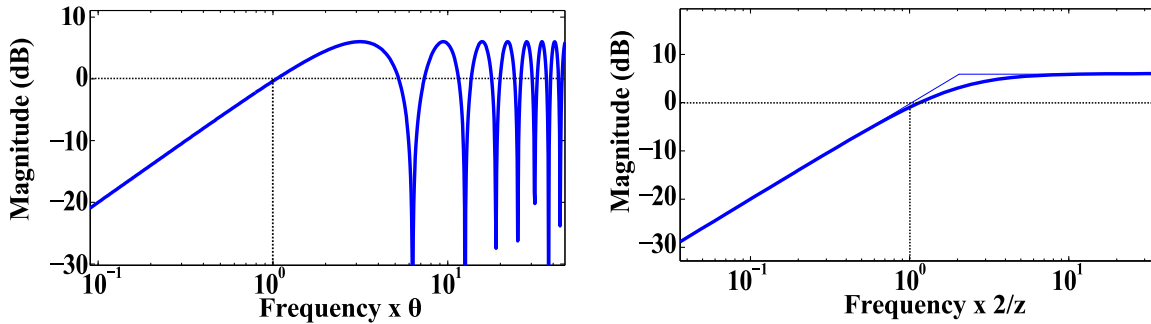


Figure A.9. Maximum bandwidth for plants with time delays (left) and RHP-zero (right).

- Consider a plant with a time delay θ , $G(s) = e^{-\theta s}$, the ideal sensitivity function will be:

$$S = 1 - T = 1 - e^{-\theta s} \quad (\text{A.45})$$

whose magnitude is plotted in the left part of Fig. A.9. As it can be seen, $|S(j\omega)|$ crosses 1 at a frequency of about $1/\theta$. So the maximum feedback bandwidth ω_c (where $|S(j\omega_c)| = 1$) of any designed controller $K(s)$ for a plant $G(s)$ with time delays will be $\omega_c = 1/\theta$.

- Consider a plant with a real RHP-zero at z , $G(s) = -s + z$, the ideal sensitivity function will be:

$$S = 1 - T = 1 - \frac{-s+z}{s+z} = \frac{2s}{s+z} \quad (\text{A.46})$$

whose magnitude is plotted in the right part of Fig. A.9. As it can be seen, $|S(j\omega)|$ low-frequency asymptote crosses 1 at a frequency $z/2$. So the maximum achievable bandwidth ω_c of any designed controller $K(s)$ for a plant $G(s)$ with a RHP-zero will be $\omega_c = z/2$.

Note that, considering the Pade approximation of a delay, $e^{-\theta s} \approx (1 - \frac{\theta}{2}s)/(1 + \frac{\theta}{2}s)$, the maximum bandwidth of a time delay θ is equal to the one of a RHP-zero at $2/\theta$.

A.7 Controllers design methodologies: main classical control design frameworks

Linear control design methodologies can be sorted in classical and optimal techniques. The main difference between both is the way the controller is derived. In the classical control paradigm, the designer obtains a controller (K) for a given plant dynamic following some heuristic rules based on its knowledge and experience, so that the closed-loop system fulfils some given objectives (e.g. good reference tracking performance, robustness etc.). In the optimal control paradigm, the controller (K) is synthesized with the same premises (i.e. plant open-loop dynamics and desired closed-loop objectives) but, this time, following some optimization rules. Optimal control is, then, better suited for applications where the derivation of the controller could be a very hard task, such as the control of complex plant dynamics (e.g. MIMO plants) or if different and complex control objectives must be fulfilled at the same time.

Some optimal control techniques are analysed in section 3.2. The main classical control design frameworks are briefly introduced next;

- Proportional-integral-derivative (PID) control: This is probably the most popular family among linear controllers, even more without its derivative part (i.e. PI). A generalized expression of this controllers is detailed next:

$$K_{PID}(s) = K_p + K_d s + \frac{K_i}{s} \quad (\text{A.47})$$

where K_p , K_d and K_i are the proportional, derivative and integral gains. The integral part of the controller provides of a high gain at low (continuous) frequencies (i.e. $\omega \rightarrow 0$), obtaining a good tracking response at them (i.e. $T(j\omega)|_{\omega \rightarrow 0} \rightarrow 1$) and, then, making possible to track step-type (non-oscillatory) reference outputs (y^*). Due to its popularity, multiple straightforward design rules had been proposed for the design of this kind of controllers, even more for the case of first-order plants. However, its biggest drawback is the poor tracking performance for periodic (i.e. non-continuous) reference outputs (y^*).

- Proportional-resonant (PR) control: In this framework, the integral part of PI controllers is substituted by a generalized integrator:

$$K_{PR}(s) = K_p + \frac{K_r s}{s^2 + 2\zeta\omega_0 s + \omega_0^2} \quad (\text{A.48})$$

where K_r is the resonant gain, ω_0 is the resonant frequency and ζ is a resonance damping factor. A high controller gain ($|K_{PR}(j\omega)|$) is obtained at a frequency $\omega = \omega_0$, resulting in a good output reference (y^*) tracking at this frequency⁸. The same design rules of PI controllers can be translated into PR controllers using some of the proposed equivalences in the literature [Zmood et al., 2001, Zmood and Holmes, 2003, Yepes, 2011, Karttunen et al., 2014]⁹.

- Zero-pole compensation networks: These networks consist on transfer functions of this form;

$$H(s) = H_c \frac{s + a}{s + b} \quad (\text{A.49})$$

⁸Note that infinite gains, and then a perfect tracking (i.e. $|Tj\omega_0| = 1$), is obtained for null damping factors ($\zeta = 0$) at frequency ω_0

⁹Note that $K_{PI} = K_{PR}|_{\omega_0=0}$

Supposing an $a < b$ definition, this network will result in a lead-lag compensator, which increases asymptotically the controller phase with a $45^\circ/\text{dec}$ slope, up to a maximum of 90° phase lead, for frequencies $0.1a < \omega < 10a$, and decreases it again with a $-45^\circ/\text{dec}$ slope, down to the initial 0° phase, for frequencies $\omega > 0.1b^{10}$. An opposite lag-lead behaviour will be obtained for an $a > b$ definition. These networks serve, then, as closed-loop dynamic modifiers, rather than high-performance controllers like the aforementioned PR and PI controllers. They are particularly well suited for loop-shaping applications, where several lead-lag or lag-lead networks can be defined in series to further modified the feedback gain and, then, the loop function ($L(s)$), or to effectively modify the disturbance (D) function by introducing them on the disturbance (d) feed-forward path (i.e. K_d gain in Figs. A.2-A.4).

Fig. A.10 shows the frequency domain representation of the aforementioned proportional-integral (PI) and proportional-resonant (PR) controllers, in addition to a lead-lag compensator.

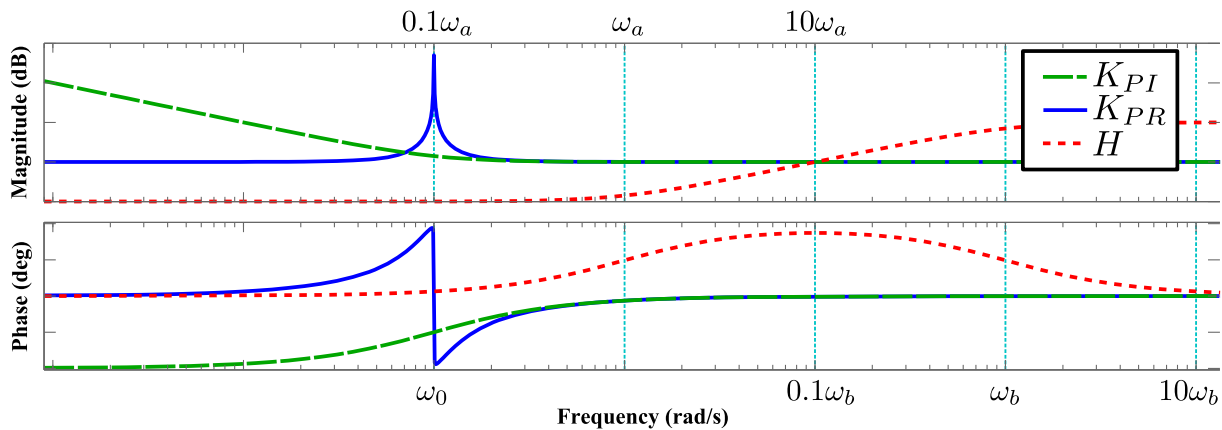


Figure A.10. Frequency domain representation of the PI (K_{PI}) and PR (K_{PR}) controllers, as well as the lead-lag compensator (H).

A.8 Lineal control applied to power converters

The application of linear controllers to power converters could be questioned bearing in mind its intrinsic non-linear nature. However, assuming the averaging hypothesis to be valid [Lindgren and Svensson, 1998, Svensson, 1997], the control of power electronic converters can be considered a linear problem. This approximation makes possible the use of well-established and known linear controller design techniques [Cóbreces, 2009].

This section summarizes the main control topologies applied to power converters (i.e. current-controlled and voltage-controlled PECs), as well as some of their most representative applications.

A.8.1 Current-controlled PECs

Current-controlled power converters are usually connected to a voltage source (e.g. the grid/micro-grid, a voltage-controlled power converter, an electric generator etc.) through an L or an LCL

¹⁰Note that the controller gain will also increase in that case with a $20\text{dB}/\text{dec}$ slope for frequencies $a < \omega < b$.

filter, as represented in Fig. A.11 and Fig. A.12, respectively.

L filter

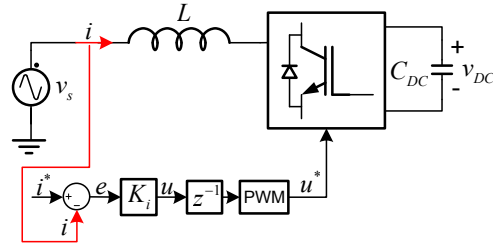


Figure A.11. Current control with an L filter.

When an L filter is used, the open loop current (i) dynamic to be controlled is as follows:

$$I(s) = \underbrace{-\frac{1}{sL + R}}_{G_L(s)} U^*(s) + \underbrace{\frac{1}{sL + R}}_{G_{dL}(s)} V_s(s) \quad (\text{A.50})$$

Two signals (inputs to the open-loop model) may modified the current (output to the open-loop model): one controlled, the VSC average output voltage $U^*(s)$, and one uncontrolled, the voltage source $V_s(s)$. Two transfer functions are derived to describe the current dynamic: the open-loop command-to-output $G_L(s)$ and admittance $G_{dL}(s)$. Their frequency domain responses are shown in Fig. A.14. Note how both have a magnitude slope of -20 dB/dec. That is, G_L has a low magnitude value at high frequencies that will filter the effect of PWM commutation noise in U^* . Increasing the inductance (L) value will result in a frequency displacement to the left of G_L magnitude, and then in lower values at high frequencies (i.e. better filtering). These transfer functions dynamics are used to design the simple one DOF controller (K_i) in Fig. A.11 to fulfil the desired current closed-loop performance.

LCL filter

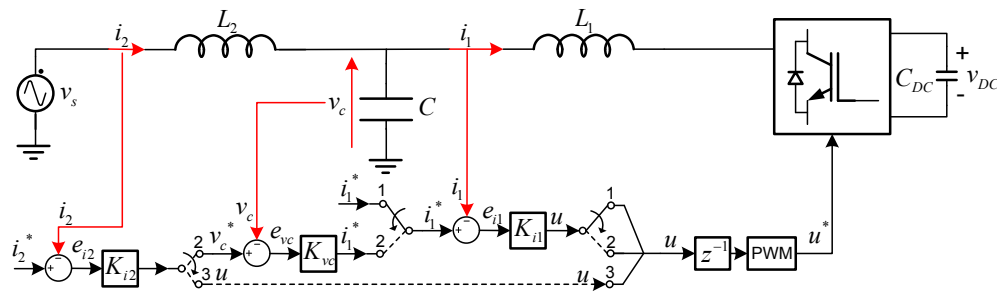


Figure A.12. Current control with an LCL filter.

If an LCL filter is used, the output current (i_2 in Fig. A.12) dynamic is more complex:

$$I_2(s) = \underbrace{-\frac{1}{sC(R_1 + sL_1)(R_2 + sL_2) + R_f + sL_f}}_{G_{LCL}(s)} U^*(s) + \underbrace{\frac{sC(R_1 + sL_1) + 1}{sC(R_1 + sL_1)(R_2 + sL_2) + R_f + sL_f}}_{G_{dLCL}(s)} V_s(s) \quad (\text{A.51})$$

with $L_f = L_1 + L_2$ and $R_f = R_1 + R_2$. The new open-loop transfer function dynamics are shown in Fig. A.14. As it can be seen, $G_{LCL}(s)$ presents a higher filtering degree than the L filter at high frequencies (-60 dB/dec). The filter size (i.e. inductance value) can be highly reduced using this topology for the same commutation noise filtering. However, both $G_{LCL}(s)$ and G_{dLCL} present a magnitude resonance that represents a risk in both stand-alone (see section A.4) and complex networks (see section 2.2.1) stability, respectively. The design of a stable one DOF current controller (K_{i_2} in Fig. A.12, with the switches in position 3) is, then, far more complex for this filter topology. Three main control alternatives are common in the literature:

- **Control the converter size current** (i_1) simplifies the plant dynamics to the L filter case (see equation (A.50)), and is often sufficient for grid power conditioning applications (i.e. the filter is usually designed so $i_1 \approx i_2$ for the fundamental frequency ω_1). The current controller structure can be simplified to the one DOF controller (K_{i_1}) shown in Fig. A.12, with the switches in position 1. Even though some papers have report the inherent damping characteristic of controlling the converter-side current [Tang et al., 2012], not modelling the filter resonance (i.e. $F_{i_1 \rightarrow i_2}$ dynamics) in the loop may still result in instabilities for high controller bandwidths [Wang et al., 2014b].
- The second alternative is control the output current (i_2) considering an equivalent L filter plant dynamic with an inductance $L_f = L_1 + L_2$, and then include additional **active damping loops** by feeding-back another filter state (e.g. v_c) or a lineal combination of states (e.g. $i_c = i_2 - i_1$). An example of these structures can be found in section 2.3.1. Active-damping techniques are, in fact, state regulators structures as the one shown in Fig. A.4, which try to modify the LCL plant dynamics so they resemble the aforementioned equivalent L filter dynamics.
- The third alternative is control the output current (i_2) with a **multi-loop structure** as the one shown in Fig. A.12, with the switches in position 2. This method consists in the design of three single-loops, one per each filter state (i_1 , v_c and i_2), where the output of the outer loops controllers are the references to the inner ones. The only design requisite is that each inner loops settling time must be much smaller than the one of the loop immediately above them (from a hierarchy point of view), so the dynamic of the former can be neglected in the design of the later (i.e. K_{i_1} loop tracking must be much faster than K_{v_c} 's, and the latter's faster than K_{i_2} 's, in turn). This simple and elegant technique has, in addition, an inherent damping effect on the LCL filter resonance [He and Li, 2012]¹¹.

Even though the design of a stable system using the last two techniques is simpler than the design of a single i_2 current loop (position 3 in Fig. A.12), they imply the design of multiple loops that may interact with each other. To simplify the process, optimal MIMO design techniques, like the ones exposed in section 3.2.4, can be used.

A.8.2 Voltage-controlled PECs

Voltage-controlled power converters are usually connected to a current source (e.g. a current-controller power converter, an electric machine etc.) through and LC filter, as represented in Fig. A.13.

¹¹This fact becomes obvious when separating the inner-loops of the multi-loop structure (i.e. i_1 and v_c loops) in references feed-forward gains and states feedback gains, transforming the structure in an equivalent state regulator or active damping loop.

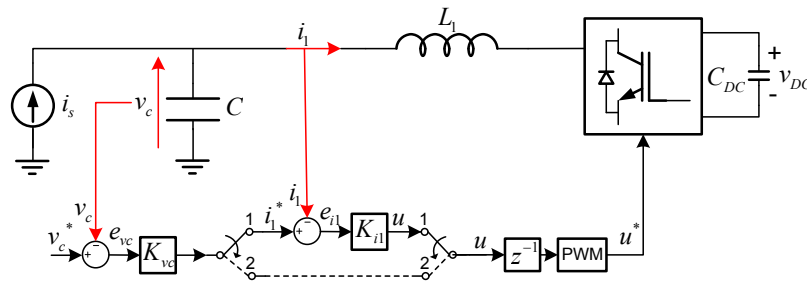


Figure A.13. Voltage control with an LC filter.

The filter open-loop output voltage (v_c) dynamic to be controlled is as follows:

$$V_c(s) = \underbrace{\frac{1}{CLs^2 + CR_1s + 1}}_{G_{LC}(s)} U^*(s) + \underbrace{\frac{L_1s + R_1}{CLs^2 + CR_1s + 1}}_{G_{dLC}(s)} I_s(s) \quad (\text{A.52})$$

The uncontrolled input signal is now a current (i_s), so $G_{dLC}(s)$ represents the system open-loop impedance. The frequency domain representations of the open-loop system dynamics are shown in Fig. A.14. Both $G_{LC}(s)$ and G_{dLC} present resonant frequencies that represent a stability risk from a stand-alone and complex network point of view, respectively. So the design of a one DOF voltage controller ($K_{vc}(s)$ in Fig. A.13, with switches in position 2) is, again, more complex than separate the control structure in different loops, with active damping techniques or with a double-loop structure like the one shown in Fig. A.13 (switches in position 1) [He and Li, 2012, Turner et al., 2013, Rahimi and Emadi, 2009].

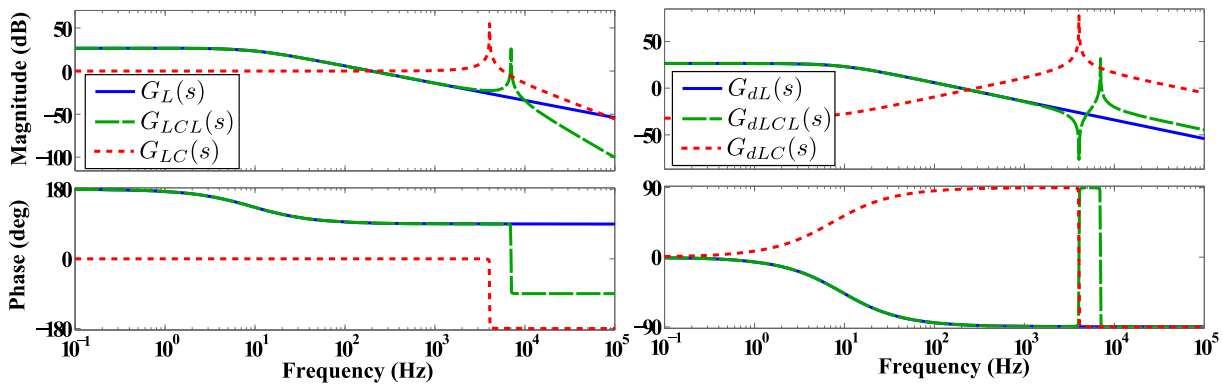


Figure A.14. Frequency domain representation of the L, LC and LCL filter plants.

A.8.3 Application examples of controlled power electronic converters.

This section introduces some of the most representative power electronic converter (PEC) based applications. They will be sorted attending to their type of connection (*shunt*, *series* or *hybrid* connection) and to their main controlled variable (current-controlled or voltage-controlled):

- **Static synchronous compensator (STATCOM):** An STATCOM is a shunt-connected current-controlled PEC-based application. A simplified diagram of it is shown in Fig. A.15.

The STATCOM is able to exchange reactive (Q) and active (P) power with the AC grid which is connected to by modifying its output voltage (u^*) module and phase, respectively.

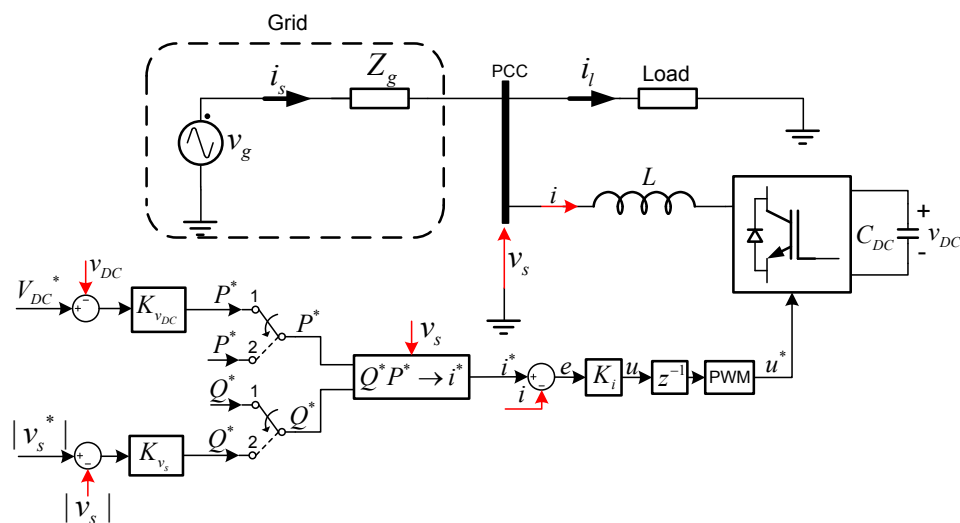


Figure A.15. Static synchronous compensator diagram.

The primary function of the STATCOM is, then, to exchange reactive and active power with the AC grid. By doing so, it is also able to regulate the PCC voltage module ($|V_s|$) and to control the DC-bus voltage (v_{DC}) by means of an outer AC voltage controller (K_{v_s}) and an outer DC voltage controller ($K_{v_{DC}}$), respectively. Even though the STATCOM is also able to control the PCC voltage phase by means of the active power control [Hill, 1997], it is not recommended for this task due to the big necessary currents [Awad, 2002].

- **Dynamic voltage restorer (DVR):** A DVR is a series-connected voltage-controlled PEC-based application. Fig. A.16 shows its simplified diagram.

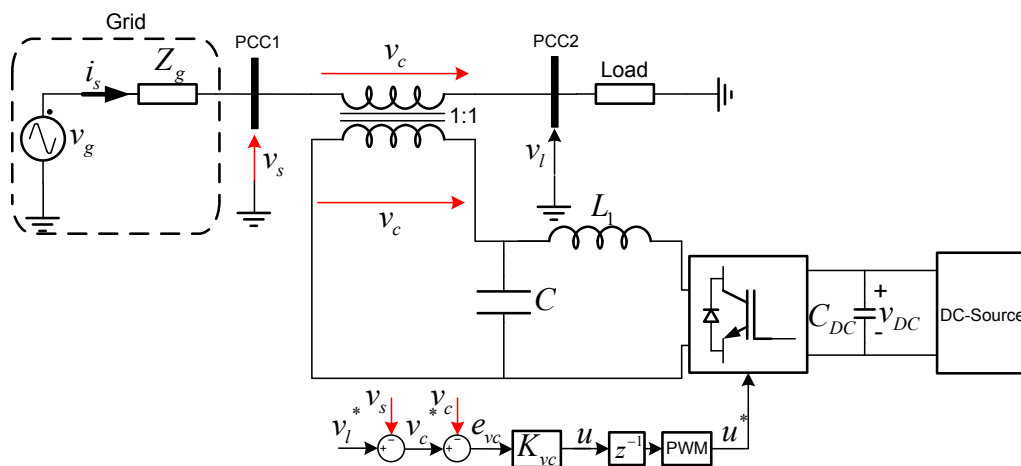


Figure A.16. Dynamic voltage restorer diagram.

The main function of a DVR is to compensate possible grid voltage (v_s in Fig. A.16) magnitude dips and/or phase jumps, so a sensitive load connected to it does not suffer from their effects. Its operation principle is very similar to an Uninterruptible power supply (UPS) but, unlike it, the DVR is specifically designed for large loads (ranging from 2MVA to 10MVA). Basically, a DVR will inject, by means of a series-connected (1:1) transformer, the voltage difference between the nominal grid voltage (v_l^* in Fig. A.16) and the current grid voltage (v_s), so that the load voltage (v_l) remains stable and equal to the

mentioned nominal grid voltage. The DVR is, then, better suited for PCC voltage regulation than the STATCOM. However, as the DC-bus voltage is not controlled and the injected voltage (v_c) often requires of an active power flow from the DVR to the load, the DC-bus voltage will decay unless an external DC-source is connected to it.

- **Active power filter (APF):** An APF is a PEC-based application which main objective is to compensate the harmonic effect of grid-connected non-linear load on the own grid. They can be either shunt or series-connected, and current or voltage-controlled. Fig. A.17 shows the simplified diagram of a current-controlled shunt-connected APF, where a grid-connected non-linear load will demand a current (i_l) contaminated with harmonics.

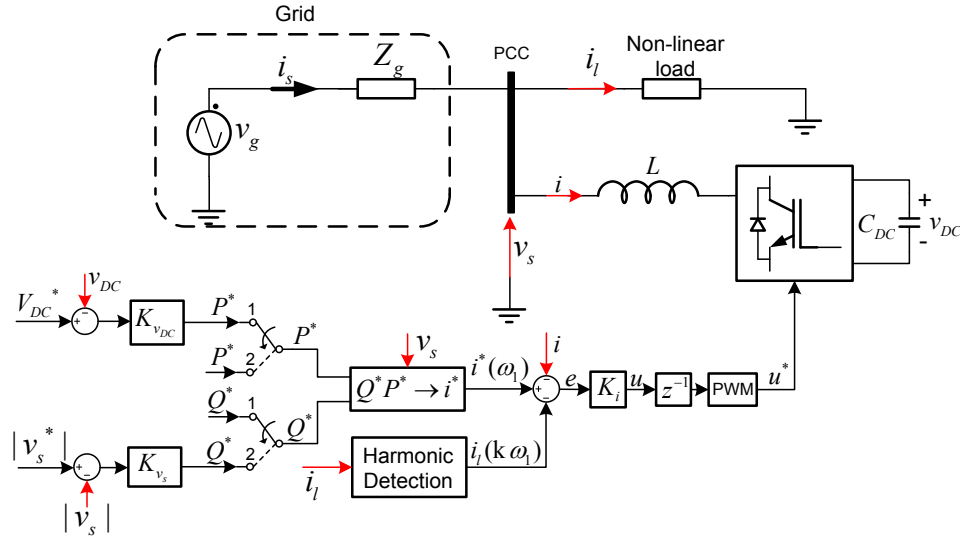


Figure A.17. Shunt active power filter diagram.

It has, basically, the same structure than a STATCOM, with a simple modification on the controlled current reference (i^*). The shunt APF will measure the non-linear load current (i_l) and, next, extract its harmonic content ($i_l(k\omega_1)$). This harmonic content serves as the APF current reference at the harmonic frequencies (i.e. $i^*(k\omega_1) = -i_l(k\omega_1)$), meanwhile its fundamental frequency tone ($i^*(\omega_1)$) is calculated from any of the aforementioned STATCOM characteristic outer-loops. Assuming that the designed current controller (K_i) provides of a good reference tracking at the harmonic frequencies (i.e. $|T(jk\omega_1)| \approx 1$ and $i = i^*(\omega_1) - i_l(k\omega_1)$), the shunt APF will inject the non-linear load harmonics again to the PCC so the grid current (i_s) and, then, the PCC voltage (v_s) only have a fundamental frequency component (i.e. $i_s = i_l + i = i_l(\omega_1) + i^*(\omega_1)$). A similar scheme can be used to compensate the effect of non-linear loads that generated voltage harmonics, this time by using a series-connected voltage-controlled APF.

- **Unified power factor controller (UPFC):** The UPFC is a PEC-based application that presents both a series and a shunt-connected converter (i.e. hybrid connection) that share a common DC-bus (i.e. back-to-back connection). Fig. A.18 shows its simplified diagram.

This topology joins, then, the main advantage of both shunt and series-connected PEC-based applications; it is able to control the power flow of both active and reactive powers and, at the same time, regulate the AC voltage effectively, in a similar way that the STATCOM and DVR do, respectively.

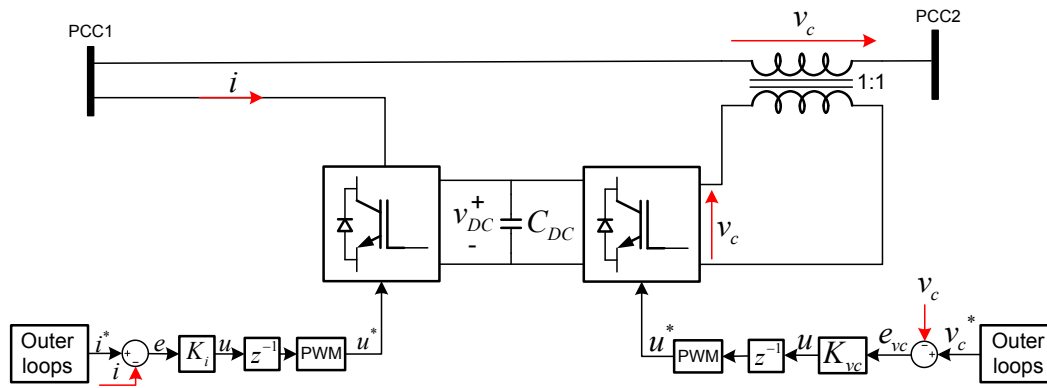


Figure A.18. Unified power factor controller diagram.

- **High-voltage direct-current (HVDC) transmission:** HVDC is an energy transmission topology based in the back-to-back connection of two VSCs. Fig. A.19 shows an schematic diagram.

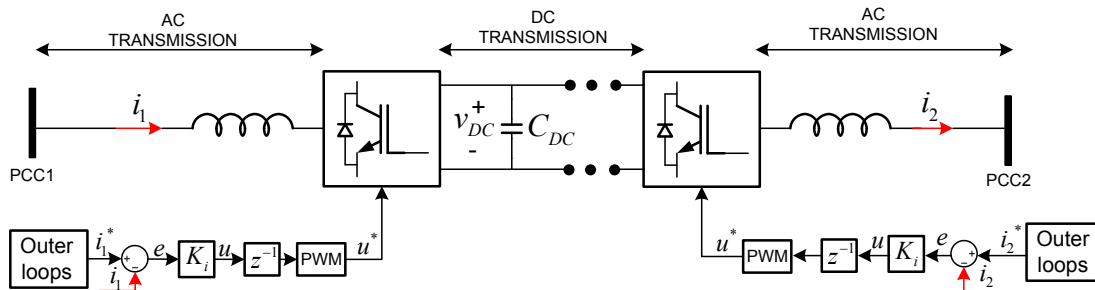


Figure A.19. High-voltage direct-current transmission diagram.

Its main purpose is the effective bulk-energy transmission between two distant points (PCC1 and PCC2 in Fig. A.19) using DC signals, as it is demonstrated that DC transmissions present some cost/efficiency benefits in that cases (e.g. asynchronous interconnection, smaller/less expensive filters and transmission cables etc.). This topology is specially suited, then, for the energy transmission between large offshore renewable energy plants and the onshore grid. Simplifying, one of the VSCs will rectify the source AC power (PCC1 in Fig. A.19, e.g. offshore energy plant) into a controlled DC-bus voltage, meanwhile the other VSC will control the power/energy flow between the common DC-side and the ending AC-side (PCC2 in Fig. A.19, e.g. onshore grid).

Appendix B

Publications

Admittance-shaped \mathcal{H}_∞ current controller for grid-connected VSC

Jorge Pérez, Santiago Cóbrecas
 Department of Electronics
 Alcala University
 Email: jorge.perez@depeca.uah.es

Robert Griño
 Industrial and Control Engineering Inst.(IOC)
 Universitat Politècnica de Catalunya (UPC)
 Email: roberto.grino@upc.edu

Abstract—This paper introduces an \mathcal{H}_∞ current controller that allows the shaping of power converters' input admittance in frequency domain, allowing to define not only its magnitude but also its phase. In addition to admittance shaping, some current tracking specification are also introduced to the algorithm demonstrating that both admittance shaping and tracking performance are possible, but not at the same frequencies. The correct performance (both in time and frequency domain) of the proposed method is demonstrated in an L-filter grid-connected single-phase VSC.

I. INTRODUCTION

The increasing presence of power electronics-based distributed energy sources, machine drives and grid support systems besides of bringing new energy and grid management capabilities is also generating technical challenges coming from interactions between the different involved systems.

This kind of problems are modifying the way power converter control is understood: while traditionally the main converter control objective was to obtain high performance current and voltage tracking controllers, recently this strategy is being questioned as it may cause stability issues. Some of the applications where conflicting situations may be found are systems connected to Constant Power Loads (CPL) elements [1] [2], High Voltage Direct Current - Voltage Source Converter (HVDC-VSC) transmission systems [3], converters used in single-phase or three phases rail networks [4], distributed power generation systems under weak grids [5] [6] [7] [8] or converters located nearby to synchronous machines [9] [10].

The nature of these stability issues is, in general, non linear. Although there are recent efforts to study the problem in its whole complexity [2], most of the existing results are limited to study the situation near an operation point, making use of a linearized approximation. One of the system transfer functions that is usually remarked on those analysis is the closed loop power converter input impedance/admittance.

The importance of the admittance in the stability of interconnected systems has been studied for a long time. In [11], R. Middlebrook introduced a new linear stability criterion for the analysis of the connection of electric subsystems. Middlebrook criterion established that the stability of two subsystem's connection (assuming that both are stable) could be analysed with the open loop function $L = Z_g(s)Y_L(s)$ by means of classical LTI criteria, where $Z_g(s)$ and $Y_L(s)$ represent input impedance and input admittance of two different subsystems (corresponding with grid and load in Fig.1).

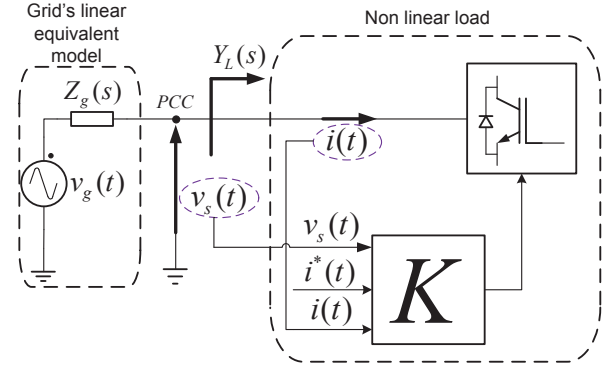


Fig. 1: Proposed admittance and current control scheme. In the figure's left part, grid is modelled as an ideal voltage source $v_g(t)$ and a linear input impedance $Z_g(s)$. In the right part, a non-linear load (closed loop power converter) is connected to the point of common coupling (PCC). $Y_L(s)$ represents the closed loop input admittance. Controller K inputs are PCC voltage $v_s(t)$, input current $i(t)$ and current reference $i^*(t)$.

The dissipative characteristic of the input admittance is known to play an important role in the stability of interconnected systems. The sign of $\Re\{Y_L(s)\}$ defines the dissipativity behaviour (positive realness, or passivity) [12] [13] of the obtained system. If every subsystem interconnected is dissipative the resulting system is dissipative, and then stable. Systems with controllers that respond fast to output perturbations usually have non-dissipative frequency ranges (e.g., CPL, active rectifiers, servo-controllers ...). The system may become unstable if that frequency range coincides with one of the system's resonance [14].

This paper is focused on shaping (in frequency domain) the input admittance $Y_L(s)$ (transfer function from input supply $v_s(t)$ to input current $i(t)$, see Fig. 1). This concept has been previously studied in [15], [4], [9], [14], [16] and [17].

The main contribution of this paper is a systematic \mathcal{H}_∞ controller design that allows admittance shaping at some frequencies and current tracking at others, fixing different objectives depending on the frequency zone. The controller is designed following a model-reference strategy. This allows to achieve admittance shaping not only in modulus, but also in phase. This may give some ease in cases where system dissipativity is desirable.

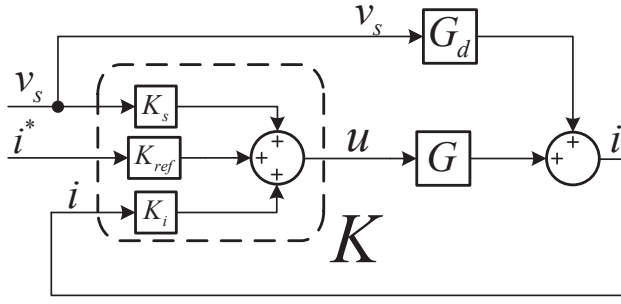


Fig. 2: Simplified control scheme. \mathbf{K} is a three degrees of freedom controller formed by three single blocks K_s , K_{ref} and K_i . G_d and G represents open loop input admittance and command-to-output transfer function, respectively.

The outline of this paper is as follows. Section II presents a theoretical background for admittance shaping. It first describes the target system (one phase VSC-grid connection through an L-filter) and the desired current controller objectives. Then summarizes \mathcal{H}_∞ controllers theory and finally applies it to admittance shaping. Section III introduces the design of the \mathcal{H}_∞ discrete controller by solving an example design. Section IV presents the obtained frequency and time domain results. Finally Section V comes to the conclusion.

II. THEORETICAL BACKGROUND

A. Objectives and system description

Fig. 12 shows the equivalent model for the plant to be controlled. It is formed by a series connection of an AC voltage supply with a voltage source converter (VSC) through an L filter. In averaged terms, the system is described by the following state equation:

$$L \frac{di(t)}{dt} = v_s - r_l i(t) - u(t), \quad (1)$$

being u and r_l the averaged VSC output voltage along a switching period, and the inductor equivalent resistance, respectively. The grid current in Laplace domain is then:

$$I(s) = G(s) \cdot U(s) + G_d(s) \cdot V_s(s) \quad (2)$$

where $G(s) = \frac{I(s)}{U(s)} = -\frac{1}{sL+r_l}$ and $G_d(s) = \frac{I(s)}{V_s(s)} = \frac{1}{sL+r_l}$ are the open-loop command-to-output and input admittance, respectively.

The control objectives are the following:

- 1) Obtain a closed-loop input admittance that follows a provided admittance reference model, namely $Y_{ref}(s)$. The closed loop system is desired to follow this model in a certain specified band.
- 2) Current tracking at the system fundamental frequency ω_1 . For uniformity in the formulation, this objective will also be introduced as reference-to-output model reference transfer function, namely $T_{ref}(s)$.

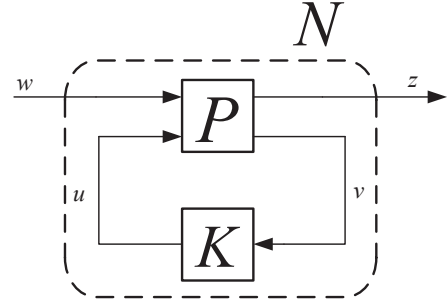


Fig. 3: Generalized plant \mathbf{P} -based \mathcal{H}_∞ controller problem.

The measurements available to achieve such objectives are the following:

- Point of common coupling (PCC) voltage measurement v_s .
- Grid current i measurement.
- Additionally a grid current reference input signal i^* is considered.

The controller structure here proposed consists in a three degrees of freedom controller. Its block diagram is displayed on Fig. 2. Note that the grid PCC voltage is usually available at no extra sensor cost as grid synchronisation algorithms use it.

The expression, in Laplace domain, of the closed-loop controlled system grid current is, then:

$$I = \underbrace{\frac{GK_{ref}}{1-GK_i}}_{T(s)} I^* + \underbrace{\frac{GK_s + G_d}{1-GK_i}}_{Y(s)} V_s, \quad (3)$$

being $T(s)$ and $Y(s)$ the closed-loop reference-to-output and input admittance transfer functions respectively. Here K_{ref} and K_s are feedforward gains of i^* and v_s respectively, meanwhile closed loop stability depends on feedback gain K_i .

B. Fundamental \mathcal{H}_∞ optimal controllers theory

The proposed controller design procedure is based on the use of the generalised plant \mathbf{P} [18] (see Fig 3),

$$\begin{bmatrix} \mathbf{z} \\ \mathbf{v} \end{bmatrix} = \mathbf{P} \begin{bmatrix} \mathbf{w} \\ \mathbf{u} \end{bmatrix} \quad (4)$$

where \mathbf{w} is the external input vector to the system, \mathbf{z} is the external output vector, which is typically wanted to be kept small, \mathbf{u} is the controller actuation vector and \mathbf{v} is the measured output vector. A (sub)optimal \mathcal{H}_∞ controller \mathbf{K} will minimize, basing on the information obtained from \mathbf{v} , the infinity norm¹ of transfer function \mathbf{N} relating exogenous inputs vector \mathbf{w} to closed-loop outputs \mathbf{z} , until it is lower than a given limit (named γ):

¹The infinity norm of a MIMO system $\mathbf{H}(s)$ in the frequency domain is defined as $\|\mathbf{H}(s)\|_\infty \triangleq \max_\omega \bar{\sigma}(\mathbf{H}(j\omega))$, where $\bar{\sigma}(\mathbf{H}(j\omega))$ are the maximum singular values of $\mathbf{H}(j\omega)$

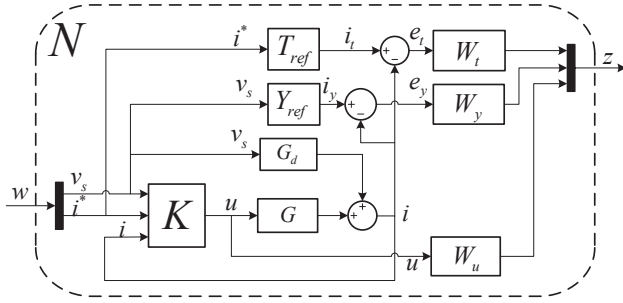


Fig. 4: Proposed signal based \mathcal{H}_∞ control for admittance shaping and current tracking.

$$z = \mathbf{N}w \quad \min_{\mathbf{K}} \|\mathbf{N}(\mathbf{K})\|_\infty \leq \gamma \quad (5)$$

C. Application to admittance shaping

The underlying design strategy follows the well-known model-reference \mathcal{H}_∞ control design scheme [18]. On this scheme, the designer specifies two reference models: T_{ref} , that is the reference-to-output desired transfer function and Y_{ref} that is the input equivalent admittance transfer function.

As can be seen in the generalised control problem displayed on Fig. 4, the output of the open-loop plant ($G + G_d$) is subtracted from the reference models, obtaining two error signals $e_y = Y_{ref}v_s - i$ and $e_t = T_{ref}i^* - i$. This error signals should be kept as small as possible to get a good model following. To weight their importance in different frequencies, two weight transfer functions are introduced W_t and W_y . The output of these transfer function are the first two closed-loop outputs specified in the generalised plant. The third one is a frequency weighted version of the actuation signal u .

The exogenous input signals considered in the problem are: the PCC voltage, v_s , that is assumed to be a disturbance input to the system and the grid current reference i^* .

The input signals to the controller \mathbf{K} , as stated in § II-A, are the PCC voltage v_s , the grid current reference i^* and the measured grid current i . The controller may have, then, three inputs and one output (actuation): u .

Summarising, the output and input signals, respectively, of generalised plant \mathbf{P} are:

$$z = \begin{bmatrix} z_1 = W_t \cdot e_t \\ z_2 = W_y \cdot e_y \\ z_3 = W_u \cdot u \end{bmatrix} \quad v = \begin{bmatrix} v_s \\ i^* \\ i \end{bmatrix} \quad w = \begin{bmatrix} v_s \\ i^* \end{bmatrix} \quad u = u \quad (6)$$

The influence of the model-reference \mathcal{H}_∞ strategy over the obtained closed loop transfer function phase deserves some additional discussion. Traditionally (sub)optimal \mathcal{H}_∞ controllers induce performance specifications/results over the closed-loop transfer function modulus. When considering the model-reference approach, however, the minimised function is, actually, the difference between the closed-loop obtained transfer functions and the reference ones. When this difference

is small it implies a close matching not only in modulus but also in phase.

The obtained phase is particularly important in the case of the equivalent closed-loop admittance, as it affects the sign of the real part of the equivalent admittance, and then the system's dissipativity

III. DESIGN

A. Reference model and frequency weight selection

The design strategy exposed in § II is general enough to handle a wide variety of control objectives. As a particular case this section will consider a dual objective. The main objective considered here will be to obtain a closed-loop equivalent admittance similar to Y_{ref} . Additionally, the grid current is desired to follow a given current reference T_{ref} at grid fundamental frequency.

The converter admittance reference is chosen, for simplicity, to be a inductive-resistive network, so that $Y_{ref} = 1/(sL_{ref} + R_{ref})$, where $L_{ref} = 3.688$ mH and $R_{ref} = 10$ Ω . This selection is often interesting as it constitutes an easy way to obtain a dissipative operation. More complex models can be introduced into the algorithm. Note, however, that the reference model is included in the controller and, hence, the order of the controller \mathbf{K} will increase the same value as the model order. For a good current tracking, a simple $T_{ref}(j\omega) = 1$ is chosen. This would imply perfect reference tracking.

An important consideration regarding this multiple objective problem is the fact that Y_{ref} and T_{ref} are, actually, not compatible. Both impose a grid injected current in the system: Y_{ref} tries to force the grid current to follow a certain relation -admittance- with respect to v_s , and T_{ref} tries to make the same grid current follow a certain reference. As it results clear, is impossible to satisfy both, so, these objectives have to be imposed over different frequency bands. Another limitation observed is that good admittance or tracking shaping can not be obtained in a unlimited frequency range. That it is due to a water-bed effect [18], which limits the width of the high performance bands.

The frequency distribution of control objectives can be easily handled by means of weight functions. In this example the admittance objective is considered to be the primary at low frequencies. Power converter's admittance shaping at low frequencies can be used to deal with subsynchronous resonances problems. Series capacitor compensation introduces subsynchronous electrical resonances in AC transmissions systems. Those may coincide with one of the shaft natural resonance in a synchronous machine. This coincidence can cause shaft fatigue and possible damage or failure [19]. This resonance can be damped using power converters [10], being input admittance shaping at low frequencies of those devices one of the solutions.

As a complementary objective, admittance shaping at super-synchronous frequencies is desired. Admittance shaping at high frequencies is convenient, as super-synchronous resonance may provoke instability in non dissipative systems [14]; super-synchronous resonance are common in weak transmission lines, as a result of its intrinsic dynamic [20],

so dissipative systems at super-synchronous frequencies are preferable when connected to weak grids.

Finally, current tracking at fundamental frequency ω_1 is added to the controller design specifications. The tracking capabilities are, however, band limited, as no fast dynamics are demanded in favour of good admittance shaping.

$W_y(s)$ is selected to allow a low frequencies (sub-synchronous) admittance emulation. To that end, a sensible shaping would be a plain transfer function with a notch around the current reference following band. Additionally, the control band must be limited; in this case this is fulfilled by means of first order low pass filter. More concretely, the chosen weight is:

$$W_y(s) = K_y \frac{s^2 + 2n_w\omega_1 s + \omega_1^2}{s^2 + 2\zeta\omega_1 s + \omega_1^2} \frac{1}{(1/\omega_y)s + 1}, \quad (7)$$

where K_y is the gain at low frequencies, n_w marks notch width, relation n_w/ζ establishes the notch's peak gain (absolute value) and ω_y is the first order low pass filter crossover frequency. The chosen parameters are $n_w = 1.2589 \times 10^{-7}$, $\zeta = 1.2589$, $K_y = 10$ and $\omega_y = 2\pi 90$ rad/s. Fig. 5 shows $W_y(s)$ in frequency domain.

$W_t(s)$ is designed in order to reduce tracking error only in a neighbourhood of the system fundamental frequency ($\omega_1 = 2\pi 50$ rad/s). The function used for this example is a resonant-like second order transfer function:

$$W_t(s) = K_t \frac{s^2 + 2n_w\omega_1 s + \omega_1^2}{s^2 + 2\zeta\omega_1 s + \omega_1^2}, \quad (8)$$

where $n_w = 1.4125$, $\zeta = 1.4125 \times 10^{-7}$ and $K_t = 10^{-1.2}$. Fig. 5 shows $W_t(s)$ in frequency domain.

As was mentioned before, admittance shaping and current tracking form a trade-off problem. For this reason, $W_y(s)$ and $W_t(s)$ are complementary weight's functions. Of main importance in this dual problem are frequencies around fundamental frequency ω_1 . Parameter n_w , in a complementary way in $W_y(s)$ and $W_t(s)$ weights, mark tracking control band (i.e., tracking performance), and therefore limits high performance admittance shaping. Notch width can be expanded if better tracking performance is desired. Note, however that this comes at the cost of a poorer input admittance emulation.

Finally, $W_u(s)$ weight is a zero-pole pair chosen to limit the band where control effort is desired:

$$W_u(s) = K_u \frac{(1/w_{u1})s + 1}{(1/w_{u2})s + 1}, \quad (9)$$

where w_{u1} is the frequency from which control effort starts to be limited (i.e., when control is not necessary, basically when W_y is less than 0 dB). The pole introduced at a high frequency w_{u2} makes $W_u(s)$ proper (necessary condition for used \mathcal{H}_∞ synthesis algorithm). The chosen parameters are $K_u = 10^{-6}$, $w_{u1} = 5100$ rad/s and $w_{u2} = 1.6 \times 10^{10}$ rad/s. Fig. 5 shows $W_u(s)$ in frequency domain.

B. Discrete time controller

Continuous plant $G(s)$ is modified in a way that it includes zero order hold (ZOH) and computational delay dynamics, both of which are convenient in any digital implementation.

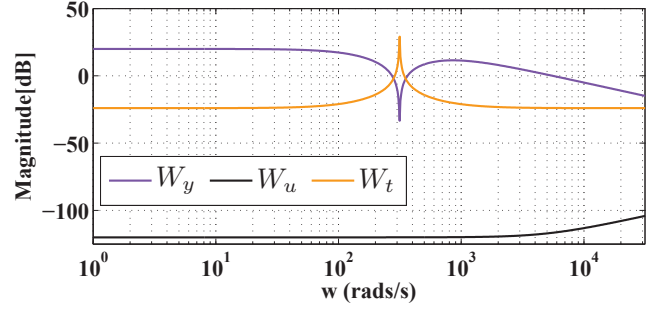


Fig. 5: Bode diagram of chosen weights

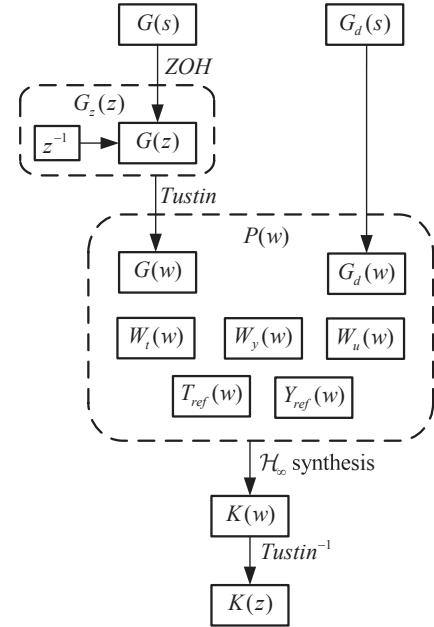


Fig. 6: Flux diagram of discretization process

Both elements will introduce phase changes (bigger as frequency increases) in the closed loop dynamics which must be taken into account in the controller design. In order to do so, continuous plant is first discretized through ZOH transformation $G(z)$. Then, discrete plant is modified so that it includes one computational delay z^{-1} , resulting in discrete plant $G_z(z)$. Discrete plant is again transformed to continuous through inverse Tustin transformation, obtaining plant $G(w)$, where w is the complex variable in continuous Tustin domain. Once reference models ($T_{ref}(w), Y_{ref}(w)$) and weighting functions ($W_u(w), W_y(w), W_t(w)$) are defined, continuous controller is obtained via \mathcal{H}_∞ synthesis. Finally, the continuous controller is discretized through Tustin transformation so that it can be implemented in a digital platform. Fig. 6 summarize followed procedure.

More close performance will be obtained between synthesized \mathcal{H}_∞ continuous controller and final discrete controller as sampling time period T_s is reduced. In addition to this, switching period T_{sw} of VSC's IGBTs determine commutation

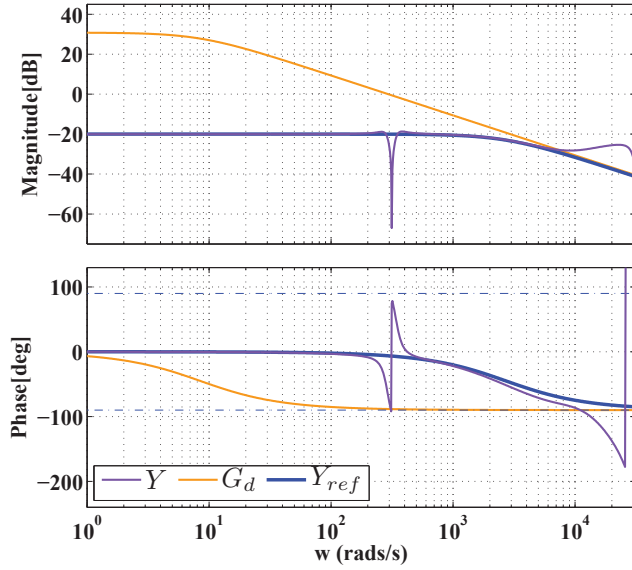


Fig. 7: Bode result of admittance shaping. Y_{ref} , Y and G_d are the desired closed loop input admittance, the obtained closed loop admittance and open loop admittance frequency response respectively. Good admittance shaping was obtained at desired frequencies, remaining passive positive real in almost all control band frequencies.

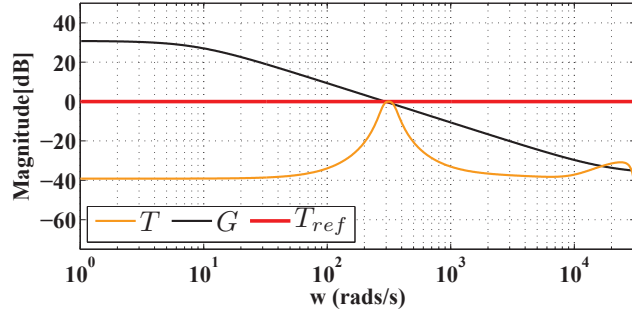


Fig. 8: Bode result of closed loop tracking. T_{ref} , T and G are the desired closed loop current tracking, obtained closed loop current tracking and open loop command-to-output transfer function frequency response respectively. Good current tracking was obtained only in frequencies nearby ω_1 as desired.

noise frequency of measured current $i(t)$. Taking these two facts into account, a sampling time $T_s = T_{sw}/4$ was chosen. Doing this, current samples are only obtained in the middle point of current commutation noise, resulting in a filtered current $i[k]$ for the controller feedback [21].

IV. RESULTS

A. Frequency analysis of the achieved controlled plant

This section presents frequency achieved results for current tracking and admittance shaping. Fig. 7 shows desired and obtained admittance magnitude and phase in frequency domain.

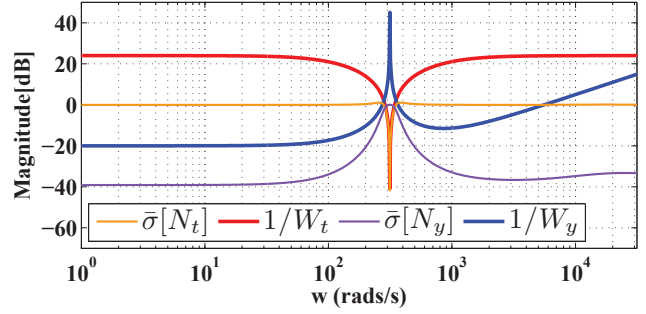


Fig. 9: Maximum singular values limitation of closed loop transfer functions N_t and N_y by the inverse of design weight W_t and W_y respectively: N_y is the transfer function from external inputs vector $w = [v_s \ i^*]^T$ to admittance shaping error e_y , meanwhile N_t is the transfer function from w to tracking error e_t .

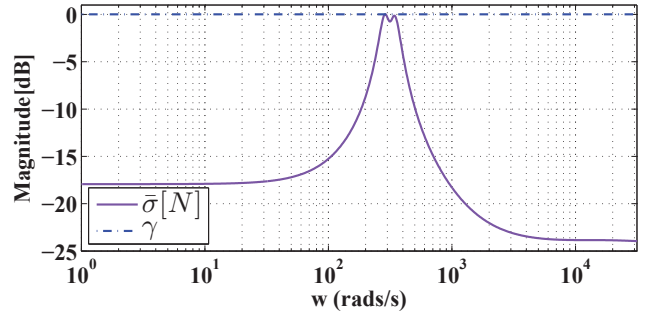


Fig. 10: Maximum singular values of closed loop transfer function N and obtained γ .

As it can be seen, obtained admittance is close enough to the desired one in low frequencies, remaining passive positive real in almost all control band frequencies. Fig. 8 depicts that obtained tracking transfer function $T(j\omega)$ is close to the desired one at frequencies nearby ω_1 as it was expected from designed weights. Fig. 9 shows how \mathcal{H}_∞ controller successfully limits $\bar{\sigma}(N_t)$ and $\bar{\sigma}(N_y)$ by means of W_t and W_y weights (where N_t and N_y are external inputs vector

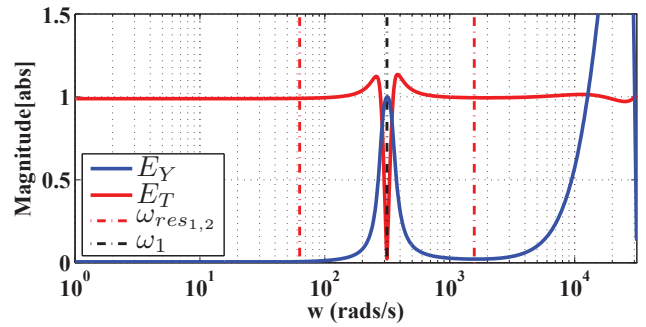


Fig. 11: Normalized tracking and admittance shaping error

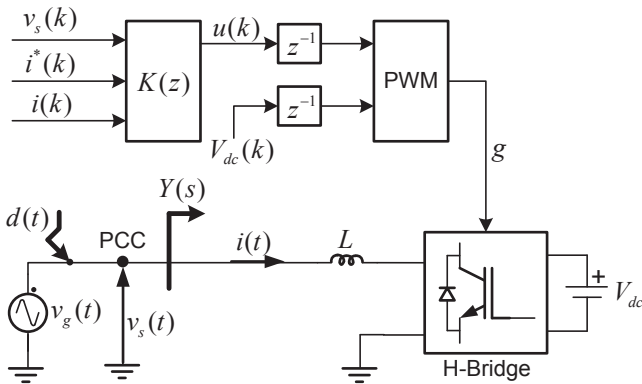


Fig. 12: Simulated test platform: Single phase H-bridge supplied by an ideal DC voltage V_{dc} , and connected to the grid through an L filter. Single phase grid is modelled as an ideal supply $v_g(t)$ that eventually suffer voltage disturbance $d(t)$.

w to tracking e_t and admittance e_y errors transfer functions respectively). Fig. 10 shows maximum singular values of closed loop transfer function N , with close to one $\gamma = 1.002$ abs.

To demonstrate the correct performance of the obtained controller two normalized error parameters E_Y and E_T are defined below:

$$E_Y = \frac{|Y_{ref}(j\omega) - Y(j\omega)|}{|Y_{ref}(j\omega)|} \quad (10)$$

$$E_T = \frac{|T_{ref}(j\omega) - T(j\omega)|}{|T_{ref}(j\omega)|} \quad (11)$$

Fig. 11 shows frequency results for both error parameters. As it can be seen, tracking error is low at ω_1 frequency, meanwhile successful admittance shaping is achieved at frequencies where W_y is big enough (mainly low frequencies).

Good stability margins were obtained [18], with a gain margin of $GM = 27.42$ dB and phase margin of $PM = 106.77$ deg.

B. Time domain simulated results

Fig. 12 shows simulated test platform, where grid voltage is set to $v_g(t) = 400 \cos(\omega_1 t)$ V, filter inductance is $L = 3.4$ mH with an associated resistance of $r_l = 28.8$ m Ω and H-Bridge inverter constant DC supply is $V_{dc} = 1000$ V. Simulated platform is tested under four different conditions:

- Test 1 (time range $t = [0, 0.08]$ s): A super-synchronous voltage disturbance $d(t) = 100 \cos(\omega_{res_1} t)$ V is introduced in the grid, where $\omega_{res_1} = 5\omega_1$ rad/s. According to desired admittance shaping, this disturbance should result in current increment of $i_y = 8.6 \cos(\omega_{res_1} t)$ A. Meanwhile, tracking current reference is set to zero.
- Test 2 (time range $t = [0.08, 0.4]$ s): A subsynchronous voltage disturbance $d(t) = 120 \cos(\omega_{res_2} t)$ V is introduced in the grid, where $\omega_{res_2} = 2\pi 10$ rad/s. According to desired admittance shaping, this

TABLE I: Simulation parameters

Simulation type	Continuous
Solver name	ode23tb (stiff/TR-BDF2)
Solver type	Variable-step
Max step size	6.1728 μ s
Relative tolerance	1×10^{-6}

disturbance should result in current increment of $i_y = 12 \cos(\omega_{res_2} t)$ A. Tracking current reference is again set to zero.

- Test 3 (time range $t = [0.4, 0.75]$ s): Voltage disturbance is set to $d(t) = 100 \cos(\omega_{res_2} t)$ V (resulting in a theoretical current increment of $i_y = 10 \cos(\omega_{res_2} t)$ A). A tracking current reference of $i^*(t) = 10 \cos(\omega_1 t)$ A is introduced to the controller.
- Test 4 (time range $t = [0.75, 1]$ s): Voltage disturbance is set to zero, meanwhile the tracking current change its phase and increment its value to $i^*(t) = 20 \cos(\omega_1 t - \pi/2)$ A.

H-Bridge uses unipolar PWM modulation with a switching period of $T_{sw} = 400$ μ s in order to inject the desired $u(t)$ voltage. The sample time is chosen to be $T_s = T_{sw}/4 = 100$ μ s so that commutation noise is filtered for the controller. Simulation results were obtained through MATLAB[®] SimPowerSystems. Table I shows used parameters.

Fig. 13 and Fig. 14 summarize time domain results, where $v_s[t]$ is the supply voltage; $i[k]$, $i_y[k]$ and $i_t[k]$ are the obtained current, admittance shaping expected current and tracking reference current in discrete time domain respectively; $u[k]$ is the actuation voltage and $i[t]$ is the obtained current in continuous time domain (commutation noise included).

V. CONCLUSION

New proposal based in \mathcal{H}_∞ controllers is presented in order to shape input admittance of power converters. The presented solution allows the designer to define the system dissipativity at the desired frequencies by means of phase and magnitude admittance references, so that stability criterion in electrical subsystem connections can be fulfilled. Controller design is a trade-off between tracking performance and admittance shaping, being possible both of them at different frequencies by means of using frequency weights. Simulated time and frequency results demonstrate good performance of the obtained controller, tested in a VSC-grid connection through an L-filter.

Obtained controller shows good stability margins, current tracking and admittance shaping. Furthermore, it is valid in discrete time domain and was simulated in a switching VSC, so is theoretically implementable in a digital platform. As controller was obtained from \mathcal{H}_∞ synthesis and its design strategy is general enough, it can handle a wide variety of other control specifications different from the presented ones in this paper (e.g., admittance shaping in a wide range or a specific frequency, better tracking performance with limited band admittance shaping, uncertainty modelling...).

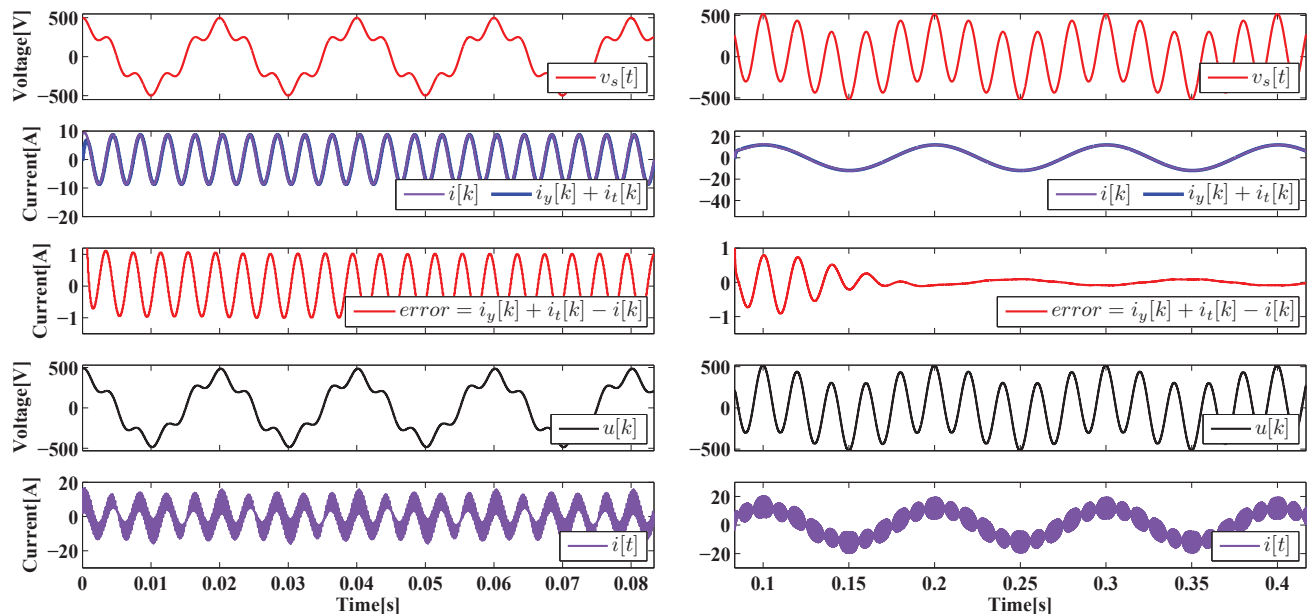


Fig. 13: Left column shows Test 1 results, that consists in a voltage disturbance of $d(t) = 100 \cos(\omega_{res1}t)$ V in the supply grid and a tracking current $i^*(t)$ set to zero. Supply voltage $v_s(t)$ is then perturbed with a super-synchronous resonance. Here, current reference is set to zero, so influence of current tracking on desired current $i_t(k) = 0$. Then, desired current only depends on admittance shaping influence $i_y = 8.6 \cos(\omega_{res1}t)$, represented in blue. Obtained current $i(k)$ is close to desired one in module, but a little phase shift result in *error* showed. Current noise in $i(t)$ is due to IGBTs commutation effect.

Right column shows Test 2 results, that consists in a voltage disturbance of $d(t) = 120 \cos(\omega_{res2}t)$ V in the supply grid and a tracking current $i^*(k)$ set to zero. Supply voltage $v_s(t)$ is then perturbed with a subsynchronous resonance. Again $i_t(k) = 0$, so desired current only depends on admittance shaping influence $i_y = 12 \cos(\omega_{res2}t)$ A. Obtained current $i(k)$ is close to desired one in module and phase.

Proposed controller has been tested in a single phase model without any outer loops, as phase-locked loop or DC-bus controller. As those outer loops affect system's final admittance [14], further studies have to be done in this direction.

ACKNOWLEDGMENT

This work was supported in part by Spanish Research Project ENE2011-28527-C04-02 (Ministerio de Economía y Competitividad). The work of Robert Griño was supported in part by the Spanish Research Project DPI2013-41224-P.

REFERENCES

- [1] S. Sudhoff, S. Glover, P. Lamm, D. Schmucker, and D. Delisle, "Admittance space stability analysis of power electronic systems," *Aerospace and Electronic Systems, IEEE Transactions on*, vol. 36, no. 3, pp. 965–973, 2000.
- [2] S. Sanchez, R. Ortega, R. Griño, G. Bergna, and M. Molinas, "Conditions for existence of equilibria of systems with constant power loads," *Circuits and systems, IEEE Transactions on*, 2014.
- [3] G. Pinares, T. Le, C. Breitholtz, and L. B. Tjernberg, "Analysis of the dc dynamics of vsc-hvdc systems using a frequency domain approach," in *IEEE PES Asia-Pacific Power and Energy Engineering Conference 2013*, 2013.
- [4] M. Jansson, A. Danielsson, J. Galic, K. Pietiläinen, and L. Harnefors, "Stable and passive traction drives," in *Proc. IEEE Nordic Power and Industrial Electronics Conf*, 2004.
- [5] M. Liserre, R. Teodorescu, and F. Blaabjerg, "Stability of grid-connected pv inverters with large grid impedance variation," in *Power Electronics Specialists Conference, 2004. PESC 04. 2004 IEEE 35th Annual*, vol. 6. IEEE, 2004, pp. 4773–4779.
- [6] —, "Stability of photovoltaic and wind turbine grid-connected inverters for a large set of grid impedance values," *Power Electronics, IEEE Transactions on*, vol. 21, no. 1, pp. 263–272, 2006.
- [7] S. Cobreces, E. Bueno, F. J. Rodriguez, F. Huerta, and P. Rodriguez, "Influence analysis of the effects of an inductive-resistive weak grid over l and lcl filter current hysteresis controllers," in *Power Electronics and Applications, 2007 European Conference on*. IEEE, 2007, pp. 1–10.
- [8] G. Liu, Y. Yang, P. Wang, W. Wang, and D. Xu, "Stability control method based on virtual inductance of grid-connected pv inverter under weak grid," in *Industrial Electronics Society, IECON 2013-39th Annual Conference of the IEEE*. IEEE, 2013, pp. 1867–1872.
- [9] L. Harnefors, "Analysis of subsynchronous torsional interaction with power electronic converters," *Power Systems, IEEE Transactions on*, vol. 22, no. 1, pp. 305–313, 2007.
- [10] M. Bongiorno, J. Svensson, and L. Angquist, "Single-phase vsc based ssc for subsynchronous resonance damping," *Power Delivery, IEEE Transactions on*, vol. 23, no. 3, pp. 1544–1552, 2008.
- [11] R. Middlebrook, "Input filter consideration in design and application of switching regulators," *IAS'76 Annual*, 1976.
- [12] B. D. O. Anderson and S. Vongpanitlerd, *Network Analysis and synthesis. A Modern Systems Theory Approach*. Dover Publications Inc., 2006.
- [13] J. C. Willems, "Dissipative dynamical systems part i: General theory," *Archive for rational mechanics and analysis*, vol. 45, pp. 321–351,

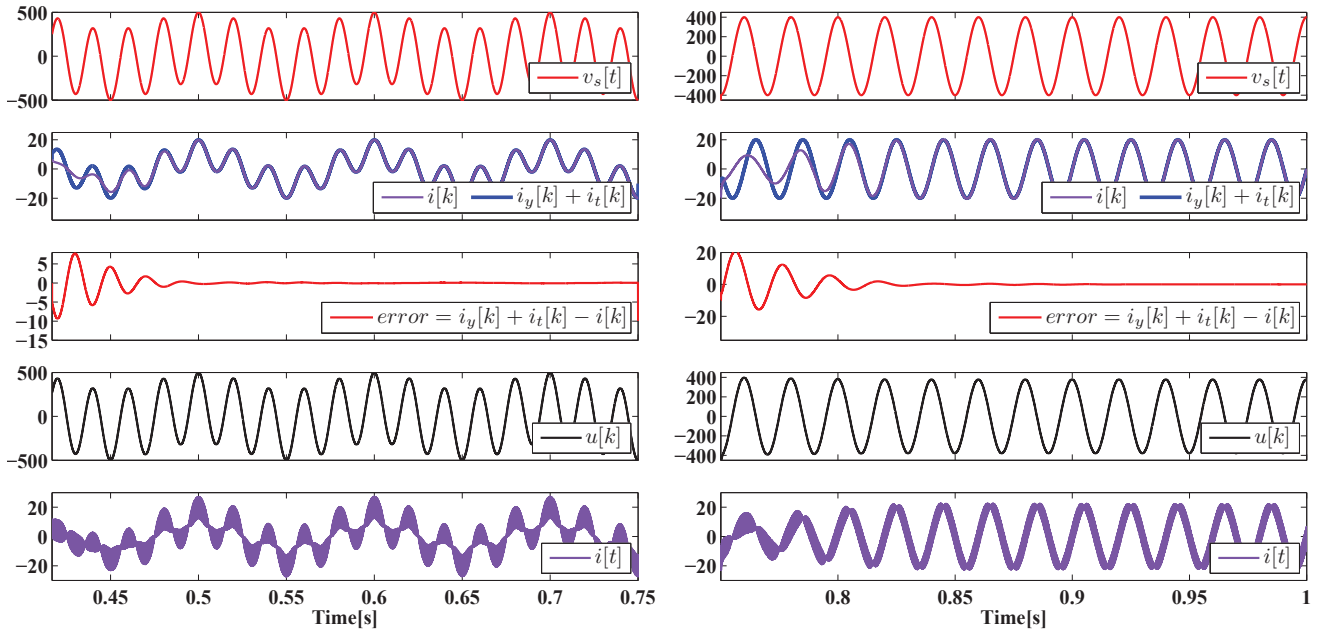


Fig. 14: Left column shows Test 3 results, that consists in a grid disturbance of $d(t) = 100 \cos(\omega_{res2}t)$ V in the supply grid and a tracking current $i^*(t) = 10 \cos(\omega_1 t)$ A. Supply voltage $v_s(t)$ is then perturbed with a subsynchronous resonance. Here, input admittance shaping $i_y = 10 \cos(\omega_{res2}t)$ A influence is added to current tracking $i_t(k) = i^*(k)$ influence on desired current representation. Obtained current $i(k)$ is close to desired one in module and phase, resulting in a minimum *error*

Right column shows Test 4 results, where no voltage disturbance in the supply grid was introduced, and tracking current change its phase and increment its value to $i^*(t) = 20 \cos(\omega_1 t - \pi/2)$ A. Supply voltage $v_s(t)$ is then equal to the nominal one $v_g(t)$, resulting in an admittance shaping influence $i_y = 0$ A in the desired current, meanwhile $i_t(k) = i^*(k)$ as always. This test demonstrate good tracking *error*, but with limited tracking response as expected.

1972.

- [14] L. Harnefors, M. Bongiorno, and S. Lundberg, "Input-admittance calculation and shaping for controlled voltage-source converters," *Industrial Electronics, IEEE Transactions on*, vol. 54, no. 6, pp. 3323–3334, 2007.
- [15] A. Emadi, "Modeling of power electronic loads in ac distribution systems using the generalized state-space averaging method," *Industrial Electronics, IEEE Transactions on*, vol. 51, no. 5, pp. 992–1000, 2004.
- [16] L. Harnefors, L. Zhang, and M. Bongiorno, "Frequency-domain passivity-based current controller design," *IET Power Electronics*, vol. 1, no. 4, pp. 455–465, 2008.
- [17] M. Cespedes and J. Sun, "Impedance shaping of three-phase grid-parallel voltage-source converters," in *Applied Power Electronics Conference and Exposition (APEC), 2012 Twenty-Seventh Annual IEEE*. IEEE, 2012, pp. 754–760.
- [18] S. Skogestad and I. Postlethwaite, *Multivariable Feedback Control*. John Wiley & Sons, 2005.
- [19] P. M. Anderson, B. L. Agrawal, and J. E. Van Ness, *Subsynchronous resonance in power systems*. Wiley.com, 1999, vol. 9.
- [20] P. Kundur, *Power system stability and control*. Tata McGraw-Hill Education, 1994.
- [21] F. Huerta Sánchez, "Aplicación de técnicas de identificación y control multivariable en convertidores en fuente de tensión conectados a la red eléctrica," Ph.D. dissertation, UNIVERSIDAD DE ALCALÁ Escuela Politécnica Superior, Alcalá de Henares (España), 2011.

\mathcal{H}_∞ simultaneous admittance and tracking current controller of three-phase active grid front-ends

Jorge Pérez, Santiago Cóbreces, Francisco Javier Rodríguez Sánchez

Department of Electronics
Alcala University
Email: jorge.perez@depeca.uah.es

Robert Griñó

Inst. of Industrial and Control Engineering.(IOC)
Universitat Politècnica de Catalunya (UPC)
Email: roberto.grino@upc.edu

Abstract—This paper proposes an \mathcal{H}_∞ current controller that allows power converter input admittance shaping, both in modulus and in phase, in a three phase voltage source converter to grid connection through an L filter. In addition to this new feature, controller allows grid current tracking. Proposed controller tries to solve then trade-off problem between stand-alone converter performance (current tracking) and its influence on global stability (admittance control) by an intuitive controller design. Time and frequency domain simulated results demonstrate the good performance of the proposed method.

I. INTRODUCTION

Controlled power electronic converters (PEC) offer a lot of advantages in electrical applications, as excellent load regulation, good transitory response and good fault tolerance. As a result of it, their presence as non-linear loads connected to the grid is increasing.

As the grid has an equivalent input impedance Z_g associated to it, interaction between the PEC based application and other electrical applications connected to the same point of common coupling (PCC) may occur. A common grid scenario is shown in Fig. 1. These interactions are not negligible as they may result in global system instability. Examples of applications with these stability problems are constant power loads [1] [2], flexible ac transmission system (FACTS) devices [3], power conversion for high voltage direct current (HVDC) transmission systems [4], distributed power generation systems (DPGSs) [5], machine drives for single-phase or three phases rail networks [6] etc.. Awareness of these issues is changing PEC's controllers design, limiting converter's stand-alone performance in favour of lower risk of global instability.

The nature of these stability issues is, in general, non linear. Even though some recent work analyse these stability problems from a non-linear point of view [2] [7], the study in an operation point, using linear approximation, is in many cases enough. PEC's input impedance/admittance receives a lot of attention on those linear stability analysis.

In [8], R. Middlebrook's linear impedance criterion established that the stability of two subsystem's connection (assuming that both are stand-alone stable) could be analysed with the open loop function $L = Z_g(s)Y_L(s)$ by means of classical LTI Nyquist criterion. Here $Z_g(s)$ and $Y_L(s)$ represent input impedance and input admittance of two different subsystems (corresponding with grid and equivalent load in Fig.1).

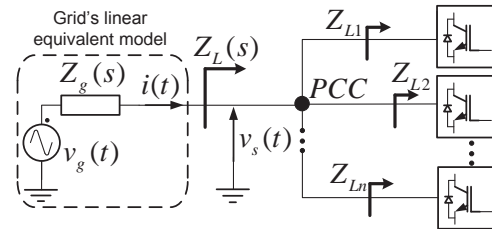


Fig. 1. Multiple power electronic converters based systems connected to the grid. As the grid input impedance Z_g is not zero, the PCC voltage v_s depends on the PCC right equivalent impedance Z_L . Then, other loads/converters connected to the grid may affect the stand-alone performance of the controlled converter under study.

Instabilities commonly start as a small oscillation in resonant frequencies of involved interacting subsystems [9]. Nearly ideal voltage and current regulation of controlled PECs may result in a non dissipative behaviour at some frequencies (i.e., PECs act as negative resistances [1]). Those small oscillation may be fed if non dissipative zones and global system resonant frequencies match, increasing the risk of global instability. If all PECs are dissipative in all frequencies the global system is stable, as the oscillation is damped. Although this is rarely the case, in [9] is demonstrated that dissipative behaviour of PECs at global resonant frequencies should be enough.

Admittance control allows, then, define system dissipativity and compliance of global stability criterion presented in [8]. This paper is focused on shaping (in frequency domain) the input admittance $Y_L(s)$ (transfer function from input supply $v_s(t)$ to input current $i(t)$, see Fig. 1). This concept has been previously studied in, among others, [6], [9], [10] and [11].

A systematic (sub)optimal \mathcal{H}_∞ controller design is presented, that allows good current tracking performance (common control objective in PECs-based applications) at some frequencies and input admittance shaping at others. As the controller is designed following a model-reference strategy, admittance shaping is achieved both in modulus and in phase. That is important, as dissipative behaviour is desired due to its positive influence on stability. Presented controller is a three phase extension of the one presented in [12].

The outline of this paper is as follows. Section II describe the considered system. Plant model is first obtained, and then research objectives are described. Section III summarizes \mathcal{H}_∞

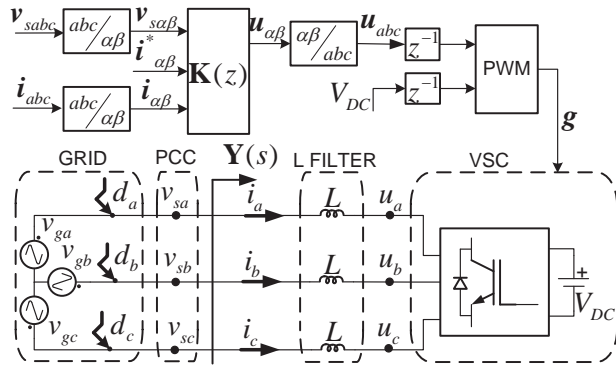


Fig. 2. Simulated test platform: VSC-grid series connection through an L filter. VSC is supplied by an ideal DC voltage V_{DC} . Grid is modelled as a nominal voltage v_g that eventually suffer from a voltage disturbance d : the PCC voltage v_s is the sum of both voltages.

controllers theory and applies it to admittance shaping. Section IV introduces the design of the \mathcal{H}_∞ discrete controller by solving an example design. Section V presents the obtained frequency and time domain results. Finally, Section VI winds up to the conclusion.

II. SYSTEM DESCRIPTION

A. Plant model

Fig. 2 shows the equivalent model for the plant to be controlled. It is formed by a series connection of an AC voltage supply with a voltage source converter (VSC) through an L filter. Three phase system is transformed to static power invariant $\alpha\beta$ reference frame for control purposes. In averaged terms, the system is described by the following state equation:

$$L \frac{d\mathbf{i}_{\alpha\beta}(t)}{dt} = \mathbf{v}_{s\alpha\beta} - r_l \mathbf{i}_{\alpha\beta}(t) - \mathbf{u}_{\alpha\beta}(t) \quad (1)$$

being $\mathbf{u}_{\alpha\beta}$, $\mathbf{i}_{\alpha\beta}$ and $\mathbf{v}_{s\alpha\beta}$ the averaged VSC output voltage along a switching period, grid current and PCC voltage equivalent $\alpha\beta$ vectors, and L and r_l the inductor and its equivalent resistance values.

$\alpha\beta$ axes allow current control even under unbalanced conditions. In this research, non-coupled $\alpha\beta$ axes were considered, so that each axis could be controlled independently and analogously. In this paper, non-bold signals refer to only one of the axes and bold signals refer to its equivalent $\alpha\beta$ vector (e.g., $i(t)$ may refer to either α or β grid current, being $\mathbf{i}_{\alpha\beta}(t)$ grid current equivalent $\alpha\beta$ vector). For simplicity in notation, transfer functions and frequency weights refer to its single-input-single-output (SISO) form. For both axes, diagonal matrix are defined (e.g., complete admittance transfer function $\mathbf{Y}(s) = \mathbf{I}_{2 \times 2} Y(s)$, where \mathbf{I} is the unitary matrix and $Y(s)$ is the SISO equivalent admittance). The grid current in Laplace domain is then:

$$\mathbf{I} = G(s) \cdot \mathbf{U} + G_d(s) \cdot \mathbf{V}_s, \quad (2)$$

where $G(s) = \frac{I}{U} = -\frac{1}{sL+r_l}$ and $G_d(s) = \frac{I}{V_s} = \frac{1}{sL+r_l}$ are the open-loop command-to-output and input admittance, respectively.

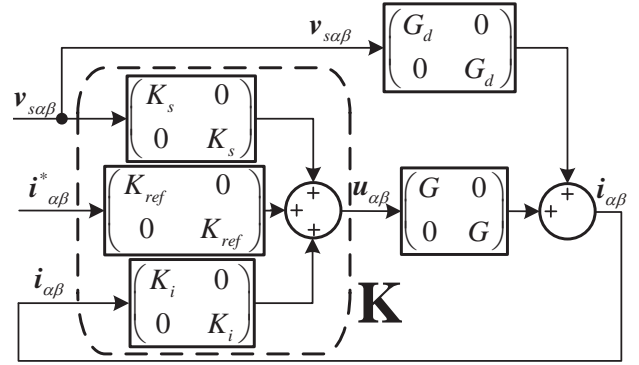


Fig. 3. Simplified control scheme for both $\alpha\beta$ axes. \mathbf{K} is a three-degrees of freedom controller formed by two feedforward gains (K_s and K_{ref}) and one feedback gain (K_i). G_d and G represent open loop input admittance and command-to-output transfer function, respectively.

B. Objectives

The objective is to find a controller $\mathbf{K}(s)$ that makes both tracking $T(s)$ and input admittance $Y(s)$ closed loop transfer function similar to given references $T_{ref}(s)$ and $Y_{ref}(s)$, respectively.

$T(s)$ relates obtained grid current $i(t)$ and its given control reference $i^*(t)$ (i.e., $T(s) = \frac{I}{I^*}$), so its shape gives information of current tracking performance (i.e., $T(s) = 1$ at a given frequency means perfect current tracking at this frequency). $Y(s)$ relates obtained grid current $i(t)$ and PCC voltage $v_s(t)$ (i.e., $Y(s) = \frac{I}{V_s}$), and it is of big importance in stability analysis of VSC-grid connections, as it was outlined in Section I. Note that fulfilling both objective at the same frequencies is not possible, as both impose conditions over output grid current. Then, dual objective is treated as a trade-off problem between admittance shaping (i.e., global stability) and tracking shaping (i.e., stand-alone performance), trying the former at both grid's sub and super-synchronous frequencies and the latter at grid's synchronous frequency ω_1 .

III. CONTROL STRUCTURE

Fig. 3 shows the equivalent simplified control scheme for both $\alpha\beta$ axes. Three-degrees of freedom current controller is chosen, that will use PCC voltage v_s and grid current i measurements, in addition to a grid current reference i^* , to fulfil dual control objective. Note that the grid PCC voltage is usually available at no extra cost as grid synchronisation algorithm use it. The resulting closed-loop controlled grid current, in Laplace domain is, then:

$$\mathbf{I} = \underbrace{\frac{GK_{ref}}{1 - GK_i}}_{T(s)} \mathbf{I}^* + \underbrace{\frac{GK_s + G_d}{1 - GK_i}}_{Y(s)} \mathbf{V}_s, \quad (3)$$

A. Basis of \mathcal{H}_∞ control

\mathcal{H}_∞ synthesis uses the generalised plant \mathbf{P} [13] defined below (see Fig. 4):

$$\begin{bmatrix} \mathbf{z} \\ \mathbf{v} \end{bmatrix} = \mathbf{P} \begin{bmatrix} \mathbf{w} \\ \mathbf{u} \end{bmatrix}, \quad (4)$$

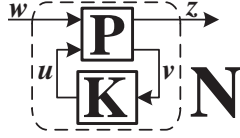


Fig. 4. Generalized plant P -based \mathcal{H}_∞ controller problem

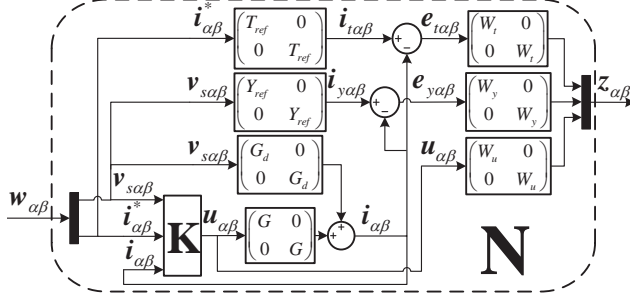


Fig. 5. Proposed signal based \mathcal{H}_∞ control to achieve admittance shaping and current tracking for both $\alpha\beta$ axes. This structure is only employed in the design process, in order to obtain the (sub)optimal controller that fits the imposed constraints.

where \mathbf{w} is the external input vector to the system, \mathbf{z} is the external output vector, \mathbf{u} is the controller actuation vector and \mathbf{v} is the measured output vector. A (sub)optimal \mathcal{H}_∞ controller \mathbf{K} will minimize, basing on the information obtained from \mathbf{v} , the infinity norm¹ of transfer function \mathbf{N} relating exogenous inputs vector \mathbf{w} to closed-loop outputs \mathbf{z} , until it is lower than a given limit (named γ):

$$\mathbf{z} = \mathbf{N}\mathbf{w} \quad \min_{\mathbf{K}} \|\mathbf{N}(\mathbf{K})\|_\infty \leq \gamma \quad (5)$$

B. Proposed control scheme

Fig. 5 shows proposed signal based \mathcal{H}_∞ control structure for both $\alpha\beta$ axes. Two reference transfer functions are added to the control scheme previously showed in Fig. 3: T_{ref} for tracking shaping and Y_{ref} for admittance shaping. Their outputs i_t and i_y represent tracking and admittance shaping reference currents, respectively. Measured current i is subtracted then from these two references, resulting in two shaping errors: e_t for tracking and e_y for admittance shaping error. Dual control objective may be solved now by minimizing this two errors. As both errors take into account the current sign, minimizing them means good shaping not only in modulus but also in phase. That means that system dissipativity can be achieved by defining an admittance reference that fulfil $-90^\circ \leq \angle Y_{ref} \leq 90^\circ$.

Tracking and admittance shaping are not possible at same frequency. As a result, dual objective is a trade-off problem that is solved by defining two frequency-weights: W_t for tracking shaping and W_y for admittance shaping. Increase

¹The infinity norm of a MIMO system $\mathbf{H}(s)$ in the frequency domain is defined as $\|\mathbf{H}(s)\|_\infty \triangleq \max_\omega \bar{\sigma}(\mathbf{H}(j\omega))$, where $\bar{\sigma}(\mathbf{H}(j\omega))$ are the maximum singular values of $\mathbf{H}(j\omega)$

some of these weights at a given frequency will reduce its corresponding error at this frequency. Designer can define, then, frequency ranges where one objective takes priority over the other. Additionally, an actuation weight is introduced to limit control effort u beyond the Nyquist frequency.

Output and input signal vectors of generalized plant P defined in Fig. 4 are then:

$$\mathbf{z} = \begin{bmatrix} W_t \cdot e_t \\ W_y \cdot e_y \\ W_u \cdot u \end{bmatrix} \quad \mathbf{v} = \begin{bmatrix} v_s \\ i^* \\ i \end{bmatrix} \quad \mathbf{w} = \begin{bmatrix} v_s \\ i^* \end{bmatrix} \quad \mathbf{u} = u \quad (6)$$

IV. CONTROLLER DESIGN

A. Reference model and frequency weight selection

Proposed \mathcal{H}_∞ controller structure is general enough to handle a wide variety of control objectives. As an example, in this research two objectives were considered:

- 1) Input admittance Y is desired to be similar to a resistive network $Y_{ref}(s) = 0.1 \Omega^{-1}$ at both sub and super-synchronous grid frequency ranges. Sub-synchronous admittance shaping takes priority over super-synchronous admittance shaping.
- 2) Grid current i should track a given reference i^* at synchronous grid frequency $\omega_1 = 2\pi 50$ rad/s. In order to do that a tracking transfer function $T_{ref}(s) = 1$ is defined.

Tracking shaping weigh $W_t(s)$ is designed in order to reduce tracking error only in a neighbourhood of grid fundamental frequency ω_1 . A resonant like second order transfer function is used for this purpose:

$$W_t(s) = K_t \frac{s^2 + 2n_w\omega_1 s + \omega_1^2}{s^2 + 2\zeta\omega_1 s + \omega_1^2}, \quad (7)$$

where K_t is the gain at low frequencies, n_w influences in notch width and relation n_w/ζ establishes the notch's peak gain (absolute value). The chosen parameters² are $n_w = 4.6528$, $\zeta = 4.6528 \times 10^{-11}$ and $K_t = 10^{-2}$. A narrow tracking bandwidth is pursued, limiting then tracking performance in benefit of wider range of admittance shaping.

Admittance shaping weight $W_y(s)$ is selected to allow sub and super-synchronous admittance emulation. A first order low pass filter with high low frequency gains and a limited control band is defined. Additionally, a notch is defined at synchronous frequency ω_1 , in order to not interact with tracking shaping frequency range. Chosen weight is presented below:

$$W_y(s) = K_y \frac{s^2 + 2\zeta\omega_1 s + \omega_1^2}{s^2 + 2n_w\omega_1 s + \omega_1^2} \frac{1}{(1/\omega_y)s + 1}, \quad (8)$$

where $n_w = 4.6528$, $\zeta = 4.6528 \times 10^{-11}$, $K_y = 3.1623$ and $\omega_y = 2\pi 200$ rad/s is the first order low pass filter crossover frequency.

Finally, $W_u(s)$ weight is a zero-pole pair chosen to limit the band where control effort is desired:

$$W_u(s) = K_u \frac{(1/w_{u1})s + 1}{(1/w_{u2})s + 1}, \quad (9)$$

²The weight's designing final parameters are obtained following an heuristic-based iterative process

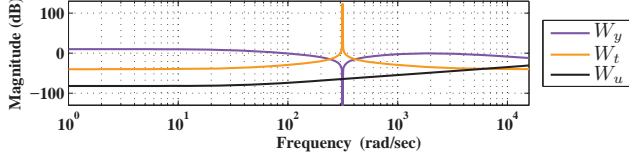


Fig. 6. Bode diagram of the chosen weights. Admittance shaping is desired at both sub and super-synchronous frequencies, where admittance weight (W_y) is bigger than tracking (W_t) and control effort (W_u) weights. At synchronous frequency, where tracking shaping is desired, W_t resonantly increases, and W_y decreases complementary. Finally W_u increases at high frequencies, in order to limit actuation beyond Nyquist frequency.

where w_{u1} is the frequency from which control effort starts to be limited. The pole introduced at a high frequency w_{u2} makes $W_u(s)$ proper (necessary condition for used \mathcal{H}_∞ synthesis algorithm). The chosen parameters are $K_u = 10^{-4.1}$, $w_{u1} = 43$ rad/s and $w_{u2} = 5.1 \times 10^6$ rad/s.

Fig. 6 shows chosen weights frequency domain representation.

B. Discrete-time controller implementation

To obtain discrete controller, this research follow the same method as the one presented in [12]. In it, a continuous controller $\mathbf{K}(s)$ is obtained from a phase shifted plant $G(s)$, that takes into account computational delay and ZOH (introduced by PWM modulation) phase effects. Then, discrete controller $\mathbf{K}(z)$ is obtained by Tustin transformation. Sampling time for this research is increased to $T_s = T_{sw}/2$, where T_{sw} is the switching period of the PWM modulation used for the converter. Samples are taken at peaks and valleys of carrier waveform, resulting in a filtered digital current $i[k]$ for the discrete controller feedback.

V. RESULTS

A. Frequency results

For the analysis of the controller performance, transfer functions shown below, derived from the structure shown in Fig. 5, will give a good insight feedback of the designing process accuracy:

$$\begin{aligned} F_y(s) &= F_{v_s \rightarrow e_y} = \frac{E_y}{V_s} = Y_{ref} - Y \\ F_t(s) &= F_{i^* \rightarrow e_t} = \frac{E_t}{I^*} = T_{ref} - T \\ F_u(s) &= \mathbf{F}_{\mathbf{w} \rightarrow u} = \begin{bmatrix} U & U \\ V_s & I^* \end{bmatrix}, \end{aligned} \quad (10)$$

where F_y and F_t give frequency-domain information of admittance and tracking shaping errors minimization, and so do F_u for control effort limitation. Generalized \mathcal{H}_∞ closed loop plant \mathbf{N} shown in Fig. 5 can be partitioned for controller performance analysis:

$$N_y = W_y F_y \quad N_t = W_t F_t \quad N_u = W_u F_u, \quad (11)$$

where N_y , N_t and N_u are the admittance, tracking and control effort partitioned \mathcal{H}_∞ closed loop functions. \mathcal{H}_∞ optimization

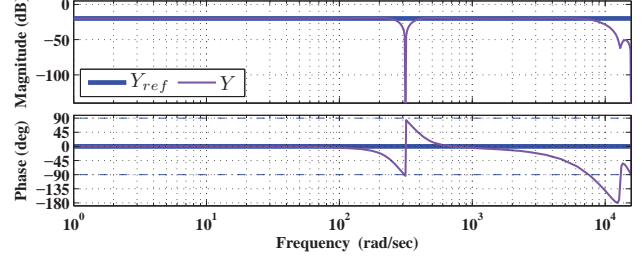


Fig. 7. Bode results of admittance shaping. Obtained closed loop input admittance Y is close to the desired one Y_{ref} at both sub and super-synchronous frequencies in modulus, with a frequency-increasing phase shift at super-synchronous frequencies. Input admittance remains passive positive real in almost all control band frequencies.

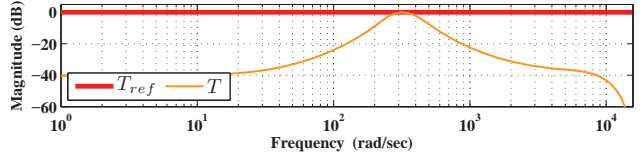


Fig. 8. Bode results of tracking shaping. Obtained closed loop tracking transfer function T is close to the desired one T_{ref} at synchronous frequency. A tracking bandwidth $B_{T(s)} = 165$ rad/s is obtained

algorithm will define then three constraints for eq. (10) transfer functions:

$$|F_t| \leq \frac{\|N_t\|_\infty}{W_t} \quad |F_y| \leq \frac{\|N_y\|_\infty}{W_y} \quad \bar{\sigma}(\mathbf{F}_u) \leq \frac{\|N_u\|_\infty}{W_u} \quad (12)$$

From a controller design point of view, that means that admittance and tracking shaping errors minimization, and control effort limitation don't depend only on its frequency weights W_x , but also on its frequency-domain closed loop function peak values $\|N_x\|_\infty$. Reduction of these peaks may be achieved by defining complementary weights (i.e., weights that don't interact with other weights' objectives at same frequency ranges).

Figs. 7 and 8 show admittance and tracking shaping obtained results. Fig. 9 shows shaping errors and control effort frequency-domain limitation. Finally, Fig. 10 shows admittance, tracking and control effort \mathcal{H}_∞ partitioned closed loop functions. Achieved frequency results fulfil defined objectives and \mathcal{H}_∞ constrains, being synchronous frequency range the most conflictive zone.

TABLE I. Simulation parameters

Solver name	ode23tb (stiff/TR-BDF2)				
Simulation type	Continuous	Solver type	Variable-step		
Relative tolerance	1×10^{-6}	Max step size	6.1728 μ s		
L	3.4 mH	r_l	28.8 m Ω	T_{sw}	400 μ s
V_{gll}	400 V	V_{DC}	1000 V	T_s	200 μ s

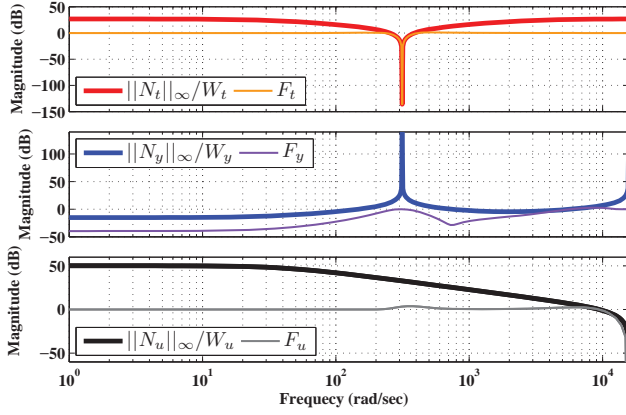


Fig. 9. Magnitude limitation of closed loop tracking shaping error F_t , closed loop admittance shaping error F_y (normalized to admittance reference modulus) and closed loop control effort F_u functions. F_t is reduced at synchronous frequency, and so do F_y at both sub and super-synchronous frequencies with a frequency-increasing error. F_u is limited at frequencies beyond Nyquist frequency

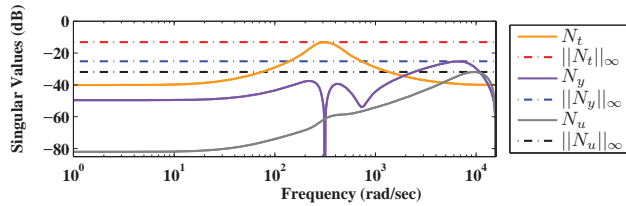


Fig. 10. Admittance N_y , tracking N_t and control effort N_u \mathcal{H}_∞ partitioned closed loop functions, and its corresponding peak values $\|N_x\|_\infty$. Attending to this results, it can be deduced that the obtained controller has more difficulties to fulfil given \mathcal{H}_∞ constraints at synchronous frequency.

B. Time results

Times results was obtained through simulation of test platform showed in Fig. 2. The VSC uses three phase PWM modulation in order to inject the desired actuation voltage $\mathbf{u}_{abc}(t)$. Simulation results were obtained through MATLAB[®] SimPowerSystems. Table I summarized used parameters, where V_{gll} is the effective line-to-line nominal grid voltage.

Fig. 11 shows time domain results. As admittance shaping is not desired at synchronous frequency ω_1 , a balanced disturbance $\mathbf{d}_{abc}(t)$ is introduced on the PCC for admittance shaping testing, at sub $\omega_{sub} = \omega_1/5$ or super-synchronous frequency $\omega_{sup} = 5\omega_1$. Therefore influence of this disturbance in expected current must be one tenth of its line-to-line value $D_{ll}(t)$, as $Y_{ref} = 0.1 \Omega^{-1}$ and power invariant $\alpha\beta$ transformation is used. Four different tests condition are simulated to demonstrate achievement of proposed objectives.

VI. CONCLUSION

This paper presents a novel technique to control power electronic converters input admittance. Proposed controller allows input admittance shaping not only in modulus but also in phase. Using it, the designer can define converter dissipativity, reducing risk of instability problems in electrical

subsystem interconnection with the grid. Controller is obtained from \mathcal{H}_∞ synthesis. Its design strategy is general enough to handle a wide variety of control specification.

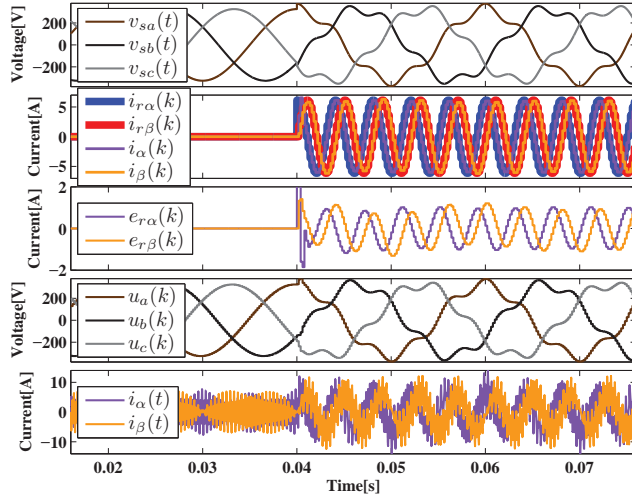
In this research, in addition to admittance shaping, current tracking is also considered as secondary control objective. Controller design is a trade-off between this two objectives, making impossible fulfil both at same frequencies. That can be easily handle by defining frequency weights transfer functions. Admittance shaping is desired at both sub and super-synchronous frequencies, meanwhile current tracking is desired in a narrow band centred at synchronous frequency. Simulated time and frequency results demonstrate good performance of the obtained controller, tested in a three phase VSC-grid connection through an L-filter.

ACKNOWLEDGMENT

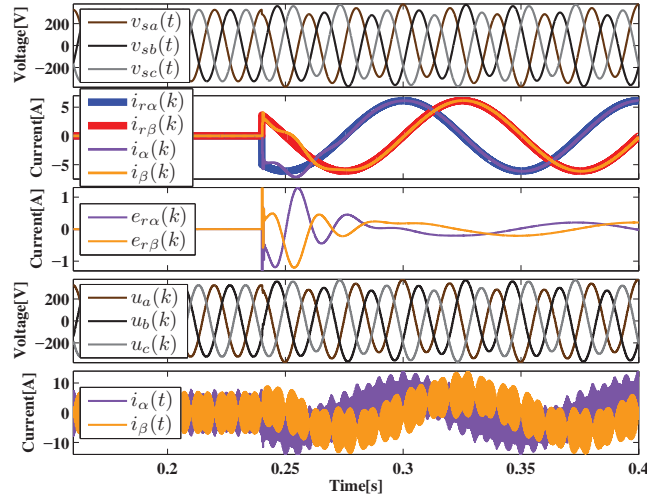
This work was supported in part by Spanish Research Project ENE2011-28527-C04-02 (Ministerio de Economía y Competitividad) and PRICAM: S2013/ICE-2933 (Consejería de educación, juventud y deporte de la Comunidad de Madrid). The work of Robert Griño was supported in part by the Spanish Research Project DPI2013-41224-P.

REFERENCES

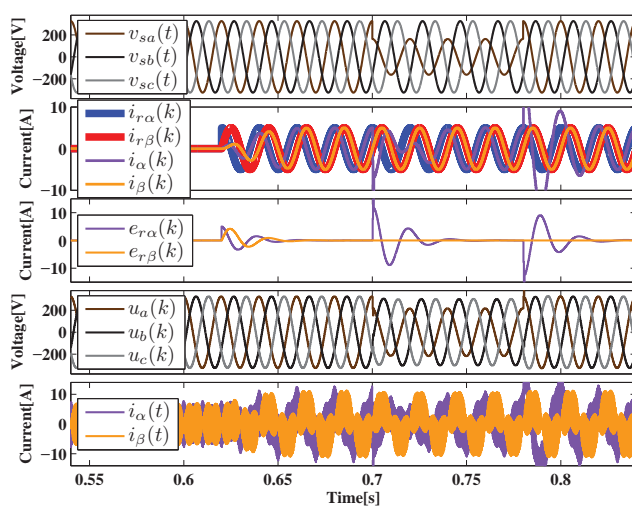
- [1] S. Sudhoff, S. Glover, P. Lamm, D. Schmucker, and D. Delisle, "Admittance space stability analysis of power electronic systems," *Aerospace and Electronic Systems, IEEE Transactions on*, vol. 36, no. 3, pp. 965–973, 2000.
- [2] S. Sanchez, R. Ortega, R. Griño, G. Bergna, and M. Molinas, "Conditions for existence of equilibria of systems with constant power loads," 2013.
- [3] M. Bongiorno, J. Svensson, and L. Angquist, "Single-phase vsc based sssc for subsynchronous resonance damping," *Power Delivery, IEEE Transactions on*, vol. 23, no. 3, pp. 1544–1552, 2008.
- [4] G. Pinares, T. Le, C. Breitholtz, and L. B. Tjernberg, "Analysis of the dc dynamics of vsc-hvdc systems using a frequency domain approach," in *IEEE PES Asia-Pacific Power and Energy Engineering Conference 2013*, 2013.
- [5] M. Liserre, R. Teodorescu, and F. Blaabjerg, "Stability of grid-connected pv inverters with large grid impedance variation," in *Power Electronics Specialists Conference, 2004. PESC 04. 2004 IEEE 35th Annual*, vol. 6. IEEE, 2004, pp. 4773–4779.
- [6] M. Jansson, A. Danielsson, J. Galic, K. Pietiläinen, and L. Harnefors, "Stable and passive traction drives," in *Proc. IEEE Nordic Power and Industrial Electronics Conf*, 2004.
- [7] C. Wan, M. Huang, C. K. Tse, S.-C. Wong, and X. Ruan, "Nonlinear behavior and instability in a three-phase boost rectifier connected to a nonideal power grid with an interacting load," *Power Electronics, IEEE Transactions on*, vol. 28, no. 7, pp. 3255–3265, 2013.
- [8] R. D. Middlebrook, "Input filter considerations in design and application of switching regulators," *IAS'76*, 1976.
- [9] L. Harnefors, M. Bongiorno, and S. Lundberg, "Input-admittance calculation and shaping for controlled voltage-source converters," *Industrial Electronics, IEEE Transactions on*, vol. 54, no. 6, pp. 3323–3334, 2007.
- [10] M. Cespedes and J. Sun, "Impedance shaping of three-phase grid-parallel voltage-source converters," in *Applied Power Electronics Conference and Exposition (APEC), 2012 Twenty-Seventh Annual IEEE*. IEEE, 2012, pp. 754–760.
- [11] D. Yang, X. Ruan, and H. Wu, "Impedance shaping of the grid-connected inverter with lcl filter to improve its adaptability to the weak grid condition," *IEEE Trans. Power Electron*, vol. 29, no. 11, pp. 5795–5805, 2014.
- [12] J. Perez, S. Cobrecas, and R. Grino, "Admittance-shaped hinf current controller for grid-connected vsc," in *Emerging Technology and Factory Automation (ETFA), 2014 IEEE*. IEEE, 2014, pp. 1–8.
- [13] S. Skogestad and I. Postlethwaite, *Multivariable Feedback Control*. John Wiley & Sons, 2005.



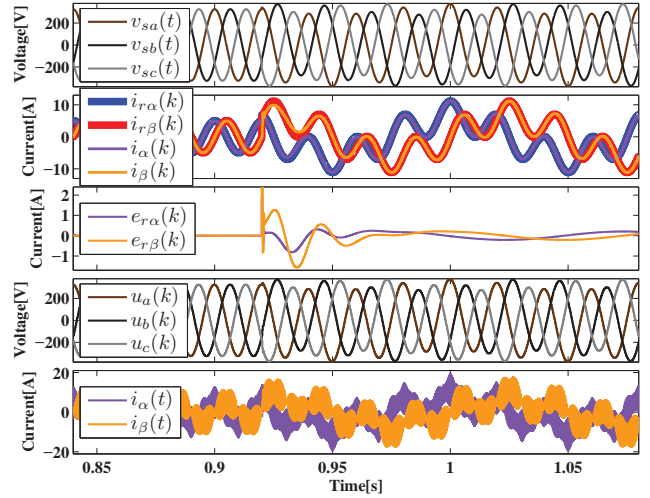
(a) Super-synchronous admittance shaping test: departing from an initial condition, where the PCC voltage $\mathbf{v}_{sabc}(t)$ is equal to the nominal grid voltage $\mathbf{v}_{gabc}(t)$ and the tracking current $\mathbf{i}_{\alpha\beta}^*(t)$ is set to zero, a balanced super-synchronous voltage disturbance $\mathbf{d}_{abc}(t)$ of 50 volts (i.e., $d_a(t) = 50 \cos(\omega_{sup}t)$ V for phase a) is added to the PCC. Then, desired current only depends on admittance shaping influence (i.e., $\mathbf{i}_{r\alpha\beta}(k) = \mathbf{i}_{y\alpha\beta}(k) = \mathbf{i}_{y\alpha\beta}(k)$). Obtained current $\mathbf{i}_{\alpha\beta}(k)$ is close to desired one in modulus, but a little phase shift is shown in total current error $\mathbf{e}_{r\alpha\beta}(k)$.



(b) Sub-synchronous admittance shaping test: departing from the same initial condition as Fig. 11(a), a balanced sub-synchronous voltage disturbance $\mathbf{d}_{abc}(t)$ of 50 volts (i.e., $d_a(t) = 50 \cos(\omega_{sub}t)$ V for phase a) is added to the PCC. Again, desired current only depends on admittance shaping influence (i.e., $\mathbf{i}_{r\alpha\beta}(k) = \mathbf{i}_{y\alpha\beta}(k) = \mathbf{i}_{y\alpha\beta}(k)$). Obtained current $\mathbf{i}_{\alpha\beta}(k)$ is close to desired one in modulus and phase with a minimum total error $\mathbf{e}_{r\alpha\beta}(k)$.



(c) Tracking shaping test: departing from the same initial condition as Fig. 11(a), balanced tracking references $i_{\alpha}^* = 5 \cos(\omega_1 t)$ and $i_{\beta}^* = 5 \cos(\omega_1 t - \pi/2)$ are introduced. After that, an unbalanced voltage dip is forced in the nominal grid, reducing phase $v_{s_a}(t)$ to a half. Since neither sub nor super-synchronous voltage disturbance are introduced, desired current $\mathbf{i}_{r\alpha\beta}(k)$ only depends on tracking shaping influence (i.e., $\mathbf{i}_{r\alpha\beta}(k) = \mathbf{i}_{t\alpha\beta}(k) = \mathbf{T}_{ref} \mathbf{i}_{\alpha\beta}^*(k)$ A). Obtained current $\mathbf{i}_{\alpha\beta}(k)$ is nearly equal to desired one in modulus and phase.



(d) Tracking and admittance shaping test: departing from an initial condition, where the PCC voltage $\mathbf{v}_{sabc}(t)$ is equal to the nominal grid voltage $\mathbf{v}_{gabc}(t)$ and tracking current references are set to $i_{\alpha}^* = 5 \cos(\omega_1 t)$ and $i_{\beta}^* = 5 \cos(\omega_1 t - \pi/2)$, a balanced sub-synchronous voltage disturbance $\mathbf{d}_{abc}(t)$ of 50 volts (i.e., $d_a(t) = 50 \cos(\omega_{sub}t)$ V for phase a) is added to the PCC. In this test then, desired current depends on both admittance and tracking shaping influence (i.e., $\mathbf{i}_{r\alpha\beta}(k) = \mathbf{i}_{y\alpha\beta}(k) + \mathbf{i}_{t\alpha\beta}(k) = \mathbf{Y}_{ref} \mathbf{d}_{\alpha\beta}(k) + \mathbf{T}_{ref} \mathbf{i}_{\alpha\beta}^*(k)$ A). Obtained current $\mathbf{i}_{\alpha\beta}(k)$ is close to desired one in modulus and phase, with minimum shown total error $\mathbf{e}_{r\alpha\beta}(k)$.

Fig. 11. Time domain results. $\mathbf{i}_{r\alpha\beta}(k)$ represents the desired current response (i.e., sum of admittance and tracking current references $\mathbf{i}_{y\alpha\beta}(k)$ and $\mathbf{i}_{t\alpha\beta}(k)$ shown in Fig. 5), meanwhile $\mathbf{e}_{r\alpha\beta}(k)$ represent the total error (i.e., sum of admittance and tracking shaping errors $\mathbf{e}_{y\alpha\beta}(k)$ and $\mathbf{e}_{t\alpha\beta}(k)$). No big control effort $\mathbf{u}_{abc}(k)$ overshoots are needed during the tests. Current noise in $\mathbf{i}_{\alpha\beta}(t)$ is due to IGBTs commutation effect. It can be reduced by means of increasing filter inductance value L , switching frequency f_{sw} or filter order (i.e., using an LC or an LCL filter).

Resonance damping of LCL filters via input admittance frequency shaping

Jorge Pérez, Santiago Cóbreces,
Daniel Pizarro, Francisco Javier Rodríguez Sánchez
Departamento de Electrónica
Universidad de Alcalá
Email: jorge.perez@depeca.uah.es

Robert Griño
Inst. of Industrial and Control Engineering.(IOC)
Universitat Politècnica de Catalunya (UPC)
Email: roberto.grino@upc.edu

Abstract—This paper presents a novel active damping technique of current-controlled grid-connected power converters through LCL filters. Based on \mathcal{H}_∞ synthesis algorithms, a grid current controller is obtained so that the grid-connected power converted-based application admittance resembles a given frequency reference. By defining a low resistive admittance as the reference, considered application resonance is effectively damped, reducing grid current oscillations under grid voltage variations and avoiding their associated stability problems. Presented grid current controller senses only the PCC grid voltage and current, and is experimentally tested in both time and frequency domains. Additionally, the effectiveness of presented damping method is proved under different grid impedance scenarios.

I. INTRODUCTION

Pulsewidth modulated (PWM) power electronic converters are usually connected to the grid through input filters in order to ensure low THD sinusoidally shaped grid currents [1]. Regarding grid current control applications, one of the most common topologies is the LCL filter [2], which has better filtering capability than simpler topologies as, for example, the L filter, but also increases control complexity [3]. That is due to the presence of two complex conjugate poles in the controlled plant, which resonantly increases its open-loop gain (i.e., its admittance value).

This resonance will generate current oscillations (at the resonant frequency) under changes in the system operating point (e.g., PCC voltage perturbations). These oscillations can be more or less durable over time and high in magnitude depending on how damped the resonance is. Moreover, they can become unstable in presence of non-dissipative closed-loop systems [4] and weak grids [5].

Damping techniques of resonant systems have received significant attention by the specialized literature. They can be sorted in two big groups; active damping [2], [3], [5]–[10], where the system controller is modified to damp the resonance, and passive damping [1], [11]–[14], where passive elements, commonly resistances, are added to the filter to displace the resonant poles. Passive damping is a simpler solution but comes at the cost of extra power loss and reduction of the high-frequency attenuation capability [13]. Active damping techniques overcome passive damping drawbacks, but its effectiveness, however, is limited by the switching frequency,

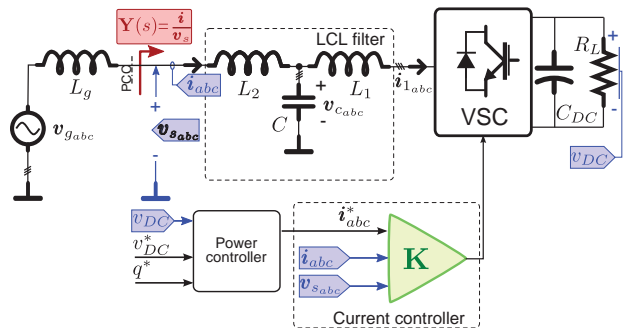


Fig. 1. One-line equivalent diagram of the considered system. In blue the measured variables, in green the current controller and in red the input admittance to be shaped.

and additional passive components may still be needed to damp high-frequency resonance [11].

This paper proposes a new active damping technique for grid-connected power electronic converters through LCL filters by directly shaping, in the frequency domain, the closed-loop input admittance of the considered application. A model-reference approach is adopted, where designer defines the desired admittance at the resonant frequency and an \mathcal{H}_∞ synthesis algorithm obtain the (sub)optimal controller that makes the closed-loop input admittance match the given reference [15]. The system resonance will be effectively damped, then, by defining a purely resistive admittance as the reference.

The rest of the paper is organized as follows. Section II models the plant of the considered application and introduce the resonant behaviour of the LCL filter. Section III develop the proposed system control, starting with the controller objectives and ending up with its design. Section IV discuss the results of the proposed controller, experimentally tested in both time and frequency domains. Additionally, it shows how robust the controller is, regarding both stand-alone stability and damping capability under different grid conditions. The paper ends with a brief discussion of its conclusions.

II. DYNAMIC MODELLING

This paper considers a grid current control of a shunt converter connected to the grid through an LCL filter (see

Fig. 1). The system is modelled in stationary (i.e., $\alpha\beta$) reference frame, which allows effective controller operation even under unbalanced conditions. Additionally, as $\alpha\beta$ axes are uncoupled, the original MIMO control problem is reduced to the control of two identical SISO problems. For the sake of notation simplicity, only one of the controlled channels is considered in this paper for both plant modelling and controller design.

Grid current i dynamic of considered system is represented in the Laplace domain as follows:

$$I(s) = G(s) \cdot U(s) + G_d(s) \cdot V_s(s), \quad (1)$$

where $I(s)$, $U(s)$ and $V_s(s)$ are the grid injected current, the VSC average output voltage and PCC voltage, respectively. Transfer functions $G(s)$ and $G_d(s)$ are the open loop command-to-output and input open loop admittance, respectively, which will follow the next dynamic expressions if an ideal PCC voltage (i.e., $L_g = 0$) is considered:

$$G(s) = -\frac{Z_c(s)}{Z_{L_1}(s) \cdot Z_c(s) + Z_{L_2}(s) \cdot (Z_{L_1}(s) + Z_c(s))}, \quad (2)$$

$$G_d(s) = \frac{Z_{L_1}(s) + Z_c(s)}{Z_{L_1}(s) \cdot Z_c(s) + Z_{L_2}(s) \cdot (Z_{L_1}(s) + Z_c(s))}, \quad (3)$$

where $Z_c(s) = 1/(sC)$, $Z_{L_1}(s) = sL_1 + R_1$ and $Z_{L_2}(s) = sL_2 + R_2$ are the capacitor, converter-side coil and grid-side coil impedances, respectively.

Both $G(s)$ and $G_d(s)$ have a pair of complex conjugate poles which will produce an increase of their respective gains at the resonance frequency $\omega_{res} = \sqrt{(L_1 + L_2)/(L_1 \cdot L_2 \cdot C)}$ rad/s. Of main importance in the stability of the considered application is the resonance in $G_d(s)$ (refer to Fig. 7 to see its frequency domain representation), as it may cause high current oscillations and even system instability under PCC voltage changes. That problem is increased if the system is connected to a weak grid (i.e., with high grid impedance) [5]. The resonance must be properly damped in order to assure the correct and robust operation of the system.

III. SYSTEM CONTROL

A. Control objectives

The main objective of this paper is the design of a grid current controller that, in addition to track a given reference i^* , can effectively damp the system resonance. In order to do so, this paper proposes the frequency shaping of two closed loop transfer function, tracking transfer function $T(s)$ and closed-loop admittance $Y(s)$, which relate the grid current reference i^* and the PCC voltage v_s to the obtained grid current, respectively.

Fig. 1 shows, in green, the integration of the proposed controller \mathbf{K} in the system. It has three inputs: the measured PCC voltage v_s , the sensed grid current i and its corresponding reference i^* . Even though the controller is obtained as a MIMO system in the synthesis process, is interesting to divide its transfer matrix in rows: $\mathbf{K}(s) = [K_s \quad K_{ref} \quad K_i]^T$. Controller actuation u dynamic can be expressed in the Laplace

domain as follows:

$$U(s) = K_s(s) \cdot V_s(s) + K_{ref}(s) \cdot I^*(s) + K_i(s) \cdot I(s). \quad (4)$$

Substituting expressions (4), (2) and (3) in (1) gives the closed loop grid current dynamic in the Laplace domain:

$$I = \underbrace{(1 - GK_i)^{-1} GK_{ref}}_{T(s)} I^* + \underbrace{(1 - GK_i)^{-1} (G_d + GK_s)}_{Y(s)} V_s, \quad (5)$$

where (stand-alone) system stability depends only on the system open-loop transfer function $L = -GK_i$.

The controller design follows a model-reference approach; that is, a controller $\mathbf{K}(s)$ is obtained in order to make the closed-loop transfer functions $Y(s)$ and $T(s)$ resemble two given model references, $Y_{ref}(s)$ and $T_{ref}(s)$. By defining a plain low admittance reference at the system resonance frequency, oscillations can be effectively damped and, as a result, derived stability problems are avoided.

As it is shown in Fig. 1, grid current reference i^* is generated by an outer loop power controller, whose objective may be, for example, maintain the DC-bus voltage v_{DC} equal to a given reference v_{DC}^* even under changes of the load R_L (i.e., the system acts as an active rectifier) [16]. Its design is out of the scope of this work, which is centred in the inner current controller design.

B. Controller design

Controller $\mathbf{K}(s)$ is obtained through an \mathcal{H}_∞ synthesis algorithm, whose input is the generalized plant \mathbf{P} [17]. It is just a virtual MIMO plant with the structure showed below:

$$\begin{bmatrix} z \\ v \end{bmatrix} = \mathbf{P} \begin{bmatrix} w \\ u \end{bmatrix}, \quad (6)$$

where w is called the exogenous inputs vector to the system, z is the so-called output error signals, u is the actuation vector that will be computed for the controller and v is the measurements output vector.

\mathcal{H}_∞ synthesis process will compute a (sub)optimal controller \mathbf{K} , which minimizes the infinity norm¹ of the closed-loop system \mathbf{N} that results from the feedback interconnection of \mathbf{P} and \mathbf{K} , and relates exogenous input vector w and error vector $z = \mathbf{N}w$:

$$\min_{\mathbf{K}} \|\mathbf{N}(\mathbf{K})\|_\infty = \min_{\mathbf{K}} \frac{\|z\|_2}{\|w\|_2} \leq \gamma \quad (7)$$

Fig. 2 shows the considered virtual plant \mathbf{P} (in red) used for obtaining the controller \mathbf{K} (in blue) and the resulting closed-loop system \mathbf{N} . \mathbf{P} is formed by the open-loop plants G and G_d (in orange) and a set of added elements only necessary for the synthesis process (in purple) which are explained below.

$T_{ref}(s)$ and $Y_{ref}(s)$ are the desired (reference model) tracking and admittance transfer functions. Their outputs, i_t and i_y ,

¹The infinity norm of a MIMO system $\mathbf{H}(s)$ in the frequency domain is defined as $\|\mathbf{H}(s)\|_\infty \triangleq \sup_\omega \bar{\sigma}(\mathbf{H}(j\omega))$, where $\bar{\sigma}(\mathbf{H}(j\omega))$ is the maximum singular value of $\mathbf{H}(j\omega)$. For SISO systems that is simplified to $\|H(s)\|_\infty \triangleq \sup_\omega |H(j\omega)|$

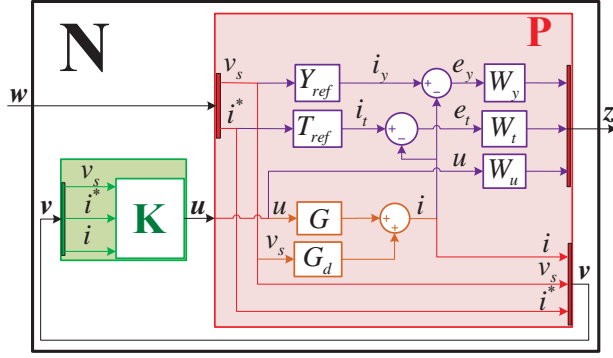


Fig. 2. Structure used for the \mathcal{H}_∞ synthesis. In red the generalized plant $\mathbf{P}(s)$. Wrapped inside of it, in orange the open loop plant $G(s)$ and open loop admittance $G_d(s)$, and in purple the references and weights added for the synthesis. Finally, the obtained controller is represented in green.

mark the reference currents due to tracking and admittance control effects, respectively. Grid current i is subtracted from both reference currents, giving two different errors: e_t for tracking and e_y for admittance control. Both controller objectives (i.e., admittance and tracking shaping) can be achieved by means of minimizing these two errors. But, as both errors depend on the grid current, they can not be minimized at the same frequencies (i.e., i can not be equal to both i_t and i_y at the same frequency). Additionally, control bandwidth must be limited by means of control effort u minimization. To handle this trade-off, three frequency-weights ($W_t(s)$, $W_y(s)$ and $W_u(s)$ respectively) multiplies each signals. Output and input signal vectors of generalized plant \mathbf{P} defined in Fig. 2 are then:

$$\mathbf{z} = \begin{bmatrix} W_t \cdot e_t \\ W_y \cdot e_y \\ W_u \cdot u \end{bmatrix} \quad \mathbf{v} = \begin{bmatrix} v_s \\ i^* \\ i \end{bmatrix} \quad \mathbf{w} = \begin{bmatrix} v_s \\ i^* \end{bmatrix} \quad \mathbf{u} = u \quad (8)$$

As synthesized controller \mathbf{K} should minimize \mathbf{z} , increasing one weight at a given frequency (while setting the other two relatively low) should result in the minimization of its input at that frequency. Following this design criterion, and given the controller objectives stated in the previous subsection, suitable frequency-weights are represented in Fig. 3. As it is shown, tracking of current reference i^* is only desired at the grid fundamental frequency, 60 Hz in this application, meanwhile admittance shaping is desired, mainly, at super-synchronous frequencies, which is the location of the LCL-filter resonance (a sub-synchronous admittance shaping is also considered to damp possible low frequency grid oscillation). Finally, control bandwidth is limited at high frequencies.

Laplace expressions of the selected weights are showed below:

$$W_t(s) = K_t \frac{s^2 + 2\zeta_n \omega_1 s + \omega_1^2}{s^2 + 2\zeta_d \omega_1 s + \omega_1^2}, \quad (9)$$

where K_t is the initial tracking gain, ω_1 is the fundamental frequency in rad/s and ζ_d and ζ_n will define both maximum

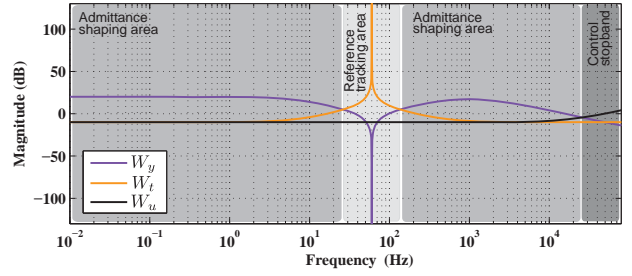


Fig. 3. Magnitude of the selected weights in the frequency domain. The frequency spectrum is divided in areas according to the controller objective in that range.

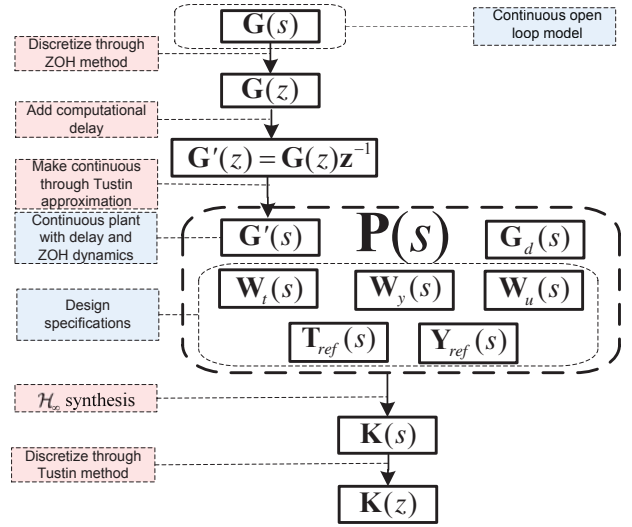


Fig. 4. Flux diagram of the inner controller \mathbf{K} synthesis and discretization process

gain peak and width of the weight resonance;

$$W_y(s) = K_y \frac{s^2 + 2\zeta_d \omega_1 s + \omega_1^2}{s^2 + 2\zeta_n \omega_1 s + \omega_1^2} \cdot \frac{1}{(1/\omega_y)s + 1} \quad (10)$$

where an initial weight $K_y > K_t$ is defined, ζ_d and ζ_n change positions to define a complementary notch to the tracking weight resonance and an additional pole is defined at high frequency ω_y to delimit the admittance shaping region;

$$W_u(s) = K_u \frac{(1/\omega_{u1})s + 1}{(1/\omega_{u2})s + 1}, \quad (11)$$

where a zero in the frequency ω_{u1} will increase the initial low actuation weight K_u , and a pole at very high frequency ω_{u2} is added just to fulfil \mathcal{H}_∞ synthesizing method requirements.

As for the reference model, a tracking reference $T_{ref} = 1$ is set, which will result in perfect current tracking at fundamental frequency (i.e., $I(j\omega_1) \approx I^*(j\omega_1)$), meanwhile a low resistive admittance of $Y_{ref} = 0.1 \Omega^{-1}$ is considered, which will result in a properly damped LCL resonance.

Synthesized controller $\mathbf{K}(s)$ is obtained in Laplace continuous domain. In order to be implemented in a digital platform,



Fig. 5. Picture of experimental set-up.

TABLE I. EXPERIMENTAL SETUP PARAMETERS

S_n	17.5 kVA	L_1	3.4 mH
V_g	120 V	R_1	28.8 m Ω
ω_1	$2\pi 60$ rads $^{-1}$	L_2	1.7 mH
V_{DC}^*	700 V	R_2	18.6 m Ω
T_{sw}	400 μ s	C	18 μ F
T_s	200 μ s	C_{DC}	4.7 mF

it must be previously discretized. The discretization process is summed up in Fig. 4. It is important to point out that the obtained controller, and then the close-loop admittance, takes into account the phase lag introduced by both PWM modulation and computational delay. For more information about the discretization process or the admittance and tracking shaping of power converters refer to [15].

IV. RESULTS

Proposed algorithm has been tested in both simulations and an experimental set-up. The latter consist of an AC programmable power supply Pacific SmartSource 345-AMX, emulating the grid, and a 17.5 kVA two-level VSC connected to it through an LCL filter. Passive loads R_L are connected to the DC-side to test the platform under different operating points. Control algorithm is implemented on a Texas Instruments DSP TMS320DSK6713. Table I sums up set-up parameters, where T_s is the sampling period of the control algorithm and T_{sw} is the converter's IGBTs switching period. A picture of the experimental set-up is shown in Fig. 5.

A. Frequency domain results

Fig. 6 shows theoretical tracking transfer function T (obtained following (5)), which is equal to its reference T_{ref} at the fundamental frequency, as was specified in the design process. Fig. 7 shows the admittance shaping results. Theoretical admittance Y is equal to the given reference Y_{ref} at both sub and super-synchronous frequencies as it was specified.

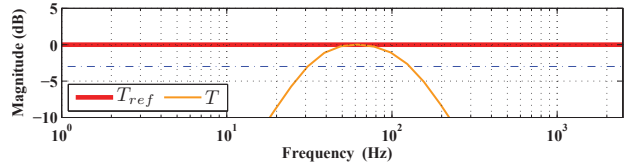


Fig. 6. Obtained tracking transfer function T and its reference T_{ref} .

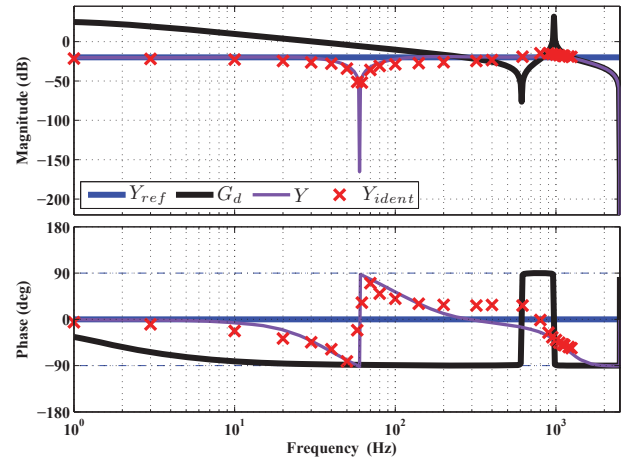


Fig. 7. Admittance frequency results. Open-loop admittance G_d is shown in black. Admittance reference model Y_{ref} is shown on blue color. The closed loop synthesised admittance (theoretical) Y is shown on purple. Red crosses show the experimentally measured admittance Y_{ident} .

Y_{ident} is an experimental admittance measurement obtained by adding a three phase controlled sinusoidal signal to the voltage generated by the AC power supply and analysing, in steady-state, the current response of the converter at that frequency. Of main importance is the resonance frequency of G_d , where more points of Y_{ident} are taken, which proves the good active damping capabilities of the proposed method.

B. System robustness

Fig. 8 shows the obtained system sensitivity function $S = (1 - GK_i)^{-1}$. Its infinity norm $\|S\|_\infty$ is a good inverse indicator of the design stand-alone robustness [17], that is, how much plant parameters may change until the designed system becomes unstable. A commonly design criterion for robust controller is to synthesize loops with $\|S\|_\infty < 6$ dB, which will assure a gain margin bigger than 6 dB and a phase margin bigger than 30° . This criterion is fulfilled, as it can be seen in Fig. 8, which proves the design robustness.

The effects of grid impedance on the presented active damping technique are tested below. Considering a non-ideal inductance L_g at the PCC, the grid current is modified as follows:

$$I(s) = G'(s) \cdot U(s) + G'_d(s) \cdot V_g(s), \quad (12)$$

where $V_g(s) = V_s(s) + Z_g(s) \cdot I(s)$ is the grid voltage, the grid impedance is considered purely inductive $Z_g(s) = s \cdot L_g$

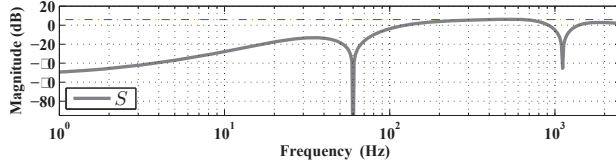


Fig. 8. Obtained sensitivity function S . Blue dash-dotted line marks the accepted 6 dB sensitivity gain limit for robust systems.

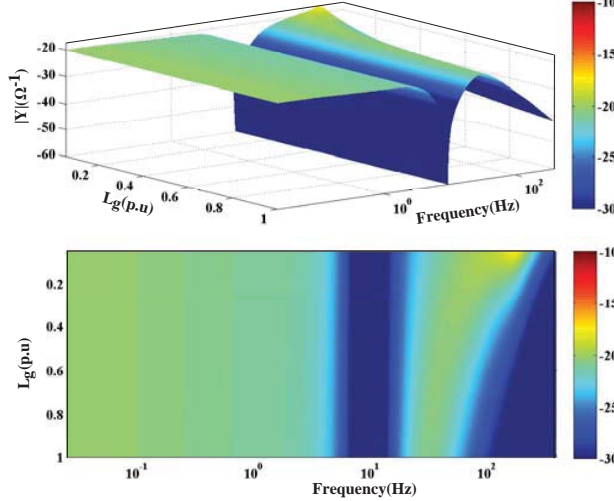


Fig. 9. Effect of modifying the grid inductance L_g on the obtained close loop admittance modulus $|Y'(s)|$.

and

$$G'(s) = -\frac{Z_c(s)}{Z_{L1}(s) \cdot Z_c(s) + (Z_g(s) + Z_{L2}(s)) \cdot (Z_{L1}(s) + Z_c(s))}, \quad (13)$$

$$G'_d(s) = \frac{Z_{L1}(s) + Z_c(s)}{Z_{L1}(s) \cdot Z_c(s) + (Z_g(s) + Z_{L2}(s)) \cdot (Z_{L1}(s) + Z_c(s))} \quad (14)$$

are the new open loop transfer functions.

Substituting expressions (4), (13) and (14) in (12) gives the new closed loop input admittance $Y'(s)$ seen from the grid voltage V_g :

$$Y'(s) = \frac{I(s)}{V_g(s)} = \frac{Y(s)}{1 + Y(s) \cdot Z_g(s)} \quad (15)$$

where $Y(s)$ is the converter input admittance given by eq. (5). Fig. 9 shows closed loop input admittance modulus $|Y'(s)|$ in the frequency domain under changes of the grid inductance $L_g \in [0.05, 1]$ p.u.². Presented damping technique is effective even under high grid inductances (i.e., weak grids), as it is shown in the minimum modulus increase over the given admittance reference of $0.1 \Omega^{-1}$.

C. Time domain results

Fig. 10 shows experimental time domain evolution of the system after the introduction of a DC-load of 4.2 kW. Fig.

² L_g is expressed in per unit values of the converter nominal impedance $Z_n = (\sqrt{3}V_g)^2/S_n$.

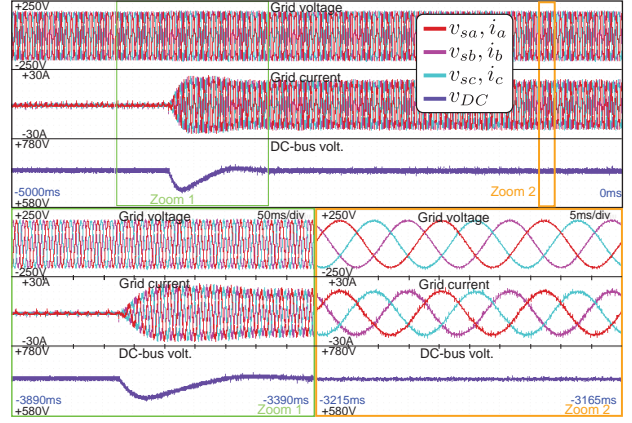


Fig. 10. Connection of a 4.2 kW DC-load with a null reactive reference. Top shows the complete transient. Zoom 1 focuses on the currents and DC-voltage evolution after the connection. Zoom 2 shows grid currents and voltages in steady-state.

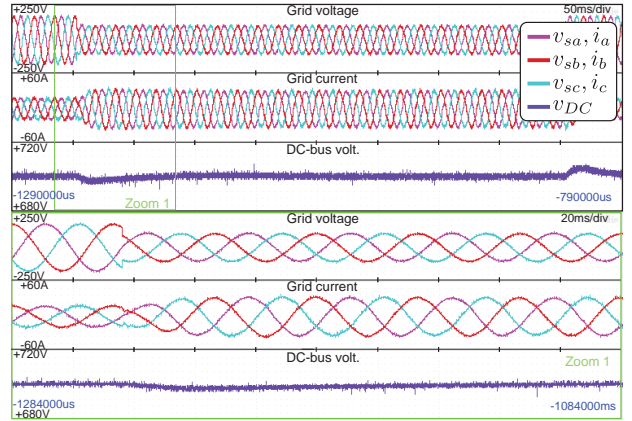


Fig. 11. Response under grid balanced voltage dip when DC-bus is loaded with 4.2 kW. All phases fall to 60% of its value keeping their phase untouched. Top view shows the complete transient in grid voltages, currents and DC-bus voltage. Lower view focuses on the dip initial edge.

11 shows the response of the system under a balanced dip of 60% of the nominal grid voltage value. Both experiments show good current tracking performance. Of main importance is the current response under the grid dip: as can be seen, no oscillation at frequency ω_{res} can be appreciated on it, which proves again the good obtained resonance damping.

V. CONCLUSION

This work presents a novel active damping technique for current-controlled grid-connected power converters through resonance filters like the LCL. Resonance damping will result in smaller current oscillations under PCC voltage variations and, as a consequence, will improve system stability in connection to weak grids.

Presented active damping technique is based on frequency shaping of the closed-loop input admittance of the considered application, and only needs grid current and grid voltage mea-

surements (i.e., no additional LCL filter sensors are needed). This is achieved by a model-reference approach, where, after designer specifies a desired admittance reference, an \mathcal{H}_∞ synthesis algorithm will obtain the (sub)-optimal controller that shapes the system admittance, in the frequency domain, to follow the given reference. By defining a resistive admittance reference the resonance can be effectively damped, and related stability problems are avoided. Current control design to achieve this goal is explained.

Experimental test of the obtained controller are done and their results are shown. Proposed method shows good current tracking and resonance damping capabilities. The latter is proved experimentally in both frequency and time domains. Moreover, damping technique is demonstrated (theoretically) effective even under extremely high grid impedance, with both good phase and gain margins.

Future works will study the resonance damping and stability robustness under filter and grid modelling uncertainties, and how they are affected by the addition of different control measurements (like filter capacitor voltage or converter side current).

ACKNOWLEDGEMENT

This work of the University of Alcalá group was supported in part by the Universidad de Alcalá research project DIANA (CCG2015/EXP-064), the spanish research projects COMPOSITE (ENE2014-57760-C2-2-R Ministerio de Economía y Competitividad) and PRICAM (S2013/ICE-2933 Consejería de educación, juventud y deporte de la Comunidad de Madrid). The work of Robert Griño was supported in part by the Spanish Research Project DPI2013-41224-P.

REFERENCES

- [1] T. Nussbaumer, M. L. Heldwein, and J. W. Kolar, "Differential mode input filter design for a three-phase buck-type pwm rectifier based on modeling of the emc test receiver," *Industrial Electronics, IEEE Transactions on*, vol. 53, no. 5, pp. 1649–1661, 2006.
- [2] J. He and Y. W. Li, "Generalized closed-loop control schemes with embedded virtual impedances for voltage source converters with lc or lcl filters," *Power Electronics, IEEE Transactions on*, vol. 27, no. 4, pp. 1850–1861, 2012.
- [3] S. G. Parker, B. P. McGrath, and D. G. Holmes, "Regions of active damping control for lcl filters," *Industry Applications, IEEE Transactions on*, vol. 50, no. 1, pp. 424–432, 2014.
- [4] L. Harnefors, L. Zhang, and M. Bongiorno, "Frequency-domain passivity-based current controller design," *IET Power Electronics*, vol. 1, no. 4, pp. 455–465, 2008.
- [5] M. Liserre, R. Teodorescu, and F. Blaabjerg, "Stability of photovoltaic and wind turbine grid-connected inverters for a large set of grid impedance values," *Power Electronics, IEEE Transactions on*, vol. 21, no. 1, pp. 263–272, 2006.
- [6] M. Liserre, A. D. Aquila, and F. Blaabjerg, "Genetic algorithm-based design of the active damping for an lcl-filter three-phase active rectifier," *Power Electronics, IEEE Transactions on*, vol. 19, no. 1, pp. 76–86, 2004.
- [7] V. Blasko and V. Kaura, "A novel control to actively damp resonance in input lc filter of a three-phase voltage source converter," *Industry Applications, IEEE Transactions on*, vol. 33, no. 2, pp. 542–550, 1997.
- [8] J. L. Agorreta, M. Borrega, J. López, and L. Marroyo, "Modeling and control of-parallelled grid-connected inverters with lcl filter coupled due to grid impedance in pv plants," *Power Electronics, IEEE Transactions on*, vol. 26, no. 3, pp. 770–785, 2011.

- [9] J. Dannehl, F. W. Fuchs, S. Hansen, and P. B. Thøgersen, "Investigation of active damping approaches for pi-based current control of grid-connected pulse width modulation converters with lcl filters," *Industry Applications, IEEE Transactions on*, vol. 46, no. 4, pp. 1509–1517, 2010.
- [10] Y. Tang, P. C. Loh, P. Wang, F. H. Choo, and F. Gao, "Exploring inherent damping characteristic of lcl-filters for three-phase grid-connected voltage source inverters," *Power Electronics, IEEE Transactions on*, vol. 27, no. 3, pp. 1433–1443, 2012.
- [11] M. Cespedes, L. Xing, and J. Sun, "Constant-power load system stabilization by passive damping," *Power Electronics, IEEE Transactions on*, vol. 26, no. 7, pp. 1832–1836, 2011.
- [12] R. D. Middlebrook, "Input filter considerations in design and application of switching regulators," *IAS Record, 1976*, 1976.
- [13] R. Pena-Alzola, M. Liserre, F. Blaabjerg, R. Sebastián, J. Dannehl, and F. W. Fuchs, "Analysis of the passive damping losses in lcl-filter-based grid converters," *Power Electronics, IEEE Transactions on*, vol. 28, no. 6, pp. 2642–2646, 2013.
- [14] R. W. Erickson, "Optimal single resistor damping of input filters," in *Applied Power Electronics Conference and Exposition*, vol. 2. Citeseer, 1999, pp. 1073–1079.
- [15] J. Perez, S. Cobrecas, F. J. R. Sanchez, and R. Grino, "H-inf simultaneous admittance and tracking current controller of three-phase active grid front-ends," in *Industrial Technology (ICIT), 2015 IEEE International Conference on*. IEEE, 2015, pp. 2092–2097.
- [16] E. J. B. Peña, "Optimización del comportamiento de un convertidor de tres niveles npc conectado a la red eléctrica," Ph.D. dissertation, Polytechnic School. University of Alcalá, 2005.
- [17] S. Skogestad and I. Postlethwaite, *Multivariable feedback control: analysis and design*. Wiley New York, 2007, vol. 2.

\mathcal{H}_∞ Current Controller for Input Admittance Shaping of VSC-Based Grid Applications

Jorge Pérez, *Student Member, IEEE*, Santiago Cobreces, *Member, IEEE*, Robert Griño, *Senior Member, IEEE*, and Francisco Javier Rodríguez Sánchez, *Member, IEEE*

Abstract—This paper presents a current controller that shapes, in the frequency domain, the input admittance of voltage-source converters connected to the grid. The controller is obtained by means of a \mathcal{H}_∞ synthesis procedure, which minimizes the difference between the application closed-loop input admittance and a model-reference defined by the designer. This formulation achieves good accuracy in both modulus and phase. The proposed methodology allows the fulfilment of other current control objectives, such as current tracking, by defining frequency regions where each objective is desired. Experimental results show the good response of the proposed controller, both in frequency and time domain.

Index Terms—Admittance, current control, \mathcal{H}_∞ control, pulse width modulated power converters.

I. INTRODUCTION

THE increasing presence of power electronics-based devices in the power system, such as machine drives, power supplies, flexible ac transmission systems (FACTS) or renewable-energy interfaces is populating the grid of complex dynamics including nonlinear behavior, constant-power loading, control-loop induced resonances, etc. The results of recent investigations seem to mark those kind of dynamics as contributors-triggers of power quality problems or even power system instabilities [1]–[4].

Although the problem, in its whole nonlinear generality, is still under scientific discussion [4], [5], power electronic-based devices input admittance [see $Y(s)$, Fig. 1], when linearized around the system operating point, is known to play a distinguished role on system stability and also on several power quality problems.

Its interest in power systems stability arises from [6], where a sufficient small-signal stability condition was derived based

Manuscript received December 23, 2015; revised April 4, 2016; accepted May 16, 2016. Date of publication May 30, 2016; date of current version January 20, 2017. The work of authors J. Pérez, S. Cobreces, and F. J. R. Sánchez was supported by research projects CONPOSITE (ENE2014-57760-C2-2-R Ministerio de Economía y Competitividad), PRICAM (S2013/ICE-2933 Consejería de educación, juventud y deporte de la Comunidad de Madrid), and DIANA (CCG2015/EXP-064 Universidad de Alcalá). The work of the author R. Griño was supported in part by the Government of Spain through the Ministerio de Economía y Competitividad Project DPI2013-41224-P and by the Generalitat de Catalunya through the Project 2014 SGR 267. Recommended for publication by Associate Editor Qing-Chang Zhong.

J. Pérez, S. Cobreces, and F. J. R. Sánchez are with the Department of Electronics, Universidad de Alcalá, Alcalá de Henares, Madrid 28871, Spain (e-mail: jorge.perez@depeca.uah.es; cobreces@depeca.uah.es; fjrs@depeca.uah.es).

R. Griño is with the Institute of Industrial and Control Engineering, Universitat Politècnica de Catalunya, Barcelona 08028, Spain (e-mail: roberto.griño@upc.edu).

Color versions of one or more of the figures in this paper are available online at <http://ieeexplore.ieee.org>.

Digital Object Identifier 10.1109/TPEL.2016.2574560

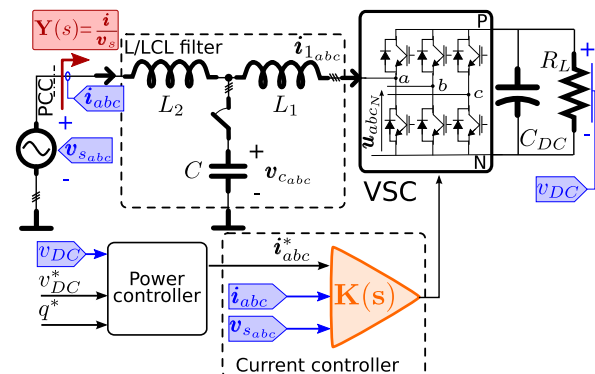


Fig. 1. Proposal block diagram: active rectifier connected to the grid via L or LCL filter. In orange color is the proposed controller. In blue color is the measured signals.

on the relation between impedances/admittances of the systems that are to be connected. More concretely, the stability relies on the Hurwitz condition of polynomial $D(s) = 1 + Z_s(s)Y_l(s)$, where Z_s and Y_l are the series equivalent impedance and admittance of the *main* power system and of the new connected *load*, respectively. The criterion has been further studied on [7]–[10].

This theoretical framework has motivated the publication of several works dealing with the shaping of converter closed-loop input admittance. A popular approach is to impose conditions over admittance module to ensure stability. Works [11]–[18] share the strategy of modifying the converter admittance on a particular problematic frequency, or in a small set of discrete frequencies, using classical control design procedures. In general terms, they offer satisfactory results on the target frequencies, but the design problem complexity induces limitations when facing wideband designs, and also in the management of the tradeoffs between the admittance at different frequencies and other control objectives such as reference tracking or relative stability. [6] has also served to enunciate stability conditions based on the phase of the admittance transfer function of the connected converter. The most important approach on this direction is based on the known result from system theory stating that the connection of a passive [19] loads improves the relative stability of the complex system. [20]–[23] propose the use of feedforward and feedback modifications to ensure admittance passivity, modifying its phase, sometimes at the cost of uncontrolled modulus modifications. Finally, an open approach to the improvement of stability of interconnected systems has emerged from the recent work [5], where it is derived that negative imaginary systems may be beneficial from this point of view, although there have not been proposals developing this line.

Admittance shaping is an interesting topic also in the field of power quality where there have been proposals on different directions. On the field of FACTS, it has been identified as a good alternative to damp resonances that facilitate the propagation of voltage and current harmonic through distribution or transport networks. The works developing this idea [24]–[30] present limitations similar to those expressed before. Finally, and although they are usually approached in a different way, active damping techniques or droop control techniques could be considered admittance shaping approaches [12], [14], [17], [31]–[33].

This paper proposes a systematic design procedure that allows to shape the converter input admittance, in modulus and phase, for wide frequency bands and handling other control objectives, such as reference tracking or stability, from a holistic point of view. The obtained flexibility may allow the use of the procedure to obtain controllers valid for all the scenarios described above.

To achieve that objective, the control problem is formulated as a model-reference-based \mathcal{H}_∞ synthesis procedure. More concretely, the designer provides the procedure with two model-reference transfer functions: one that specifies the desired input admittance and another that specifies the desired reference-tracking dynamic model (relationship between current reference, and grid injected current). As both objectives are not achievable at the same frequency, the designer also provides the algorithm with a frequency distribution of both control objectives. The process result is a discrete-time controller suitable for being programmed and executed in a DSP. The proposal is illustrated using a pulse width modulation (PWM) rectifier application but is flexible enough to be applied to different control schemes and converter topologies.

This approach has been already explored by authors in [34], [35] obtaining promising preliminary results for simplified ideal scenarios. This paper extends the procedure to deal also with *LCL* filter structures, simplifies three-phase approach and integrates the controller in a realistic application with several hierarchical controllers in operation. This paper also gives a wide exploration of the possibilities and inherent limitations of the control design procedure, suggesting important design guidelines for the practical application of the method. In addition, a complex experimental setup has been prepared to obtain an actual experimental testing of the proposal.

The solution of the problem in the \mathcal{H}_∞ framework transfers part of the design complexity to a computational algorithm, allowing the designer to deal with different complex control objectives in an tractable way. Following a model-reference design allows an accurate shaping in both modulus and phase. The convex nature of the underlying optimization algorithm guarantees that an (sub)optimal controller is found. Although its presence on the control of dc/ac converters is still incipient, some approaches have been published in the field of current and voltage control reference tracking control, robust control, etc. [36]–[44].

The next section is dedicated to describe the theoretical basis of the design procedure. Section III gives practical insight into the design procedure, the underlying existing limitations and the implementation details. Section IV gives a summary of the

different experimental tests followed to verify the proposals. The paper ends with a discussion of the conclusions extracted from the presented work.

II. THEORETICAL BACKGROUND

A. System Description and Control Objectives

The proposed current control design scheme has been applied to a PWM Voltage-source Converter (VSC)-based active rectifier (see Fig. 1). This application represents a good benchmark plant, allowing a simultaneous testing of the current reference tracking (which comes from the power controller, Fig. 1) capabilities and of the admittance (\mathbf{i}/\mathbf{v}_s) emulation accuracy. Additionally, it is general enough to suggest that obtained results could be extrapolated to other common grid topologies or applications such as machine-drive front-end, FACTS, etc.

The control structure is divided in a classical two-hierarchical-levels control scheme: in the highest level, the load voltage is regulated to a given reference v_{DC}^* by the power controller (Fig. 1). This voltage reference, together with a possible reactive power reference q^* , will serve as inputs for the power controller block that will generate an ac current reference, namely \mathbf{i}_{abc}^* that satisfies the desired power balance for a given measured point of common connection (PCC) voltage $\mathbf{v}_{s_{abc}}$.

To achieve both objectives, the design follows a model-reference approach: the designer gives two reference models \mathbf{Y}_{ref} and \mathbf{T}_{ref} . The former describes the desired relationship between the grid PCC voltage \mathbf{v}_s and the grid current \mathbf{i} ; in other words, the system input admittance. The latter describes the desired relationship between the grid current reference \mathbf{i}_{abc}^* and the actual grid current \mathbf{i}_{abc} . It will later become evident that both objectives cannot be fulfilled at the same frequency so, additionally, the designer has to make a frequency distribution of the control objectives.

B. Dynamic Modeling

The active rectifier, shown in Fig. 1, is controlled in the $\alpha\beta$ stationary reference frame [45]. Expressing a three-wire converter control problem in the $\alpha\beta$ reference frame allows to operate under unbalanced conditions in a natural way, removing component coupling and, thus, reducing the original multiple input multiple output (MIMO) problem to the control of two identical single-input single-output uncoupled systems. The theory and procedures exposed on this proposal are expressed for only one control channel (α or β) and, similarly, the obtained controller will have to be executed twice, once for each component. As a consequence, the obtained closed-loop admittance will be equal for both components, being it a balanced three-phase admittance. It is also worth to remark that the design procedure could be translated into other typical reference frames, for instance, in synchronous dq axes.

Focusing on the inner control level process, the grid current in Fig. 1 follows the next linear dynamic expression, expressed in Laplace domain

$$I(s) = G(s) \cdot U(s) + G_d(s) \cdot V_s(s) \quad (1)$$

where I and V_s are the grid injected current and the PCC voltage, respectively. $U(s)$ represents the averaged value, over a PWM half-period (T_s), of the voltage \mathbf{u}_{abcN} (VSC block on Fig. 1) that is generated by the PWM signals applied to the power devices gates. Transfer functions $G(s)$ and $G_d(s)$ are the open-loop command-to-output and input open-loop admittance, respectively.

These last transfer functions are extracted from the differential equations that describe the system dynamics and are dependent on the grid filter that is used. For the L filter the transfer function are

$$G(s) = -\frac{1}{sL_f + R_f} \quad G_d(s) = \frac{1}{sL_f + R_f} \quad (2)$$

where $L_f = L_1 + L_2$ and $R_f = R_1 + R_2$ are the filter inductance and its parasitic equivalent resistance, respectively.

In the case of using an LCL filter, the following transfer functions are obtained:

$$G(s) = -\frac{1}{sC(R_1 + sL_1)(R_2 + sL_2) + R_f + sL_f} \quad (3)$$

$$G_d(s) = \frac{sC(R_1 + sL_1) + 1}{sC(R_1 + sL_1)(R_2 + sL_2) + R_f + sL_f} \quad (4)$$

where L_1 , R_1 , L_2 , and R_2 are the converter-side and grid-side inductance and resistance, respectively.

The outer dc-bus voltage controller is designed using a classical active power balance approach similar to the one described in [46]. Its design is out of the scope of this work that will only consider its main characteristics.

C. Controller Structure and Synthesis

Fig. 1 shows the structure where the proposed controller is integrated. The current controller, in orange color, $\mathbf{K}(s)$, has three inputs: the PCC grid voltage measurement, namely \mathbf{v}_s , the grid reference current \mathbf{i}^* , and the sensed grid current \mathbf{i} . From the information provided by these three inputs, the controller computes the average voltage at VSC ac terminal outputs, \mathbf{u} , needed to achieve control objectives. The controller transfer matrix is computed as a whole by the control design algorithm, however, it is interesting to observe that, dividing the transfer matrix in rows: $\mathbf{K}(s) = [K_s(s) \quad K_{\text{ref}}(s) \quad K_i(s)]^T$, the actuation signal can be calculated as

$$U(s) = K_s(s)V_s(s) + K_{\text{ref}}(s)I^*(s) + K_i(s)I(s). \quad (5)$$

Controller \mathbf{K}^1 can be considered, thus, to be formed by the addition of a grid voltage feedforward action K_s , a current reference precompensation action K_{ref} , and a grid current feedback action K_i .

Expressing the closed-loop grid current I using the aforementioned structured transfer function, the following expression is

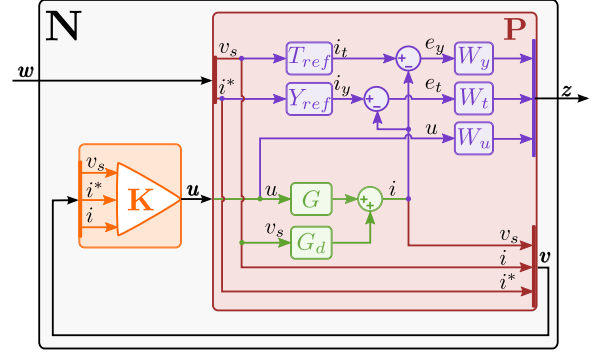


Fig. 2. General Control Problem (for any of the $\alpha\beta$ components) used for the \mathcal{H}_∞ synthesis. The open-loop transfer functions are colored in green, purple elements are added in the design process for controller synthesis. \mathbf{P} , in red color, wraps around both. The desired controller \mathbf{K} is shown in orange. Closed-loop system, \mathbf{N} , in black, results from connection of \mathbf{P} and \mathbf{K} .

obtained:

$$I = \underbrace{(1 - GK_i)^{-1} GK_{\text{ref}}}_{T(s)} I^* + \underbrace{(1 - GK_i)^{-1} (G_d + GK_s)}_{Y(s)} V_s \quad (6)$$

where T and Y are the closed-loop tracking and admittance transfer functions. It is important to note that system stability depends only on the system open-loop transfer function $L = -GK_i$.

Controller \mathbf{K} is obtained through an \mathcal{H}_∞ synthesis process that uses, as its entry point, the general control problem formulation, or generalized plant $\mathbf{P}(s)$ [47]. This virtual plant is a mathematical instrument that incorporates the open-loop plant and admittance transfer functions, G and G_d , respectively, a set of extra transfer functions that are used by the designer to specify the main control objectives and restrictions and, also, the control loop architecture. Structurally, \mathbf{P} is a plant with two (vector) inputs and two (vector) outputs

$$\begin{bmatrix} \mathbf{z} \\ \mathbf{v} \end{bmatrix} = \mathbf{P} \begin{bmatrix} \mathbf{w} \\ \mathbf{u} \end{bmatrix} \quad (7)$$

where \mathbf{w} is called exogenous inputs vector to the system, usually composed of references and disturbances. \mathbf{z} is the vector of the so-called output error signals, that are to be minimized in some sense to meet control objectives, \mathbf{u} is the actuation vector that will be computed by the controller, and \mathbf{v} is the measurements output vector that will enter the controller.

With the implicit information provided by \mathbf{P} , the \mathcal{H}_∞ synthesis process computes a (sub)optimal controller \mathbf{K} , which minimizes the infinity norm² of the closed-loop system \mathbf{N} that results from the feedback interconnection of \mathbf{P} and \mathbf{K} , and relates exogenous input vector \mathbf{w} and error vector $\mathbf{z} = \mathbf{N}\mathbf{w}$, as shown in Fig. 2.

Minimizing the closed-loop function infinity norm is equivalent to minimizing the ratio between the energies (norm-2) of

¹For notation compactness, the Laplace variable “ s ” is omitted when its presence results obvious attending to the context.

²The infinity norm of a MIMO system $\mathbf{H}(s)$ in the frequency domain is defined as $\|\mathbf{H}(s)\|_\infty \triangleq \sup_\omega \bar{\sigma}(\mathbf{H}(j\omega))$, where $\bar{\sigma}(\mathbf{H}(j\omega))$ is the maximum singular value of $\mathbf{H}(j\omega)$.

the *error vector* \mathbf{z} and the exogenous vector \mathbf{w}

$$\min_{\mathbf{K}} \|\mathbf{N}(\mathbf{K})\|_\infty = \min_{\mathbf{K}} \frac{\|\mathbf{z}\|_2}{\|\mathbf{w}\|_2} \leq \gamma. \quad (8)$$

In other words, the synthesis process computes the controller that minimizes the energy of the error signals for the considered set of disturbances, references, and other exogenous signals. The designer task is, then, to choose the appropriate error signals and shape them to accomplish the control objective. In fact, choosing an inner structure for \mathbf{P} , that is, effective in practice is the design keystone in this control paradigm.

The principle behind this control proposal is the minimization of the difference between the output current of a designer provided Y_{ref} and that of the actual converter; if, given the grid PCC voltage, this difference is *small*, the converter would be following the admittance model, accomplishing the main objective of this work. Current tracking is approached in a similar manner.

Fig. 2 shows the proposed structure for \mathbf{P} . Over the diagram, green elements represent the actual plant under control. The plant output i is the result of adding the outputs of G and G_d transfer functions. These components model the contributions of the control actuation u and grid voltage v_s over i , respectively. Purple elements are added in the design process for controller synthesis. e_t is the difference between plant output i and the tracking reference model T_{ref} output i_t . In a similar way, e_y is the difference between i and i_y , the output of the admittance reference model Y_{ref} . Controller actuation u has also to be added as a minimization signal in order to avoid unnecessary or impossible control efforts. All these three variable are then multiplied by frequency weights (W_t , W_y , W_u , respectively), that emphasize the range of frequencies where each variable has to be minimized. Their outputs compose the \mathbf{z} output vector. Finally, the controller that is produced from the synthesis process is displayed on orange color. Note that the inputs to the controller are all the exogenous signals (\mathbf{w} vector) together with the plant measurements, i signal, namely \mathbf{v} in the standard notation of (7). The controller output is the plant actuation signal u .

Summing up, output and input signal vectors of generalized plant \mathbf{P} defined in Fig. 2 are then

$$\mathbf{z} = \begin{bmatrix} W_t \cdot e_t \\ W_y \cdot e_y \\ W_u \cdot u \end{bmatrix} \quad \mathbf{v} = \begin{bmatrix} v_s \\ i^* \\ i \end{bmatrix} \quad \mathbf{w} = \begin{bmatrix} v_s \\ i^* \end{bmatrix} \quad \mathbf{u} = u. \quad (9)$$

It is important to stress on the way i_y and i are compared: e_y is calculated as the subtraction of both signals. As a consequence good admittance control can be achieved not only in modulus, but also in phase. Admittance transfer function phase is a key parameter because important dynamical properties, as for example, dissipativity[19], depend on it.

Design of frequency weights has also a strong influence on the obtained controller \mathbf{K} : the signals involved in the \mathbf{z} vector are actually incompatible from a minimization point of view as it is not possible to mimic a certain admittance in the frequency bands, where good tracking is required, and also, it is not possible to minimize control effort at the same frequencies. The

correct design of the functions inside \mathbf{P} is, to a large extent, application dependent and is dealt in more detail in the next section.

III. PRACTICAL CONSIDERATIONS

A. Design of Current Controller: Reference Model and Weighting Function Selection

The generalized plant presented in Section II-C is general enough to handle a wide variety of VSC control problems. The objective of this section is to settle some design heuristic rules that have been found to be useful by the authors.

As stated in previous sections, a designer following the described control architecture and methodology is requested to define five transfer functions, grouped in two classes. The first group is composed of the transfer functions that serve as reference models for current tracking or admittance shaping purposes. The second group is integrated by those transfer functions that emphasize—weight—the importance of the different reference models, or the control effort, for the different frequency bands.

1) *Reference Model Selection*: The reference models are used to specify, by the designer, how the grid injected current i (in Fig. 2) tracks the exogenous current reference i^* (in Fig. 2) and the converter input admittance.

In typical applications, the grid current is required to accurately track the provided reference, at least in a band around the fundamental frequency and, possibly, also in some of its lower order harmonics. Facing the design from a reference-model point of view, the easiest approach is to choose a $T_{\text{ref}} = 1$. Such a broadband tracking objective is clearly unachievable (and incompatible with any non null admittance objective). The tracking reference weighting function W_t will serve as an effective tracking band-limiter.

The range of possibilities for admittance reference model Y_{ref} is wider and more application dependent. Although usually low-valued power-dissipative (resistive) responses are preferred, other behaviors could be considered. Section III-B, below, shows some different example designs that can give an idea of the design method flexibility.

2) *Weighting Functions Selection*: The control strategy presented in this proposal is a tradeoff problem generated by several inherent incompatibilities and constraints.

- 1) Tracking and admittance control objectives are incompatible as they try to make the grid injected current follow the tracking and the admittance reference model output current, which are, in general, different. The designer has to choose which model is important for the different frequency bands.
- 2) Control effort magnitude has to be reasonable inside the control band. For this reason, it has to be included in the output error vector \mathbf{z} : if it were not, the optimization of $\|\mathbf{N}\|_\infty$ would possibly arrive to an optimum solution with not realistic actuation signals that would saturate the plant input (maximum duty cycle on PWM).

- 3) *Control-Band Limitation*: Given the sampled-time nature of the proposed control algorithm, actuation should be attenuated to a great extent before Nyquist frequency f_{Ny} . This limitation represents a maximum limit on the band where control objectives can be achieved. Other band limitations are to be added in the case that the plant exhibits nonminimum phase behavior or a delay in the control input. These important topics will be more deeply dealt in Section III-C.

The designer deals with these tradeoffs by means of the frequency weighting functions. To properly understand its utility it helps to remember that the \mathcal{H}_∞ controller synthesis algorithm tries to obtain a controller that keeps the error output vector \mathbf{z} small. This way, a frequency weight that (relatively) amplifies a signal in a band, would yield a controller that keeps the unweighted actual signal smaller inside that band. In a similar fashion, a weight (relatively) attenuating a signal in a band will induce a bigger actual unweighted signal in the closed-loop system. This paper proposes the use of three different weighting functions.

- 1) $W_t(s)$ transfer function weights the error with respect to the tracking reference model. If $T_{\text{ref}} = 1$ has been chosen, it weights the tracking error. High values are used for bands where good reference tracking is desired. In the case, the controller is used in a PWM rectifier application, the designer has to take into account that the tracking band should be about ten times wider than the band of the dc-bus/power controller that generates the current reference, to ensure the current accurately tracks it.
- 2) $W_y(s)$ weights the error with respect to the admittance reference model. High values are used for bands where good admittance shaping is desired. It has to be remembered that admittance and reference tracking are not compatible, so their respective weighting functions should be complementary.
- 3) $W_u(s)$ weights the actuation in two senses: it is used to limit the maximum control bandwidth but also to limit the maximum control effort within the control band. Thus, typically, W_u is a high-pass function. The transition between the low- and high-gain bands marks the frequency where control actuation is desired to be small, i.e., the stop-band beginning. The maximum control effort in the control band is adjusted by modifying the gain of W_u in that band: lower values allow a bigger control effort and vice versa. This value is usually adjusted to get a control effort near the saturation limit under nominal transients and disturbances as, for instance, voltage dips.

Fig. 3 presents a possible selection of the aforementioned weighting functions. The plot divides the spectrum in four different frequency zones. In first zone, placed at subsynchronous frequency range, W_y gets the bigger value, indicating that the objective is to follow the admittance reference model. The same applies to the third-band, on supersynchronous frequencies. Around the grid fundamental frequency, W_t gets a very high value. This is used to achieve null error in tracking sinusoidal references and, in practice, will yield a controller with (almost)

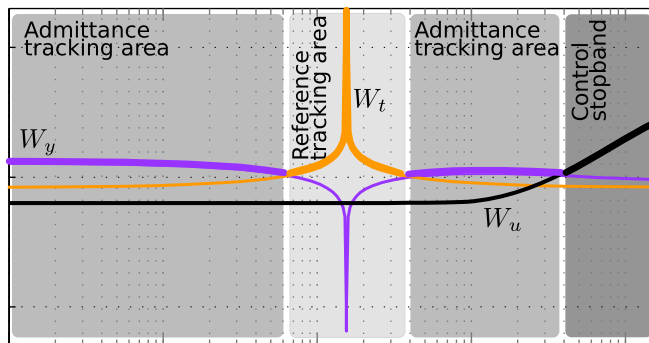


Fig. 3. Typical weighting function selection scenario.

a resonant-part on that frequency. Finally, in the fourth interval W_u gain gets higher signaling the end of the control band.

B. Design Examples

This section presents three study cases. The objective is to give more insight into the design process, emphasize the designer typical work flow and strategy and demonstrate the flexibility of the procedure respect to the plant model and control objectives.

1) *Broad-Band Admittance Control (L Filter)*: The first case proposes the design of an active rectifier whose admittance, outside the fundamental frequency range, presents purely resistive behavior. The energy absorbed by the converter due to this dissipative behavior is evacuated, by the dc-bus voltage controller, through the grid fundamental frequency. It is necessary, then, to provide the controlled system with fundamental frequency tracking capabilities. This objective may be achieved selecting, for instance, $Y_{\text{ref}} = 0.1\bar{U}$ and $T_{\text{ref}} = 1$.

To distribute the different objectives along the spectrum this design uses the weights displayed on Fig. 4: W_t is chosen as a resonance in the grid fundamental frequency. A high gain ensures an accurate tracking. W_t bandwidth controls tracking transient response. Concretely, it follows the structure:

$$W_t(s) = K_t \frac{s^2 + 2\zeta_n \omega_1 s + \omega_1^2}{s^2 + 2\zeta_d \omega_1 s + \omega_1^2} \quad (10)$$

where $\omega_1 = 2\pi 60$ rad/s is the grid fundamental frequency ζ_n varies the resonance bandwidth and ζ_n/ζ_d can be used to adjust the resonance peak maximum value.

Similarly, a complementary admittance weight W_y is defined using a notch characteristic in the fundamental frequency.

$$W_y(s) = K_y \frac{s^2 + 2\zeta_d \omega_1 s + \omega_1^2}{s^2 + 2\zeta_n \omega_1 s + \omega_1^2} \cdot \frac{1}{(1/\omega_y)s + 1} \quad (11)$$

where ω_y marks the maximum frequency where impedance emulation is desired. The notch part of the transfer function is designed following W_t criteria.

Finally, control effort is limited by the next weight

$$W_u(s) = K_u \frac{(1/\omega_{u1})s + 1}{(1/\omega_{u2})s + 1} \quad (12)$$

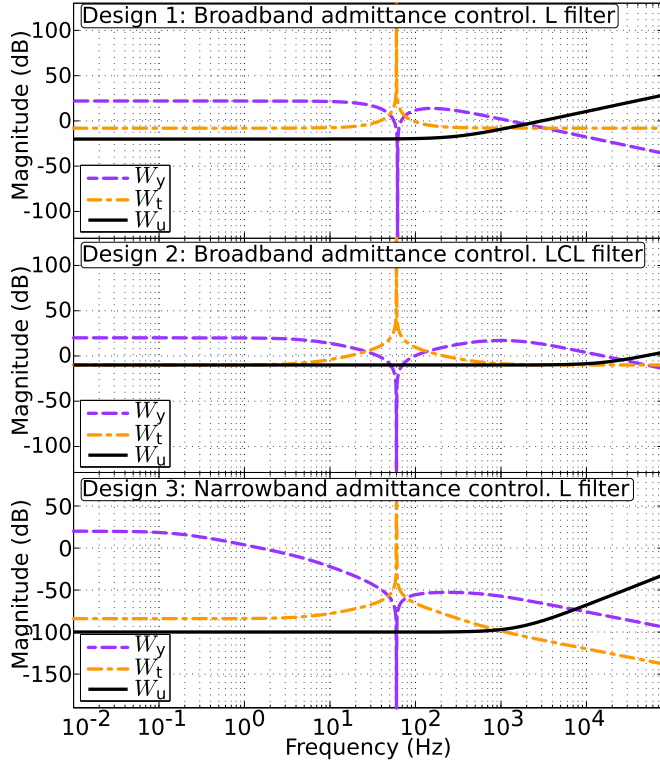


Fig. 4. Frequency weights for the different design examples.

where the zero in ω_{u1} defines the frequency where control effort starts to be limited, in the beginning of the crossover band. The pole in ω_{u2} marks the control stop band and the end of the crossover band. This pole is also needed to make W_u (and P , Fig. 2) strictly causal, as required by \mathcal{H}_∞ synthesis algorithm.

2) *Broad-Band Admittance Control (LCL Filter)*: This second example describes how the plant model affects the design flow. The control objective is the same as in the first example but the plant order has been increased by considering an LCL filter connection. Admittance reference is, again, a pure resistance $Y_{\text{ref}}(s) = 0.1\bar{U}$. In this case, the LCL resonance is also desired to be shaped, so control objectives spread over a wider band, using W_y equal to (11), but with a bigger ω_y .

Tracking reference is also kept as $T_{\text{ref}}(s) = 1$. This example has been designed to present a faster tracking behavior. W_t follows, thus, (10) but selecting a wider bandwidth.

Control effort is shaped with W_u equal to (11). Again, the active control band is wider and ω_{u1} and ω_{u2} are selected to obtain actuation limitation at higher frequencies.

3) *Narrow-Band Admittance Control (L Filter)*: The objective of the third example is to illustrate the validity of the design proposal when considering higher order reference models: process model is again an L-filter grid connected VSC but the desired admittance (outside the fundamental frequency) shows a resonant-like behavior. From a hypothetical application point of view, this could be used, for instance, as a lossless damper for a resonance placed at a known frequency. By using this resonance behavior, admittance achieved on the desired frequency is larger than in previous examples, also minimizing the

influence over the rest of the spectrum and leaving more room for reference tracking, if needed.

The new admittance reference is

$$Y_{\text{ref}}(s) = 0.01 \frac{s^2 + 2\zeta_n \omega_{\text{res}} s + \omega_{\text{res}}^2}{s^2 + 2\zeta_d \omega_{\text{res}} s + \omega_{\text{res}}^2} \cdot \frac{1}{(1/\omega_{y\text{ref}})s + 1} \quad (13)$$

where ω_{res} is the frequency where the maximum admittance is reached. The high frequency pole at $\omega_{y\text{ref}}$ is used to make the admittance reference-model (Y_{ref}) more similar to the open-loop one (G_d), avoiding excessive control efforts on that frequencies.

Frequency range of admittance control is defined through a W_y equal in structure to (11) but with the real pole placed at lower frequencies to enhance its importance in subsynchronous frequencies.

Tracking reference is, again, $T_{\text{ref}}(s) = 1$; W_t changes slightly

$$W_t(s) = K_t \frac{s^2 + 2\zeta_n \omega_1 s + \omega_1^2}{s^2 + 2\zeta_d \omega_1 s + \omega_1^2} \cdot \frac{1}{(1/\omega_t)s + 1}. \quad (14)$$

The new pole at ω_t makes admittance control more dominant at frequencies above the fundamental (supersynchronous frequencies, where admittance resonance peak is placed) and below the control band upper limit (where W_u is dominant).

Control effort is again limited at high frequencies, with a weight W_u with similar dynamics to (12). This time it has double order to reduce crossover range, and be able to control admittance at higher frequencies.

$$W_u(s) = K_u \left(\frac{(1/\omega_{u1})s + 1}{(1/\omega_{u2})s + 1} \right)^2. \quad (15)$$

C. Controller Limitations

The presented controller design and synthesis is subjected to the following known limitations.

1) *Sampled-Time Implementation Limitations*: An inherent limitation in the practical implementation of discrete-time controllers is the impossibility of applying to the plant, in time k , an actuation computed with measurements also acquired in time k . In most power converter control scenarios, signal acquisition time and controller actuation computation last for a nonnegligible part of the controller sample time. The typical workaround is to postpone the actuation application until the arrival of the next sampling period. This is usually modeled placing a one-sample pure delay in the control input, z^{-1} in z -domain, of the plant discrete-time model. The existence of this delay introduces a high bound on the controller bandwidth, limiting the achievable bandwidth to [47]

$$f_c < \frac{1}{2\pi T_s} \quad (16)$$

which is, approximately, one third of f_{Ny} .

It is important to remark that this bound affects to both the feedforward and feedback components of the controller actuation, because both are affected by the input delay.

2) *Waterbed Limitations*: The transfer function of the plant under control presents, as can be seen in (3), a relative degree: $rd(G(s)) = 3$. This fact makes applicable the Bode sensitivity integral theorem (first waterbed formula) [47] establishing a

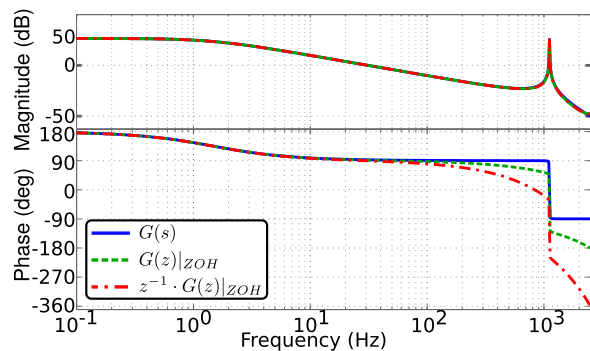


Fig. 5. Frequency responses of the continuous open-loop plant, $G(s)$, its zero-order hold discrete-time equivalent, $G(z)|_{\text{ZOH}}$, and the delayed ZOH discrete-time equivalent, $z^{-1} \cdot G(z)|_{\text{ZOH}}$.

tradeoff design decision between closed-loop performance and system robustness: increasing closed-loop performance at some frequencies comes at the cost of increasing the achieved sensitivity function infinity norm $\|S(j\omega)\|_{\infty}$, which is a good inverse indicator of the design robustness. A commonly accepted design criterion is to synthesize loops with $\|S(j\omega)\|_{\infty} < 2$ (in natural units). This condition implies that the polar plot of $L(j\omega)$ lies outside of a circumference of radius 0.5 centred at $(-1 + 0j)$, and, consequently, a gain margin bigger than 6 dB and a phase margin bigger than 30° .

3) *Weight Design Limitations*: In addition to the previous limitations, which actually have a clear indirect impact on the design of the weighting functions, the latter are also subject to two additional limitations that have to be considered in the design process: 1) Weights must be strictly stable and proper. Pure resonators and integrators are, thus, not allowed to be present in weight functions as they present poles over the $j\omega$ axis. There is no theoretical limitation, however, in placing them arbitrary close to the $j\omega$ axis. From a practical point of view, this limitation has no implication as the behavior is practically equivalent. 2) Weight transfer function order. The order of the synthesized controller is that of the augmented $\mathbf{P}(s)$ plant transfer function. The three design weights are contained inside \mathbf{P} so, an increase in their order implies an increase in the final controller \mathbf{K} order. The designer has to evaluate whether the performance improvement obtained by an extra state in a weight is worth the corresponding controller complexity increase.

D. Controller Synthesis and Implementation

The \mathcal{H}_{∞} synthesis tools are designed to work with continuous-time plants. The presented controller, however, is executed in a DSP, and thus, a discrete-time controller transfer function is needed. Using a direct discrete-time approximation of a continuous-time controller neglects important dynamics such as the presence of a PWM modulator, that may be modeled as a zero-order hold (ZOH), and the presence of a one-sample delay at the plant control input. To include such important elements, the ZOH discrete-time equivalent of $G(s)$ is computed and a one-sample delay element z^{-1} is added to it in the z domain. Fig. 5 shows a comparison of the frequency responses

of $G(s)$, $G(z)|_{\text{ZOH}}$ and $z^{-1} \cdot G(z)|_{\text{ZOH}}$. It can be observed that, while the modulus of the transfer functions are similar, there are important differences in their phases that increase with frequency. While these differences could be neglected in the case of a reference-tracking controller with a conservative tracking bandwidth (relative to the switching frequency), in the case of the admittance shaping it would yield phase errors in the obtained closed-loop admittance.

After introducing these dynamic elements in the process, a continuous approximation of this plant is obtained via Bilinear transformation, making a frequency prewarping to accurately preserve *LCL* resonance frequency. The open-loop admittance G_d can be directly included in the augmented plant $\mathbf{P}(s)$ as the grid voltage is, in fact, a continuous disturbance of the process. Frequency weights may also be directly expressed in continuous time, being conscious of the bandwidth limitations that are present because of the final objective of obtaining a discrete-time controller. Once the plant \mathbf{P} is specified, the continuous-time controller $\mathbf{K}(s)$ is obtained through a regular \mathcal{H}_{∞} synthesis process. The final discrete-time controller $\mathbf{K}(z)$ is then obtained by computing a Bilinear transformation.

The algorithm synthesis is performed using MATLAB standard library and also its Robust Control Toolbox.³ The transfer functions used in \mathbf{P} are created using standard `tf`, `ss` commands. Continuous to discrete conversions, and vice versa, are performed using `c2d` and `d2c`. Once they are created, process \mathbf{P} is assembled using the scripting tool `sysic`. The controller is then synthesized using `hinfsyn` command. The snippet displayed on Alg. 1 describes the procedure used to obtain the final controller.

Once the controller is obtained, it is programmed in C code using a state-space description of the controller

$$\begin{aligned} \mathbf{x}_{k+1} &= \mathbf{A}\mathbf{x}_k + \mathbf{B}\mathbf{v}_k \\ \mathbf{u}_k &= \mathbf{C}\mathbf{x}_k + \mathbf{D}\mathbf{v}_k \end{aligned} \quad (17)$$

where, \mathbf{x} , \mathbf{v} , and \mathbf{u} vectors stand for the controller state, plant outputs measured by the controllers and controller actuation, respectively, and $[\mathbf{A}, \mathbf{B}, \mathbf{C}, \mathbf{D}]$ are the controller state matrices. Fig. 6 shows a diagram of the different tasks executed during a sample period in the DSP. The period starts updating PWM signals with the actuation computed during the previous sampling period, u_{k-1} . This time shift is reflected as the one-sample delay at the plant input. Next, signals from sensors are acquired. With those data, higher hierarchy loops, in this case the dc-bus voltage controller, are computed, obtaining the appropriate references for the current controller. The controller is executed in two steps. First, the actuation to be applied in the next period u_k is computed. Finally, the controller internal states are updated, calculating x_{k+1} , before the DPS goes idle until the next period arrives.

³The synthesis procedure here described represents only one alternative that has been found particularly intuitive by the authors but similar results could be obtained by different approaches.

Algorithm 1 Controller synthesis procedure

```

1: procedure Controller Synthesis(G,Gd,ts)
2: Weight definition:
3: Wu=tf(...); Wt=tf(...); Wy=tf(...);
4: Process model:
5: delay=tf([1],[1 0],ts);
6: G_z=delay*c2d(G,ts,'zoh');
7: G_eq_cont= d2c(Gz,'bilin',...);
8: P assembly:
9: systemnames='G Gd Yr Wy Tr Wt Wu';
10: inputvar = '[e;i_ref;u]';
11: outputvar=' [Wy;Wt;Wu;e;i_ref;G+Gd]';
12: input_to_Wy=' [Yref-G-Gd]';
13: input_to_Wt=' [Tref-G-Gd]';
14: input_to_Wu=' [u]';
15: input_to_Yr=' [e]';
16: input_to_Tr=' [i_ref]';
17: input_to_G= '[u]';
18: input_to_Gd= '[e]';
19: P=sysic;
20: K synthesis:
21: [K_cont,gamma]=hinfsyn(P,...);
22: if(gamma>gmax) then goto Weight definition
23: K=c2d(K_cont,'bilin',...);
24: end
    
```

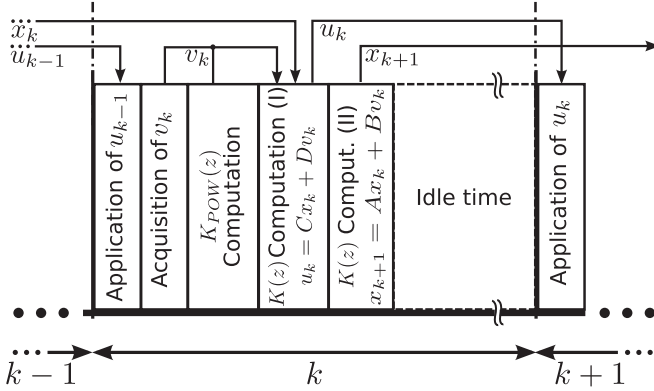


Fig. 6. Chronogram of the implemented control algorithm. The blocks show the different tasks executed in the processor unit. The arrows show the data flow between tasks and sample periods.

IV. RESULTS

The proposed control scheme has been verified by both simulation and experimental testing. The experimental setup (see Fig. 7) consists of the connection between an ac programmable power supply Pacific SmartSource 345-AMX, emulating the grid, and a 17.5 kVA two-level VSC connected to it through an LCL or an L filter (Table I shows the main parameters of the setup). A bank of passive loads is connected to the dc-bus to test the application under different operating points. Control application is implemented on a Texas Instruments DSP TMS320DSK6713 based control platform described in detail in [48].



Fig. 7. Experimental Set-up.

TABLE I
EXPERIMENTAL SETUP PARAMETERS

S	17.5 kVA	L_1	3.4 mH
V_g	120 V	R_1	28.8 m Ω
ω_1	2 π 60 rad/s	L_2	1.7 mH
V_{dc}	700 V	R_2	18.6 m Ω
T_{sw}	400 μ s	C	18 μ F
T_s	200 μ s	C_{DC}	4.7 mF
$K_{POW}(z)$	$K_p + \frac{K_I T_s}{(z-1)}$	K_I, K_P	0.2893, 0.0369

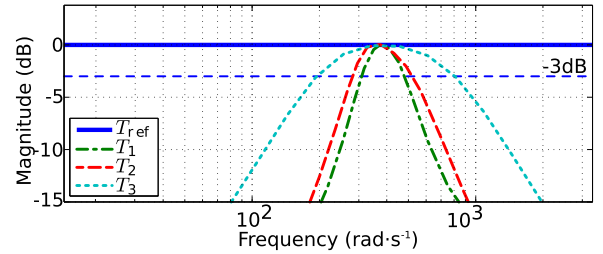


Fig. 8. Closed-loop analytic reference-tracking transfer function for the example designs $T_n(s)$, where n is the number of the design (refer to Section III-B). Blue color shows the reference model for all designs.

The experimental values of the closed-loop system admittance are obtained by adding a three-phase controlled sinusoidal signal to the voltage generated by the ac power supply. The ac power supply has a connector (J5), with three analog inputs where the user can place reference voltage signals. These voltage signals are internally amplified and added to each one of the phases of the main power supply output. To obtain the experimental admittance value on a particular frequency, a three-phase balanced sinusoidal signal of a particular frequency was added to the main ac voltage. The generated voltage signal and the corresponding injected currents are then acquired at 5 kHz, ensuring that the possible transient effects have already finished and that the data registry contains several cycles of the injected signal. Voltage and current data are, then, converted to the $\alpha\beta$

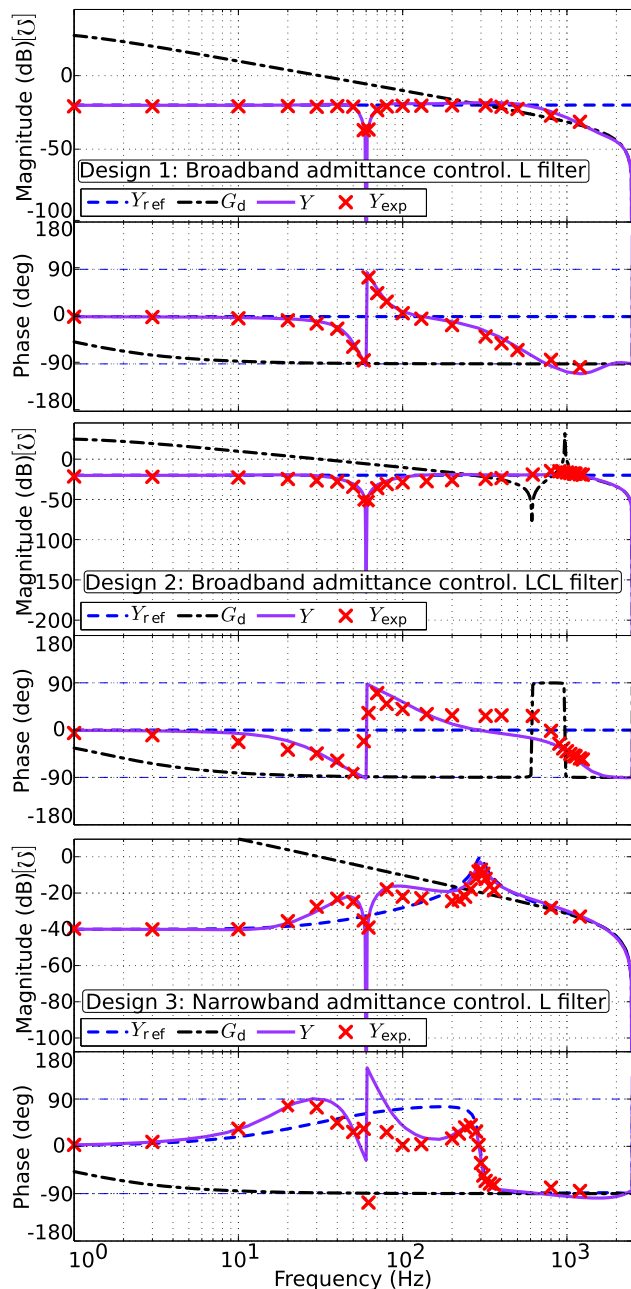


Fig. 9. Admittance frequency results. Open-loop admittance G_d is shown in black. Admittance reference model is shown in blue color. The closed-loop synthesized admittance (theoretical) is shown in purple. Red crosses show the experimentally measured admittance.

reference frame, analyzed with the MATLAB `fft` command, and divided to obtain the experimental value of the converter input impedance/admittance.

A. Frequency Domain Results

The three design cases described in Section III-B have been implemented and tested to verify the validity of the described control proposal. Fig. 8 shows the closed-loop analytic tracking function for the three designs. It can be observed that all designs achieve good tracking capabilities. The achieved bandwidth is

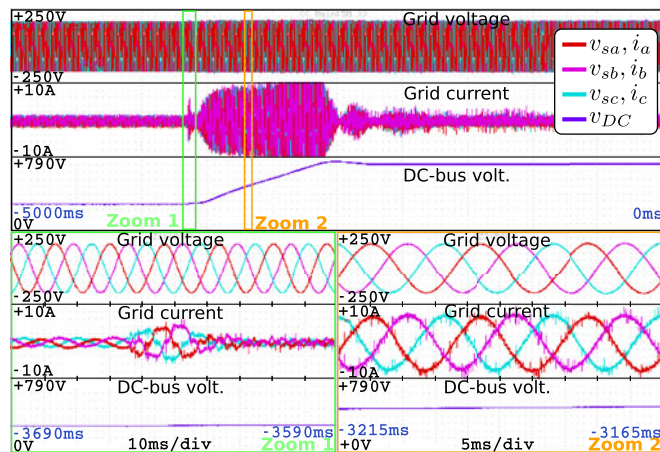


Fig. 10. Initial grid connection. General view shows dc-bus charging from the diode-rectified level to the nominal value (700 V). Zoom 1 shows the current transient when PWM starts. Zoom 2 details system signals during bus boosting. After elevation currents go null because bus is unloaded.

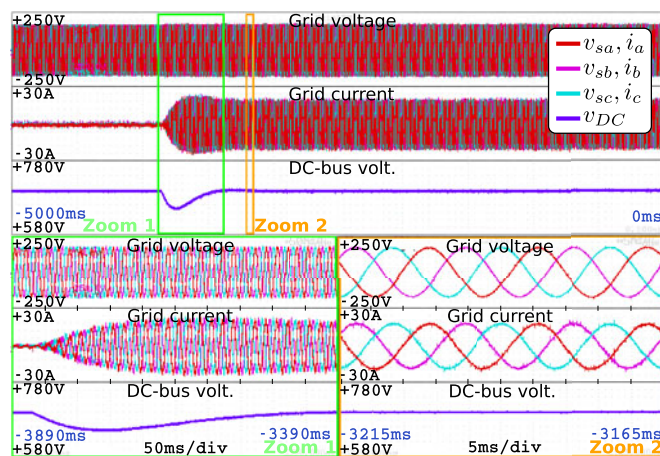


Fig. 11. Connection of a 4.2-kW dc-load with a null reactive reference. Top shows the complete transient. Zoom 1 focuses on the currents and dc-voltage evolution after the connection. Zoom 2 shows grid currents and voltages in steady state.

different for the three designs, because it was specified that way during the design process.

Similarly, Fig. 9 evaluates the admittance shaping capabilities of the proposed control scheme. Over the figures, it can be seen the open-loop admittance G_d , the desired admittance reference model Y_{ref} , the theoretical closed-loop admittance (using the theoretical plant G and G_d and the synthesized controller, K) and the experimentally identified system admittance, for a discrete number of frequencies. It can be observed that the synthesized controller effectively shapes the system admittance in the three cases: as expected the admittance follows the reference below and above the fundamental frequency, up to the system control bandwidth. Around the fundamental frequency, there is a transition zone, that may be shortened, if needed, by increasing resonators order in the corresponding weights.

The system admittance that has been experimentally identified accurately tracks the theoretical closed-loop admittance.

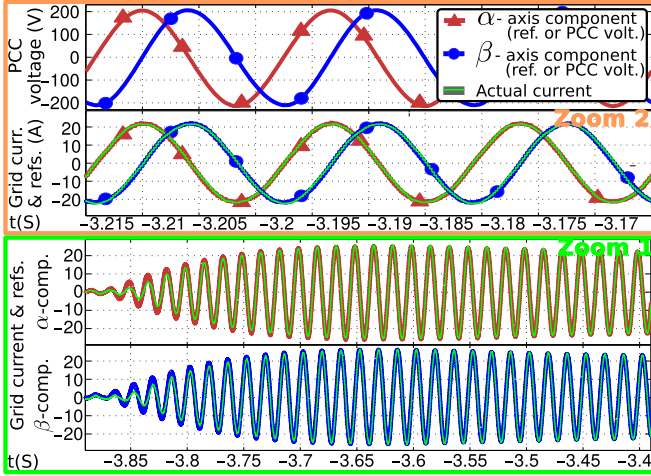


Fig. 12. $\alpha\beta$ components evolution for zoom ranges of transient in Fig. 11. (Zoom 2) Top: PCC $\alpha\beta$ voltages. Bottom: $\alpha\beta$ grid consumed currents and references. (Zoom 1) Top and bottom: Grid consumed current and the reference provided by the outer controller for the α and β components, respectively.

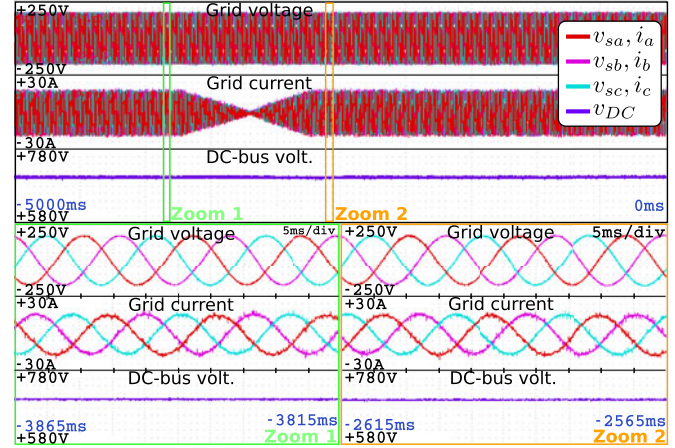


Fig. 14. Change in the reactive power reference. With the dc-bus unloaded, reactive power reference goes from 4 to -4 kVar. Power controller forces the transient to follow a slope. Top view shows the complete transient. Zoom 1 and 2 focus on the phase between grid voltage and currents for both references.

V. CONCLUSION

This paper presents a new current controller design methodology for simultaneous input admittance and current tracking control in power converter-based application. Presented controller is based on \mathcal{H}_∞ synthesis, and allows admittance frequency shaping, in both magnitude and phase, by means of defining frequency-based admittance references for complete frequency bands. This feature allows, for example, defining system dissipativity, the active damping of system's resonance, define high/low impedance paths, or fulfilment of impedance stability criterion (commonly used to predict stability in multiconverter networks). This feature extends the capabilities of previous approaches to the problem of closed-loop admittance shaping.

Proposed methodology is verified in a three-phase active rectifier, which simultaneously fulfills a dual control objective: tracking of a current reference which comes from a dc-side voltage, whose design lies out of the scope of this proposal, and control of the applications input admittance. This is possible if the frequency ranges of both control objectives do not overlap, which can be achieved by defining frequency-weights in the \mathcal{H}_∞ controller structure. Control operates in $\alpha\beta$ axes and was tested for both L and LCL filter topologies, measuring only the grid current and voltage, as well as the dc-bus voltage.

Designing criteria for the proposed controller is given. To demonstrate the proposed admittance control generality and feasibility, three different admittance references were considered: admittance control over a broadband for both L and LCL filter topologies, making the active rectifier behave as a resistance and actively damping the LCL resonance, and a design that defines a low impedance path around a given frequency, and a high impedance path for the rest.

All the proposed designs are experimentally implemented and tested, with both good frequency and time domain results. Future works would consider the effect and capabilities of the proposed algorithm in more complex grid connected scenarios, with several active components connected to the same ac grid and its effect over the proposed control algorithm.

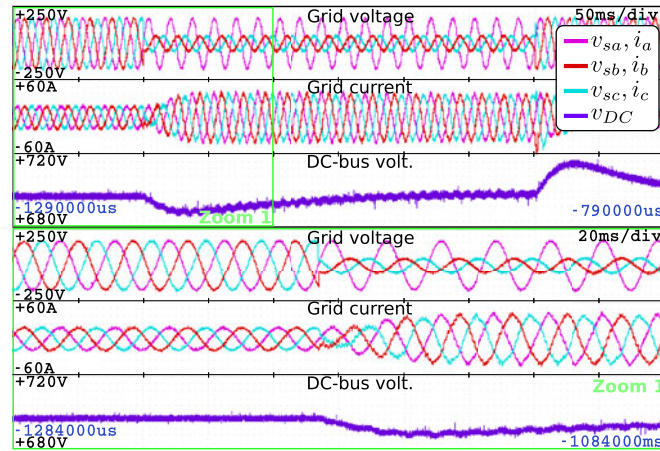


Fig. 13. Response under grid voltage dip (type E[49]) when dc-bus is loaded with 4.2 kW. Phases b and c fall to 30% of its value keeping their phase untouched. Top view shows the complete transient in grid voltages, currents and dc-bus voltage. Lower view focuses on the dip initial edge.

Some minor errors on the phase values, probably due to inductance modeling errors, can be observed above the fundamental frequency.

B. Time Domain Results

The second design example (Section III-B) is used to validate the transient and tracking capabilities obtained with the proposed design procedure. Fig. 10 shows the initial converter connection and dc-bus charging to its nominal value (700 V). Fig. 11 and 12 show the system behavior when a 4.2 kW load is connected to the dc-bus. Finally, Fig. 13 shows system evolution when the grid suffers an unbalanced dip. Fig. 14 shows the system behavior under a soft reactive power change.

REFERENCES

- [1] P. Liutanakul, A. B. Awan, S. Pierfederici, B. Nahid-Mobarakkeh, and F. Meibody-Tabar, "Linear stabilization of a DC bus supplying a constant power load: A general design approach," *IEEE Trans. Power Electron.*, vol. 25, no. 2, pp. 475–488, Feb. 2010.
- [2] M. Cespedes, L. Xing, and J. Sun, "Constant-power load system stabilization by passive damping," *IEEE Trans. Power Electron.*, vol. 26, no. 7, pp. 1832–1836, Jul. 2011.
- [3] J. Wang and D. Howe, "A power shaping stabilizing control strategy for DC power systems with constant power loads," *IEEE Trans. Power Electron.*, vol. 23, no. 6, pp. 2982–2989, Nov. 2008.
- [4] S. Sanchez, R. Ortega, R. Griño, G. Bergna, and M. Molinas, "Conditions for existence of equilibria of systems with constant power loads," *IEEE Trans. Circuits Syst. I, Reg. Papers*, vol. 61, no. 7, pp. 2204–2211, Jul. 2014.
- [5] N. Barabanov, R. Ortega, R. Griño, and B. Polyak, "On existence and stability of equilibria of linear time-invariant systems with constant power loads," *IEEE Trans. Circuits Syst. I, Reg. Papers*, vol. 63, no. 1, pp. 114–121, Jan. 2016.
- [6] R. D. Middlebrook, "Input filter considerations in design and application of switching regulators," in *Proc. Inf. Assurance Security Rec. Conf.*, 1976.
- [7] S. Hiti, V. Vlatkovic, D. Borojcic, and F. C. Lee, "A new control algorithm for three-phase PWM buck rectifier with input displacement factor compensation," *IEEE Trans. Power Electron.*, vol. 9, no. 2, pp. 173–180, Mar. 1994.
- [8] J. Sun, "Impedance-based stability criterion for grid-connected inverters," *IEEE Trans. Power Electron.*, vol. 26, no. 11, pp. 3075–3078, Nov. 2011.
- [9] S. D. Sudhoff, S. F. Glover, P. T. Lamm, D. H. Schmucker, and D. Delisle, "Admittance space stability analysis of power electronic systems," *IEEE Trans. Aerosp. Electron. Syst.*, vol. 36, no. 3, pp. 965–973, Jul. 2000.
- [10] C. M. Wildrick, F. C. Lee, B. H. Cho, and B. Choi, "A method of defining the load impedance specification for a stable distributed power system," *IEEE Trans. Power Electron.*, vol. 10, no. 3, pp. 280–285, May 1995.
- [11] K. M. Alawasa, Y. A.-R. Mohamed, and W. Xu, "Active mitigation of subsynchronous interactions between PWM voltage-source converters and power networks," *IEEE Trans. Power Electron.*, vol. 29, no. 1, pp. 121–134, Jan. 2014.
- [12] M. Cespedes and J. Sun, "Modeling and mitigation of harmonic resonance between wind turbines and the grid," in *Proc. IEEE Energy Convers. Congr. Expo.*, 2011, pp. 2109–2116.
- [13] M. Céspedes and J. Sun, "Impedance shaping of three-phase grid-parallel voltage-source converters," in *Proc. 27th IEEE Annu. Appl. Power Electron. Conf. Expo.*, 2012, pp. 754–760.
- [14] X. Wang, F. Blaabjerg, M. Liserre, Z. Chen, J. He, and Y. Li, "An active damper for stabilizing power-electronics-based AC systems," *IEEE Trans. Power Electron.*, vol. 29, no. 7, pp. 3318–3329, Jul. 2014.
- [15] X. Wang, F. Blaabjerg, and P. C. Loh, "Proportional derivative based stabilizing control of paralleled grid converters with cables in renewable power plants," in *Proc. 2014 IEEE Energy Convers. Congr. Expo.*, 2014, pp. 4917–4924.
- [16] M. Cespedes and J. Sun, "Adaptive control of grid-connected inverters based on online grid impedance measurements," *IEEE Trans. Sustain. Energy*, vol. 5, no. 2, pp. 516–523, Apr. 2014.
- [17] M. Céspedes and J. Sun, "Mitigation of inverter-grid harmonic resonance by narrow-band damping," *IEEE J. Emerg. Sel. Topics Power Electron.*, vol. 2, no. 4, pp. 1024–1031, Dec. 2014.
- [18] D. Dujic *et al.*, "Power electronic traction transformer-low voltage prototype," *IEEE Trans. Power Electron.*, vol. 28, no. 12, pp. 5522–5534, Dec. 2013.
- [19] J. C. Willems, "Dissipative dynamical systems part I: General theory," *Archive Rational Mech. Anal.*, vol. 45, no. 5, pp. 321–351, 1972.
- [20] L. Harnefors, M. Bongiorno, and S. Lundberg, "Input-admittance calculation and shaping for controlled voltage-source converters," *IEEE Trans. Ind. Electron.*, vol. 54, no. 6, pp. 3323–3334, Dec. 2007.
- [21] L. Harnefors, A. Yepes, A. Vidal, and J. Doval-Gandoy, "Passivity-based controller design of grid-connected VSCs for prevention of electrical resonance instability," *IEEE Trans. Ind. Electron.*, vol. 62, no. 2, pp. 702–710, Feb. 2015.
- [22] L. Harnefors, L. Zhang, and M. Bongiorno, "Frequency-domain passivity-based current controller design," *IET Power Electron.*, vol. 1, no. 4, pp. 455–465, 2008.
- [23] L. Harnefors, X. Wang, A. Yepes, and F. Blaabjerg, "Passivity-based stability assessment of grid-connected VSCs—An overview," *IEEE J. Emerg. Sel. Topics Power Electron.*, vol. 4, no. 1, pp. 116–125, Mar. 2016.
- [24] H. Akagi, E. H. Watanabe, and M. Aredes, *Instantaneous Power Theory and Applications to Power Conditioning*, vol. 31. Hoboken, NJ, USA: Wiley, 2007.
- [25] J. He and Y. W. Li, "Generalized closed-loop control schemes with embedded virtual impedances for voltage source converters with LC or LCL filters," *IEEE Trans. Power Electron.*, vol. 27, no. 4, pp. 1850–1861, Apr. 2012.
- [26] T. Takeshita and N. Matsui, "Current waveform control of PWM converter system for harmonic suppression on distribution system," *IEEE Trans. Ind. Electron.*, vol. 50, no. 6, pp. 1134–1139, Dec. 2003.
- [27] X. Wang, F. Blaabjerg, and Z. Chen, "Synthesis of variable harmonic impedance in inverter-interfaced distributed generation unit for harmonic damping throughout a distribution network," *IEEE Trans. Ind. Appl.*, vol. 48, no. 4, pp. 1407–1417, Jul./Aug. 2012.
- [28] D. Yang, X. Ruan, and H. Wu, "Impedance shaping of the grid-connected inverter with LCL filter to improve its adaptability to the weak grid condition," *IEEE Trans. Power Electron.*, vol. 29, no. 11, pp. 5795–5805, Nov. 2014.
- [29] X. Wu, X. Li, X. Yuan, and Y. Geng, "Grid harmonics suppression scheme for LCL-type grid-connected inverters based on output admittance revision," *IEEE Trans. Sustain. Energy*, vol. 6, no. 2, pp. 411–421, Apr. 2015.
- [30] J. Kwon, X. Wang, and F. Blaabjerg, "Impedance based analysis and design of harmonic resonant controller for a wide range of grid impedance," in *Proc. IEEE 5th Int. Symp. Power Electron. Distrib. Generation Syst.*, 2014, pp. 1–8.
- [31] A. A. A. Radwan and Y. A.-R. Mohamed, "Assessment and mitigation of interaction dynamics in hybrid AC/DC distribution generation systems," *IEEE Trans. Smart Grid*, vol. 3, no. 3, pp. 1382–1393, Sep. 2012.
- [32] J. M. Guerrero, D. Vicuña, L. García, J. Matas, M. Castilla, and J. Miret, "Output impedance design of parallel-connected UPS inverters with wireless load-sharing control," *IEEE Trans. Ind. Electron.*, vol. 52, no. 4, pp. 1126–1135, Aug. 2005.
- [33] R. Pena-Alzola, M. Liserre, F. Blaabjerg, R. Sebastián, J. Dannehl, and F. W. Fuchs, "Analysis of the passive damping losses in LCL-filter-based grid converters," *IEEE Trans. Power Electron.*, vol. 28, no. 6, pp. 2642–2646, Jun. 2013.
- [34] J. Perez, S. Cobrecas, and R. Grino, "Admittance-shaped \mathcal{H}_∞ current controller for grid-connected VSC," in *Proc. IEEE Conf. Emerg. Technol. Factory Autom.*, 2014, pp. 1–8.
- [35] J. Perez, S. Cobrecas, F. J. R. Sanchez, and R. Grino, " \mathcal{H}_∞ simultaneous admittance and tracking current controller of three-phase active grid front-ends," in *Proc. IEEE Int. Conf. Ind. Technol.*, 2015, pp. 2092–2097.
- [36] H. Mosskull, "Optimal stabilization of constant power loads with input LC-filters," *Control Eng. Practice*, vol. 27, pp. 61–73, 2014.
- [37] Q.-C. Zhong and T. Hornik, *Control of Power Inverters in Renewable Energy and Smart Grid Integration*, vol. 97. Hoboken, NJ, USA: Wiley, 2012.
- [38] T. Hornik and Q.-C. Zhong, "Parallel pi voltage \mathcal{H}_∞ current controller for the neutral point of a three-phase inverter," *IEEE Trans. Ind. Electron.*, vol. 60, no. 4, pp. 1335–1343, Apr. 2013.
- [39] G. Weiss, Q.-C. Zhong, T. C. Green, and J. Liang, " \mathcal{H}_∞ repetitive control of DC-AC converters in microgrids," *IEEE Trans. Power Electron.*, vol. 19, no. 1, pp. 219–230, Jan. 2004.
- [40] G. Rigatos, P. Siano, and C. Cecati, "An \mathcal{H}_∞ feedback control approach for three-phase voltage source converters," in *Proc. IEEE 40th Annu. Conf. Ind. Electron. Soc.*, 2014, pp. 1227–1232.
- [41] S. Cobrecas, E. J. Bueno, F. J. Rodriguez, D. Pizarro, and F. Huerta, "Robust loop-shaping \mathcal{H}_∞ control of LCL-connected grid converters," in *Proc. IEEE Int. Symp. Ind. Electron.*, 2010, pp. 3011–3017.
- [42] S. Yang, Q. Lei, F. Z. Peng, and Z. Qian, "A robust control scheme for grid-connected voltage-source inverters," *IEEE Trans. Ind. Electron.*, vol. 58, no. 1, pp. 202–212, Jan. 2011.
- [43] R. Naim, G. Weiss, and S. Ben-Yaakov, " \mathcal{H}_∞ control applied to boost power converters," *IEEE Trans. Power Electron.*, vol. 12, no. 4, pp. 677–683, Jul. 1997.
- [44] T.-S. Lee, S. Chiang, and J.-M. Chang, " \mathcal{H}_∞ loop-shaping controller designs for the single-phase UPS inverters," *IEEE Trans. Power Electron.*, vol. 16, no. 4, pp. 473–481, Jul. 2001.
- [45] P. C. Krause, O. Wasynczuk, and S. D. Sudhoff, *Analysis of Electric Machinery and Drive Systems*, 2nd ed. Piscataway, NJ, USA: IEEE Press, 2002.
- [46] E. J. B. Peña, "Optimización del comportamiento de un convertidor de tres niveles NPC conectado a la red eléctrica." Ph.D. dissertation, Polytechnic School, Univ. Alcalá, Alcalá de Henares, Spain, 2005.

- [47] S. Skogestad and I. Postlethwaite, *Multivariable Feedback Control: Analysis and Design*, vol. 2. New York, NY, USA: Wiley, 2007.
- [48] E. J. Bueno, A. Hernandez, F. J. Rodriguez, C. Giron, R. Mateos, and S. Cobreces, "A DSP-and FPGA-based industrial control with high-speed communication interfaces for grid converters applied to distributed power generation systems," *IEEE Trans. Ind. Electron.*, vol. 56, no. 3, pp. 654–669, Mar. 2009.
- [49] M. H. Bollen, *Understanding Power Quality Problems*, vol. 3. New York, NY, USA: IEEE Press, 2000.



Jorge Pérez (S'16) was born in Madrid, Spain, in 1988. He received the B.Sc. and M.Sc. degrees in industrial electronics and industrial automation process from the University of Alcalá (UAH), Alcalá de Henares, Spain, in 2011 and 2013, respectively. He is currently working toward the Ph.D. degree from UAH, Alcalá de Henares.

Since 2012, he has been a Researcher for the Electronic Engineering Applied to Renewable Energies Research Group of the UAH. His research interests include automatic control applied to power electronic systems, power quality, and distributed power generation systems.



Santiago Cobreces (S'03–M'09) was born in Alcalá de Henares, Spain, in 1980. He received the B.Sc. and M.Sc. degrees in telecom engineering and the Ph.D. degree in electronics engineering from the University of Alcalá, Alcalá de Henares, Spain, in 2003 and 2009, respectively.

Since 2012, he is an Associate Professor with the Department of Electronics, University of Alcalá, where he is a member of the Research Group "Electronics Engineering Applied to the Renewable Energies." His current research interests include automatic control and system identification applied to power electronic systems power quality, and distributed power generation systems.



Robert Griño (M'99–SM'12) received the M.Sc. degree in electrical engineering and the Ph.D. degree in automatic control from the Universitat Politècnica de Catalunya (UPC), Barcelona, Spain, in 1989 and 1997, respectively.

From 1990 to 1991, he was a Research Assistant with the Instituto de Cibernética, UPC. From 1992 to 1998, he was an Assistant Professor with the Automatic Control Department, UPC, where he has been an Associate Professor since 1998. His research interests include digital control, nonlinear control, stability theory, and control of power electronics converters.

Dr. Griño is an affiliate Member of International Federation of Automatic Control and a Member of the Spanish Society on Automation and Control-IFAC.



Francisco J. R. Sánchez (S'99–M'00) received the B.Sc. degree in technical telecommunication engineering from the University of Alcalá, Alcalá de Henares, Spain, in 1985, the M.Sc. degree in telecommunication from the Technical University of Madrid, Madrid, Spain, in 1990, and the Ph.D. degree in electronics engineering from the University of Alcalá, Alcalá de Henares, in 1997.

He worked in the private electronic industry for two years. Since 1986, he has been a Lecturer with the Department of Electronics, University of Alcalá, where now he is a Professor. He is the author of more than 142 refereed publications in international journals, book chapters, and conference proceedings. Also, he has directed more than 45 investigation projects funded by public institutions and private industry. His research interests include the areas of control electronics, real-time processing, and embedded systems applied to power electronic systems.

A robust grid current controller with grid harmonic and filter resonance damping capabilities using a closed-loop admittance shaping

Jorge Pérez, Santiago Cóbrecas Xiongfei Wang, Frede Blaabjerg
Department of Electronics Department of Energy Technology
Universidad de Alcalá Aalborg Universitet
Email: jorge.perez@depeca.uah.es Email: xwa@et.aau.dk, fbl@et.aau.dk

Robert Griñó
Inst. of Industrial and Control Engineering.(IOC)
Universitat Politècnica de Catalunya (UPC)
Email: roberto.grino@upc.edu

Abstract—This paper presents a grid current control of a grid connected Voltage Source Converter (VSC) with an LCL filter. The control method enables to shape the input admittance of the converter in addition to track a given current reference. By specifying a low resistive admittance profile, a suitable controller is obtained by using an \mathcal{H}_∞ synthesis, which will actively damp the filter resonance and the harmonics/inter-harmonics from the grid in a wide frequency range. Additionally, the proposed system presents good robustness with respect to grid uncertainty.

I. INTRODUCTION

This work presents a new grid current controller structure for a Voltage Source Converter (VSC) connected to the grid through an LCL filter. The topology is very common in renewable energy source based power plants, as it has superior output performance. However, the resonant behaviour of the LCL filter presents some drawbacks for its effective and stable current control from the points of view of power quality and system robustness:

From the former point of view, system resonances -in grid or filter- may lead to system oscillations, and even to instabilities of the controlled grid current [1], [2]. Many papers have focused on design of the resonance dampers that improve the overall current dynamics. They can be classified into active [2]–[9] and passive [10]–[14] damping techniques. A related issue is the effect of grid voltage harmonics and inter-harmonics in the control loop. The most usual approach is to design the current controllers with harmonic rejection capabilities, mainly by using PR (proportional + resonant) controllers tuned at the most common harmonics in order to reject them [15]–[17]. However, the harmonic rejection effectiveness depends on different factors, such as the model uncertainties, the discretization process and the presence of computational delays in the system, which may result in ineffective harmonic damping [18]. Additionally, the use of high feedback-gain controllers may lead to poor stability margins [19], and its stable operation becomes more difficult as the harmonics to be rejected approach to the filter resonance [20].

From the robustness point of view, it is known that the stability of the control loop of the LCL-filtered grid-connected

VSC may be compromised by the uncertainty in the grid equivalent impedance, which may lead to the uncontrolled displacement of resonances inside the control band. Several approaches to obtain robust controllers have been explored in the related literature [21], [22] being achieved at the cost of a conservative performance -control bandwidth- reduction, as a consequence of the need complying with Small Gain Theorem [23].

This paper translates the aforementioned problems into the frequency domain input admittance specifications, following the design procedure presented in [24]. This recent method allows to shape the input admittance transfer function of a VSC, in both modulus and phase, while maintaining tracking performance at selected harmonic frequencies.

This new capabilities open the door to face the robustness problem from an alternative point of view: in stead of the classical approach, based on the fulfilment of the Small Gain Theorem, it allows to face the problem trying to comply with certain input admittance conditions described in Middlebrook's criterion [12], [25], which may decrease the closed-loop performance reduction induced by uncertainty. If that admittance, additionally, is low out of the fundamental frequency, the converter will present good inter-harmonic behaviour. That condition also implies a good damping of the LCL-filter resonance [26]. The proposed controller will, in addition, track a given current reference in a band around the fundamental frequency.

The rest of the paper structure is as follows: Section II serves as a theoretical background to the rest of the paper, modelling the considered system and analysing its stability in both stand-alone and grid-connected conditions. Section III explains the proposed method and its limitations, in addition to give some guidelines for the design parameters tuning. Section IV presents the achieved experimental results in both time and frequency domain. It demonstrates the damping capabilities of the proposed method of both LCL filter resonance and grid voltage -inter-harmonics effect. Finally, it analyses its robustness for different grid impedances. The paper concludes with Section V.

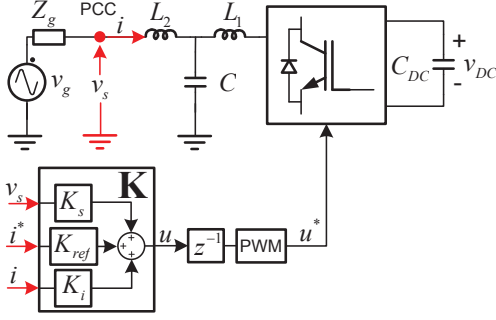


Fig. 1. Simplified single phase equivalent of the considered system.

II. THEORETICAL BACKGROUND AND OBJECTIVES STATEMENT

A. System modelling

Fig. 1 shows a single-phase equivalent of the considered system: grid current i control of a grid-connected VSC with an LCL filter. This single-phase system is considered for both modelling and controller design procedure. Obtained controller can be easily translated and implemented in a three-phase system using $\alpha\beta$ stationary reference frame transformations [27] for its input and output signals.

Open-loop grid current can be expressed in Laplace domain as follows:

$$I(s) = G(s)U(s) + G_d(s)V_s(s), \quad (1)$$

where $I(s)$, $U(s)$ and $V_s(s)$ are the grid current, controller output voltage and point of common coupling (PCC) voltage, respectively, and $G(s)$ and $G_d(s)$ are the open-loop command-to-output and admittance transfer functions;

$$G(s) = -\frac{1}{sC(R_1 + sL_1)(R_2 + sL_2) + R_f + sL_f} \quad (2)$$

$$G_d(s) = \frac{sC(R_1 + sL_1) + 1}{sC(R_1 + sL_1)(R_2 + sL_2) + R_f + sL_f} \quad (3)$$

where C , L_1 and L_2 are the filter capacitor and the converter-side and grid-side filter inductance values, respectively, and R_1 and R_2 are their respective resistive inductance losses.

The controller \mathbf{K}^1 has three inputs; the PCC voltage v_s , the grid current i and the reference current i^* . The only measurements necessary for the controller implementation are, then, the grid currents and voltages, which means a reduced costs in sensors. Note, in addition, that the grid PCC voltage is usually available at no extra sensor cost as grid synchronisation algorithms use it. Dividing the controller matrix in rows $\mathbf{K}(s) = [K_s(s) \ K_{ref}(s) \ K_i(s)]^T$ results in the closed-loop current dynamic shown below;

$$I|_{Z_g(s)=0} = \underbrace{\frac{GK_{ref}}{1 - GK_i}}_{T(s)} I^* + \underbrace{\frac{G_d + GK_s}{1 - GK_i}}_{Y(s)} V_s, \quad (4)$$

¹For notation compactness, the Laplace variable 's' is omitted when its presence results obvious attending to the context

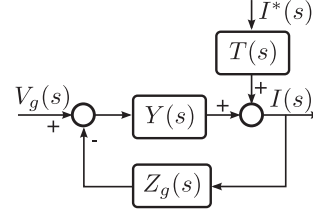


Fig. 2. Block diagram representation of the interconnection of a current-controlled VSC to a non-ideal grid with equivalent serial impedance $Z_g(s)$.

where $T(s)$ and $Y(s)$ are the closed-loop tracking and admittance transfer functions for an ideal grid (i.e., grid impedance $Z_g(s) = 0$).

B. Stability robustness of the Grid-VSC interaction

When a current-controlled VSC is connected to an ideal grid, whose PCC voltage $v_s = v_g$ is independent of the grid current, system stability depends on the closed-loop system formed by the converter and the current controller, as defined (4). Assuming linearity, that amounts to place the roots of $1 - GK_i$ in the left hand side of the complex plane, or to comply with one of the multiple equivalent formulations.

When this controlled-system is connected to a grid with non-negligible equivalent series grid impedance, the system behaves following the block diagram of Fig. 2, described by the following equations:

$$I|_{Z_g(s) \neq 0} = \underbrace{\frac{T}{1 + Z_g Y}}_{T'(s)} I^* + \underbrace{\frac{Y}{1 + Z_g Y}}_{Y'(s)} V_g, \quad (5)$$

where V_g is the ideal grid voltage and $Y'(s)$ and $T'(s)$ are the modified closed-loop admittance and tracking transfer functions, respectively. From (5), it can be seen that the system stability no longer depends only on the stand-alone conditions, but also on the new impedances loop function $L'(s) = Z_g Y$.

Provided that the system is stand-alone stable, the connection stability relies on the relationship between Z_g and Y . Several criteria have been proposed in the literature [12], [28]. One particularly interesting approach is to take advantage of the Strictly Positive Realness of function $Z_g(s)$ [29]: if the rendered Y is positive real, the product $Z_g Y$ will not get negative values, ensuring stability regardless of the functions respective modules.

A system that behaves like a low resistive admittance in a wide range will damp both grid voltage harmonic/interharmonics and the LCL filter resonance, in addition to the improved stability robustness in weak grids. Designing a current controller with good stand-alone stability margins that fulfils this condition is the main objective of this work.

III. DESIGN PROCEDURE AND LIMITATIONS

A. Model-reference approach for controller design

The desired controller is obtained following a model reference \mathcal{H}_∞ design approach [23]. Readers can refer to previous

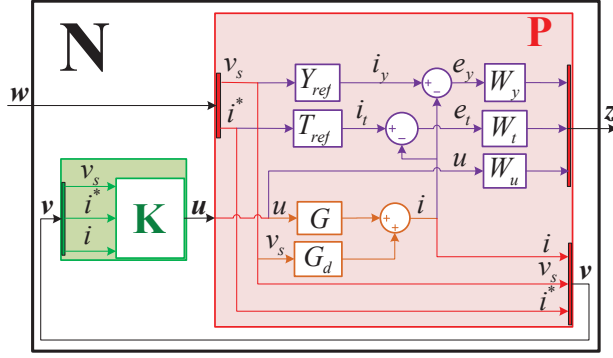


Fig. 3. \mathcal{H}_∞ model-reference approach for admittance shaping control. In red the generalized plant $\mathbf{P}(s)$. Inside of it, the open loop command-to-output G and admittance $G_d(s)$ transfer function, in orange. In purple, a set of elements added for the \mathcal{H}_∞ controller synthesis. They serve as the design parameters. Finally, the obtained controller is represented in green.

work presented by the authors for a more detailed explanation of the underlying theory [24].

The keystone of the \mathcal{H}_∞ control paradigm is the definition of the inner structure (i.e., its input and output vectors) of the generalized plant \mathbf{P} [23]. Fig. 3 shows, in red, the structure of the plant for the presented method. It is formed by the open-loop current dynamic in (1), shown in orange, and the addition of some design parameters shown in purple. \mathbf{P} has the next inputs and outputs; input vector \mathbf{w} , formed by the perturbation signals of the closed-loop system v_s and i^* (see equation (4)), input \mathbf{u} and output vector \mathbf{v} , which are equal to the inputs and outputs of the controller \mathbf{K} output and inputs, respectively, and the output vector \mathbf{z} , which is formed by the signals to be minimized in the design. Once the plant \mathbf{P} is defined, an \mathcal{H}_∞ synthesis process will be used to compute the controller that minimises the energy (norm-2) of the output vector \mathbf{z} with respect to the exogenous input vector \mathbf{w} (i.e., the one that minimize $\|\mathbf{N}\|_\infty$).

In Fig. 3, $Y_{ref}(j\omega)$ represents the desired behaviour, in the frequency domain, of the closed-loop admittance $Y(j\omega)$, as so does $T_{ref}(j\omega)$ for the desired tracking transfer function $T(j\omega)$. Obtained controller should fulfil either $T(j\omega) \approx T_{ref}(j\omega)$ or $Y(j\omega) \approx Y_{ref}(j\omega)$ at a given frequency, resulting in the minimization of the tracking shaping e_t or admittance shaping e_y error signals. Which one is fulfilled depends on the magnitude of the tracking $W_t(j\omega)$ and admittance $W_y(j\omega)$ frequency weights. If the magnitude of $W_y(j\omega)$ is higher than $W_t(j\omega)$ at a given frequency ω_x the synthesized controller $\mathbf{K}(j\omega)$ will fulfil $Y(j\omega_x) \approx Y_{ref}(j\omega_x)$; tracking shaping works analogously. A third weight $W_u(j\omega)$ is added to limit the controller output (i.e., control effort) u . Similarly, high $W_u(j\omega)$ values will result in higher actuation limitation and vice-versa.

Fig. 4 summarizes the design process. First, the desired behaviour of the closed-loop tracking T_{ref} and admittance transfer functions Y_{ref} are chosen. Next, controller objectives are divided in different frequency zones by means of the

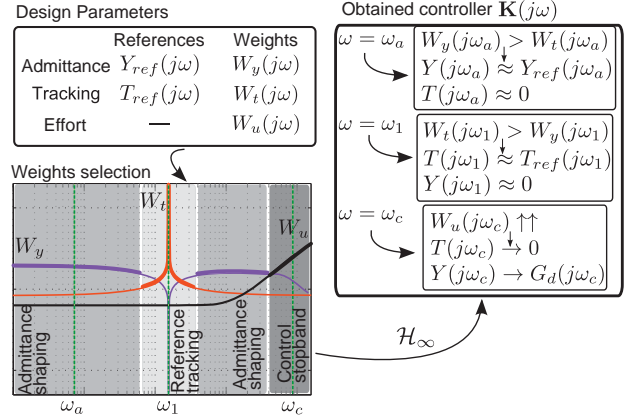


Fig. 4. Simplified scheme of the controller design process.

frequency shaped weights, as depicted in the weight selection of Fig. 4. In this work, controller \mathbf{K} should result in a low resistive closed-loop admittance profile $Y(s)$, with good stand-alone stability margins and good tracking of the current reference at the grid fundamental frequency ω_1 (i.e., $T(j\omega_1) \approx 1$).

B. Design procedure

$T_{ref}(s)$ is defined constant and equal to one, which will result in a good current tracking (i.e., $i \approx i^*$) at the desired frequencies. $Y_{ref}(s)$ is defined constant (i.e., resistive) and with the lowest possible value. This value is usually, as will be justified later on, the open-loop admittance $G_d(j\omega)$ magnitude at the end of the control bandwidth.

For this design, a good admittance shaping (i.e., $Y(j\omega) \approx Y_{ref}(j\omega)$) is desired at both sub- and super-synchronous frequencies and good tracking (i.e., $T(j\omega) \approx T_{ref}(j\omega)$) is desired around the grid synchronous (i.e., fundamental) frequency ω_1 . Additionally, the controller effort u , and then the controller bandwidth, must be limited at high frequencies. The next weighting functions are hence proposed below:

$$W_t(s) = K_t \frac{s^2 + 2\zeta_n \omega_1 s + \omega_1^2}{s^2 + 2\zeta_d \omega_1 s + \omega_1^2} \quad (6)$$

$$W_y(s) = K_y \frac{s^2 + 2\zeta_d \omega_1 s + \omega_1^2}{s^2 + 2\zeta_n \omega_1 s + \omega_1^2} \cdot \frac{1}{(1/\omega_y)s + 1} \quad (7)$$

$$W_u(s) = K_u \frac{(1/\omega_{u1})s + 1}{(1/\omega_{u2})s + 1} \quad (8)$$

A frequency domain magnitude representation of them is shown in Fig. 4. Tracking weight is formed by an initial low gain K_t and a resonant-like gain centred at fundamental frequency ω_1 . Admittance weight is a low pass function with an initial gain $K_y > K_t$ and a pole at ω_y to limit the admittance shaping band. A notch is added at ω_1 , complementary to W_t resonance, to improve the reference tracking shaping inside its frequency range. Finally, control effort weight W_u is a high-pass function with a small initial gain K_u , increasing at high frequencies by means of a zero in ω_{u1} . A pole at ω_{u2} is added at high frequencies to make W_u proper.

Some heuristic rules that have been found to be useful for the weights parameters tuning are presented below. A graphical interpretation of them is summarised in Fig. 5:

1) *Admittance shaping range*: It is recommended to first tune the admittance weight W_y parameters K_y and ω_y . These parameters will define the maximum frequency where tight admittance control is desired. It is important to respect the maximum bandwidth limits that will be described in the next subsection.

2) *Actuation limitation range*: The next step is to consider the controller effort weight W_u . The controller bandwidth is defined by the relative relation between W_y and W_u . It is modified, then, by means of the zero at ω_{u1} , along with the previously fixed W_y pole at ω_y . The controller bandwidth must be kept inside certain limits to obtain good system stability margins. Additionally, the amount of controller effort u within this bandwidth is controlled by the initial gain K_u relative to K_y . This is adjusted to get a controller effort near the saturation limit under nominal transients and disturbances (e.g., voltage dips). That constitutes the first trade-off to be solved, between admittance error minimization and allowed controller actuation / stability robustness.

3) *Tracking shaping range*: The last step is the tuning of the reference tracking band. The tracking weight W_t is included along with the complementary notch-like part in W_y . The minimization of the tracking shaping error e_t at ω_1 depends on the W_t resonance height, which is the ratio $n_h = \zeta_n / \zeta_d$. The higher this ratio is, the smaller the error (i.e., perfect current tracking $i \approx i_{ref}$ can be obtained for very high n_h values). The reference tracking bandwidth is mainly determine by the range where $W_t > W_y$. It can be modified by increasing the initial value K_t in W_t relative to the previously fixed initial value K_y in W_y , or by increasing ζ_n value in both W_t and W_y to increase the resonance/notch width². The wider this band is, the faster the current reference tracking will be, to the detriment of a reduced admittance shaping range around fundamental frequency. Moreover, as current reference tracking strongly relies on feedback action, an increase of the tracking bandwidth will also result in poorer stability margins. A compromise is hence needed in the tuning of these controller parameters.

C. Method and controller limitations

Elements in \mathbf{P} must be LTI and proper. This implies that designed weights can not have infinite gain states (i.e., pure integrators/resonators); however, they can be placed arbitrarily close to the $j\omega$ axis.

The obtained controller \mathbf{K} has the same order of \mathbf{P} , so an increase of the design parameters (i.e., weights or model references) order will provoke an equal increase of \mathbf{K} order. Order reduction techniques can be used, if necessary, to reduce the computation burden of the implemented controller. Alg. 1 in [24] summarizes the modulator modelling process, generalized plant \mathbf{P} generation, controller synthesis process and its discretization for its implementation in a digital controller.

²In order to preserve the ratio n_h , ζ_d must increase equally to ζ_n .

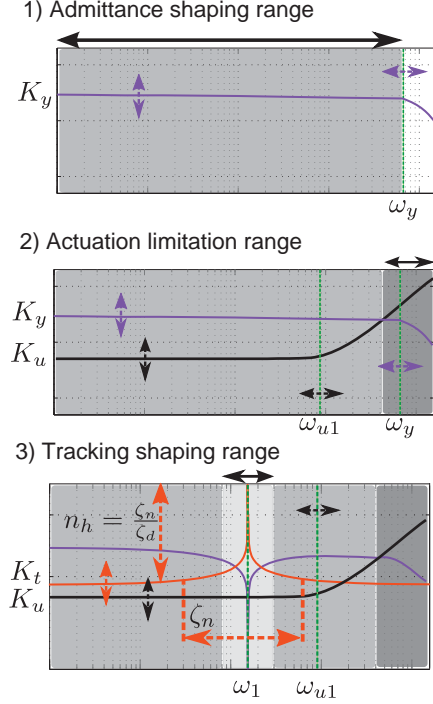


Fig. 5. Step-by-step weights design graphic guideline.

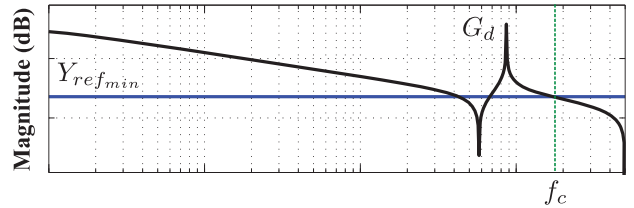


Fig. 6. Minimum obtainable resistive admittance reference Y_{refmin} as a function of the open-loop admittance G_d and the maximum admittance shaping bandwidth f_c .

The control of the system by PWM signals generated by a digital control platform induces bandwidth limitations. A high bound in controller bandwidth limitation is $f_c = 1/(2\pi T_s)$ Hz [23]. It is important to note that this limitation affects both feedforward and feedback terms because both are affected by the modulator and the delay. This means that admittance shaping can not be obtained above this frequency, making impossible to reduce the closed-loop admittance $Y(s)$ below its open-loop value $G_d(s)$ at f_c . From an application design point of view, this implies that the minimum obtainable resistive admittance reference Y_{ref} is equal to $G_d(s)$ magnitude at f_c , and, to reduce it, either the sampling time T_s must be reduced or the filter inductances must be increased, as both will result in a smaller magnitude of $G_d(s)$ at f_c (see Fig. 6).

The loop function $L(s)$ relative degree complies with the conditions for appliance of the Bode sensitivity integral theorem (first waterbed formula) [23]. It states that an increase in the feedback action of the controller inside a given frequency

TABLE I. EXPERIMENTAL SETUP PARAMETERS

V_{gN}	120 V	ω_1	$2\pi 60$ rad/s
S_n	2.6 kVA	C_{DC}	600 μ F
V_{DC}^*	650 V	C	15 μ F
L_1	5.2 mH	L_2	4 mH
R_1	28.8 m Ω	R_2	18.6 m Ω
T_s	100 μ s	T_{sw}	100 μ s

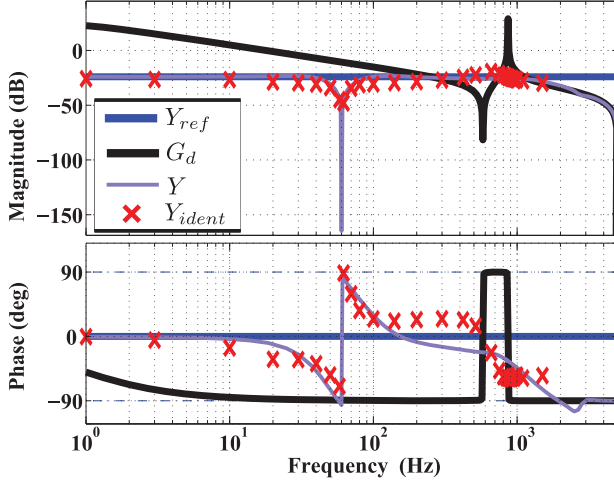


Fig. 7. Obtained input admittance by the proposed method.

band (i.e., frequencies where $|S(s)| < 1$) comes at the cost of a higher $\|S(s)\|_\infty$ value and, then, in a reduction of the stability margins. Design parameters must take into account this trade-off between close-loop performance and system robustness.

IV. RESULTS

Table I shows the main parameters considered for the experimental set up. S_n , V_{gN} and ω_1 are the nominal power, grid voltage and grid frequency, respectively. V_{DC}^* and C_{DC} are the DC-bus reference voltage and capacitor value, respectively. Finally, T_s is the sampling period of the digital controller and T_{sw} is the switching period of the Danfoss VSC. The controller is implemented in a DS1007 dSPACE system. An AC programmable power supply Chroma 61845 is used to emulate the grid in order to generate different harmonics and inter-harmonics in the PCC.

A. Frequency domain results

Fig. 7 shows the obtained closed-loop admittance Y , its open-loop value G_d and the given admittance reference Y_{ref} in purple, black and blue lines respectively. Obtained admittance Y follows given reference $Y_{ref} = 0.06 \Omega^{-1}$ in the desired frequencies (i.e., sub and super synchronous). Y_{ident} shows experimental measurements of the controlled admittance³. The

³To obtain them, three phase small controlled voltage signals are added to the nominal grid voltage at different frequencies by means of the AC power supply. The steady-state current response is, then, measured. Y_{ident} marks the magnitude/phase relation between the introduced voltage and measured current at each frequency.

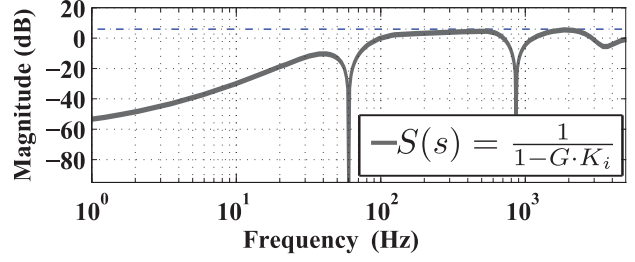


Fig. 8. Sensitivity function magnitude.

experimental admittance results show a well damped LCL resonance seen in G_d . Additionally, it demonstrates that any harmonic/inter-harmonics in the PCC will be damped to a current oscillation of, at most, 6 % of the introduced voltage perturbation.

B. Robustness results

Fig. 8 shows the magnitude of the sensitivity transfer function $S(s)$. Its maximum peak value fulfils the stand-alone stability condition $\|S(s)\|_\infty < 6$ dB, marked in the figure by a blue dashed line. As stated before, that will assure good stand-alone stability margins, with a gain margin $GM > 6$ dB and a phase margin $PM > 30^\circ$.

The presented application is next tested for two different grid impedance topologies: a purely inductive grid $Z_g(s) = L_g s$ and a resonant inductive-capacitive grid $Z_g(s) = (L_g s) / (L_g C_g s^2 + 1)$. Fig. 9 shows modified admittance $Y'(s)$ closed loop poles (i.e., roots of $1 + Z_g Y$) for changes of L_g in the inductive grid and C_g capacitance in the inductive-capacitive grid: L_g is fixed to 0.11 pu⁴ in the latter. The system is stable for all inductive grids considered⁵. However, it has some unstable zones for inductive-capacitive grids (red lines in Fig. 9). These instabilities appear when the resonance of Z_g matches, in frequency, the two non-dissipative zones of the obtained admittance Y in Fig. 7: the first in the fundamental frequency ω_1 , that interacts with the grid for a C_g inside the interval $[9, 10]$ pu, and the second at high frequencies outside the controller bandwidth f_c , for a C_g inside the interval $[0.003, 0.025]$ pu.

Fig. 10 and Fig. 11 show $Y'(s)$ magnitude for some of the previous inductive and inductive-capacitive grid changes, respectively. As it can be seen, an inductive behaviour of the grid decreases even more the obtained admittance and don't affect the LCL resonance damping. However, the interaction between the LC grid and the high frequency non-dissipative zone of the converter admittance generates a resonance in Y' : the red box in Fig. 11 represents the zone where this resonance is unstable. The capacitive behaviour of Z_g interacts in this case with

⁴Grid impedance parameters are expressed in per unit values of the system nominal impedance $Z_N = 3V_{gN}^2/S_N$ (i.e., $L_N = Z_N/\omega_1$ and $C_N = 1/(Z_N\omega_1)$)

⁵It is important to remark that some of these grid impedances are not feasible in practice, as their high values will require huge controller actuation for grid current tracking. This analysis only shows the stability robustness of the method.

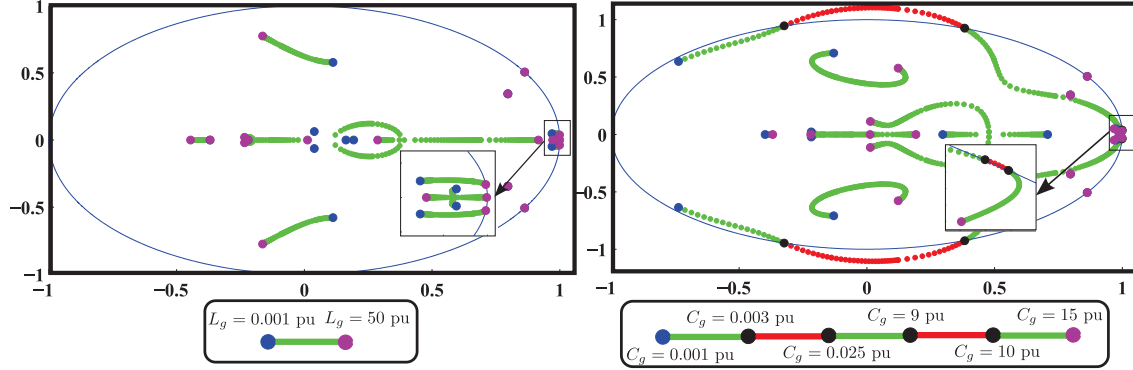


Fig. 9. The admittance $Y'(s)$ poles for changes of inductive grid (left) and changes of capacitive grid (right). The red lines represents unstable cases.

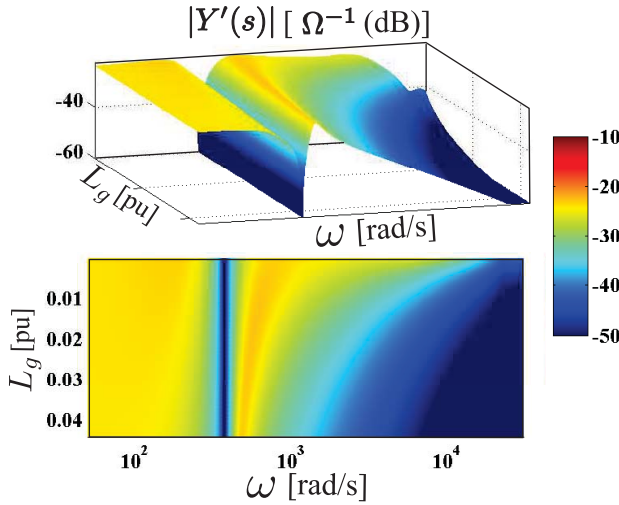


Fig. 10. Admittance magnitude $|Y'(s)|$ for changes of an inductive grid.

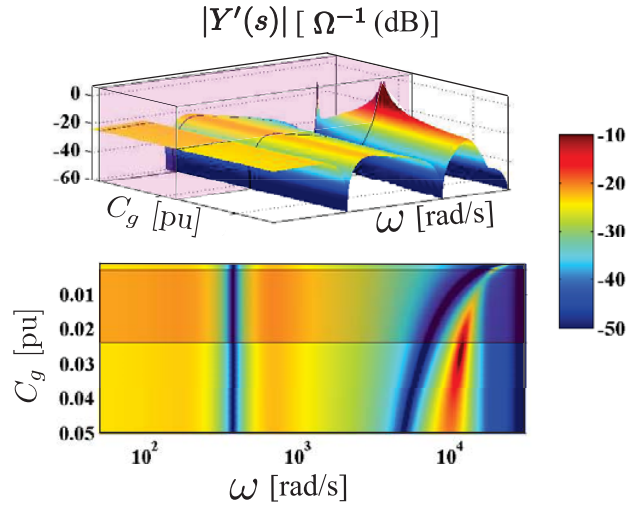


Fig. 11. Admittance magnitude $|Y'(s)|$ for changes of an inductive-capacitive grid. The red box represents C_g interval where the complex system becomes unstable.

the inductive and non-dissipative behaviour of the converter at high frequencies. As this non-dissipative zone is beyond the admittance control bandwidth, it can only be reduced by a more complex admittance reference that increases system admittance phase (and, then, magnitude) enough prior to the end of controller bandwidth. Some previous works have study this by including derivative terms in their current controllers [17], [30]. However, this phase increase will provoke bigger actuations and, if feedback is involved, smaller stand-alone margins. In any case, the result in Fig. 11 shows the worst case scenario, where the grid resonance is not damped by any resistive element, which is rarely the real case. Additionally, as shown in Fig. 7, experimental results Y_{exp} presents a more resistive behaviour at high frequencies than the theoretical obtained admittance Y , which means that this non-dissipative zone could even not exist in the real application.

C. Time domain results

This subsection presents some time domain experimental results of the obtained grid current control for different grid

conditions, grouped in Fig. 12. Fig. 12(a) shows the tracking results for a sudden change of the grid current reference i^* with ideal grid conditions (i.e., $Z_g = 0$ and PCC voltage v_s equal to its nominal value). As it can be seen, the grid current successfully follows its reference. Fig. 12(b) shows a similar experiment, this time with an LC resonant grid impedance connected between the LCL filter and the AC power supply. Again, the current is stable and quickly track the given reference. Note that the grid impedance resonance is perfectly damped by the converter resistive admittance. This behaviour is expected attending to admittance magnitude $|Y'(s)|$ in Fig. 11 for the chosen grid impedance parameters (i.e., $L_g = 0.11$ pu and $C_g = 0.05$ pu).

The grid voltage harmonic rejection capabilities of the proposed method are tested below. Fig. 13 shows the total harmonic distortion (THD) for four different simulated test cases and different operational points: In test 1 (T1) a 5th harmonic of 0.12 pu is introduced in the grid; in test 2 (T2)

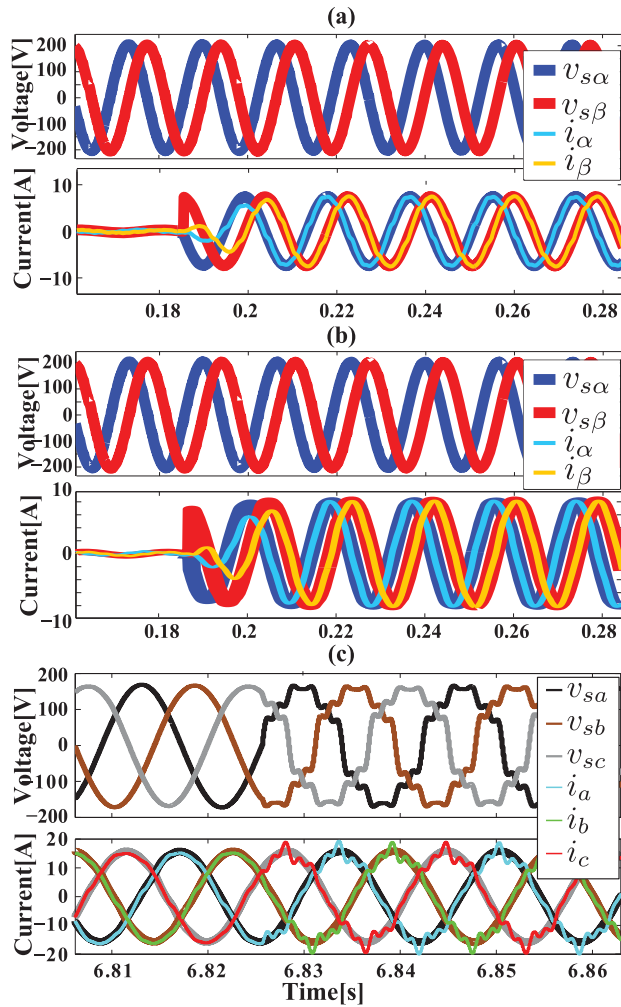


Fig. 12. (a) Experimental time domain tracking results for an ideal grid impedance $Z_g = 0$. (b) Experimental time domain tracking results for a resonant LC grid: $L_g = 0.11$ pu and $C_g = 0.05$ pu. (c) Experimental time domain results to test 4 with an ideal grid impedance $Z_g = 0$.

a 7^{th} harmonic of 0.1 pu is added to T1; in test 3 (T3) two more harmonics, $11^{th} = 0.7$ pu and $13^{th} = 0.6$ pu, are added; finally test 4 (T4) is completed with many high frequency harmonics $19^{th} = 0.6$ pu, $23^{th} = 0.6$ p.u, $25^{th} = 0.6$ pu, $29^{th} = 0.5$ pu, $31^{th} = 0.3$ pu, $35^{th} = 0.3$ pu and $37^{th} = 0.3$ pu. Fig. 12(c) shows the experimental time domain results to test 4. The grid currents i still follows its (reactive) reference i^* after the introduction of grid voltage harmonics in v_s , with reduced current distortion thanks to its low admittance profile.

V. CONCLUSION

A grid current controller for a VSC connected to the grid through an LCL filter using a shaped closed loop admittance is presented. With the presented method, a low resistive admittance can be obtained, which will simultaneously damp the filter resonance and reduce the effect of grid voltage

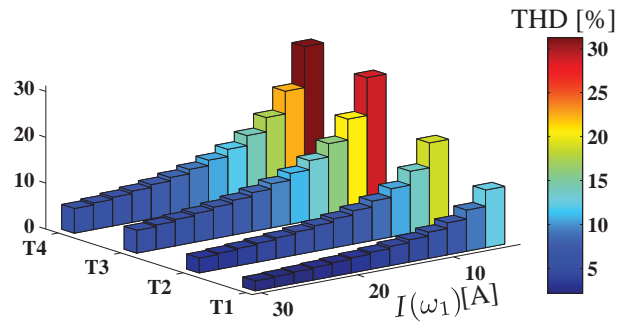


Fig. 13. Obtained THD for different harmonic test.

harmonics and inter-harmonics in a wide frequency range, even at high frequencies closed to the filter resonance. In terms of damping, the main advantage of the method is the reduced number of sensors needed to its implementation. In terms of harmonics damping, the presented method is probably not as effective as the classical PR gains tuned at certain frequencies (if a good system modelling is considered, including discretization and time delays effects); the main advantage of the method is that it damps the disturbance from the grid voltage in a wider frequency range, both harmonics and inter-harmonics and in both sub and super synchronous frequencies. Additionally, the system has good stand-alone stability margins, which is a known concern when multiple PR feedback gains are introduced. Finally, the low resistive admittance obtained makes the system very robust for changes of the grid impedance.

Future studies will analyse the effect of more complex admittance profiles, whit bigger magnitude reduction at the main grid harmonic frequencies, to improve the current controller response to the main PCC voltage perturbations.

ACKNOWLEDGEMENT

The work of the University of Alcalá group was supported in part by the spanish research projects CONPOSITE (ENE2011-28527-C04-02 Ministerio de Economía y Competitividad), PRICAM (S2013/ICE-2933 Consejería de educación, juventud y deporte de la Comunidad de Madrid) and DIANA (CCG2015/EXP-064 Universidad de Alcalá). The work of Robert Griño was supported in part by the Government of Spain through the *Ministerio de Economía y Competitividad* Project DPI2013-41224-P and by the *Generalitat de Catalunya* through the project 2014 SGR 267.

REFERENCES

- [1] L. Harnefors, L. Zhang, and M. Bongiorno, "Frequency-domain passivity-based current controller design," *IET Power Electronics*, vol. 1, no. 4, pp. 455–465, 2008.
- [2] M. Liserre, R. Teodorescu, and F. Blaabjerg, "Stability of photovoltaic and wind turbine grid-connected inverters for a large set of grid impedance values," *IEEE transactions on power electronics*, vol. 21, no. 1, pp. 263–272, 2006.
- [3] M. Liserre, A. D. Aquila, and F. Blaabjerg, "Genetic algorithm-based design of the active damping for an lcl-filter three-phase active rectifier," *IEEE Transactions on Power Electronics*, vol. 19, no. 1, pp. 76–86, 2004.

- [4] V. Blasko and V. Kaura, "A novel control to actively damp resonance in input lc filter of a three-phase voltage source converter," *IEEE Transactions on Industry Applications*, vol. 33, no. 2, pp. 542–550, 1997.
- [5] J. L. Agorreta, M. Borrega, J. López, and L. Marroyo, "Modeling and control of paralleled grid-connected inverters with lcl filter coupled due to grid impedance in pv plants," *IEEE Transactions on Power Electronics*, vol. 26, no. 3, pp. 770–785, 2011.
- [6] J. Dannehl, F. W. Fuchs, S. Hansen, and P. B. Thøgersen, "Investigation of active damping approaches for pi-based current control of grid-connected pulse width modulation converters with lcl filters," *IEEE Transactions on Industry Applications*, vol. 46, no. 4, pp. 1509–1517, 2010.
- [7] J. He and Y. W. Li, "Generalized closed-loop control schemes with embedded virtual impedances for voltage source converters with lc or lcl filters," *IEEE Transactions on Power Electronics*, vol. 27, no. 4, pp. 1850–1861, 2012.
- [8] Y. Tang, P. C. Loh, P. Wang, F. H. Choo, and F. Gao, "Exploring inherent damping characteristic of lcl-filters for three-phase grid-connected voltage source inverters," *IEEE Transactions on Power Electronics*, vol. 27, no. 3, pp. 1433–1443, 2012.
- [9] S. G. Parker, B. P. McGrath, and D. G. Holmes, "Regions of active damping control for lcl filters," *IEEE Transactions on Industry Applications*, vol. 50, no. 1, pp. 424–432, 2014.
- [10] T. Nussbaumer, M. L. Heldwein, and J. W. Kolar, "Differential mode input filter design for a three-phase buck-type pwm rectifier based on modeling of the emc test receiver," *IEEE Transactions on Industrial Electronics*, vol. 53, no. 5, pp. 1649–1661, 2006.
- [11] M. Cespedes, L. Xing, and J. Sun, "Constant-power load system stabilization by passive damping," *IEEE Transactions on Power Electronics*, vol. 26, no. 7, pp. 1832–1836, 2011.
- [12] R. D. Middlebrook, "Input filter considerations in design and application of switching regulators," in *Proc. of IAS*, 1976.
- [13] R. Pena-Alzola, M. Liserre, F. Blaabjerg, R. Sebastián, J. Dannehl, and F. W. Fuchs, "Analysis of the passive damping losses in lcl-filter-based grid converters," *IEEE Transactions on Power Electronics*, vol. 28, no. 6, pp. 2642–2646, 2013.
- [14] R. W. Erickson, "Optimal single resistor damping of input filters," in *Proc. of Applied Power Electronics Conference and Exposition*, vol. 2. Citeseer, 1999, pp. 1073–1079.
- [15] F. Rodriguez, E. Bueno, M. Aredes, L. Rolim, F. A. Neves, and M. C. Cavalcanti, "Discrete-time implementation of second order generalized integrators for grid converters," in *Proc. of 34th Annual Conference on IEEE Industrial Electronics Society IECON 2008*. IEEE, 2008, pp. 176–181.
- [16] A. Vidal, F. D. Freijedo, A. Yepes, P. Fernandez-Comesana, J. Malvar, O. Lopez, and J. Doval-Gandoy, "Assessment and optimization of the transient response of proportional-resonant current controllers for distributed power generation systems," *IEEE Transactions on Industrial Electronics*, vol. 60, no. 4, pp. 1367–1383, 2013.
- [17] L. Harnefors, A. Yepes, A. Vidal, and J. Doval-Gandoy, "Passivity-based controller design of grid-connected vsos for prevention of electrical resonance instability," *IEEE Transactions on Industrial Electronics*, vol. 62, no. 2, pp. 702–710, 2015.
- [18] A. G. Yepes, "Digital resonant current controllers for voltage source converters," Ph.D. dissertation, UNIVERSITY OF VIGO, 2011.
- [19] A. G. Yepes, F. D. Freijedo, O. Lopez, and J. Doval-Gandoy, "Analysis and design of resonant current controllers for voltage-source converters by means of nyquist diagrams and sensitivity function," *IEEE Transactions on Industrial Electronics*, vol. 58, no. 11, pp. 5231–5250, 2011.
- [20] X. Wang, F. Blaabjerg, and P. C. Loh, "Virtual rc damping of lcl-filtered voltage source converters with extended selective harmonic compensation," *IEEE Transactions on Power Electronics*, vol. 30, no. 9, pp. 4726–4737, 2015.
- [21] S. Cobreces, E. J. Bueno, F. J. Rodriguez, D. Pizarro, and F. Huerta, "Robust loop-shaping h-inf control of lcl-connected grid converters," in *Proc. of IEEE International Symposium on Industrial Electronics (ISIE)*. IEEE, 2010, pp. 3011–3017.
- [22] I. J. Gabe, V. F. Montagner, and H. Pinheiro, "Design and implementation of a robust current controller for vsi connected to the grid through an lcl filter," *IEEE Transactions on Power Electronics*, vol. 24, no. 6, pp. 1444–1452, 2009.
- [23] S. Skogestad and I. Postlethwaite, *Multivariable feedback control: analysis and design*. Wiley New York, 2007, vol. 2.
- [24] J. Perez, S. Cobreces, R. Grino, and F. Rodriguez, "H-inf current controller for input admittance shaping of vsc-based grid applications," *IEEE Transactions on Power Electronics*, vol. PP, 2016.
- [25] J. Sun, "Impedance-based stability criterion for grid-connected inverters," *IEEE Transactions on Power Electronics*, vol. 26, no. 11, pp. 3075–3078, 2011.
- [26] J. Perez, S. Cobreces, D. Pizarro, F. J. Rodriguez Sanchez, and R. Grino, "Resonance damping of lcl filters via input admittance frequency shaping," in *Proc. of the 2016 IEEE 25th International Symposium on Industrial Electronics (ISIE)*. IEEE, 2016, pp. 516–521.
- [27] P. C. Krause, O. Wasynczuk, and S. D. Sudhoff, *Analysis of Electric Machinery and Drive Systems. 2nd Edition*. IEEE Press. Wiley-Interscience, 2002.
- [28] L. Harnefors, M. Bongiorno, and S. Lundberg, "Input-admittance calculation and shaping for controlled voltage-source converters," *IEEE Transactions on Industrial Electronics*, vol. 54, no. 6, pp. 3323–3334, 2007.
- [29] S. V. Brian D. O. Anderson, *Network Analysis and Synthesis: A Modern Systems Theory Approach*. Dover Publications, 2006.
- [30] X. Wang, F. Blaabjerg, and P. C. Loh, "Proportional derivative based stabilizing control of paralleled grid converters with cables in renewable power plants," in *Proc. of IEEE Energy Conversion Congress and Exposition (ECCE)*. IEEE, 2014, pp. 4917–4924.

Bibliography

- [Acharya et al., 2008] Acharya, K., Mazumder, S. K., and Basu, I. (2008). Reaching criterion of a three-phase voltage-source inverter operating with passive and nonlinear loads and its impact on global stability. *IEEE Transactions on Industrial Electronics*, 55(4):1795–1812.
- [Agorreta et al., 2011] Agorreta, J. L., Borrega, M., López, J., and Marroyo, L. (2011). Modeling and control of-paralleled grid-connected inverters with lcl filter coupled due to grid impedance in pv plants. *IEEE Transactions on Power Electronics*, 26(3):770–785.
- [Akagi, 2005] Akagi, H. (2005). Active harmonic filters. *Proceedings of the IEEE*, 93(12):2128–2141.
- [Akagi et al., 1986] Akagi, H., Nabae, A., and Atoh, S. (1986). Control strategy of active power filters using multiple voltage-source pwm converters. *IEEE transactions on industry applications*, (3):460–465.
- [Akagi et al., 2007] Akagi, H., Watanabe, E. H., and Aredes, M. (2007). *Instantaneous power theory and applications to power conditioning*, volume 31. John Wiley & Sons.
- [Alawasa et al., 2013] Alawasa, K. M., Mohamed, Y. A.-R., Xu, W., et al. (2013). Modeling, analysis, and suppression of the impact of full-scale wind-power converters on subsynchronous damping. *IEEE Systems Journal*, 7(4):700–712.
- [Alawasa et al., 2014] Alawasa, K. M., Mohamed, Y. A.-R., Xu, W., et al. (2014). Active mitigation of subsynchronous interactions between pwm voltage-source converters and power networks. *IEEE Transactions on Power Electronics*, 29(1):121–134.
- [Alepuz et al., 2006] Alepuz, S., Busquets-Monge, S., Bordonau, J., Gago, J., González, D., and Balcells, J. (2006). Interfacing renewable energy sources to the utility grid using a three-level inverter. *IEEE Transactions on Industrial Electronics*, 53(5):1504–1511.
- [Altowati et al., 2007] Altowati, A., Zenger, K., and Suntio, T. (2007). Qft based robust controller design for a dc-dc switching power converter. In *2007 European Conference on Power Electronics and Applications*, pages 1–11. IEEE.
- [Areerak et al., 2012] Areerak, K., Bozhko, S., Asher, G., De Lillo, L., and Thomas, D. (2012). Stability study for a hybrid ac-dc more-electric aircraft power system. *Aerospace and Electronic Systems, IEEE Transactions on*, 48(1):329–347.
- [Ariyasinghe and Vilathgamuwa, 2008] Ariyasinghe, D. P. and Vilathgamuwa, D. M. (2008). Stability analysis of microgrids with constant power loads. In *Proc. of IEEE International Conference on Sustainable Energy Technologies, ICSET*, pages 279–284. IEEE.
- [Awad, 2002] Awad, H. (2002). Vector control of static series compensator for mitigation of voltage dips.

- [Azémar et al., 2015] Azémar, J., Gueguen, P., and Yole Développement (2015). Power electronics overview: What are the markets and trends? *Semicon Europa 2015*.
- [Belkhat, 1997] Belkhat, M. (1997). Stability criteria for ac power systems with regulated loads.
- [Belkhat et al., 1995] Belkhat, M., Cooley, R., and Witulski, A. (1995). Large signal stability criteria for distributed systems with constant power loads. In *Proc. of 26th Annual IEEE Power Electronics Specialists Conference, PESC*, volume 2, pages 1333–1338. IEEE.
- [Blaabjerg and Wang, 2015] Blaabjerg, F. and Wang, X. (2015). Harmonic modeling and stability in power electronic based power systems. *The 6th international symposium on power electronics for distributed generation systems*.
- [Blasko and Kaura, 1997] Blasko, V. and Kaura, V. (1997). A novel control to actively damp resonance in input lc filter of a three-phase voltage source converter. *IEEE Transactions on Industry Applications*, 33(2):542–550.
- [Bollen, 2000] Bollen, M. H. (2000). *Understanding power quality problems*, volume 3. IEEE press New York.
- [Bueno et al., 2009] Bueno, E. J., Hernandez, A., Rodriguez, F. J., Giron, C., Mateos, R., and Cobrecas, S. (2009). A dsp-and fpga-based industrial control with high-speed communication interfaces for grid converters applied to distributed power generation systems. *IEEE Transactions on Industrial Electronics*, 56(3):654–669.
- [Burgos et al., 2010] Burgos, R., Boroyevich, D., Wang, F., Karimi, K., and Francis, G. (2010). On the ac stability of high power factor three-phase rectifiers. In *Proc. of IEEE Energy Conversion Congress and Exposition (ECCE)*, pages 2047–2054. IEEE.
- [Canay, 1982] Canay, I. (1982). A novel approach to the torsional interaction and electrical damping of the synchronous machine part i: theory. *IEEE Transactions on Power Apparatus and Systems*, (10):3630–3638.
- [CEI/IEC 1000-2-1:1990, 1990] CEI/IEC 1000-2-1:1990 (1990). Electromagnetic Compatibility, Part 2: Environment, Sect. 1: Description of the environment – Electromagnetic environment for low-frequency conducted disturbances and signalling in public power supply systems. Standard, International Electrotechnical Commission, Geneva, CH.
- [Céspedes and Sun, 2009] Céspedes, M. and Sun, J. (2009). Renewable energy systems instability involving grid-parallel inverters. In *Proc. of Twenty-Fourth Annual IEEE Applied Power Electronics Conference and Exposition APEC 2009.*, pages 1971–1977. IEEE.
- [Céspedes and Sun, 2011] Céspedes, M. and Sun, J. (2011). Modeling and mitigation of harmonic resonance between wind turbines and the grid. In *Proc. of IEEE Energy Conversion Congress and Exposition (ECCE)*, pages 2109–2116. IEEE.
- [Céspedes and Sun, 2012] Céspedes, M. and Sun, J. (2012). Impedance shaping of three-phase grid-parallel voltage-source converters. In *Proc. of Twenty-Seventh Annual IEEE Applied Power Electronics Conference and Exposition (APEC)*, pages 754–760. IEEE.
- [Céspedes and Sun, 2014a] Céspedes, M. and Sun, J. (2014a). Adaptive control of grid-connected inverters based on online grid impedance measurements. *IEEE Transactions on Sustainable Energy*, 5(2):516–523.

- [Cespedes and Sun, 2014b] Cespedes, M. and Sun, J. (2014b). Mitigation of inverter-grid harmonic resonance by narrow-band damping. *IEEE Journal of Emerging and Selected Topics in Power Electronics*, 2(4):1024–1031.
- [Cespedes et al., 2011] Cespedes, M., Xing, L., and Sun, J. (2011). Constant-power load system stabilization by passive damping. *IEEE Transactions on Power Electronics*, 26(7):1832–1836.
- [Chen et al., 2016] Chen, C., Xiong, J., Wan, Z., Lei, J., and Zhang, K. (2016). Time delay compensation method based on area equivalence for active damping of lcl-type converter. *IEEE Transactions on Power Electronics*, PP.
- [Chen and Francis, 2012] Chen, T. and Francis, B. A. (2012). *Optimal sampled-data control systems*. Springer Science & Business Media.
- [Chiang and Chang, 2001] Chiang, S. and Chang, J. (2001). Parallel control of the ups inverters with frequency-dependent droop scheme. In *Proc. of 32th Annual IEEE Power Electronics Specialists Conference, PESC*, volume 2, pages 957–961. IEEE.
- [Ciezki and Ashton, 2000] Ciezki, J. G. and Ashton, R. W. (2000). Selection and stability issues associated with a navy shipboard dc zonal electric distribution system. *IEEE Transactions on Power Delivery*, 15(2):665–669.
- [Cóbreces, 2009] Cóbreces, S. (2009). *Optimization and analysis of the current control loop of VSCs connected to uncertain grids through LCL filters*. PhD thesis, Ph. D. Thesis, University of Alcalá, Madrid, Spain.
- [Cóbreces et al., 2007] Cóbreces, S., Bueno, E., Rodriguez, F. J., Huerta, F., and Rodriguez, P. (2007). Influence analysis of the effects of an inductive-resistive weak grid over l and lcl filter current hysteresis controllers. In *Proc. of European Conference on Power Electronics and Applications*, pages 1–10. IEEE.
- [Cóbreces et al., 2010] Cóbreces, S., Bueno, E. J., Rodriguez, F. J., Pizarro, D., and Huerta, F. (2010). Robust loop-shaping h-inf control of lcl-connected grid converters. In *Proc. of IEEE International Symposium on Industrial Electronics (ISIE)*, pages 3011–3017. IEEE.
- [Dahono, 2002] Dahono, P. A. (2002). A control method to damp oscillation in the input lc filter. In *Proc. of 33th Annual IEEE Power Electronics Specialists Conference, PESC*, volume 4, pages 1630–1635. IEEE.
- [Dannehl et al., 2010] Dannehl, J., Fuchs, F. W., Hansen, S., and Thøgersen, P. B. (2010). Investigation of active damping approaches for pi-based current control of grid-connected pulse width modulation converters with lcl filters. *IEEE Transactions on Industry Applications*, 46(4):1509–1517.
- [Dannehl et al., 2011] Dannehl, J., Liserre, M., and Fuchs, F. W. (2011). Filter-based active damping of voltage source converters with filter. *IEEE Transactions on Industrial Electronics*, 58(8):3623–3633.
- [del Toro et al., 2016] del Toro, J. M., Pérez, J., Cóbreces, S., and Rodríguez, F. J. (2016). Robust qft current control design for dc/ac grid converter. In *Proc. of 42nd Annual Conference of the IEEE Industrial Electronics Society, IECON 2016*, pages 7221–7226. IEEE.
- [Deng et al., 2008] Deng, H., Oruganti, R., and Srinivasan, D. (2008). A simple control method for high-performance ups inverters through output-impedance reduction. *Industrial Electronics, IEEE Transactions on*, 55(2):888–898.

- [Dias et al., 2008] Dias, R., Neves, F., Bueno, E., and Cavalcanti, M. (2008). Robust virtual flux oriented direct power control for three-phase rectifiers. In *Proceedings of the VII Conferência Internacional de Aplicações Industriais. INDUSCON*, volume 8.
- [Dujic et al., 2013] Dujic, D., Zhao, C., Mester, A., Steinke, J. K., Weiss, M., Lewdeni-Schmid, S., Chaudhuri, T., and Stefanutti, P. (2013). Power electronic traction transformer-low voltage prototype. *IEEE Transactions on Power Electronics*, 28(12):5522–5534.
- [Durrant et al., 2004] Durrant, M., Werner, H., and Abbott, K. (2004). Synthesis of multi-objective controllers for a vsc hvdc terminal using lmis. In *43rd IEEE Conference on Decision and Control, 2004. CDC.*, volume 4, pages 4473–4478.
- [Emadi, 2004] Emadi, A. (2004). Modeling of power electronic loads in ac distribution systems using the generalized state-space averaging method. *IEEE Transactions on Industrial Electronics*, 51(5):992–1000.
- [Emadi et al., 1999] Emadi, A., Fahimi, B., and Ehsani, M. (1999). On the concept of negative impedance instability in the more electric aircraft power systems with constant power loads. Technical report, SAE Technical Paper.
- [Emadi et al., 2006] Emadi, A., Khaligh, A., Rivetta, C. H., and Williamson, G. A. (2006). Constant power loads and negative impedance instability in automotive systems: definition, modeling, stability, and control of power electronic converters and motor drives. *IEEE Transactions on Vehicular Technology*, 55(4):1112–1125.
- [Erickson, 1999] Erickson, R. W. (1999). Optimal single resistor damping of input filters. In *Proc. of Applied Power Electronics Conference and Exposition*, volume 2, pages 1073–1079. Citeseer.
- [Familiant et al., 2009] Familiant, Y., Huang, J., Corzine, K., Belkhatat, M., et al. (2009). New techniques for measuring impedance characteristics of three-phase ac power systems. *IEEE Transactions on Power Electronics*, 24(7):1802–1810.
- [Feng et al., 2002] Feng, X., Liu, J., and Lee, F. C. (2002). Impedance specifications for stable dc distributed power systems. *IEEE Transactions on Power Electronics*, 17(2):157–162.
- [Francis et al., 2011] Francis, G., Burgos, R., Boroyevich, D., Wang, F., and Karimi, K. (2011). An algorithm and implementation system for measuring impedance in the dq domain. In *Proc. of IEEE Energy Conversion Congress and Exposition (ECCE)*, pages 3221–3228. IEEE.
- [Freijedo et al., 2015] Freijedo, F., Chaudhary, S., Teodorescu, R., Guerrero, J., Bak, C., Kocewiak, L., and Jensen, C. (2015). Harmonic resonances in wind power plants: Modeling, analysis and active mitigation methods. In *PowerTech, 2015 IEEE Eindhoven*, pages 1–6. IEEE.
- [Freijedo et al., 2016] Freijedo, F. D., Rodriguez-Diaz, E., Golsorkhi, M. S., Vasquez, J. C., and Guerrero, J. M. (2016). A root-locus design methodology derived from the impedance/admittance stability formulation and its application for lcl grid-connected converters in wind turbines. *IEEE Transactions on Power Electronics*.
- [Gabe et al., 2007] Gabe, I. J., Massing, J. R., Montagner, V. F., and Pinheiro, H. (2007). Stability analysis of grid-connected voltage source inverters with lcl-filters using partial state feedback. In *European Conference on Power Electronics and Applications*, pages 1–10. IEEE.

- [Gabe et al., 2009] Gabe, I. J., Montagner, V. F., and Pinheiro, H. (2009). Design and implementation of a robust current controller for vsi connected to the grid through an lcl filter. *IEEE Transactions on Power Electronics*, 24(6):1444–1452.
- [Guerrero et al., 2005] Guerrero, J. M., Vicuña, D., García, L., Matas, J., Castilla, M., and Miret, J. (2005). Output impedance design of parallel-connected ups inverters with wireless load-sharing control. *IEEE Transactions on Industrial Electronics*, 52(4):1126–1135.
- [Haddadi et al., 2015] Haddadi, A., Boulet, B., Yazdani, A., and Joós, G. (2015). A μ -based approach to small-signal stability analysis of an interconnected distributed energy resource unit and load. *IEEE Transactions on Power Delivery*, 30(4):1715–1726.
- [Harnefors, 2007] Harnefors, L. (2007). Analysis of subsynchronous torsional interaction with power electronic converters. *IEEE Transactions on Power Systems*, 22(1):305–313.
- [Harnefors, 2011] Harnefors, L. (2011). Proof and application of the positive-net-damping stability criterion. *IEEE Transactions on Power Systems*, 1(26):481–482.
- [Harnefors et al., 2007] Harnefors, L., Bongiorno, M., and Lundberg, S. (2007). Input-admittance calculation and shaping for controlled voltage-source converters. *IEEE Transactions on Industrial Electronics*, 54(6):3323–3334.
- [Harnefors and Nee, 1998] Harnefors, L. and Nee, H.-P. (1998). Model-based current control of ac machines using the internal model control method. *IEEE transactions on industry applications*, 34(1):133–141.
- [Harnefors et al., 2017] Harnefors, L., Wang, X., Finger, R., Haofeng, B., and Blaabjerg, F. (2017). Vsc input-admittance modeling and analysis above the nyquist frequency for passivity-based stability assessment. *IEEE Transaction on Industrial Electronics*.
- [Harnefors et al., 2015a] Harnefors, L., Wang, X., Yepes, A., and Blaabjerg, F. (2015a). Passivity-based stability assessment of grid-connected vscs-an overview. *IEEE Journal of Emerging and Selected Topics in Power Electronics*, 4(1):116 – 125.
- [Harnefors et al., 2014] Harnefors, L., Yepes, A., Vidal, A., and Doval-Gandoy, J. (2014). Passivity-based stabilization of resonant current controllers with consideration of time delay. *Power Electronics, IEEE Transactions on*, 29(12):6260–6263.
- [Harnefors et al., 2015b] Harnefors, L., Yepes, A., Vidal, A., and Doval-Gandoy, J. (2015b). Passivity-based controller design of grid-connected vscs for prevention of electrical resonance instability. *Industrial Electronics, IEEE Transactions on*, 62(2):702–710.
- [Harnefors et al., 2008] Harnefors, L., Zhang, L., and Bongiorno, M. (2008). Frequency-domain passivity-based current controller design. *IET Power Electronics*, 1(4):455–465.
- [He and Li, 2011] He, J. and Li, Y. W. (2011). Analysis, design, and implementation of virtual impedance for power electronics interfaced distributed generation. *IEEE Transactions on Industry Applications*, 47(6):2525–2538.
- [He and Li, 2012] He, J. and Li, Y. W. (2012). Generalized closed-loop control schemes with embedded virtual impedances for voltage source converters with lc or lcl filters. *IEEE Transactions on Power Electronics*, 27(4):1850–1861.
- [He et al., 2012] He, J., Li, Y. W., and Munir, M. S. (2012). A flexible harmonic control approach through voltage-controlled dg-grid interfacing converters. *IEEE Transactions on Industrial Electronics*, 59(1):444–455.

- [Hill, 1997] Hill, J. (1997). A practical example of the use of distribution static compensator (d-statcom) to reduce voltage fluctuations. In *IEE Colloquium on Power Electronics for Renewable Energy (Digest No: 1997/170)*, pages 7–1. IET.
- [Hiti et al., 1994] Hiti, S., Vlatkovic, V., Borojevic, D., and Lee, F. C. (1994). A new control algorithm for three-phase pwm buck rectifier with input displacement factor compensation. *IEEE Transactions on Power Electronics*, 9(2):173–180.
- [Hornik and Zhong, 2013] Hornik, T. and Zhong, Q.-C. (2013). Parallel pi voltage h-inf current controller for the neutral point of a three-phase inverter. *IEEE Transactions on Industrial Electronics*, 60(4):1335–1343.
- [Huang et al., 2009] Huang, J., Corzine, K., Belkhat, M., et al. (2009). Small-signal impedance measurement of power-electronics-based ac power systems using line-to-line current injection. *IEEE Transactions on Power Electronics*, 24(2):445–455.
- [Huang et al., 2016] Huang, M., Wang, X., Loh, P. C., and Blaabjerg, F. (2016). Active damping of llcl-filter resonance based on lc-trap voltage or current feedback. *Power Electronics, IEEE Transactions on*, 31(3):2337–2346.
- [Huerta et al., 2016] Huerta, F., Pérez, J., Moranchel, M., and Rodríguez, F. J. (2016). Two-degree-of-freedom current control for shunt active power filters. In *Proc. of the 42nd Annual Conference of the IEEE Industrial Electronics Society, IECON 2016*, pages 3787–3792. IEEE.
- [Huerta et al., 2012] Huerta, F., Pizarro, D., Cobrecas, S., Rodriguez, F. J., Giron, C., and Rodriguez, A. (2012). Lqg servo controller for the current control of grid-connected voltage-source converters. *IEEE Transactions on Industrial Electronics*, 59(11):4272–4284.
- [IEEE 1547-2003, 2008] IEEE 1547-2003 (2008). IEEE Standard for Interconnecting Distributed Resources with Electric Power Systems. Standard, Institute of Electrical and Electronics Engineers, Piscataway, NJ.
- [IEEE 519-2014, 2014] IEEE 519-2014 (2014). IEEE recommended practices and requirements for harmonic control in electrical power systems. Standard, Institute of Electrical and Electronics Engineers, Piscataway, NJ.
- [IEEE 929-2000, 2000] IEEE 929-2000 (2000). IEEE Recommended Practice for Utility Interface of Photovoltaic (PV) Systems. Standard, Institute of Electrical and Electronics Engineers, Piscataway, NJ.
- [Jansson et al., 2004] Jansson, M., Danielsson, A., Galic, J., Pietiläinen, K., and Harnefors, L. (2004). Stable and passive traction drives. In *Proc. of IEEE Nordic Power and Industrial Electronics Conference*.
- [Jessen and Fuchs, 2015] Jessen, L. and Fuchs, F. W. (2015). Modeling of inverter output impedance for stability analysis in combination with measured grid impedances. In *Proc. of IEEE 6th International Symposium on Power Electronics for Distributed Generation Systems (PEDG)*, pages 1–7. IEEE.
- [Jiang-Häfner et al., 2002] Jiang-Häfner, Y., Duchen, H., Linden, K., Hyttinen, M., De Toledo, P. F., Tulkiewicz, T., Skytt, A.-K., and Björklund, H. (2002). Improvement of subsynchronous torsional damping using vsc hvdc. In *Proc. of International Conference on Power System Technology, PowerCon*, volume 2, pages 998–1003. IEEE.

- [Jung and Tzou, 1996] Jung, S.-L. and Tzou, Y.-Y. (1996). Discrete sliding-mode control of a pwm inverter for sinusoidal output waveform synthesis with optimal sliding curve. *IEEE Transactions on Power Electronics*, 11(4):567–577.
- [Karttunen et al., 2014] Karttunen, J., Kallio, S., Peltoniemi, P., and Silventoinen, P. (2014). Transforming dynamic system models between two-axis reference frames rotating at different angular frequencies. In *Proc. of 16th European Conference on Power Electronics and Applications*, pages 1–10. IEEE.
- [Krause et al., 2002] Krause, P. C., Wasynczuk, O., and Sudhoff, S. D. (2002). *Analysis of Electric Machinery and Drive Systems. 2nd Edition*. IEEE Press. Wiley-Interscience.
- [Kundur et al., 1994] Kundur, P., Balu, N. J., and Lauby, M. G. (1994). *Power system stability and control*, volume 7. McGraw-hill New York.
- [Kwon et al., 2014] Kwon, J., Wang, X., and Blaabjerg, F. (2014). Impedance based analysis and design of harmonic resonant controller for a wide range of grid impedance. In *Proc. of IEEE 5th International Symposium on Power Electronics for Distributed Generation Systems (PEDG)*, pages 1–8. IEEE.
- [Lascu et al., 2009] Lascu, C., Asiminoaei, L., Boldea, I., and Blaabjerg, F. (2009). Frequency response analysis of current controllers for selective harmonic compensation in active power filters. *Industrial Electronics, IEEE Transactions on*, 56(2):337–347.
- [Lazbin and Needham, 1993] Lazbin, I. and Needham, B. R. (1993). Analysis of the stability margins of the space station freedom electrical power system. In *Proc. of 24th Annual IEEE Power Electronics Specialists Conference, PESC'93*, pages 839–845. IEEE.
- [Lee et al., 2001] Lee, T.-S., Chiang, S., and Chang, J.-M. (2001). H-inf loop-shaping controller designs for the single-phase ups inverters. *IEEE Transactions on Power Electronics*, 16(4):473–481.
- [Lindgren and Svensson, 1998] Lindgren, M. and Svensson, J. (1998). Control of a voltage-source converter connected to the grid through an lcl-filter-application to active filtering. In *Power Electronics Specialists Conference, 1998. PESC 98 Record. 29th Annual IEEE*, volume 1, pages 229–235. IEEE.
- [Liserre et al., 2004a] Liserre, M., Aquila, A. D., and Blaabjerg, F. (2004a). Genetic algorithm-based design of the active damping for an lcl-filter three-phase active rectifier. *IEEE Transactions on Power Electronics*, 19(1):76–86.
- [Liserre et al., 2005] Liserre, M., Blaabjerg, F., and Hansen, S. (2005). Design and control of an lcl-filter-based three-phase active rectifier. *IEEE Transactions on Industry Applications*, 41(5):1281–1291.
- [Liserre et al., 2002] Liserre, M., Dell'Aquila, A., and Blaabjerg, F. (2002). Stability improvements of an lcl-filter based three-phase active rectifier. In *Proc. of 33th Annual IEEE Power Electronics Specialists Conference, PESC*, volume 3, pages 1195–1201. IEEE.
- [Liserre et al., 2004b] Liserre, M., Teodorescu, R., and Blaabjerg, F. (2004b). Stability of grid-connected pv inverters with large grid impedance variation. In *Proc. of 35th Annual IEEE Power Electronics Specialists Conference, PESC*, volume 6, pages 4773–4779. IEEE.
- [Liserre et al., 2006] Liserre, M., Teodorescu, R., and Blaabjerg, F. (2006). Stability of photovoltaic and wind turbine grid-connected inverters for a large set of grid impedance values. *IEEE transactions on power electronics*, 21(1):263–272.

- [Liu et al., 2014] Liu, F., Liu, J., Zhang, H., and Xue, D. (2014). Generalized stability criterion for multi-module distributed dc system. *Journal of Power Electronics*, 14(1):143–155.
- [Liu et al., 2003] Liu, J., Feng, X., Lee, F. C., and Borojevich, D. (2003). Stability margin monitoring for dc distributed power systems via perturbation approaches. *IEEE Transactions on Power Electronics*, 18(6):1254–1261.
- [Liu et al., 2007] Liu, X., Forsyth, A. J., and Cross, A. M. (2007). Negative input-resistance compensator for a constant power load. *IEEE Transactions on Industrial Electronics*, 54(6):3188–3196.
- [Liu et al., 2016] Liu, Y., Wu, W., He, Y., Lin, Z., Blaabjerg, F., and Chung, H. S.-H. (2016). An efficient and robust hybrid damper for-or-based grid-tied inverter with strong grid-side harmonic voltage effect rejection. *IEEE Transactions on Industrial Electronics*, 63(2):926–936.
- [Liu et al., 2015] Liu, Z., Liu, J., Bao, W., and Zhao, Y. (2015). Infinity-norm of impedance-based stability criterion for three-phase ac distributed power systems with constant power loads. *IEEE Transactions on Power Electronics*, 30(6):3030–3043.
- [Liutanakul et al., 2010] Liutanakul, P., Awan, A.-B., Pierfederici, S., Nahid-Mobarakeh, B., and Meibody-Tabar, F. (2010). Linear stabilization of a dc bus supplying a constant power load: A general design approach. *Power Electronics, IEEE Transactions on*, 25(2):475–488.
- [Mao et al., 1998] Mao, H., Boroyevich, D., and Lee, F. C. (1998). Novel reduced-order small-signal model of a three-phase pwm rectifier and its application in control design and system analysis. *IEEE Transactions on Power Electronics*, 13(3):511–521.
- [Messo et al., 2013] Messo, T., Jokipii, J., Makinen, A., and Suntio, T. (2013). Modeling the grid synchronization induced negative-resistor-like behavior in the output impedance of a three-phase photovoltaic inverter. In *Proc. of 4th IEEE International Symposium on Power Electronics for Distributed Generation Systems (PEDG)*, pages 1–7. IEEE.
- [Middlebrook, 1976] Middlebrook, R. D. (1976). Input filter considerations in design and application of switching regulators. In *Proc. of IEEE Industrial Applications Society Annual Meeting (IAS)*, pages 366–382. IEEE.
- [Miret et al., 2004] Miret, J., de Vicuña, L. G., Castilla, M., Cruz, J., and Guerrero, J. M. (2004). A simple sliding mode control of an active power filter. In *Power Electronics Specialists Conference, 2004. PESC 04. 2004 IEEE 35th Annual*, volume 2, pages 1052–1056. IEEE.
- [Mohamed et al., 2012] Mohamed, Y. A.-R., Rahman, M., Seethapathy, R., et al. (2012). Robust line-voltage sensorless control and synchronization of lcl-filtered distributed generation inverters for high power quality grid connection. *IEEE Transactions on Power Electronics*, 27(1):87–98.
- [Moharana and Dash, 2010] Moharana, A. and Dash, P. (2010). Input-output linearization and robust sliding-mode controller for the vsc-hvdc transmission link. *IEEE Transactions on Power Delivery*, 25(3):1952–1961.
- [Möllerstedt and Bernhardsson, 2000] Möllerstedt, E. and Bernhardsson, B. (2000). Out of control because of harmonics—an analysis of the harmonic response of an inverter locomotive. *Proc. of IEEE Control Systems*, 20(4):70–81.

- [Morán et al., 1995] Morán, L. A., Dixon, J. W., and Wallace, R. R. (1995). A three-phase active power filter operating with fixed switching frequency for reactive power and current harmonic compensation. *IEEE Transactions on Industrial Electronics*, 42(4):402–408.
- [Morari and Zafiriou, 1989] Morari, M. and Zafiriou, E. (1989). *Robust process control*, volume 488. Prentice hall Englewood Cliffs, NJ.
- [Mosskull, 2014] Mosskull, H. (2014). Optimal stabilization of constant power loads with input lc-filters. *Control Engineering Practice*, 27:61–73.
- [Naim et al., 1997] Naim, R., Weiss, G., and Ben-Yaakov, S. (1997). H-inf control applied to boost power converters. *IEEE Transactions on Power Electronics*, 12(4):677–683.
- [Nussbaumer et al., 2006] Nussbaumer, T., Heldwein, M. L., and Kolar, J. W. (2006). Differential mode input filter design for a three-phase buck-type pwm rectifier based on modeling of the emc test receiver. *IEEE Transactions on Industrial Electronics*, 53(5):1649–1661.
- [Olalla et al., 2009] Olalla, C., Leyva, R., El Aroudi, A., and Garces, P. (2009). Qft robust control of current-mode converters: application to power conditioning regulators. *International Journal of Electronics*, 96(5):503–520.
- [Orellana and Griñó, 2012] Orellana, M. and Griñó, R. (2012). On the stability of discrete-time active damping methods for vsi converters with a lcl input filter. In *Proc. of 38th Annual Conference on IEEE Industrial Electronics Society IECON 2012*, pages 2378–2383. IEEE.
- [Park et al., 2008] Park, S.-Y., Chen, C.-L., Lai, J.-S., and Moon, S.-R. (2008). Admittance compensation in current loop control for a grid-tie lcl fuel cell inverter. *Power Electronics, IEEE Transactions on*, 23(4):1716–1723.
- [Parker et al., 2014] Parker, S. G., McGrath, B. P., and Holmes, D. G. (2014). Regions of active damping control for lcl filters. *IEEE Transactions on Industry Applications*, 50(1):424–432.
- [Peña, 2005] Peña, E. J. B. (2005). *Optimización del comportamiento de un convertidor de tres niveles NPC conectado a la red eléctrica*. PhD thesis, Politechnic School. University of Alcalá.
- [Pena-Alzola et al., 2013] Pena-Alzola, R., Liserre, M., Blaabjerg, F., Sebastián, R., Dannehl, J., and Fuchs, F. W. (2013). Analysis of the passive damping losses in lcl-filter-based grid converters. *IEEE Transactions on Power Electronics*, 28(6):2642–2646.
- [Perez et al., 2014] Perez, J., Cobreces, S., and Grino, R. (2014). Admittance-shaped h-inf current controller for grid-connected vsc. In *Proc. of IEEE Emerging Technology and Factory Automation (ETFA)*, pages 1–8. IEEE.
- [Perez et al., 2016a] Perez, J., Cobreces, S., Grino, R., and Rodriguez, F. (2016a). H-inf current controller for input admittance shaping of vsc-based grid applications. *IEEE Transactions on Power Electronics*, 32(4):3180–3191.
- [Perez et al., 2017] Perez, J., Cobreces, S., Grino, R., Rodriguez, F., and Huerta, F. (2017). Active damping: an h-inf model-reference approach. *Submitted to IEEE Transactions on Power Electronics (Under review)*.
- [Perez et al., 2016b] Perez, J., Cobreces, S., Pizarro, D., Rodriguez Sanchez, F. J., and Grino, R. (2016b). Resonance damping of lcl filters via input admittance frequency shaping. In *Proc. of the 2016 IEEE 25th International Symposium on Industrial Electronics (ISIE)*, pages 516–521. IEEE.

- [Perez et al., 2013] Perez, J., Cobreces, S., Rodriguez, F. J., Bueno, E. J., Sanz, I., Huerta, F., and Grino, R. (2013). Static reference frame lqr optimal state-feedback control for static-series compensators. In *Proc. of 39th Annual Conference of the IEEE Industrial Electronics Society, IECON*, pages 3776–3781. IEEE.
- [Perez et al., 2015] Perez, J., Cobreces, S., Sanchez, F. J. R., and Grino, R. (2015). H-inf simultaneous admittance and tracking current controller of three-phase active grid front-ends. In *2015 IEEE International Conference on Industrial Technology (ICIT)*, pages 2092–2097. IEEE.
- [Pérez et al., 2017a] Pérez, J., Cóbreces, S., Wang, X., Blaabjerg, F., and Griño, R. (2017a). A robust admittance shaping approach to grid harmonic attenuation and filter resonance damping. *To be submitted to IEEE Transactions on Power Electronics*.
- [Pérez et al., 2017b] Pérez, J., Cóbreces, S., Wang, X., Blaabjerg, F., and Griño, R. (2017b). A robust grid current controller with grid harmonic and filter resonance damping capabilities using closed-loop admittance shaping. In *Proc. of IEEE Applied Power Electronics Conference and Exposition (APEC)*, pages 2625–2632. IEEE.
- [Piwko and Larsen, 1982] Piwko, R. J. and Larsen, E. (1982). HvdC system control for damping of subsynchronous oscillations. *IEEE Transactions on Power Apparatus and Systems*, (7):2203–2211.
- [Radwan et al., 2013] Radwan, A. A., Mohamed, Y. A.-R., et al. (2013). Analysis and active-impedance-based stabilization of voltage-source-rectifier loads in grid-connected and isolated microgrid applications. *IEEE Transactions on Sustainable Energy*, 4(3):563–576.
- [Radwan et al., 2012] Radwan, A. A. A., Mohamed, Y. A.-R., et al. (2012). Assessment and mitigation of interaction dynamics in hybrid ac/dc distribution generation systems. *IEEE Transactions on Smart Grid*, 3(3):1382–1393.
- [Rahim and Kandlawala, 2004] Rahim, A. and Kandlawala, M. (2004). Robust statcom voltage controller design using loop-shaping technique. *Proc. of Electric Power Systems Research*, 68(1):61–74.
- [Rahimi and Emadi, 2009] Rahimi, A. M. and Emadi, A. (2009). Active damping in dc/dc power electronic converters: A novel method to overcome the problems of constant power loads. *IEEE Transactions on Industrial Electronics*, 56(5):1428–1439.
- [Rigatos et al., 2014] Rigatos, G., Siano, P., and Cecati, C. (2014). An h-infinity feedback control approach for three-phase voltage source converters. In *Proc. of 40th Annual Conference of the IEEE Industrial Electronics Society, IECON*, pages 1227–1232. IEEE.
- [Rissik, 1941] Rissik, H. (1941). *Mercury-arc current converters*. Sir Isaac Pitman And Sons Ltd., London.
- [Rivetta et al., 2006] Rivetta, C. H., Emadi, A., Williamson, G. A., Jayabalan, R., and Fahimi, B. (2006). Analysis and control of a buck dc-dc converter operating with constant power load in sea and undersea vehicles. *Industry Applications, IEEE Transactions on*, 42(2):559–572.
- [Rodriguez et al., 2008] Rodriguez, F., Bueno, E., Aredes, M., Rolim, L., Neves, F. A., and Cavalcanti, M. C. (2008). Discrete-time implementation of second order generalized integrators for grid converters. In *Industrial Electronics, 2008. IECON 2008. 34th Annual Conference of IEEE*, pages 176–181. IEEE.

- [Rodríguez Monter, 2013] Rodríguez Monter, A. (2013). *Contributions to cascade linear control strategies applied to grid-connected Voltage-Source Converters*. PhD thesis, Ph. D. Thesis, University of Alcalá, Madrid, Spain.
- [Rosenwasser and Lampe, 2012] Rosenwasser, E. N. and Lampe, B. (2012). *Computer controlled systems: analysis and design with process-orientated models*. Springer Science & Business Media.
- [Sanchez et al., 2014] Sanchez, S., Ortega, R., Griño, R., Bergna, G., and Molinas, M. (2014). Conditions for existence of equilibria of systems with constant power loads. *IEEE Transactions on Circuits and Systems I: Regular Papers*, 61(7):2204–2211.
- [Skogestad and Postlethwaite, 2007] Skogestad, S. and Postlethwaite, I. (2007). *Multivariable feedback control: analysis and design*, volume 2. Wiley New York.
- [Sudhoff et al., 2000] Sudhoff, S. D., Glover, S. F., Lamm, P. T., Schmucker, D. H., and Delisle, D. (2000). Admittance space stability analysis of power electronic systems. *IEEE Transactions on Aerospace and Electronic Systems*, 36(3):965–973.
- [Sun, 2009] Sun, J. (2009). Small-signal methods for ac distributed power systems—a review. *IEEE Transactions on Power Electronics*, 24(11):2545–2554.
- [Sun, 2011] Sun, J. (2011). Impedance-based stability criterion for grid-connected inverters. *IEEE Transactions on Power Electronics*, 26(11):3075–3078.
- [Svensson, 1997] Svensson, J. (1997). Inclusion of dead-time and parameter variations in vsc modelling for predicting responses of grid voltage harmonics. In *European conference on power electronics and applications*, volume 3, pages 3–216. Proceedings published by various publishers.
- [Tabesh and Iravani, 2004] Tabesh, A. and Iravani, R. (2004). Frequency-response analysis of torsional dynamics. *IEEE Transactions on Power Systems*, 19(3):1430–1437.
- [Tabesh and Iravani, 2005] Tabesh, A. and Iravani, R. (2005). On the application of the complex torque coefficients method to the analysis of torsional dynamics. *IEEE Transactions on Energy Conversion*, 20(2):268–275.
- [Takeshita and Matsui, 2003] Takeshita, T. and Matsui, N. (2003). Current waveform control of pwm converter system for harmonic suppression on distribution system. *IEEE Transactions on Industrial Electronics*, 50(6):1134–1139.
- [Tang et al., 2012] Tang, Y., Loh, P. C., Wang, P., Choo, F. H., and Gao, F. (2012). Exploring inherent damping characteristic of lcl-filters for three-phase grid-connected voltage source inverters. *IEEE Transactions on Power Electronics*, 27(3):1433–1443.
- [Teodorescu et al., 2003] Teodorescu, R., Blaabjerg, F., Liserre, M., and Dell’Aquila, A. (2003). A stable three-phase lcl-filter based active rectifier without damping. In *Proc. of 38th Industry Applications Conference, IAS*, volume 3, pages 1552–1557. IEEE.
- [Thandi et al., 1999] Thandi, G., Zhang, R., Xing, K., Lee, F. C., and Boroyevich, D. (1999). Modeling, control and stability analysis of a pebb based dc dps. *Power Delivery, IEEE Transactions on*, 14(2):497–505.
- [Towati, 2008] Towati, A. A. (2008). *Dynamic Analysis and QFT-based Robust Control Design of Switched-mode Power Converters*. Helsinki University of Technology.

- [Turner et al., 2013] Turner, R., Walton, S., and Duke, R. (2013). A case study on the application of the nyquist stability criterion as applied to interconnected loads and sources on grids. *IEEE Transactions on Industrial Electronics*, 60(7):2740–2749.
- [Twining and Holmes, 2003] Twining, E. and Holmes, D. G. (2003). Grid current regulation of a three-phase voltage source inverter with an lcl input filter. *Power Electronics, IEEE Transactions on*, 18(3):888–895.
- [Vesti et al., 2013] Vesti, S., Suntio, T., Oliver, J., Prieto, R., Cobos, J., et al. (2013). Impedance-based stability and transient-performance assessment applying maximum peak criteria. *IEEE Transactions on Power Electronics*, 28(5):2099–2104.
- [Vidal et al., 2013] Vidal, A., Freijedo, F. D., Yepes, A., Fernandez-Comesana, P., Malvar, J., Lopez, O., and Doval-Gandoy, J. (2013). Assessment and optimization of the transient response of proportional-resonant current controllers for distributed power generation systems. *Industrial Electronics, IEEE Transactions on*, 60(4):1367–1383.
- [Vinnicombe, 2000] Vinnicombe, G. (2000). *Uncertainty and Feedback: H-inf loop-shaping and the ν -gap metric*. World Scientific.
- [Wan et al., 2015] Wan, C., Huang, M., Tse, C. K., and Ruan, X. (2015). Effects of interaction of power converters coupled via power grid: A design-oriented study. *IEEE Transactions on Power Electronics*, 30(7):3589–3600.
- [Wang and Howe, 2008] Wang, J. and Howe, D. (2008). A power shaping stabilizing control strategy for dc power systems with constant power loads. *IEEE Transactions on Power Electronics*, 23(6):2982–2989.
- [Wang et al., 2012] Wang, X., Blaabjerg, F., and Chen, Z. (2012). Synthesis of variable harmonic impedance in inverter-interfaced distributed generation unit for harmonic damping throughout a distribution network. *IEEE Transactions on Industry Applications*, 48(4):1407–1417.
- [Wang et al., 2014a] Wang, X., Blaabjerg, F., Liserre, M., Chen, Z., He, J., and Li, Y. (2014a). An active damper for stabilizing power-electronics-based ac systems. *IEEE Transactions on Power Electronics*, 29(7):3318–3329.
- [Wang et al., 2014b] Wang, X., Blaabjerg, F., and Loh, P. C. (2014b). Proportional derivative based stabilizing control of paralleled grid converters with cables in renewable power plants. In *Proc. of IEEE Energy Conversion Congress and Exposition (ECCE)*, pages 4917–4924. IEEE.
- [Wang et al., 2015] Wang, X., Blaabjerg, F., and Loh, P. C. (2015). Virtual rc damping of lcl-filtered voltage source converters with extended selective harmonic compensation. *IEEE Transactions on Power Electronics*, 30(9):4726–4737.
- [Weiss et al., 2004] Weiss, G., Zhong, Q.-C., Green, T. C., and Liang, J. (2004). H-inf repetitive control of dc-ac converters in microgrids. *IEEE Transactions on Power Electronics*, 19(1):219–230.
- [Wen et al., 2013] Wen, B., Boroyevich, D., Mattavelli, P., Shen, Z., and Burgos, R. (2013). Influence of phase-locked loop on input admittance of three-phase voltage-source converters. In *Proc. of Twenty-Eighth Annual IEEE Applied Power Electronics Conference and Exposition (APEC)*, pages 897–904. IEEE.

- [Wessels et al., 2008] Wessels, C., Dannehl, J., and Fuchs, F. W. (2008). Active damping of lcl-filter resonance based on virtual resistor for pwm rectifiers—stability analysis with different filter parameters. In *Proc. of Annual IEEE Power Electronics Specialists Conference, PESC*, pages 3532–3538. IEEE.
- [Wildrick et al., 1995] Wildrick, C. M., Lee, F. C., Cho, B. H., and Choi, B. (1995). A method of defining the load impedance specification for a stable distributed power system. *IEEE Transactions on Power Electronics*, 10(3):280–285.
- [Willems, 1972a] Willems, J. (1972a). Dissipative dynamical systems part i: General theory. *Proc. of Archive for Rational Mechanics and Analysis*, 45(5):321–351.
- [Willems, 1972b] Willems, J. C. (1972b). Dissipative dynamical systems part ii: Linear systems with quadratic supply rates. *Proc. of Archive for Rational Mechanics and Analysis*, 45(5):352–393.
- [Wu and Lehn, 2005] Wu, E. and Lehn, P. W. (2005). Digital current control of a voltage source converter with active damping of lcl resonance. In *Proc. of Twentieth Annual IEEE Applied Power Electronics Conference and Exposition APEC 2005*, volume 3, pages 1642–1649. IEEE.
- [Wu et al., 2015] Wu, X., Li, X., Yuan, X., and Geng, Y. (2015). Grid harmonics suppression scheme for lcl-type grid-connected inverters based on output admittance revision. *Sustainable Energy, IEEE Transactions on*, 6(2):411–421.
- [Xu and Fan, 2013] Xu, L. and Fan, L. (2013). Impedance-based resonance analysis in a vsc-hvdc system. *IEEE Transactions on Power Delivery*, 28(4):2209–2216.
- [Yang et al., 2014] Yang, D., Ruan, X., and Wu, H. (2014). Impedance shaping of the grid-connected inverter with lcl filter to improve its adaptability to the weak grid condition. *Power Electronics, IEEE Transactions on*, 29(11):5795–5805.
- [Yang et al., 2011] Yang, S., Lei, Q., Peng, F. Z., and Qian, Z. (2011). A robust control scheme for grid-connected voltage-source inverters. *IEEE Transactions on Industrial Electronics*, 58(1):202–212.
- [Yepes, 2011] Yepes, A. G. (2011). *Digital resonant current controllers for voltage source converters*. PhD thesis, UNIVERSITY OF VIGO.
- [Yepes et al., 2011] Yepes, A. G., Freijedo, F. D., Lopez, O., and Doval-Gandoy, J. (2011). Analysis and design of resonant current controllers for voltage-source converters by means of nyquist diagrams and sensitivity function. *IEEE Transactions on Industrial Electronics*, 58(11):5231–5250.
- [Zhang et al., 2015] Zhang, C., Wang, X., and Blaabjerg, F. (2015). Analysis of phase-locked loop influence on the stability of single-phase grid-connected inverter. In *Power Electronics for Distributed Generation Systems (PEDG), 2015 IEEE 6th International Symposium on*, pages 1–8. IEEE.
- [Zhong and Hornik, 2012] Zhong, Q.-C. and Hornik, T. (2012). *Control of power inverters in renewable energy and smart grid integration*, volume 97. John Wiley & Sons.
- [Zmood and Holmes, 2003] Zmood, D. N. and Holmes, D. G. (2003). Stationary frame current regulation of pwm inverters with zero steady-state error. *IEEE Transactions on Power Electronics*, 18(3):814–822.

- [Zmood et al., 2001] Zmood, D. N., Holmes, D. G., and Bode, G. H. (2001). Frequency-domain analysis of three-phase linear current regulators. *IEEE Transactions on Industry Applications*, 37(2):601–610.